

XXIII

**International
Conference on
Phenomena in
Ionized
Gases**



Proceedings

Contributed Papers

Vol. II

Friday, July 18

Public reporting burden for this collection of information is estimated to average 1 hour per response, including the time for reviewing instructions, searching existing data sources, gathering and maintaining the data needed, and completing and reviewing the collection of information. Send comments regarding this burden estimate or any other aspect of this collection of information, including suggestions for reducing this burden to Washington Headquarters Services, Directorate for Information Operations and Reports, 1215 Jefferson Davis Highway, Suite 1204, Arlington, VA 22202-4302, and to the Office of Management and Budget, Paperwork Reduction Project (0704-0188), Washington, DC 20503.

1. AGENCY USE ONLY (Leave blank)		2. REPORT DATE 1 December 1998	3. REPORT TYPE AND DATES COVERED Conference Proceedings	
4. TITLE AND SUBTITLE XXIII International Conference on Phenomena in Ionized Gases, VOL 2			5. FUNDING NUMBERS F6170897W0048	
6. AUTHOR(S) Conference Committee				
7. PERFORMING ORGANIZATION NAME(S) AND ADDRESS(ES) Universite Paul Sabatier 118 Route de Narbonne Toulouse Cedex 31062 France			8. PERFORMING ORGANIZATION REPORT NUMBER N/A	
9. SPONSORING/MONITORING AGENCY NAME(S) AND ADDRESS(ES) EOARD PSC 802 BOX 14 FPO 09499-0200			10. SPONSORING/MONITORING AGENCY REPORT NUMBER CSP 97-1013	
11. SUPPLEMENTARY NOTES One book of Invited Papers and five volumes of Proceedings and Contributed Papers				
12a. DISTRIBUTION/AVAILABILITY STATEMENT Approved for public release; distribution is unlimited.			12b. DISTRIBUTION CODE A	
13. ABSTRACT (Maximum 200 words) The Final Proceedings for XXIII International Conference on Phenomena in Ionized Gases, 17 July 1997 - 22 July 1997 kinetic, thermodynamics, and transport phenomena; elementary processes; low pressure glows; coronas, sparks, surface discharges, and high pressure glows; arcs; high frequency discharges; ionospheric magnetospheric, and astrophysical plasmas; plasma diagnostic methods; plasma surface effects; plasma processing; plasma flows; non ideal plasmas; waves and instabilities; non-linear phenomena; particle and laser beam interactions with plasmas; plasma sources of radiation; modeling; plasma for environmental issues; plasma thrusters; surface treatment; high pressure, non-thermal plasmas.				
14. SUBJECT TERMS EOARD, Space Environment, Pulsed Power, Astrodynamics, Coatings, Fluids & Lubrication, Electromagnetics, High Power Generation, Lasers			15. NUMBER OF PAGES Too Many to Count	
			16. PRICE CODE N/A	
17. SECURITY CLASSIFICATION OF REPORT UNCLASSIFIED	18. SECURITY CLASSIFICATION OF THIS PAGE UNCLASSIFIED	19. SECURITY CLASSIFICATION OF ABSTRACT UNCLASSIFIED	20. LIMITATION OF ABSTRACT UL	

NSN 7540-01-280-5500

Standard Form 298 (Rev. 2-89)
Prescribed by ANSI Std. Z39-18
298-102

F61708-97-W0048

CSP97-1013

**X
X
I
I
I**

**I nternational
C onference on
P henomena in
I onized
G ases**

Editors: M.C. Bordage and A. Gleizes

19981216 003



Proceedings

Contributed Papers

Vol. II

Friday, July 18

Organizers :

Centre de Physique des Plasmas et leurs Applications de Toulouse (CPAT)
Laboratoire de Génie Electrique de Toulouse (LGET)
From the Université Paul Sabatier, Toulouse France.

International Scientific Committee

R. d'Agostino	Italy
J. Allen	Great Britain
A. Bouchoule (Chairman)	France
E. Desoppere	Belgium
H. Kikuchi	Japan
E.E. Kunhardt	USA
J. Mentel	Germany
B. Milic	Yugoslavia
D. Morrow	Australia
A.H. Oien	Norway
A.A. Rukhadze	Russia
M. Sicha	Czech. Republic

Local Organizing Committee

J.P. Bœuf	M.C. Bordage (Sec.)
H. Brunet (co-Chair.)	J.P. Couderc
B. Despax	M. Dziadowiec
A. Gleizes	B. Held
F. Massines	L.C. Pitchford (co-Chair.)
Y. Segui	S. Vacquie
M. Yousfi	G. Zissis

Sponsors

Association pour le Développement de la Physique Atomique (ADPA)
International Union of Pure and Applied Physics (IUPAP)
Centre National de la Recherche Scientifique (CNRS)
Université Paul Sabatier (UPS) of Toulouse
Direction de la Recherche et Technologie (DRET)
Commissariat à l'Energie Atomique (CEA), Cycle de Combustible
Electricité de France through :
 Club Arc Electrique, Club Chimie des Hautes Températures and Novelect
Conseil Régional de la Région Midi-Pyrénées
Conseil Général du Département de la Haute-Garonne
Mairie de Toulouse
CRT Plasma-Laser
Union Radio Scientifique Internationale (URSI)
US Department of Energy, US BMDO
US Air Force through the EOARD

The Local Organizing Committee wishes to express appreciation to the following corporations for their support :

AGA S.A.	Thomson Tubes Electroniques
Motorola Semiconducteurs S.A.	Schneider Electric
Osram-Sylvania Inc.	Philips Lighting (for the Penning Award)

FOREWORD

This volume is the second of five volumes which contain contributed papers that were accepted by the Local Organizing Committee of the XXIII ICPIG for presentation in poster sessions. These papers are to be listed in the INSPEC data base.

The contributions were submitted in camera-ready form by the authors. Therefore, the responsibility for the contents and the form of the papers rests entirely with the authors.

The first four volumes have been arranged by topics, the sequence of which corresponds to that of the respective poster sessions. The fifth volume is comprised of 'late' papers, those for which the authors registered after the deadline for printing of their papers.

The texts of the invited talks are to be published shortly after the conference in a special issue of Journal de Physique.

The editors would like to acknowledge the contributions of Mrs L. Fourmeaux, Mr J.M. Barachet and Mr J.P. Chaucheprat in the preparation of these volumes. The computer file of contributed papers and authors was prepared by C. de Peco, and her careful execution of this task is gratefully acknowledged.

April 1997

The Editors

For additional copies of this publication, please contact :

M.C. Bordage, CPAT, Université Paul Sabatier, 118 Route de Narbonne, 31062
Toulouse cedex 4 France

Printed in France, in the Université Paul Sabatier of Toulouse , 1997

Topic number	SCHEDULE FOR POSTERS	
VOLUME 1 THURSDAY, JULY 17		
MORNING		
1	Kinetics, thermodynamics and transport phenomena (Part A)	
2	Elementary processes (Part A)	
6	High frequency discharges (Part A)	
13	Waves and instabilities, including shock waves (Part A)	
AFTERNOON		
1	Kinetics, thermodynamics and transport phenomena (Part B)	
2	Elementary processes (Part B)	
6	High frequency discharges (Part B)	
12	Non-ideal plasmas. Clusters and dusty plasmas	
13	Waves and instabilities, including shock waves (Part B)	
18	Plasmas for environmental issues	
VOLUME 2 FRIDAY, JULY 18		
MORNING		
3	Low pressure glows (Part A)	
5	Arcs (Part A)	
17	Numerical modeling (Part A)	
AFTERNOON		
3	Low pressure glows (Part B)	
5	Arcs (Part B)	
11	Generation and dynamics of plasma flows	
14	Non-linear phenomena and self-organization processes	
17	Numerical modeling (Part B)	
VOLUME 3 SATURDAY, JULY 19		
7	Ionospheric, magnetospheric, and astrophysical plasmas	
16	Plasma sources of radiation	
19a	Highly ionized, low pressure plasmas	
19b	High pressure, non-thermal plasmas	
VOLUME 4 MONDAY, JULY 21		
MORNING		
4	Coronas, sparks, surface discharges and high pressure glows (Part A)	
8	Plasma diagnostic methods (Part A)	
10	Physical aspects of plasma chemistry, plasma processing of surface and thin film technology (Part A)	
AFTERNOON		
4	Coronas, sparks, surface discharges and high pressure glows (Part B)	
8	Plasma diagnostic methods (Part B)	
9	Plasma wall interactions, electrode and surface effects	
10	Physical aspects of plasma chemistry, plasma processing of surface and thin film technology (Part B)	
15	Particle and laser beam interaction with plasmas	
VOLUME 5 LATE PAPERS		

CONTENTS

Topic 3 : Low pressure glows.

EXPERIMENTAL EVALUATION OF A HOLLOW CATHODE PLASMA SOURCE Alcaide I., Conde L.	II-2
COMPARISON OF KINETIC AND DIFFUSION THEORIES OF POSITIVE COLUMN OF A DISCHARGE Golubovskii Yu.B., Porokhova I.A., Behnke J., Behnke J.F., Deutsch H.	II-4
WALL RECOMBINATION IN THE PLASMA OF POSITIVE COLUMN IN LOW CURRENT DISCHARGE Behnke J.F., Bindemann Th., Deutsch H., Golubovskii Yu.B., Porokhova I.A.	II-6
DETERMINATION OF FIRST EXCITED STATES NUMBER DENSITIES OF ARGON ATOMS IN A CYLINDRICAL MAGNETRON DISCHARGE : LASER DIODE ABSORPTION SPECTROSCOPY AND MODELLING Csambal C., Behnke J.F., Helbig V., Hennig A., Passoth E.	II-8
3D MODELING OF DIRECT CURRENT GLOW DISCHARGES IN DIFFERENT CELL GEOMETRIES Bogaerts A., Gijbels R.	II-10
STATISTICAL STUDIES OF HOLLOW CATHODE EVENTS IN A TRANSIENT HOLLOW CATHODE DISCHARGE Favre M., Moreno J., Choi P., Zambra M., Chuaqui H., Wyndham E.	II-12
JOINING SHEATH TO PLASMA IN A LOW PRESSURE NEGATIVE ION DOMINATED DISCHARGE Franklin R.N., Snell J.	II-14
STUDY OF A NITRIDING PLASMA REACTOR : COMPARISON BETWEEN EXPERIMENTAL RESULTS AND MODELLING OF THE DISCHARGE Guiberteau E., Henrion G., Hugon R., Bonhomme G.,	II-16
STUDY OF RADIAL PROFILES OF EXCITED NEUTRAL SPECIES IN THE POSITIVE COLUMN OF THE GLOW DISCHARGE IN RARE GASES Kanka A., Hrachova V., Hava O., Zicha J.	II-18
INFLUENCE OF THE NEON AND ARGON ON THE OXYGEN SPECTRA IN THE GLOW DISCHARGE Hrachova V., Kanka A.	II-20
RADIAL DEPENDENCE OF ELECTRON ENERGY IN HE AND N ₂ POSITIVE COLUMNS Kimura T., Ieda Y., Ohe K.	II-22
THE STRUCTURE OF LOW PRESSURE HIGH-CURRENT DIFFUSE DISCHARGE Fetisov I.K., Khodachenko G.V., Kurnaev V.A., Mozgrin D.V., Savjlov A.S.	II-24
PENNING DISCHARGE IN REGIME OF RF AUTOGENERATION Vizgalov I.V., Kirnev G.S., Kurnaev V.A., Sarytchev D.V., Savjlov A.S.	II-26
EXPERIMENTAL AND THEORETICAL STUDY OF THE NON-LOCALITY EFFECTS OF THE ELECTRON ENERGY SPECTRUM IN O ₂ DC GLOW DISCHARGE Ivanov V.V., Klopovskiy K.S., Lopaev D.V., Popov A.M., Rakhimov A.T., Rakhimova T.V.	II-28

A PLASMA MIRROR FOR ELECTRONIC MICROWAVE BEAM STEERING Manheimer W., Mathew J., Fernsler R., Meger R., Gregor J., Murphy D., Pechacek R.	II-30
CHARACTERISTICS OF THE INITIATION AND OPERATION OF A REPETITIVE PULSED HOLLOW CATHODE GLOW DISCHARGE Gavrilov N.V., Mesyats G.A.	II-32
EXPERIMENTAL STUDY ON STANDING/ MOVING STRIATIONS AND STANDING/ MOVING HELICES Mori A., Matsuoka M., Kawaguchi M.	II-34
REALIZATION OF HIGH-CURRENT MODE OF GLOW DISCHARGE WITH OSCILLATING ELECTRONS AT LOWERED PRESSURE Nikulin S.P.	II-36
EXPERIMENTAL INVESTIGATIONS OF THE ANODE REGION OF A LOW-PRESSURE GLOW DISCHARGE IN HELIUM Otte M., Pfau S., Rohmann J.	II-38
THE ELECTRON VELOCITY DISTRIBUTION FUNCTION OF THE RADIAL INHOMOGENEOUS PLASMA OF THE POSITIVE COLUMN IN A HELIUM GLOW DISCHARGE -MEASUREMENTS AND CALCULATIONS - Otte M., Pfau S., Rohmann J.	II-40
NEUTRAL GAP DEPLETION IN PSS REPETITION MODE Courtois L., Rivaletto M., Paillol J., Brasile J.P., Pignolet P.	II-42
A SIMPLE, LOCAL EQUILIBRIUM MODEL OF NEGATIVE DIFFERENTIAL RESISTANCE Vrhovac S.B., Stefanovic I., Petrovic Z.Lj.	II-44
TRANSITION FROM AMBIPOLAR TO FREE DIFFUSION IN NITROGEN AFTERGLOW Markovic V.Lj., Petrovic Z.Lj., Pejovic M.M.	II-46
CORRELATED EXPERIMENTS ON CATHODE-DOMINATED, LOW PRESSURE DISCHARGES IN AR Phelps A.V.	II-48
TIME AND SPACE RESOLVED ENERGY DISTRIBUTION OF AN ELECTRON BEAM PRODUCED IN A FILAMENTARY TRANSIENT DISCHARGE Modreanu G., Ganciu M., Mandache N.B., Pointu A.M., Dewald E., Nistor M., Popescu I.I., Udrea M.	II-50
INTENSE PULSED ELECTRON BEAMS PRODUCED IN MULTIGAP AND SINGLE GAP PCOHC Dewald E., Frank K., Pointu A.M., Hoffmann D.H.H., Stark R., Ganciu M., Mandache N.B., Nistor M., Popescu I.I.	II-52
THE INFLUENCE OF ANODE REGION OF A GLOW DISCHARGE ON THE EEDF IN S- AND P- MOVING STRIATIONS Golubovskii Y.B., Nekuchaev V.O., Ponomarev N.S.	II-54
ION AND NEUTRAL DISTRIBUTION FUNCTIONS AT THE CATHODE OF DC GLOW DISCHARGES IN ARGON Revel I., Pitchford L.C., Bœuf J.P.	II-56

CRITICAL FIELD AND POTENTIAL DISTRIBUTION IN A MAGNETIZED SF ₆ /HE MIXTURE GAS POSITIVE COLUMN Sato H., Wakabayashi Y., Nishioka T., Matsumoto M.	II-58
INFLUENCE OF OXYGEN ADMIXTURE ON GAS HEATING IN N ₂ -O ₂ MIXTURE OF PULSE DISCHARGE Ershov A.P., Kalinin A.V., Shibkov V.M., Shibkova L.V., Singh D.P., Vaselli M.	II-60
ON THE NONHYDRODYNAMIC KINETICS OF THE ELECTRONS IN S - AND P-STRIATIONS OF NEON DC GLOW DISCHARGE PLASMAS Sigeneger F., Golubovski Y.B., Porokhova I.A., Winkler R.	II-62
ELECTRON AND ION KINETICS IN HYDROGEN OBSTRUCTED GLOW DISCHARGE Simko T., Donko Z., Rozsa K.	II-64
THE CATHODE END OF A DC HELIUM POSITIVE COLUMN AS A PLACE OF ORIGINATION OF IONIZATION WAVES Sirghi L., Ohe K., Popa G.	II-66
CONSTITUTIONAL STUDY OF TWO PARALLEL-PLATES CATHODE FOR ATTAINING THE HOLLOW-CATHODE EFFECT Onoda H., Yatsu M., Sugawara M.	II-68
EFFECT OF WALL TREATMENT ON OXYGEN ATOMS RECOMBINATION Cartry G., Magne L., Cernogora G., Touzeau M., Vialle M.	II-70
RELAXATION OF EXCITED STATES IN OXYGEN NITROGEN MIXTURES IN A LOW PRESSURE AFTERGLOW Cartry G., Magne L., Cernogora G., Touzeau M., Vialle M.	II-72
IMPROVED DESCRIPTION OF A NEON GLOW DISCHARGE BY RATE EQUATIONS Franke St., Deutsch H., Uhrandt D., Wilke C.	II-74
ELECTRIC DISCHARGE IN CROSSED ELECTRIC AND MAGNETIC FIELDS Bugrova A.I., Lipatov A.S., Morozov A.I., Kharchevnickov V.K.	II-76

Topic 5 : Arcs.

COMPUTATIONAL RECONSTRUCTION AND VISUALISATION OF SWITCHING ARC Aubrecht V., Busov B., Hanacek P., Masek J., Peska L., Stefka J.	II-78
SOME REMARKS TO CALCULATION OF IONIZATION AND RECOMBINATION COEFFICIENTS IN SF ₆ ARC PLASMA Bartlova M., Aubrecht V.	II-80
DIAGNOSTICS OF THE ARC PLASMA BY AUTOCOLLIMATION INTERFEROMETER Masek J., Peska L., Houska A., Gross B., Aubrecht V.	II-82
THE PLASMA MODEL OF NEW MODE HOT ANODE VACUUM ARC Beilis I.I., Boxman R.L., Goldsmith S.	II-84

SIMULATION OF A DECAYING SF ₆ ARC PLASMA Belhaouari J.B., Gonzalez J.J., Gleizes A.	II-86
DEPARTURES FROM EQUILIBRIUM IN THE ANODE REGION OF A TRANSFERRED ARC AT ATMOSPHERIC PRESSURE Bouaziz M., Razafinimanana M., Gleizes A.	II-88
DYNAMICAL ANALYSIS OF A LOW PRESSURE NITROGEN PLASMA GENERATED BY A TRANSFERRED DOUBLE ARC Bultel A., Maheu B., Lemeur F., Cheron B.G.	II-90
STUDY OF THE COMMUTATION OF AN ELECTRIC ARC IN A BREAKING DEVICE Cajal D., Laurent A., Mercier M., Velleaud G., Gary F., Servant S.	II-92
HIGH-CURRENT PLASMA GENERATOR RADIATION Chinnov V.F., Isakaev E.H., Iserov A.D., Spector N.O., Tereshkin S.A., Zobnin A.V.	II-94
RADIAL TEMPERATURE DISTRIBUTION IN AR-CO ₂ PLASMA Maouhoub E., Coitout H., Parizet M.J.	II-96
ESTIMATION OF THE METALLIC PLASMA PRESSURES IN THERMAL ARC COLD CATHODE SPOTS Coulombe S., Meunier J.L.	II-98
2-D HYDRODYNAMIC MODEL OF THE ELECTRODE VAPORIZATION IN AN ELECTRICAL CIRCUIT BREAKER IN SF ₆ AND COMPARISON WITH EXPERIMENTS Ciobanu S.S., Chevrier P., Fleurier C.	II-100
EXPERIMENTAL STUDY OF THE ELECTRODE VAPORIZATION IN AN ELECTRICAL CIRCUIT BREAKER IN SF ₆ Ciobanu S.S., Fleurier C., Fievet C.	II-102
ELECTRICAL CONDUCTIVITY OF AN SF ₆ THERMAL PLASMA AT LOW TEMPERATURE (T<5000 K) Chervy B., Gleizes A., Krenek P.	II-104
CALCULATION OF MEAN ABSORPTION COEFFICIENTS FOR THERMAL PLASMAS APPLICATIONS TO AIR, METHANE AND ARGON-IRON Gleizes A., Erraki A., Naghizadeh-Kashani Y., Riad H.	II-106
IONISATION EFFICIENCY IN A PINCHED CASCADED ARC CHANNEL Burm K.T.A.L., Goedheer W.J., Van der Mullen J.A.M., Schram D.C.	II-108
DIAGNOSTICS OF A THERMAL ARGON-BROMINE PLASMA CREATED IN A WALL-STABILIZED CASCADE ARC FOR DETERMINATION OF ATOMIC STRUCTURE CONSTANTS Baclawski A., Golly A., Ksiazek I., Wujec T.	II-110
MODELING AND SPECTROSCOPY STUDIES ON A CUTTING PLASMA TORCH Gonzalez-Aguilar J.A., Pardo C., Rodriguez-Yunta A., Calderon M.A.G.	II-112
DETERMINATION OF THE RADIAL TEMPERATURE DISTRIBUTION OF PULSED SODIUM ARC DISCHARGES Kettlitz M., Schopp H.	II-114

HIGHLY STRUCTURED ELECTRON ENERGY DISTRIBUTION FUNCTIONS UNDER EXPANDING ARC CONDITIONS Capitelli M., Dyatko N., Hassouni K., Gorse C., Longo S.	II-116
ENERGETIC IONS IN TVA (THERMIONIC VACUUM ARC) GENERATED PURE METAL VAPOR PLASMAS Musa G., Popescu A., Mustata I., Salabas A., Leu F., Ehrich H., Schumann J.	II-118
DC PLASMA TORCH THEORETICAL AND EXPERIMENTAL RESULTS Pacheco J., Razafinimanana M., Bauchire J.M., Vacquie S., Gonzalez J.J.	II-120
PHENOMENA IN THE ELECTRIC ARC CATHODE REGION Pokrzywka B., Musiol K., Pellerin S., Pawelec E., Cormier J.M., Chapelle J.	II-122
INFLUENCE OF THE ARC MOTION ON THE HYDRODYNAMIC FLOW IN A THREE-PHASE AC PLASMA REACTOR Ravary B., Fulcheri L., Fabry F., Flamant G.	II-124
EXPERIMENTAL ANALYSIS OF THE CARBON ARC FOR FULLERENE SYNTHESIS Saidane K., Razafinimanana M., Pousse J., Gleizes A., Vacquie S.	II-126
STABILIZATION OF PLASMA ARCS WHEN FEEDING WITH RECTANGULAR ALTERNATING CURRENTS OF MEDIUM FREQUENCY Scheibe H.J., Musikowski H.D.	II-128
RF-EXCITATION OF CU ION LASER TRANSITIONS IN HE(NE)-CUBR DISCHARGE Grozeva M., Schulze J., Teuner D., Telbizov P., Petrov T., Sabotinov N., Mizeraczyk J., Mentel J.	II-130
INVESTIGATION OF ARC SPOT IGNITION ON COLD ELECTRODES BY EMISSION SPECTROSCOPY Schumann M., Nandelstadt D., Korbel A., Schein J., Mentel J.	II-132
EXPERIMENTAL STUDY OF CATHODE REGION OF PULSE HIGH CURRENT FREE BURNING ARC IN ARGON AT ATMOSPHERIC PRESSURE Mitrofanov N.K., Shkol'nik S.M.	II-134
EXPERIMENTAL MEASUREMENTS ON A DC PLASMA TORCH: COMPARISON WITH THEORETICAL MODEL Singh N., Bauchire J.M., Razafinimanana M., Gonzalez J.J., Gleizes A.	II-136
STUDY OF THE PHYSICS PHENOMENA IN THE DISCHARGE CHAMBER OF AIR PLASMA GENERATOR WITH COPPER ELECTRODE FOR METALS CUTTING Stanciu T., Pogora V., Protuc I.	II-138
STUDY OF CIRCUIT BREAKER ARC DURING THERMAL CURRENT INTERRUPTION Trusca A., Gleizes A., Gonzalez J.J.	II-140
TWO-DIMENSIONAL MODEL OF THE ANODE AREA OF A LOW PRESSURE DISCHARGE Ulyanov K.N., Filippov A.A.	II-142
EFFECT OF ANODE VAPOURS ON THE HC VACUUM ARC CATHODE STREAM DECELERATION Ulyanov K.N., Londer J.I.	II-144

A COMPREHENSIVE STUDY OF ARCING ON ALUMINIUM ANODIZED PLATES IMMERSSED IN LOW DENSITY PLASMAS Doreswamy C.V., Ferguson D.C., Galofaro J.T., Snyder D.B., Vayner B.V.	II-146
THE EFFECTS OF SELF-INDUCED MAGNETIC FIELD ON A HIGH CURRENT SF ₆ ARC IN A SUPERSONIC NOZZLE Yan J.D., Fang M.T.C.	II-148
THE STABILITY OF ARGON ARCS IN AXIALLY ACCELERATING FLOW Blundell R.E., Fang M.T.C., Yan J.D.	II-150
THE INTERRELATION BETWEEN THE DEPARTURE FROM LTE AND THE SPACE MODES OF ELECTRIC ARC PLASMA AND DIAGNOSTIC PROBLEMS Zhovtyansky V.A.	II-152
INVESTIGATIONS OF FREE-BURNING ELECTRIC ARC IN COPPER VAPOURS Babich I.L., Veklich A.N., Cheredarchuk A.I., Zhovtyansky V.A.	II-154

Topic 11 : Generation and dynamics of plasma flows.

GENERATION OF MAGNETIC FIELD BY ACCELERATION OF HALL PLASMA AND SOME CONSEQUENCES OF THIS PROCESS Alekseeva L.M.	II-156
COMPUTATIONAL ANALYSIS OF A THREE-DIMENSIONAL PLASMA SPRAY JET Dussoubs B., Vardelle A., Vardelle M., Fauchais P.	II-158
AN ATTEMPT TO SIMULATE RADIATIVE EMISSION FROM NONEQUILIBRIUM HYPERSONIC AIR FLOWS Epifanie A., Sarrette J.P., Gomes A.M.	II-160
COLLECTION OF ISOTOPICALLY ENRICHED LITHIUM IN PLASMA BY MEANS OF ION CYCLOTRON RESONANCE Dolgolenko D.A., Ezubchenko A.N., Laz'ko V.S., Karchevsky A.I., Muromkin Yu.A., Pashkovsky V.G., Ustinov A.L.	II-162

Topic 14 : Non-linear phenomena, self-organization and chaos.

CONTROL OF THE CHAOTIC REGIMES OF A DRIVEN THERMIONIC DISCHARGE Arnas-Capeau C., Pierre Th.	II-164
DYNAMICAL FORCE-FREE ZERO-NET-CURRENT LAYER IN COMPRESSING TURBULENT PLASMA Djakov A.F., Bobrov Yu.K., Sorokin A.V.	II-166
ADIABATIC EVOLUTION OF FORCE-FREE PLASMOID WITH SURFACE CURRENTS Djakov A.F., Bobrov Yu.K., Sorokin A.V.	II-168

SPATIOTEMPORAL DYNAMICS AND CONTROL OF IONIZATION WAVES IN AN UNDRIVEN NEON GLOW DISCHARGE Atipo A., Pierre Th., Bonhomme G.	II-170
COMPARATIVE STUDIES PERFORMED ON « FIREBALLS » FORMED IN DIRECT CURRENT AND HIGH FREQUENCY DISCHARGES Sanduloviciu M., Borgia C., Melnig V., Gherman C.	II-172
SELF-ORGANIZATION OF AUTONOMIC CHAOTIC REGIMES IN STRIATED LOW-TEMPERATURE PLASMA OF A GLOW DISCHARGE Chirkin M.V., Solonin V.V., Stepanov V.A.	II-174
PARAMETRIC AND NONLINEAR EFFECTS IN A UHF RESONATOR LOADED BY A PLASMA LAYER PERTURBED BY ION-SOUND OSCILLATIONS Cicconi G., Rosatelli C.	II-176
THE WAVES SCATTERING PROCESSES IN THE MAGNETIZED PLASMA WITH UPPER HYBRID PUMP Pavlenko V.N., Panchenko V.G., Rosum I.N.	II-178
INFLUENCE OF DENSITY GRADIENT ON ABSORPTION OF UPPER HYBRID PUMP ENERGY IN TURBULENT PLASMA Pavlenko V.N., Panchenko V.G., Rosum I.N.	II-180
INTERACTION OF FILAMENTS IN ANA.C.-DRIVEN PLANAR GAS DISCHARGE SYSTEM Muller I., Ammelt E., Purwins H.G.	II-182
CELL LIKE STRUCTURES FORMED IN PLASMA AFTER SELF-ORGANIZATION Sanduloviciu M., Lozneau E., Leu G.	II-184
ON THE SO CALLED TURING STRUCTURES FORMED IN GAS DISCHARGES Lozneau E., Leu G., Sanduloviciu M.	II-186
ON THE TEMPORAL STRUCTURES GENERATED BY A THERMIONIC VACUUM ARC DISCHARGE Sanduloviciu M., Stan C., Musa G., Popescu A., Mustata I., Leu F.	II-188
THE EFFECT OF THE MAGNETIC FIELD ON THE HOLLOW CATHODE GENERATED ELECTRON BEAM Biborosch L., Toma M., Sanduloviciu M.	II-190
FILAMENTATION OF SURFACE WAVE SUSTAINED DISCHARGES Dzermanova N., Grozev D., Kirov K., Shivarova A., Tsvetkov T.S.	II-192
ON BEHAVIOUR OF ELECTRON BEAM EXCITING STRONG LANGMUIR TURBULENCE IN PLASMA Sychov I.A.	II-194
RADIATION SPECTRA OF LANGMUIR CAVITIES IN A WEAK MAGNETIZED TURBULENT PLASMA Sergeichev K.F., Sychov I.A.	II-196

OBSERVATION OF INTERMITTENT CHAOTIC PHENOMENA CAUSED BY ION ACOUSTIC INSTABILITY Taniguchi K., Kuwae H., Hayashi N., Kawai Y.	II-198
OBSERVATION OF THE ECKHAUS INSTABILITY IN A GLOW DISCHARGE PLASMA Dinklage A., Bruhn B., Deutsch H., Gubsch S., Koch B.P., Wilke C.	II-200
HOT IONS IN MULTI-COMPONENT PLASMAS Anschutz F.B., Awakowicz P., Scheubert P., Valentini H.B.	II-202

Topic 17 : Numerical modeling.

A HYDRODYNAMIC MODEL FOR A CYLINDRICAL LANGMUIR PROBE IN A LOW PRESSURE DISCHARGE Scheubert P., Awakowicz P., Anschutz B., Wachutka G.	II-204
METALLIC POWDERS IN A PLASMA TORCH : NUMERICAL MODELLING OF THE CURRENT INTENSITY EFFECT Bauchire J.M., Gonzalez J.J., Proulx P.	II-206
SIMULATION OF POSITIVE STREAMERS IN AIR I. TWO-STEP ALGORITHM BASED ON VAN LEER TYPE UPWIND SCHEMES Djakov A.F., Bobrov Yu.K., Solntsev I.A., Yurghelenas Yu.V.	II-208
SIMULATION OF POSITIVE STREAMERS IN AIR II. POSITIVE STREAMER PROPAGATION IN A NON-UNIFORM FIELD Djakov A.F., Bobrov Yu.K., Scherbakov Yu.V., Yurghelenas Yu.V.	II-210
SPUTTERED PARTICLES TRANSPORT STUDY IN A RF MAGNETRON DISCHARGE Clenet F., Briaud Ph., Lemperiere G., Turban G.	II-212
NUMERICAL MODELLING OF THE IGNITION TRANSIENT IN INDUCTIVELY COUPLED PLASMA TORCHES Taddei F., Colombo V., Coppa G.G., M., Panciatichi C.	II-214
RECENT HIGH-RESOLUTION STUDIES OF PSEUDOSPARK DISCHARGE Al-Hussany A., Davies A.J.	II-216
A STABLE HIGH RESOLUTION INTEGRATION SCHEME FOR DISCHARGE SIMULATION Al-Hussany A., Davies A.J.	II-218
ANALYSIS OF A H ₂ SHORT-GAP SPARK CHANNEL WITH A HYBRID MODEL OF NEUTRAL AND CHARGED PARTICLE DYNAMICS Jugroot M., Eichwald O., Yousfi M., Bayle P.	II-220
A 2-D FLUID MODEL FOR DUST PARTICLES IN AN RF DISCHARGE Goedheer W.J.	II-222

MODELING RESULTS OF SiH_4 - H_2 RF/VHF DEPOSITION DISCHARGES COMPARED TO EXPERIMENTS Nienhuis G.J., Goedheer W.J., Hamers E.A.G., Bezemer J.	II-224
MODELLING OF ECR DISCHARGES Hemmers D., Biel W., David M., Kempkens H., Uhlenbusch J.	II-226
ONE-DIMENSIONAL HYBRID FLUID-MONTE CARLO MODEL OF A AC MATRIX PLASMA DISPLAY PANEL CELL Hirech A., Boeuf J.P.	II-228
STUDY OF PLASMA OXIDATION OF METALS: CHARGE TRANSPORT THROUGH PLASMA Hrach R.	II-230
SIMPLIFIED PARTICLE MODEL OF COLLISION PROCESSES IN AR PLASMA Hrach R., Entlicher M., Horvath M.	II-232
ONE-DIMENSIONAL HYBRID MODEL OF PLASMA DISPLAY CELL Ivanov V.V., Klopovskiy K.S., Mankelevich Yu.A., Proshina O.V., Rakhimov A.T., Rakhimova T.V.	II-234
PULSED CORONA IN AN ELECTROSTATIC PRECIPITATOR CONFIGURATION Egli W., Kogelschatz U., Gerteisen E.	II-236
NUMERICAL SIMULATION OF HYPERSONIC AIR NOZZLE FLOW IN THERMAL AND CHEMICAL NON-EQUILIBRIUM Leroux A., Domingo P., Vervisch P.	II-238
SOLUTION OF THE FOKKER-PLANCK EQUATION FOR AZIMUTHALLY-SYMMETRIC 2V-DISTRIBUTION FUNCTION USING SPLITTING SCHEME Telegov K.V., Levchenko V.D.	II-240
DIRECT SIMULATION MONTE CARLO MODELING OF VIBRATIONAL RELAXATION Bruno D., Capitelli M., Ivanov M.S., Longo S.	II-242
NUMERICAL MODELING OF A FAST AXIAL-FLOW CO_2 LASER Si-Serir F., Louhibi D., Mokhtari A.E.	II-244
SIMULATION OF POSITIVE STREAMER PROPAGATION IN FLUE GASES Babaeva N.Yu., Naidis G.V.	II-246
STUDY OF ELECTRICAL PROPERTIES OF THE SHEATH IN A DIRECT CURRENT GLOW DISCHARGE Novak S.	II-248
NUMERICAL SIMULATION OF A TRICHEL PULSE IN AIR AT ATMOSPHERIC PRESSURE Reess T., Paillol J.	II-250
ION DENSITY DISTRIBUTIONS IN THE CATHODE REGION OF GLOW DISCHARGES IN GAS MIXTURES Pedoussat C., Pitchford L.C., Boeuf J.P.	II-252
PROPAGATION OF HIGH POWER MICROWAVES AROUND A LOCAL PERTURBATION Peres G., Boeuf J.P., Theroude C.	II-254

THEORETICAL DETERMINATION OF THE ELECTRON DISTRIBUTION FUNCTION IN AN ELECTRON CYCLOTRON RESONANCE ION SOURCE Perret C., Girard A., Lecot C.	II-256
MODELLING OF THE PLASMA KINETICS IN THE ELECTRODE SHEATH REGIONS OF A PULSED COPPER VAPOUR LASER Satoh K., Morrow R., Carman R.J.	II-258
SELF-CONSISTENT DETERMINATION OF THE ELECTRIC FIELD IN A STATIONARY LOW PRES- SURE GLOW DISCHARGE USING MICROSCOPIC TREATMENT FOR THE MOTION OF ELECTRONS Zahraoui A., Segur P., Alkaa A.	II-260
TRANSMISSION OF CHARGED PARTICLES THROUGH PROBE APERTURES IN MAGNETIZED AND DRIFTING PLASMAS Tramontin L., Serianni G., Antoni V., Bagatin M., Desideri D.	II-262
CREATION OF DOUBLE LAYER IN ASYMMETRIC DC DISCHARGE Vrba P.	II-264
AN EFFICIENT PROCEDURE FOR DETERMINING ELECTRON KINETIC PROPERTIES IN THE CATHODE REGION OF DC GLOW DISCHARGES Winkler R., Petrov G.	II-266
IMITATION MODELS OF CHARGED PARTICLE UNIPOLAR BEAM FORMATION AND ACCELERATION PROCESSES Tchuyan R.K.	II-268

Topic 3

Low pressure glows.

Experimental evaluation of a hollow cathode plasma source.

I. Alcaide and L. Conde
Departamento de Física Aplicada.
ETSI Aeronáuticos. UPM.
28040 Madrid, (Spain).

1 Introduction

Hollow cathodes have been employed with different configurations to produce dense plasma clouds, as well as electron emitters in the laboratory [1 - 3]. The plasma is generated by a high voltage discharge, and the particular electrode configuration of these devices increase the generated plasma density over usual electric discharges of similar characteristics [2].

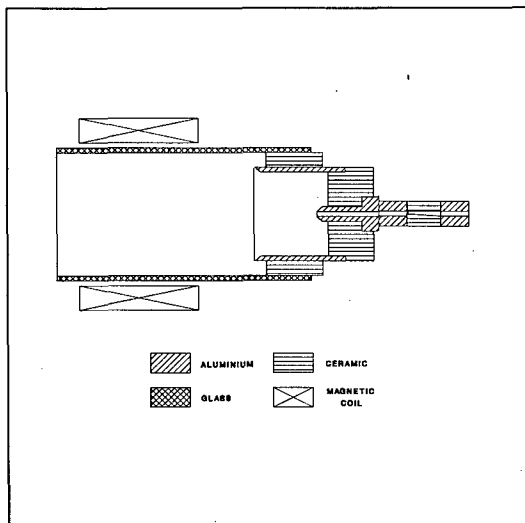


Figure 1: *Detail of the hollow cathode assembly.*

In this paper we describe a simple and unexpensive hollow cathode plasma source. Our device, of small size, employs moderate discharge voltages (always below 1 Kilovolt). The hollow cathode is used as a primary plasma source to

create a quiescent and magnetized plasma column with 10 cm of diameter and 30 of length. This device is based in previous experiments with hollow cathode discharges [4] and is intended for basic plasma studies.

2 Experimental setup

The details of the plasma chamber and vacuum equipment have been described in previous papers [4, 5]. An scheme of the hollow cathode is presented in Figure 1. The cathode was a small hollow metallic cylinder with a drill of 0.1 cm in its center. Neutral gas (Ar or Xe) was injected through this drill, which is in turn connected by means of a ceramic tube to the gas feed. This permits the electrical insulation of the hollow cathode set holding the thermal contact for external cooling. The neutral gas mass flow rate (between 1-20 standard cubic centimeters per minute) was controlled by means of a needle valve. The anode was made of a coaxial cylinder electrically insulated by ceramic rings. The electric discharge was produced by a high voltage ($V_{dis} = 200-1000$ Volts) in the choked flow of neutral gas leaked. This assembly was covered by a pyrex glass tube which supports a coaxial magnetic coil which provides a maximum magnetic field of 4×10^{-2} Tesla. This enhance the ionization rate of remaining neutral gas by electrons originated in the electric discharge. In addition, the hollow cathode could be polarized with a bias voltage (V_{bias} between -40 and +40 Volts) with respect to either, the grounded chamber walls or a metallic target plate located at the

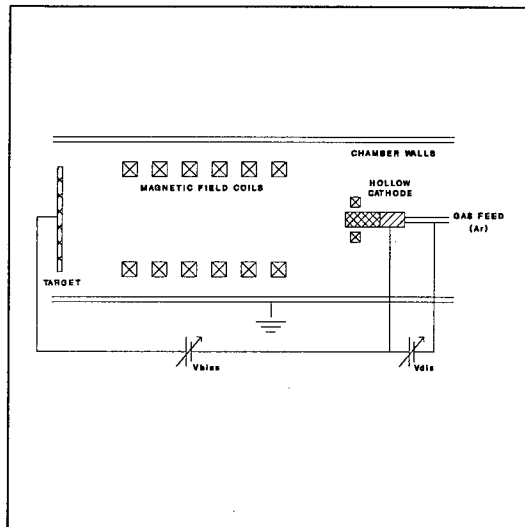


Figure 2: Scheme of the experimental setup.

end of the plasma column.

In Figure 2 is presented an scheme of the plasma device. The uniform magnetic field was generated by six equally spaced Hemholtz coils with 30 cm of diameter disposed along 33 cm. This configuration holds a uniform magnetic field into a volume of 10 cm of radius and 30 cm of length, with a maximum value of 3.0×10^{-3} Tesla.

The properties of the magnetized plasma column were ascertained using collecting Langmuir probes biased to the anode of the hollow cathode. These probes were placed inside the plasma volume with a resolution of ± 0.1 cm. The plasma potential V_p , electronic temperature T_e and density n_e were obtained from voltage current probe traces by means of the usual techniques for plasma diagnose. The smallness of the electronic Larmor radius, always larger than the probe dimensions, permits to make use of the simplified Langmuir theory [6].

3 Experimental results

The plasma parameters were measured under stationary conditions of both mass flow rate and background pressure. The typical electron densi-

ties measured at a fixed point located at the exit of the hollow cathode plasma source lie between $6.5 \times 10^8 \text{ cm}^{-3}$ and $7 \times 10^9 \text{ cm}^{-3}$, depending on the different experimental conditions. The electronic temperatures were between 1 and 2 eV.

The plasma emission properties were evaluated by measuring the current I_{col} collected at either, end target plate and/or the grounded plasma chamber walls for different bias voltages. For positive values the current I_{col} is increased with V_b up to a maximum value which depends on the electron density n_e at the exit of the hollow cathode. This maximum saturation current is also increased with the current I_{dis} of the hollow cathode discharge. The intense magnetic field applied in the plasma source also contributes to the increment the electron density, and therefore, the emitted current I_{col} .

4 References

1. Vannaroni, G. et al. *J. Appl. Phys.* **71**, (10), (1992), 4709.
2. D.E. Parks, I. Katz, B. Buchholtz and P.J. Wilbur, *J. Appl. Phys.* **74**, (1993), 7094.
3. Y.P. Raizer, *Gas Discharge Physics*, Berlin, Springer Verlag, (1991), Ch. VIII.
4. L. Conde, L. León and L.F. Ibañez. Accepted for its publication in *IEEE Transactions of Plasma Science*.
5. L. Conde and L. León, *Phys. Plasmas*, **1**, (8), (1994), 2441.
6. Hershkowitz, N. How Langmuir probes work, in *Plasma diagnostics. Discharge parameters and Chemistry*, O. Auciello and D.L. Flamm, Editors. London, (1989), Academic Press.

Comparison of Kinetic and Diffusion Theories of Positive Column of a Discharge.

Yu.B. Golubovskii*, I.A. Porokhova*, J. Behnke, J.F. Behnke, H. Deutsch,

Department of Physics, D-17487 Greifswald, Germany

* Department of Optics, Saint-Petersburg University, Uljanovskaja 1, 198904 S.Petersburg, Russia.

1 Introduction

The proper self-consistent description of a positive column of an inert gas discharge under low pressures and small currents should base on a joint solution of kinetic equation for electrons and of motion equation for ions. The attempts to describe electron motion under these conditions in terms of diffusion and mobility can lead to results considerably different from those of kinetic description.

In the present paper the kinetic (nonlocal) and diffusion (local) theories of positive column in neon are developed and compared under the same cross-sections of elementary processes.

2 Nonlocal theory

The basic equations are the kinetic equation where the term with radial gradients of electron distribution function (EDF) is present, the ion motion equation and Poisson equation.

$$\frac{(eE)^2}{3} \frac{\partial}{\partial \varepsilon} \frac{v^3}{v} \frac{\partial f_0(\varepsilon, r)}{\partial \varepsilon} + \frac{1}{3r} \frac{\partial}{\partial r} \frac{v^3}{v} \frac{\partial f_0(\varepsilon, r)}{\partial r} =$$

$$vv^*(v)f_0(\varepsilon, r) - v'v^*(v')f_0(\varepsilon + \varepsilon_1, r) \quad (1)$$

$$\left. \frac{\partial f_0(\varepsilon, r)}{\partial r} \right|_{r \approx r_0(\varepsilon)} = 0; \quad f_0(\varepsilon, r)|_{r=R} = 0$$

$$n_e(\varphi) = \int_{\varepsilon_{\text{ex}}}^{\infty} f_0(\varepsilon, r) \sqrt{\varepsilon - \varepsilon_{\text{ex}}(r)} d\varepsilon \quad (2)$$

$$I_d(\varphi) = \int_{\varepsilon_i + \varepsilon_{\text{ex}}}^{\infty} v_i(\varepsilon - \varepsilon_{\text{ex}}(r)) f_0(\varepsilon, r) \sqrt{\varepsilon - \varepsilon_{\text{ex}}(r)} d\varepsilon \quad (3)$$

$$I_s(\varphi) = \gamma(\varphi) \int_{\varepsilon_i + \varepsilon_{\text{ex}}}^{\infty} v^*(\varepsilon - \varepsilon_{\text{ex}}(r)) f_0(\varepsilon, r) \sqrt{\varepsilon - \varepsilon_{\text{ex}}(r)} d\varepsilon \quad (4)$$

Here $\varepsilon = w + \varepsilon_{\text{ex}}(r)$, ($\varepsilon, w, \varepsilon_{\text{ex}}$ are total, kinetic and potential energies), E is constant axial field, v, v^*, v_i are the transport frequencies of elastic and inelastic impacts and the frequency of direct ionization, velocities v and v' are related by $mv'^2/2 = mv^2/2 + \varepsilon_1$, ε_1 is excitation threshold, ε_i is ionization potential, ε_{ex} is the wall potential, $\gamma(\varphi)$ is the ratio of stepwise ionization probability to total probability of decay of metastable and resonance levels involved in stepwise ionization, $n_e(\varphi)$ is electron density, $I_d(\varphi), I_s(\varphi)$ are direct and stepwise ionization rates as the functions of radial potential.

The closed system of equations for calculation of discharge parameters is

$$j_i = b_i E_r n_i(\varphi) \quad \left. \frac{n_i - n_e}{n_e} \right|_{r=0} = \left. \frac{I_d + I_s}{4\pi e n_e^2 b_i} \right|_{r=0} \quad (5)$$

$$\text{div } j_i = I_d(\varphi) + I_s(\varphi) \quad j_i(0) = 0 \quad (6)$$

$$\text{div } E_r = 4\pi e(n_i(\varphi) - n_e(\varphi)) \quad E_r(0) = 0 \quad (7)$$

$$E_r = -\text{grad } \varphi \quad \varphi(0) = 0 \quad (8)$$

j_i is the radial flux of ions, n_i is ion density, E_r is radial field, b_i is ion mobility. The solution of kinetic equation (1) has been found by method of averaging over radial motions of electrons [1] in trial potential with wall potential $\varepsilon_{\text{ex}}^{(0)}$. Then the set of equations (2)-(8) has been solved by varying of parameters in order to satisfy conditions

$$j_e(R) = j_i(R) = \frac{1}{R} \int_0^R (I_d + I_s) r dr; \quad \varepsilon_{\text{ex}}^{(0)} = \varepsilon_{\text{ex}}^{(1)}$$

$j_e(R)$ is electron flux on the tube wall, in this model it is determined mostly by electron flux in energy space into energy region $\varepsilon > \varepsilon_{\text{ex}}$.

3 Local theory

The model bases on kinetic equation where the term with radial gradients is omitted, on equations for ion and electron fluxes and on Poisson equation

$$\frac{(eE)^2}{3} \frac{\partial}{\partial w} \frac{v^3}{v} \frac{\partial (n(r)f_0(w))}{\partial w} =$$

$$vv^*(v)n(r)f_0(w) - v'v^*(v')n(r)f_0(w + \varepsilon_1) \quad (9)$$

$$I_d(n, E) = n \int_{\varepsilon_i}^{\infty} v_i(w) f_0(w) \sqrt{w} dw \quad (10)$$

$$I_s(n, E) = \gamma(n, E) n \int_{\varepsilon_i}^{\infty} v^*(w) f_0(w) \sqrt{w} dw \quad (11)$$

$$b_e = \frac{e}{3} \sqrt{\frac{m}{2}} \int_0^{\infty} \frac{v^3}{v} \frac{\partial f_0}{\partial w} dw \quad (12)$$

$$D_e = \frac{1}{3} \sqrt{\frac{m}{2}} \int_0^{\infty} \frac{v^3}{v} f_0 dw \quad (13)$$

$$j_{ir} = b_i E_r n_i \quad (14)$$

$$j_{er} = -b_e E_r n_e - D_e \text{grad } n_e \quad (15)$$

$$j_{ir} = j_{er} \quad (16)$$

$$\text{div } j_{ir} = I_d + I_s \quad (17)$$

$$\text{div } E_r = 4\pi e(n_i - n_e) \quad (18)$$

$$E_r = -\text{grad } \varphi \quad (19)$$

The system of equations (14)-(19) has been integrated numerically, parameter E has been varied until the boundary condition at the tube wall $n_e(R) = j_z(R)/\sqrt{T_e/m}$ would have been satisfied.

4 Results

The results of calculations by nonlocal and by local theories are shown in the Figures 1,2,3,4 and Table for neon discharge under $pR=1$ torr.cm, $i/R=10$ mA/cm.

The main differences are:

the nonlocal EDF $f_0(w, r)$ is considerably depleted with fast electrons in the column periphery (Fig.1). This lead to compression of ionization sources and densities of charged particles (Fig.2). The wall potentials in nonlocal theory are considerably smaller than in local theory. Contrast to the local theory the axial current density $j_z(r)$ does not coincide with electron density profile, and mean energy of electrons decreases towards the tube wall. The sizes of space charge sheath L_d differ in about two times.

	$n_0 \cdot 10^{10}$ cm^{-3}	E V/cm	$e\Phi_w$ eV	$e\Phi_{pl}$ eV
NLT	1.6	4.25	28	18.5
LT	1.35	4.55	44	17
	L_d cm	I_{d0}/n_0 $\cdot 10^5 \text{s}^{-1}$	I_{s0}/n_0 $\cdot 10^5 \text{s}^{-1}$	$2\pi R j_R$ $\text{cm}^{-1} \text{s}^{-1}$
NLT	0.075	2.5	2.1	$1.16 \cdot 10^{15}$
LT	0.18	0.8	0.82	$1.5 \cdot 10^{15}$

Acknowledgments

This study was supported by the Deutsche Forschungsgemeinschaft under SFB 198.

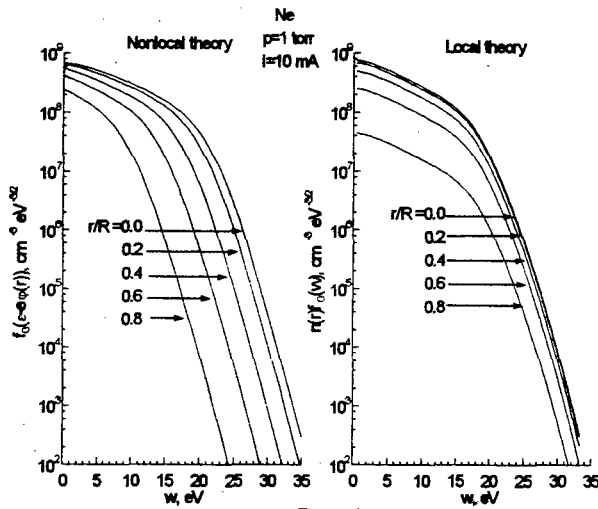


Figure 1.

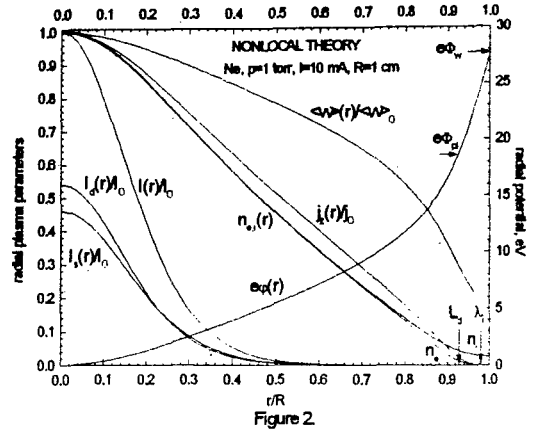


Figure 2.

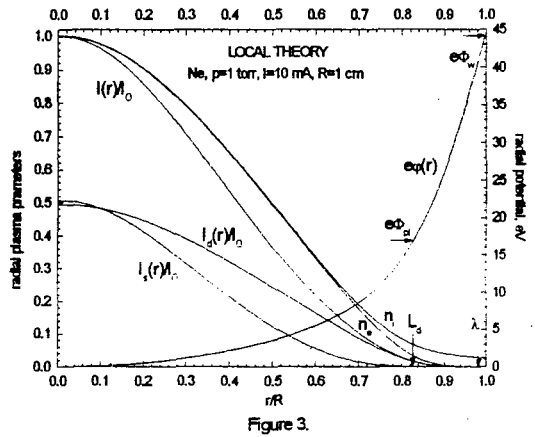


Figure 3.

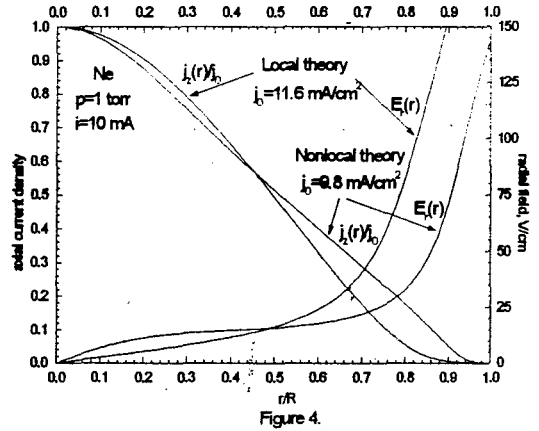


Figure 4.

Reference

- [1] J. Behnke, Yu.B. Golubovskii, S.U. Nisimov, I.A. Porokhova
Contr. Plasmaphys. V.36, 1, p.75, 1996..

Wall Recombination in the Plasma of Positive Column in Low Current Discharge

J.F. Behnke, Th. Bindemann, H. Deutsch, Yu.B. Golubovskii*, I.A. Porokhova*,
 Institute for Physics, Ernst-Moritz-Arndt University of Greifswald, D-17487 Greifswald, Germany
 * Department of Optics, Saint-Petersburg University, Uljanovskaja 1, 198904 S.Petersburg, Russia.

1 Introduction

Plasma wall interaction is of fundamental importance for the understanding of the properties of a plasma and also of great interest in many plasma technological applications such as plasma etching and plasma-assisted deposition processes.

We have developed a model in which the electron kinetics in the bulk-plasma and the sheath is based on the so-called non local approach of the BOLTZMANN-equation [1],[2] which describes the EEDF and the density profile of the electrons as a function of the radial potential ϕ .

In contrast to earlier models we show that the necessary plasma boundary conditions result from a system of balance equations of the charged carriers on the insulated wall surrounding the positive column [3].

For a special neon discharge, the radial distribution function of several plasma parameters calculated from the model are compared with experimental results [4].

2 Theoretical Concept

The following set of equations was used in order to describe the plasma including the plasma sheath in front of the wall:

The BOLTZMANN-equation written in the non local form [1], [2], the continuity equation for charged particles, the impuls balance equation for the ions, and the POISSON-equation [2].

The following ionization processes have been considered: direct ionization and stepwise ionization via metastable atoms. Furthermore, according to [1] the stepwise ionization process has been used in an approximational solution.

In an effort to develop a more detailed model of the plasma interaction and to find realistic boundary conditions, the following elementary processes at the insulating wall have to be taken into account:

- adsorption of incoming carrier (negative and positive),
- desorption of charge carriers,
- surface diffusion and wall recombination of carriers on the wall.

In addition, the modelling of the plasma interaction has been carried out in the framework of a two dimensional wall plasma [5], i.e. the ions on the wall are fixed and the electrons can move in two dimensions by surface diffusion. These assumptions lead to two balance equations for the adsorbed charged particles.

$$S_e j_{rw} - \sigma_e / \tau_e - \alpha_R \sigma_e \sigma_i = 0,$$

$$S_i j_{rw} - \sigma_i / \tau_i - \alpha_R \sigma_e \sigma_i = 0$$

The negative charge at the wall $\Delta\sigma_e = \sigma_e - \sigma_i$ is related to the radial electric field E_r normal to the wall by:

$$E_r = e_0 / \epsilon_0 \Delta\sigma_e$$

where σ_e and σ_i denote the number densities of electrons and of positive ions on the wall, j_{rw} is the charged particle current density on the wall, $S_e, S_i \approx 1$ are the sticking coefficients of electrons and ions, respectively. $\tau_e = \tau_{e0} \exp(E_{se}/kT_w)$, $\tau_i = \tau_{i0} (E_{si}/kT_w)$ the residence time of the charged particle of the wall,

$$\alpha_R = \alpha_0 (T_w/300)^{1/2}$$

denotes the recombination coefficient of charged particles on the wall, e_0 is the electron charge and ϵ_0 is the permittivity of the vacuum.

This means that the properties of the surface determine the flux of the charge carriers to the wall, because $\Delta\sigma_e$ is determined by the properties of the wall.

3 Results and Discussion

The model was applied to a Neon glow discharge with the following parameters:

- pressure: $p_0 = 150$ Pa
- discharge current: $i = 9$ mA
- radius of the discharge tube: $r_0 = 1.27$ cm

The main results can be summarized as follows:

- the radial distributions of the charged particles are contracted in relation to the BESSEL-function of zero order, within the limits of probe measurements the measured distribution function [4] corresponds to the calculated (fig. 1), larger deviations in experimental and theoretical results exist for the mean electron energy in the bulk plasma (fig. 1);
- the model describes the bulk of the plasma and the formation of the sheath region and shows the known increase of the radial components of electric potential (fig. 2), the electric radial potential (fig. 3) and the increase of the degree of deviation from the quasi-neutrality $\Delta g = (g - g_0)/g_0$ (fig. 4). The level of agreement between experimentally determined [4] and calculated radial potential and radial electric field strength is satisfactory.

First estimations of elementary data of the wall recombination mechanism are given in tab. 1 and first results for the temperature dependence of different kinds of plasma sheath and wall data are represented in tab. 2:

- under our experimental condition the axial electric field strength E_z does not change with gas and wall temperature, ($T_g = T_w$);

- the radial electric field strength at the wall $E_r(r_0)$, the negative net charge $\Delta\sigma_0$ and the wall potential $\phi(r_0)$ show a maximum at $T_g = T_w = 350$ K;
- the current density of ions $j_i(r_0)$ and the ion drift velocity $v_i(r_0)$ at the wall decrease with increasing temperature.

Acknowledgments

This study was supported by the Deutsche Forschungsgemeinschaft under SFB 198..

Reference

- [1] J. Behnke, Yu.B. Golubovskii, et al *Contr. Plasmaphys.* V.36, 1, p.75, 1996..
- [2] Yu.B. Golubovskii et al. XXIII ICPIG Contr. Papers. Toulouse 1997, submitted
- [3] J.F. Behnke et al. XXII ICPIG Contr. Papers. 4 p 43 Hoboken 1995
- [4] H. Sievers, Diplomarbeit Greifswald 1993
- [5] K.G. Emeleus, J.R.M. Coulter, *Il Nuovo Cimento* 7D,79 (1986), *IEEE Proc.* 135, 76 (1988)

Tabel 1: Estimated elementary data of the wall recombination mechanism

E_{se} /eV	E_{si} /eV	τ_{e0} /s	τ_{i0} /s	α_0 cm ² /s
0.095	0.18	$9 \cdot 10^{-8}$	$2 \cdot 10^{-12}$	30

Tabel 2 : The change of the sheath parameters ($E_r(r_0)$, $\phi(r_0)$, $j_i(r_0)$ and $v_i(r_0)$) and the wall properties ($\Delta\sigma_0$) in dependence of the gas temperature and the wall temperature ($T_g = T_w$).

T / K	E_r V/cm	$E_r(r_0)$ V/cm	$\Delta\sigma_0$ cm ⁻²	$\phi(r_0)$ V	$j_i(r_0)$ cm ⁻² s ⁻¹	$v_i(r_0)$ cm/s
300	3.15	92.4	$5.1 \cdot 10^7$	23.32	$6.8 \cdot 10^{13}$	$2.6 \cdot 10^5$
350	3.15	100.2	$5.5 \cdot 10^7$	25.1	$6.5 \cdot 10^{13}$	$2.7 \cdot 10^5$
400	3.15	93.4	$5.2 \cdot 10^7$	23.41	$6.2 \cdot 10^{13}$	$2.4 \cdot 10^5$
450	3.15	82.0	$4.5 \cdot 10^7$	21.18	$5.9 \cdot 10^{13}$	$2.0 \cdot 10^5$

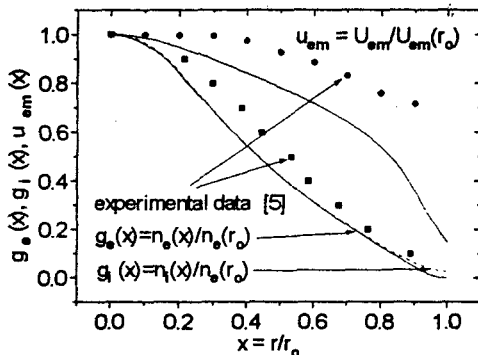


Fig. 1 : The radial dependence of the normalized charged particle density distributions g_e , g_i and the

normalized mean electron energy u_{em} , comparison between model calculation and experiments [4].

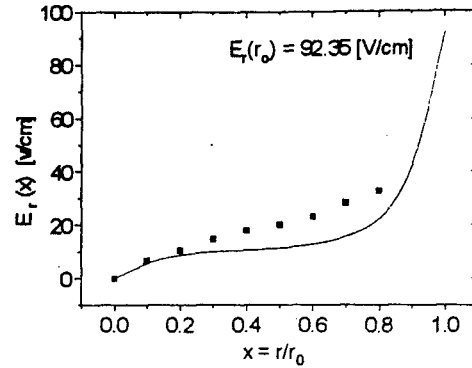


Fig. 2 The radial electric field strength in dependence on the radial coordinate; comparison between model calculation and experiment[4]., $T_g = T_w = 300$ K

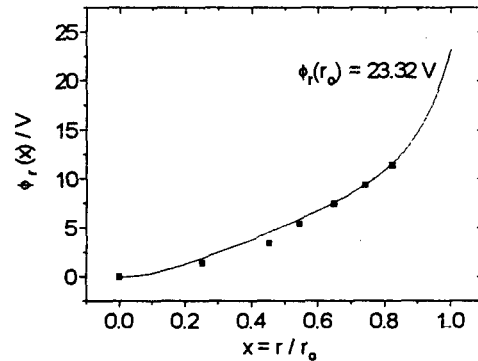


Fig 3. The calculated radial potential in comparison with experimental data [4], $T_g = T_w = 300$ K

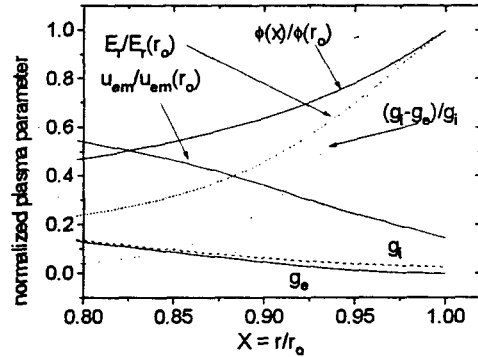


Fig. 4 The radial dependencies of the calculated normalized plasma parameters in the sheath region.

Determination of first excited states number densities of argon atoms in a cylindrical magnetron discharge: laser diode absorption spectroscopy and modelling

C. Csambal, J.F. Behnke, V. Helbig*, A. Hennig and E. Passoth

Departement of Physics, Ernst-Moritz-Arndt University D-17487 Greifswald,

*Departement of Physics, Christian-Albrechts University, D-24118 Kiel

Introduction

Magnetron discharges of various designs are widely employed in plasma enhanced deposition technologies to reach high sputtering rates. Because of the $E \times B$ -drift of the electrons near the cathode the collision frequency of the direct ionization at pressures of about 1 Pa is significantly higher than under non-magnetic conditions. Thus the input of the electrical power at relatively low voltages is very effective. In magnetron discharges used in technology the magnetic field is inhomogeneous in all directions. A quantitative description of the plasma in such types of discharges becomes more simple in a cylindrical magnetron discharge where inhomogeneities of the plasma parameters only occur in radial direction and where the magnetic field is generated by coils and not by permanent magnets.

Absorption spectroscopy using narrow bandwidth single mode diode lasers is a sensitive method to obtain number densities and temperatures in gasdischarge research. This technique especially allows access to the first four excited levels of the rare gases that are important for the carrier production in the discharge. Two of those are connected to the ground state the other two levels are metastable. Because of the large population density of the metastable states the absorption lines usually are influenced by optical thickness. This requires special care when reducing the data to obtain the number densities.

Since we are dealing with a magnetic field the lines additionally show Zeeman splitting which has to be mentioned in the later fitting procedure.

Experimental set-up

The cylindrical magnetron discharge consist of a coaxial non magnetic stainless steel vacuum vessel that can be pumped down to pressures of the order of 10^{-3} Pa. The inner stainless steel cylinder is water-cooled, isolated from the vacuum system body and serves as cathode. The magnetic field is created by means of a couple of special formed coils in order to guarantee homogeneity over the whole discharge length.

The laser set-up consists of a grating stabilized diode laser in Littrow configuration [1]. In contrast to the free running spectrak linewidth of the order of 100 Mhz we obtained a band-width of 4.5 Mhz and a tuning range of approximately 25 Ghz. The wavelength scanning

was achieved by a computer controlled voltage ramp to a highly stabilized current source. The whole laser set-up was actively temperature stabilized by a peltier element. The set-up of the magnetron and the laser can be seen in figures 1 and 2.

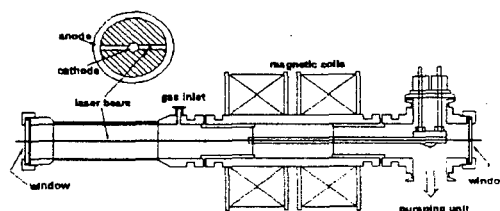


Fig. 1 Set-up of the cylindrical magnetron discharge

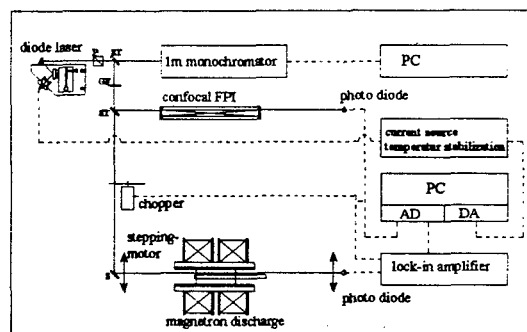


Fig. 2 Set-up of the diode laser system

Experiments

Spectroscopic measurements were done on the argon transitions $3p^4s-3p^4p$ in the range 810-826 nm. To obtain radial density and temperature profiles an efficient least-squares routine [2] was used to fit the Gaussian absorption profiles for the different Zeeman-transitions in a longitudinal magnetic field with known values of the magnetic field, Landé factors [3] and oscillator strenghts. Especially for the Ar 1s₁ level care has to be taken of optical thickness which affected the absorption profile. The model function used in the least-squares routine concerning for this effect is described in [4]. The single Zeeman-transitions are fitted with Doppler profiles. From the Doppler width one can deduce the temperature of the argon atoms.

Results and modelling

A typical example for the radial particle density variation of a Ar resonance level is shown in fig. 3.

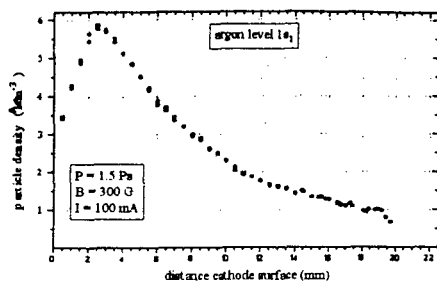


Fig. 3 Radial particle density of Ar $1s_2$ level

The number density raises rapidly near the cathode. From maximum to the anode it decreases smoothly, since the electron density also decreases and their energy gain is significantly reduced in the positive column. The densities of the metastable levels exhibit another decrease, because of diffusion toward the anode due to their long durability. In fig. 4 the different courses can be seen.

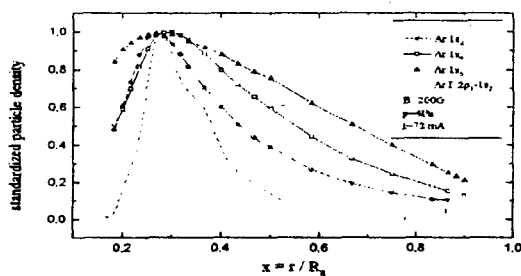


Fig. 4 Comparison of radial courses for three different first excited state levels of argon

The variation of the density profile with applied magnetic field strength is shown in fig. 5 for the Ar $1s_4$ level. The maximum shifts towards the cathode with increasing field strength.

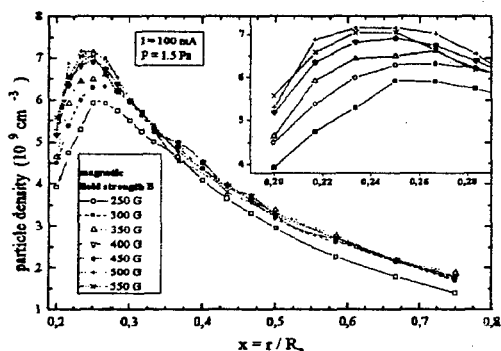


Fig. 5 Radial Ar $1s_4$ particle density in dependence of applied magnetic field strength

To build a theoretical model of the discharge mechanisms we used in a first step the number densities of the metastable $1s_2$ level to gain information about the excitation and deexcitation processes of this level. The modelling of the resonance levels is more complicate because of influence of the escape factors. The radial density profiles of the rare gas metastables in the cylindrical magnetron discharge are calculated from the continuity equation of the radial metastable current density j_m which describes the radial flow of these excited state atoms in dependence of their local source and drain terms

$$\frac{1}{r} \frac{d}{dr} (r j_m) = \sum_i S_{mi} - \sum_j D_{mj}$$

and the diffusion ansatz for the metastable current density

$$j_m = -D_m \frac{dn_m}{dr}$$

To solve this differential equation system, beside the initial and boundary conditions a detailed knowledge of the excitation and deexcitation processes of the metastables is necessary. A summary of these processes is given in [5].

Recognizing only important excitation and deexcitation processes we were able to simulate the metastable distributions with the aid of measured electron energy distribution function.

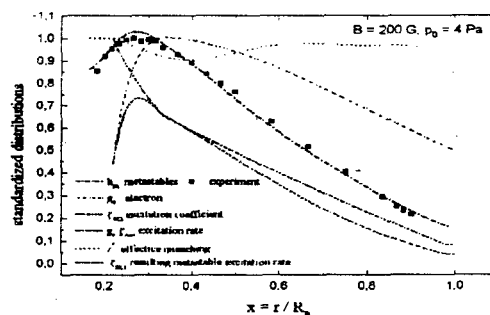


Fig. 6 Modelling of discharge processes

- [1] C. Csambal: doctor thesis, University of Kiel 1996
- [2] K. Jess et al: JQSRT 41(1) 1989, pages 69-78
- [3] C.E. Moore Circular 467, Nat. Bureau of Standards Washington D.C. 1949
- [4] C. Csambal et al: „Interpretation of absorption profiles in the case of longitudinal Zeeman-splitting“, submitted to JQSRT
- [5] J. Delcroix, C.M. Ferreira and A. Richard: Principles of laser plasmas, ed. Bekefi, John Wiley & Sons New York 1976

3D modeling of direct current glow discharges in different cell geometries

Annemie Bogaerts and Renaat Gijbels

Department of Chemistry, University of Antwerp (UIA),
Universiteitsplein 1, B-2610 Wilrijk-Antwerp, Belgium.

Glow discharges are used in a large number of application fields, ranging from the semi-conductor industry (deposition, etching) and the lighting and gas laser industry to analytical chemistry. In the latter application field, the material to be analyzed is used as the cathode of the glow discharge cell, which is sputter-bombarded by ions and atoms from the plasma. The sputtered atoms arrive in the plasma where they can be ionized and excited, and hence detected by mass spectrometry and optical emission spectrometry.

To acquire better results in all these application fields, a good insight in the glow discharge is desirable. We try to achieve this by mathematical modeling. A set of three-dimensional models has been developed to obtain an overall picture of the argon direct current glow discharge, used in analytical chemistry [1,2]. The species assumed to be present in the plasma, are argon gas atoms at rest, uniformly distributed over the discharge, singly charged positive argon ions, fast argon atoms created by charge transfer collisions from the argon ions, argon metastable atoms, fast and slow electrons, and sputtered cathode atoms and the corresponding ions.

These plasma species are described with Monte Carlo models (for the fast plasma particles, which are not in equilibrium with the electric field) and with fluid models (for the slow particles, which can be considered in equilibrium with the electric field).

The fast electrons are treated with a Monte Carlo model; collision processes incorporated are elastic collisions with argon atoms, electron impact excitation and ionization from the argon ground state and from the metastable level, and ionization of sputtered copper atoms.

The behavior of the slow electrons and the argon ions is calculated in a fluid model; the continuity and transport equations are coupled with the Poisson equation to obtain a self-consistent electric field distribution.

Moreover, the argon ions are described with a Monte Carlo model in the cathode dark space (CDS), as well as the fast argon atoms which are created by charge transfer and elastic collisions from the argon ions. The collision processes taken into account are symmetric charge transfer for the argon ions, elastic collisions with argon atoms for both argon ions and fast atoms, and fast argon ion and atom impact ionization and excitation of argon atoms.

The argon metastable atoms are handled with a fluid model, consisting of a balance equation with different production and loss processes.

The thermalization process of the sputtered cathode atoms is described with a Monte Carlo model. The subsequent diffusion, the creation of cathode ions and the transport of these cathode ions, are handled in a fluid model. The ionization processes for the cathode atoms incorporated in the model, are Penning ionization by argon metastable atoms, asymmetric charge transfer by argon ions, and electron impact ionization. Finally, the behavior of the cathode ions in the CDS is also treated with a Monte Carlo model.

All these models are combined into a comprehensive modeling network, and solved iteratively until final convergence is reached, to obtain an overall picture of the glow discharge. The models are developed in three dimensions (or in two dimensions for the fluid models, due to the cylindrical symmetry of the cells investigated), and applied to typical cell geometries used in analytical chemistry.

Typical results of the models are the electrical current when pressure and voltage are given, the density profiles, fluxes and energy distributions of the different plasma species, the potential and electric field distributions throughout the discharge, information about the relative importance of different collision processes in the plasma, the crater profiles and etching rates due to sputtering at the cathode, etc. The results obtained for different cell geometries (e.g., cells with flat and with pin-type cathodes) are compared with each other, to investigate which cell geometries yield the best results.

To test the validity of the models, the results are compared with experimental observations. Laser induced fluorescence spectrometry has been carried out to measure three-dimensional number density profiles of the argon metastable atoms, the sputtered cathode atoms and ions, in a direct current glow discharge in argon with a tantalum cathode [3,4].

For the argon metastable atoms, a Ti:sapphire (continuous) laser, tunable from 780 to 825 nm, was used. The primary excitation line was taken to be the one at 794.818 nm, whereas the 852.144 nm line was used as fluorescence line.

For the tantalum atoms and ions, a dye laser pumped by a copper vapor laser was used. The primary excitation lines were taken to be those at 269.131 nm and 270.28

nm, respectively, whereas the fluorescence was measured using the 358.42 nm and the 304.2 nm lines, respectively. From the fluorescence intensities, the absolute number density profiles were deduced.

Moreover, for the tantalum atoms, atomic absorption measurements with a hollow cathode lamp were performed as well, to check the fluorescence results; the 271.467 nm line was selected for this purpose.

The glow discharge chamber was mounted on a table which could be moved in the x, y and z directions, so that three-dimensional distributions could be recorded. In general, good agreement is reached between the calculated and experimental density profiles (see for example figures 1a and b), which illustrates that our models present already a realistic picture of the glow discharge.

References

- [1] A. Bogaerts, R. Gijbels and W. J. Goedheer: *Anal. Chem.*, **68** (1996) 2296.
- [2] A. Bogaerts and R. Gijbels: *Anal. Chem.*, **68** (1996) 2676.
- [3] A. Bogaerts, E. Wagner, B. W. Smith, J. D. Winefordner, D. Pollmann, W. W. Harrison and R. Gijbels, *Spectrochim. Acta B*, **52** (1997: in press).
- [4] A. Bogaerts, R. D. Guenard, B. W. Smith, J. D. Winefordner, W. W. Harrison and R. Gijbels, *Spectrochim. Acta B*, **52** (1997: in press).

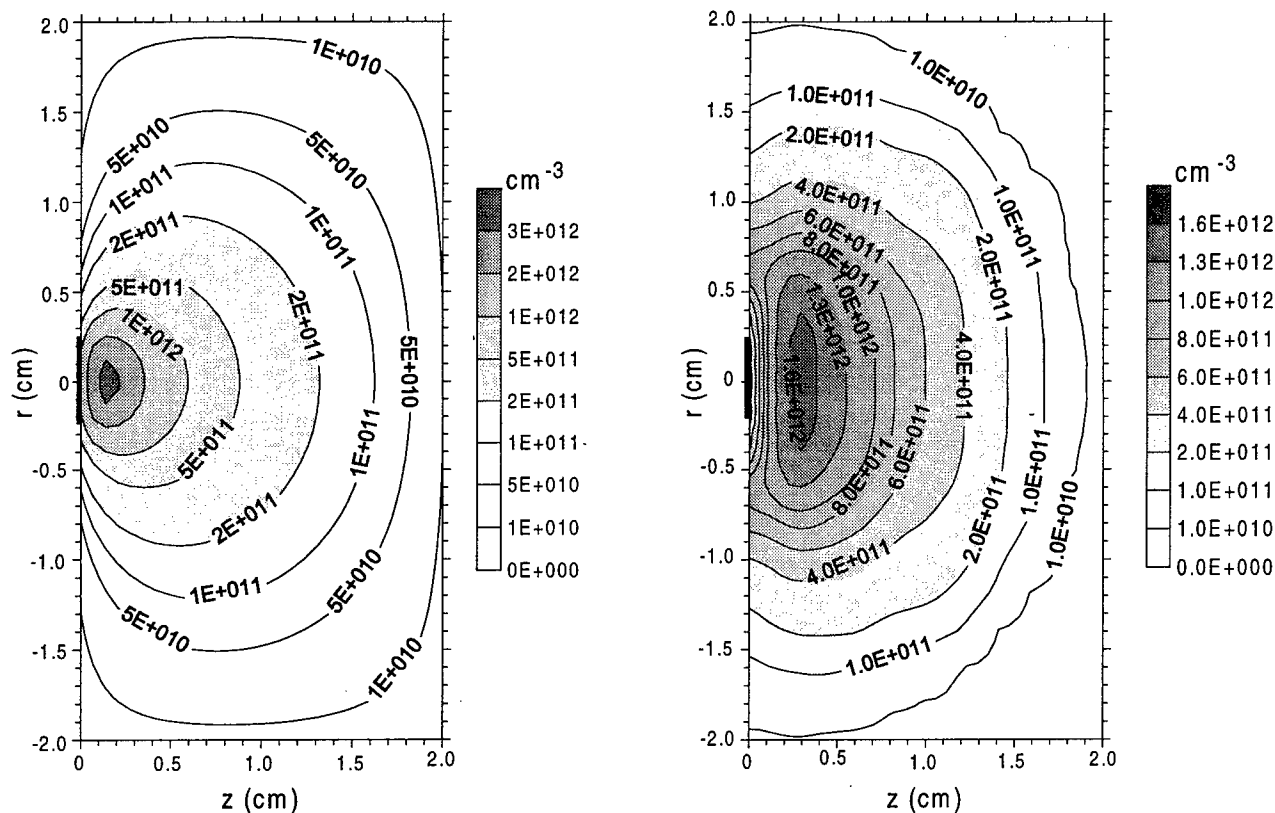


Figure 1: Comparison between calculated (left) and experimentally measured (right) density profiles of the sputtered tantalum atoms, at 1000 V, 1 torr and 2 mA (tantalum cathode in argon).

Statistical Studies of Hollow Cathode Events in a Transient Hollow Cathode Discharge

M. Favre, J. Moreno, P. Choi*, M. Zambra**, H. Chuaqui, and E. Wyndham

Facultad de Física, Pontificia Universidad Católica de Chile

Casilla 306, Santiago 22, Chile

*LPMI, Ecole Polytechnique, Palaiseau 91128, France

** Chilena de Energía Nuclear, Casilla 188-D, Santiago

1. Introduction

It has been found¹ that electric breakdown in a transient hollow cathode discharge (THCD) proceeds through the formation of a moving virtual anode, which propagates from anode towards cathode, under the assistance of electron beams emitted from the hollow cathode region (HCR). In a previous publication² we have presented a statistical study of breakdown formation in transient hollow cathode discharges, where three distinct regimes of ionization growth were identified. 1) initial ionization growth with plasma formation close to the anode, 2) extension of this plasma region towards the cathode, and 3) ionization growth inside the HCR under enhanced field due to the close proximity of the anode potential. Regime 1) was found to be essentially random, whereas regime 2) exhibited a deterministic nature. The statistics of regime 3) indicated more than one competing ionization processes, whose nature was not possible to infer from the data. In this paper we present a further statistical study of ionization processes associated with regime 3). The arrival of the virtual anode at the proximity of the cathode, the formation of plasma inside the HCR, the penetration of the anode potential into the HCR through the cathode aperture and the peak in the high energy component of the electron beams, are time correlated with respect to electric breakdown in the A-K gap. A well defined sequence of events is established and some properties of the characteristic statistics are identified.

2. Experimental Details

The experiments were performed in Hydrogen, at pressures between 50 and 400 mTorr, at 30 kV applied voltage. A-K separation was kept at 10 cm, and a 5 mm cathode aperture was used. Further details of the experimental apparatus has been published elsewhere³. The previous study was based on measurements with a capacitive probe array, whose signal is proportional to the time derivative of the product between the plasma potential and the coupling capacitance of the probe relative to the plasma⁴. In

this case we have used two capacitive Probes, A_C located at 15 mm from the cathode face, inside the A-K gap, and A_{HC} , located inside the HCR, at 4 mm from the back face of the cathode. Plasma formation is monitored by collecting light from a small region inside the HCR, on the axis and at the same position of A_{HC} . The light is fed through an H_α filter into a fiber optic-photomultiplier arrangement. The high energy component of the electron beams is measured with the usual optical fiber scintillator- photomultiplier combination.

3. Experimental Results

Figure 1 shows characteristic signals at 200 mTorr. From top to bottom, the signals are the capacitive probe inside the A-K gap (A_C), the capacitive probe inside the HCR (A_{HC}), the electron beam (e-b), and the H_α emission.

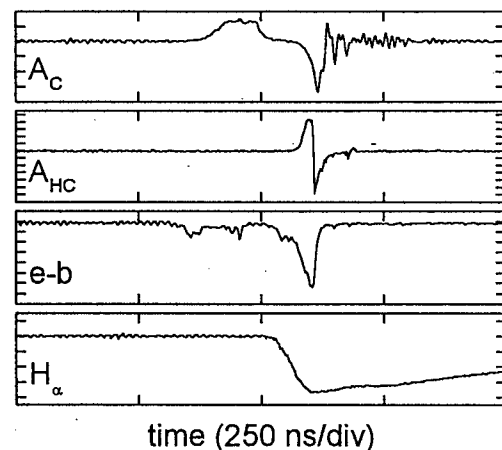


Figure 1: characteristics signals at 200 mTorr

To characterize the different ionization events associated with the signals shown in Fig. 1, the following convention has been adopted: the arrival of the virtual anode at the vicinity of the cathode is marked by the peak value in A_C , the initial growth of a significant plasma density inside the HCR is marked by the onset of signal in H_α emission, the penetration of the anode potential inside the HCR is marked by the peak

value in A_{HC} , and the enhanced period of electron beam activity is marked by the peak value in e-b. Figure 2 shows characteristic times associated with these four ionization events, in the 100 to 400 mTorr pressure range, measured over 150 shots. The size of the distribution is of the same order of the 128 points used in previous studies, which was found to statistically be statistically sufficient for analysis².

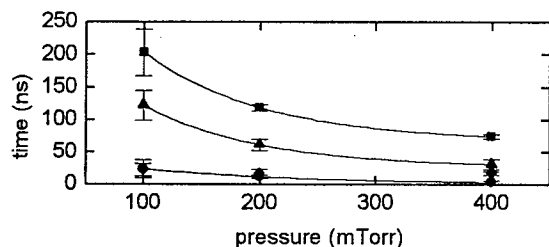


Figure 2: characteristic time intervals for the different ionization events: ■ A_C , ▲ H_{α} , ● A_{HC} , and ◆ e-b.

To visualize the statistical nature of the different characteristic times, the cumulative probability of the time intervals were plotted using the von Laue formalism⁵. The results for the different ionization events are shown in figure 3.

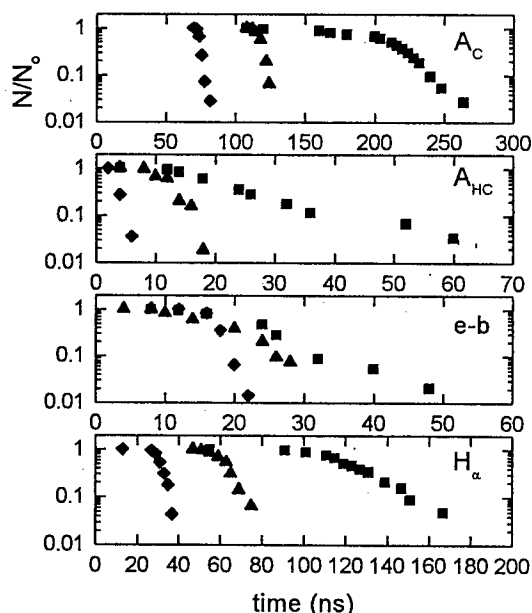


Figure 3: von Laue plots of the different characteristic times: ■ 100 Mtorr, ▲ 200 mTorr, and ◆ 400 mTorr.

At low operating pressure becomes difficult to identify the defining features for each particular event. This is shown in figure 4, for different situations at 50 mTorr.

3. Discussion

For a Gaussian distribution, the von Laue plot fits a parabolic envelope. The characteristic time for the

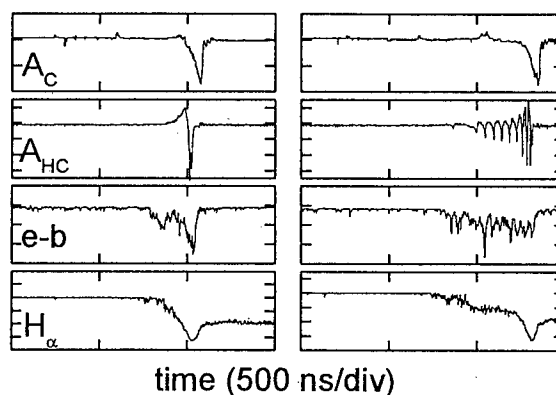


Figure 4: different behaviors at 50 mTorr.

particular process is given by the 50% cumulative data point in the plot. If the 50% cumulative data point intersect of a simple spline fit to the von Laue plots in Fig. 3 is compared with the average values shown in Fig. 2, it is found that the corresponding values are almost identical. This is a good indication that the statistical distribution of times for the different ionization events broadly follows a Gaussian distribution. The data in Fig. 2 establish a clear sequence of events which gives rise to regime 3) presented above. First: the virtual anode arrives to the vicinity of the cathode, second: significant ionization develops inside the HCR, close to the cathode aperture, under an enhanced electric field due to the proximity of the anode potential, third: the anode potential diffuses inside the HCR through the conducting HCR plasma, and fourth: enhanced electron beam emission takes place from the HCR, due to electron acceleration in the enhanced field. At low operational pressure or small cathode aperture the hollow cathode does not play the dominant role in the ionization events, as it is shown in Fig. 4. For the same operational pressure two distinctive situations are observed. On the left hand plot the situation is similar to that shown at 200 mTorr in Fig. 1, whereas in the right hand plot, A_{HC} exhibits a pulsing feature, with a well defined periodicity. This situation can not be described by a simple Gaussian statistics and a plausible explanation is still not available.

Acknowledgments

This work has been funded by FONDECYT grant N° 1950798 and a CNRS-CONICYT collaboration. J. Moreno holds a doctoral studies scholarship awarded by CONICYT.

References

- ¹P. Choi et al., *Appl. Phys. Lett.* **63**, 2750 (1993)
- ²P. Choi et al., *IEEE Trans. Plasma Sci.* **23**, 221 (1995)
- ³M. Favre et al., *IEEE Trans. Plasma Sci.* **23**, 212 (1993)
- ⁴P. Choi and M. Favre., *Rev. Sci. Instrum.* **65**, 2281 (1994)
- ⁵M. von Laue, *Ann. Phys.* **76**, 721 (1925)

Joining Sheath to plasma in a low pressure negative ion dominated discharge

by R N Franklin and J Snell

City University, Northampton Square, London EC1V OHB

There has been a considerable amount of interest in negative ion plasmas arising, particularly, from their use in the plasma processing of semi-conductors. The structure of such plasmas determines the energy of the ions and their spread of energy impacting on the substrate. A number of treatments have shown that in general, there is a central region which is an ion-ion plasma surrounded by an electron-ion sheath [1-7]. The joining of sheath to plasma has been discussed earlier [8] and this paper extends that work giving a method that is capable of generalization for different values of the negative ion/electron density A , the electron temperature/negative ion temperature ϵ and the ratio of Debye length/discharge dimension α . In such a form it can be related to earlier work at low pressures for an electron-ion plasma in the limit $A \rightarrow 0$ [9, 10].

The Sheath Solution

The model for the sheath is the conventional one assuming no generation of charges in the sheath and acceleration of the positive ions in the electrostatic field of the sheath. Scaling the equations to the Debye length so that the linear dimension is $Y = \alpha X$ and defining the potential ψ with respect to the potential at the plasma edge ϕ^* , all potentials being normalized to the electron temperature, gives -

$$\frac{d\psi}{dY} = P, \quad \frac{dP}{dY} = I - N - E, \quad U \frac{dU}{dY} = P$$

and $IU = \text{const.}$

The first two equations are Poisson's equation, the third the ion motion and the fourth the constancy of ion flux. I , N and E are the normalized positive ion, negative ion and electron densities and U is the ion velocity normalized to the Bohm velocity $(kT_e/M)^{1/2}$.

Writing $I = I^*$, $N = N^*$, $E = E^*$ at the plasma 'edge' and $U^2 (= W) = W^*$ we find $IU = I^*U^*$, $W = 2\psi + W^*$.

The equations have a first integral

$$\frac{1}{2} P^2 = I^*U^* \sqrt{(W^* + 2\psi)} - I^*W^* - E^* [1 - \exp(-\psi)] - \frac{N^*}{\epsilon} [1 - \exp(-\epsilon\psi)]$$

The wall is located at the point where $E = \frac{I^*U^*}{\delta}$, δ being given by

$$(M/2\pi m)^{1/2} \text{ according to kinetic theory. Thus } \psi_b = \ln \left(\frac{E^*}{I^*U^*} \right) \text{ where}$$

the starred variables are derived from the plasma solution given below. Given ψ_b we can calculate W_b , (U_b) , E_b and $\left(\frac{d\psi}{dY}\right)_b$.

The plasma solution (quasi neutral approximation $\alpha = 0$)

This has been given previously [4] and can be written as $I = E + N = \exp(-\phi) + A \exp(-\epsilon\phi)$

$$\frac{dU}{dX} = \frac{E}{I} \frac{I + U^2(E + \epsilon N)}{I - U^2(E + \epsilon N)}, \quad (1)$$

$$\frac{d\phi}{dX} = \frac{2UE}{I - U^2(E + \epsilon N)} \quad (2)$$

ϕ^* is given by the zero of the denominator or

$$W^* = \frac{\exp(-\phi^*) + A \exp(-\epsilon\phi^*)}{\exp(-\phi^*) + A \epsilon \exp(-\epsilon\phi^*)} \text{ and}$$

$$= \frac{(1 - \exp(-\phi^*)) + A\epsilon(1 - \exp(-\epsilon\phi^*))}{\exp(-\phi^*) + A \exp(-\epsilon\phi^*)}$$

With ϕ^* known E^* , N^* , I^* can be calculated and used to determine ψ_b , etc, above.

The general plasma solution

In this case, quasineutrality is not assumed and equations (1) and (2) are supplemented by

$$\alpha \frac{d^2\phi}{dX^2} = I - N - E. \quad (3)$$

It can be shown that for there to be a solution symmetric about $X = 0$ i.e. $\frac{d\phi}{dX} = 0$ requires

$$I_0^2(I_0 - A - 1) = 2\alpha^2 \text{ and then the integration from } X = 0 \text{ outwards can}$$

be carried out given that $E_0 = 1$, $N_0 = A$, $U_0 = 0$.

Physical interest centres around values of $\alpha < 10^{-2}$ and this presents numerical difficulties in the sheath region where, in general, there is required to be a transition layer to go smoothly from the plasma to the sheath.

Matching the solutions

For the reasons just given, it is more convenient to integrate the equations (1, 2 and 3) outwards to say $\phi = \phi^*$ and then join them to the modified sheath solution obtained by integrating inwards from the wall, but now allowing for charged particle generation so that $\frac{d}{dy}(IU) = -\alpha E$ replaces $IU = \text{const.}$

This modified sheath solution will correspond to modified boundary values which have to be determined in order to achieve a smooth join to the plasma solution. Thus, we write $\phi_b^I = \phi_b + \Delta\phi_b$, $P_b^I = P_b + \Delta P_b$, $U_b^I = U_b + \Delta U_b$ with $E_b^I = E(\phi_b^I)$ and $I_b^I = E_b^I \cdot S/U_b^I$ and determine $\Delta\phi_b$, ΔP_b , ΔU_b to achieve continuity of I , P and U and their derivatives at $\phi = \phi^*$.

The eigenvalue of the problem, the value of X_b , we know can be written $X_b = X_b^*(A, \epsilon) + X_b^*(\alpha, A, \epsilon) + \alpha Y^*(\alpha, A, \epsilon)$
 $X_b^*(A, \epsilon)$ is given in Table I

A \	1	10	100
0	0.5765	0.5709	0.5708
0.1	0.6279	0.5721	0.5708
1	1.142	0.5881	0.5714
10	6.279	1.870	0.5891
100	57.67	16.27	5.091

Table I

and when $A = 0$

X_b
0 0.5708
10^{-3} 0.5782
10^{-2} 0.6239
10^{-1} 0.9694

Table II

Tables of $X_b^*(\alpha, A, \epsilon)$ and $X_b(\alpha, A, \epsilon)$ will be presented at the conference.

- [1] Ferreira C M et al, 1988. J.Phys.D 21, 1403-13.
- [2] Daniels P G and Franklin R N, 1989. J.Phys.D 22, 780-5.
- [3] Daniels P G et al, 1990. J.Phys.D 23, 823-31.
- [4] Franklin R N and Snell J, 1992. J.Phys.D 25, 453-7.
- [5] Volynets et al, 1993. J.Phys.D 26, 647-56.
- [6] Franklin R N et al, 1993. J.Phys.D 26, 1638-49.
- [7] Franklin R N and Snell J, 1994. J.Phys.D 27, 2102-6.
- [8] Franklin R N and Snell J, 1995. ICPIG XXII, pp101-2.
- [9] Forrest J R and Franklin R N, 1968. J.Phys.D 1, 1357-68.
- [10] Franklin R N and Ockendon J R, 1970. J.Plasma Phys. 4, 371-85.

STUDY OF A NITRIDING PLASMA REACTOR : COMPARISON BETWEEN EXPERIMENTAL RESULTS AND MODELLING OF THE DISCHARGE

Emmanuel GUIBERTEAU, Gérard HENRION, Robert HUGON and Gérard BONHOMME

Laboratoire de Physique des Milieux Ionisés (CNRS URA 835); Université Henri Poincaré - Nancy I,
BP 239, F- 54506 Vandoeuvre les Nancy Cedex, France.
Tél. (+33) (0)3 83 91 20 63 Fax. (+33) (0)3 83 27 34 98. - e-mail henrion@lpmi.u-nancy.fr

Introduction

Though plasma nitriding is a well know process that is widely used at an industrial scale, the processes that occur in the vapour phase and that are responsible for the surface treatment need to be better understood in order to improve the process and allow its control by means of plasma diagnostic measurements.

In this way we carry out experimental investigations by means of optical emission spectroscopy and Langmuir probes of a DC pulsed plasma nitriding reactor (figure 1) working under the following main conditions : Nitrogen gas pressure = 0.4 to 2 Torr (1 Torr=133 Pa); Plasma pulse duration (t_d) = 0.1 to 10 ms; Afterglow (between two successive pulses) duration (t_{pd}) = 0.1 to 100 ms. The two electrodes have 50 mm in diameter. The cathode consists of an iron disk (\varnothing 30 mm) to be nitrided which is inserted in a insulator holder and surrounded by a metallic shield. The gap between anode and cathode is fixed at a value of 40 mm.

Previous results showed that t_d and t_{pd} have to be chosen so that the plasma reactivity be high enough and that the gas cooling during the afterglow be minimised [1,2, 3]. In fact, a long afterglow ($t_{pd} > 5$ ms) leads to a strong cooling of the neutral gas and consequently implies a more difficult plasma inception as well as a change in the discharge structure.

In order to better understand the effect of the energy transfer from the discharge to the neutral gas, we have carried out a comparison between experimental results and those obtained from a numerical modelling of the reactor, that is based on a model developed by P. Bayle and A. Perrin [4]. This one dimensional model is established from the first three moments of the Boltzmann equation coupled with the Poisson equation. The source terms and the transport coefficients are computed taking into account the breakdown of the local field approximation in the cathode fall. This model has been improved by adding a monoenergetic electron beam issued from the cathode in order to take into account the high energy electrons in the cathode fall and in the negative glow.

Results

We present here a comparison between results obtained from the model and from plasma diagnostics for different plasma conditions (pressure ; voltage).

In order to separate the gas heating from the other discharge phenomena, the plasma measurements have been performed with a short plasma pulse ($t_d = 0.1$ ms) and a long afterglow ($t_{pd} = 50$ ms) so that the neutral gas temperature remains constant (equal to the room temperature) during both the discharge and the post-discharge. Under these conditions, the numerical description of the discharge agrees well with the experimental results, as can be seen on figure 2 showing current-voltage characteristics measured and computed for different working pressures.

The optical measurements shown on figure 3a correspond to the space variation of the intensity of the first negative system of N_2 ($N_2^+(B^2\Sigma_u^+, v=0) \rightarrow N_2^+(X^2\Sigma_g^+, v'=0) + h\nu$) averaged over the plasma pulse (100 μ s). The space resolution of the fibre optic is 1.5 mm. These curves point out the extension of the negative glow in the whole interelectrode gap. This phenomenon is clearly increased by increasing the discharge voltage owing to an increase in energy of the electrons issued from the cathode ($z=0$ mm). The same behaviour is obtained from the numerical results (figure 3b) which show a similar decrease of the line intensity from the cathode to the anode. The small intensity peak observed in the numerical simulation can be explained by the fact that in the model, the electrons of the beam are issued from the cathode with a very low energy and are accelerated in the cathode fall, thus getting in the near vicinity of the cathode the energy needed to ionise and to excite the $N_2^+(B)$ level. This is not observed on the experimental curves owing to the poor resolution of the optical device.

In order to take into account the neutral temperature and density gradient in the interelectrode gap, the next step of this work consisting in coupling this numerical model with a two dimensional hydrodynamic model of the neutral gas is under way.

References

- [1] R. Hugon, Thesis (1994) Université Henri Poincaré, Nancy1
- [2] R. Hugon, M. Fabry, G. Henrion: J Phys D 29 (1996) 761
- [3] G. Henrion, R. Hugon, M. Fabry: 5th Int Conf Plasma Surface Engineering, 9-13 Sept 96, Garmisch Partenkirchen (Germany)
- [4] P. Bayle, A. Perrin: Phys. Rev. E 47 (1993) 612

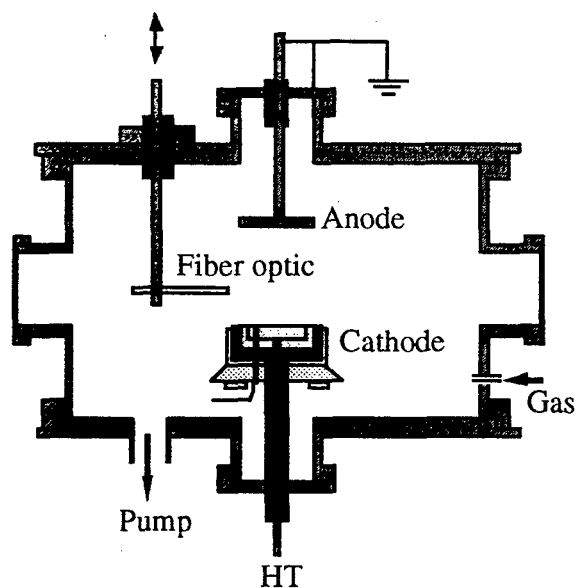
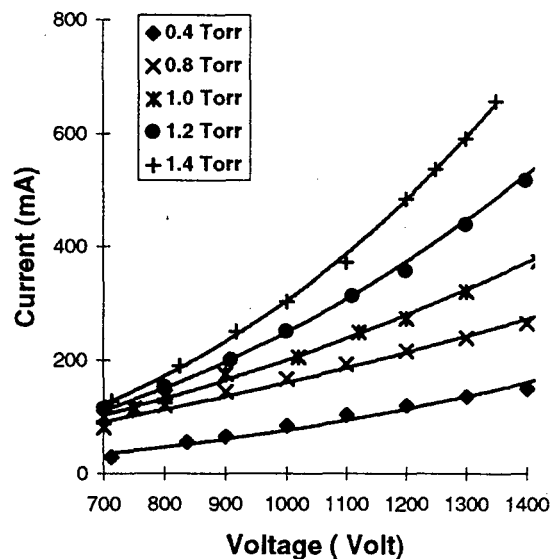
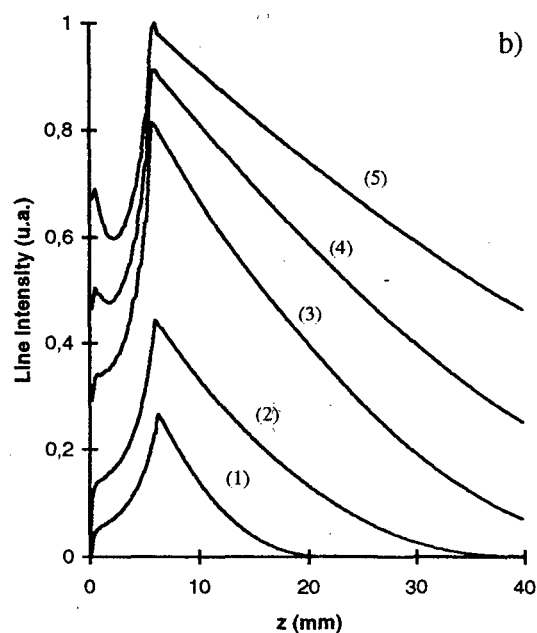
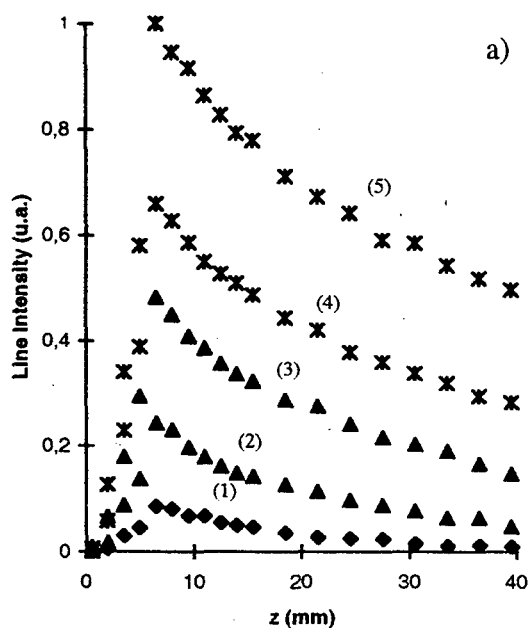


Figure 1: schematic drawing of the experimental reactor

Figure 2: I-V characteristics
Experimental measurement: symbols;
Simulation: solid lineFigure 3: Line intensity of the first negative system of $N_2^+(B)$ (391.4 nm) versus distance from cathode for different discharge voltage : (1) 600 V ; (2) 800 V ; (3) 1000 V ; (4) 1200 V ; (5) 1400 V.

a) Experimental data - b) Numerical data

(Discharge duration : 100 μ s - Post Discharge duration : 40 ms - Pressure : 0.4 Torr)

Study of Radial Profiles of Excited Neutral Species in the Positive Column of the Glow Discharge in Rare Gases

A. Kaňka*, V. Hrachová*, O. Háva* and J. Zicha*

* Department of Electronics and Vacuum Physics, Faculty of Mathematics and Physics, Charles University, V Holešovičkách 2, 180 00 Prague 8, Czech Republic

+ Department of Precision Mechanics and Optics, Faculty of Mechanical Engineering, Czech Technical University, Horská 3, 128 00 Prague 2, Czech Republic

1. Introduction

Low-temperature plasma generated by using discharges in pure rare gases or mixtures containing rare gases forms active medium in gaseous lasers. They are to be applied as carrier gases to various technological applications. Processes occurring in this medium are influenced by the diffusion of the excited neutral species. Assuming the positive column of the glow discharge to be cylindrically symmetrical the radial distribution of different excited neutral atoms in neon, argon and helium has been studied by means of emission spectroscopy. Results achieved contribute to the investigation of the diffusion processes in glow discharge.

2. Experimental

Measurements were realised in the Pyrex glass tube of the U-shape whose length is 700 mm. The central part of the discharge tube (length 390 mm, internal diameter 31.8 mm) is equipped with Pyrex head-on plane windows. The original scanning system for the investigation of the radial alterations of the intensities of the spectral lines is described in [1] in greater details. This arrangement consisting of the negative and positive cone mirrors (apex angle 90°) selects from all rays emitted by positive column rays parallel to the optical axis having the form of the hollow cylinder whose base is a circular zone concentric with the axis of the central part of the discharge tube. Both optical surfaces of the mirrors are coated with aluminium. Having the thickness of the testing cylinder about 10 % of the internal diameter of the discharge tube D the same spectrum is to be obtained compared to the case when the testing bundle has the form of the cylinder with the diameter $0.1D$ but the intensity is increased by the factor of $80r/D$ (r is the radius of the wall of the testing cylinder). The optical system improves total balance of power of the radiation detected especially from the parts of the discharge tube near the wall. The motion of the mirrors in the direction of the common axis of symmetry is related by a linear function to the radius of the zone which forms the base of the testing bundle. The thickness of the zone is to be altered in the range from 0 to 4 mm by two diaphragms. The spectral analysis of the radiation was performed by means of the monochromator SPM 2 (produced by Zeiss Jena) equipped with the grating having the groove density

651 grooves per mm. Monochromatic radiation is detected by the photomultiplier tube Hamamatsu R 928. Spectral resolution 0.8 nm was achieved. Radial scanning was performed with the step 2 mm. The experimental arrangement is to be used for radiation whose wavelength ranges from 350 to 850 nm. Spectral range is limited by the transmittance of the window material and by radiant sensitivity of the multialkali photocathode of the photomultiplier tube. Pressure ranges from 0.5 to 6 Torr and discharge currents do not exceed 30 mA. Spectrally pure gases manufactured by Moravské chemické závody Ostrava were employed for filling discharge tube.

3. Results and discussions

The course of the radial profile of the persistent neon line 585.3 nm[2] is shown in Figure 1. Intensities are related to values at the axis of the central part of the discharge tube. Radial positions are related to inner radius $R = 15.9$ mm. The excited states of the neutral neon atoms whose deexcitation is associated with the emission of the lines investigated (spectral range 580-725 nm) are mainly formed in collisions of the neon atoms in fundamental quantum state with electrons (i.e. $e + \text{Ne} \rightarrow e + \text{Ne}^*$). Considering pressures up to 2 Torr pressure alteration of the radial profile of the electron density is negligible [3]. For this reason the radial diffusion of this excited state of neon depends on pressure slightly.

The radial alterations of the intensity of the line 471.3 nm corresponding to deexcitation of the excited neutral atom of helium are plotted in Figure 2 for pressures 0.5, 1 and 2 Torr (discharge current 20 mA). The pressure dependence of the radial profile of the intensity can be explained by the changes of the diffusion coefficient which is inversely proportional to pressure. Assuming higher pressure excited helium atoms collide with neutral species more frequently. This process results in deexcitation (i.e. $\text{He}(4^3\text{S}_1) + \text{He} \rightarrow \text{He}(2^3\text{P}_{1/2}) + \text{He}$).

Investigating positive column generated in pure argon ionizing waves in the space from which radiation is collected by the optical system were detected. This instability influences the radial profile of the lines, especially at the radial position $r/R = 0.31$. Figure 3 exhibits the radial profile of the intensity of the persistent argon line 696.5 nm[2] in the pressure range

1 - 6 Torr. The courses are practically the same for discharge currents 20 and 30 mA.

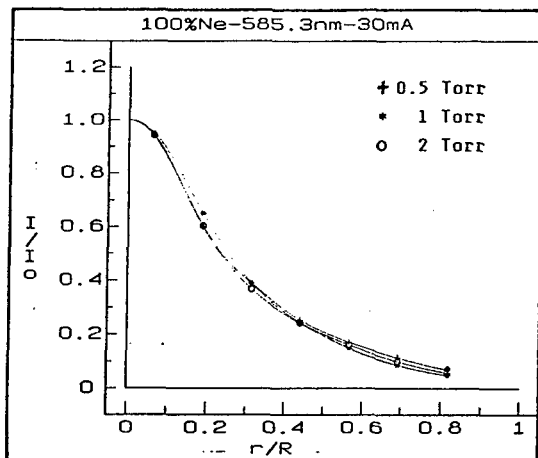


Fig. 1: Radial intensity profile of the persistent line 585.3 nm of the neutral neon atom (transition $3s'[1/2]-3p'[1/2]$, energy of initial state 18.96 eV, energy of final state 16.85 eV, see e.g. [4]).

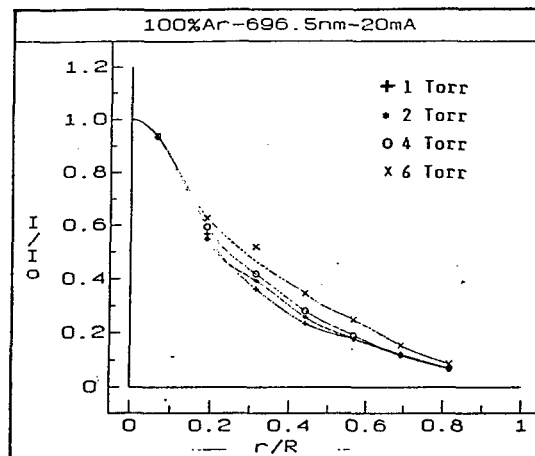


Fig. 3: Radial intensity profile of the persistent line 696.5 nm of the neutral argon atom (transition $4s[1/2]^0-4p'[1/2]$, energy of initial state 13.33 eV, energy of final state 11.55 eV, see e.g. [4]).

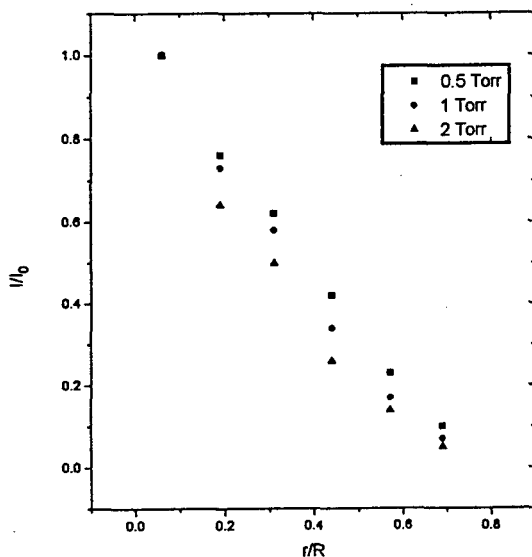


Fig. 2: Radial intensity profile of the line 471.3 nm of the neutral helium atom (transition $4^3S_1-2^3P_{1/2}$, energy of initial state 23.58 eV, energy of final state 20.96 eV, see e.g. [4]).

4. References

- [1] J. Zicha, V. Hrachová, A. Kaňka, Š. Němcová: Proc. 41th International Scientific Colloquium, Technical University of Ilmenau(1996)405
- [2] R.W.B. Pearse, A.G. Gaydon: The Identification of Molecular Spectra, Whitefriars Press Ltd., London, 1965
- [3] V. Hrachová, A. Kaňka: Acta Phys. Slov., 41(1991)293
- [4] A.R. Striganov, N.S. Sventickij: Tables of Spectral Lines of Neutral and Ionized Atoms, Atomizdat, Moskva, 1966

Acknowledgements

The research was financially supported by the grant of the Charles University GA UK-15.

Influence of the neon and argon on the oxygen spectra in the glow discharge

V. Hrachová and A. Kaňka

Department of Electronics and Vacuum Physics, Faculty of Mathematics and Physics, Charles University
V Holešovičkách 2, Prague 8, Czech Republic

1. Introduction

The spectra emitted by glow discharge positive column in the pure oxygen and in its mixtures with neon and argon are studied. In this paper we are concentrating on the dominant wave lengths of the pure oxygen in the glow discharge. It means both the lines corresponding to transition between atomic oxygen levels (777.4 nm and 844.7 nm) and the atmospheric A-band corresponding to neutral oxygen molecule transitions and represented by its head (759.4 nm) and origin (761.9 nm) are studied. Influence of neon and argon on these lines in the dependence on the pressure, discharge current and portion of rare gas in the mixture is analysed.

2. Experimental

All our measurements were realised in the discharge tube of U - shape, the length of which was 700 mm and the internal diameter 32 mm. The central part of the discharge tube, 390 mm long, had Pyrex head-on windows. The radiation across the discharge tube in the direction of the axis of symmetry was collected by a positive lens to the entrance slit of the monochromator and after that was detected by photomultiplier tube. Range of analysed wave lengths was from 350 nm to 850 nm. Our study was realised for the pressures up to 800 Pa and discharge currents up to 30 mA. Under such discharge conditions the radiant power was very weak (mainly in the pure oxygen) and only arrangement described above and relatively large slits on monochromator allowed us to detect sufficient signal of the lines and bands. The spectral resolution was 0.8 nm. In the mentioned discharge condition in the pure oxygen there are exist two forms of the positive column - H form with higher axial electric field and T form with lower one [1]. If both forms in the discharge tube exist simultaneously, it is not possible to use our experimental device for optical analyses. For this reason we will focus on such pressures, discharge currents and composition of the oxygen rare gas mixture, where the H form is in the all straight part of the discharge tube.

3. Results and discussion

3.1 Pure oxygen

Considering our experimental conditions, T form of the positive column exists for 800 and 530 Pa simultaneously with the H form so that, our analyses will be concentrated on the pressures 65, 130 and 270 Pa. Dependence of the relative intensity of the head and

origin of the A-band it is seen in the figure 1. The increasing intensity of both lines is evident if discharge current or oxygen pressure are increased.

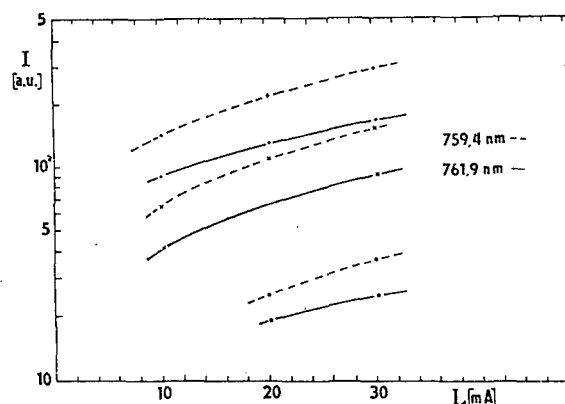


Fig. 1: Dependence of relative intensity of the head (759.4 nm) and origin (761.9 nm) of A-band on oxygen pressure (•..65 Pa, ×..130 Pa, +..270 Pa) and discharge current.

Because excited oxygen molecule is created by direct electron impact $e + O_2 = e + O_2^*$, the increase of A-band characteristic lines is connected both with increasing electron density with pressure and with discharge current in the discharge; and with increasing concentration of the neutral molecules with pressure. Similar dependence of the relative intensities for lines 777.2 nm and 844.7 nm is shown in the figure 2.

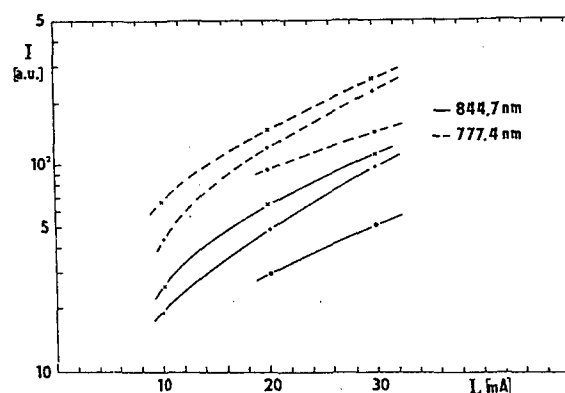


Fig. 2: The dependence of relative intensity of lines 777.4 nm and 844.7 nm on the discharge current and oxygen pressure (•..65 Pa, ×..130 Pa, +..270 Pa).

These triplets correspond to the deexcitation of the oxygen atom, whose creation is predicted or by dissociative excitation $e + O_2 = e + O + O^*$ or by direct excitation of oxygen atom $e + O = e + O^*$ [2]. From the figure 2 it is seen that the greatest relative intensity corresponds to the pressure 130 Pa for both lines. It follows that additional contribution of oxygen causes the lower level of dissociative excitation and also of dissociation.

3.2 Mixtures

The same lines in the mixtures with neon or argon were analysed, instead of origin of A-band by mixtures with argon, where the intensive argon lines near its wave length are more significant. It was possible to detect by means of our optical arrangement also our analysed lines at higher pressures with higher portion of inert gas, where T-form did not exist more. It is possible to say generally that lines of oxygen atoms are very intensive in the mixtures, argon influence being more significant. On the other hand the atmospheric band is less important, for instance for 130 Pa in the mixture with argon is practically undetected. It means that inert gas helps to dissociate the oxygen. Situation for head of A-band is depicted in the figure 3 for the discharge current 20 mA. The same results for measured 10 and 30 mA were obtained.

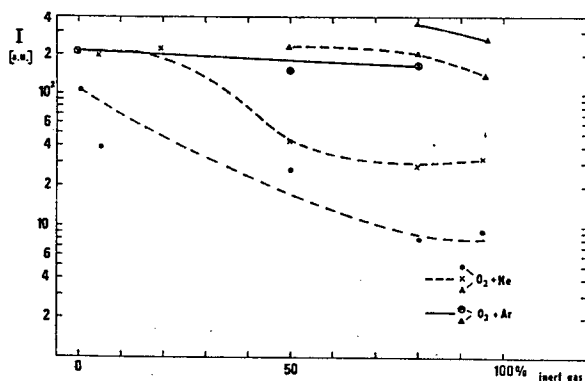


Fig. 3.: Dependence of the relative intensity of the head of A-band (759.4 nm) on the portion of neon and total mixture pressure (●..130 Pa, ×..270 Pa, ▲..530 Pa) and on the portion of argon and total mixture pressure (⊗..270 Pa, Δ..530 Pa).

From this figure it is seen that relative intensity of the A-band head decreases relatively slowly with increasing portion of the inert gas. Similar situation was found for the origin of this band in the mixture with the neon. It can be explained by the fact that upper level for A-band is highly populated and has the long radiative life time [3]. In the figure 4 the situation for the line 777.4 nm of atomic oxygen is shown for the discharge current 20

mA and mixture pressure 270 Pa. The same dependence was found for the line 844.7 nm.

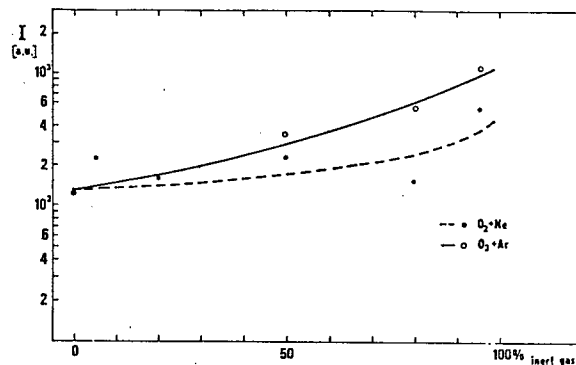


Fig. 4: Relative intensity dependence of the oxygen atom line 777.4 nm as a function of portion of neon (●) and argon (°) for 270 Pa and 20 mA.

From this figure it is seen that inert gas causes decrease of excited oxygen atoms. Similar situation for others measured pressures and discharge currents was found, not only for line 777.4 nm but also for line 844.7 nm. There are several mechanisms for explanation of this effect. Instead of higher dissociation degree, it is possible also transfer of excitation. This fact corresponds with the fact that influence of the argon is more significant due to its levels above 11 eV, which is near the uppers levels of these triplets [4].

4. References

- [1] R. Seeliger, A. Wichmann : *Annalen der Physik*, 9 (1951) 235
- [2] R.W. Dreyfus, Y.M. Jasinski, R.E. Walkup : *Pure & Applied Chemistry*, 57 (1985) 1265
- [3] M. Touzeau, M. Vialle, A. Zellagui, G. Gousset, M. Lefebvre, M. Pealat : *J.Phys. D: Appl.Phys.*, 24 (1991) 41
- [4] G. Gousset, A.R. De Souza, J. Jolly, M. Touzeau, M. Vialle : *Proc. 9th ISPC, Pugnuchiuso, Italy* (1989) 223

Acknowledgements

The research was supported by grant of Charles University GAUK-15 and by grant of EC Copernicus No. CIPA-CT94-0183.

Radial Dependence of Electron energy in He and N₂ Positive columns

T. Kimura, Y. Ieda and K. Ohe

*Department of Systems Engineering, Nagoya Institute of Technology
Showa-ku, Nagoya, 466, Japan*

1 Introduction

Recently, theoretical and experimental investigations of inhomogeneous plasmas which include RF and DC glow discharges have been developed, being related to the electron kinetics [1,2]. For example, such an inhomogeneity can be observed in the radial direction of DC positive column which is classic and representative. At present time, a nonlocal kinetic approach proposed by Bernstein and Holstein [3] has been used to describe the electron behavior in collisional DC discharge plasmas. Electron behavior in collision-dominated plasma is governed by the collision processes. The electron momentum is easily relaxed within a short length corresponding to the electron mean free path, while the electron energy is relaxed in a distance much longer than the mean free path [2].

The bulk of EEDF in He discharges nonlocally depends on the ambipolar potential, since the majority electrons can behave collisionless-like due to a long energy relaxation length. On the other hand, the bulk of EEDF in N₂ discharges may be locally determined by the local electric field due to a short relaxation length related to the vibrational collision processes. Such a difference of the electron behavior may be attractive from view point of the physical interest.

The aim of the present paper is to investigate the radial dependence of EEDF in N₂ and He positive columns.

2 Experimental

The discharge is produced in a 1.8 cm- ϕ (2R) glass chamber, in which the gas pressure p is from

0.32 Torr to 1.0 Torr and the discharge current I_d range from 20 mA to 100 mA. A single probe (0.08 mm- ϕ and 1 mm in length), which is movable, is installed to detect the EEDF. According to Druyvesteyn formula, the EEDF can be deduced by using a finite impulse response filter method [4].

3 Results and Discussion

Typical radial dependences of the electron energy probability function (EEDF) in He and N₂ of $p=0.96$ Torr and $I_d=80$ mA with respect to the total energy are shown in Figs. 1(a),(b), respectively. In He discharges, the bulk of the EEDF at any radial position r are shifted by the corresponding DC ambipolar potential, since the energy relaxation length for electrons with the energy below 20 eV is much longer than the tube radius. The electron behavior is described by the non-local kinetics based on the potential, while there is ambiguity in applying the non-local kinetics to electrons with the energy higher than 23 eV.

On the other hand, the bulk of EEDF measured at r is independent of the ambipolar potential, while its tail ($\varepsilon \geq 4$ eV : ε the electron kinetic energy) depends on the potential, since the relaxation length for low energy electrons which may be correlated with the vibrational collision, is much shorter than the tube radius and that for high energy electrons ($\varepsilon \geq 4$ eV) is much longer. Thus, the behavior of electrons with such a low energy can be determined by the local electric field. However, the effective electron temperature T_{eff} , which can be estimated by the measured slope of the bulk ($d \log(f(r, \varepsilon))/d\varepsilon$: $f(r, \varepsilon)$ the

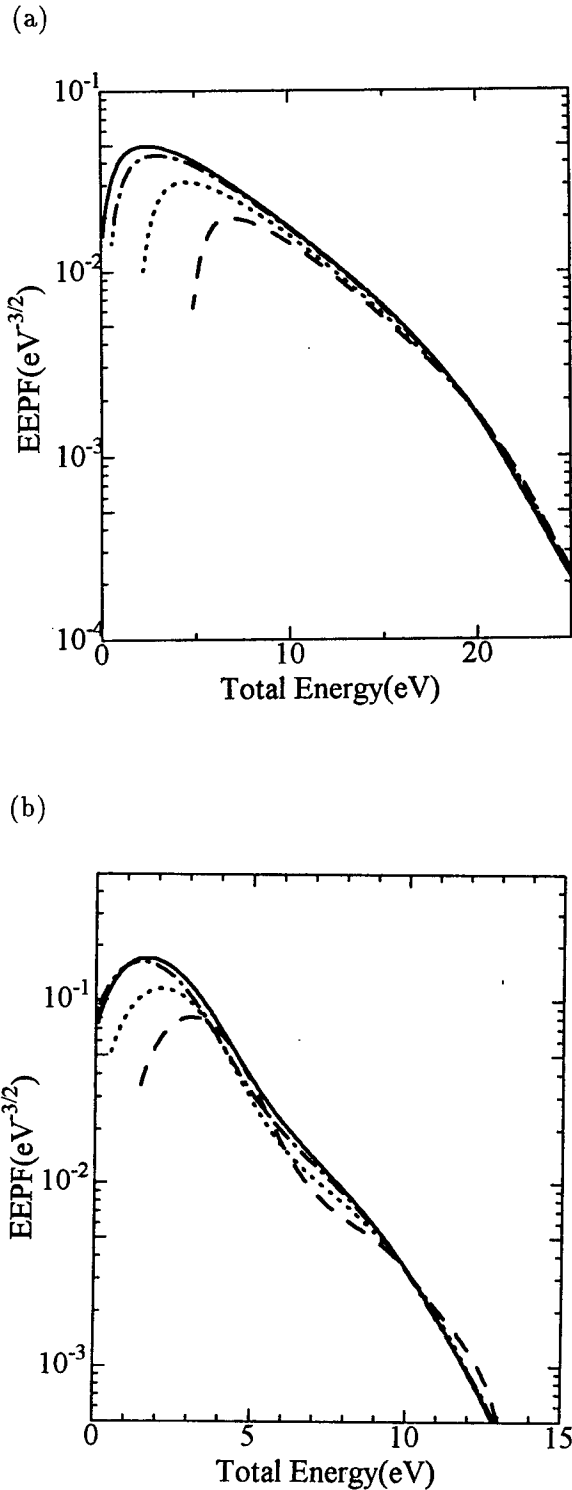


Fig.1 Radial dependence of the EEPF for He in (a) and N₂ in (b), where $r=0, 2, 4$ and 6 mm are shown by —, — · —, ···, — —, respectively.

local EEPF), gradually decreases from the axis to the wall, as shown in Table 1. This phenomenon may be caused by the diffusion cooling and the decrease of the superelastic collision towards the wall. Further experimental and theoretical investigations for the variation of effective temperature towards the wall will be necessary.

Table 1. Radial variation of T_{eff} (eV), where $I_d=40\text{mA}$, 80mA and $p=0.96$ Torr

$r(\text{mm})$	$T_{eff} _{40\text{mA}}$	$T_{eff} _{80\text{mA}}$
0	1.82	1.99
2	1.76	1.96
3	1.76	1.91
4	1.75	1.78
5	1.74	1.68
6	1.64	1.55
7	1.42	1.22

4 Concluding remark

In the He discharge, the EEDF measured at r can be approximated by shifting the EEDF measured at the tube axis by the ambipolar potential from the axis to the wall except for its tail. On the other hand, the bulk of EEDF measured at r in the N₂ discharge is independent of the ambipolar potential, while its tail ($\varepsilon \geq 4$ eV) depends on the potential.

References

- [1] V.I.Kolobov and V.A.Godyak: IEEE Trans. Plasma Sci. 23 (1995) 503.
- [2] U.Kortshagen, C.Busch and L.D.Tsendin: Plasma. Sources Sci. Technol. 5 (1996) 1.
- [3] I.B.Bernstein and T.Holstein: Phys. Rev. 94 (1954) 1475.
- [4] T. Kimura, A. Yoneya and K. Ohe, Jpn. J. Appl. Phys., **30**, (1991) 1877.

THE STRUCTURE OF LOW PRESSURE HIGH-CURRENT DIFFUSE DISCHARGE.

Fetisov I.K., Khodachenko G.V., Kurnaev V.A., Mozgrin D.V. and Savjolov A.S.

Department of Plasma Physics, Moscow State Engineering and Physics Institute.
115409 Moscow, Russia

Introduction

The structure of the high-current diffuse discharge in magnetic field is considered in this work. Experimental research of the powerful quasi-stationary discharge in magnetic field [1] allowed to establish existence of steady state forms which did not transform in arc at high current density: 1) high-current magnetron discharge, having an increasing volt-ampere characteristics and the current up to 250 A (cathode current density up to 25 A/cm²) and 2) high-current diffuse discharge, existing at currents up to 2000 A (current density up to 90 A/cm²). The later form of discharge had burned at constant voltage of 75-120 V, which practically did not depend on current, pressure, and geometry of crossed electrical and magnetic fields. Life time of the discharge was 1.5-40 ms.

Model of the discharge structure.

Analysis of the experimental volt-ampere characteristics at various pressures, inductions of a magnetic together with analyses of parameters of discharge plasma (density and electron temperature) allowed to assume, that the structure of the high-current diffuse discharge essentially differs from that of both magnetron discharge, which is characterized by prevalence secondary (photo- and ion - electron) emission from the cathode and Townsend mechanism of ionisation, and arc discharge, which is characterized by prevalence thermal-autoelectronic emission and thermal mechanism of ionization.

From experimental data follows, that transformation of magnetron discharge in high-current diffuse discharge is possible if the density of plasma can reach some critical value ($n_c \approx 5 \cdot 10^{13} \text{ cm}^{-3}$) corresponding to small Debye's radius. Comparison of the thickness of positive charge layer near the cathode surface

$$l_c = \left(\frac{8}{9}\right)^{\frac{1}{2}} \left(\frac{M}{m}\right)^{\frac{1}{2}} \left(\frac{eU_c}{kT_e}\right)^{\frac{1}{2}} \left(\frac{kT_e}{4\pi e^2 n}\right)^{\frac{1}{2}}, \quad \text{which}$$

corresponding to the electron density of discharge transformation to the high-current diffuse mode, with the free path between electron-atom or electron-ion collisions $\lambda_{e-am,e-i}$ (high pressure) and the height of electrons trajectory over the cathode surface when moving in cross fields $h_e = \frac{2mc^2}{e} \frac{\langle E_c \rangle}{B^2}$ (low pressure), allows to suggest that the cathode layer is collision free.

Increase of the plasma density with current even strengthens the condition $l_c < \lambda_{e-am,e-i} h_e$

Puasson equation for collisionless layer of the discharge can be written as:

$$\begin{aligned} -\frac{d^2 U}{dx^2} &= 4\pi e(n_i - n_e), & j_e &= Sj = en_e V_e, \\ j_i &= (1-S)j = en_i V_i, & V_e &= \left(\frac{2eU}{m}\right)^{\frac{1}{2}}, \\ V_i &= \left(\frac{2e(U_c - U)}{M}\right), & S &= \frac{\gamma}{1+\gamma} = \frac{j_e}{j_e + j_i} \end{aligned}$$

where $\gamma = \gamma_w + \gamma_{hv}$ - coefficient of secondary emission, caused both by ion - electron and photo electron emission. This equation determines intensity of electric field near the cathode surface and magnitude of the cathode potential [2]:

$$\begin{aligned} E_c &= \left\{ \frac{16\pi}{(2e)^{\frac{1}{2}}} \left[(1-S)M^{\frac{1}{2}} - sm^{\frac{1}{2}} \right] \right\}^{\frac{1}{2}} U_c^{\frac{1}{4}} j^{\frac{1}{2}}, \\ U_c &= \left\{ \frac{12\pi}{(2e)^{\frac{1}{2}}} \left[(1-S)M^{\frac{1}{2}} - sm^{\frac{1}{2}} \right] \right\}^{\frac{2}{3}} j^{\frac{2}{3}} U_c^{\frac{1}{3}} \end{aligned}$$

From probe measurements follows that dependence of plasma density on the discharge current is practically linear. Besides, it follow that $l_c \approx 1/(n_c^{\frac{1}{2}})$,

i.e. $U_c \approx j^{\frac{2}{3}} \{1/j^{\frac{1}{3}}\}^{\frac{2}{3}}$ does not depend on j , as is observed experimentally. Presence of the collisionless cathode layer make impossible prevalence of the Townsend mechanism of ionization in the cathode fall potential. This allows to assume that the basic ionization processes go in the discharge plasma.

Balance of power in the high-current quasi-stationary diffuse discharge can be written as

$$I_d U_d = \frac{I_d}{e} \left(E_i + \frac{3}{2} kT_e + \frac{3}{2} kT_i \right) + P_g + P_r,$$

where $I_d U_d$ - total power deposition in the discharge

volume; $\frac{I_d}{e} \left(E_i + \frac{3}{2} kT_e + \frac{3}{2} kT_i \right)$ - power spent on ionization, and removed from the discharge area by charged particles; P_g - power, spent for heating of gas; P_r - power of radiation; E_i - ionization energy. Following [3] power of radiation can be written as

$$P_r = VJ = 1.95 \cdot 10^{-34} T_e^{1/2} Z n_i n_e \exp \left\{ \frac{E_g}{kT_e} \right\} [\text{kW/cm}^3]$$

where V - volume, occupied by plasma of the discharge, J - integrated radiation ability including collision radiation, recombination radiation and radiation in the linear spectrum; E_g - binding energy of the lowest level.

From the balance of energy in the discharge and quasi-stationary equation of thermal balance of gas in discharge area it follow

$$P_g = (T_0 - T_g) M_g C_p \nu_T$$

That is, the temperature of ions and gas can reach significant value

$$T_g = \frac{I_d U_d - \frac{I_d}{e} (E_i + \frac{3}{2} k T_g) - P_r}{\frac{\lambda \pi^2 S}{L} + \frac{3}{2} k \frac{I_d}{e}}$$

where T_g - quasi-stationary temperature of gas, T_0 - temperature of electrodes, M_g - weight of gas in the discharge volume, C_p - heat capacity at constant pressure,

$\nu_T = \chi / \Lambda_T^2$ - heat removal frequency, $\chi = \frac{\lambda}{M n_g C_p}$,

Λ_T - characteristic heat removal length, λ - thermal conductivity of gas temperature T_g , M - atomic weight; n_g - concentration of gas molecules S - cross-section. For plane layer with distance between electrode L , Λ_T equals L/π .

For example for typical parameters of the high-current diffuse discharge, $I_d = 540$ A, and $U_d = 90$ V, $p = 0.1$ torr, $B = 0.8$ kGs, temperature of gas with taking into account of radiation, is $T_g = 3.2$ eV, while for $I_d = 1500$ A, $T_g = 5.4$ eV.

These values of temperatures and the respective plasma densities allow to assume, that the basic mechanisms of ionization in the high-current diffuse discharge are ionization by fast electrons in bulk plasma and thermal ionization.

Determination of the average density of the discharge current.

One of major parameters, characterizing the mechanism of the discharge maintenance and the electron emission from the cathode is the cathode current density (j_c). The value of j_c was determined from simultaneous measurements of time dependencies of the current and voltage of the discharge combined with photography of the discharge area using the high-speed frame camera in the shot mode of time scanning (resolution 50 μ s/shot). The measurements were carried out in the range of current 5+2000 A in the planar magnetron in argon.

In the area of the preliminary discharge, the luminescence occupies a thin ring with $S \approx 3.5$ cm² corresponding to area of maximum induction of the magnetic field. In case when the discharge transforms in the high-current diffuse mode, the luminescence area becomes a homogeneous ring or sector with $S \approx 20+40$ cm². The density of the cathode current in this case becomes as high as reaches 40+90 A/cm².

The high-speed photography allows to establish difference between arc discharges, characterized by a luminescence having the form of bright point in the region of the cathode spot, development, which is moved by the magnetic field, and high-current diffuse discharge having the homogeneous luminescence that allows to limit mean density of the cathode current down to 90 A/cm².

Spectral structure of radiation from the plasma high-current diffuse discharge.

Spectral structure of radiation from plasma of quasi-stationary high-current diffuse discharge of low pressure was determined. The discharge was formed in the magnetic field with the induction down to 1 kGs in argon at pressure down to 1 torr and had the following parameters: the current 350+800 A, voltage - 90 V, pulsing power 30+80 kW, density of plasma (2+6) 10^{14} cm⁻³. The measurement was made in the range of wave lengths 440+900 nm. The experimental spectrum did not contain lines which belonged to the material of the cathode (Cu) or other metal impurity. This result shows that there was neither significant cathode sputtering nor evaporation of the electrodes materials. This means that the average energy of ions, accelerated by the discharge cathode layer less that the sputtering threshold, and the surface temperature of the cathode (average, and in period of a current pulse) was less then the evaporation temperature.

Conclusions about limitations of bought cathode current density and cathode surface temperature together with calculations of the electrical field intensity near the cathode surface allowed to conclude that contribution of thermal autoelectron emission in the net emission current is small and can be excluded as the prevailing mechanism of maintenance of the high-current diffuse discharge.

Conclusion.

From experimental results and model estimations it follows that the structure of the high-current diffuse discharge is characterized by

1. Existence of a collisionless cathode layer and area a bulk plasma, being an active zone of the discharge with prevalence of thermal mechanism of ionization;
2. Prevalence of the mechanism of secondary (photo- and ion - electron) cathode emission, that distinguishes it from classical magnetrons and arcs of the discharges.

This work supported by Russian Foundation of Basic Researches (grant 95-2-04429a).

References.

1. Mozgrin D.V., Fetisov I.K., Khodachenko G.V. " Physics of plasma " т.21, n5, p. 422-433.
2. Granovsky V.L. An electrical current in gases. M.: Science, 1971
3. Raiser J.P. Physics of the gas discharge. M.: Science, 1987.

Penning discharge in regime of RF autogeneration.

I.V. Vizgalov, G.S. Kirnev, V.A. Kurnaev, D.V. Sarytchev, A.S. Savjolov
Moscow Engineering Physics Institute, Moscow 115409, Russia

It has been reported previously [1,2], that under certain conditions an interaction of negatively biased electrodes with plasma flows produced by means of the electron beam driven discharge sets unstable. The main factor determining the instability development is bombardment of the surface exhibiting enhanced secondary emission with superthermal electrons. So, the current versus voltage characteristic (CVC) for such an electrode has a strongly marked current drop (similar to N-shaped CVC of tunnel diodes but expanded by 3-4 orders of I-U magnitudes). Tuneable RF high voltage electromagnetic oscillations can arise in the coupled LC-contour. Superthermal electrons occur not only in beam-plasma discharges. They are pronounced in glow discharges and particularly, in Penning discharge. So, it is of interest to investigate the possibility of self-excitation of RF oscillations in this type of discharge. The test cell with Penning geometry has been constructed to meet the conditions for autogeneration of RF oscillations in the cold cathode circuit. Its concept and experimental results on transitions to self-maintained auto-oscillating regimes are presented.

The schematic diagram of the experimental apparatus is shown in fig.1a. It consists of the cylinder anode (50 mm in diameter and 800 mm long), water cooled magnetic coils,

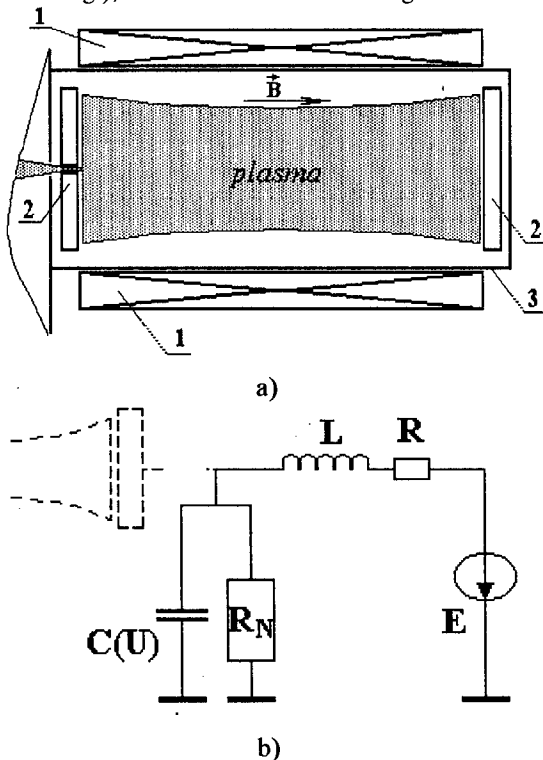


Fig.1. a) Schematic diagram of the experimental Penning cell (1 - magnetic field coils, 2 - cathode plates, 3 - vacuum vessel); b) equivalent electrical scheme.

two cathodes with removable and water cooled plates. The working gas pressure can be varied in the range 10^{-3} -10 Pa, the maximum magnetic field is 0.2T. Cathodes have separate biasing supplies and the anode is under ground potential. Cathode currents and voltages can be observed on the oscilloscope monitor by means of Rogovsky coils and RF voltage dividers. Discharge plasma parameters are controlled by Langmuir probes, mass- and energy analysers (not shown). One of the cathodes has a diagnostic orifice.

The operation principle of the apparatus can be cleared up by a simplified model, if at first the initial mechanism of discharge excitation is left out and cathodes are considered under bombardment of ternary flows: ions, thermal electrons ($T_e \sim 10$ eV) and superthermal electrons with energies distributed in the range of some hundreds of eV. The cathode plate is assumed to be made of a material with enhanced electron-electron secondary emission. Notably high secondary e-e emission is peculiar to materials, which form stable oxide films, thin enough to be conductive at low potential drops (Al, Mg, Be, for instance). Fig.2 shows an example of the instantaneous cathode CVC obtained by computer integration with use of experimental (time-averaged) data on ion and electron saturation currents, discharge plasma potential, electron energy distribution function and literature data on energy dependencies for secondary ion-electron $\gamma(E)$ and electron-electron $\sigma(E)$ emissions [3,4]. Oxide films on the surface of Al-Mg cathodes used in experiments have $\sigma \sim 5$ -10 under bombardment by electrons with energies in the range of 200-600 eV. Other emissive mechanisms are neglected, though in real conditions a photoemission, microdischarges and a direct electron tunnelling through dielectric films can take place. Calculated CVC depicts a steep

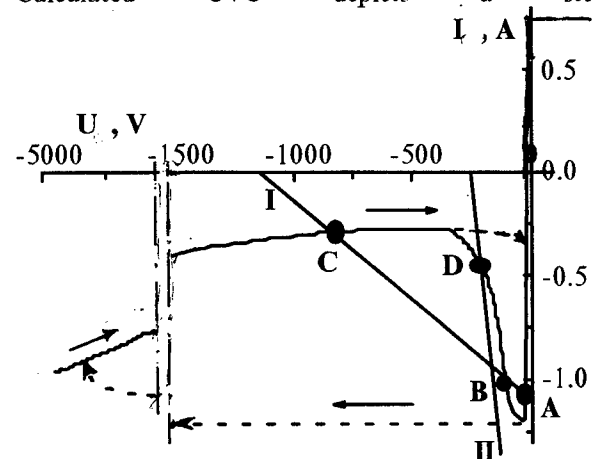


Fig.2. Simulated instantaneous CVC for one cathode; I, II - two types of loading characteristics; dashed lines and arrows - an imaginary phase cycle.

change of the current with cathode negative bias relative to plasma potential (which approaches the anode potential) due to both repulsion of thermal electrons and backward acceleration of secondary electrons. Further increase of the negative bias above 500V results in repulsion of almost all superthermal electrons. So, the cathode current decreases to much lower values dependent only on ions bombardment of the cathode surface.

The principle electrical scheme of the cathode circuit is presented in fig.1b. Its outer part includes the DC bias supply E, the inductance L, the active resistance R. The cathode-plasma contact is assumed as non-linear resistance R_N and plasma sheath capacity $C(U)$ coupled in parallel. It is convenient to characterise the circuit state by cathode voltage $U(t)$ and full current $I(t)$. The circuit behaviour can be described by the equations:

$$\frac{dU}{dt} = \frac{1}{C(U)} [I - I_N(U)] \quad (1)$$

$$\frac{dI}{dt} = \frac{1}{L} (E - IR - U), \quad (2)$$

where $I_N(U)$ is instantaneous cathode CVC. The phase trajectory $[U(t), I(t)]$ is determined by concrete circuit parameters and has always the clockwise direction. The equilibrium points A and C are stable, the point B is never stable and cannot be achieved. The auto-oscillations arise around D, provided $L/CR > |R_d|$ (R_d - differential negative resistance at D). In A and C states, external pulses or inherent fluctuations can trigger transition to metastable states. A negative high voltage pulse can be formed by one cycle motion along the phase trajectory for A-type working point and a positive - for C. When L is large enough, dI/dt is small and phase trajectory transitions from one CVC branch to the other one are almost parallel to U axis. U in maximum can reach extremely high values due to the gentle slope of the high voltage CVC branch, the dU/dt rate increasing with voltage bias (up to $10^{12}V/s$) through the decrease of $C(U)$.

Three operation modes with generation of auto-oscillations have been observed in test

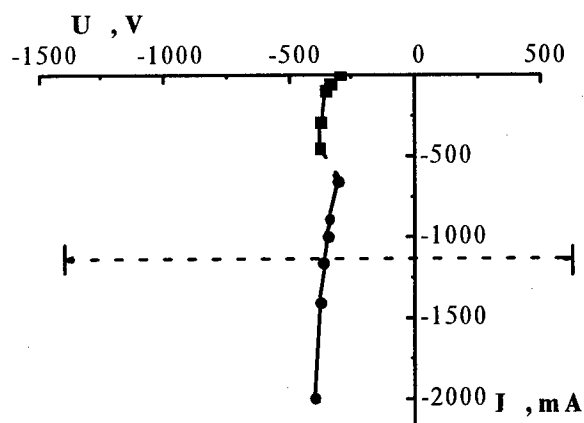


Fig.3. Average discharge current vs applied voltage. Working gas H_2 , $p=3.8 \cdot 10^{-4}$ Torr. The dashed line determines a range of voltage oscillations.

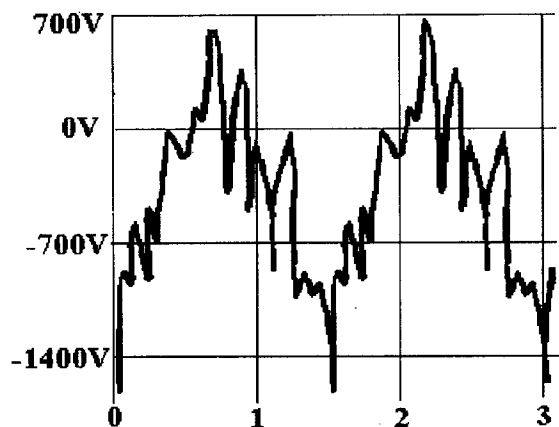


Fig.4. Voltage oscillogram for discharge parameters: H_2 , $p=3.8 \cdot 10^{-4}$ Torr, average discharge current $I_c=1.2A$, applied voltage $U_c=-360V$ ($0.2\mu s/unit$).

experiments: 1 - auto-oscillations are excited in only one cathode circuit (similar mode can be realised for one cathode discharge cell by replacement of the other cathode with magnetic plug); 2 - auto-oscillations are excited in both circuits independently; 3 - the circuits are coupled through inductances.

Though voltage pulses exceeding 10 kV are realised experimentally, the unperturbed auto-oscillation regimes (without external discharges) are limited by electric strength of the cathode assembly to moderate $U(t)$ amplitudes - 1-2 kV. Fig.3 corresponds to the third operation mode, when two identical cathode circuits are counter-phased. The disruption in the time-averaged CVC is accounted for self-excitation of powerful auto-oscillations. Fig.4 demonstrates high voltage cathode oscillations with rather complicated harmonic spectrum. It is interesting to note that at some intervals cathode plate obtains a positive potential. According to probe measurements the plasma potential oscillations have much lower amplitude compared with cathode voltage oscillations (tens of volts near the ground potential).

The experimental results show that in contrast to the conventional Penning discharge the observed auto-oscillation modes exhibit some features peculiar to the γ -form of RF capacitive discharges. The detailed model including self-correlated effects in the discharge bulk volume, in the sheath and on the plasma facing surfaces is to be developed.

References

- [1] Vizgalov I.V., Dimitrov S.K., Chernyatjev Yu.V. I.C.P.I.G.-20, Pica, Italy, (1991), 683-684.
- [2] Vizgalov I.V., Kirnev G.S., Kurnaev V.A., Sarichev D.V., Chernyatjev Yu.V. I.C.P.I.G.-22, Hoboken, NJ, USA (1995), v.3, 23-24.
- [3] Krutchenko OH, Chizhikov AE Sov. Electron Techniques. Electrovacuum and Discharge Devices 119(4) 1987 62.
- [4] Soukup R.J. J. Appl. Phys. 48(3) 1977 1098.

Experimental and theoretical study of the non-locality effects of the electron energy spectrum in O₂ DC glow discharge

V.V. Ivanov, K.S. Klopovskiy, D.V. Lopaev, A.M. Popov, A.T. Rakhimov, T.V. Rakhimova
119899, Nuclear Physics Institute, Moscow State University, Moscow, Russia

In general case, the electron distribution function (EDF) in a spatially non-uniform electric field can be found by solving the Boltzmann kinetic equation. In the case, when the characteristic non-uniformity length L is higher than the energy relaxation length, the EDF is not determined by local values of the electric field and becomes spatially "non-local". Note that in experiment, the EDF non-locality is observed at low pressure, when the spatial dependence of the EDF is determined only by the electron potential energy in the space charge electric field [1,2]. A physical foundation for this assumption are the following considerations: for low gas pressure, the motion of electrons in the space charge electric field is determined by their total energy $\varepsilon = W_k - eV$, where W_k and $(-eV)$ is the kinetic and potential energies respectively. In this case, the experimentally measured EDFs for different spatial points should coincide when we take into account the shift in the energetic space equal to the potential difference between the corresponding points. Such an effect has been found experimentally in measurements of the EDF in Ar RF discharge [3,4].

In this work, using the experimentally measured EDF in various spatial points in the O₂ DC discharge [5], we have carried out the analysis of the applicability of the two-term approximation (TTA) for the EDF calculation taking into account the spatial non-locality. As a rule, for a DC discharge in a cylindrical tube, the radial electric field E_r is taken into account only in macroscopic electrodynamical equations, but it is ignored in the kinetic equation for the EDF, which is assumed to depend only on the uniform axial field E_z . The field E_r , which is due to the space charge, is a "cooling" one with respect to E_z . It is obvious that the EDF non-locality should be observed when $E_z \sim E_r$.

The scheme of the experimental set-up and its detailed description is given in [5], where the effect of non-locality of the electron energy spectrum in an electronegative gas has been experimentally shown at first using as an example O₂ DC discharge.

It has been shown that for the case of low pressures $p=0.15-0.3$ Torr ($R^*p=0.09-0.18$ cm*Torr) the approximation in which the EDF depends only on the total electron energy is valid. With the increase of pressure, beginning from some energy, the EDFs cease to coincide in various space points. This fact means that, beginning from some values of Rp , the approximation in which the EDF is a function of only

the total electron energy becomes not valid. However, this does not mean that the EDF is spatially local. In this case, in order to describe the experimental data, it is necessary to compare the experimental EDF (as a function of the kinetic energy) with results of the accurate methods of calculation (Monte-Carlo technique).

However, high volume of numerical calculations needed by these methods leads to the necessity of studying more simple methods of accounting for the EDF non-locality. In this work, the applicability of TTA for the EDF calculation (taking into account the spatially non-uniform radial electric field E_r) is analysed in comparison with the results obtained by the Monte-Carlo technique (MC) and the experimental data. The spatial dependences of the field E_r used in calculations were taken from the experiment.

a) The EDF calculation in TTA.

This is the most widely used method of the EDF calculation in the glow discharge plasma. In this work, we used the same equation for the symmetrical part of the EDF as in [6].

b) The EDF calculation using the MC technique.

In order to study the applicability of TTA (when finding the EDF in spatially non-uniform case), we solved the Boltzmann equation by MC technique also. The components E_r and E_z of the electric field were taken from the experiment. The value of the wall potential was obtained in calculations using the steady-state condition for the EDF similarly to the case of TTA.

Calculations of the EDF were carried out for the discharge current density $j=5$ mA/sm². The experimental values of the axial field E_z and of the electric potential radial distribution were used in the calculations. As has been noted above, the radial field in the plasma hinders the electrons moving along the tube and makes equal one to another the effective coefficients of electron and ion diffusion. Therefore, knowledge of the wall potential $U=U(r=R)$ is very important for the modelling, because it controls the number of electrons which are able to overcome the ambipolar field and leave the plasma. Unfortunately, it was very difficult to determine the value of the wall potential in the conditions of our experiment. Thus, in calculations, this potential was chosen in such a way that the EDF were stationary. Deviation of its value in any direction led to the exponential increase (or decrease) of the electron concentration. As a result, the

values of U obtained in calculations in TTA and using the MC technique are different. But the closeness of these values proves (to our opinion) the closeness of the results of calculations in TTA and the MC technique.

Fig. 2 (a,b) shows the EDFs calculated by means of TTA and MC technique in various points of the discharge for the values of total neutral species concentration (a) $N = 4.8 \cdot 10^{15} \text{ cm}^{-3}$ ($p = 0.15 \text{ Torr}$) and (b) $N = 3.2 \cdot 10^{16} \text{ cm}^{-3}$ ($p = 1 \text{ Torr}$). In the first case, the EDF non-locality should be significant. The experimental EDFs (as a function of the kinetic energy) are shown in Fig. 2 (a,b). For the case (b), it is reasonable to assume that the EDF should be close to the local one everywhere except for the thin wall sheath. Fig. 2 shows that the experimental values and results of calculations (both the ones taking into account the spatial non-locality and the local ones) are close to each other. For the case of low pressure (Fig. 2a), the role of spatial non-locality increases. As can be seen from comparison of the calculations carried out by the two methods, TTA leads to a significantly stronger non-locality of the electron energy spectrum for high electron energies. However, this difference in EDFs produces only a very small effect on the calculated values of the ionization coefficient (as well as on the other kinetic coefficients in oxygen plasma). Indeed, there is a significant difference between the EDFs (at the tube axis) calculated by different techniques near 20 eV, and this energy is significantly higher than the thresholds of all the inelastic processes (including the ionization of O_2 -molecule). Therefore, even at this low pressure, the calculations using different techniques lead to practically the same results. This fact is illustrated by Fig. 3, which shows (together with the experimental results) the radial distributions of the mean electron energy, calculated by various techniques. As can be seen from Fig. 3, the results of calculations made by different methods are close to each other.

The work is supported by the Russian Foundation of Fundamental Research (grants 95-02-06326 and 96-02-18747).

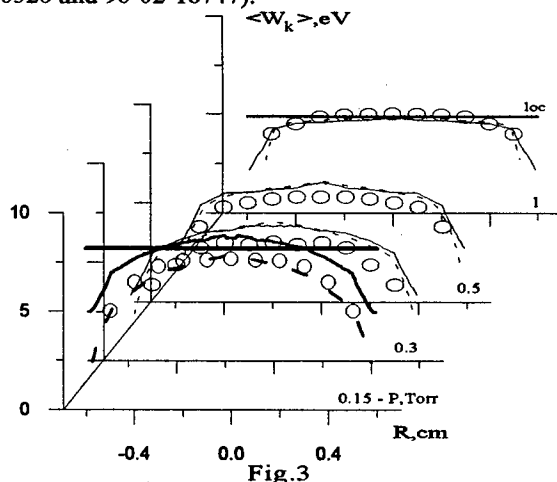


Fig. 3
The radial distribution of mean electron energy at various pressures. Symbols are the experimental data, dashed lines are the calculations by TTA model and solid lines are the calculations by MC model.

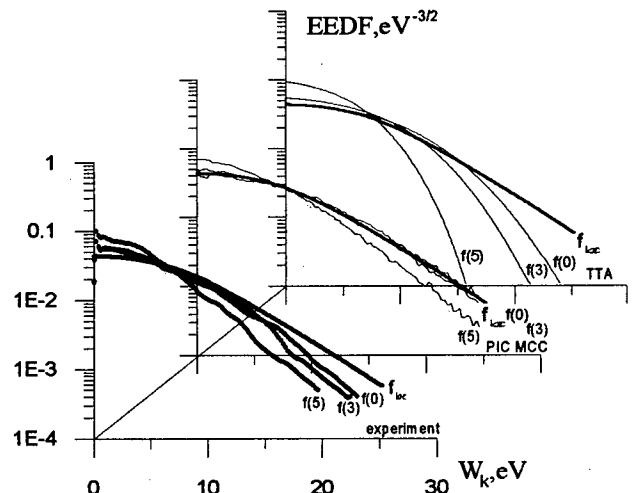


Fig. 1

EEDF at pressure - 0.15 Torr and at current density - 5 mA/cm for three radial positions - $R = 0, 3$ and 5 mm. The results of experiment and calculations by MC and TTA methods are compared with local EEDF.

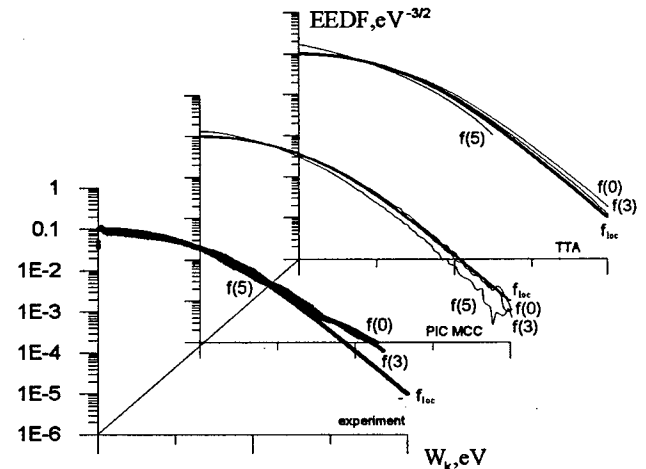


Fig. 2

All is the same as in Fig. 1 only at pressure - 1 Torr.

References

- [1] I.B. Bernstein, T. Holstein: Phys. Rev., 94 (1954) 1475
- [2] Tsandin L.D.: Sov. Phys. JETP. 39 (1974) 805.
- [3] V.A. Godyak, R.B. Piejak, B.M. Alexandrovich: Plasma Sources Sci. Technol., 1(1992) 36.
- [4] U. Kortchagen: Phys. Rev., E 49(1994) 4369.
- [5] V.V. Ivanov, K.S. Klopovskii et al: JETP Lett., 63(7) (1996) 537.
- [6] A.M. Popov, A.T. Rakhimov and T.V. Rakhimova: Fiz. Plazmy (Rus), 19 (1993) 1241.

A Plasma Mirror for Electronic Microwave Beam Steering

W. Manheimer, J. Mathew, R. Fernsler, R. Meger, J. Gregor, D. Murphy, and R. Pechacek
Plasma Physics Division, Naval Research Laboratory, Washington DC 20375, USA

Abstract

A planar plasma may be used as a reflector for microwaves if the plasma frequency (at the angle of incidence) is greater than the microwave frequency. If this plasma mirror can be repositioned electronically, it could have the capability of redirecting microwave beams on a very fast time scale, and as such it could have important applications to radar and communication systems.

The Plasma

The goal is the generation of planar plasmas which have the potential of reflecting microwave beams [1-4]. The plasma is formed with a unique hollow cathode glow discharge. The hollow cathode is three sides of a metal rectangle, about 1.2 cm deep and 1.6 cm wide, and of length 60 cm. It produces a sheet plasma, square and about 60 cm on a side. This plasma has been studied mostly in air, although other gases have been used also with similar results. The background pressure is about 100 mtorr, and a uniform magnetic field of about 100 G is present. The field is oriented along the plasma and perpendicular to the rear face of the hollow cathode.

The discharge is struck at voltages of about 3-5 keV and currents of 5-20 Amps. As detected both by Langmuir probes and particle detectors beneath the anode, the plasma is generated by a beam of electrons, produced at the cathode, which have nearly the full cathode potential. However this beam current is only a small fraction of the total current in the discharge. Electric field measurements in the plasma also show that the electric field in the discharge is not large enough to create avalanche breakdown. Nevertheless, the plasma, generated by the beam has very high electron density, larger than 10^{12} cm^{-3} at the highest current. This seems to be a new mode of discharge operation, and we have called it the enhanced glow mode. It is characterized by lower current and higher voltage than the normal hollow cathode mode, and lower voltage and lower current than the abnormal glow. Nevertheless, it produces a higher electron

density plasma than either one of them.

Preliminary theoretical analysis of the enhanced glow assume an ion sheath of dimension much smaller than the hollow cathode dimension, and reflexing electrons in the cathode hollow. It gives qualitative agreement for the voltage dependence of the discharge and beam current in the plasma. Also it gives qualitative agreement for the electron density in the plasma.

Furthermore, it shows that the power into the plasma is almost all dissipated on the cathode, anode and outer wall; very little (but still enough to be a concern) is dissipated in the gas.

Microwave Measurements

Many measurements of the characteristics of the plasma as a microwave reflector have been made. In order for the plasma to be a viable beam director, at least for a radar system, it is important that the quality of the microwave beam be unaffected by the plasma. Thus the plasma must be flat, be stationary and have very low noise temperature. Experiments on the flatness have been done in two ways. First of all the microwave reflection from the plasma has been compared to reflection from a metal plate. The measurements were done at a frequency of 10 GHz, so the fact that the plasma reflects means that the electron density is at least 10^{12} cm^{-3} .

Absolute measurements of reflected power as a function of angle show identical characteristics within the main lobe. In each case, side lobes are reduced by about 25 dB, and the sidelobe patterns are similar, but not identical. As an additional check, imaging spectroscopy has been done on the enhanced glow plasma to look for variations in the emitted spectrum of the optical emission. In the enhanced glow mode the spectrum is dominated by emission of two transition lines at about 400 nm, and this emission is nearly uniform, possibly decreasing slightly from cathode to anode. Thus the plasma is very uniform in the enhanced glow mode.

A crucial figure of merit for a radar is suppression of clutter with doppler filtering. In order for this to be viable, the plasma must be stationary, that is the motion of the critical

surface must be sufficiently slow. With a microwave heterodyne system, we have measured the velocity of the critical surface. When the plasma has settled down, the motion of the critical surface is less than 2 meters per second. However there is an initial transient of about 50 μ s (out of a 300 μ s pulse) during which the plasma moves first outward, and then inward with a velocity of about 100 m/s.

An additional important quality of the plasma reflector is its noise temperature. This is particularly important for the radar receiver, where it is receiving a signal which may be extremely weak. One might at first think that where the plasma temperature is an electron volt or so (about 10^4 degrees Kelvin), the effective antenna temperature would be very high. However this is not the case, because at frequencies of interest, the plasma is a reflector, not an absorber. Theory shows that the temperature should be about 200-300°K. Recently we have performed measurements of the temperature and have confirmed that it is between 500 and 1000°K, a value reasonable for a radar or communication system.

The Agile Mirror

In order for the plasma to develop into a viable component of a radar system, it must not only provide a high quality microwave reflection, but must also provide agility for the microwave beam on a time scale of perhaps 10 μ s. There are two separate systems which we envision as giving rise to this agility. The first is a segmented cathode with different parts of the cathode electronically addressable. Thus by designating the emitting portion of the cathode, we specify one edge of the mirror, and we anticipate that this can be done on the required time scale. To achieve agility in the other plane, we envision a transverse magnetic field which can be varied also on a 10-20 microsecond time scale. Preliminary experiments on designating one of two cathodes have been done, but not on a 10 μ s time scale. The same is true for varying the magnetic field. We hope that by the time of the meeting, both capabilities are demonstrated on a 10 μ s time scale.

Acknowledgment: This work has been supported by the Office of Naval Research.

References:

1. W. Manheimer, IEEE Trans. Plasma Sci. PS- 19, 1228, (1991)
2. A. Robson, R. Morgan, and R. Meger, IEEE Trans. Plasma Sci. PS-20, 1036 (1992)
3. R. Meger, J. Mathew, J. Gregor, R. Pechacek, R. Fernsler, W. Manheimer, and A. Robson, Phys. Plasmas 2, 1532, (1995)
4. J. Mathew, R. Fernsler R. Meger, J. Gregor, D. Murphy, R. Pechacek, , W. Manheimer, Phys. Rev. Let. 77, 1982 (1996)

Characteristics of the initiation and operation of a repetitive pulsed hollow-cathode glow discharge

N.V. Gavrilov, G.A. Mesyats

Institute of Electrophysics, Ural Division of the Russian Academy of Sciences
Yekaterinburg 620049, Russia

1. Introduction

The pulsed low-pressure glow discharge with oscillating electrons is used in sources of electrons [1] and gas ions [2] where the limiting frequency of beam generation is determined by the dynamics of discharge initiation in a large volume. The low electric field (0.1-1 kV/cm) in extended (~ 10 cm) interelectrode gaps, the high degree of the surface conditioning, the large area of the cathode surface ($\sim 10^3$ cm²), and the low pressure of the inert gas in the gap (< 0.1 Pa) are responsible for the dominant effect of the dynamics of generation of initial electrons and of the gas adsorption and desorption processes at the cathode on the time required for a discharge to be initiated and on the discharge characteristics in the quasi-steady stage of its operation.

2. Experiment

Used in the experiments was the coaxial electrode system of the gas ion source [2], consisting of a stainless steel hollow cathode with dimensions $L = D = 150$ mm and a tungsten rod anode of diameter $d = 3$ mm and length $l = 100$ mm. The anode is inserted into the cathode cavity through a hole of diameter 10 mm made in the end of the hollow cathode. The opposite end of the cathode is perforated. A longitudinal magnetic field with an induction $B \sim 1$ mT was created by a solenoid. The working gas (Ar, N₂) was fed into the cathode cavity. The gas pressure in the vacuum chamber was $p \sim (1-2) \cdot 10^{-2}$ Pa, the average pressure in the discharge gap was two or three times higher. Evacuation was produced by a vapor-oil pump having no nitrogen trap. The discharge was initiated in the repetitive pulse mode (RPM) with the pulse repetition rate f varied from 10 to 1200 Hz. The pulse duration τ was 100 μ s; the risetime was no longer than ~ 5 μ s. The amplitude of the voltage applied to the gap V_0 (0.8-2 kV) was stable within 5%. The discharge current was controlled in the range 0.04-2 A. The temperature T_k of the cathode with the surface area $S_k \sim 10^3$ cm² was controlled in the range from 20 to 150 °C.

The time required to initiate a glow discharge, t_i , was measured from the instant the V_0 was applied to the gap to the onset of its abrupt fall to the level $0.9V_0$. The discharge formative time, t_2 , was determined

within the current pulse risetime from 0.1 I to 0.9 I , with I being the steady-state discharge current.

The time t_i as a function of f for $T_k = 20^\circ\text{C}$, $V_0 = 2$ kV, $B = 1$ mT, and various values of I and of Ar pressure p is given in Fig. 1. Both the time t_i and the statistical spread in t_i values decrease as increasing f . An increase in the current I results in a decrease in t_i . The time t_2 and the steady-state values of the discharge operating voltage V and I as functions of f for $B = 1$ mT and $T_k = 20^\circ\text{C}$ are given in Fig. 2. Increasing f increases the discharge impedance in the steady-state mode. As T_k is increased, the discharge impedance increases, too. The changes of T_k in the range 20-150 °C affects only weakly on the $t_i(f)$ dependence. For a discharge in N₂ this dependence is similar to that for a discharge in Ar; however, the steady-state values of V and I are weakly dependent on f .

3. Discussion

The characteristics of a glow discharge initiated in RPM can be affected by the transient processes occurring in the discharge gap on cessation of current, provided that the time constants of these processes are comparable with the value of $1/f$. These processes are the gas adsorption on the cathode surface and the post-discharge electron emission.

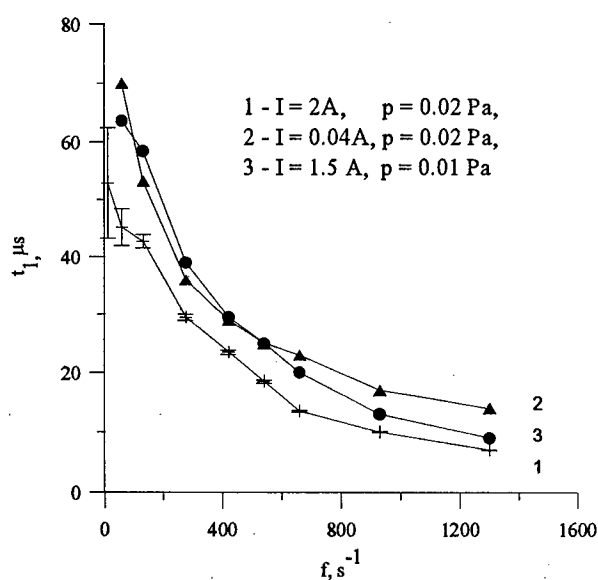


Fig. 1

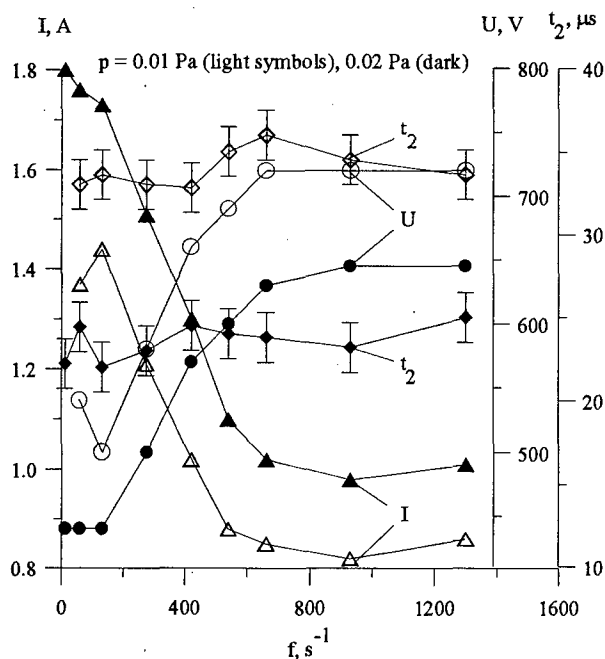


Fig. 2

The experimental conditions are such that in the original state a layer of adsorbed gas atoms is present on the cathode surface, the number of the atoms being much over their number in the gas space. For a discharge operating in RPM, the number of the atoms desorbed in a time τ comes into equilibrium with the number of the atoms adsorbed on the cathode in the time of the cycle $1/f$. An increase in f has the result that this equilibrium is established at a lower density N of adsorbed atoms. The change in N may result in a change in the coefficient of ion- electron emission γ from the cathode and in an impulsive increase in pressure near the cathode and in the whole gas space. The increase in pressure near the cathode may lead to a change in the effective value of γ_e taking into account the probability that the primary electrons will return to the cathode, while the increase in pressure in the whole gap affects the ionization rate in the discharge.

Estimates show that the change in N with increasing f corresponds to some fraction of the monolayer, which may result in changes in gas pressure and in discharge impedance. The effective coefficient of electron emission from the cathode of a glow discharge in the presence of adsorbed argon atoms, may be 1-1.5 orders of magnitude lower than that for a clean metal surface [3]. However, even this substantial change in γ is too low to account for the 5-6-fold decrease in the formative time of a discharge, t_1 , with increasing f .

The decrease in the statistical spread in t_1 values with increasing f testifies to an increase in the frequency of appearance of initial electrons, f_e . The spread $\sim 10 \mu s$ measured for $f = 10 \text{ Hz}$ corresponds to the frequency $f_e \sim 10^5 \text{ s}^{-1}$. Several mechanisms for the postdischarge electron emission with no external electric field are

known [4]; among these are the exoemission and the electron emission through thin dielectric films. The rate of change of the post-emission intensity abruptly decreases with time. Increasing f and raising f_e to values at which $1/f_e \gg t_1$, leads to a speed-up of the discharge development due to multi-electron initiation. The avalanche-like current rise in the gap during the initiation of a discharge is described by the relation

$$I(t) = I(0) \exp(t\mu/\tau_1). \quad (1)$$

Here, $I(0)$ is the current of the initial electrons, μ is the current enhancement factor, and τ_1 is the time required for a single avalanche to develop. For the current at which the discharge goes into a glow, $I(t_1)$, being constant, in order that the time t_1 be reduced to one fifth or one sixth, the current $I(0)$ should be increased by five or six orders of magnitude, i.e., the initial electron current density should be $10^{-11} - 10^{-12} \text{ s}^{-1} \text{ cm}^{-2}$.

For cathodes with oxide films present on the surface, higher (by 3 orders of the magnitude) current densities of post-emission was observed for a long time [5]. A distinctive feature of the experiment performed was the high pulse repetition rate, which allowed an investigation of the post-emission with high temporal resolution (10^{-3} s). So we are able to detect the high rate of decrease in the efficiency of the post-emission in a system with the electrodes cleaned in a glow discharge.

4. Conclusions

In initiation a low-pressure glow discharge with a hollow cathode in a repetitive pulse mode, the dynamic processes of gas adsorption and desorption on the large-size cold cathode may affect substantially the discharge impedance, provided that the pulse duration is shorter than the time constant for the transition of the gas conditions in the gap to a steady state.

A decrease in interpulse period decreases the formative time of a glow discharge. This may be accounted for by the increase in the current density of the post-discharge emission of electrons and by the onset of the multielectron mode of discharge initiation.

5. References

- [1] N.V.Gavrilov, M.A. Zavjalov, S.P.Nikulin, et al.: Pisma J. Tekh. Fiz, V.19(21) (1993) 57 (In Russian)
- [2] N.V. Gavrilov, G.A. Mesyats, S.P. Nikulin, et al. J. Vac. Sci. Technol.: A14(3) (1996) 1050
- [3] S. Brown, Elementary processes in gas discharge plasma, Moscow, Gosatomizdat (1960) (In Russian)
- [4] Yu.D. Korolev, G.A. Mesyats. Physics of pulse breakdown in gases, Moscow, Nauka Publishers (1991)
- [5] P.N.Chistjakov, N.V.Tatarinova: J. Tekh. Fiz, V.35(7) (1965) 1333 (In Russian)

Experimental Study on Standing / Moving Striations and Standing / Moving Helices

Asuka Mori, Mamoru Matsuoka and Motoichi Kawaguchi
Department of Industrial and Technical Education, Mie University
Tsu, Mie 514, Japan

1. Introduction

Standing striations or moving striations are often observed in a dc discharge at low pressure not much exceeding 100 Pa. Standing striations often appear in the gas composed of polyatomic molecule such as air [1], while moving striations are observed mainly in rare gases [2].

We observed that a standing striation transformed itself into a standing helix continuously when a longitudinal magnetic field was applied. Similarly, a moving striation transformed itself into a moving helix. In this paper, we describe the experimental observation on the transition from striations to helices. We also report the dependence of a standing striation on the discharge condition.

2. Experimental Apparatus and Methods

The experiment was performed in a hot cathode dc discharge in helium. Figure 1 shows the schematic diagram of the experimental setup. The discharge was produced in a cylindrical glass tube with internal radius of 73 mm in a longitudinal magnetic field. The anode with diameter of 55 mm was situated inside the magnetic coils. The cathode with diameter of 77 mm was situated outside them. The distance between the anode and

cathode was 1135 mm. To keep the discharge stable, two stainless meshes were set up near two electrodes. Pressure was varied from 1 Pa to 22.5 Pa. Applied magnetic field was up to 100 mT. Discharge current was between 50 mA and 225 mA.

The transition from a standing or moving striation to a standing or moving helix caused by an external magnetic field was monitored by a CCD color camera.

3. Experimental Results

Figure 2 shows the pattern of discharge. In the absence of the magnetic field, a standing striation spread throughout the discharge region. With increasing the magnetic field, striations near the anode leaned and combined with each other and became a standing helix at $B \approx 28$ mT. Thus there appeared a standing helix on the anode side of the discharge region and a standing striation on the cathode side. As the magnetic field increased further, the standing helix became clearer. With increasing the magnetic field more up to 100 mT, the standing striation and the standing helix changed their forms gradually into a uniform discharge column spreading throughout the discharge region, though we do not draw in this diagram.

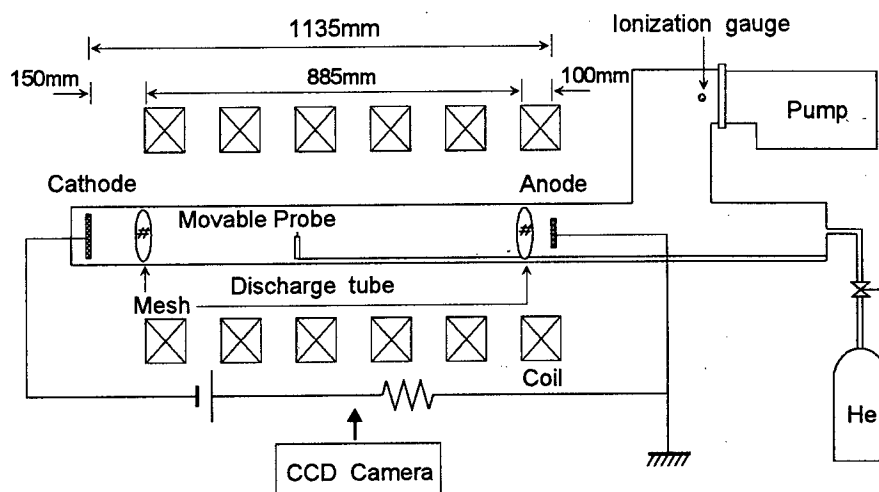


Fig.1 Experimental apparatus.

The direction of helix depended on the direction of magnetic field. The standing helix twisted clockwise (as a usual screw) in the case when the magnetic field was in the same direction as that of the discharge current, and it did counterclockwise in the case when the magnetic field was in the opposite direction as of the discharge current.

Figure 3 shows the dependence of the distance between the centers of two neighboring standing striations on pressure, in the absence of the magnetic field. The distance between striations decreases with increasing pressure. The relation between the distance and pressure showed hysteresis characteristics. The following form is known as Wehner's relation [2] between the distance L and pressure P ;

$$\frac{L}{R} = \frac{C}{(PR)^m}$$

We fitted this relation to our experimental result. The values of C and m were calculated in the gas pressure range of $P=12.5\sim22.0$ Pa for $R=3.65$ cm. When the pressure was increased, $C=12$, $m=0.28$, and $C=13$, $m=0.29$ with decrease of the pressure. The curves in Fig.3 shows Wehner's relation drawn by using the calculated values of C and m .

It is noted that the experimental result agrees with Wehner's relation, and that the value of m is 0.28 and independent of increase / decrease of the pressure. The value of m is usually 0.53 for hydrogen and 0.32 for nitrogen [2]. The value of m obtained in our experiment is close to that for nitrogen, which may suggest that the discharge was contaminated by nitrogen or air.

4. Summary

In this paper, we described the transition from a standing or moving striation to a standing or moving helix caused by the applied magnetic field. The direction of helix was clarified. Also it is suggested that the occurrence of standing striations or helices is related to the existence of nitrogen molecules in the discharge.

[1] K. Honda: "Kitai Houden Gensho" (Phenomena in Gas Discharges), Publication Bureau in Tokyo Denki University, (1973) 137 (in Japanese)

[2] The Institute of Electrical Engineers of Japan: "Houden Handbook" (Handbook on Discharge - revised edition -), Ohm Company, (1975) 122 (in Japanese)

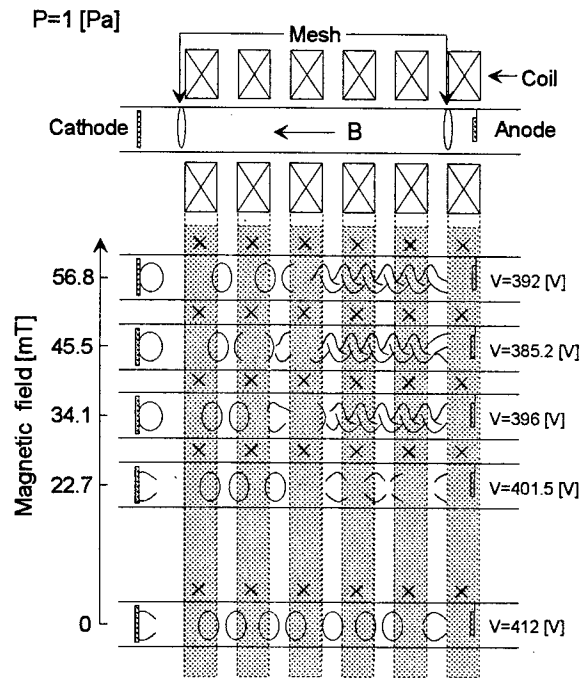


Fig.2 Discharge pattern with striation and standing helix.

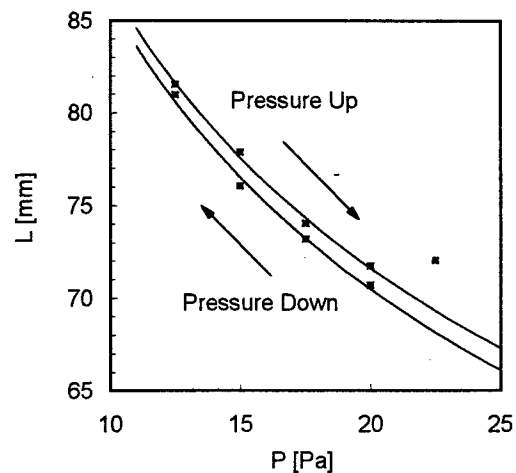


Fig.3 Dependence of the distance between standing striations on pressure: Magnetic field $B=0$ mT, discharge current $I=100$ mA, discharge volts $V=270\sim387$ V.

Realization of high-current mode of glow discharge with oscillating electrons at lowered pressure

S. P. Nikulin

Institute of Electrophysics, Ural Branch of RAS, 34, Komsomolskaya str., Ekaterinburg, Russia

1. Introduction

The operation of glow discharges with oscillating electrons, such as discharge in a magnetic field and hollow cathode discharge, is possible in two modes: a high-voltage one characterized by predominance of an electron charge in the discharge gap, and a high-current mode, in which almost the whole gap is filled with plasma at a potential close to that of the anode, and the discharge voltage concentrates in a narrow near-cathode ion layer [1]. The use of the latter mode is preferable for the development of powerful and effective discharge devices. However, this mode is realized at higher pressures, which can complicate its use in those applications, where the operation at low pressures is of prime importance, e.g. in the development of sources of charged particles, in which low pressure is necessary to prevent the breakdown of the accelerating gap. So, the determination of conditions promoting the realization of the high-current mode at lowered pressure is an urgent task. The purpose of the present work is the scrutiny of analytical models allowing the determination of major factors influencing the bottom boundary of the operating pressure range for glow discharges with hollow cathode and in a magnetic field.

2. Hollow cathode discharge

The discharge maintenance mechanism is the following: ions move from the gap to the cathode and cause an emission of electrons, which are accelerated in the cathode sheath and then spend their acquired energy in collisions with neutral atoms, in particular, on their ionization. Each of these fast electrons should make I/γ ionizations, where γ is coefficient of ion-electron emission. As to secondary electrons, their contribution to ionization is negligible, because they do not obtain sufficient energy from the weak electric field existing in plasma. In a wide range of initial energies of fast particles it is necessary to spend a fixed quantity of energy W to create one pair of charged particles. Taking also into account, that the frequency of ionization ν_i is can be considered to be constant in the 100 - 1000 eV energy range, which is characteristic of fast particles of the discharge, one can write down

the following expression for the relaxation time of fast particles

$$\tau_r = \frac{eU_c}{\nu_i W}, \quad (1)$$

where e is the charge of electron, U_c is cathode fall. On expiration of time τ_r fast particles lose their ionizing ability. Besides, a part of fast particles escape from the gap to the anode. So, the balance equation for fast particles can be written as

$$\frac{I_c}{e} - \frac{n_f V}{\tau_r} - \frac{n_f v S_a}{4} = 0, \quad (2)$$

where I_c is the ion current at the cathode, V is the volume of the cavity, n_f and v are the concentration and average velocity of fast particles, respectively, S_a is the area of the anode. Considering, that all emerging ions come to the cathode, one can obtain the self-maintenance condition in the following form

$$\frac{2\sqrt{u/3}}{3p(1-1/u)} = 1, \quad (3)$$

where

$$u = U_c / U_0, \quad p = P / P_0, \quad (4)$$

$$U_0 = \frac{W}{e\gamma}, \quad P_0 = \frac{\sqrt{27kTS_a}}{16\gamma V\sigma(eU_0)}, \quad (5)$$

P and T are gas pressure and temperature, respectively, σ is the ionization cross-section, k is the Boltzmann constant. Condition (3) determines implicitly the dependence of discharge voltage on pressure (Fig.1).

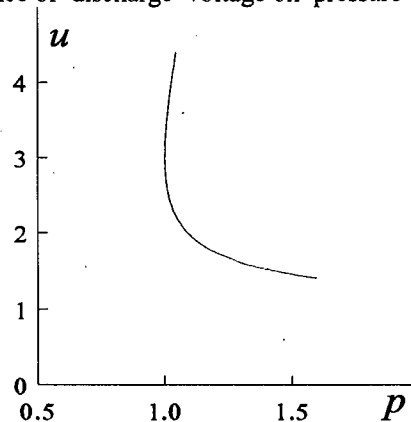


Fig.1.

The dependence is two-valued, however, the states corresponding to the top branch are unstable and are not observed in experiments. The introduced parameter U_0 is the discharge voltage on condition, that the fast

electrons lose their energy completely in the gap, and P_0 is the critical pressure, below which discharge operation in the considered mode is impossible. P_0 is proportional to anode area and one would think that it would be possible to decrease pressure down to any desirable level by reducing S_a . However with $S_a < \sqrt{m/M} S_c$, where m and M are electron and ion mass, respectively, and S_c is the cathode area, an electron layer forms near the anode and the discharge transforms to the high-voltage form [2]. Thus, expression (5) for P_0 is correct when $S_a > \sqrt{m/M} S_c$, and one can obtain the following estimation

$$P_1 = \frac{\sqrt{27m/M} k T S_c}{16 \gamma \sigma (e U_0)} \quad (6)$$

for the minimum possible pressure P_1 in the hollow cathode glow discharge.

3. Discharge in magnetic field

Let us consider the problem in plane geometry. The anode and the cathode are located in planes $x = 0$ and $x = d$, respectively. The following equations of motion and continuity for fast particles were used

$$n_f v_f = D_f \frac{dn_f}{dx}, \quad \frac{d(n_f v_f)}{dx} = \frac{n_f}{\tau_r}, \quad (7)$$

where v_f and D_f are the average velocity of directed motion and the coefficient of diffusion of fast particles, respectively. The appropriate equations for plasma electrons were used in the following form

$$n_e v_e = D \frac{dn_e}{dx} - \mu n_e \frac{d\phi}{dx}, \quad \frac{d(n_e v_e)}{dx} = -v_i n_f, \quad (8)$$

where n_e and v_e are the concentration and the average velocity of directed motion of plasma electrons, respectively, D and μ are the coefficients of diffusion and mobility of electrons across magnetic field, respectively, ϕ is potential. There is no drift term in (7), because the weak electric field existing in the plasma does not influence significantly the motion of fast particles. As for ions, they are not practically affected by the magnetic field and leave the gap in collisionless mode. The following equations of ion balance and motion were used

$$\frac{d(n_i v_i)}{dx} = v_i n_f, \quad \frac{d(n_i v_i^2)}{dx} = -\frac{en_i}{M} \frac{d\phi}{dx}, \quad (9)$$

where n_i and v_i are the concentration and the average velocity of ions, respectively. Neglecting the contribution of fast particles to the complete electron charge one can use the condition of quasineutrality as

$$n_e = n_i \quad (10)$$

The analysis of system of equations (7) - (10) allows one to obtain the self-maintenance condition as

$$u(1 - ch^{-1}(2.61b/u)) = 1, \quad (11)$$

where

$$b = B/B_0, \quad (12)$$

B is magnetic induction, and parameter B_0 is determined by expression

$$B_0 = 1.5 \frac{\sqrt{mWv_f/v_i}}{\gamma ed}, \quad (13)$$

where v_f is the effective collision frequency of fast particles. Expression (11) is an implicit form of dependence $u(b)$ presented in Fig. 2. The curve

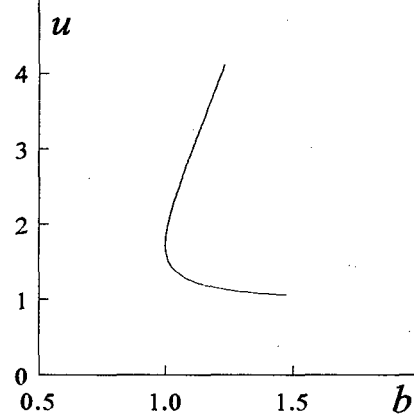


Fig.2.

resembles qualitatively like the dependence $u(p)$ obtained earlier for hollow cathode discharge. With $b < 1$ or $B < B_0$ operation of the considered discharge mode is impossible at any voltage, while with $b > 1$ the dependence is two-valued. As in the previous case, only the states corresponding to the bottom branch are observed experimentally. Besides the fulfilment of the self-maintenance condition, for the realization of the high-current discharge mode it is necessary that the gap be filled with the plasma from the cathode sheath up to the anode. This is ensured at pressures above some value P_2 determined by the following expression

$$P_2 = \frac{0.78 W v_f}{\gamma^2 d v_i v_0 \sqrt{k T_e M}}, \quad (14)$$

where T_e is electron temperature, and v_0 is the effective collision frequency for plasma electrons at a pressure accepted as a unit of measurement. At $P = P_2$ the operation of the discharge is possible only at a single value of magnetic induction $B = B_0$, but the operating range of magnetic fields expands abruptly, when P increases.

*This work was supported by U.S. Department of Energy through LANL (Contract No. 0248U0016-35).

4. References

- [1] M. D. Gabovich, Physics and engineering of plasma ion sources. Moscow, Atomizdat (1972), 304 p.
- [2] A. S. Metel', Zh. T. F., 54 (1984) 2, pp. 241-247.

Experimental Investigations of the Anode Region of a Low-Pressure Glow Discharge in Helium

M. Otte¹, S. Pfau¹, J. Rohmann²

¹ Department of Physics, Ernst-Moritz-Arndt-University, Domstraße 10a, D-17487 Greifswald, FRG

² Institute of Low Temperature Plasma Physics, Robert-Blum-Straße 8-10, D-17489 Greifswald, FRG

1. Introduction

Recently intensified investigations were carried out to describe the weakly ionized plasma in quantity in the different spatially nonuniform sections of the glow discharge. There in the centre of the investigations was the determination of the velocity distribution function of the electrons with respect to the spatial inhomogeneity [1], [2], [3]. A verification of the theoretical statements and calculations in discharge plasmas using a nonlocal electron kinetic treatment requires reliable experimental data of the most important plasma parameters. In this paper a choice of spatially resolved measurements in the anode region of a low-current and low-pressure glow discharge is presented.

2. Experimental conditions

In a collision dominated plasma of a low-current helium glow discharge measurements of important plasma parameters were carried out in the anode region. The cylindrical discharge tube, with a diameter of $2r_0 = 40\text{mm}$, contained a circular disc-shaped nickel anode with $2r_A = 36\text{mm}$ in diameter. By using a moveable electrical probe the electron velocity distribution functions, the density and the mean energy of the electrons as well as the electrical potential distribution were determined in the anode region and in the positive column in their radial and axial dependence. In the following presentation we mostly confine ourselves to the reproduction of results on the axis of the discharge tube.

The current and the pressure of the investigated discharge were varied within the limits :

$$1\text{ mA/cm} \leq i/r_0 \leq 25\text{ mA/cm} \text{ and} \\ 100\text{ Pa cm} < p_0 r_0 < 350\text{ Pa cm}.$$

3. Results

The peculiarity of the anode region is to be seen in the two dimensional nonuniform structure of the plasma. Fig. 1 shows the potential behaviour in the axis of the discharge tube $V_s(x, r=0)$ from the anode as far as to the axial homogeneous part of the positive column. This observed shape of the potential does clearly deviate from previous investigations under comparable conditions. A typical feature of its behaviour is the

development of a plateau near the anode. The potential only raises in the vicinity of the anode due to the development of a negative space charge sheath within a *DEBYE*-length onto the value of the anode potential $V_s(x=0, r)=0$.

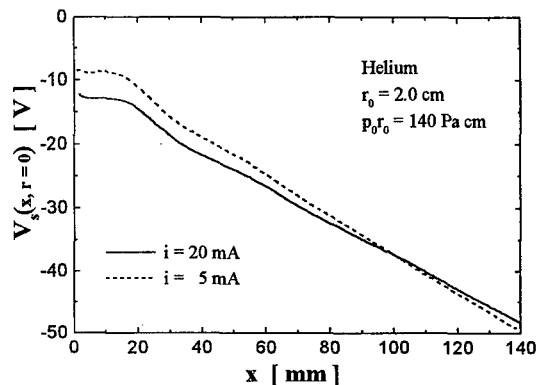


Fig. 1. Measured electrical potential $V_s(x, r=0)$ as a function of the distance x from the anode, with an anode fall of $U_{A1} = 8.8\text{V}$, $U_{A2} = 12.9\text{V}$ for $i = 5\text{mA}$ resp. $i = 20\text{mA}$

The axial electric field strength, that can be seen in Fig. 2, has a very small value ($E_x \approx 0$) within the plateau zone. While approaching the positive column we can observe a distinct overswing of the axial field strength above the value in the positive column.

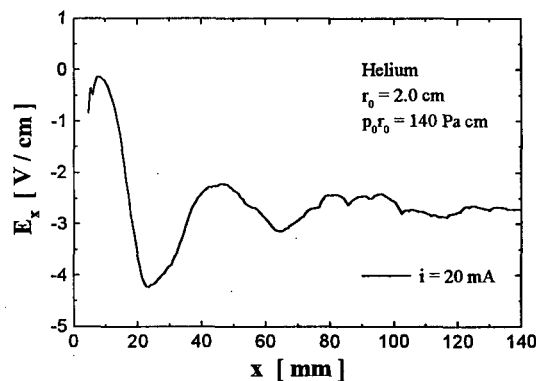


Fig. 2. Damped periodical structure of the axial electric field strength $E_x(r=0)$ versus the distance x from the anode

This transient process is less clearly to observe in the behaviour of the mean electron energy $u_m(x)$ (Fig. 3).

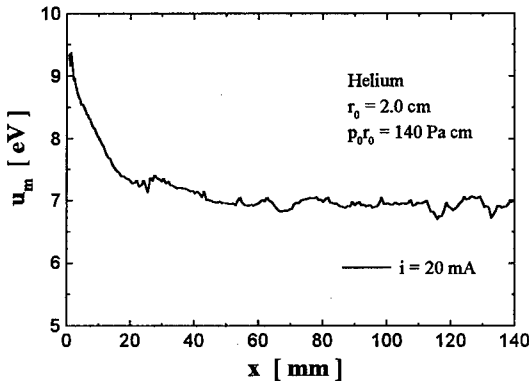


Fig. 3. Mean electron energy $u_m(x)$

The electron density n_e nearly rises up to the column density as an exponential function (Fig. 4).

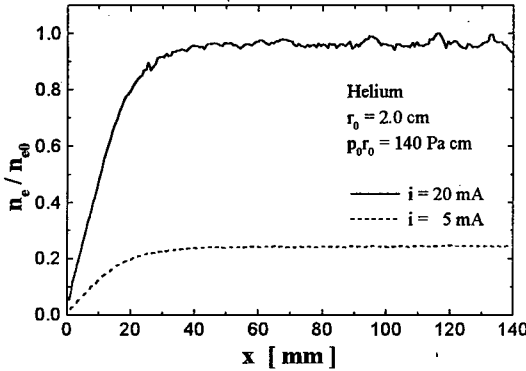


Fig. 4. Relative electron densities $n_e(x)$, normalized on the maximum value n_{e0} for $i = 20$ mA

In contrast to the column plasma, where the electron velocity distribution function in a low-current regime suffers a change in the radial diffusion field, which means a drop of the mean energy, the mean electron energy increases by approaching the anode (Fig. 3 and 5).

The radial variation of the electron velocity distribution function far from the anode in an axial homogeneous section of the column plasma is shown in Fig. 6. The course of the curves in Fig. 6 demonstrate, that the distribution functions under the investigated discharge conditions depends only on the total energy ε of the electrons.

A theoretical description of the plasma in the anode region requires an appropriate treatment of the distinct nonequilibrium electron kinetics taking into account the specific plasma conditions. Such calculations were carried out under special simplifications [1] - [4].

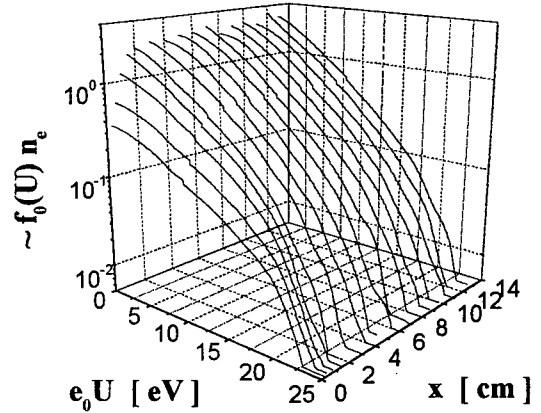


Fig. 5. Electron velocity distribution function in the axis versus kinetic energy $e_0 U$ and axial position x with $i = 20$ mA and $p_0 r_0 = 140$ Pa cm

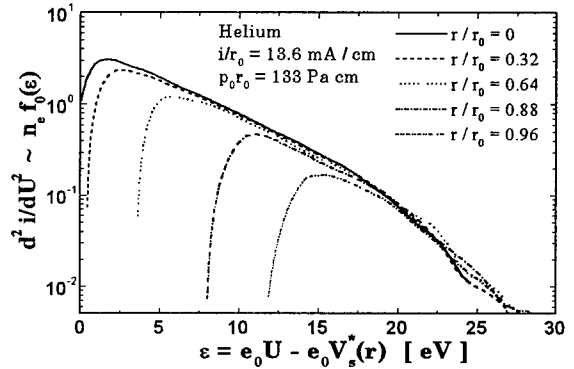


Fig. 6. Electron velocity distribution function versus the total energy ε on different radial positions with $V_s^*(r) = V_s(x, r) - V_s(x, 0)$ and $x = 140$ mm

A comparison of the present measurements with appropriate calculations of the nonlocal electron kinetics shows a satisfactory agreement between the theoretical and the experimental quantities within the presupposed limits.

4. References

- [1] V. J. Kolobov, V.A. Godyak, IEEE Transaction on Plasma Science 23(1995) 503.
- [2] Y.B. Golubowskii, S.H. al Havat, L.D. Tsendin, Sov. Phys. Tech. Phys. 32(1987) 760.
- [3] S.Pfau, J. Rohmann, D. Uhrlandt, R. Winkler, Contrib. Plasma Phys. 36(1996) 449.
- [4] D. Uhrlandt, R. Winkler, J. Phys. D29(1996) 115.

The Electron Velocity Distribution Function of the Radial Inhomogeneous Plasma of the Positive Column in a Helium Glow Discharge

- Measurements and Calculations -

M. Otte¹, S. Pfau¹, J. Rohmann²

¹ Department of Physics, Ernst-Moritz-Arndt-University, Domstraße 10a, D-17487 Greifswald, FRG

² Institute of Low Temperature Plasma Physics, Robert-Blum-Straße 8-10, D-17489 Greifswald, FRG

Introduction

The strict kinetic description of the electrons in the spatially inhomogeneous plasma of a cylindrical positive column is an extremely difficult problem. To obtain the electron velocity distribution function under non-uniform plasma conditions, the kinetic equation of the electrons has to be solved.

The aim of the following contribution is to compare measured distribution functions with special solutions of the electron *BOLTZMANN*-equation under specific simplifications of the problem. For this comparison will be taken into account the conventional homogeneous approach (CHA), the local field approximation (LFA) and the non-local approach (NLA) [1], [2].

Special solutions of the *BOLTZMANN*-equation

The following numerical treatment of the problem considers an axially homogeneous column plasma.

a) Conventional homogeneous approach (CHA)

This solution neglects the influence of the radial inhomogeneity and of the column plasma on the electron kinetics. The distribution function can be obtained from the *BOLTZMANN*-equation with a constant axial electric field E_z neglecting the radial inhomogeneity taking into account the elastic and relevant inelastic collision processes [1], [2].

$$\frac{d}{dU} \left[E_z^2 \frac{U}{3K(U)} \frac{d}{dU} f_0(U) + 2 \frac{m_e}{M} U^2 n_0 Q_d(U) f_0(U) \right] = U \sum_k n_k Q_k^*(U) f_0(U) - S_0$$

b) Local field approximation (LFA)

The local field approximation considers the equilibrium of the energy gain of the electrons in the total electric field $E = (E_z^2 + E_r^2)^{1/2}$ and the energy loss by collisions. To obtain this approximation we have to replace in the upper equation E_z by E .

c) Nonlocal approach (NLA)

The replacement of the kinetic energy $e_0 U$ by the total energy ε allows a transformation of the *BOLTZMANN*-equation in a more simple form. Assuming that the energy relaxation length λ_ε is large in comparison to

the radius of the discharge tube, and integrating the kinetic equation at a fixed ε over the relevant cross section of the plasma column, we obtain an ordinary differential equation for $f_0(\varepsilon)$ [1].

$$\frac{d}{d\varepsilon} \left[E_z^2 \frac{U}{3K(U)} \frac{d}{d\varepsilon} f_0(\varepsilon) + 2 \frac{m_e}{M} U^2 n_0 Q_d(U) f_0(\varepsilon) \right] = U \sum_k n_k Q_k^*(U) f_0(\varepsilon) - \bar{S}_0(U),$$

with $\varepsilon = e_0 U - e_0 V_s$, $\bar{b}(U) = \int_0^R b(\varepsilon, r) r dr$ and

R defined by $-e_0 V_s(R) = \varepsilon$ for $0 \leq \varepsilon < -e_0 V_s(r_0)$ and $R = r_0$ for $\varepsilon \geq -e_0 V_s(r_0)$.

Comparison with measurements

Measurements of the EDF in the positive column of helium a glow discharge were carried out under the following conditions: discharge current $i = 25$ mA, pressure $p_0 = 110$ Pa, tube radius $r_0 = 10$ mm. Under these conditions we can find for the energy relaxation length: $\lambda_\varepsilon > r_0$ for $U \leq \varepsilon_1$ and $\lambda_\varepsilon \approx r_0$ for $U > \varepsilon_1$, ε_1 threshold energy of the excitation.

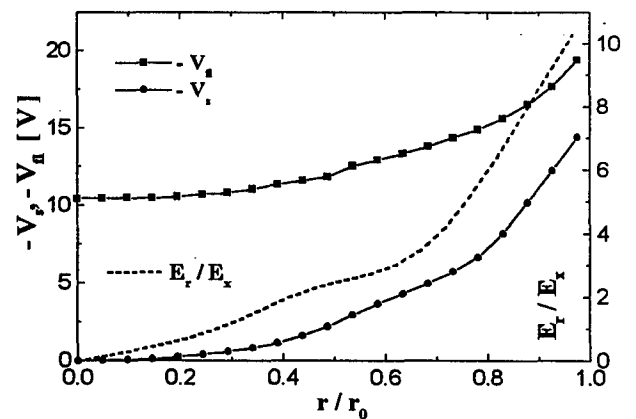


Fig. 1 Radial potential and field strength profiles

In Fig. 1 the measured floating and space potentials and the proportion of radial and axial field strength are presented. The radial component of the electrical field

strenght E_r increases by approaching the wall and exceeds the axial one by more than one order. These measured radial profiles of the potential and the electric field strength were used to calculate the distribution function from the modified *BOLTZMANN*-equation. Fig. 2 shows for the axis of the discharge tube that the calculated EDF's in nonlocal approach in the region of inelastical collisions significantly deviate from the measured ones. A good agreement can be found in comparison to the conventional solution.

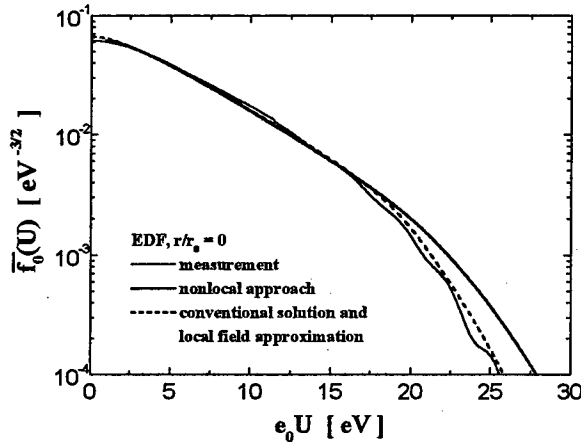


Fig. 2 Calculated and measured EDF's, $r/r_0 = 0$, $\bar{f}_0(U)$ is normalized to one

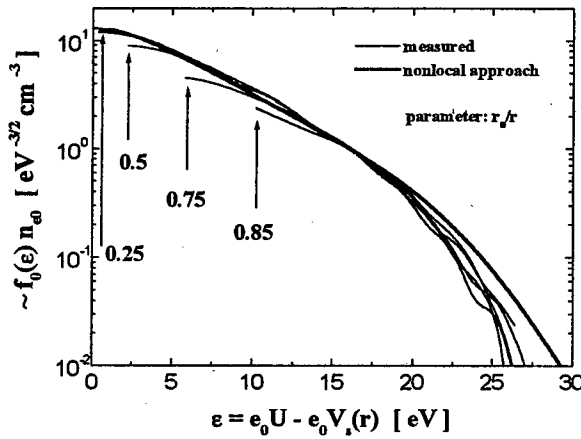


Fig. 3 Radial EDF's vs. total energy ϵ

Fig. 3 demonstrates that the radial dependence of the EDF's is described in a good manner by the nonlocal approach. On the other hand the local field approximation deviates drastically from the measured EDF's as to be seen in Fig. 4.

In Fig. 5 the measured electron density profile is compared with results of the nonlocal approach.

$$n_e(r) = n_{e0} \int_{-e_0 V_s(r)}^{\infty} f_0(\epsilon) \sqrt{\epsilon + e_0 V_s(r)} d\epsilon$$

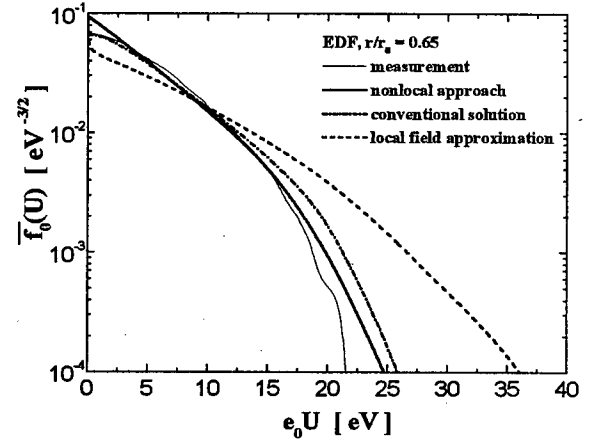


Fig. 4 Calculated and measured EDF's, $r/r_0 = 0.65$

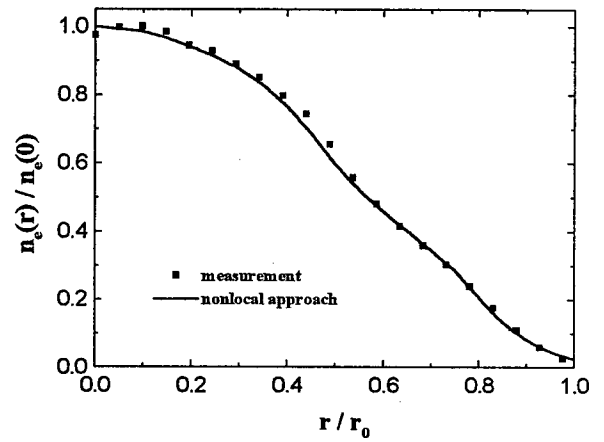


Fig. 5 Measured and calculated electron density profiles

Final Remarks

The measured electron velocity distribution function (EVDF) under our discharge conditions show a distinct change of the EVDF in dependence of the radial position. The discussed three cases of the simplified treatment of the inhomogeneous electron kinetics deliver different radial variations of the EVDF. Though the supposition for the validity of the NLA under our discharge conditions are only approximately fulfilled, the NLA alone describes the radial dependence of the EVDF in a satisfactory agreement with the experimental results.

References

- [1] Tsendin, L. D., Plasma Sources Sci. Technol. 4 (1995) 200-211.
- [2] Pfau, S., Rohmann, J., Uhrlandt, D., Winkler R., Contrib. Plasma Phys. 36 (1996) 4, 449-469

Neutral gap depletion in PSS repetition mode

L. Courtois, M. Rivaletto, J. Paillol, J-P. Brasile*, P. Pignolet

Université de Pau, Laboratoire de Génie Electrique, Hélioparc, 2 av. du Président Angot 64 000 PAU, France

* Thomson Shorts Systemes S.A., 9 rue des Mathurins, 92 223 BAGNEUX Cedex, France

Abstract

Analysis of repetition rate influence on the PSS operation characteristics is presented. Depletion of neutral densities in the main gap as function of repetition rate is carried out.

I Introduction.

In the 1980s' a new class of switches, so called PseudoSpark Switches (P.S.S.) has been developed.

The Pseudo-spark discharge is a low pressure gas discharge working on the left side of the Paschen-like hold-off curve. The P.S.S. is characterized by a fast current breakdown phase during which the corresponding high current density can be achieved with a diffuse aspect discharge over a large cathodic area. Moreover, it is able to operate at high repetition rate.

These features make the P.S.S. very attractive. Consequently that one becomes an alternative of usual high power switches.

The purpose of this paper is the investigation of the repetition rate influence on the gas heating and subsequently on the operating characteristics of the P.S.S.

II Experimental set-up.

The PSS trigger design corresponds to those of Mechttersheimer et al [1]. It consists to inject electrons, in the hollow cathode, provided by the mean of a pulsed low pressure glow discharge created back of the cavity.

During the tests [2], two types of hole are used : a central hole, and a ring hole allowing to increase the active surface of the hole while preserving a large hold-off voltage.

The dumping circuit is composed of a 6nF total equivalent capacitor. The inductance of the circuit is 32nH. The capacitors are charged by a D.C. power supply (10kV, 2kJ.s). Thus, the P.S.S. absorbs 300mJ.

The repetition rate is limited to 2kHz. In these conditions, the P.S.S. dissipates 600W mean.

III Preliminary investigation

III-1 Results

On figure 1, at 1Hz for a 10^{-2} mbar air pressure, we note a $0.9\mu\text{s}$ delay which corresponds to the hollow cathode glow discharge inception. When the repetition rate slightly increases (10Hz), due to the decreasing of the gas dielectric strength, the delay decreases. However, above 25Hz, the delay increases significantly. At 250Hz, the delay reaches $1.9\mu\text{s}$. By increasing the pressure from 1 to 1.8×10^{-2} mbar, the delay falls down

to $0.9\mu\text{s}$. At 2kHz, to obtain a value close of the initial delay of $0.9\mu\text{s}$, the pressure has to be 12×10^{-2} mbar.

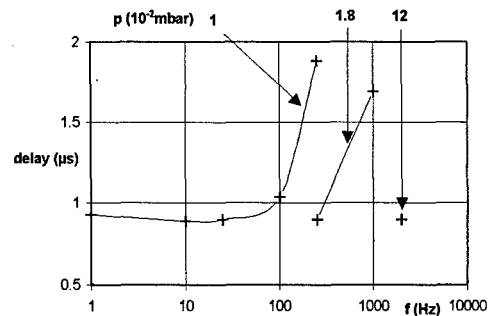


figure 1: triggering delay versus repetition rate and pressure

We can deduced the following conclusions :

- 1) The operating at high repetition rate in air increases the delay.
- 2) Contrary to what we could expect, the repetition rate operation increases the switch dielectric strength. This significant feature is shown in the figure 2, where the hold-off voltage (DC) versus the pressure is compared to that which was obtained in the preliminary experiment in repetition rate operation.

Thus, the 2kHz operation corresponds to a hold-off voltage of 2kV.

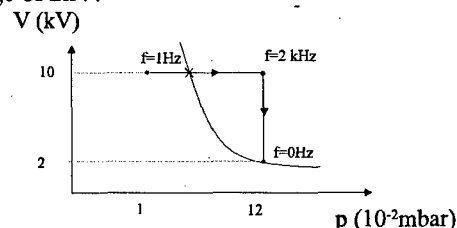


figure 2 : Working point according the pressure breakdown.

III-2 Interpretation

First, we have supposed that the Townsend dark discharge conditions were modified by increasing the repetition rate, i.e. reducing the time duration between two successive switchings. Nevertheless, by drastically varying the repetetive rate from 250Hz to 2kHz, the new steady delay value is reached only after several seconds. Consequently, hold-off voltage conditions are not only depending on the electrical parameters but, in addition, on internal modifications of the medium .

In single shot experiment, the hold-off voltage can be considered as a function of the pressure. Nevertheless, as reduced fields are high, due to low pressure and small dimensions, the electrons energy is larger than the neutral one. Therefore the hold-off

voltage can be expressed rather as a function of the neutral density, i.e. the collision frequency.

Besides, it is necessary to note that the neutral density is a decreasing function of the delay. When the collision frequency increases, we reach self-breakdown conditions.

The interpretation of the initial experience is given below, on the figure 3 where numbers indicate the sequence.

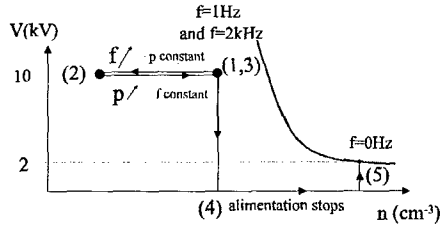


figure 3 : Experiment interpretation (step by step)

When the frequency increases, the delay increases, i.e. the neutral density decreases. So, the delay can be compensated by increasing the pressure, corresponding to a new neutral density. Thus, we can explain that, at 2kHz, the self-breakdown voltage has not reached. When the power supply has stopped, the increased pressure corresponds to a neutral density ten times higher, and consequently the hold-off voltage is only 2kV.

The delay increase is interpreted therefore by a decrease of neutral density in all the interval (gap + hollow cathode).

Assuming, in all parts of the switch, the thermodynamic equilibrium, the interval depletion corresponds to the heating of the medium. When the injected energy in the medium increases, the neutral temperature increases and the neutral density decreases, according to the $p = nkT$ law.

IV Measures at constant delay

IV-1 Results

As delay depends on neutral density, it is possible to measure the pressure variation at constant neutral density, i.e. at constant delay.

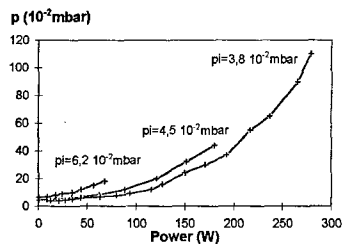


figure 4 : Pressure to keep delay constant versus power

So, the pressure variation is plotted on the figure 4 versus the power injected at constant delay and for three different initial pressures p_i .

We observe that variations increase as p_i . However, we must notice that the maximum allowed power depends on the plasma radial expansion that makes a short-circuit along the charged insulator.

IV-2 Interpretation

Assuming that current mainly correspond to an electron beam [3], which yielded energy to the medium, the probability that an electron of the beam collides by crossing the interval is proportional to the neutral density.

Thus, the energy E yielded to maintain the plasma is expressed as:

$$E \propto W \cdot n \propto W \cdot p_i$$

where W corresponds to the power dissipated in the P.S.S. and n the neutral density.

Moreover, assuming the thermodynamic equilibrium for neutral species, we write :

$$\frac{T_g}{T_{g_i}} = \frac{p}{p_i} = f(W \cdot p_i)$$

By using the previous experimental data, we obtain the following curves (figure 5 ring curve).

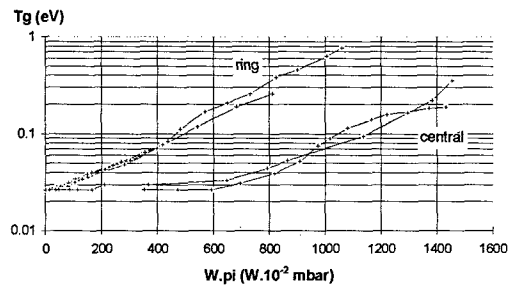


figure 5: Gas temperature versus product of initial pressure and power

The curves behaviours for the three pressures p_i , at constant delay are very similar especially for a product $W \cdot p_i$ lower than to $400 \cdot 10^{-2} \text{ W} \cdot \text{mbar}$. That means that the gas temperature mainly depends on the energy injected in the plasma ($W \cdot p_i$) and on the cooling. Because this depends on the repetition rate and on physical conditions, the neutral temperature variations can be written :

$$\ln(T_g/T_{g_i}) = k \cdot W \cdot p_i \quad k : \text{a constant}$$

In addition, others experiments made for a cathodic central hole P.S.S. are reported and compared with previous results on figure 5. We observe a same feature in function of $W \cdot p_i$. In this case, the gas is heated with higher power. This is due to the fact that the electrode temperature for a same total power absorbed by the switch is lower for the cathodic central hole than for the cathodic ring hole. That corresponds to a best cooling of the plasma.

V Conclusion

A depletion effect in the gap is due to neutral heating. The energy loss in the gas is function of $W \cdot p_i$. This argues in favour of a beam electron transport mode during the superdense glow. The cooling mainly depends on the electrodes and so on their designs.

References

- [1] G. Mechttersheimer., R. Kohler., T. Lasser., R. Meyer. J Phys E SI-19 (1986), p 466
- [2] L. Courtois, Thèse, Université de PAU (1996)
- [3] G. Kickman-Anemiya, R.L. Liou, T.Y. Hsu, M.A. Gundersen. Physics and applications of Pseudosparks Edited by M.A. Gundersen and G. Schaefer, Plenum Press, NY, 1990

A simple, local-equilibrium model of negative differential resistance

S. B. Vrhovac, I. Stefanović and Z. Lj. Petrović
Institute of Physics, University of Belgrade, P.O. Box 57,
11001 Belgrade, Yugoslavia

Introduction

The negative resistance plays a crucial role in the theory of instabilities and oscillations of the low-current discharges in parallel-plane geometry [1, 2, 3, 4]. In this paper we extend the simple model developed by Phelps and coworkers [3] of the negative differential resistance.

Recently the interest in low current diffuse discharges has increased. The reasons are that there are still some unsolved properties of such very simple discharges which were believed to be exactly described by a uniform field and Townsend's theory based on effective spatial coefficients. In addition those discharges may be used to determine transport coefficients and when operated at very high E/N they reveal some properties of sheaths such as nonlocal, non-equilibrium behaviour and excitation induced by heavy particles. As a result of their simplicity and accuracy of the available experimental data such discharges have recently become interesting to test numerical models which would later be applied to the inhomogeneous, higher current, discharges [5].

A linear theory was developed by Phelps and coworkers [3] which overcomes some of the limitations of the inherently nonlinear, similar theory of Melekhin and coworkers [4]. Experiments have revealed that under some circumstances, the effective negative differential resistance (voltage to current ratio) becomes nonlinear [6] behavior of low-current electrical discharges needed to describe the experimental results. Therefore we have attempted to extend the theory of low current discharges of Phelps and coworkers [3] but in the process we became aware that Phelps [7] has developed a theory similar to ours with details which are still not available to us. The non-linearity in negative differential resistance is the precursor of a series of non-linear phenomena observed in those discharges that lead eventually to constriction [8].

In this paper analytic expressions for differential resistance are developed using the steady-state, local-equilibrium model for electron and ion motion and a *second-order* perturbation treatment of space-charge electric fields.

Theoretical evaluation

In this section we will calculate the negative differential resistance of the discharge R_D caused by space-charge distortion of the electric field. We limit the discharge current so that the perturbation of the applied electric field is small. Thus we calculate the space charge to the *second-order* using the steady-state ion and electron current densities appropriate to a spatially uniform electric field.

The space-charge-induced electric field E_s is found by solving Poisson's equation:

$$\frac{dE_s}{dz} = \frac{1}{\epsilon_0} \frac{j}{W_+} [1 - \exp(\alpha_0(z-d))]. \quad (1)$$

Here ϵ_0 is the permittivity of free space, j is the total current density, W_+ is the positive ion drift velocity and α_0 is the spatial ionization coefficient appropriate to the unperturbed electric field E_0 . The z -axis is directed from cathode to anode and d is the separation of the parallel-plane electrodes. By integrating Eq. (1) we obtain

$$E_s(z) - E_s^{(C)} = \frac{1}{\epsilon_0} \frac{j}{W_+} \frac{1}{\alpha_0} [\alpha_0 z - \exp(\alpha_0(z-d)) + \exp(-\alpha_0 d)] \quad (2)$$

where $E_s^{(C)}$ is the electric field at the cathode caused by the space charge ($E_s^{(C)}$ - unknown boundary condition). From Eq. (2) we can calculate

$$\begin{aligned} \delta V_s^{(1)} &:= - \int_0^d (E_s(z) - E_s^{(C)}) dz \\ &= - \frac{1}{\epsilon_0} \frac{j}{W_+} f^{(1)}(\alpha_0, d) \end{aligned} \quad (3)$$

and

$$\begin{aligned} \delta V_s^{(2)} &:= - \int_0^d (E_s(z) - E_s^{(C)})^2 dz \\ &= - \frac{1}{\epsilon_0^2} \frac{j^2}{W_+^2} f^{(2)}(\alpha_0, d). \end{aligned} \quad (4)$$

Functions $f^{(1)}$ and $f^{(2)}$ are known.

The second part of derivation is the evaluation of the potential change δV between electrodes caused

by the space-charge-induced electric field E_s :

$$\delta V := - \int_0^d E_s(z) dz. \quad (5)$$

We first expand α and γ (ion-induced electron yield at the cathode) in Taylor series in the vicinity of the unperturbed field E_0 to the *second* order in E_s :

$$\begin{aligned} \alpha(E) &= \alpha(E_0) + \alpha'(E - E_0) \\ &\quad + \frac{1}{2} \alpha''(E - E_0)^2 + o(E_s^2), \end{aligned} \quad (6)$$

$$\begin{aligned} \gamma(E^C) &= \gamma(E_0) + \gamma'(E^C - E_0) \\ &\quad + \frac{1}{2} \gamma''(E^C - E_0)^2 + o[(E_s^C)^2] \end{aligned} \quad (7)$$

where $E^C = E_0 - E_s^{(C)}$ is the (perturbed) electric field at the cathode. Substituting these expressions into the discharge maintenance condition

$$1 = \gamma(E^C) \left[\exp \left(\int_0^d \alpha[E(z)] dz \right) - 1 \right] \quad (8)$$

and keeping only the terms to the *second* order in E_s , leads after some algebra to the equation of the second order in δV . General solution can be obtained in an analytical form:

$$\begin{aligned} \delta V = -\frac{1}{2k_1} \left\{ k_2 + k_3 \delta V_s^{(1)} \pm \left[(k_2 + k_3 \delta V_s^{(1)})^2 \right. \right. \\ \left. \left. - 4k_1 \left(k_4 \delta V_s^{(1)} + k_5 (\delta V_s^{(1)})^2 + k_6 \delta V_s^{(2)} \right) \right]^{\frac{1}{2}} \right\} \end{aligned} \quad (9)$$

where

$$\begin{aligned} k_1 &= k_1(\alpha_0, \gamma_0, \alpha', \gamma', \alpha'', \gamma'', d) \\ k_2 &= k_2(\alpha_0, \gamma_0, \alpha', \gamma', d) \\ k_3 &= k_3(\alpha_0, \gamma_0, \alpha', \gamma', \gamma'', d) \\ k_4 &= k_4(\gamma_0, \gamma', d) \\ k_5 &= k_5(\alpha_0, \gamma_0, \alpha'', \gamma'', d) \\ k_6 &= k_6(\alpha_0, \gamma_0, \alpha'', \gamma'', d) \end{aligned} \quad (10)$$

Finally, negative differential resistance R_N is defined [3] as

$$R_N := \frac{A \delta V}{I d^2} \quad (11)$$

where A is the electrode area, I total current and δV can be calculated from Eq. (9). Equations (9)–(11) show that for a given set of electrode and gas parameters, R_N is a function of the variables $W_+(E/n)$, $\alpha/n(E/n)$ and γ . The final result is too complex to be presented here but is open to analytical analysis and easy numerics as it is a purely algebraic result.

Discussion

The predictions of our model of negative differential resistance when compared with published data [1, 2, 3] and our experimental data for low-current hydrogen discharges give an insight into the mechanisms that lead to development of negative differential resistance, self sustained oscillations in low current diffuse discharges and their transition to constricted regime. The present theory only includes the second order effects in ionization coefficient and secondary electron yield due to ion bombardment. The basic feedback mechanism assumed is the ion drift to the cathode and secondary electron production. At higher pressures [7], however excitation of resonant states may lead to emission which can produce initial electrons at the cathode and also diffusion of metastables may lead to negative differential resistance as well. Those processes will have different non-linearities inherent in them. Generally however, description of the development of constrictions will also require inclusion of non-linear effects due to electric field deviation.

References

- [1] Z. Lj. Petrović and A. V. Phelps, Phys. Rev. E **47**, 2806 (1993)
- [2] B. M. Jelenković, K. Rózsa and A. V. Phelps Phys. Rev. E **47**, 2816 (1993)
- [3] A. V. Phelps, Z. Lj. Petrović and B. M. Jelenković Phys. Rev. E **47**, 2825 (1993)
- [4] V. N. Melekhin and N. Yu. Naumov, Sov. Phys. Tech. Phys. **29**, 888 (1984)
- [5] I. Peres and L. C. Pitchford, J. Appl. Phys. **78**, 774 (1995)
- [6] Z. Lj. Petrović and A. V. Phelps, unpublished (1992)
- [7] A. V. Phelps (personal communication)
- [8] Z. Lj. Petrović and A. V. Phelps, IEEE Trans. Plasma Sci. **PS 24**, 107 (1996)

Transition from ambipolar to free diffusion in nitrogen afterglow

V. Lj. Marković*, Z. Lj. Petrović† and M. M. Pejović**

* Department of Physics, University of Niš, P.O. BOX 91, 18001 Niš, Yugoslavia

† Institute of Physics, P. O. BOX 57, 11000 Belgrade, Yugoslavia

** Faculty of Electronic Engineering, P.O. BOX 73, 18001 Niš, Yugoslavia

1. Introduction

The subject of this paper is to establish processes of charged particle decay in nitrogen afterglow from the breakdown time delay data and determine the variation of the effective diffusion coefficients from the ambipolar to the free diffusion limit. Hence, the breakdown time delay data (\bar{t}_d) as a function of the afterglow period or relaxation time (τ) (the memory curve) are modeled on the basis of a simple diffusive model. The values of the effective diffusion coefficients from the ambipolar diffusion limit to the free diffusion limit and effective electron temperature in the afterglow are determined.

2. Experiment

The memory curves represent the plots of the mean value of breakdown time delay (\bar{t}_d) as a function of the afterglow period or relaxation time (τ). The memory curves were obtained for a gas tube made of molybdenum glass with volume $V = 160 \text{ cm}^3$ and area $S_W = 180 \text{ cm}^2$. The electrodes were copper rods, with area $S_E = 1.3 \text{ cm}^2$ and gap $d = 2 \text{ mm}$. The tube was filled with Matheson research grade nitrogen at 6.6 mbar pressure.

During the experiment a series of pulses is applied to the discharge tube. The time between the voltage pulses τ and the breakdown time delay t_d were measured. The voltage of the pulse is $U_s + \Delta U$, where $\Delta U/U_s$ is the fractional overvoltage given in percents and U_s is the static breakdown voltage. The glow current was $I_g = 0.5 \text{ mA}$ and glow time $t_g = 1 \text{ s}$. The mean values of the time delay were established from series of 100 measurements. More details can be found in [1-3].

The total time delay comprises of the statistical time delay t_s and the formative time t_f , i.e. $t_d = t_s + t_f$ [4]. The statistical time delay can be expressed as $\bar{t}_s = 1/YP$, where Y represents a number of generated electrons in the inter-electrode space per second (electron yield), and P the probability of one electron to cause the breakdown. If we assume that the breakdown probability is $P \approx 1$ at $\Delta U/U_s = 50\%$, the effective electron yield in the

interelectrode space can be obtained as $Y \approx 1/\bar{t}_s$. Since standard deviation of statistical time delay is equal to the mean value of statistical time delay $\sigma(t_s) = \bar{t}_s$ [4] and $\sigma(t_d) \approx \sigma(t_s)$, we obtain the mean value of statistical time delay in the form $\bar{t}_s = \sigma(t_d) = 1/Y$ which is associated with electron production and used for modeling of relaxation processes in afterglow [3].

3. Charged particle decay in afterglow by simple diffusive model

The temporal behavior of the breakdown time delay due to decay of ions as discharge precursors can be followed by numerically solving the following two equations for the diffusion and loss of ions on surfaces and for the yield of secondary electrons [3]:

$$\frac{\partial N_i}{\partial \tau} = D_{eff} \nabla^2 N_i - k_{rec} N_i^2, \quad (1)$$

$$Y_I = P_I N_i|_E (V_C/2)/\Delta T. \quad (2)$$

The first term on the right-hand side of (1) designates the transitional diffusion with the effective ion diffusion coefficient extending from an ambipolar diffusion limit to a free diffusion limit [5], and the second one is the dissociative recombination term. The value for the dissociative recombination coefficient $k_{rec} \sim 10^{-7} \text{ cm}^3 \text{ s}^{-1}$ [6] is taken. The equation (1) is solved by the finite difference method. The grid is developed that corresponds to our mostly cylindrical geometry with exact representation of geometry, assuming completely absorbing electrode and glass surface for ions ($N_i|_{E,W} = 0$). In previous equations $N_i|_E$ is the ion number density at the front electrode surface ($N_i|_W$ corresponds to the wall surface), V_C is the volume of the inter-electrode space and ΔT is the numerical time step.

In the first step, the stationary density distribution is calculated on the basis of estimated concentration in the inter-electrode space ($N_{i0} \sim 10^{10} \text{ cm}^{-3}$). In the second step, the density distribution during the decay is followed. The value for the effective diffusion coefficient is varied ranging

from an ambipolar diffusion limit to the free diffusion limit [5] in order to fit the experimental data. The fitting of experimental data with constant and transitional effective diffusion coefficient and probability $P_I \approx 10^{-4}$ is shown in Figs 1,2. For the early afterglow times of the order of ~ 0.1 ms all the conditions for the ambipolar diffusion are met, i.e. $\Lambda/\lambda_{Di} > 100$, where $\lambda_{Di} = \sqrt{(\epsilon_0 k T_i)/(N_i e^2)}$ is Debye length for ions [5]. For those times however dissociative recombination dominates and diffusion coefficient cannot be determined. For greater times the effective diffusion coefficient can be obtained and $D_{eff} = 110 \text{ cm}^2 \text{ s}^{-1}$ gives the best fit up to 20 ms (Figs 1,2), and Λ/λ_{Di} from about 100 to 1. Above 20 ms a relatively rapid transition to the free diffusion coefficient ($D_i \sim 8 \text{ cm}^2 \text{ s}^{-1}$) is needed to fit the data (Figs. 1,2), and D_{eff} should be a linear function of Λ/λ_{Di} . According to our calculations, the region of transition to free diffusion coincides with $\Lambda/\lambda_{Di} \sim 1 - 0.1$.

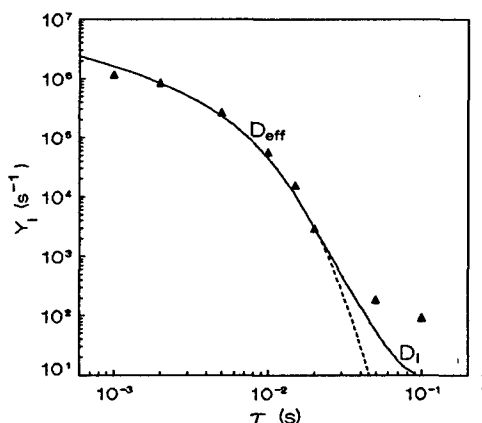


Fig. 1. The electron yield Y_I in the inter-electrode space vs τ at $D_{eff} = \text{const}$ (broken curve) and with transitional D_{eff} (solid curve).

According to the theoretical calculations of the temporal evolutions in discharge and post-discharge regimes of electronically and vibrationally excited molecules as well electron energy distribution function [7] the very early afterglow is characterized by very fast relaxation of initial electron energy distribution function to a quasi-stationary state where superelastic vibrational collisions compensate the inelastic vibrational losses and the mean electron energy \bar{E}_e decreases to a quasi-stationary value of 0.45 eV in times of the order ($10^{-7} - 10^{-6}$) s. The quasi-stationary state described by vibrational temperature and quasi-stationary \bar{E}_e value change self-consistently (in times of the order of $10^{-3} - 10^{-2}$ s) as a result of the variation of a vibrational distribution [7]. In this time interval the diffusion is the predominant relaxation process (Figs 1,2). If D_{eff} is expressed as $D_{eff} \sim D_i(T_e/T_i)$ (like in am-

bipolar diffusion limit [5]) and assuming that the ion temperature T_i is equal to the gas temperature $T_g = 300 \text{ K}$ and $D_i \sim 8 \text{ cm}^2 \text{ s}^{-1}$ under our conditions, it follows that the electron temperature is $T_e \approx 4000 \text{ K}$ ($\bar{E}_e \approx 0.5 \text{ eV}$).

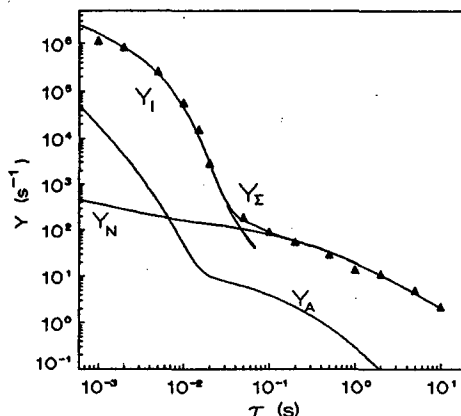


Fig. 2. The net electron yield Y_E vs τ from the ion induced secondary electron emission Y_I , from the gas phase $N_2(A^3\Sigma_u^+)$ metastable states Y_A and from the surface-catalyzed excitation mechanism Y_N [1].

The constant diffusion coefficient and electron temperature (comparable with the vibrational temperature [7]) in the above calculations indicate that the superelastic heating of electrons in collisions with vibrationally excited molecules is the dominant channel and not with the $N_2(A^3\Sigma_u^+)$ state since its number density decays several orders of magnitude in this afterglow period (Fig. 2). In the late afterglow (Fig. 2) the second order breakdown initiation mechanism begins to dominate which is assigned to the atomic recombination of nitrogen atoms on the cathode surface as a source of secondary emitted electrons [1].

4. References

- [1] V. Lj. Marković, M. M. Pejović, and Z. Lj. Petrović, J. Phys. D 27 (1994) 979
- [2] V. Lj. Marković, Z. Lj. Petrović, and M. M. Pejović, J. Chem. Phys. 100 (1994) 8514
- [3] V. Lj. Marković, Z. Lj. Petrović, and M. M. Pejović, to be published
- [4] J. M. Meek and J. D. Craggs, *Electrical Breakdown of Gases* (Oxford at the Clarendon Press, 1953).
- [5] A. V. Phelps, J. Res. Natl. Ins. Stand. Technol. 95 (1990) 407
- [6] A. V. Elefski and B. M. Smirnov, Usp. Phys. Nauk 136 (1982) 25
- [7] M. Capitelli, C. Gorse and A. Ricard, in *Nonequilibrium Vibrational Kinetics*, ed. M. Capitelli (Springer-Verlag, Berlin, 1986)

Correlated experiments on cathode-dominated, low-pressure discharges in Ar

A. V. Phelps

JILA, University of Colorado and National Institute of Science and Technology, Boulder, CO

1. Introduction

We present correlations among the extensive set of experimental measurements on low-pressure, parallel-plane discharges in Ar carried out at JILA between 1984 and 1994. The solid curve of Fig. 1 shows representative steady-state, discharge voltage versus current data at 2 Torr for a 1 cm electrode spacing and a 3.9 cm radius [1,2]. The arrows lead from the steady-state values to measured radial spatial distributions of emission or to transient voltages and currents. Similar plots will correlate other data cited below.

2. Townsend, subnormal, or dark discharges

Discharges operating at currents from zero to values at which constrictions are observed (near 0.2 mA in Fig. 1) are called "Townsend," subnormal, or "dark" discharges. At the lower currents, measurements using dc and pulsed voltages show a linear decrease of voltage with current, i.e., a constant negative differential voltage to current ratio (NDVCR) [1]. Digital photographs of the discharge emission taken through a semitransparent anode [1,3] show that these discharges are diffuse (lower, left insert in Fig. 1). The transient voltage and current (upper, left insert) show a damped oscillatory approach to the steady-state [1,2]. As the average current is increased the oscillation frequency increases and the damping decreases until self-sustained oscillations occur (top, center insert in Fig. 1) [1,2]. The oscillatory discharges are highly constricted (bottom, center insert) [3]. Reduction of the circuit capacitance minimizes the current range of the self-sustained oscillations [1,2,4]. Models [2,4] including the effects of space-charge fields on the ion-induced electron yield at the cathode give frequencies of damped oscillations in agreement with experiment at 0.3 to 2 Torr, but not at 0.12 Torr [1]. Measurements of charge collected following laser induced avalanches test models of ionization growth and of secondary electron production [1]. Axial scans of emission show the importance of excitation in collisions of fast Ar with Ar [5]. A small angle between the nominally parallel electrodes results in an asymmetry of the discharge that switches sides with pressure to reflect the pressure dependence of the breakdown voltage [6].

3. Constricted or normal discharges

At intermediate currents (0.2 mA to 5 mA in Fig. 1)

the discharges are constricted to an area smaller than the area of the cathode. At 2 Torr pressure analyses of digital photographs of the emission taken through the semitransparent anode [1,3] show the flat-topped radial distributions (lower, right inset in Fig. 1) that expand with current as previously observed visually. Analyses [1] of the photographs show that the average current density in the constricted region is nearly constant at the "normal" value and that the constriction area is in rough agreement with recent theories [7]. The quasi-steady-state voltage is very nearly independent of current as reported previously. At pd values below 0.3 Torr-cm the onset of the constriction is delayed by roughly 0.5 millisecond before moving to the wall and rotating [1].

4. Above normal or abnormal discharges

As the current is increased the discharge expands until it fills the discharge tube (near 5 mA in Fig. 1). The current density for this condition ($100 \mu\text{A}/\text{cm}^2$) is the "normal" current density and is within the spread of published values. Our voltage-current data for "abnormal" discharges is shown in Fig. 1. Transient, axial spatial distributions of emission and voltage and current waveforms [8] at currents near the normal current show the development of the cathode fall and the importance of fast atom collisions. Window blackening by sputtering prevented photographs of the radial emission distribution at these currents.

5. References

- [1] Z. Lj. Petrović and A.V. Phelps, Phys. Rev. E (submitted) (1997) and unpublished.
- [2] Z. Lj. Petrović and A.V. Phelps, Phys. Rev. E 47, 2806 (1993); B. M. Jelenković, K. Rózsa, and A.V. Phelps, Phys. Rev. E 47, 2816 (1993); A.V. Phelps, Z. Lj. Petrović and B. M. Jelenković, Phys. Rev. E 47, 2825 (1993).
- [3] Z. Lj. Petrović and A.V. Phelps, IEEE Trans. on Plasma Sci. 24, 107 (1996).
- [4] V. N. Melekhin and N. Yu. Naumov, Zh. Tekh. Fiz. 54, 1521 (1984); I. D. Kagonovich, M. A. Fedotov, and L. D. Tsandin, Zh. Tekh. Fiz. 64, 22 (1994).
- [5] A.V. Phelps and B. M. Jelenković, Phys. Rev. A 38, 2975 (1988); D. A. Scott and A. V. Phelps, Phys. Rev. A 43, 3043 (1991).
- [6] B. M. Jelenković and A. V. Phelps, Bull. Am. Phys. Soc. 39, 1490 (1994).

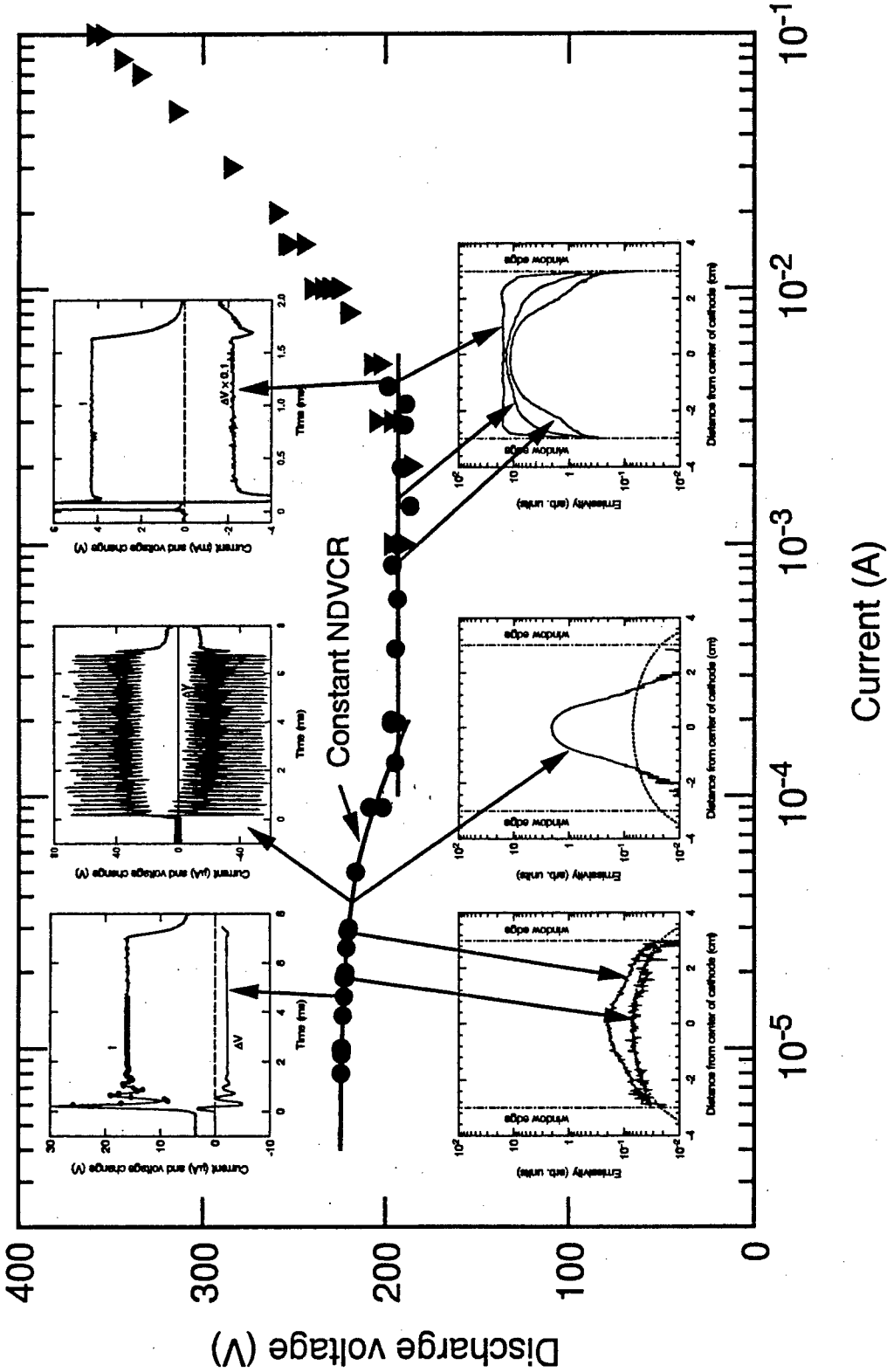


Figure 1. Discharge voltage versus current for Ar at 2 Torr. The upper set of insets shows the transient current and voltage, while the lower set shows the radial distribution of emission. The arrows connect the insets with their respective steady-state voltages and currents.

TIME AND SPACE RESOLVED ENERGY DISTRIBUTION OF AN ELECTRON BEAM PRODUCED IN A FILAMENTARY TRANSIENT DISCHARGE

G. Modreanu, M. Ganciu*, N.B. Mandache*, A.M. Pointu

LPGP, Université Paris-Sud -CNRS, 91405 Orsay Cedex, France

E. Dewald*, M. Nistor, I. Iovitz Popescu, M.V. Udrea

Institute of Atomic Physics, Plasma Department, PO Box MG-6 Bucharest, Romania

* permanent adress: Institute of Atomic Physics, Plasma Department, PO Box MG-6 Bucharest, Romania

+ actual adress: Physics Department, University of Erlangen-Nuernberg, 91058 Erlangen, Germany

1-Experiment

A method to generate electron beams in the same range of operating parameters as in pseudo-sparks has been reported recently^[1]: it uses the basic principle of superposition of two discharges, the main one being established by applying high voltage pulses between an open hollow cathode and an anode, the auxiliary one creating a preliminary plasma in the cathodic region.

Among possible configurations, the one under study (Fig.1) allows to extend to some 10cm the beam length. It uses a 3cm diameter discharge tube presenting a common K_1K_2 hollow cathode to serve both as the main pulsed discharge cathode and the auxiliary dc discharge cathode. A_1 and A_2 are the pulsed discharge and the dc discharge anodes, respectively. The anode A_2 plays the role of a diaphragm for the main discharge. A metallic grid around the discharge tube at the same potential as the diaphragm is used to increase the stability of the electron beam. The beam develops longitudinally on the tube axis between K_1 and A_1 , very stable and finely controlled by the auxiliary discharge. It is associated with a filamentary discharge, appearing as a 1 to 2mm diameter plasma channel produced homogeneously along the beam path.

The beam current is extracted through a circular hole drilled in anode A_1 and collected by a Faraday cup coupled to a non inductive shunt of 0.6Ω through a serial resistor, giving a total equivalent resistor R . When passed by the beam current $I_b(t)$, the Faraday cup is self biased to a repulsive voltage $RI_b(t)$ such that selection is operated in the beam energy distribution function $g(u)$ following the relation

$$I_b(t) = c \int_{RI_b(t)}^{\infty} (u)^{1/2} g(u) du$$

where c is a constant involving electron charge and mass and extraction hole area A , given by $c = e^{3/2} A (2/m)^{1/2}$. The knowledge of curves $I_b(t)$ for several values of R allows deconvoluting previous relation to determine at each t value the corresponding $g(u)$ through relation :

$$cg(RI_b) = - [dI_b / d(RI_b)] / (RI_b)^{1/2}$$

2-Results

Let denote with index $j=1,2$ the quantities relative to the cases of 1 mm and 2 mm anodic aperture respectively. Fig.2 shows oscillograms of recorded $I_b(t)$, for several values of R between 0.6Ω and 500Ω . Common discharge conditions were 0.1Torr pressure of Argon and 50kV breakdown voltage.

Fig.3 gives calculated $g_1(u)$, evidencing at earlier times a "fast" electron tail evolving later to a slower quasi maxwellian distribution. As an example, corresponding n_1 and T_1 values are estimated respectively around $1.2 \cdot 10^{13} \text{ cm}^{-3}$ and 80 eV for $t=40\text{ns}$.

The distribution $g_2(u)$ exhibits the same evolution, with a lower ratio between fast and slow population, as evidenced in Fig.4 where are shown simultaneously $g_1(u)$ and $g_2(u)$ at time of the common first maximum value, I_{bm} , of I_b (i.e. $t=32\text{ns}$). The comparison between cases $j=1$ and $j=2$ gives a rough indication on the radial distribution in g : in fact, the mean distribution function for beam electrons out of axis by a distance between 0.5 and 1mm can be estimated from the relation

$$g_3 = (4 g_2 - g_1)/3$$

It is shown on Fig. 4 at time $t=32\text{ns}$.

Finally, using comparison of I_{b2} for 0.6Ω and 500Ω and the mean energy of energetic electrons ($\approx 15\text{keV}$), as measured in [2], we estimate that, at time of I_{bm} that we have previously shown to coincide with energetic electron beam emission, these energetic electrons carry electron density and current respectively around $n_2/10$ and $1/30$ of I_{bm} (0.6Ω). It appears thus that electron beam is dominated by medium energy electrons in the range of 100 eV, very interesting for laser and physico-chemical applications.

3-References

- [1] M. Ganciu, G. Modreanu, A. M. Pointu, I. I. Popescu, J. Phys.D:Appl. Phys., **27**, 1370 (1994)
- [2] N.B. Mandache, A.M. Pointu, E. Dewald, M. Nistor, M. Ganciu, G. Musa, I. I. Popescu, to appear in Plasma Sources Sci. Technol. (1997)

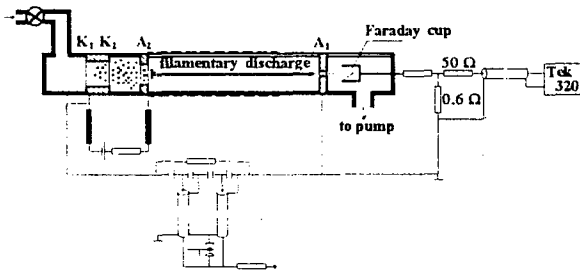


Fig. 1 Experimental set-up

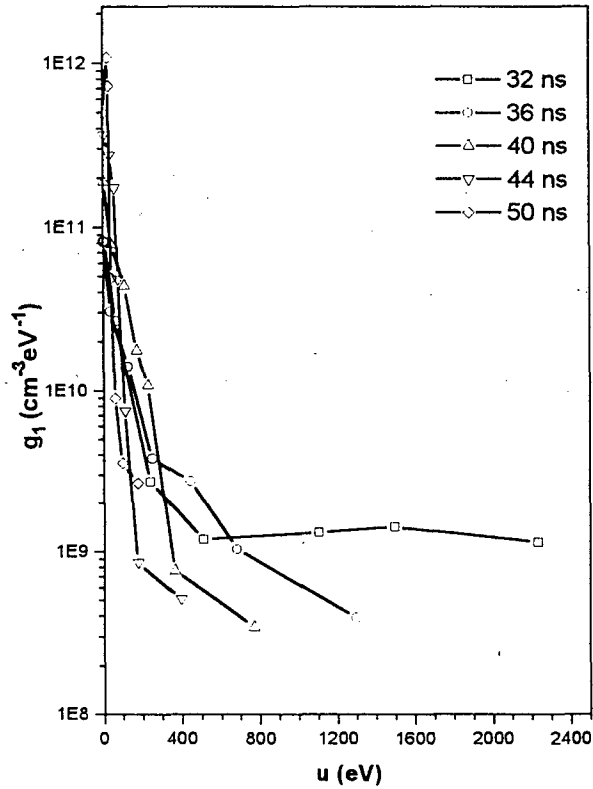


Fig. 3 Electron distribution function for 1 mm anodic aperture

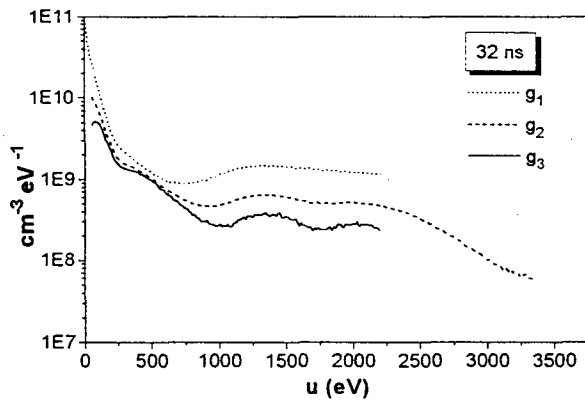


Fig. 4 g_1 and g_2 distributions for two extraction holes and out of axis (0.5 mm to 1 mm) g_3 distribution

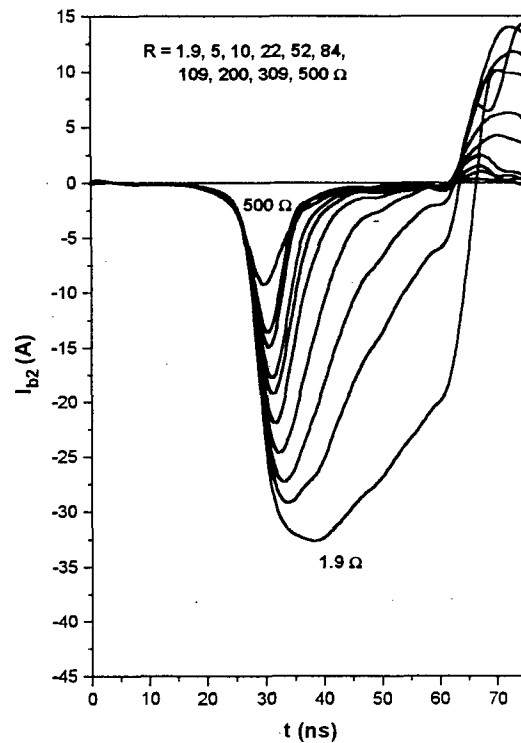
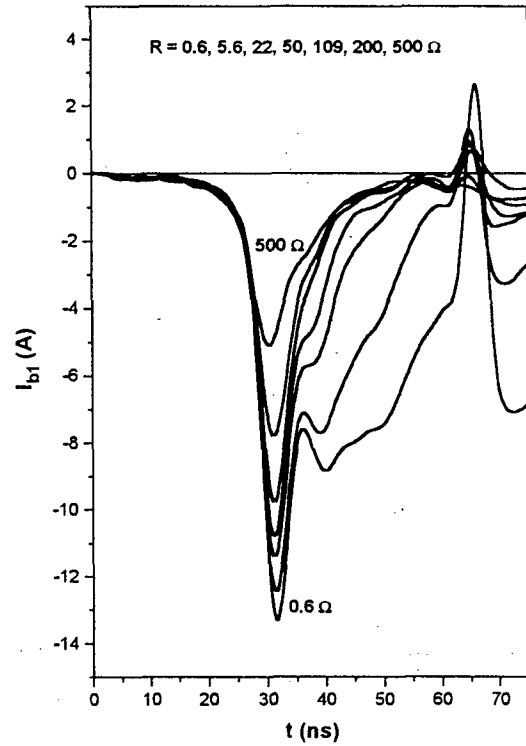


Fig. 2 Recorded beam currents I_{b1} and I_{b2} for several resistor values

Intense pulsed electron beams produced in multigap and single gap PCOHC

E. Dewald^{1,4}, K. Frank¹, A.M. Pointu², D. H. H. Hoffmann¹, R. Stark¹
M.Ganciu³, N.B. Mandache³, M. Nistor³, and I.-Iovitz Popescu³

¹Physics Department, University of Erlangen-Nuremberg, Erwin-Rommel-Str. 1 D-91058 Erlangen, Germany

²Universite Paris Sud, 91405 Orsay, France

³Institute of Physics and Technology of Radiation Devices, Bucharest - Magurele, Romania (⁴Permanent address)

1. Introduction

High voltage hollow-cathode glow discharges are used to generate pulsed intense electron beams with remarkable parameters. Recently such pulsed electron beams were generated with high efficiency in a preionization controlled open ended hollow cathode configuration (PCOHC) [1]. This configuration can work either with metallic or dielectric electrodes and the generated electron beams turned out to have a very good spatial stability and reproducibility. The electron beam parameters are similar to those of the electron beams generated in pseudospark discharges [2,3]. Some parameters of the extracted electron beams such as intensity were improved by using a multielectrode device similar to those used in pseudosparks [4]. In this work the dependence of the beam intensity from breakdown voltage, external capacity and distance from the anode back face is studied for both single gap and multigap configurations.

2. Set-up and results

The single-gap and multigap configurations have 70 mm length and 34 mm diameter metallic open ended hollow cathodes. The six-electrode system and the anode (for single gap configuration) have 2 mm central bore holes, 20 mm bore holes in the insulators and the thicknesses for both the electrodes and insulators are of 2 mm. The hollow cathode is placed 1.5 cm from the first floating electrode. The anode-cathode gap in the single gap configuration is about 2 cm long. The working gas is air at pressures between 30 and 50 Pa, measured at the drift chamber level. The optimal preionization current [2] was of 1 mA for the single gap configuration and of 0.1-0.8 mA for the multigap configuration. The optimal preionization current is increasing with the discharge voltage in the multigap case. External capacities between 0.9 and 10 nF were used. The discharge voltage was measured with a Tektronix P6015A high voltage probe and the beam current was measured behind the anode bore hole at distances between 1.5 and 12 cm with a moveable Faraday cup having an internal resistance of about 1.2 Ω . In Fig. 1 the dependencies of the beam peak current with the breakdown voltage are given for both multigap and single gap configurations.

The beam currents were measured at 1.5 cm behind the anode. As it can be observed, the beam peak current is strongly dependent on the breakdown voltage and is more than two times increased when the multielectrode system is used.

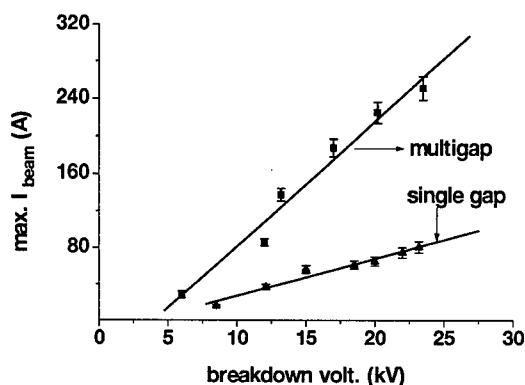


Fig. 1 Beam peak current versus breakdown voltage for multigap and single gap configurations

Similar with pseudosparks [5], the beam current has two or more different peaks which can be better separated for longer distances between the Faraday cup and the anode. For small distances (1.5 cm) the separation of the peaks is better when the breakdown lasts longer and for higher breakdown voltages. In the multigap configuration the different peaks of the beam are better separated (Fig. 2) and therefore it was possible to observe the attenuation of two different beam peaks.

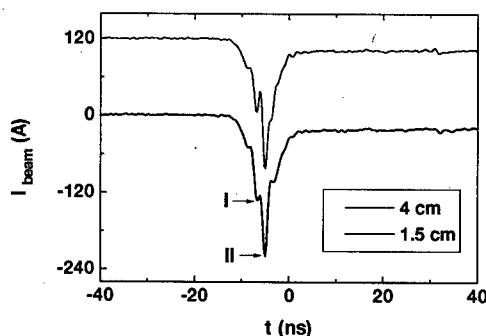


Fig. 2 Beam current waveforms measured at 1.5 and 4 cm respectively behind the anode hole (22 kV, air at 40 Pa, C=0.9 nF)

Fig. 2 presented one current waveform, obtained in the multigap configuration for 22 kV breakdown voltage, measured at 1.5 and 4 cm behind the anode. The FWHM of the beam current was of about 4-6 ns in the single gap configuration and of about 7-10 ns in the multigap one. It was observed that, by using external capacities between 0.9 and 10 nF the maximum beam current do not depend on the external capacitor. However, the beam duration is slightly increased when higher capacities are used (from 7.5 ns for 0.9 nF to aprox. 9 ns for 10 nF). In Fig. 3 are given the peak current attenuation curves for different breakdown voltages obtained in the single gap configuration (air at 50 Pa, 0.9 nF external capacitor).

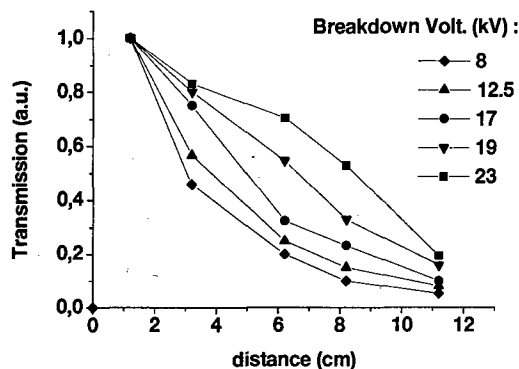


Fig. 3 Beam peak attenuation curves for different breakdown voltages (air at 50 Pa)

All the peak currents for each attenuation curve were divided to the peak current of the first measuring point placed at 1.2 cm behind the anode hole and the current maximum value was obtained on the second peak (see Fig. 2). Analysing the attenuation curves one can observe that, by increasing the breakdown voltage not only the energy of the beam energetic component [4]

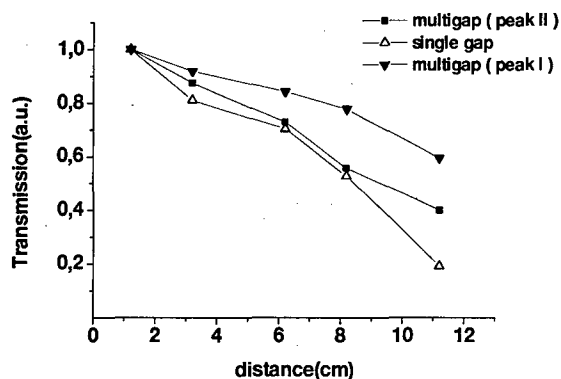


Fig. 4 Beam attenuation curves for single gap and multigap (peak I and II) configurations (air at 50 Pa, 22 kV breakdown voltage)

(that forms most of the first peak) is increased, but also the energy of the low energy component (forming the second peak). In Fig. 4 normalized beam attenuation curves are given for single gap configuration and

multigap configuration (max. beam - II peak and for I peak). For both curves shown in Fig. 3 and 4 the errors were estimated to be less than 10 %. Due to the relatively large diameter of the Faraday cup, at distances between 1.2 and 8 cm the beam divergence may not play an important role. Here only a sensible improvement of beam transmission can be observed in the multigap configuration in comparison with the single gap one, suggesting that not the average beam energy is the modified parameter. It is very possible for the beam divergence to be the main parameter that is changing, explaining thus the strong improvement of the beam transmission at high distances. The much lower attenuation of the first peak confirms the hypothesis that the electron energy is much higher for the first peak [6] and the emittance of this peak is better than the one of the second peak [7].

3. Discussion

As it was discussed before [6], the electron beam peak current does not depend on the external capacity, but only on breakdown voltage, gas pressure and self-capacitance of the discharge tube. The same also was observed in a similar pseudospark configuration using the same investigation methods at similar gas pressures (15-20 Pa). The present results confirm the different electron energy structure within the different beam peaks and the varying beam energy of the low energy component for different breakdown voltages. In next future time resolved optical spectroscopy performed by fast open shutter and streak photography will be used in parallel under the present conditions in order to explain decisive aspects of beam formation and propagation.

4. References

- [1] M. Ganciu, G. Modreanu, A.M. Pointu and I.I. Popescu, J. Phys. D: Appl. Phys., **27**, (1994) 1
- [2] N. B. Mandache, A. M. Pointu, E. Dewald, M. Nistor, M. Ganciu, G. Musa and I-Iovitz Popescu, to appear in Plasma Sources Sci. and Techn., **6** (1997)
- [3] J. Christiansen and C. Schultheiß, Z. Phys., **A 290**, (1979) 35
- [4] E. Dewald, M. Ganciu, N. B. Mandache, G. Musa, M. Nistor, A. M. Pointu, I-Iovitz Popescu, K. Frank, D. H. H. Hoffmann and R. Stark, to be published in IEEE Trans. on Plasma. Sci.
- [5] R. Stark, J. Christiansen, K. Frank, F. Mucke, and M. Stetter, IEEE Trans. Plasma Sci., **23**, (1995) 258.
- [6] E. Dewald, K. Frank, D. H. H. Hoffmann, R. Stark, M. Ganciu, N. B. Mandache, M. Nistor, A. M. Pointu I-Iovitz Popescu to be published in IEEE Trans. on Plasma. Sci.
- [7] L. C. Pitchford, J. Appl. Phys., **75**, (1994) 7227

The influence of anode region of a glow discharge on the EEDF in S- and P-moving striations

Y. B. Golubovskii*, V. O. Nekuchaev, N. S. Ponomarev

*Department of Optics, St. Petersburg University, Uljanovskaja 1, Peterhof, St. Petersburg, 198904, Russia
Department of Physics, Ukhta Industrial Institute, Pervomajskaja 13, Ukhta, 169400, Russia

Nowadays the kinetic nature of S- and P-striations in the glow discharge under low pressures and not high currents is proved undoubtedly both experimentally and theoretically [1-4]. The mechanism of these waves origin is determined by nonlocal character of electron energy distribution function (EEDF) formation in the space-periodic fields and does not have a hydrodynamic analogy in principle. The other example of successful application of nonlocal approach is the description of near-anode region of the DC nonstratified glow discharge [5].

In the present work the experimental and theoretical investigation of the EEDF behaviour in the S- and P-striations as they pass through the near-anode region of neon discharge under low pressures is carried out ($p = 1 \div 2 \text{ torr}$, $i = 10 \div 20 \text{ mA}$,

$R = 1.4 \text{ cm}$). Plasma potential and EEDF measurements at different distances from anode and in the different phases of strata were performed by means of mobile probe that allows to exclude the plasma potential oscillations as a whole with respect to anode and therefore to make correct measurements of potential space dependence along strata length [4]. The experimentally measured potential dependence (dots) and its approximation (solid curve $x_1(\epsilon)$) for P-striations ($p = 1 \text{ torr}$, $i = 20 \text{ mA}$) is represented in Fig.1 for the moment just after an abrupt potential curve drop as a whole with respect to anode that is connected with the passing of strong field range of strata through the anode region. At this moment the potential wells and reverse electric fields near the anode are absent. In Fig.2 the transformation of EEDF

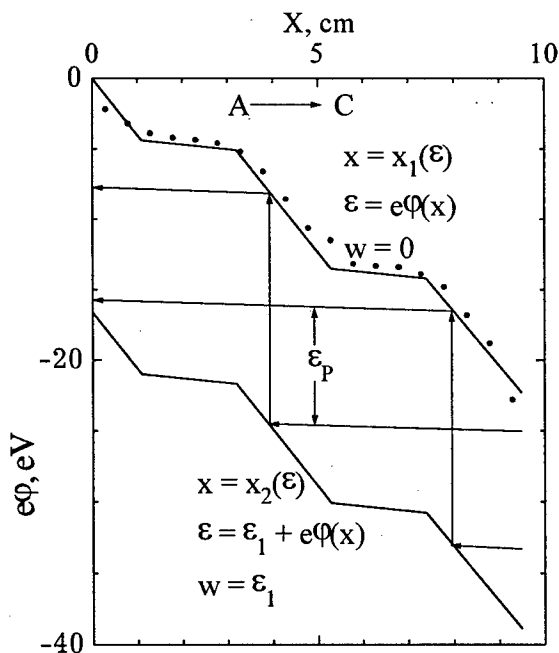


Fig.1. Potential profile for P-striation. $X=0$ corresponds to anode.

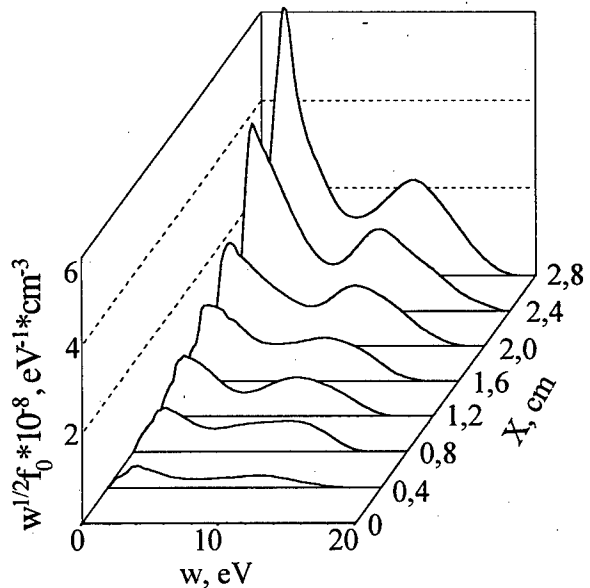


Fig.2. EEDF measured in the near-anode region for P-striation. $X=0$ corresponds to anode

measured in P-striations as they pass through the anode region at the different distances from anode is shown. One can see a decrease of EEDF amplitude as he approaches nearer to the anode where at first a decrease of slow electrons takes place and then this process involves more and more fast electrons. At the distance 4 mm the electron density falls by more than one order. The EEDF measured in the undisturbed positive column do not reveal the similar decrease and are reproduced quite well from one strata to another as we move further from the anode.

The theoretical calculations of EEDF in the near-anode region of stratified discharge can be carried out on the basis of kinetic equation [2] in variables $\varepsilon = w + e\varphi(x)$, x (ε - total energy, w - kinetic energy) for the energy values $0 < w < \varepsilon_1$:

$$\frac{\partial}{\partial x} \frac{v^3}{3v(v)} \frac{\partial f_0(\varepsilon, x)}{\partial x} + \frac{\partial}{\partial \varepsilon} \frac{m^2}{M} v(v) v^3 f_0(\varepsilon, x) = 0$$

It is supposed that in the balance of energy the inelastic impacts prevail and electron-electron collisions can be neglected. If the EEDF drop in the inelastic range is quite sharp it is possible to use a zero boundary condition for the EEDF on the first excitation level of atoms ε_1

$$f_0(\varepsilon, x) \Big|_{w=\varepsilon_1} = 0$$

$$\frac{v^3}{v} \frac{\partial f_0}{\partial x} \Big|_{x=x_2(\varepsilon)} = \frac{v^3}{v} \frac{\partial f_0}{\partial x} \Big|_{x=x_1(\varepsilon)}$$

The solution of these equations may be written as follows

$$f_0(\varepsilon, x) = \Phi(\varepsilon) \int_{x_2(\varepsilon)}^{x(\varepsilon)} \frac{v(\varepsilon, x')}{v^3(\varepsilon, x')} dx' = \Phi(\varepsilon) F_0(\varepsilon, x)$$

where $\Phi(\varepsilon)$ - amplitude of EEDF. The kinetic energy on the curve $x_2(\varepsilon)$ equals the first excitation level ε_1 . The calculation of integral $F_0(\varepsilon, x)$ depends on the form of $x_2(\varepsilon)$, in

addition on the anode $F_0(\varepsilon, x) \Big|_{x=0} = 0$. Amplitude $\Phi(\varepsilon)$ was found by analogy with [4], where there are two maxima in the energy interval $0 \div \varepsilon_1$, which are shifted on the value ε_p - the potential drop on P-strata. The $\sqrt{w} f_0(w, x)$ calculations results in the near-anode region are represented in Fig.3. It is clear that the nonlocal theory describes quite well the EEDF decrease measured as strata moves to the anode.

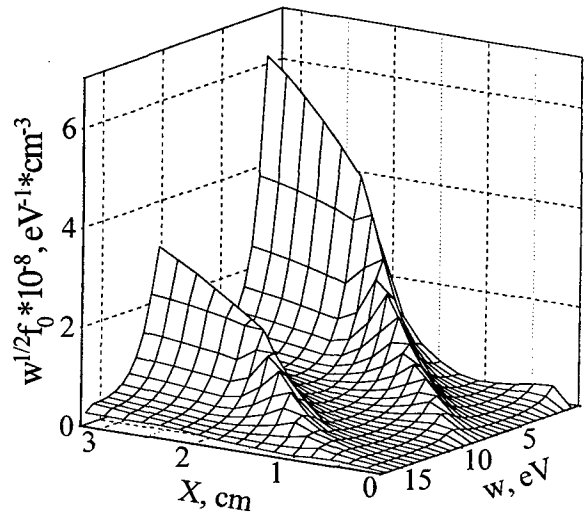


Fig.3. EEDF calculated in the near-anode region for P-striation. $X=0$ corresponds to anode.

References

- [1] T. Ruzicka, K. Rohlena: Czech. J. Phys., **22** (1972) 906
- [2] L. D. Tsendin: Sov. J. Plasma Phys., **8** (1982) 228
- [3] Y. B. Golubovskii, S. U. Nisimov: Sov. Phys. Tech. Phys., **40** (1995) 24
- [4] Y. B. Golubovskii, V. O. Nekuchaev, N. S. Ponomarev: XIII ESCAMPIG, Poprad (1996) Contr. Pap. 119
- [5] Y. B. Golubovskii, S. H. al Havat, L. D. Tsendin: Sov. Phys. Tech. Phys., **32** (1987) 760

Ion and neutral distribution functions at the cathode of DC glow discharges in argon

I. Revel, L.C. Pitchford and J.P. Boeuf

Centre de Physique des Plasmas et Applications de Toulouse (E.S.A. 5002), UPS,
118 route de Narbonne, 31062 Toulouse Cedex, France

1. Introduction

We have used a Monte Carlo simulation to determine the energy distribution of the ion and fast neutral fluxes at the cathode in low pressure DC glow discharges in argon at 1 torr. The electrodes are plane and parallel and separated by a distance of 4 cm. The relative sputtering rates of a gold cathode due to the incident ion and fast neutral fluxes were also calculated, and we find that the fast neutrals cause most of the sputtering. The long term goal of this work is the development of a self-consistent model of cathode sputtering in glow discharges for mass spectrometry [1]. The point P2 of Table I is representative of the discharge conditions for this application.

2. Description of the model

The Monte Carlo simulations were performed for different points along the voltage-current characteristic for argon at 1 torr. The discharge current density, voltage and sheath length were taken from previous calculations and are given in Table I for two points.

Our Monte Carlo simulation is standard. The ion trajectories are followed from the sheath edge to the cathode. The electric field is supposed to be purely axial and to vary linearly with distance from the cathode. Ionization in the sheath is taken into account for the point P1, but this has little effect on our results. Ionization in the sheath is neglected for the point P2. Fast neutrals, created in collisions between the ions and the background gas (at 300°K), are simulated until they reach the cathode or until their energy drops below a certain cut-off (0.5 eV in the results shown here).

The collision processes we consider are charge transfer collisions and elastic collisions (between ions and slow neutrals and between fast neutrals and slow neutrals). In charge transfer collisions, the neutrals exit the collision events with the energy of the incident ion. The energy transfer in elastic collisions is calculated supposing that the elastic collisions are isotropic in the center of mass frame. We have used cross sections (ion-neutral & neutral-neutral) for these processes recommended by Phelps [2].

	Point P1	Point P2
INPUT		
voltage (V)	196.	1000.
current density (mA/cm ²)	0.52	30.
sheath length (cm)	0.15	0.053
RESULTS		
mean ion energy at the cathode (eV)	18.4	294.
average number of collisions per ion in the sheath	26	8
mean energy of fast neutrals at the cathode (eV)	6.0	80.
average number of collisions per fast neutral in the sheath	3	1.5
ion contribution to sputtering	23%	29%
fast neutral contribution to sputtering	77%	71%

Table I Discharge conditions used as input and a summary of the results of the simulations. The voltage, current density and sheath length for P1 are taken from Fiala et al [3] and those for P2 are referenced in Phelps [2]. The term 'fast neutrals' refers to neutrals with an energy greater than 0.5 eV.

3. Results of our model

Certain results from our calculations are summarized in Table I, and the ion and fast neutral flux energy distributions are shown in figs. 1 and 2 for points P1 and P2, respectively. The mean energy of the fast neutrals (neutrals with energies greater than 0.5 eV) incident on the cathode is considerably less than that of the ions. Nevertheless, the flux of fast neutrals to the cathode is greater than the incident ion flux for particles with energies less than 150 eV and 500 eV, respectively, for points P1 and P2. The ion and the fast neutral fluxes decrease almost exponentially with energy, except for the low energy component of the neutral flux.

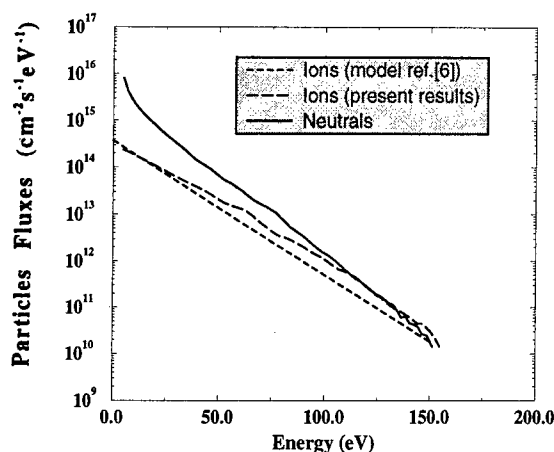


Figure 1. Energy resolved flux distributions of ions and fast neutrals for the conditions of point P1.

We use the data for the sputtering yield vs incident particle energy given by Yamamura et al [4] to determine the sputtered atom flux due to the incident ions. Consistent with theory, we suppose that the sputtering yield is independent of the charge of the incident particle. From these data and the ion flux energy distributions, we calculate the sputtered atom flux. For the conditions here, the neutrals cause most of the sputtering. This is consistent with the findings of Bogaerts et al [5] in argon at 1 keV.

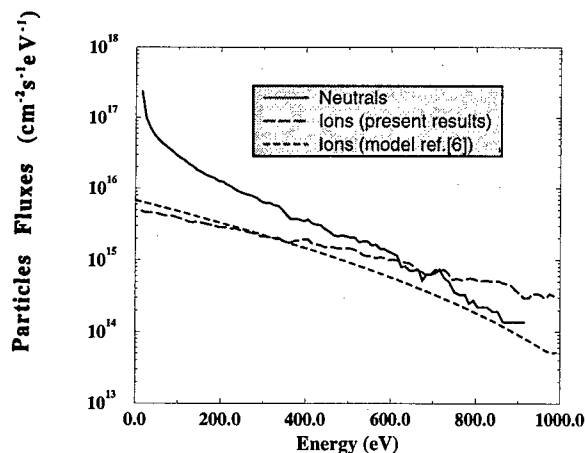


Figure 2. Energy resolved flux distributions of ions and fast neutrals for the conditions of point P2.

Davis and Vanderslice [6] have developed a simple analytical model for the ion flux energy distribution function in DC glow discharges. This model is often cited and used to estimate the importance of cathode sputtering from sputtering yields. This model is based on several simple hypotheses: (1) the electric field is supposed linearly decreasing from the cathode; (2) ionization in the sheath is neglected; (3) elastic collisions are neglected; and (4) the charge transfer cross section is independent of energy. With these hypotheses, ion flux energy distribution can be expressed as a function of C , the number of collisions per ion in the sheath, and the discharge

voltage. In general, C is not known *a priori* because the charge exchange cross section depends on energy. The ion flux distributions from this model are compared to our simulations in figs. 1 and 2, where we have used the value of C from our simulations. For both P1 and P2, the simple model underestimates the flux of sputtered atoms due to the incident ion flux.

4. Conclusion

These results show that, for the range of discharge conditions studied, cathode sputtering is largely controlled by incident flux of fast neutrals. Calculations for a wider range of discharge conditions and for other cathode materials are in progress.

5. References

- [1] R. K. Marcus, ed. Glow Discharge Spectroscopies. New York: Plenum Press (1993).
- [2] A. V. Phelps, J. Appl. Phys. 76, 747 (1994).
- [3] A. Fiala, L.C. Pitchford and J.P. Boeuf, Phys. Rev. E, 49, 5607 (1994).
- [4] Y. Yamamura and H. Tawara, Atom. Nucl. Dat. Tab. 62, 149 (1996).
- [5] A. Bogaerts, M. Van Straaten and R. Gijbels, Spectrochim. Acta. 50B, 2 (1995)
- [6] W. D. Davis, T. A. Vanderslice, Phys. Rev. 131, 219 (1963).

Critical Field and Potential Distribution in a Magnetized SF₆/He Mixture Gas Positive Column

H.Satoh, Y.Wakabayashi, T.Nishioka and M.Matsumoto

Faculty of Textile Science and Technology, Shinshu University, Tokita 3-15-1, Ueda 386, JAPAN

1 Introduction

It is well known that the helical instability can be excited in the inert gas positive column in the applied axial magnetic field B [1]. Lately, ionization waves or helical waves in the electronegative gas-positive column in the field B greater than a certain critical field B_c were theoretically studied by Daniel et al.[2], and Matsumoto, one of the present authors[3]. Volynets et al. have shown that existence of negative ions leads to a significant difference of the charged particle radial distributions from the zeroth order Bessel function type [4].

We here report some experimental results about relations between the critical field B_c and a small amount of mixed SF₆ gas. Further, we discuss those experimental results comparing with the theoretical analysis.

2 Experiment

The basic arrangement used throughout the present experiments is shown in Fig.1. A discharge tube with inner radius 1.3cm is 150cm long, and of hot cathode type.

The enclosed He gas is in a range of pressure $P=(0.1 \sim 0.5)$ Torr, and mixed with a small amount of SF₆ gas equal to or less than 5%. Here, SF₆ gas is put in through a microgase valve (S) on the anode side. Discharge currents I_p are in (50~200) mA.

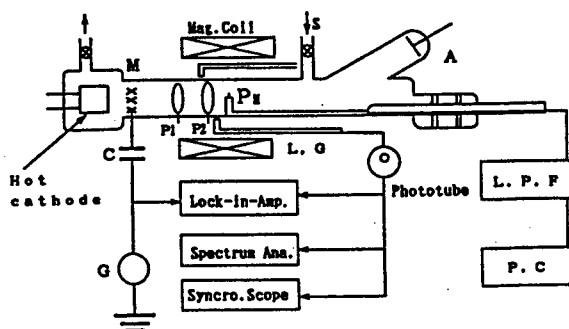


Fig. 1 Scheme of the experimental system

The instability waves are analyzed by Lock-in-Amp. using the light signal through movable Light Guide(L.G). The strength of the axial electric field E_0 is measured by two probes P_1 and P_2 . The mean potentials $V(r)$ are measured along the radial direction using the rotational probe (P_M) with low path filter (L.P.F.) of the cut off frequency $f_c = 10$ Hz. Here, electrical signals through the probe (P_M) are arranged by a personal computer.

Figure 2 shows the characteristic features of the discharge voltage V_{PK} to the strength of field B depending on the amount of mixed SF₆ gas, each ratio of which is given to SF₆/He = 0.0%, = 0.5%, = 2% and = 3%.

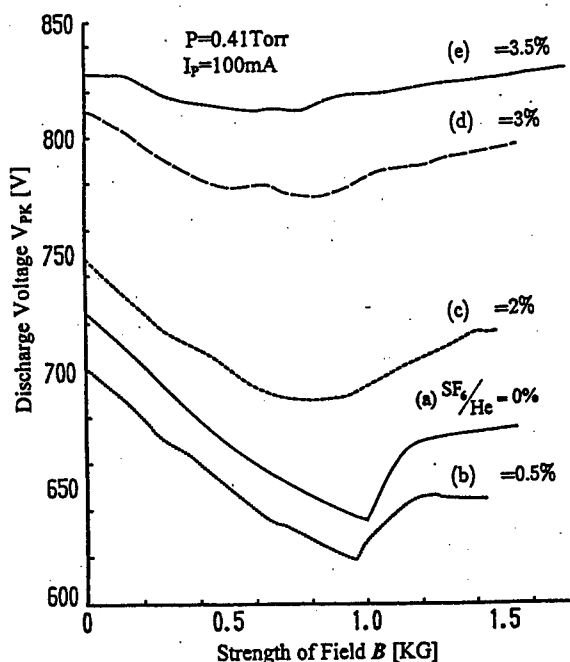


Fig. 2 Characteristic features of the discharge voltage V_{PK} to the mixture ratios SF₆/He

The discharge voltage V_{PK} in the positive column mixed less than SF₆/He = 1% is small compared with the case of He gas, and also the critical field B_c becomes smaller, i.e. the column plasma becomes more unstable as to the helical wave. Further, with the

increase of SF_6 , the frequency of an excited $m = 1$ mode helical wave increases. As the amount of SF_6 gas increases more than 1% of He gas, potential oscillations extended to 10kHz are excited, even at the field $B = 0$. The discharge voltage V_{PK} increases with the amount of SF_6 gas, and the critical field B_c comes to be obscure.

Then, we show the frequency of the $m = 1$ wave as a function of the critical field B_c in Fig.3. Curve (a) shows the results for He positive column, and Curve (b) for various gas pressures in the mixture ratios SF_6/He less than 1%.

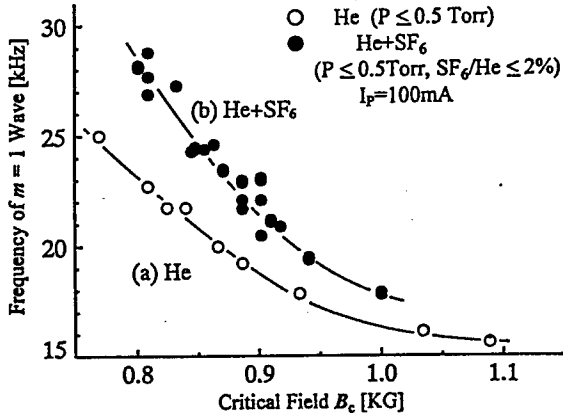


Fig.3 Frequency of the $m = 1$ wave at the critical field B_c depending on mixture ratios SF_6/He in He gas pressure less than 0.5 Torr

Figures 4(a) and (b) show the dependence of the radial potential distribution ($V(r)-V(0)$) on the ratios SF_6/He and on the strengths of the field B , respectively. Figure 4(a) shows that magnitudes of $V(r)$ become larger as increasing the ratios SF_6/He , each of which is given to $\text{SF}_6/\text{He} = 0.0\%$, 0.2% and 0.8% .

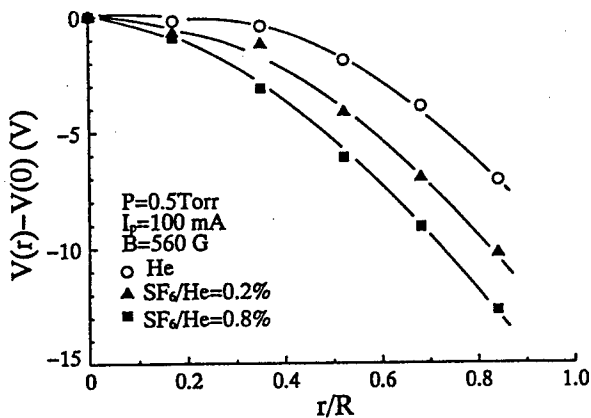


Fig.4 (a) Radial potential distribution depending on the ratios SF_6/He

The injection effect of a small amount of SF_6 gas on the potential distribution is corresponded to the case of the rare gas positive column at reduced gas pressure.

And Fig.4 (b) shows that the potential distributions are according to the ambipolar diffusion theory in tendency for the strengths of B , similar to the rare gas positive column.

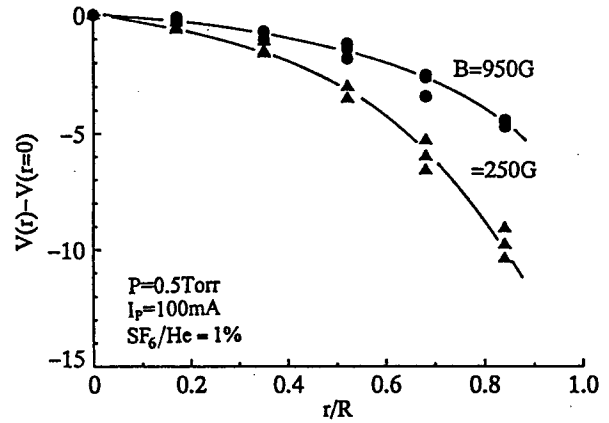


Fig.4 (b) Radial potential distribution depending on the strength of B

3 Discussion

The amount of negative ions is considered to increase with the ratios SF_6/He . With this increase, as shown in Figs.2 and 3, the frequency of $m = 1$ helical wave increases and their critical field B_c decreases, i.e the positive column becomes more unstable as to the helical wave, as proposed by Matsumoto. The frequency of the $m = 1$ wave is understood to originate in the magnetized $E \times B$ drift due to the ambipolar field E_A as shown in Fig.4. By the field E_A which is mainly proportional to the logarithmic derivative of the electron density with respect to r , the negative ions tend toward the axis. With the space charge neutrality, the plasma contracts and E_A is considered to become larger.

4 References

- [1] B.B.Kadomtsev and A.V.Nedospasov : J. Nuclear Energy, Vol. C-1, (1960), 230
- [2] P.G.Daniels, R.N.Franklin and J.Snell : J.Phys.D : Appl. Phys. 23, (1990), 823
- [3] M.Matsumoto : J.Phys. Soc. Jap. 62, (1993), 3919
- [4] V.N.Volynets, A.V.Lukyanova, A.T.Rokhimov, D.I.Slovetsky and N.V.Suetine : J.Phys. D : Appl. Phys. 26, (1993), 647

INFLUENCE OF OXYGEN ADMIXTURE ON GAS HEATING IN N₂-O₂ MIXTURE OF PULSE DISCHARGE

A.P.Ershov, A.V.Kalinin, V.M.Shibkov, L.V.Shibkova

Department of Physics, Moscow State University, 119899, Moscow, Russia

D.P.Singh, M.Vaselli

Istituto di Fisica Atomica e Molecolare. Via del Giardino, 7-56127, Pisa, Italy

In [1,2] the fast gas heating at high values of E/n was fixed for two types of discharge in air: freely localized microwave discharge in focused beam and pulse-periodic discharge limited by chamber walls. For explanation of such fast heating the kinetics model was used, in which the quenching of electronically excited states of nitrogen molecules was taken into account. In [3] the model of kinetics processes in nitrogen-oxygen mixture was worked out. This model describes the dynamics of main components of such mixture excited by discharge with high values of reduced electric field. The characteristic feature of suggested model at description of gas heating in discharge is taking into account quenching metastables atoms $O(^1D)$ by oxygen atoms and atoms $O(^1D)$ by nitrogen molecules. It is proposed that 70 % of excitement energy $O(^1D)$ is spent on gas heating. The results of calculations with the help of model [3] of the kinetics of gas heating are in good agreement with experiment [1,2]. For explanation the fast gas heating at high values of E/n at air pressure $p > 100$ torr the kinetics model is proposed in [4], in which the gas heating is conditioned by cascaded quenching at VT-relaxation of high electronic excited states of nitrogen

molecules. The calculations following this model satisfactorily coordinates with experimental data connected with gas heating in freely localized microwave discharge in air [1,5]. For elucidation of concrete channel of gas heating at high values E/n in present work kinetics of the molecular gas heating was studied for the pulsed discharge burned up in a tube with the diameter of 1 cm in nitrogen-oxygen mixture under the pressure of 0.1-1.0 torr. The partial pressure of oxygen in mixture is changed from 0 to 20 %. Modulator produced the pulses duration up to 100 μs , voltage from 0.5 to 25 kV discharge current from 0.1 to 20 A. The time dependence of the gas temperature, the density of atomic oxygen, the electric field in plasma, the electron energy distribution function, their temperature and density were determined by using spectral and probe methods.

Investigations of gas heating kinetics and EEDF showed (Fig.1, $p = 0.8$ torr, $i = 0.65$ A, $\delta[O_2], \%$: 1-1.5; 2-7.5; 3-20) that value of electric field was large at initial stage of pulse and, because of it, the number of fast electrons on EEDF was great. It leads to increasing the rate of excitation of high electronic states of molecules; in turn, this leads to increasing the concentration of these molecules. Deexcitation

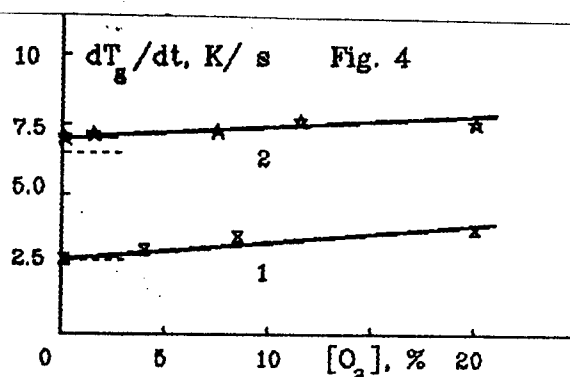
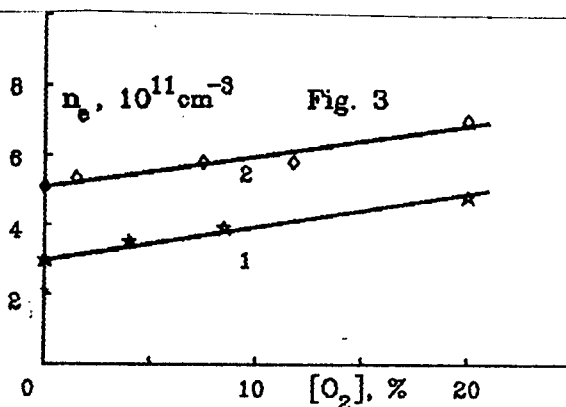
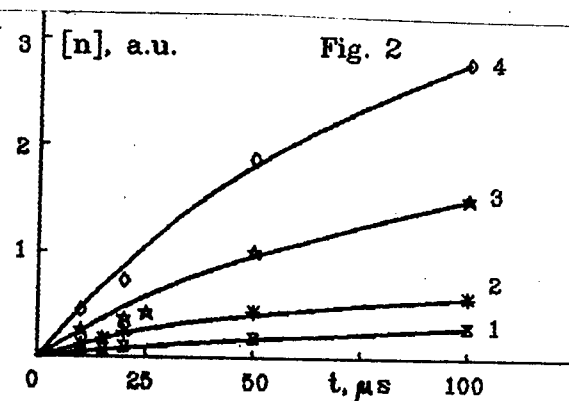
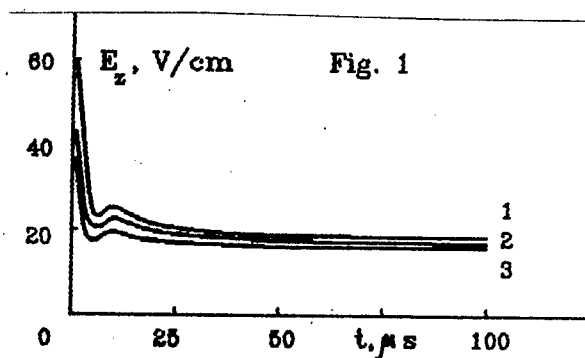
these molecules leads to fast gas heating. At this the number of fast electrons decrease at relaxation of EEDF to stationary state. It leads to decreasing gas heating rate at pulse ending. On Fig.2 the dependence of relate density of oxygen atoms from time for full pressure of nitrogen-oxygen mixture $p=0.4$ torr and discharge current $i = 0.65$ A at different partial pressure of molecular oxygen $\delta, \%$: 1 - 0.5; 2 - 4.0; 3 - 8.5; 4 - 20 is presented. It is showed, that with increasing of oxygen part in nitrogen-oxygen mixture the quantity of atomic oxygen increases and that necessary time for working out the atomic oxygen is higher than $100 \mu\text{s}$ in conditions of experiment.

On Fig. 3, 4 the electron density and the rates of gas heating in dependence on partial molecular oxygen pressure are presented (p, torr : 1-0.4; 2-0.8, dotted lines are result of calculation [6]).

The results of our investigations let us conclude that for high values of reduced electric field $E/n > 100$ Td quenching of longlived electronically excited states of nitrogen molecules is one of the main mechanisms resulting in gas heating, while contribution of quenching channel of oxygen metastable atoms does not exceed 30%.

References

1. Devyatov A.M., Shibkov V.M., et.al. -Vestnik MSU, 1991, v.32, N2, p.29-33 (Rus).
2. Alexandrov A.F., Shibkov V.M., et.al. - Prikladnaya Fizika, 1994, v.4, p.20-29 (Rus).
3. Popov N.A. -Fizika plazmi, 1994, v.20, N3, p.335-343 (Rus).
4. Bezmenov I.B., Silakov V.P. -Precinct N30, M., IPM RAN, 1993, 30p (Rus).
5. Berdishev A.V., et. al. -Teplofizika Visokih Temperatur, 1988, v.26, N4, p.661-666 (Rus).
6. Zarin A.S, Kuzovnikov A.A., Shibkov V.M. Freely localized microwave discharge in air. -M.: Oil & gas, 1996, 204p (Rus).



On the Nonhydrodynamic Kinetics of the Electrons in s- and p-Striations of Neon DC Glow Discharge Plasmas

F. Sigeneger¹, Yu.B. Golubovski², I.A. Porokhova², and R. Winkler¹

¹Institut für Niedertemperatur-Plasmaphysik, Greifswald, Germany

²Institute of Physics, St. Petersburg University, Russia

1. Introduction

The periodic structures of plasmas caused by s- and p-striations represent an interesting subject in the context of the nonlocal kinetic behaviour of the electrons in collision dominated plasmas. An important aspect of this problem concerns the electron kinetics under the action of periodic electric fields. Several efforts [1, 2] have been undertaken in order to treat this problem. Recently, an efficient approach for solving the one-dimensional inhomogeneous Boltzmann equation has been developed. Using this approach, the electron relaxation behaviour under the action of homogeneous electric fields has been comprehensively studied [3]. At moderate field strengths periodic structures have been generally found in the electron velocity distribution function. The idea that these structures are of the same basic nature as those occurring in striations is analysed. Furthermore, the relaxation of the electrons to unique periodic states maintained by the strongly modulated electric fields in the striations is investigated.

2. Basic Aspects of the Kinetics

The theoretical investigations are based on the solution of the space-dependent Boltzmann equation

$$\vec{v} \cdot \nabla_{\vec{r}} f - \frac{e_0}{m} \vec{E} \cdot \nabla_{\vec{v}} f = C^{el}(f) + \sum_k C_k^{in}(f) \quad (1)$$

for the velocity distribution $f(\vec{v}, \vec{r})$ of the electrons with the charge $-e_0$ and the mass m . This equation includes the impact of the periodic electric field $\vec{E}(z) = E_0(1 + \beta \sin(2\pi z/\Lambda_E))\vec{e}_z$ with a modulation degree $0 \leq \beta < 1$. The action of elastic collisions (C^{el}) and various kinds of conservative inelastic collision processes (C_k^{in}) of electrons with neutral particles are taken into account by appropriate collision integrals. As the direction of the electric field and its inhomogeneity are parallel to the z -direction, the velocity distribution function gets the reduced dependence $f(v, v_z/v, z)$ and can be expanded in Legendre polynomials. In two term approximation the distribution function has the representation

$$f(U, \frac{v_z}{v}, z) = \frac{1}{2\pi} \frac{1}{(2/m)^{3/2}} [f_0(U, z) + f_1(U, z) \frac{v_z}{v}],$$

$$U = \frac{m}{2} v^2, \quad v = |\vec{v}|. \quad (2)$$

The substitution of this expansion into the Boltzmann equation yields finally a parabolic differential equation system for the isotropic and anisotropic part $f_0(U, z)$ and $f_1(U, z)$ of the velocity

distribution function. By introducing the total energy $\varepsilon = U - \int_0^z E(\tilde{z}) d\tilde{z} \cdot (-e_0)$ and eliminating the anisotropic distribution part f_1 this equation system is transformed into a parabolic equation of standard form which can be solved with appropriate boundary conditions as initial boundary value problem in a nonrectangular region of ε and z [4]. In the numeric calculations performed for the neon plasma three lumped cross sections for the excitation of the s-states (Q_1), of the p- and all higher bound states (Q_2), and for the ionization (Q_3) has been used with the corresponding energy losses $U_i, i = 1, 2, 3$. The ionization has been treated as an excitation process.

3. Results

Former investigations [3] of the electron relaxation in homogeneous fields E_h showed that spatially limited disturbances excite periodic structures in the electron distribution function which are caused by the interplay of electron acceleration in the field and backscattering in inelastic collisions. If the energy loss in elastic collisions is neglected and only the lowest excitation process is taken into account these structures are undamped and have a period length of $\Lambda^* = U_1/(-e_0 E_h)$. The inclusion of the energy loss in elastic collisions and of the excitation of higher atomic states leads to a damping of the periodic structures and enlarges their period length. This enlargement is shown in Fig. 1 for a range of the normalized electric field strength E_h/p where the enlargement of the period length and the damping is mainly caused by the energy loss in elastic collisions. Period lengths $p\Lambda$ obtained from the solution of (1) for homogeneous fields E_h are compared in Fig. 1 with those ($p\Lambda_s, p\Lambda_p$) measured in s- and p-striations

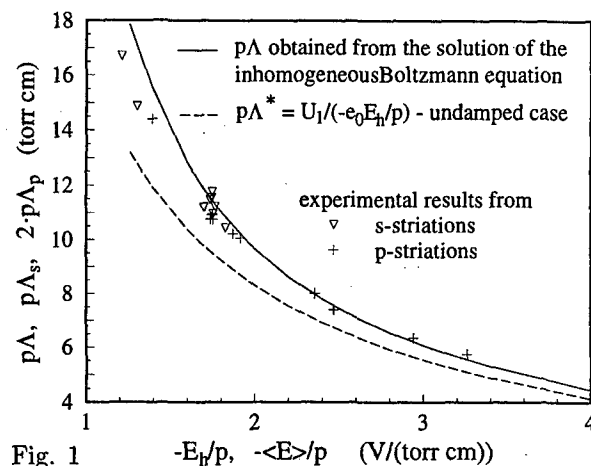


Fig. 1 $-E_h/p, -\langle E \rangle/p$ (V/(torr cm))

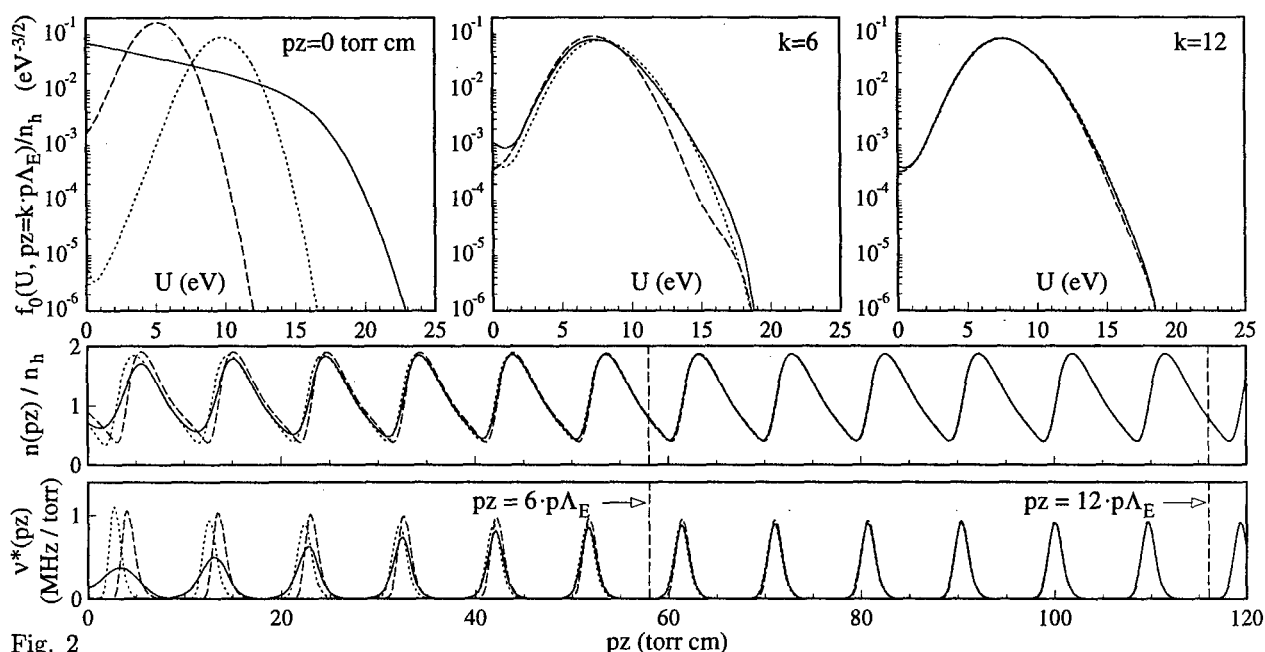


Fig. 2

as a function of the period averaged field $\langle E \rangle / p$ of the striations. The good agreement of calculated and measured lengths confirms that the periodic structures occurring in the striations are mainly caused by the nonlocal electron kinetic properties.

In order to clarify whether under the action of a periodic field an unique state is established in the velocity distribution, Fig. 2 shows at the space positions $zp = k \cdot p\Lambda_E$, $k = 6, 12$ for the above sinusoidal field the calculated isotropic distribution for the spatial relaxation initiated by three different boundary values at $pz = 0$. The calculations have been performed for the period averaged field strength $E_0/p = -2\text{V}/(\text{torr cm})$, the modulation degree $\beta = 0.9$ typical of the striations, and the period length $p\Lambda_E = 9.67$ torr cm determined from the corresponding periodic structures occurring in a homogeneous field with $E_h/p = E_0/p$. All isotropic distributions are normalized on the same magnitude of the electron particle current density and formally divided by a common density n_h . The spatial evolution of the isotropic distributions distinctly demonstrates that a unique periodic state is reached for all three boundary values. In the lower part of Fig. 2 the spatial evolution of the corresponding normalized density $n(zp)/n_h = \int_0^\infty U^{1/2} f_0(U, pz) dU / n_h$ and of the normalized excitation frequency of the s-states $\nu^*(zp) = \frac{1}{pn_h} \sqrt{\frac{2}{m}} \int_0^\infty UNQ_1(U) f_0(U, pz) dU$ are displayed for all three relaxation processes. Almost over the same distance both macroscopic quantities are established into their unique periodic state.

Figure 3 presents the spatial evolution of the isotropic distribution over three periods of its established periodic state. The strong modulation of the periodic electric field which is shown in the upper part of this figure enforces a similarly strong modulation of the distribution function. The evolution of the distribution maxima clearly illustrates the resonance path of the electrons under the action of the periodic field.

Further results related to the electron behaviour in s-striations as well as in p-striations will be reported and discussed in the poster presentation.

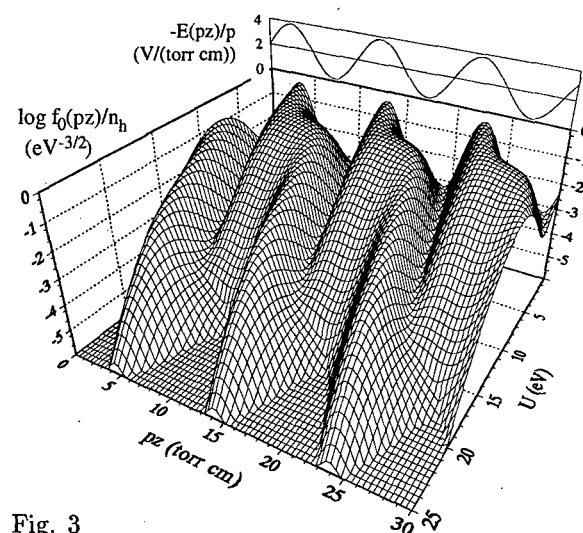


Fig. 3

4. References

- [1] R. Winkler: Contrib. Plasma Phys., **10** (1970) 79; **11** (1971) 201
- [2] L. D. Tsensin: Plasma Sources Sc. Technol., **4** (1995) 200
- [3] F. Sigeneger and R. Winkler: Plasma Chemistry and Plasma Processing, **17** (1997) 1
- [4] F. Sigeneger and R. Winkler: Contrib. Plasma Phys., **36** (1996) 551

Electron and ion kinetics in hydrogen obstructed glow discharge

T. Šimko*, Z. Donkó† and K. Rózsa†

*Department of Plasma Physics, Comenius University, Mlynská dolina F2, 84215 Bratislava, Slovakia

†Research Institute for Solid State Physics, Hungarian Academy of Sciences, P.O.Box 49, H-1525 Budapest, Hungary

1. Introduction

Obstructed regime of a DC glow discharge is characterized by low pd product (p being the gas pressure and d the electrode separation) so that even the cathode fall region is not completely developed [1,2]. The electrode separation is smaller than the normal cathode-fall thickness, which obstructs the usual electron multiplication mechanism. In order to maintain the discharge, higher electric field is therefore required (the ratio of the electric field intensity to gas density E/n can achieve several kTd). The field decreases towards the anode, but it remains considerably high even at the anode, especially at low pd values [2].

Plane-parallel obstructed glow discharges have been extensively studied both experimentally and theoretically [3]. They provide the possibility to test available scattering models and transport theories at high and spatially-dependent electric fields [2].

2. Experiment

The experimental electrical characteristics of hydrogen DC glow discharge were measured in the plane-parallel discharge tube consisting of 20 mm diameter graphite electrodes separated by gap of 4.6 mm [2]. Changing the gas pressure enabled us to vary the degree of the discharge obstruction. Experimental values of the discharge voltage vs pressure at a constant value of current are used as input parameters to our model.

3. Model

In this paper, we have improved our previously developed self-consistent Monte Carlo model of the discharge [4]. The improvements concern mainly (i) the inclusion of fast neutral species produced in reactions of energetic ions with gas molecules [5,6], (ii) inclusion of various heavy-particle impact ionization processes [5,6] and (iii) the possibility of electron and ion reflection from the electrodes [3,7]. The basic model is briefly summarized as follows.

The motion of electrons, ions (H^+ , H_2^+ , H_3^+ , H^-) and fast neutrals (H , H_2) inside the discharge gap is followed by the Monte Carlo technique. The scattering processes with background gas molecules and the corresponding cross sections are based on [5,6,8]. An electron avalanche spreading from the cathode creates H^+ and H_2^+ ions through (dissociative) electron impact ionization. These ions can convert to other ionic species or

produce new ions and neutrals as they move to the cathode. All the secondary particles are treated within the simulation. Fast neutrals are considered as thermalized when their energy decreases below 0.05 eV and in that case are no longer treated in the simulation.

The spatial dependence of the electric field is determined iteratively [2]. The initial approximation is usually a constant or a linearly falling electric field. Starting from this initial guess, the electron simulation part is run and the ion source function is produced. It serves as input for the ion simulation part, which produces space-charge densities for the Poisson equation solver. In order to close the iteration cycle, the relation of electron and ion current at the cathode is required. We have used the experimental current value to deduce this relation [2]. The new electric field profile is finally obtained from the Poisson solver with the aid of the experimental voltage value. Extra electrons produced during the ion simulation part are used to modify the distribution of their starting positions for the next iteration. Usually, two or three iterations suffice to achieve the convergence of the field profile.

The reflection of electrons at the anode was modeled according to the theoretical reflection coefficient as a function of incident electron energy and the angle of incidence, obtained for graphite in [7]. The reflection of hydrogen ions and neutrals at the cathode is known to produce almost exclusively H atoms as reflected species [3]. The reflection coefficient per incident nucleus for graphite surface was taken from [3]. The results we obtained showed only a very limited effect of both electron and heavy-particle reflection.

Monte Carlo simulation method provides the detailed information about the kinetics of various species in the discharge. This enables us to study the role of these species in the discharge maintenance. Using experimentally measured voltage-current characteristics to relate the electron and ion current at the cathode makes it possible to deduce the secondary electron yields corresponding to the experiment.

4. Results

Experimental characteristics of the discharge are shown in Fig. 1. Corresponding spatial distributions of calculated electric field are presented in Fig. 2. Note the sensitivity of the discharge voltage and the intensity of the field at the anode on the value of pressure.

As an example of the discharge kinetics, we present in Fig. 3 relative abundances of the ion and fast neutral species at the cathode for various discharge operat-

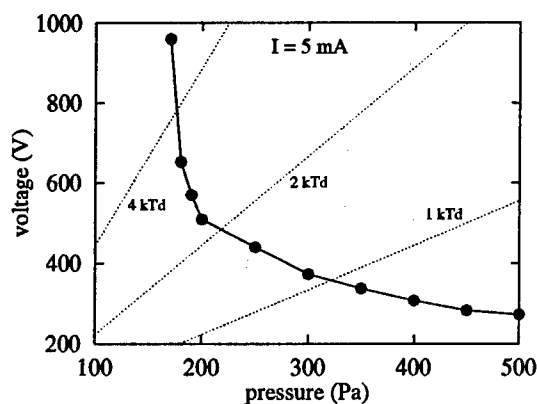


Fig. 1: Experimental voltage-pressure characteristics.

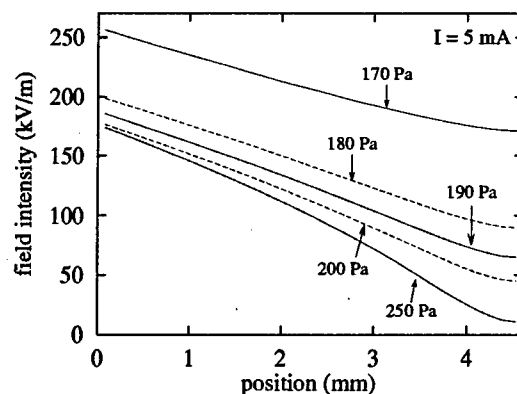


Fig. 2: Spatial distribution of calculated electric field.

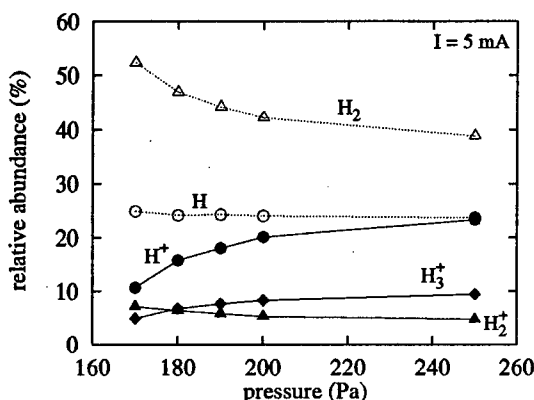


Fig. 3: Relative abundances of ions and fast neutrals in particle flux at the cathode.

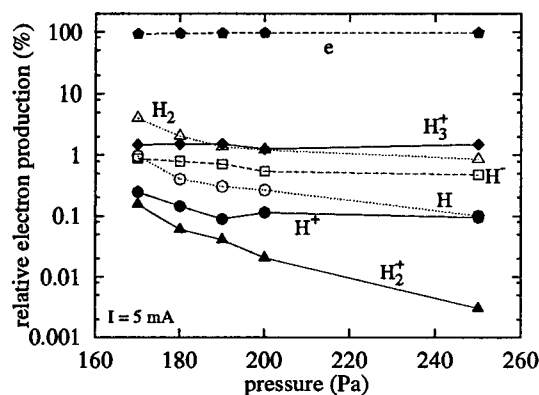


Fig. 4: Relative contributions of various species to the overall electron production in the discharge.

ing conditions. It can be seen that the flux of fast neutrals is about 1.5 to 3.5 times higher than that of ions, depending on pressure. Note that the dominant incident ion species is H^+ at all pressures, while in our previous model it was mainly H_3^+ [4]. This results from different discharge kinetics in present model; however, when comparing the present electric field profiles from Fig. 1 to those obtained in our previous model [4], one can see that they are almost unchanged. A sensitivity study indicates the relative independence of the field profiles on scattering model details [4].

The abundance of H^+ in the total ion flux at the cathode under similar E/n conditions was also found in low-pressure Townsend discharge both experimentally and theoretically [5]. Note that the relative abundances at the cathode are not related to relative contributions to the total space charge; at lower pressures, H_2^+ gives the major contribution as found in [4]. At higher pressures, H_3^+ gives the dominant contribution at the anode side and both H^+ and H_3^+ at the cathode side.

The contribution to the overall electron production within the discharge is plotted in Fig. 4 as a function of pressure. It can be seen that the ionization by heavy particles does not exceed 10%. Note the important role of fast neutral species H , H_2 even at higher pressures as well as the efficiency of H^- ions in spite of their low density.

Acknowledgments

The authors thank A. V. Phelps for discussions and encouragement. This work was supported in part by the Slovak Grant Agency (grant No 1/2312/95) and the Hungarian Science Foundation (grant No F-015502).

References

- [1] A. Güntherschulze: Z. Phys. **61** (1930) 581
- [2] Z. Donkó, K. Rózsa, R. C. Tobin and K. A. Peard: Phys. Rev. E **49** (1994) 3283
- [3] See, for example, Z. Lj. Petrović, B. M. Jelenković and A. V. Phelps: Phys. Rev. Lett. **68** (1992) 325
- [4] Z. Donkó, T. Šimko and K. Rózsa: Europhys. Conf. Abstracts **20E** (1996) 149
- [5] T. Šimko, J. Bretagne, G. Gousset, M. V. V. S. Rao, R. J. Van Brunt, J. K. Olthoff, Y. Wang, B. L. Peko and R. L. Champion: Bull. Am. Phys. Soc. **41** (1996) 1332
- [6] A. V. Phelps: J. Phys. Chem. Ref. Data **19** (1990) 653
- [7] K. Ohya, K. Nishimura and I. Mori: Jap. J. Appl. Phys. **30** (1991) 1093
- [8] S. J. Buckman and A. V. Phelps: JILA Information Center Report No 27 (1985)

The Cathode End of a dc Helium Positive Column as a Place of Origination of Ionization Waves

L. Sirghi*, K. Ohe and G. Popa**

Department of Systems Engineering, Nagoya Institute of Technology, Showa-ku, Nagoya 466, Japan

**Faculty of Physics, "Al. I. Cuza" University, b-dul Copou, no. 11, Iasi 6600, Romania

1. Introduction

The plasma of the positive column (PC) of a dc discharge in rare gases is known to be the subject of either self- or externally- induced ionization waves [1, 2]. Although, some early hydrodynamic models have been successfully used to explain some important characteristics of the ionization waves [3], it became clear that only a kinetic model provides a proper base for a theoretical approach [4]. Because of the small energy losses in the elastic collision range, the electron energy distribution (EEDF) in PC plasma of a dc discharge in inert gases has a strong nonlocal character [5]. An initial perturbation in the body of the EEDF, i.e. an injection of a number of low energy electrons, in a certain place of an axially homogeneous PC, leads, via acceleration in axial electric field, E_z , and inelastic collisions, to a downstream reproduction of the initial perturbation. Because of the fluctuations in plasma density, fluctuations of E_z also occurs, fact which can lead, in certain conditions, to a downstream development of ionization waves [6].

The aim of the present work is to provide experimental evidence on the role of the cathode inhomogeneity of the PC as a place of "injection" of the initial disturbance in the EEDF. It is known that the cathode end of a PC in a dc discharge in helium appears as a series of highly damped standing striations [7]. Following an initial pulse disturbance in the discharge current, I_d , a bunch of low energy electrons appear on the anode side of the first striation (cathode end of the PC). This bunch of electrons, which is formed as an effect of local increase of the ionization rate, evolves following the above described scenario into an ionization wave packet.

2. Results and discussion

The experiments were carried out in a dc hot cathode discharge, the discharge tube having 4.5cm in diameter and 60 cm in length, in helium at 0.75 Torr and discharge current of 200 mA, conditions in which the PC was ionization wave free. In order to observe the response of PC to an

external perturbation, a 50 μ s width pulse in I_d was periodically applied, via a coupling capacitor, to the discharge. An axially movable Langmuir probe was used to measure the EEDF, plasma potential, V_s , electron mean energy, ε , and electron density, n_e [8] in either the stationary or perturbed state of the PC [9].

The axial patterns of the radially emitted light intensity (389 nm), n_e , ε , and V_s , are presented in Fig. 1, the cathode being at $z = 0$. The cathodic parts of the discharge can be distinguished as the cathodic fall (1 cm), the negative glow (3 cm), the Faraday Dark Space (FDS) (2 cm) and the cathode head of the PC. The electrons emitted by the hot cathode are accelerated in the cathodic fall and, due to the inelastic collisions generate the high density plasma of the negative glow. The FDS is the region of low E_z , where the current continuity is assured by the strong axial diffusion [9]. At a distance of 6 cm from the cathode E_z increase again due to the opposite diffusion of the electrons in the standing striation formed at the cathode end of the PC. Here, the electrons coming from the FDS are accelerated by E_z , so that the plasma production (and n_e) increases towards the anode.

As a result of an initial pulse disturbance applied to I_d , fluctuations in the EEDF occur. Figs. 2 present the temporal evolution of the EEDF and n_e (regarded as EEDF integral over the energy space) at an incipient (Fig. 2 a) and at a later (Fig. 2 b) stages of the formation of an ionization wave packet. An increase in the low energy electron density occurs on the anode side of the first standing striation of PC ($z = 9$ cm), immediately after the initial disturbance (Fig. 2 a). It seems that whole column is affected by the initial disturbing pulse, but a perturbation in the EEDF appears, immediately after, only in the region of the axial inhomogeneity formed the cathode end of the PC. The positive pulse in I_d corresponds to an increase in charge particle

*Permanent address: Faculty of Physics, "Al. I. Cuza" University, b-dul Copou, no 11, Iasi 6600, Romania

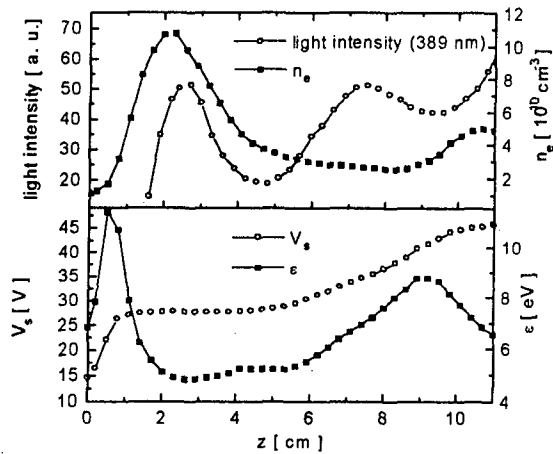


Fig. 1 Axial distributions of light intensity (389 nm), n_e , V_s and ϵ

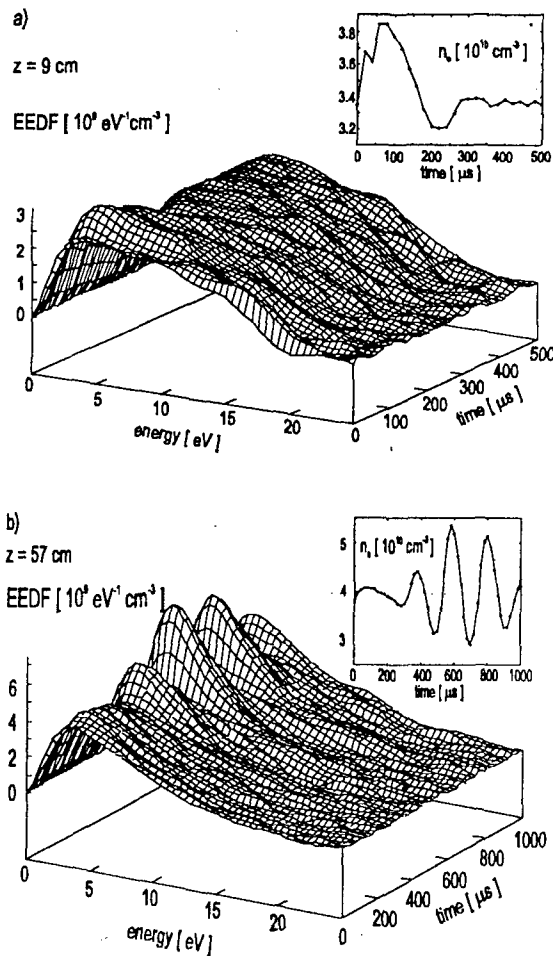


Fig. 2 Temporal fluctuations of EEDF induced by a I_d pulse disturbance at: a) the cathode end of PC; b) at large distance from the cathode.

production rate, i.e. n_e , and/or in E_z . An increase in E_z , along the region of axial inhomogeneity formed at the cathode end of plasma column (where E_z has larger values than those in the rest of the PC), leads to an increase in the number of high energy electrons in the EEDF tail and, as a result, to an increase in the charge particle production. Thus, a low energy electron bunch is generated at the anode side of the first striation of the cathode end of the PC. No relevant fluctuations in the body of the EEDF are observed immediately after the disturbing pulse at places situated far from the cathode end of the PC (Fig. 2 b).

3. Conclusion

The cathode end of a PC of a dc discharge in helium was investigated using the Langmuir probe technique in order to provide experimental evidence on the incipient stage of development of a ionization wave packet. It is shown that, as a result of a pulse disturbance applied to the discharge current, a low energy bunch of electrons is produced at the anode side of the first striation formed at the cathode end of PC.

Because the electron energy relaxation length is long in the elastic collision energy domain and relatively short in the inelastic collision one, a perturbation in EEDF at the cathode end of the positive column becomes the cause of the formation of other downstream fluctuations in the electron distribution, n_e and E_z , thus leading to the development of an ionization wave packet.

References

- [1] W. Pupp, Z. Phys., **33** (1932) 844
- [2] L. Pekarek, Czech. J. Phys., **4** (1954) 221
- [3] L. Pekarek and V. Krejci, Czech. J. Phys., **B12**, (1962), 450
- [4] V. Perina, K. Rohlena, T. Ruzicka, Czech. J. Phys. **B25** (1975) 660
- [5] V. I. Kolobov, V. A. Godyak, IEEE Trans. on Plasma Science **4** (1995) 503
- [6] L. D. Tsendin, Sov. J. Plasma Phys. **8** (1982) 96
- [7] A. W. Cooper, J. R. M. Coulter, and K. G. Emeleus, Nature **181**, (1958) 1326
- [8] M. J. Druyveinstein, Z. Phys. **64** (1930) 781
- [9] S. W. Rayment, N. D. Twiddy, Brit. J. Appl. Phys. (J. Phys. D) **2** (1969) 1747
- [10] Yu. M. Kagan, C. Cohen, P. Avivi, J. Appl. Phys. **63** (1988)

Constitutional Study of Two Parallel-Plates Cathode for Attaining the Hollow-cathode Effect

Hajime ONODA, Masaki YATSU, and Minoru SUGAWARA*

Kimmon Electric Company, TM-21 Building, 1-53-2, Itabashi, Itabashi-ku, Tokyo

*Department of Electrical Engineering, Hachinohe Institute of Technology, 88-1, Ohbiraki, Myo, Hgachinohe, Japan.

1. Introduction

The hollow-cathode discharge has features of high current density and low maintaining voltage^{(1),(2)}. In this aspect, the hollow-cathode discharge is often used to generate high density and low temperature plasmas. But, when designing the geometry of the hollow-cathode, sufficient information of the optimal shape of the cathode is not known. It is first pointed out⁽³⁾ that when the separation between two parallel plates of the cathode is sufficiently reduced the two negative glows coalesce and the light emission as well as the cathode current density rise greatly. At smaller values of the separation, the current densities are $10\text{-}10^3$ times of the normal glow discharge current density.

Aims of this research are to pursue experimentally the optimal separation of the plates with respect to the gas pressure and to discuss effect of longitudinal dimension of the plate on the hollow-cathode effect.

2. Experiments and results

Experiments have been carried out in a cylindrical glass(Pyrex) discharge tube of outer diameter of 91mm and length of 338mm. Measurements were made using two assemblies of cathode: one two parallel discs 40mm in diameter with variable separation from 0 to 10mm (type 1) and the other two parallel plates of the same size(39 in width, 15mm in depth) with variable depth of 0-15mm (type 2). We have employed two electrode materials, C and Ni. Measurements have been taken in gases of Ar, Ne, and N_2 of 99.999% purity.

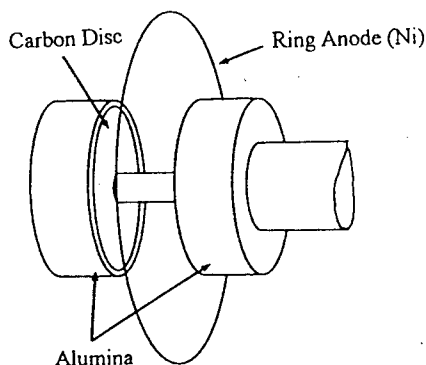


Fig.1 Electrode assembly of type 1 electrode.

The discharge tube was evacuated using turbo-molecular pump, the final vacuum obtained was 2×10^{-6} Torr. A schematic drawing of the cathode (type 1) is shown Fig.1. The separation between the two is varied from 0 to 10mm by adjusting the attached micrometer. Working pressure range is from 0.5 to 5 Torr. In the present paper, results obtained by the combination of Ar gas and C electrode are described.

2.1 Experiments on the optimal separation

One of mechanisms of the current multiplication in the hollow-cathode region is that the contribution is from the photo-electron emission from the cathodes⁽³⁾. Another existing theory suggests that electrons are trapped between two cathode sheaths and thus enhance ionization in the space by so-called pendulum motion of electrons. Therefore, varying the separation of the two, we have measured distribution of light emission across the two plates using CCD camera(model; KP-M1, Hitachi), output from which is displayed on a personal computer.

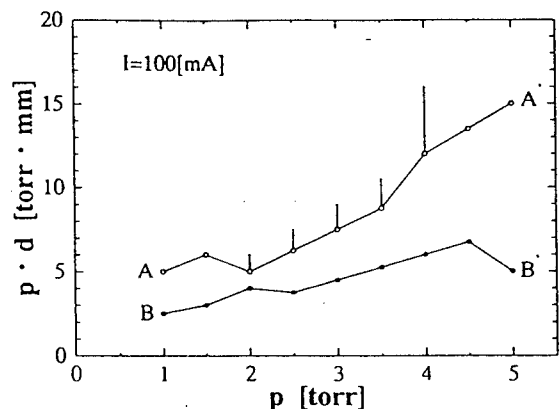


Fig.2 Measurements of the optimal separation($p \cdot d$) with respect to the pressure. Between two lines A-A' and B-B' the merged negative glow and enhanced hollow-cathode effect are observed.

We have observed that when reducing the separation, two separate negative glows of both plates are merged into one negative glow and at the same time light emission is also enhanced. We have plotted the merged

separation d multiplied by p as a function of p as shown in Fig.2. The separation (pd) of the merged negative glow is marked line A-A, below which the merged negative glow is observed. Further decrease of the separation causes the negative glow to be pushed out from the region between the two plates and at the same time the current to decrease and the maintaining voltage to increase which could be seen from the figure. The line B-B' below which the pushed-out negative glow is drawn in the figure. Experimental study of this type of discharge has been reported^{(4),(5)}. Therefore, between two lines, one can obtain merged negative-glow and the enhanced hollow cathode effect. Furthermore, we have measured the discharge current at a constant maintaining voltage and also the maintaining voltage at a constant discharge current with variable of the separation. One of typical data is shown in Fig.3. The hollow-cathode effect that is large increase in the current and large decrease in the maintaining voltage with reduced separation d is clearly seen from the figures.

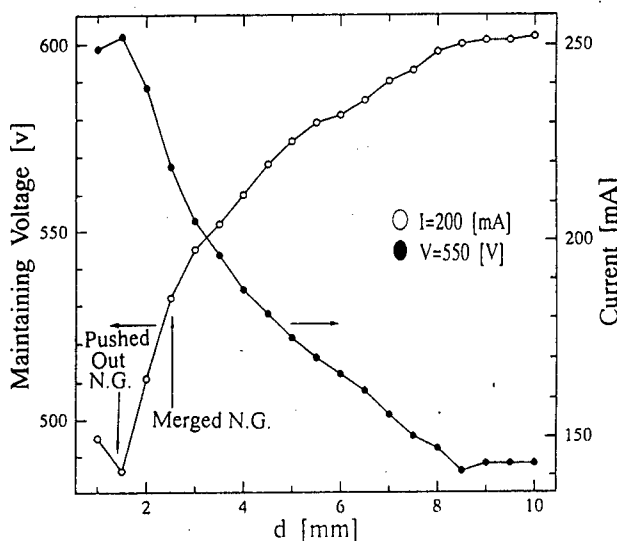


Fig.3. Measurements of the current multiplication ($V=500V$) and the voltage decrease ($I=200mA$). Taken at $p=3$ Torr.

2.2 Effect of the longitudinal dimension of the plate on the hollow-cathode effect.

If a pair of two narrow and long plates with wide separation d is used as a cathode, majority of electrons may not be trapped between the two plates and escape from the spacing. Therefore, it is easily suspected that there will be the minimum ratio (D/d) of the depth (D) of the plate to the separation (d) of the two plates in order to sustain the hollow-cathode effect. Effect of the lateral and longitudinal dimension of the plate must be similar as far as the hollow-cathode effect is concerned. We have used a pair of square plates with variable depth (0-15mm)

with a fixed lateral dimension of 38mm. Keeping the current density at $1.05 \times 10^{-3} (mA/mm^2)$ independent of variable depth, we have taken the maintaining voltage at separations of 2 and 5 mm as a function of the depth, from which sudden decrease of the maintaining voltage was noticed. This sudden decrease coincides with transition from the hollow-cathode region to the normal glow region, which is confirmed by the visual observation. Results are shown in Fig.4. Below this line, discharges tend to expand outward from the spacing.

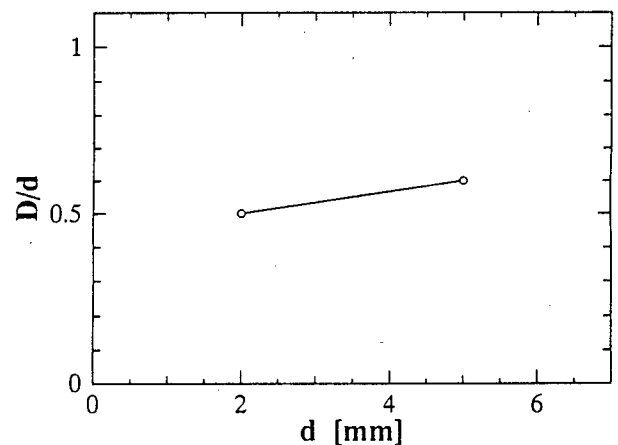


Fig.4. Effect of the longitudinal dimension (D) on the hollow-cathode effect.

3. Conclusion

We have studied the effect of the constitutional dimension of the cathode on the hollow-cathode effect. It has been shown experimentally that there have been the observed optimal separations (pd) in order to observe the enhanced hollow-cathode effect. The second experiments on effects of lateral and longitudinal dimension on the effect of the hollow-cathode effect has shown that the minimum depth (D/d) is about 0.6.

4. References

- (1) V.S.Borodin and Yu.M.Kagan, Sov. Phys.-Tech. Phys., **11**(1996)131
- (2) V.S.Borodin, Yu.M.Kagan and R.I.Lyagushenko, Sov.Phys.Tech.Phys., **11**(1967),
- (3) P.F.Little and A. von Engel, Proc. Roy. Soc., **A**, **224**(1954), 209
- (4) H.Onoda, M.Abe, M.Taira, and M.Sugawara, I.C.P.I.G.-XXI, **II**(1993),335.
- (5) H.Onoda, M.Abe, and M.Sugawara, Trans. IEE of Japan, **115**(1995), 668

EFFECT OF WALL TREATMENT ON OXYGEN ATOMS RECOMBINATION.

G. Cartry, L. Magne, G. Cernogora, M. Touzeau and M. Vialle

Laboratoire de Physique des Gaz et des Plasmas
Université Paris-Sud, Bât 212
91405 Orsay cedex FRANCE.

1. Introduction.

Low pressure glow discharges in oxygen, nitrogen and their mixtures are used in numerous applications such as surface treatments like nitridation, oxidation, atoms sources.... Therefore, the knowledge of volume kinetics and recombination of atoms at the wall is of great interest. The purpose of this work is to study the oxygen atoms recombination at the wall of a discharge tube for different surface conditions.

In oxygen low pressure glow discharges, atoms are mainly lost at the wall. The recombination strongly depends on the surface composition. For instance, atoms recombination is known to be more efficient on metal than on glass. The recombination efficiency, or catalytic property of the material, is described with the recombination probability γ : $\gamma \approx 1$ for metal and $\gamma \approx 10^{-4}$ for silica [1] or glass. Low catalytic materials are requested for the coating with refractory material of Space Orbiter in order to reduce the heating due to atoms recombination during the atmospheric re-entry trajectory. For a given material, the recombination depends also of the surface state as for instance, cleanliness, roughness, temperature. It is the reason why, published values of recombination probability γ on « Pyrex » glass range from 3.1×10^{-5} to 2×10^{-3} . A lot of measurements are done in flowing afterglow. The higher values of γ are obtained in time afterglow for which the glass wall has been submitted to the discharge [2]. Moreover, recombination increases with wall temperature. This effect is important in the temperature range (300K-1000K) commonly obtained in discharges [1].

Whereas a lot of studies are done in pure gas, recombination at the wall in gas mixtures are less known. The mixture composition induces variations on the dissociation. For instance, in N_2 - O_2 low pressure DC discharges, the concentration of atomic oxygen strongly increases with a small percentage of N_2 [3]. This effect is attributed to the

modification of dissociation by the electrons collisions, chemical reactions in the volume and at the wall [4]. The aim of this is to study only wall recombination. In order to free from electrons collisions we study the decay of the O concentration in the time afterglow of a pulsed discharge. In this paper are presented the first results concerning the influence of adsorbed species on recombination at the wall.

2. Experiment.

The experimental device is described in details in [3]. The pulsed discharge is produced in a 50 cm length and 15 mm diameter « Pyrex » tube closed with MgF_2 windows for the following experimental conditions: pressure $P = 1$ Torr, gas flow 5 sccm, pulse duration 20 μs , repetition rate 0.4 Hz, discharge current 60 mA within the pulse. The pulse duration and the discharge current have been chosen to create measurable concentrations of atoms and negligible gas heating. For this very low repetition frequency the atomic density relaxes to a negligible value at the end of the afterglow.

Absolute oxygen atoms density is measured by absorption of the atomic oxygen resonance lines at 130 nm. The light source is a low pressure discharge (Damany lamp) working in a O_2 - N_2 -He (1-1-98) mixture. The lines profiles have been measured using the very high resolution spectrometer at Meudon Observatory [3]. Oxygen atoms concentrations [O] are calculated from the transmitted signal in the time afterglow as described in [3].

The detection system is composed of a VUV 50 cm focal length monochromator with a solar blind photomultiplier. The signal is amplified and transmitted to a multichannel analyser working in photon counting mode.

Before working in the pulsed mode, the discharge tube wall is treated, during a long time; using a 80 mA DC discharge in pure N_2 or in pure O_2 with a gas flux of 20 sccm.

3. Results and discussion.

3.1 Pure oxygen afterglow.

Figure 1 shows $[O]$ concentration versus time during the afterglow for two different wall treatments. In the first case (curve a) the wall was submitted to a pure N_2 DC discharge during 4 hours. The second curve (b) is the same measurement after 4 hours of treatment in pure N_2 followed by treatment in a pure O_2 DC discharge during 1 hour.

We observe that the loss of oxygen atoms is slower for the case a. Then, nitrogen treatment reduce oxygen atoms recombination. In order to verify if this effect is a wall or a volume effect due desorbed nitrogen atoms or molecules we study now time after glows in N_2 - O_2 mixtures.

3.2 Oxygen nitrogen mixture.

We measure the variation of $[O]$ versus time during the afterglow in nitrogen oxygen mixtures for oxygen percentage varying from 2% to 80%. As in the case a of the figure 1, the wall is submitted to a pure N_2 DC discharge during 4 hours. The results are presented in figure 2. We observe, in the afterglow, the increase of $[O]$ with O_2 percentage. On the other hand, we can point out that N_2 percentage in the gas mixture have no measurable influence on characteristic decay time of $[O]$. This clearly demonstrates that the main loss process for oxygen atoms is recombination at the wall.

Therefore it can be deduced from the results presented in figure 1 that O recombination at the discharge tube wall strongly depends on the absorbed species.

Work is in progress to precise the kinetics at the wall in collaboration with V.Guerra, J.Loureiro, V.Zvonicek and A.Talsky [5].

References.

- [1] Kim J.C., Boudart M., Recombination of O, N and H atoms on silica: Kinetics and mechanism, *Langmuir* 7 (1991) 2999.
- [2] Sabadil H., Pfau S., Measurement of the Degree of dissociation..., *Plasma Chem. Plasma Process.* 5 (1985) 67.
- [3] Magne L., Coitout H., Cernogora G., Gousset G., Atomic oxygen recombination at the wall in a time afterglow, *J.Phys.III France* 3 (1993) 1871.
- [4] Gordiets B., Ferreira C.M., Nahorny J., Pagnon D., Touzeau M., Vialle M., Surface kinetics of N and O atoms in N_2 - O_2 discharges, *J.Phys D:Appl. Phys.* 29 (1996) 1021.
- [5] Zvonicek V., Guerra V., Loureiro J., Talsky A., Touzeau M., Surface and volume kinetics of $O(^3P)$ atoms in a low pressure O_2 - N_2 microwave discharge, *ICPIG XXIII*.

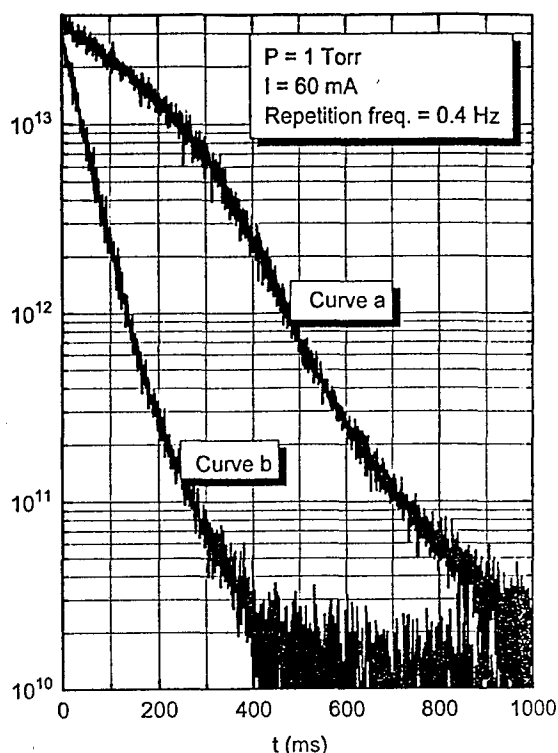


Figure 1. $[O]$ decay in a pure O_2 afterglow case a: after N_2 treatment; case b: after O_2 treatment

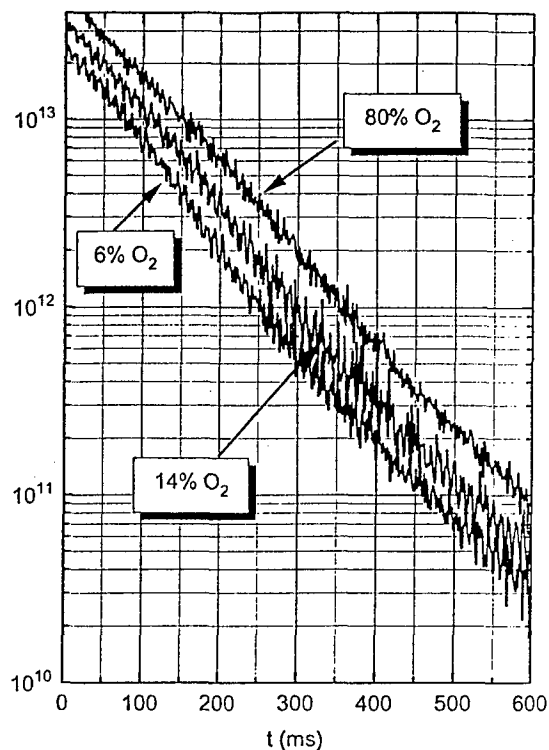


Figure 2. $[O]$ decay in a N_2 - O_2 mixture after glow for several O_2 percentages.

RELAXATION OF EXCITED STATES IN OXYGEN NITROGEN MIXTURES IN A LOW PRESSURE AFTERGLOW

G. Cartry, L. Magne, G. Cernogora M. Touzeau and M. Vialle.

Laboratoire de Physique des Gaz et des Plasmas
Université Paris-Sud, Bât 212
91405 Orsay Cedex FRANCE.

1. Introduction.

Oxygen nitrogen mixture discharges are used in wide range of applications as for instance atoms sources for surfaces treatments. A study has been undertaken in our laboratory for several years to establish surface and volume kinetics in low pressure DC discharges. In order to free from electronic processes we are now investigating the time afterglow of a pulsed discharge. The aim of this work is to present volume kinetics in such an afterglow. The surface kinetics is studied in a coupled paper submitted to this conference [1]. Relaxation of N_2 and NO excited states during the afterglow are deduced from optical spectroscopy time resolved measurements. Oxygen and nitrogen atomic concentrations are measured by VUV absorption spectroscopy. A simple model for heavy species kinetics supported by these experimental results is presented.

2. Experiment

The pulsed discharge is created in a 50 cm length Pyrex tube closed with two MgF_2 windows. The oxygen percentage δ varies from 0% to 20% for a total pressure $P = 1$ Torr of the N_2 - O_2 mixture and a gas flow of 5 sccm maintained to remove impurities.

The pulsed discharge parameters are 50 μs pulse duration, 1 kHz repetition frequency and 400 mA discharge current within the pulse. These parameters have been adjusted to create measurable concentrations of active species and a negligible gas heating.

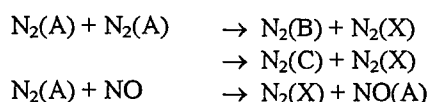
The intensities of the first positive and second positive systems of N_2 and NO(γ) bands are measured by emission spectroscopy in the visible and near UV using a 60 cm focal length monochromator. The output signals are amplified and connected to a multichannel analyser working in photon counting mode.

The absolute concentration of oxygen and nitrogen atoms are measured by VUV absorption spectroscopy at 130 nm and 120 nm respectively. The lamp is a low pressure discharge (Damany lamp) working in a N_2 - O_2 -He (1-1-98) mixture. The source line profiles have previously been measured using the very high resolution

spectrometer at Meudon Observatory [3]. The detection system is composed of a 50 cm focal length VUV monochromator and a solar blind photomultiplier.

3. Results and discussion.

The emissions of these excited states $N_2(B)$, $N_2(C)$ and NO(A) are observed in the time afterglow for duration up to 500 μs whereas their radiative lifetimes are respectively 9.8 μs , 37 ns and 187 ns. Consequently, these states are repopulated during the afterglow. In our experimental conditions, the reexcitation of these state can only result from energy transfers from metastable species. In N_2 - O_2 mixture discharges, the main processes for populating excited states are [2]:



Figures 1 and 2 present respectively the emissions from $N_2(C, v=4)$ and NO(A) as a function of time for δ from 0% to 20%. The fluorescences in the near afterglow can be described by exponential laws:

$$I = I_0 \cdot e^{-\nu_F t}$$

where ν_F is a characteristic fluorescence frequency. ν_F is measured for $N_2(C)$, $N_2(B)$ and NO(A). We found that ν_F increases with increases oxygen percentage. Furthermore for δ lower than 5%, $\nu_F(C) \sim 2 \cdot \nu_F(NO)$.

This result is in agreement with the proposed crude kinetics if $[N_2(A)]$ is assumed to follow a monoexponential decay. As a matter of fact, $N_2(C)$ production involves two $N_2(A)$ molecules whereas only one is needed for NO creation.

In the same experimental conditions, oxygen and nitrogen atoms densities are measured [3]. We observe that O density increases with oxygen amount. On the other hand, [O] remains constant in the afterglow during the decay of the observed radiative states. Nitrogen atoms concentration is strongly dependent on δ . Figure 3 shows the time evolution of [N] for several values of δ . We observe that [N] decreases with increasing δ and, the higher is δ , the faster is [N] decay. In afterglows,

recombination of N atoms at the wall is very slow (recombination probability $\gamma \sim 10^{-4}$ [4]) therefore, the kinetics of nitrogen atoms is mainly controlled by volume reactions.

Work is in progress to develop a kinetic model including volume reactions and reactions at the wall in collaboration with V.Guerra, J.Loureiro, V.Zvonicek and A.Talsky [5].

References.

- [1] Cartry G., Magne L., Cernogora G., Touzeau M., Vialle M.; Effect of the wall treatment on oxygen atoms recombination; ICPIG XXIII.
- [2] Coitout H., Cernogora G., Magne L., Nitrogen atom and triplet states $N_2(B^3\Pi_g)$, $N_2(C^3\Pi_u)$ in nitrogen afterglow; J.Phys.III France 5 (1995) 203.
- [3] Magne L., Coitout H., Cernogora G., Gousset G.; Atomic oxygen recombination at the wall in a time afterglow, J.Phys.III France 3 (1993) 1871.
- [4] Gordiets B., Ferreira C.M., Nahorny J., Pagnon D., Touzeau M., Vialle M.; Surface kinetics of N and O atoms in N_2 - O_2 discharges; J.Phys D:Appl. Phys.29 (1996) 1021.
- [5] Zvonicek V., Guerra V., Loureiro J., Talsky A., Touzeau M.; Surface and volume kinetics of $O(^3P)$ atoms in a low pressure O_2 - N_2 microwave discharge, ICPIG XXIII.

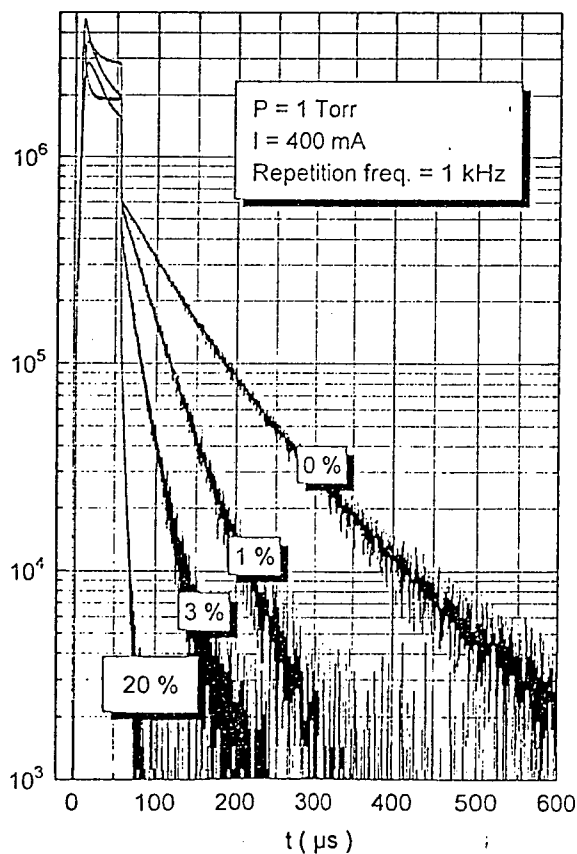


Figure 1. Emission of $N_2(C,v=4)$ (arbitrary units) during the after-glow for different oxygen percentages

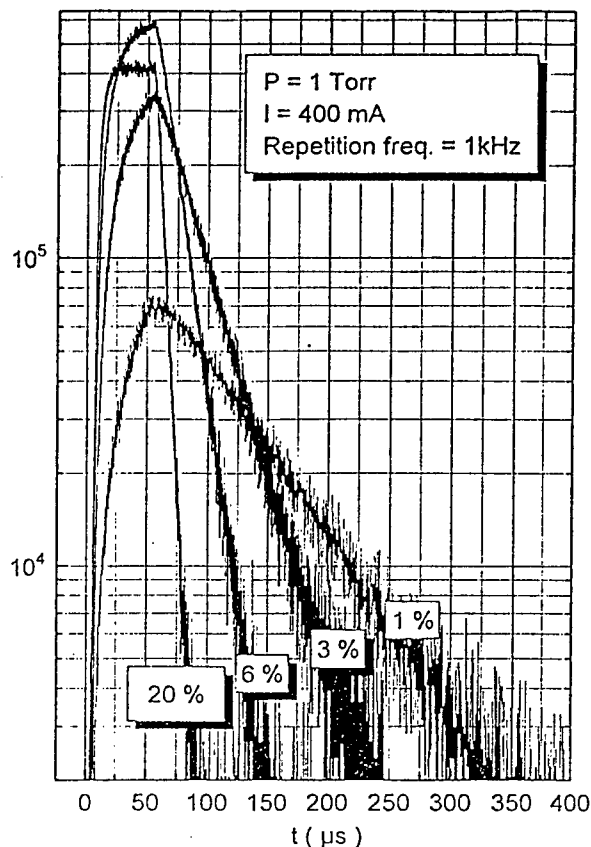


Figure 2. Emission of NO (γ) (arbitrary units) during the after-glow for different oxygen percentages

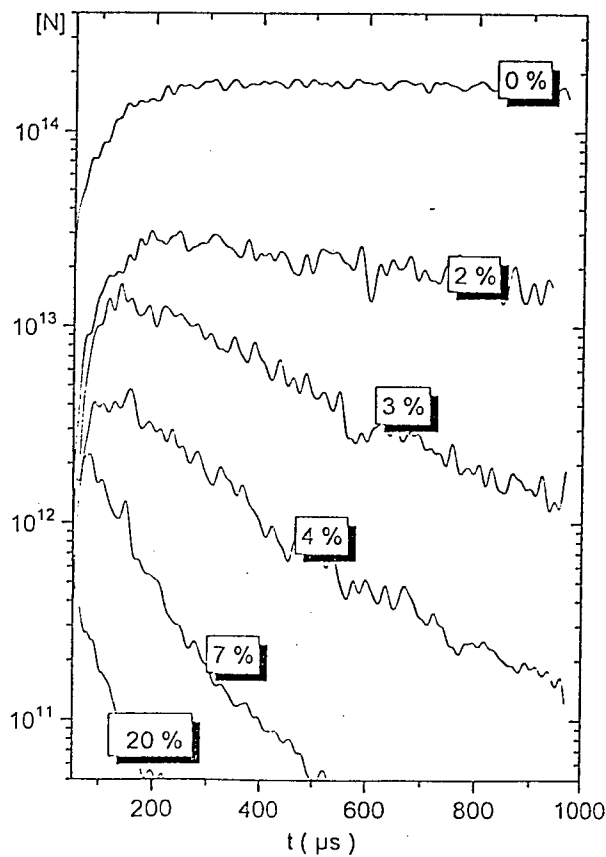


Figure 3. Nitrogen atoms density in the after-glow for different oxygen percentages

Improved Description of a Neon Glow Discharge by Rate Equations

St. Franke¹, H. Deutsch¹, D. Uhrlandt² and C. Wilke¹

¹ Institut für Physik, Ernst-Moritz-Arndt Universität Greifswald, Domstr. 10a, D-17487 Greifswald, Germany

² Institut für Niedertemperatur-Plasmaphysik, R.-Blum-Str. 8-10, D-17489 Greifswald, Germany

1. Introduction

Rate equations are known to represent excellent tools for a simple description of the positive column of low pressure glow discharges. The situation may be simplified further by radially averaged rate coefficients. Compared with Monte Carlo simulations [1] or a rigid solution of the BOLTZMANN equation [2], these rate equations provide an extraordinarily tractable approach for the description of typical properties of the positive column.

It was shown by RUTSCHER and PFAU (1967) [3] that the stationary current voltage characteristics can be described with an empirical set of rate and transport coefficients. However, a proper description of the impedance behaviour of the plasma fails with this set. WELTMANN et al. (1992) [4] gave another empirical set of coefficients for the impedance characteristics only.

Thus, there are two differing sets of coefficients for the stationary and the impedance characteristics, obviously representing an insufficient physical description. The present paper deals with approaches to remove these discrepancies for a neon glow discharge.

2. Theoretical approach

We started with a critical comparison of the atomic data available in the current literature. The most striking feature is the large discrepancy for excitation cross sections of metastable levels (see Fig. 1) [5] near threshold energies. Owing to the enormous importance of excited species for the formation of the plasma the choice of data may falsify the solution of the rate equation approach.

If the electron energy distribution function is calculated for a cylindrical, stationary, axial homogenous plasma by a 2-term approximation of the BOLTZMANN equation, it can be shown that rate coefficients must be considered to be radially dependent. A comparison of radially averaged rate coefficients of the radially inhomogenous BOLTZMANN equation with rate coefficients derived from the radially homogenous BOLTZMANN equation yields considerable deviations which must be taken into account.

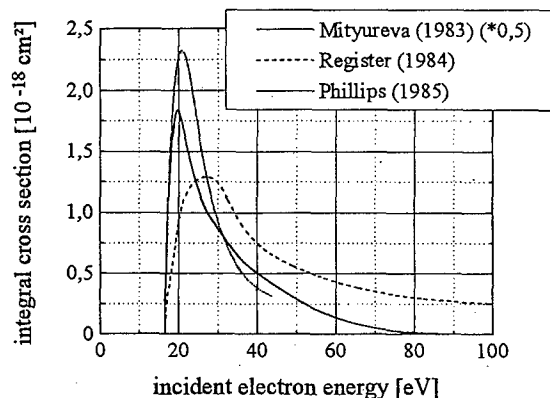


Figure 1: Cross section for collisional excitation of ground state neon to metastable excited states by electron impact.

However, experimentally derived cross sections are unknown for many elementary processes, e.g. pair collisions of excited atoms or stepwise excitation cross sections are unknown. These parameters have to be adapted by a critical comparison to experimental results.

3. Experimental results

We performed measurements for both the stationary current voltage characteristics and the impedance behaviour (see Fig. 2) of a neon glow discharge.

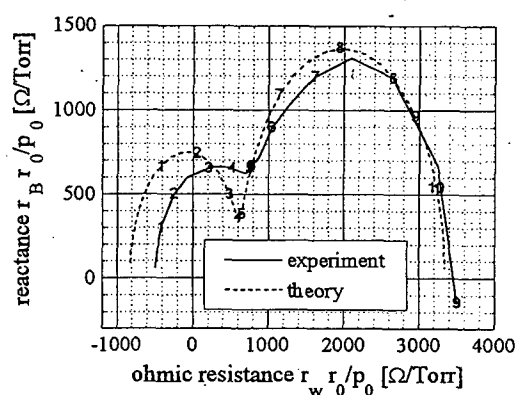


Figure 2: Comparison of the experimentally and theoretically derived impedance behaviour of a neon glow discharge ($r_0=1\text{cm}$, $p_0=1.51\text{Torr}$, $I_0=1\text{mA}$).

Although rate coefficients of some elementary processes (see above) have been adapted, the agreement of experimental values with theoretically derived impedance behaviour was insufficient.

However, if we take into account the radially dependence of rate coefficients, a consistent set of rate and transport coefficients properly describing both the stationary and the impedance behaviour can be given for different $p_0 r_0$. The result is displayed in Figure 2.

4. Conclusions

We have improved the description of the positive column and its electrical properties by rate equations. It was shown that radial dependencies of rate and transport coefficients are necessary for a consistent description of the stationary and impedance behaviour even if additional elementary processes are taken into account. Our experimental results support theoretical considerations concerning the influence of radial dependencies of the BOLTZMANN equation.

This work was funded by the Sonderforschungsbereich 198 'Kinetik partiell ionisierter Plasmen', Projekt A7 of the Deutsche Forschungsgemeinschaft.

5. References

- [1] A. Fiala, L.C. Pitchford, J.P. Boeuf: Phys. Rev. E **49** (1994) 5607; J.P. Boeuf, E. Marode: J. Phys. D **15** (1982) 2169
- [2] S. Pfau, J. Rohmann, D. Uhrlandt, R. Winkler: Contrib. Plasma Phys. **36** (1996) 449
- [3] A. Rutscher, S. Pfau: Beitr. Plasmaphys. **7** (1967) 187
- [4] K.-D. Weltmann, H. Deutsch, H. Unger, C. Wilke: Contrib. Plasma Phys. **32** (1992) 565; St. Franke: Diploma Theses, Greifswald: Institut für Physik der Ernst-Moritz-Arndt-Universität (1996)
- [5] A.A. Mityureva and N.P. Penkin: Optika i Spektroskopiya **55** (1983) 393; D.F. Register, S. Trajmar and G. Steffensen: Phys. Rev. A **29** (1984) 1793; M.H. Phillips, L.W. Anderson and C.C. Lin: Phys. Rev. A **32** (1985) 2117.

Electric discharge in crossed electric and magnetic fields.

A.I. Bugrova, A.S. Lipatov, A.I. Morozov, V.K. Kharchevnikov

Moscow State Institute of Radio Engineering, Electronics and Automation (MIREA), Moscow, Russia

Characteristic properties of toroidal electric discharge which is created and confined by crossed E-H fields are investigated. Integral and local characteristics of the discharge are obtained and oscillations are studied. The system is based on two parallel ring coils (Fig.1) with small cross-section, rigidly fixed, having currents of the same direction.

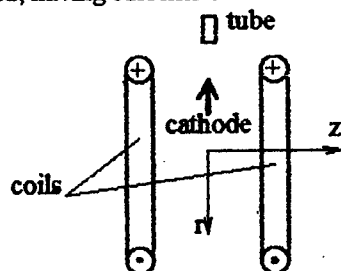


Fig.1

Distance between rings is equal to 10 cm, each diameter is 30 cm. The coils were installed in the vacuum chamber with diameter ~ 100 cm. Electric current in the coils produced magnetic field with separatrix having figure of eight and corresponding "zero" circumference where the magnetic field strength is zero. Magnetic field is sufficiently less outside the coils; its maximum is $H_0 \approx 20$ Oe when electric current in the coil is $J_m = 1.5 \cdot 10^3$ A.

Working substance (Xe) is bled into the region between the coils with 5 mm diameter tube. Just opposite the bleeding tube the pointwise thermoemission cathode was placed at "zero" line of magnetic field. The anode surfaces were the vacuum chamber and outer surfaces of magnetic coils covered with aluminium foil. The discharge voltage $U_d = 70-400$ V was applied between the anode and cathode; anode being at earth potential, cathode being at negative potential.

Electric discharge appeared as glowing ring with small cross section (~ 2 cm in diam.) placed between the rings along zero line of magnetic field. We may interpret the dynamics of plasma charged particles as below. Since the discharge glows at small magnetic field ($H_0 \approx 20$ Oe) then only electrons are confined by magnetic field. The ions, at the same time, are confined by electric field. Fig.2 represents the distribution of local plasma parameters in direction orthogonal the median plane of the system on straight line passing through zero field (z-axis). The parameters were obtained with aid of electric probe. When $H_0 = 20$ Oe the maximal concentration of electrons, electron temperature and plasma potential are: $(n_e)_{\max} = 5 \cdot 10^{10} \text{ cm}^{-3}$, $(T_e)_{\max} = 25$ eV, $\Phi = 80$ V.

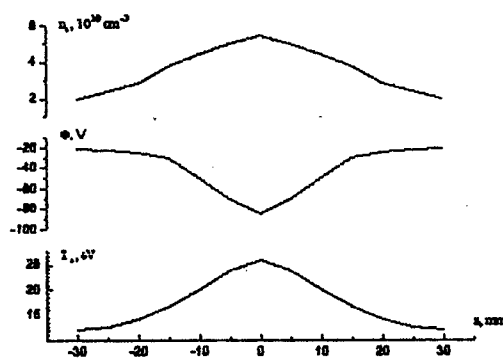


Fig.2

The great attention was paid to studying of oscillations in the system. Reason is, that, for our system dimensions value of electron density plasma volume is sufficiently transparent for neutral Xe atoms going from the tube and vacuum chamber. The dynamic Xe pressure in the chamber is $p_0 = 10^{-4}$ Torr and continuous partial ionization of atoms penetrating the whole plasma volume takes place. So, there is accumulation of appearing ions. The stationary regime may occur only if ion lifetime is

$$\tau_p = \frac{1}{n_0 \langle \sigma v_e \rangle_{\text{ion}}}$$

where n_0 is mean atom concentration in the system. When p_0 and T_e are as mentioned above, $\tau_p \sim 10$ mks and ion energy $\epsilon_i < e |\Phi_{\min}|$. If oscillations are absent the system would be overfilled with ions (ion concentration would increase by e -times during time τ_p). One can easily check that ion run-off to the cathode is ineffective in our case due to small ion velocity. So it is natural to expect the existence of powerful "waste" oscillations. The oscillations of parameters were detected by probes separated by angles $100^\circ, 180^\circ$. The oscillations of ion and electron currents at the operating mode $\dot{m}_{\text{Xe}} = 2$ mg/s, $U_d = 180$ V, $H_0 = 20$ Oe were measured. As it happens the period of oscillations $\tau_{pi} \sim \tau_{pe} \sim 15$ mks, an ion current modulation is at the level 50 - 100 %. At the same time discharge current oscillations are relatively small (≤ 10 %). We have also measured ion current oscillations varying H_0 from 16 Oe to 25 Oe. We obtained when H_0 increases τ_{pi} decreases from 15 mks to 10 mks. This τ_{pi} change can be associated with better electron confinement and subsequently more rapid accumulation of ion in the system during ionization. The data represented here indicate synonymously ion run-off due to oscillations withstands to ion accumulation and oscillation period is in reasonable consent with characteristic accumulation time.

Topic 5

Arcs.

COMPUTATIONAL RECONSTRUCTION AND VISUALISATION OF SWITCHING ARC

Aubrecht V., Bušov, B., Hanáček P., Mašek J., Peška L., Štefka J.

Technical University of Brno, Dept. of Elect. Machines and Apparatus, 602 00 Brno, Czech Republic

Introduction

Breaking of an electric circuit is accompanied by the formation of an electric arc between the circuit breaker contacts. A reliable function of the circuit breaker depends on several factors, the most important of which include: mechanical resistance of the individual components, circumstances of the switching arc extinction and the associated recovery of the dielectric strength of the medium between the circuit breaker contacts. A great influence on the switching process exert also the aerodynamic relations in the quenching chamber, the direct measurement of which is hardly feasible using contemporary techniques. Therefore the shape of the arc plasma burning between the circuit breaker contacts is scanned with a high-speed camera. The switching arc in the quenching chamber was simultaneously photographed from two fixed rectangular directions photographs from the high-speed camera represent a time analysis of the studied process which allows through their digital processing the determination of the time changes of the arc plasma shape. The negative film from the high-speed camera holds series of frames with the plasma shapes of the switching arc at the moments of exposure of the individual pictures.

Experimental methods

In our laboratory we use an equidensitometry evaluation [1] of the negative which brings an enhancement of the quality of the evaluation process and which represents apparently the most suitable procedure for the evaluation of the frames from the high-speed camera film. The method of equidensitometry diagnostics is based on digitising of the frames of the analysed object. When using the high-speed camera, a sequence of frames on the negative film is formed. Each frame represents a fixed shape of the arc plasma at the exposure time.

The term „equidensitometry“ denotes a complex of procedures which allow the obtaining of curves with the same blackening (grey level) of the photographic emulsion on the evaluated frame, and methods of their interpretation which make possible to obtain required properties of the scanned object from them. In the case of the electric arc these are mainly changes of its shape in time and the rate of its movement in the monitored equipment.

The magnitude of blackening of the photographic emulsion corresponds to the intensity of incidence

radiation. The curve connecting points with the same blackening is called *equidensity*. From the form of particular equidensities we can draw conclusions about properties of the recorded plasma.

A diagram with the set of equidensities is made using software DIPS r.5.0 (Digital Image Processing System). Particular equidensities are plotted with the step depending on optional isolines transform filter.

In Fig 1 we show the equidensitometry analysis of one frame of the negative film from high speed camera with projection of the SF₆ switching arc into two mutually perpendicular planes. Parameters of experiment in this case were as follows: rupturing current of 2.8 kA, voltage of 7.2 kV, SF₆ over-pressure of 0.4 MPa [2].

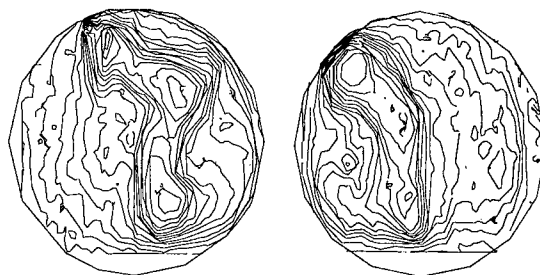


Fig. 1 Equidensitometry analysis of the arc image.

Two contour equidensities which define the arc boundary are plotted in Fig.2

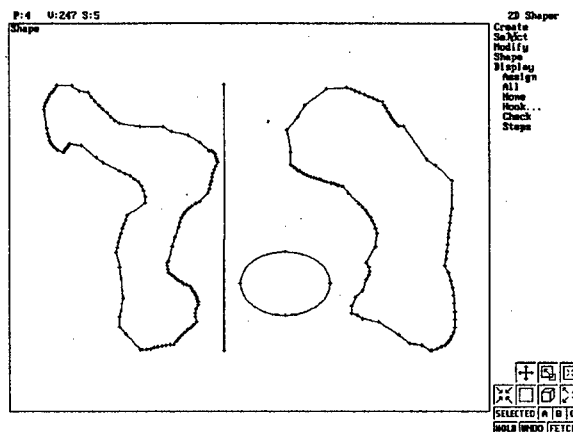


Fig.2. Pair of corresponding equidensities which determine the arc contour in rectangular planes.

A pair of such appropriate contour equidensities processed by CAD package [3] allows a reconstruction of the switching arc in a space. The reconstruction of the arc image was carried out by the method of several parallel sections through a pair of the equidensities. A section cuts selected equidensities in four points which define in first approximation an ellipse in the cutting plane [4] (see Fig.3).

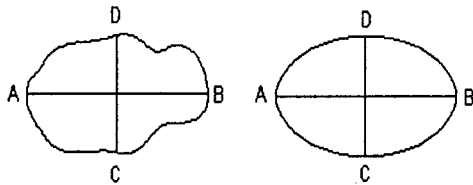


Fig.3. Approximation of the arc section by an ellipse.

The envelope around such ellipses obtained in several planes of space represents the surface of the 3D arc image (Fig.4).

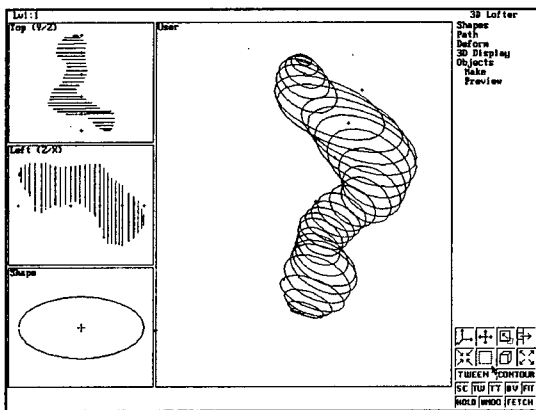


Fig.4. Several parallel sections of the arc image with elliptic contours.

The final result of the computer arc reconstruction is presented in Fig.5.

Conclusion

Computer techniques offer a new possibility of analysing and processing of experimental data into an accessible and inspiring form. 3D reconstruction and visualisation provides information about the switching arc in a form readily understandable for students and inspiring for research and development workers. It is possible to monitor changes of the arc shape in time and space via computer animation of sequence of the 3D arc images.

Such approach to the switching arc research can significantly contribute to the computation of further physical quantities that are required for assembly of the theoretical models of the switching process in the quenching chamber of power circuit breakers.

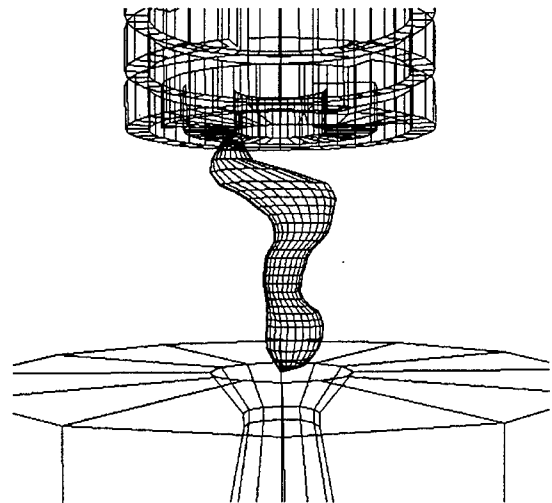


Fig. 5: Spatial reconstruction of the arc image in the quenching chamber of the circuit breaker model.

References

- [1] Gross B.: *Equidensitometry diagnostics of the switching arc plasma I, II*, Library A-38, Technical University of Brno, 1989 (in Czech).
- [2] Busov B.: *Influence of the switching arc onto the functional arrangement of a high voltage switch with SF₆*, PhD Thesis, Technical University of Brno, 1986 (in Czech).
- [3] Bušov B., Jadrný P., Aubrecht V., Gross B., Maloch J.: *Switching arc diagnostic and CAD* Proc. of XXIth ICPIG, Vol.II, pp.42-43, Bochum, September 19-24, 1993, Germany.
- [4] Bušov B., Aubrecht V.: *Plasma Diagnostic and CAD*. Proc. of Conf. on Physics and Technology of Plasma, Vol. I, pp.402-405, Minsk, 13-15 Sept.1994, Minsk, Belarus

Authors gratefully acknowledge financial support from the GACR, Projects No. 102/94/0430 and 102/95/0059.

Some remarks to calculation of ionization and recombination coefficients in SF₆ arc plasma

M. Bartlová, V. Aubrecht*

TU Brno, Faculty of Electrical Engineering & Computer Science,
Dept. of Spec. Electrical Engineering and Quality, Božetěchova 2, 612 00 Brno, Czech Republic
*Dept. of Electrical Machines and Apparatus, Údolní 19, 602 00 Brno, Czech Republic

1. Introduction

Electron-ion recombination is one of the main reactions (together with dissociative electron attachment) which are responsible for decay of free electrons in plasma and consequently protect the dielectric breakdown in extinguishing SF₆ arc. Different methods have been proposed in the past for calculating the atomic electron-ion recombination coefficient of plasma (e.g. [1]-[3]). The aim of this paper is to give a simple method for calculation of ionization and recombination coefficient which in addition takes into account radiative processes and atom-atom collisions.

2. Modified diffusion approximation

The modified diffusion approximation [4] is based on the assumption that due to collision processes the bound electron diffuses in the discrete atomic energy spectrum. The Fokker-Planck equation in finite differences is derived

$$\frac{dn_k}{dt} = \Delta j_k \quad (1)$$

where the net flow is given by (for optically thin plasma)

$$j_k = n_k z_{k,k+1} - n_{k+1} z_{k+1,k} + n_k w_{k,k+1}^a - n_{k+1} w_{k+1,k}^a - n_{k+1} A_{k+1}^R$$

where

$$z_{k,k+1} = \frac{B_k}{\Delta E_k (E_{k-1} - E_{k+1})}$$

and

$$z_{k+1,k} = \frac{A_{k+1}}{\Delta E_k} + \frac{B_{k+1}}{\Delta E_k (E_k - E_{k+2})}$$

are effective probabilities of single-quantum electron-induced transitions, 'diffusion' coefficients A_k, B_k are expressed by means of amount of energy

transfer; n_k is concentration of atoms in the state k , E_k denotes the energy of the level k , $w_{k,k+1}^a$ are transition probabilities by atom-atom collisions, A_k^R includes the sum of radiative transition probabilities.

The solution of equation (1) in quasi-stationary conditions

$$\frac{dn_k}{dt} = 0 \Rightarrow j_k = \text{konst} = j$$

is

$$j = \left(\frac{n_1}{n_1^0 \Pi_1} - \frac{n_e n^+}{n_e^0 (n^+)^0} \right) / R_{1e} \quad (2)$$

in which

$$R_{1e} = \sum_{k \geq 1} R_{k,k+1}$$

$$R_{k,k+1} = \frac{n_k^0 z_{k,k+1} \Pi_k}{1 + \frac{w_{k,k+1}^a}{z_{k,k+1}}}$$

and the radiative factor Π_k is given by

$$\Pi_k = \prod_{n \geq k} \left(1 + \frac{A_{n+1}^R}{z_{n+1,n}} + \frac{w_{n+1,n}^a}{z_{n+1,n}} \right) / \left(1 + \frac{w_{k,k+1}^a}{z_{k,k+1}} \right).$$

n_1^0 , n_e^0 , $(n^+)^0$ denote the equilibrium concentrations of atoms in the ground state, free electrons, and ions, respectively.

Comparing Eq. (2) with

$$j = n_1 n_e \beta - n_e n^+ \alpha$$

in which α and β denote recombination and ionization coefficients respectively, and including direct recombination ionization to the ground level it is obtained

$$\alpha = \frac{1}{n_e} (w_{el} + A_{el}) + [n_e n_e^0 (n^+)^0 R_{le}]^{-1} \quad (3)$$

$$\beta = \frac{1}{n_e} w_{le} + [n_e n_1^0 \Pi_1 R_{le}]^{-1}$$

where A_{el} , w_{el} , w_{le} are probabilities of both direct radiative and collisional recombinations, and collisional ionization respectively.

3. Results and discussion

From the relations (3) the recombination and ionization coefficients of electron-induced collisions, collisional-radiative processes and atom-atom collisions were determined for atoms S and F in the temperature range 2500 - 10000 K for two different pressures $p = 0.1$ MPa and $p = 1.0$ MPa. The concentrations of electrons, atoms and ions are determined for given temperature by calculation of equilibrium composition of the system of products of SF_6 - decomposition [5]

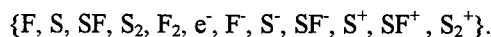


Fig. 1 and 2 give the temperature (and consequently also particle concentrations) variations of recombination and ionization coefficients for S. α is higher (β lower) for collisional-radiative processes and for atom-atom collisions than for electron-induced collisions because the plasma is assumed to be optically thin. With increasing temperature the difference decreases, this being due to decreasing of influence of radiative processes and increasing of electron concentration in the system. For low temperature where $n_a \gg n_e$ the influence of atom-atom collisions is notable.

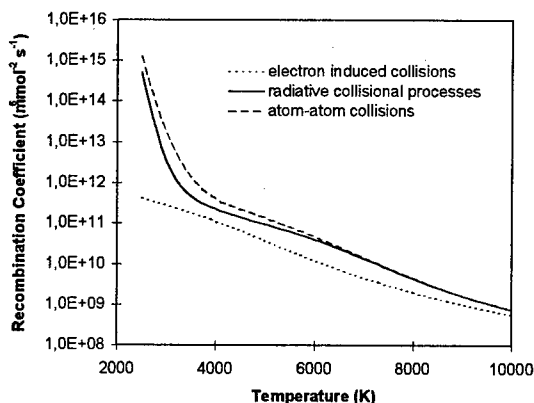


Fig. 1. Recombination coefficient of S at a pressure $p=0.1$ MPa

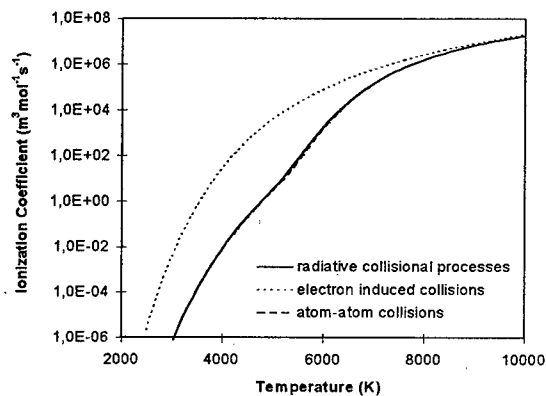


Fig. 2. Ionization coefficient of S at a pressure $p=1.0$ MPa

In Table 1 the values of recombination coefficient of atoms S and F are given. In this computation the collisional-radiative processes at a pressure $p=0.1$ MPa were taken into account. With increasing temperature α decreases more rapidly for F than for S but for higher temperature this decreasing is slower.

Table 1. Collisional-radiative coefficient for S and F at a pressure $p=0.1$ MPa

T [K]	α for S [$m^6 mol^{-2} s^{-1}$]	α for F [$m^6 mol^{-2} s^{-1}$]
3000	3.449×10^{12}	1.630×10^{12}
6000	4.141×10^{10}	6.058×10^9
10000	7.809×10^8	9.237×10^8

4. References

- [1] A. Gleizes, A.A.M. Habib, S. Vacquie: J. Phys. D: Appl. Phys. **22** (1989) 1464
- [2] H.W. Drawin, F. Emard: Beitr. Plasmaphys. **15** (1975) 273
- [3] L.M. Biberman, J.N. Toropkin, K.N. Uljanov: J. Tech. Phys. **32** (1962) 827
- [4] L.M. Biberman, V.S. Vorobev, J.T. Jakubov: Kinetics of nonequilibrium low-temperature plasma (in Russian). Nauka, Moscow, 1982
- [5] O. Coufal: Acta Technica CSAV **37** (1992) 209

The work described in this paper was carried out with the support of the grant project GACR number 102/96/1120.

DIAGNOSTICS OF THE ARC PLASMA BY AUTOCOLLIMATION INTERFEROMETER

J. Mašek, L. Peška, A. Houška*, B. Gross, V. Aubrecht

Institute of Electrical Machines and Apparatus, FEECS, TU of Brno

Údolní 19, 602 00 Brno, Czech Republic

* Institute of Physics Engineering, FME, TU of Brno

Technická 2, 619 69 Brno, Czech Republic

1. Introduction

In the contribution is described the measurement method of the temperature field of the electric arc plasma. The temperature field was determined by the interference method. The temperature field distribution in the vicinity of the plasma of the electric switching arc is one of the most important parameters which influence the construction of electric switchgear. Prior to this the temperature field was measured by probe methods. The latter are not capable of measuring continuously the examined space. Therefore it is highly advantageous to employ interference method which allow the obtainment of temperature values in all points of the space which is being examined.

2. Experimental

The subject of the measurements was an electric arc fed with a DC current with the values 20, 40 and 60 A. The arrangement of the electrodes was vertical whereby the bottom electrode was the cathode and the top one the anode. The electrodes were of a cylindrical shape with a diameter of 6 mm. The material of the electrodes was carbon.

The measurements were carried out with an autocollimation interferometer which is illustrated in Fig.1.

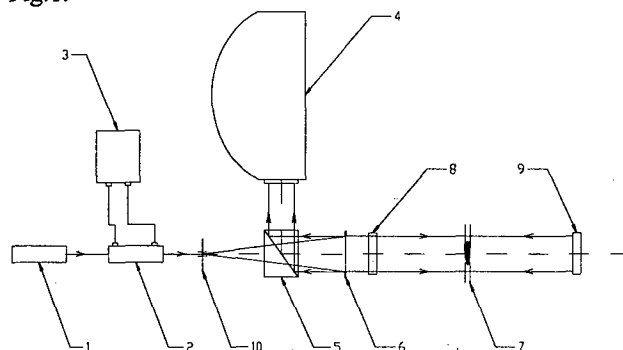


Fig.1: Experimental arrangement

- 1- He-Ne laser,
- 2- pulse laser,
- 3- power supply of the pulse laser
- 4- high-speed camera,
- 5- bundle splitter (prism),
- 6- lens,
- 7- arc discharge,
- 8,9-semi-transparent mirrors,
- 10- aperture.

The light source was a pulse-type ruby laser ($\lambda=694.8\text{nm}$) with an output energy of 1 to 5 Joule/pulse. There was also used an optical monochromatic filter for the wavelength $\lambda=694\text{ nm}$. The laser operated in a free generation mode. In our case was employed a diaphragm for setting the laser energy onto a value of 1 Joule/pulse. The pulse length was 250 μsec which corresponds to a laser performance of approx. 4 kW.

For adjusting the interferometer was used a He-Ne laser ($\lambda=632.8\text{ nm}$) which operated in a continuous mode with a performance of approx. 3mW.

For scanning the interference patterns was employed a high-speed camera with a rotating mirror. The high-speed camera was synchronized with the start of the laser pulse in such a way that at the moment when the mirror is in such a position that the laser beam can impinge onto the location of the first photo, the camera hands over a signal into the circuitry for controlling the high-speed camera. The circuits generate a HV pulse with a magnitude of 12 kV, a breakdown of the spark gap occurs and the current which has passed through the discharge on the spark gap induces in the coil a voltage pulse. This pulse triggers a sawtooth generator with a voltage of 3 V. The generated sawtooth pulse triggers the power supply of the laser and this applies onto the pulse-type laser a voltage which is necessary for the formation of a light pulse.

The high-speed camera utilized a rotating mirror with a speed of 30 000 r.p.m. At the moment of a laser pulse generation began the recording of a set of interference

patterns. Between two consecutive interference patterns is a time delay of 5 μsec whereby the exposure of every picture is 1 μsec . The high-speed camera operates with two display planes. The first one is the plane of the lens L_1 . This plane is focused onto the electric arc (end the electrodes, respectively) and displays it onto the photographic emulsion. In the second plane operates the lens L_2 which displays the diaphragm onto a set of small lenses L_3 . Only the upper diaphragm was utilized, so that the interference fields were displayed only on the unscreened locations (in this case the time interval between the individual pictures is 10 μsec). The exposure of every interference pattern was for both cases 1 μsec . The recording material was a negative film with a sensitivity of ISO-450.

The result of the experiment are photos of interference patterns which correspond to changes caused by the temperature field of the electric arc plasma.

Through the evaluation [1] of the interferograms was obtained the temperature field distribution of the plasma of the electric arc fed by a DC current. The result of the evaluation are radial temperature waveform in the plasma illustrated in Fig. 2.

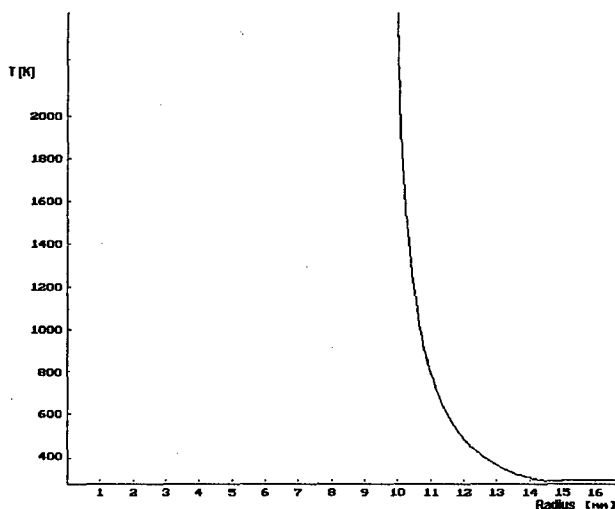


Fig. 2: Temperature waveform in the surroundings of an arc discharge in relation to the distance in a radial direction from the arc axis for current 20 A.

3. Conclusion

The method employed in the paper allows a relatively accurate measurement of the temperature field in the plasma of an electric discharge and in its immediate surroundings. This is the first step towards the measurement of temperature fields in quenching chambers of switchgear. It will allow the determination of thermal stressing of the quenching chamber wall. We consider the procedure adequate for practical applications. The results are comparable with

measurements carried out by spectroscopic methods and it can thus be assumed that the error of measurement is 10%.

4. References

- [1] L. Peška, A. Houška, B. Gross, V. Aubrecht, *Processing of interferograms of an electric arc discharge*. Proc. EOS Annual Meeting Digest, Vol.3. Zaragoza, (1993).
- [2] J. Mašek, L. Peška, A. Houška, B. Gross *Hysteresis of the temperature field in the vicinity of the electric arc plasma*. Proc PDP-I'96, Minsk, (1996).

We gratefully acknowledge the financial support from the „Task 102/95/0059“ sponsored by the Grant Agency of the Czech Republic.

The authors would like to express his gratitude to the Institute of Molecular and Atomic Physics, Academy of Sciences of Belarus, in the laboratories of which he had the opportunity to carry out the experiment and to the staff of the same Institute for their assistance in its realisation.

THE PLASMA MODEL OF NEW MODE HOT ANODE VACUUM ARC

I. I. BEILIS, R. L. BOXMAN and S. GOLDSMITH

Electrical Discharge and Plasma Laboratory
Tel Aviv University, P. O. B. 39040, Tel Aviv 69978, ISRAEL

1. INTRODUCTION

The hot anode vacuum arc (HAVA) is of interest because of its potential application in the deposition of high quality thin films (without the liquid droplets), in the high temperature synthesis of materials, and for application as a metallic plasma source[1].

In our previous experiments[2,3] the HAVA was studied using a planar Cu cathode and a thermally isolated solid graphite cylindrical anode with radius $R=16$ mm, length $L=30$ mm and interelectrode gap $h=10$ mm. A new mode of HAVA operation was established. A copper plasma was re-evaporated from the hot anode when its temperature was above 1900K, and no carbon vapor or carbon plasma were detected even when anode temperature reached 2300 K[2,3]. The transition of the arc from the multi-cathode-spot mode to the HAVA is characterized by the formation of a radiating plasma plume near the anode that expands towards the cathode. The measured electron temperature is about 1 eV.

The objective of this paper is to formulate a plasma model for this new mode of HAVA operation (with a refractory anode) which, given the arc current and the electrode geometry and materials, can predict quantities which have been observed experimentally[2,3].

2. THE PLASMA MODEL

During the initial discharge period, when the anode is not yet hot, the cathodic plasma flux condenses on the anode. The coefficient of atom condensation (k_c) is close to 1, and a thin film of cathode material is deposited on the anode surface. When anode surface is heated to a sufficiently high temperature, the film will be re-evaporated and $k_c < 1$, and depend on the anode surface temperature.

The thickness of the film assuming that all of the material eroded from the cathode is deposited uniformly on the anode surface, is $G I t / (A \gamma)$, where G is the cathode erosion rate, I is arc current, t is the duration, A is anode surface area and γ is mass density. In a case of a copper cathode, $G=100 \mu\text{g/C}$, $\gamma=9 \text{ g/cm}^3$ and, if $A \sim 10 \text{ cm}^2$ and $I=300 \text{ A}$, the film thickness can reach $\sim 30 \mu\text{m}$ in 10 s. During the discharge, the anode surface temperature increases and the deposited copper film is re-evaporated with an evaporation rate $W(T)$ [4]. The value of $k_c(T)$ can be obtained from the heavy particle balance at the anode surface as:

$$k_c(T) = 1 - \frac{W(T_a) A_a}{G I} \quad (1)$$

Using Eq. (1) for a Cu cathode shows that $k_c(T)=1$

0.02 for anode temperatures $T=1000-1800\text{K}$. The heavy particle density in the interelectrode plasma can be obtained from the particle balance, taking into account particle flows from the interelectrode plasma towards the cathode and in the radial direction. The particle balance is given by:

$$IG[1-k_c(T)]/m = \Gamma_{ik} + \Gamma_{ir} \quad (2)$$

where Γ_{ir} and Γ_{ik} are the particle flux per unit time in radial direction and towards cathode respectively. In Eq.2, the particle currents are obtained assuming that the plasma is fully ionized. This assumption is based on the relatively high electron temperature in the cathode plasma jet. In a first approximation the problem can be considered as one-dimensional with a uniform plasma density, and the plasma flux towards cathode can be disregarded. The particle losses in the radial directions can be written as:

$$\Gamma_{ir} = 2\pi R h n V_R \quad (3)$$

In the considered conditions, from Eq. 3 and Eq. 2 it follows that plasma density n in the gap with length $h=0.01 \text{ m}$ for the hot anode ($k_c=0$) depends on the radial plasma velocity V_R as $n \sim 10^{21} \frac{I}{V_R}$. In the

extreme case V_R is about thermal velocity $V_{th} \sim 10^3 \text{ m/s}$, the density is minimal and $n_{\min} \sim (2-3) \cdot 10^{20} \text{ m}^{-3}$ for $I=175-340 \text{ A}$. In general, k_c is not zero, and the plasma density changes during the discharge. Therefore, the mean free path, determined by the elastic, ionization and excitation collisions between the plasma beam ions and electrons with interelectrode (background) plasma ions and electrons, are time dependent. Therefore the intensity of cathode plasma beam interaction with the background anode plasma also is time depended.

It should be noted that even for the n_{\min} the random electron current to the anode is approximately $4 \cdot 10^3 \text{ A}$, i.e. much larger than the arc current (200 A), and, thus the anode will have a negative potential U_a with respect to the adjacent plasma.

3. THERMAL MODEL

The anode temperature distribution can be determined by the following non-stationary and nonlinear heat conductivity equations:

$$\rho(T)c(T) \frac{dT}{dt} = \frac{dT}{dx} \left[\lambda(T) \frac{dT}{dx} \right] + \rho_e(T) J^2 \frac{2}{R} \epsilon_{\text{eff}}(x) \sigma_{\text{SB}} T^4 \quad (4)$$

The boundary and initial conditions are:

$$\lambda(T) \frac{dT}{dx} \text{ (at } x=0) = q_{\text{in}}(T) - q_{\text{ro}}(T) - q_{\text{ev}}(T) \quad (5)$$

$$\lambda(T) \frac{dT}{dx} \text{ (at } x=L) = q_{rL}(T) \quad (6)$$

$$T(t=0, x) = T_0 \quad (7)$$

where $q_{ro}(T) = \epsilon_g \sigma_{SB} T^4$, $q_{rL}(T) = \epsilon_g \sigma_{SB} T^4 \rho(T)$, $c(T)$, $\lambda(T)$, $\rho_e(T)$, ϵ_g are anode material mass density, heat capacity, thermal and electrical conductivity, and surface emissivity, respectively; $q_{in}(T)$, $q_{ro}(T)$, $q_{rL}(T)$, $q_{ev}(T)$ are the temperature dependent incoming heat flux, the flux radiated by upper surface, flux radiated by the lower surface, and the evaporation heat flux, respectively. The radiation from the side surface of the anode is taken into account in the last term of Eq.4, where the parameter $\epsilon_{eff}(x)$ is the effective emissivity, which takes into account the fraction of the radiation flux which escapes from the sides of anode via the gap between the anode and the radiation shields [2].

In order to solve the Eq.4 the expression for $q_{in}(T)$ is needed. In our previous work[2] the q_{in} was taken as empirical. Here the expression for the incoming heat flux q_{in} is based on the above mentioned plasma model in following. In general, the anode can be heated by electrons q_{eb} and ions, q_{ib} from the cathode plasma beam, and by the electron flux q_{ep} from background plasma. The total heat flux to the anode is

$$q_{in} = q_{eb} + q_{ib} + q_{ep} \quad (8)$$

$$q_{ep} = \Gamma_{ep} (2T_{ep} + \phi) \quad (9)$$

$$q_{eb} = I(1+f)(2T_{ek} + \phi) \exp(-h/L_{ef}) \quad (10)$$

where ϕ is the electrode work function, L_{ef} is the effective mean free path and Γ_{ep} is plasma electron flux towards anode. The expressions for these fluxes are:

$$q_{ib} = I f \exp(-h/L_{if}) [\sum f_{iz} (U_{iz} + T_{ib}) + \sum E_{kin}^z - \sum f_{iz} \phi_z] \quad (11)$$

$$I_{ep} = e \Gamma_{ep} = I_{rd} \exp\left(-\frac{U_a}{T_{ep}}\right); \quad U_a = T_{ea} \ln\left(\frac{I_{rd}}{I_p}\right) \quad (12)$$

$I_p = I - I_{eb}(0, t) - I_{ib}(0, t)$ (13)
where e is electron charge, I_{rd} is random electron current from the plasma to the anode surface, f_{iz} is multicharge ion current fraction, $z=1,2,3$ is ionicity, U_{iz} is potential of ionization The ion beam energy flux

includes the ion potential energy and ion kinetic energy with jet velocity V ($E_{kin} = mV^2/2$).

The plasma electron energy balance is :

$$I(1+f)2T_{ek}(1-\exp(-(h-x)/L_{ef})) + (I-I_e(x))U_p = \Gamma_{ep}(2T_{ep} + U_a) + \Gamma_{er}2T_{ep} + \Gamma_{ir}(2T_{ip} + U_{il}) \quad (14)$$

where U_p is plasma potential drop and.

The heavy particles density in background plasma is:

$$n(T) = \frac{IG[1-k_c(T_a)]}{2\pi R m h V_r} \quad (15)$$

4. RESULTS

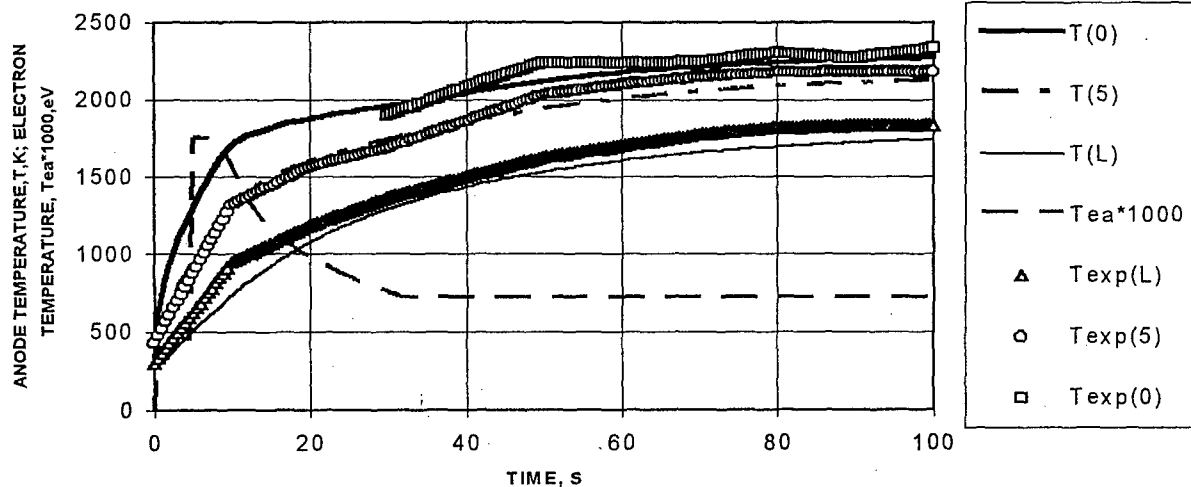
The ion temperature was assumed to be equal to the anode surface temperature $T(0)$ and the plasma radial velocity equal to thermal velocity of the heavy particles. The solution of Eq.4 for $I=340$ A and experimental data are presented in the figure, showing the time dependence of the temperature on the upper anode surface $T(0)$, in the anode body 5 mm from the surface $T(5)$ and on the lower surface $T(L)$. The curves agree well with the corresponding experimental data $T_{exp}(0)$, $T_{exp}(5)$, $T_{exp}(L)$ [2]. The plasma electron temperature T_{ea} (in the fig. is shown $T_{ea} \cdot 1000$) decreases with time from the initial value to the steady state value within 30s, and approximately agree with the experimental value[3].

ACKNOWLEDGMENTS

The authors gratefully acknowledge the support from the USA-Israel Foundation (BSF), No 94-00290.

REFERENCES

- [1] *Vacuum Arc Science and Technology*, Editors R.L. Boxman, P. Martin, D. Sanders (1995) by Noyes Publications (Park Ridge, NJ).
- [2] H. Rosenthal, I.I. Beilis, S. Goldsmith, R.L. Boxman, J. Phys. D: Appl. Phys, (1995), Vol. 28, 353
- [3] H. Rosenthal, I.I. Beilis, S. Goldsmith, R.L. Boxman, J. Phys. D: Appl. Phys, (1996), Vol. 29, 1245
- [4] S. Dushman, *Scientific Foundation of Vacuum Technique*. Ed. J. Lafferty, (1966) NY: Wiley.



SIMULATION OF A DECAYING SF₆ ARC PLASMA

J.-B. Belhaouari, J.-J. Gonzalez, A. Gleizes

Centre de Physique des Plasmas et de leurs Applications de Toulouse
ESA n° 5002, Université Paul Sabatier, 118 route de Narbonne 31062 Toulouse cedex 4, France
Phone: +33-05-61-55-68-55 Fax: +33-05-61-55-63-32 e-mail: jjg@cpa11.ups-tlse.fr

1. Introduction

During the arc extinction in H.V. circuit breakers there is a strong blowing leading to phenomena of turbulence. These mechanisms are responsible for the energy transfer necessary to the recovery of the dielectric rigidity. So a modelling based only on thermal phenomena cannot explain the behaviour of the plasma where it exists chemical non-equilibrium resulting from turbulence or strong cooling (-10^8 K.s^{-1}). All the models based on the hypothesis of the local thermodynamic equilibrium (LTE) lead to a post-arc current, contrary to the experimental results where the post-arc current is often non-existent after the zero of the alternative current. To interpret this difference, we have to consider that molecular species may be present in the hot regions. So the plasma column should be cut by a portion of gas with a small electrical conductivity unlucky to the circulation of the electric current.

The general aim of this work is to simulate the decaying arc behaviour taking non equilibrium effects into account. So we have built a mathematical model coupling a hydrodynamic and kinetic study for an SF₆ gas in a two dimensions flow in a transient state. The coupling between hydrodynamics kinetics is made through the pressure and the mass density.

2. Mathematical model

The model treats a two dimensional SF₆ arc in transient state. It is based on the following main assumptions: the plasma has a cylindrical symmetry; we consider that the transport coefficients: electrical conductivity σ , thermal conductivity κ , specific heat C_p , viscosity μ [2], net emission coefficient ϵ_N [3] are only functions of temperature. For the net emission we assume an isothermal and homogeneous cylindrical plasma of radius R_p ($R_p = 2 \text{ mm}$). Diffusion of particles is neglected. The calculation domain and boundary conditions are given in figure 1 and table 1. The dimensions of the calculation domain are respectively 2 cm and 0.5 cm on the axial and radial directions for a grid of 40 x 40 points. On the electrode (line EF) we made a preliminary study, resolving in a one dimension the equations (1) and (2) in order to give the boundary condition for the resolution of the 2D

stationary model and to give the temperature and radial velocity components for the transient state. The conservation equation that we use in stationary and transient state are the following.

on the electrode (line EF)

$$\frac{\partial \rho}{\partial t} + \frac{1}{r} \frac{\partial}{\partial r} (r \rho v) = 0 \quad (1)$$

$$\rho C_p \frac{\partial T}{\partial t} + \rho v C_p \frac{\partial T}{\partial r} = \frac{1}{r} \frac{\partial}{\partial r} \left(r K \frac{\partial T}{\partial r} \right) + \sigma E^2 - 4 \pi \epsilon_N \quad (2)$$

$$\text{species} \quad \frac{\partial n_i}{\partial t} + \vec{v} \cdot (n_i \vec{v}) = Ca_i - n_i Da_i \quad (3)$$

$$\text{momentum} \quad \rho \frac{\partial \vec{v}}{\partial t} + \vec{v} \cdot (\rho \vec{v} \vec{v}) = -\vec{\nabla} P + \vec{\nabla} \cdot (\mu \vec{\nabla} \vec{v}) \quad (4)$$

energy

$$\rho \frac{\partial h}{\partial t} + \vec{v} \cdot (\rho \vec{v} h) = \vec{\nabla} \cdot \left(\frac{K}{C_p} \nabla h \right) + \sigma E^2 - 4 \pi \epsilon_N + \vec{v} \cdot \vec{\nabla} P \quad (5)$$

Coupling

$$P = \sum_i n_i k_b T \quad \rho = \sum_i m_i n_i \quad (6)$$

where \vec{v} is the vector velocity (u and v are the axial and the radial components of the velocity), P is the pressure, h the specific enthalpy, n_i represents the particle density of species 'i', Ca_i the number of particles created, $n_i Da_i$ the number of particles 'i' destroyed by unit of time and volume. The terms Ca_i and Da_i are functions of chemical reaction rates, calculated by Borge [4]. The resolution of these equations is based on the algorithms of Patankar [5].

3. Calculation

In stationary state the calculation is made for current intensity I equal to 50 A and mass flow rate D_0 equal to 0.2 g.s^{-1} . The electric field E is constant and uniform. The gas entry is situated on the line DE where the axial velocity profile $u(r)$ of the inlet flow is parabolic. In order to limit the axis temperature in stationary state (the reaction rates were computed for $T \leq 12000 \text{ K}$) and to have a rather strong blowing during the extinction, we have imposed an increase of the inlet flow in transient state given by: $D = D_0 (1 + 29 t/2 \cdot 10^{-5}) \text{ g.s}^{-1}$. The initial SF₆ plasma composition is calculated by a kinetic model given in [6].

After the current zero the electric field $E = 0$. We have considered 19 species: (e^- , S, S⁻, S⁺, S₂, S₂⁺, F,

F, F⁺, F₂, F₂⁺, SF, SF⁺, SF₂⁺, SF₃, SF₄, SF₅, SF₆, SF₂, SF₃). More than 66 chemical reactions between these species have been taken into account and have been described in [4]. The direct reaction rates and the reverse rates are given in [6]. The initial profiles of temperature, velocities and the 19 species densities are given by the stationary model. The models (hydrodynamic and chemical) are coupled with the mass density (7) and the pressure (6). The time step, Δt is chosen using a chemical criterion: $\Delta t = [(Da)_{Max}]^{-1}$, where $(Da)_{Max}$ represents the maximum destruction rate of any species.

4. Results

The results are presented for a time equal to 20 μ s. The temperature field is plotted in figure 2. We can note a pinching on the entrance resulting of the strong convection. The maximal velocity on the entrance is 1622 m.s⁻¹. In figure 3 we have plotted the relative electron density field (the relative density is defined as the ratio of the calculated density on the equilibrium value $n_{LTE}(T,P)$). Our results show mainly an under-population of electron density in the edges of the arc that means in the temperature range 5000 K < T < 7000 K. In figure 4 we have plotted the relative density of S₂⁺. We can note an overpopulation of S₂⁺ density in the edges of the arc. The under-population of electron density is explained by the electron recombination on the molecules S₂⁺, this effect is strengthened by the convection of the cold gas.

These results on the influence of the convection are in good agreement with the expected behaviour. In effect an higher convection or phenomena of turbulence can lead to an under-population of electron density in a critical temperature range for the post-arc phase.

6. References

[1] Gleizes A., Sakalis I., Razafinimanana M., Vacquié S., 1987, J. Appl. Phys., **61**, 510.
 [2] Chervy B., Gleizes A., Razafinimanana M., 1994, J. Phys. D.: Appl. Phys., **27**, 1193.
 [3] Gleizes A., Gonzalez J. J., Liani B. and Raynal G., 1993, J. Phys. D: Appl. Phys., **26**, 1921.
 [4] Borge E., 1995, Doctorat de l'Université Paul Sabatier n° 2051.
 [5] Patankar S. V., 1980, 'Numerical Heat Transfert and Fluid Flow'.
 [6] Gonzalez J. J., Belhaouari J. B., Gleizes A., XIIth Symposium on Physics of Switching Arc, Brno, 1, 45, 1996

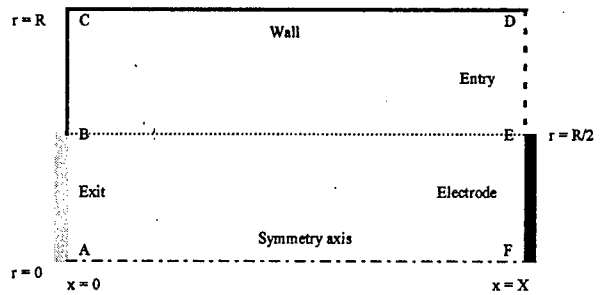


Figure 1: Calculation domain

	AB	BCD	DE	EF	FA
u	$\frac{\partial u}{\partial x} = 0$	0	u(r,t)	0	$\frac{\partial u}{\partial r} = 0$
v	0	0	0	Electrode model	0
T	$\frac{\partial T}{\partial x} = 0$	3000 K	3000 K		$\frac{\partial T}{\partial r} = 0$
n	$\frac{\partial n}{\partial x} = 0$	$\frac{\partial n}{\partial r} = 0$	n_{LTE}	n_{LTE}	$\frac{\partial n}{\partial r} = 0$

Table 1: Boundary conditions

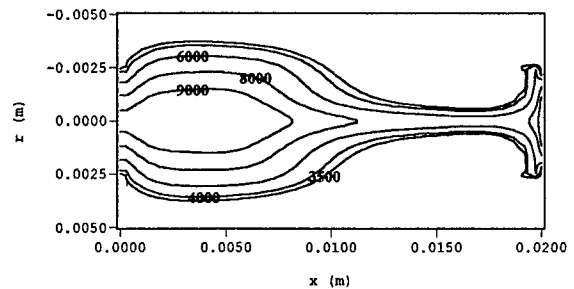


Figure 2: Plasma temperature field

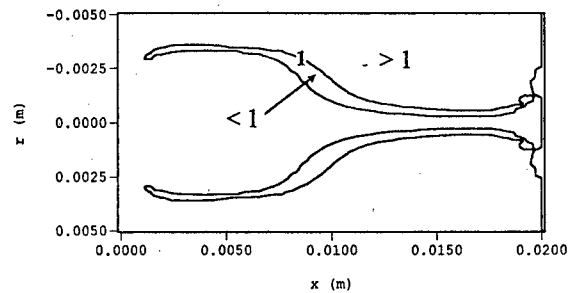


Figure 3: Relative density field (electron)

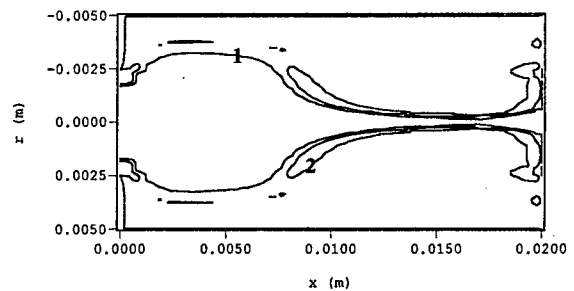


Figure 4: Relative density field (S₂⁺)

DEPARTURES FROM EQUILIBRIUM IN THE ANODE REGION OF A TRANSFERRED ARC AT ATMOSPHERIC PRESSURE

M.Bouaziz, M. Razafinimanana and A. Gleizes

Centre de Physique des Plasmas et de leurs Applications de Toulouse (ESA 5002)
118 route de Narbonne, F 31062 Toulouse cedex 4

Introduction

Several studies have shown that departures from local thermodynamic equilibrium (LTE) exist in stationary arc plasma at atmospheric pressure in the vicinity of the anode of an argon transferred arc. El Hamidi [1] has studied these departures by comparing the experimental values of particle densities and the computed values deduced from the equilibrium plasma composition. He showed that the experimental values could be different from the theoretical values obtained at LTE. In this paper we present a spectroscopic study in decaying argon and argon-copper arc plasmas at atmospheric pressure. We present the results measured first in stationary state (these results are necessary in the analysis of the phenomena), and then in transient state during the extinction.

Arc chamber

The arc chamber was described in [2]. The transferred arc was struck in argon at atmospheric pressure, between a thoriated tungsten cathode and a copper plate anode. The distance between the electrodes was adjustable from 0 to 10cm. In the area near the anode it was possible to obtain either pure argon plasma or a mixture of argon and copper vapour arising from the erosion of the anode by altering the degree of cooling of the anode. Electrical power was supplied by three DC sources of 100V and 100A each. Our working conditions were 18mm arc length, 25-40 and 90A current intensities and argon flow rate of 8l/min.

Experimental set up

The light emitted by the plasma was collected by a mobile optical unit and focused onto the entrance slit of a 1m focal length monochromator. At the outlet focal plane, an array of 1024 photodiodes or a photomultiplier were placed and allowed to analyse the radiation. Arc cut-off was produced by means of fast thyristor connected to the electrodes which short-circuits the discharge with a turn of time close to 1 or 2 μ s. The thyristor trigger was activated automatically using a procedure that minimises the effects of signal instability. The signals were recorded with a 100 MHz oscilloscope. The interruption set up was schematically represented in figure 1.

Stationary state study

We have firstly studied the plasma in the stationary state. Temperature profiles were measured by emission spectroscopic methods. In pure argon, equilibrium temperature was obtained by measuring the absolute intensity of the 696.5nm ArI line under LTE conditions. In the argon-copper mixtures, excitation temperature was deduced using the ratio between the relative intensities of 510.5 and 515.3nm CuI lines. The intensity calibration was performed with a tungsten ribbon lamp. The local values were obtained using Abel inversion of the recorded signals.

In the table 1 we presented the temperature, the electron density deduced from the equilibrium composition and the total copper concentration values obtained in pure argon and in argon-copper mixtures, on the axis of the discharge, for three current intensities and at $z=1$ mm above the anode.

I (A)	pure argon		argon-copper		
	T(K)	N_e (m^{-3})	T(K)	N_e (m^{-3})	χ_{Cu}
90	11500	4.10^{22}	9000	7.10^{21}	3.10^{-3}
40	9800	1.10^{22}	8800	6.10^{21}	1.10^{-3}
25	9300	8.10^{21}			

Transient state

The presence of LTE implies that the temperature of the species is equal ($T_e=T_g$), and the internal state distribution of the particles obeys the Saha and Boltzmann laws. However, in a stationary arc plasma, the electron temperature T_e may be higher than the gas temperature T_g because the electric field heats first the electrons, and then the electrons transfer their energy to the heavy particles through elastic collisions.. When $T_e>T_g$ in stationary state, immediately after arc interruption, T_e decreases rapidly and reaches T_g value, then the thermal equilibrium is established. The behaviour of a total line intensity during the first microseconds after the power interruption gives an idea about the equilibrium departure.

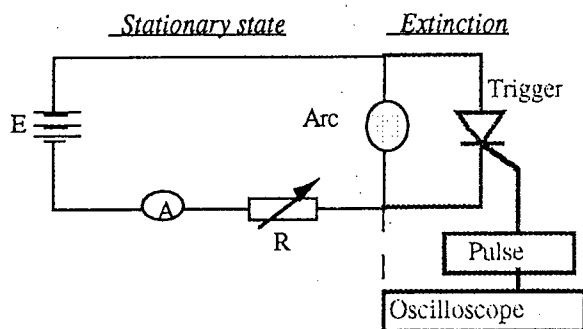
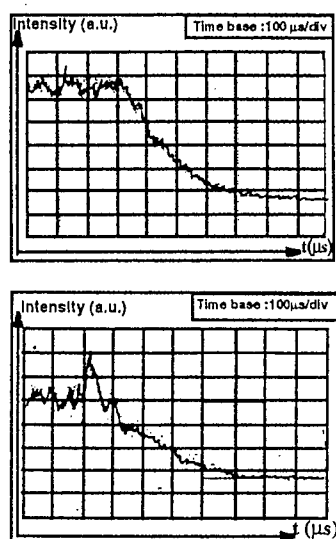


Figure 1 : Arc interruption set up

Argon case : The variations (before and immediately after the arc interruption) of the total intensity of the 696.5nm ArI line measured along the arc diameter at $z=1\text{mm}$ above the anode, for two values of current intensity (90 and 25A) are represented in figure 2.

Figure 2 : Transient evolution of the 696.5nm ArI line intensity: a) $I=90\text{A}$; b) $I=25\text{A}$

We can notice that the total line intensity variations during the arc decay are not analogous for 90A and 25A current intensities. At low current, a jump of the intensity is observed immediately after the arc interruption and indicates the existence of a departure from LTE. This phenomenon can be interpreted as following : the upper level of the 696.5nm transition is strongly correlated with the free electron and its population follows the Saha's law. The sudden interruption of the electric field induces a rapid thermalisation of the electron temperature; T_e decreases down to the gas temperature T_g in less than $1\mu\text{s}$ [3]. The electron density n_e decreases with a typical time scale of $100\mu\text{s}$ [4]. Therefore, during this thermalisation phase, n_e remains roughly constant and the atom density n_j on the level j increases. This results in a jump of the intensity of the line emitted by the level j . The intensity of the jump increases with the difference $T_e - T_g$.

Copper case : When copper vapours arising from the anode erosion were present in the plasma, we have measured the total intensity of the 515.3nm CuI line during the arc extinction at $z=1\text{mm}$ and for 90 and 40A current intensities. The transient evolution of this intensity as reported in figure 3, shows a slow decrease ($t=300\mu\text{s}$) at high current and a very rapid decrease during a first step at low current.

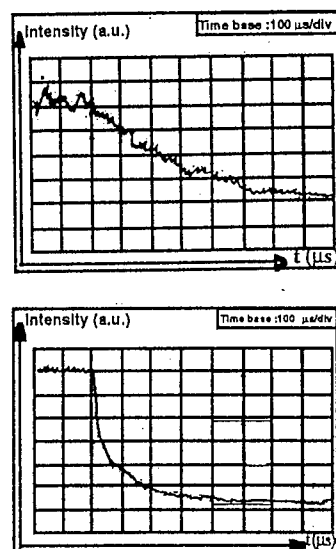


Figure 3 : Transient evolution of 515.3nm of CuI line intensity at 90A and 40A

This downward jump may be explained by the fact that the excited levels are situated at low energy; they are more correlated to the ground state than to the electrons and their populations are given by the Boltzmann law. Thus the decrease of T_e to T_g without the evolution of the density of total atom n_0 leads to a sudden decrease in the number density of the observed excited atoms level.

Conclusion

This study is the first of its kind where departures from Saha and Boltzmann equilibrium with the same transferred arc device were observed simultaneously. Similar observations were remarked with an ICP torch [5].

References

- [1] L. El Hamidi : These de l'Université Paul Sabatier, n° 1675, Toulouse 1993
- [2] J.J. Gonzalez, M. Bouaziz, M. Razafimanana and A. Gleizes : Plasma Sources Sci. Technol. 6 (1997), 1
- [3] A. Gleizes, H. Kafrouni, H. Dang Duc and C. Maury : J. Phys. D : Appl. Phys., 15 (1982), 1031
- [4] H. Kafrouni, J.M. Bagnoux, A. Gleizes : J. quant. Spectrosc. radiat. Transfer, 21 (1979), 457
- [5] J.M. de Regt, J.A.M. van der Mullen, and D. C. Schram : Physical Review E, 52 (1995), 3, 2982

Dynamical analysis of a low pressure nitrogen plasma generated by a transferred double arc

A.Bultel, B.Maheu, F.Lemur, B.G.Chéron
UMR 6614 - CORIA - Université de Rouen
76821 Mont Saint Aignan Cedex

Previous studies in our laboratory [1],[2] have been focused on the characterisation of a supersonic low pressure nitrogen plasma jet. These works were intended to validate some chemical rates and transport coefficients involved in the numerical simulation of the space shuttle re-entry. The interest here is in studying the stability of our plasma source by considering it as a non-linear dynamical system. This work intends to emphasize the temporal coupling between the electrical parameters of our double arc (voltages and currents) and the optical emission intensity inside the arc chamber and at the exit of the plasma source.

The involved methods are either classical (Fourier analysis and temporal correlations) or specifically relevant to nonlinear systems dynamics.

The experiments have been performed in a low density plasma wind tunnel (chamber pressure 100 Pa, nitrogen mass flow 0.22 g.s^{-1}). A primary arc (38V, 280 A) is ignited between the tip of a cone-shaped tungsten cathode and the throat (5mm in diameter) of a nozzle-shaped copper anode. A secondary arc (40V, 100A) is then ignited between the cathode and an annular anode (25 mm in diameter) set in the extension of the primary anode divergence. Tungsten and copper have been successively used as secondary anode materials. This plasma source is supplied by a set of triphase asynchronous motors linked to dc generators. The hydrodynamic stability and the emissivity of the plasma are greatly enhanced by this increase of the applied power.

Holes bored through the primary anode give the static pressure in the arc chamber. The 'reservoir' pressure is 30 kPa and the nozzle is not pressure-adapted. In the vacuum chamber the plasma spread is 14 cm in diameter and 150 cm in length.

A schematic draw of the experiment is shown in figure 1. Operating tensions between cathode and primary anode $U_1(t)$ between cathode and secondary anode $U_2(t)$ and the intensity of the 410.9 nm line of the atomic nitrogen are simultaneously recorded.

The primary current intensity $I_1(t)$ is directly drawn from a shunt. At the secondary anode four copper intakes have been symetrically arranged for draining the current. The secondary current intensities are measured by using Hall effect clamps.

Optical observation of the primary arc has been achieved by symetrically arranging four optical fibers (N.A=0.4) in the arc chamber. They are connected to UVP photo-

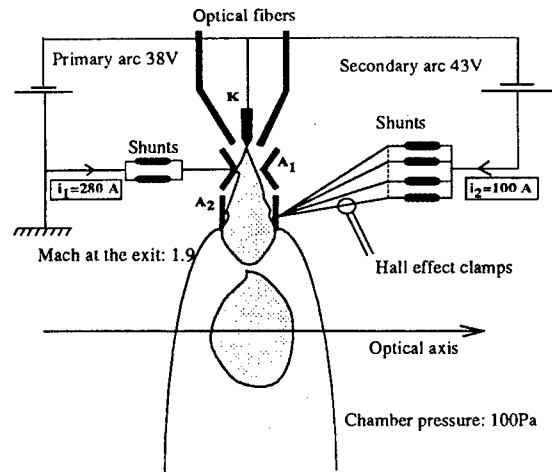


Fig.1: schematic draw of the experiment

multipliers. Cardinal points (N, W, S, and E) mark the location of the current intakes and of the optical fibers.

First experiment:

The secondary anode is a tungsten ring. As a first step in dynamical analysis, Fourier spectra are computed from the three different time series $U_1(t)$, $U_2(t)$ and $I_1(t)$. A low frequency peak is found to be located at 100 Hz which comes from the current generators. Conversely, two principal frequencies are exhibited (fig 2) on tension time series at 10250 Hz and 6560 Hz while no high frequency may be distinguished from time series $I_1(t)$.

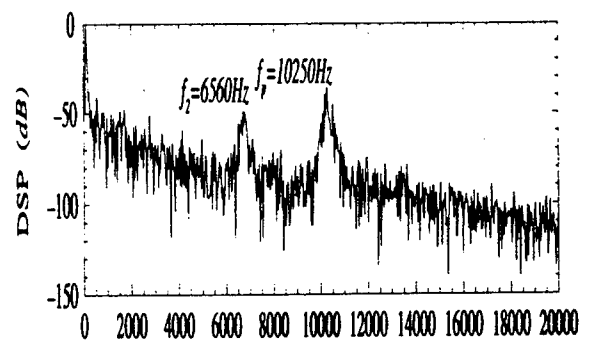


Fig.2: Fourier spectra of secondary tension time serie

As expected time correlations between tensions are strong. Both tensions approximately evolve with the

same phase. No modulations of the correlation coefficients are found at high frequency meaning that there is no stable phase relationship between HF evolution of $U_1(t)$ and $U_2(t)$. A dynamical analysis in a reconstructed phase space has been achieved by using delay coordinates. The phase portraits exhibit very jittery trajectories in all cases and especially for $I_1(t)$. Nevertheless a much regular LF evolution can be extracted from the time series by using a low-pass filter. The three LF portraits then present very similar shapes according to the LF correlations. These similarities confirm that the LF fluctuations are transferred from the electrodes to the plasma jet. Conversely the phase portrait associated with high frequency seems to induce a very high dimensional dynamics i.e corresponding to a more stochastic behaviour since no structure can be exhibited.

Second experiment:

The tungsten secondary ring anode is replaced by a copper anode. The cooling circuit is much more efficient than in the previous case. The Fourier analysis of the tension and current signals exhibits strong peaks located at the multiples of 50 Hz the weight of which depends on the observed variable. For instance see the phase portrait of the secondary voltage shown in figure 3.

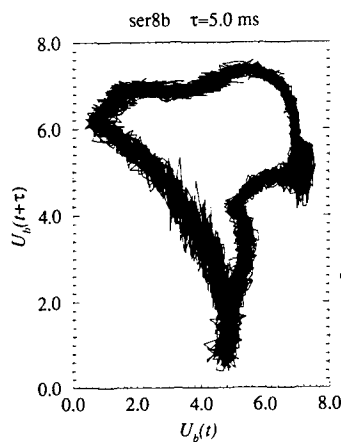


Fig.3: phase portrait of secondary tension time serie

Unlike the previous case no HF peak has been observed. We ascribe this fact to the improvement of the secondary anode cooling circuit.

Typical time series of the optical fibers are displayed in figure 4: they exhibit the rotation of the primary arc by glidding of the arc root on the anode nozzle throat. The behaviour of the arc root in direction and rate seems stochastic.

In conclusion, LF and HF fluctuations have been observed in electrode tensions of a low pressure double transferred nitrogen arc. Some physical interpretations relying on the discussion of arc root displacement can explain these observations. In the present case phase portraits allow to conclude that the number of degrees of freedom is reduced under anode erosion. Forthcoming works could allow to precise future applications of tools arising from nonlinear dynamical systems theory.

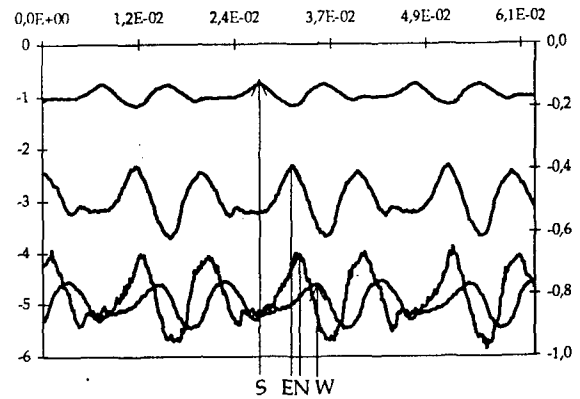


Fig.4: optical fibers signals

- [1] A. Bultel, B.G. Chéron and P. Vervisch; Plasma Sources Sci. Technol. 4 (1995) 597
- [2] B.G. Chéron; 19th ISSW 26-30 July pp3-8

Study of the commutation of an electric arc in a breaking-device

D. Cajal, A. Laurent, M. Mercier, G. Velleaud, F. Gary

Université Blaise Pascal de Clermont-Ferrand. Laboratoire d'Electrotechnique de Montluçon.
Av. A. Briand 03100 MONTLUÇON. FRANCE

S. Servant

Groupe Schneider, Centre de Recherches de Grenoble, 38050 GRENOBLE. FRANCE

1. Introduction

We have developed a "magnetic camera" which allows one to visualize the evolution of an electric break-arc assimilated to a series of segments [1]. This means of analysis is non-intrusive because the magnetic probes that are used to detect the movement of the arc are placed outside the breaking-chamber. Furthermore, it has the advantage, over optical means, of giving a picture of the electronic beam of the arc and not the phenomena linked to it, among which, light.

This device has already enabled us to contribute to the survey of the behaviour of the arc in a particular configuration [2].

The object of the study presented here is to define more accurately how it moves in a breaking-system whose structure is close to that of the low-voltage automatic circuit-breakers used in industry (figure 1).

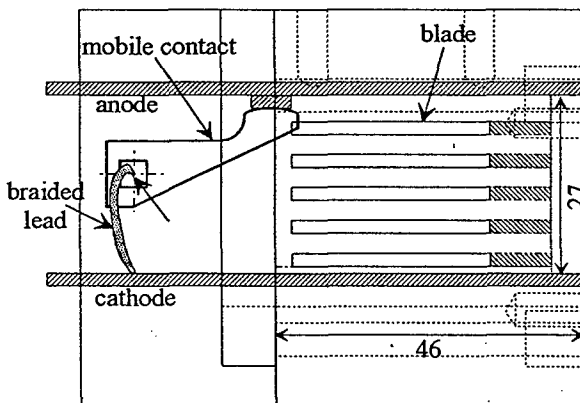


Figure 1. Breaking circuit.

In order to produce the arc, the oscillating discharge of a battery of capacitors (60 mF max.) is triggered off into an inductance before tilting the mobile contact. Once the circuit tuned, a half-wave of current, assumed to have a peak of 7300 A, is obtained.

2. The magnetic camera

Some fifty microcoils (made of 60 turns contained within a 1 mm³ volume) are positioned along the Y-axis so as to survey the air gap between the electrodes, the Y-axis being perpendicular to the plane in which the arc evolves (figure 2). The microcoils placed 11 mm away from this plane form a matrix of 5 lines for every 8 or 10 columns. Along Z the step is 4 mm, while it is 4.5 mm along X.

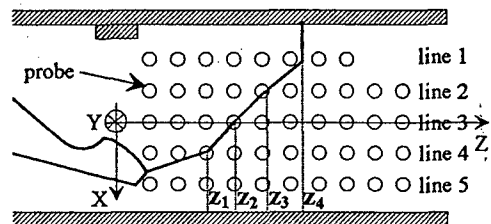


Figure 2. Location of probes.

Associated with amplifying and integrating circuits they enable us to measure, at any point, the component, along the Y-axis, of the magnetic induction $B_y(t)$ generated by the whole electric circuit.

If the magnetic influence of the current leads and electrodes is neglected, $B_y(t)$ changes signs when the arc moves past one of the probes. The signals from the probes are recorded during the break-phase with a sampling period of 8 μ s. A processing programme allows for the determination of those instants when the induction becomes zero.

3. Computation of the average line of current

In order to take into account the other components of the electric circuit, an algorithm has been developed to compute the average line of current. With this aim in mind, the arc will be supposed to evolve at a constant speed between two consecutive probes.

The procedure is carried out in the following way :

For a given time, the position where B_y becomes zero along the Z-axis is computed for each line of probes. Let (x_{s_i}, z_{s_i}) be the coordinates of such a point on line n°i. Consequently the problem consists in determining a polygonal line that, together with the other parts of the electric circuit, might produce a magnetic induction $B_y = 0$ at the points under consideration.

Mathematically, this amounts to solving system (1) where z_1, z_2, \dots are the coordinates of the polygonal line wanted (figure 2).

$$\begin{cases} B_y(x_{s_1}, z_{s_1}, z_1, z_2, \dots) = 0 \\ B_y(x_{s_2}, z_{s_2}, z_1, z_2, \dots) = 0 \\ \dots \end{cases} \quad (1)$$

Since such a system is not linear, one is compelled to use iterative calculation : one begins with the shape assumed by the link between the points where $B_y = 0$, say $z_1 = z_{s_1}, z_2 = z_{s_2}$ etc.... It is then moved until it satisfies each equation of the system (to the nearest 0.4 mT, given the digitization of the signal).

4. Results

Several tests have been carried out for several values of the assumed current, with or without copper or stainless steel blades. The test presented hereunder has been made with the following characteristics : charging voltage of the capacitor 300 V, assumed current 2900 A, stainless steel blades. Fig. 3 shows the evolution of the arc current and voltage. The commutation signal is the voltage between the ends of the cathode. This voltage which, among other things, is function of the length of the electrode through which the arc current flows, increases when the arc commutes onto the cathode.

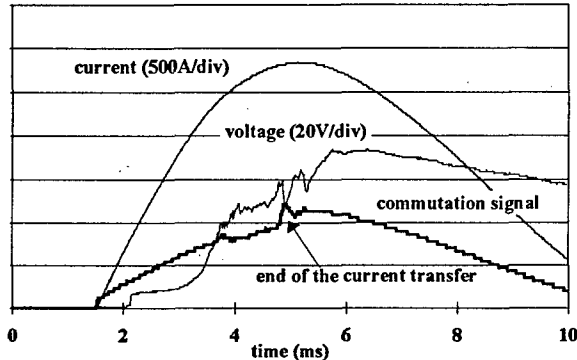


Figure 3. Arc voltage, current and commutation signal.

For each probe of the matrix, the moment when the signal becomes zero is noted. These times are listed in hereunder (time in ms).

3.47	3.36	3.67	3.71	3.73	3.73	3.76	4.00			Line 1
3.67	3.46	3.69	3.71	3.72	3.73	3.74	3.80	4.00	4.02	Line 2
3.67	3.72	3.74	3.73	3.72	3.74	3.76	4.01	4.31	4.62	Line 3
3.73	3.74	3.73	3.74	3.80	3.86	3.80	3.86	5.35	5.55	Line 4
4.19	3.82	3.74	3.77	3.74	3.81	4.19	4.98	5.24	5.50	Line 5

The figures in the first column result from the movement of the mobile contact rather than that of the arc.

Up to $t_1 = 4.19$ ms, the cathodic root is supposed attached to the mobile contact. Beyond t_1 , the resolution of system (1) compels us to consider that the root is attached to the lower electrode, i.e. the cathode. In order to define the evolution of the arc, the shapes are drawn with a constant $100 \mu\text{s}$ step (figure 4).

It is to be noted that the anodic root starts migrating towards the back of the chamber as soon as the contact opens. The curvature of the arc, at that moment, is highly pronounced. Once the current transfer is over, the elevation of the cathodic root equalizes that of the anodic root. The arc, then, straightens out.

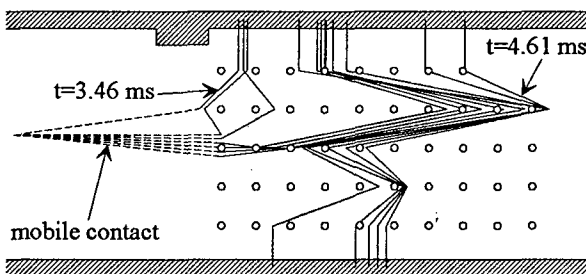


Figure 4. Shapes of the arc with a $100 \mu\text{s}$ step.

5. Commutation of the arc

In the table, one notices an area where the chronological order of the "zeros" is inverted in relation to the direction in which the arc spreads (lines 4 and 5 especially). This inversion is characteristic of a transfer of current from one arc to another, as will be shown.

In order to achieve this, lines of iso-induction, such as $B_y = 0$ in the probe plane during commutation, have been simulated. For this calculation the circuit has been simplified (figure 5). Two branches exchange their current in a linear way. I_1 decreases from 2000 A to 0 during a $640 \mu\text{s}$ Δt whereas I_2 increases. Δt is the period of time separating t_1 from the time corresponding to a rapid increase of the commutation signal.

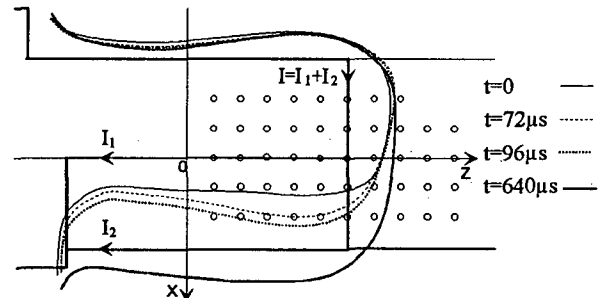


Figure 5. Simulation of the current transfer.

On the same figure, the lines $B_y = 0$ have been drawn for different values of time. Instant 0 is taken as the origin of the commutation phase.

At the beginning, the line $B_y = 0$ is almost horizontal, which explains the simultaneousness of the "zeros" on line 4. The first probes on this line might thus be used to detect commutation when it starts. The curvature of the line $B_y = 0$ with respect to its transfer does account for the chronological inversion of the "zeros" on line 5.

6. Conclusion

The use of the magnetic camera led us to draw the shapes of an electric arc evolving in the breaking-device, provided it is modelled into an average line of current. The analysis of the commutation phase presented here will allow us to determine the moment it starts as well as how long it lasts.

7. References

- [1] A. Laurent, F. Gary, D. Cajal, G. Velleaud and M. Mercier : « A magnetic camera for studying the electric break-arc » Meas. Sci. Technol. 4 (1993) 1043-1049
- [2] M. Mercier, D. Cajal, A. Laurent, G. Velleaud and F. Gary : « Evolution of a low-voltage electric arc » J. Phys. D: Appl. Phys. 29 (1996) 95-98

High-current plasma generator radiation

V.F.Chinnov, E.H.Isakaev, A.D.Iserov, N.O.Spector, S.A.Tereshkin, A.V.Zobnin

Associate Institute for High Temperature, Russian Academy of Science, Izhorskaya 13/19 Moscow RUSSIA

1. Plasma generator

Plasma source is a watercooled plasma generator with the point W - cathode and stabilizing spacer - anodes, which forms the expansive channel with minimal diameter of 6 mm and diverge angle of 12° . The working gas (Ar, N_2) comes in cathode assembly with flow rate of $1,5 \div 2,5$ g/s. The duty arc with current of 40 A maintains the break-down of between electrode spacing, and the base arc has variable current up to 500 A. System includes the computer, which measures necessary parameters, controls and regulates the power supply.

2. Spectroscopy systems

In experiments we used two systems of spectra's detection, which were under the control of a single PC. First system is based on the monochromator consists monochromator MDR-41, block of control, ensuring the scanning with the given speed and the control of the current wavelength, photoelectric multiplier FEU-100, plate ACP L-1250, inserted into the computer, and the software. Working wavelength band is limited by the sensitivity of the photo-cathode of the FEU-100 and is 200-830 nm. To this range correspond the diffractive gratings 3000 (200-500 nm) and 1500 (400-1000 nm) slits per millimetre, with dispersion 1 and 2 nm/mm.

The second system consists of the diffraction spectrograph DFS-452 and of multichannel optic spectra's analyser. System includes two photometer heads with photo-diode PZS rulers Toshiba TDS1250A and the interface plate, inserted to one of the computer ports. Photometer heads are fixed on the plate that is located at the cassette's place. Each photo-diode rule contains 3648 light-sensitive elements $8 \mu\text{m}$ long and $200 \mu\text{m}$ height. Spectral region of the sensitivity is 180-1000 nm. Time of signal's accumulation is given by the period of the interrogation of the rulers and can be changed in the range 80-20000 ms. Since 12-digit analog-to-digital converter is included as a component in each of the photometer heads then only the digital signals are transmitted to the computer. It ensures a relatively high noise immunity of the system.

Chart of the optic measurements is represented in Fig.1. Image of the arc was projected to the inlet slits of the monochromator 1 and of the spectrograph 2 with the help of the quartz condensers 3 with the focal lengths 112 and 240 mm.

At the inlet slit of the monochromator there was mounted the Gartman slit 1 mm height, that was

cutting the near axis part of plasma image. The spectrograph had the high slit. The central part of plasma image was projected to the photo-diode ruler, located along the spectra's scan. The ruler, located in the perpendicular direction, detected the distribution of radiation intensity in the lateral direction of the filament.

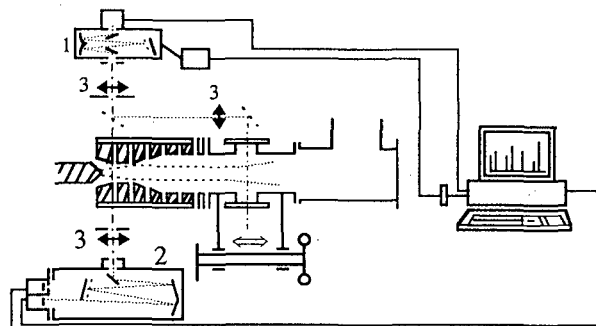


Fig.1

For the standard of the wavelengths there was used the radiation of lamps of the high frequency exciter of the spectra PPBL-3M with the vapour of Hg, Ag, and other metals. Small size tungsten tape lamp TRSH-2880 was used as the standard of the brightness. Its brightness temperature at the pyrometer wavelength was 2850 K.

3. Argon plasma radiation spectra

Typical spectrum of Ar plasma radiation from the near cathode region, obtained by DFS-452 with PZS ruler in the ultraviolet part of spectrum is represented in Fig.2

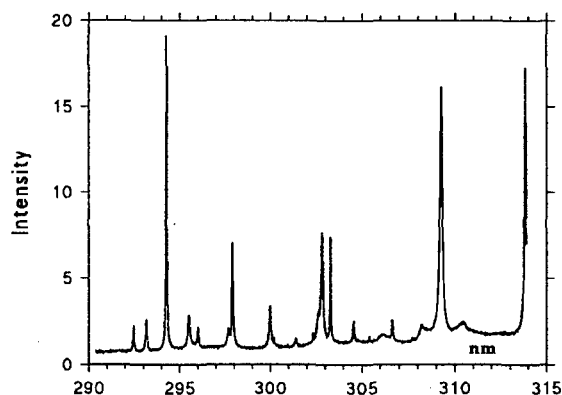


Fig.2

Spectral resolution of both automatic systems was about 0.15 \AA , what gave possibility to

detect the outlines of spectral lines of ArI and ArII, typical half-width of which is about 1Å . In Fig.3. there is represented the dependence of the spectral intensity of radiation in the near cathode region of the discharge at the current of the arc 400 A. It was obtained by the summary of the results of measurement of plasma radiation with the use of the spectrograms detected by both automatic systems of information collection.

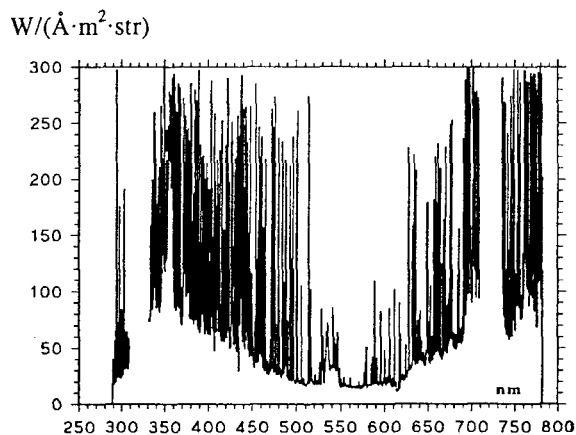


Fig.3

4. Results

Set of data represented in part 3 included the data on the absolute intensity of a great number of the ion ArII lines, on a number of atomic ArI lines, on the width (and outlines) of the isolated ArII lines, and on the absolute intensity of the continuous radiation in the range of wavelength 250-800 nm. It gives possibility to evaluate the electronic concentration n_e and electronic temperature T_e .

For determination of T_e by use of the ratio of the atomic and ion lines there were chosen the isolated spectral lines of the sufficient (on the continuum ground) intensity and of known atomic constants that well correlate between each other at the analysis in coordinates $N_k/g_k = f(E_k)$. The use of different pairs of lines leads to the electronic temperature at the discharge axis in the near electrode region ($z=4$ mm):

$$T_e(r=0, z=4) = 1.2 \pm 0.2 \text{ eV}.$$

Approximately the same value of the electronic temperature at the arc axis can be obtained from the analysis in the coordinates $T_e(I/d)$ of the experimental results [1] of the stabilised arcs in argon.

By the use of measured in the work values of the intensity of the continuum at the frequency $\nu=23000 \text{ cm}^{-1}$ ($\lambda \approx 430 \text{ nm}$), for which in [2] there is represented the dependence $\epsilon_\nu(T)$, and of obtained estimate value $T_e \approx 15000 \text{ K}$, we can obtain the value $n_e = (1.1 \pm 0.2) \cdot 10^{17} \text{ cm}^{-3}$.

Stark component of the half width of a number of lines was obtained by the subtraction of the device width: $\delta_{st} = \delta_{1/2}^{\text{exp}} - \delta_0^{\text{dev}}$

For the ion lines the Stark width is 0.5 Å , what corresponds to

$$n_e(\delta_{st}, T \approx 15000 \text{ K}) \approx 1.4 \cdot 10^{17} \text{ cm}^{-3}.$$

Hence, conducted on the basis of measured data estimates of n_e and T_e are as follows:

$$T_e = 1.2 \pm 0.2 \text{ eV}; n_e = (1.2 \pm 0.3) \cdot 10^{17} \text{ cm}^{-3}.$$

Spectrum of Ar plasma radiation, represented in Fig.3, illustrates the relationship in the radiant energy between the transferred in the continuous spectrum and in spectral lines, mainly in ArII. The estimate integration of the radiant energy in the range of the wavelength 250÷800 nm shows that by the optical thin radiation is transferred from the plasma in the radial direction:

$$\text{div} Q_R = 2\pi \int_{250}^{800} I_\lambda d\lambda \approx 1000 \text{ W/cm}^3.$$

Specific energy put in the near cathode region is: $j \cdot E \approx 800 \text{ A/cm}^2 \cdot 30 \text{ V/cm} \approx 24000 \text{ W/cm}^3$, so the radiation losses (in the given range of frequency) are about 4%.

According to [3] the experimental value of the electric conductivity $\sigma = j/E \approx 27 \text{ mo/cm}$ corresponds to the plasma temperature $T \approx 13000 \text{ K}$. In the near cathode region - the region of the main energy input, and the ionization degree is sufficiently high. In this case the losses caused by the coulombic interactions with ions Q_i are the main component of the elastic losses $Q_{el} = Q_a + Q_i$, $Q_i/Q_a \approx n_e \cdot q_{ei}/(n_a \cdot q_{eAr}) > 1$ [3]. Neglecting the inelastic losses Q_{in} (what increases the role of Q_i) we can obtain the upper estimation of the separation of electronic temperature T_e from the gas one T_a :

$$(T_e - T_a) \approx \frac{jE}{(3m/M_{Ar})(kn_e n_i q_{ei}(T_e) v_e)}.$$

Inserting into this equation the experimental values jE and $n_e = n_i$, we can obtain that

$$(T_e - T_a)_{\text{max}} \approx 7000 \text{ K}.$$

Such significant separation between the electronic and the gas temperatures at the initial region of energy input ($z=4 \text{ mm}$) at the presence of the stabilizing high velocity flow is possible (see for example [1]) and is worthy of the experimental investigation.

References

- [1] Low temperature plasma, v1, Novosibirsk, Nauka, (1990).
- [2] Asinovsky E.I., Kirillin A.V., Nizovsky V.L.: Stabilized electric arcs and their application in thermophysical experiment, Moscow, Nauka, (1992).
- [3] Biberman L.M., Vorobiev V.S., Yakubov I.T.: Kinetics of non equilibrium low temperature plasma. Moscow, Nauka, (1982).

RADIAL TEMPERATURE DISTRIBUTION IN AN AR-CO₂ PLASMA

E.MAOUHOUB, H.COITOUT, M.J. PARIZET

Laboratoire Arc Electrique et Plasmas Thermiques, U.R.A. 828 CNRS
Université Blaise Pascal,
24 avenue des landais, 63177 AUBIERE Cedex France.

INTRODUCTION

Carbon dioxide is one of the most abundant chemical found in nature. The CO₂ molecule is used in several plasma processes [1]. CO₂ is of special interest in thermal treatment of waste. CO₂ and rare gas mixture have been studied because of the great interest of this mixture in order to understand chemical mechanisms of reactions [2], and to use them for the production of carbon monoxide [3]. We present in this paper results on the effects of CO₂ molecule upon an argon thermal plasma. The radial temperature distributions are performed by optical emission spectroscopy on atomic line of argon and carbon after Abel inversion.

EXPERIMENT

The experimental device is shown in figure 1. The wall stabilized arc is produced in a modified Maecker chamber which is made of copper hollow cupels cooled with water. Bakelite cupels isolate electrically the copper cupels one from another; tangential injection to the arc column of the studied gas (Ar-CO₂ mixture) is made. The copper anode and the tungsten cathode are protected with argon. Mass flow controllers regulate the gas flow and adjust the ratio of different gases in the mixture. Discharge current is adjusted with a DC generator from 12 A to 50 A. The light emitted is observed perpendicularly to the arc column. In order to obtain a good spatial resolution we used a 25 cm focal lens. The wavelength selection is carried out by a high resolution monochromator (THR 1500 Jobin Yvon). The light is detected with an optical multichannel analyser (OMA 4000 EG&G) fitted with a 512 × 512 pixel matrix controlled by a microcomputer. The chamber translation is obtained by a micrometric screw. The plasma diameter can be estimated ranging from 6 to 8 mm. All the measurements are performed at atmospheric pressure.

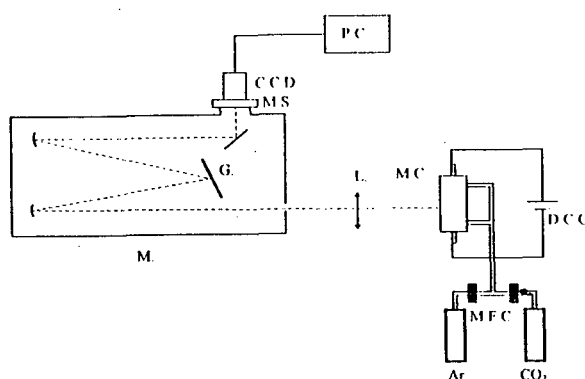


Figure 1 : Experimental set up. M.C. : Maecker chamber, M.F.C. : mass flow controllers, D.C.G. : DC generator, L. : lens, M. : monochromator, G. : grating, M.S. : mechanic shutter, C.C.D. : CCD matrix, P.C. : microcomputer.

RESULTS

The temperature is deduced from the absolute intensities of Ar I line ($\lambda=696.54$ nm) and C I line ($\lambda=538.03$ nm). Measurements are fitted using a spline function before the Abel inversion [4]. The concentration calculations are performed with the hypothesis of the local thermal equilibrium.

Figure 2 presents the electronic temperature T_e versus the radius of the plasma column in a pure argon plasma for different currents. Temperature ranges from 10000 K on the axis of the plasma to 7000 K in the sides. T_e increases with the discharge current; T_e gradient is weak and decreases with the discharge current.

Figure 3 presents the T_e radial distribution for different Ar-CO₂ mixtures. Temperature ranges from 10000 K on the axis of the plasma to 7000 K in the sides. T_e decreases with the CO₂ concentration increasing.

Figure 4 shows that $T_e(r=0)$ is 1000-2000 K greater than $T_e(r=2 \text{ mm})$ independently of the mixture composition. For $r=0$, T_e decreases weakly when the CO_2 percentage increases. For $r=2 \text{ mm}$ T_e decrease is about 1500 K from 0.9% to 12% of CO_2 .

T_e increases with the discharge current (Figure 5). The gradient of temperature decreases when current increases.

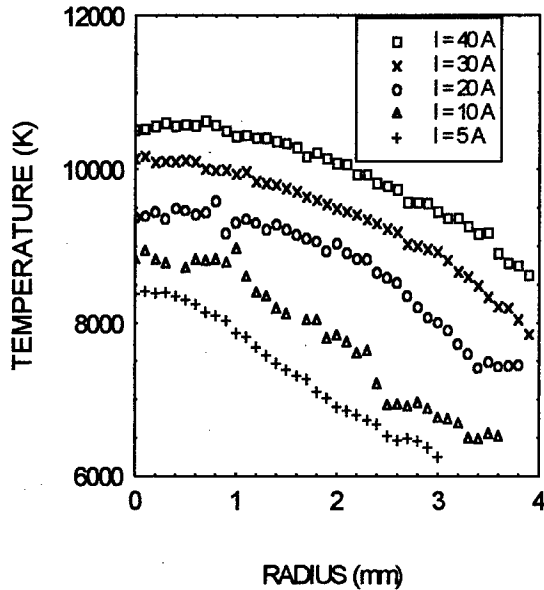


Figure 2 : Electronic temperature versus the radius of the plasma column in a pure Ar plasma for different discharge currents.

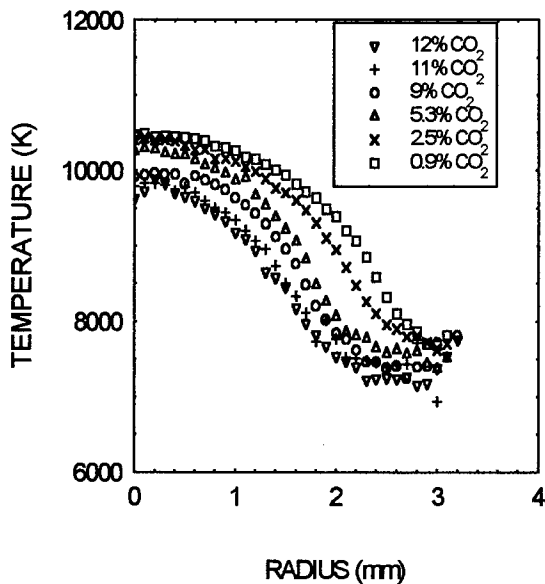


Figure 3 : Electronic temperature versus the radius of the plasma column for different plasma composition, $I = 30 \text{ A}$.

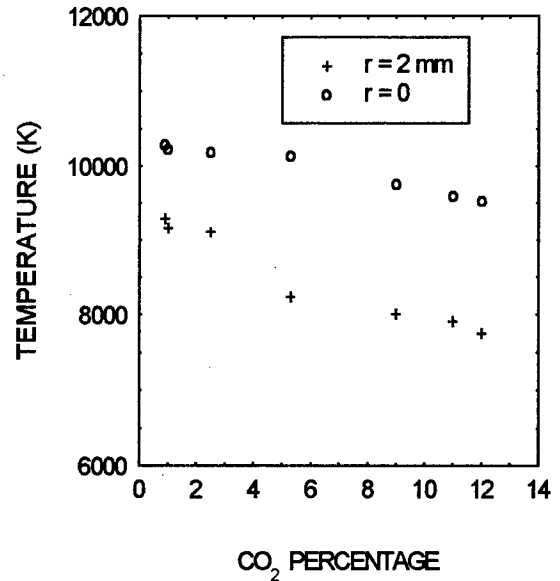


Figure 4 : Electronic temperature versus the Ar- CO_2 mixture composition for $r=0$ and $r=2 \text{ mm}$, $I = 30 \text{ A}$.

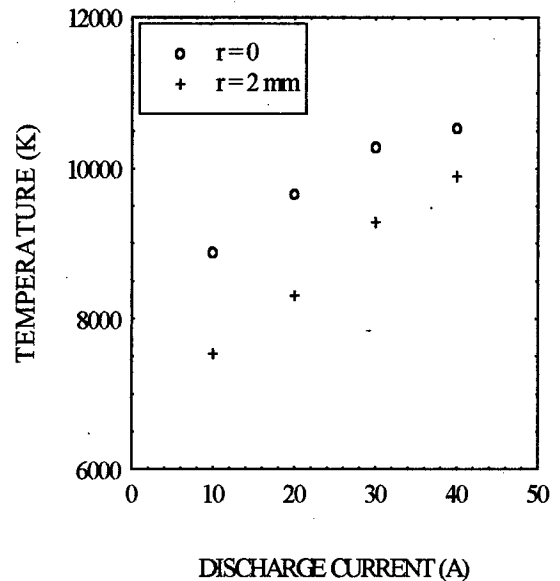


Figure 5 : Electronic temperature versus the discharge current for $r=0$ and $r=2 \text{ mm}$ in a 99.1% Ar - 0.9 CO_2 mixture.

REFERENCES

- [1] A. Huczko, A. Szymanski, Plasma Chem. and Plasma Prosc., Vol.4,n°1, 59 (1984).
- [2] J.S. CHANG, T.G. Beuthe, J. High Temp. Chem. Proc. 1, 333 (1992).
- [3] F.W. Giacobbe and D.W. Schmerling, Plasma Chem. and Plasma Prosc., Vol.3,n°4, 383 (1983).
- [4] P. Andanson, B. Cheminat, and A.M. Halbique, J. Phys.D : Appl. Phys. vol. 11,209 (1978).

Estimation of the Metallic Plasma Pressures in Thermal Arc Cold Cathode Spots

Sylvain Coulombe and Jean-Luc Meunier

Plasma Technology Research Centre (CRTP)

Department of Chemical Engineering

McGill University

3480, University Street

Montréal, Québec, Canada, H3A 2A7

Abstract

Using a model for the cathode sheath of a thermal arc interacting with a cold Cu cathode, it is shown that metallic plasma pressures exceeding 12 atm within the cathode spots are needed to account for the experimentally estimated current densities. For those pressures, the current at the cathode is almost entirely transported by the ions generated by ionization of the vaporized atoms.

1. Introduction

It is known that the current transport within the cathode spots of thermal arc systems can not be entirely assumed by the thermo-field emission electrons but also by the ions. This phenomenon is particularly true for cold cathode spots of thermal arcs which are expected to carry current densities higher than 10^9 A m^{-2} [1],[2] (compared to 10^7 - 10^8 A m^{-2} for thermionic cathodes [3]). Indeed, cold cathodes which are made of low boiling point materials cannot sustain the high temperatures needed for strong thermal emission, so the contribution of the ions to the current transport is expected to become considerable. However, the plasma conditions prevailing within the cold cathode spots and giving rise to such high current densities are not well-known.

As suggested by the works of [4] and [5], these plasma conditions might be similar to those of the vacuum arc: the cathode spots are made up of a high density metallic plasma ($>10^{25} \text{ m}^{-3}$) formed by the strong erosion of the cathode material and expanding into the ambient gas. Such high densities of plasma combined with the relatively low electron temperatures expected (1-2 eV in vacuum arcs on Cu [6]) would lead to metallic plasma pressures within the cathode spots above 10 atm.

In this study, the model for the cathode sheath of a thermal arc plasma interacting with a cold cathode [7] is briefly resumed and used to estimate the minimum metallic plasma pressures needed to account for the estimated current densities flowing through a Cu cathode.

2. Cathode Sheath Model

A net positive space charge sheath of total voltage drop V_c is formed at the plasma-cathode boundary due to the presence, in different amounts, of three different charge carriers: 1) the metal atoms evaporated from the

cathode surface, ionized in the presheath, and moving back towards the cathode carrying a current density j_{ion} , 2) the thermo-field (T-F) emission electrons carrying a current $j_{\text{T-F}}$, and 3) the plasma electrons retro-diffusing towards the cathode carrying a current j_{bde} .

The different densities of species at the cathode sheath edge are calculated using the modified Saha equation [8] and the Dalton's law for a plasma pressure p , a temperature T_e^{se} for the electrons and a temperature T_h^{se} for the heavy species. T_h^{se} is set equal to the cathode spot surface temperature T_s and related to the plasma pressure via a vapor pressure curve ($T_h^{\text{se}} = T_s = T_{\text{vap}}(p)$); the cathode spot surface is assumed to be in equilibrium with its vapor.

The z -charged ion species of density n_i^{se} at the cathode sheath edge are assumed monoenergetic and to enter the sheath at the Bohm velocity (Bohm criterion). Only a fraction $\exp(-eV_c/kT_e^{\text{se}})$ of the Boltzmann distributed plasma electrons of density $n_{\text{bde}}^{\text{se}}$ at the cathode sheath edge reach the cathode surface at their thermal velocity. The expressions for the ion, back-diffusing electron and T-F emission current densities are therefore:

$$j_{\text{ion}} = \sum_i z_i e n_i^{\text{se}} \left[k \left(\frac{T_e + T_h}{m_i} \right) \right]^{1/2} \quad (1)$$

$$j_{\text{bde}} = -\frac{1}{4} e n_{\text{bde}}^{\text{se}} \exp \left(\frac{-eV_c}{kT_e^{\text{se}}} \right) \left[\frac{8kT_e^{\text{se}}}{\pi m_e} \right]^{1/2} \quad (2)$$

$$j_{\text{T-F}} = j_{\text{T-F}}^0 \beta \quad (3)$$

for a total current density:

$$j_{\text{tot}} = j_{\text{ion}} + j_{\text{T-F}} + j_{\text{bde}} \quad (4)$$

The equations of [9] were used to calculate the T-F emission current density $j_{\text{T-F}}^0$. The values for β , the T-F emission enhancement factor induced by the presence of ions close to the cathode, were taken from [10]. The surface electric field strength E_s is obtained from the resolution of the Poisson's equation over the entire cathode sheath assuming conservation of energy and current density for the three types of charge carrier. The model forms a self-consistent set of equations solvable for given values of p , T_e^{se} and V_c .

3. Results and Discussion

Values of $V_c \sim 7$ V and $j_{tot} \sim 1.35 \times 10^9$ A m⁻² obtained recently by [2] for a 100 A atmospheric pressure argon arc on a cold Cu cathode are used to estimate the plasma parameters within the cathode spots. Fig. 1 shows a contour plot of the total current density j_{tot} calculated using the model with $V_c = 7$ V. The results show that metallic plasma pressures exceeding ~ 12 atm for electron temperatures at cathode sheath edge ranging from 0.9 to 1.2 eV are needed to account for the estimated current density. The corresponding cathode spot temperatures exceed 3400K. Under those conditions, the ratio of the flux of vaporized atoms to the flux of thermo-field electrons is ~ 10 ; this shows how potentially large can be the flux of returning ions.

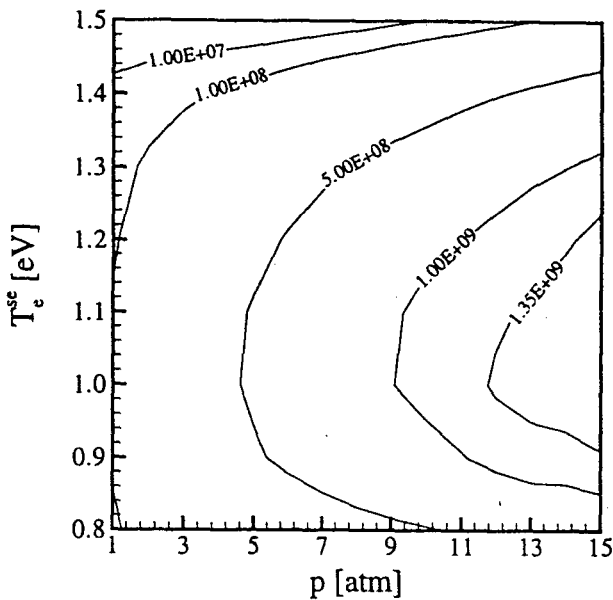


Fig. 1. Contour plot of the total current density j_{tot} in the $p - T_e^{se}$ plane for $V_c = 7$ V.

Fig. 1 also shows that, for a given metallic plasma pressure, the total current density peaks for $T_e^{se} \sim 1$ eV. This value of the electron temperature is a function of the cathode material; it corresponds to the electron temperature at which the electron density for a specific material, and therefore the ion density, reaches a maximum value. For this electron temperature, the ion current j_{ion} , the surface electric field strength E_s , and the enhancement factor β all take their maximum values giving rise to the maximum current; for $p = 12$ atm and $T_e^{se} = 1$ eV, the surface electric field strength E_s is $\sim 6.1 \times 10^8$ Vm⁻¹ while β is ~ 1.8 . Under these conditions, the thickness of the cathode sheath is $\sim 2.2 \times 10^{-8}$ m which is ~ 14 times the Debye length of the metallic plasma.

Fig. 2 shows the evolution with p of the different contributions to the total current density j_{tot} for $T_e^{se} = 1$ eV and $V_c = 7$ V. An overview of Fig. 2 shows clearly that the ion current is dominant over both electron currents. For $p = 12$ atm, the ratio j_{ion}/j_{tot} is ~ 0.88 and decreases to ~ 0.78 for $p = 15$ atm while the ratio j_{T-F}/j_{tot} is ~ 0.23 for $p = 12$ atm

and increases to ~ 0.29 for $p = 15$ atm. For the same pressure range, the ratio j_{bde}/j_{tot} decreases from ~ 0.11 to ~ 0.09 . The contribution from the retro-diffusing plasma electrons is relatively small due to the important potential drop to overcome. One observes here an interesting feature of thermal arc cold cathode spots: due to the high metallic plasma pressures, the current distribution among the main charge carriers (ions and T-F emission electrons) is inverted when compared to thermionic cathodes (see [3] for example).

Finally, this study suggests that the attachment of thermal arcs on cold cathodes is a high pressure phenomenon similar to vacuum arc behavior.

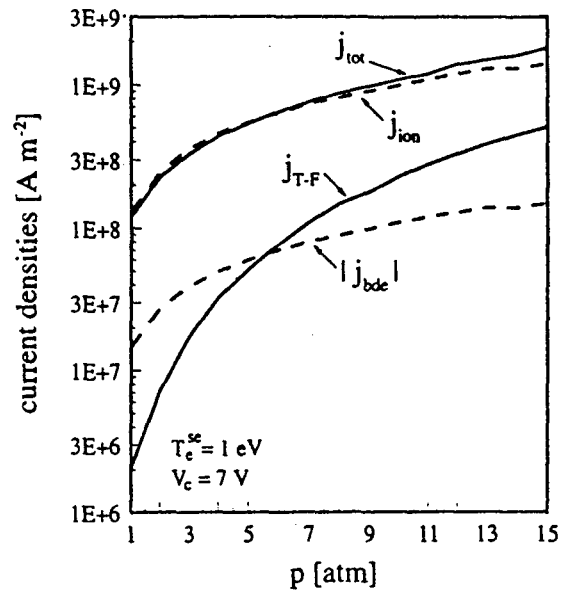


Fig. 2. Contributions to the total current density j_{tot} as a function of p for $T_e^{se} = 1$ eV and $V_c = 7$ V.

Acknowledgment

The authors would like to thank the FCAR of Québec and the NSERC of Canada for financial support.

References

- [1] T. H. Lee: J. Appl. Phys., **30** (1959) 166
- [2] A. Marotta, L. I. Sharakovsky: J. Phys. D: Appl. Phys., **29** (1996) 2395
- [3] X. Zhou, J. Heberlein: Plasma Sources Sci. Technol., **3** (1994) 564
- [4] C. W. Kimblin: J. Appl. Phys., **45** (1974) 5235
- [5] P. R. Emtage: J. Appl. Phys., **46** (1975) 3809
- [6] B. Jüttner: IEEE Trans. Plasma Sci., **15** (1987) 474
- [7] S. Coulombe, J.-L. Meunier: IEEE Trans. Plasma Sci. (Special Issue on High Pressure Arcs...) **25** (Oct. 1997) to be published.
- [8] E. Richley, D.T. Tuma: J. Appl. Phys., **53** (1982) 8537
- [9] E.L. Murphy, R.H. Good: Phys. Rev., **102** (1956) 1464
- [10] R. Gayet, C. Harel, T. Josso, H. Jouin: J. Phys. D: Appl. Phys., **29** (1996) 3063

2-D Hydrodynamic Model of the Electrode Vaporization in an Electrical Circuit Breaker in SF₆ and Comparison with Experiments

S.S. Ciobanu^{§*}, P.Chévrier[#], C. Fleurier[§]

[§]GREMI, Université d'Orléans, CNRS UMR 6606, BP 6759, 45067 Orléans Cedex 2, France

[#]Centre de Recherches Schneider Electric, 38050 Grenoble Cedex, France

*On leave of absence from the Institute of Atomic Physics, INFLPR L-22, P.O.Box MG-7, 76900 Bucharest-Magurele, Romania

The electrode vaporization during the electrode separation in an electrical circuit breaker influences strongly its interruption capabilities. In order to reduce the long and expansive testing in developing these devices, it is necessary to realize a correct simulation of their behavior. This simulation must include also the effect of metal vapor presence on the transport coefficients of the SF₆ quenching gas used industrially in such devices.

Previously, a medium voltage circuit breaker operated in a 3 atm SF₆ gas was experimentally studied with temporal resolution [1,2]. The electrodes were made out of copper or a sintered mixture of copper and tungsten. The copper temperature and density were obtained by spectroscopic measurements, as the total copper quantity present in the arc.

These values can be compared with the results of a 2D hydrodynamic simulation including the electrode vaporization and the copper effect on transport coefficients.

The model describes the time evolution of a cylindrical plasma in local thermodynamic equilibrium between two cylindrical electrodes. The physical quantities are functions of time and spatial (radial and axial) coordinates. The mass, momentum and energy conservation equations in the laminar approximation for the plasma and the Fourier equation for the heat diffusion in the anode are solved by a finite element method [3]. We did not consider the magnetic force in the momentum conservation equation, neither the presence of an externally generated magnetic field which produces the arc rotation in a real circuit breaker. To reproduce the experimental conditions, an externally generated sinusoidal current with a 22 ms period and 4.8 kA peak value was considered between the electrodes. The electrical circuit opened 1 ms after the beginning of the current. The electric field is represented only by its axial component. The plasma is heated by Joule dissipation. The model includes also the anode vaporization by an energy balance equation (at the anode) and the copper diffusion in the S-F plasma. We used theoretically calculated mass density, internal energy, specific heat, viscosity, electrical resistivity and thermal diffusion coefficient [4,5]. The radiation transfer was considered by means of two emission and absorption coefficients depending on local temperature and composition. The plasma was considered as a gray body for the whole spectrum.

2-D maps of temperature field in the plasma present a cooler region near to the anode and a warmer central region, as obtained experimentally by emission spectroscopy. This effect is explained by a higher emission coefficient for an S-F plasma containing copper particles. The copper localization close to the electrodes experimentally seen by time and spectral resolved photography [1] is well reproduced by this 2-D simulation, as showed in figures 1 and 2.

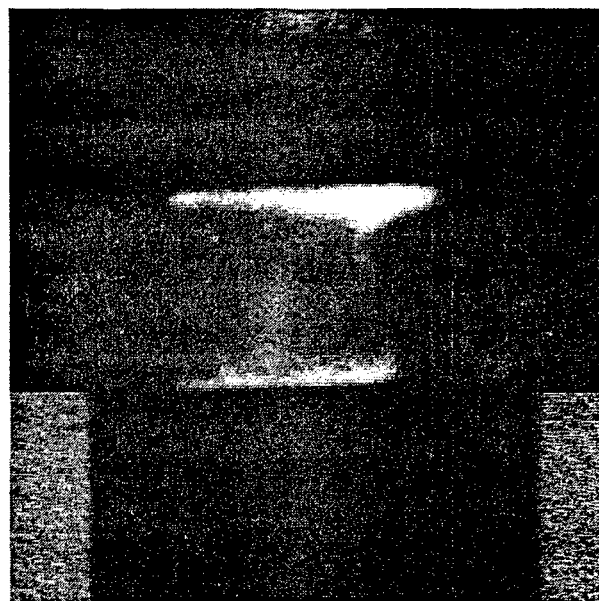


Figure 1 Copper localization in the arc as obtained by time and spectral resolved photograph (at 6 ms after the electrode separation)

The copper mass between the electrodes as obtained from simulation and from experiments is presented in figures 3 and 4 respectively. The maximum simulated current density is about $8 \cdot 10^3$ A/cm² and the simulated flow velocity is about 100 m/s.

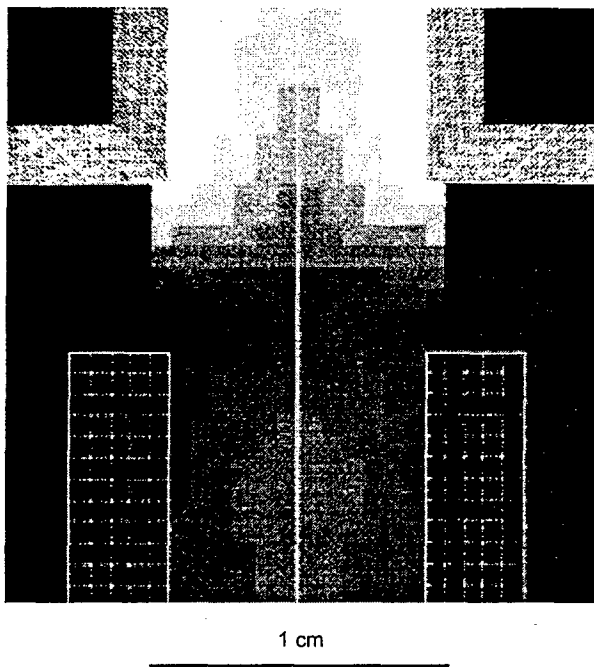


Figure 2 Copper localization in the arc as obtained by 2D hydrodynamic simulation (at 6 ms after the electrode separation)

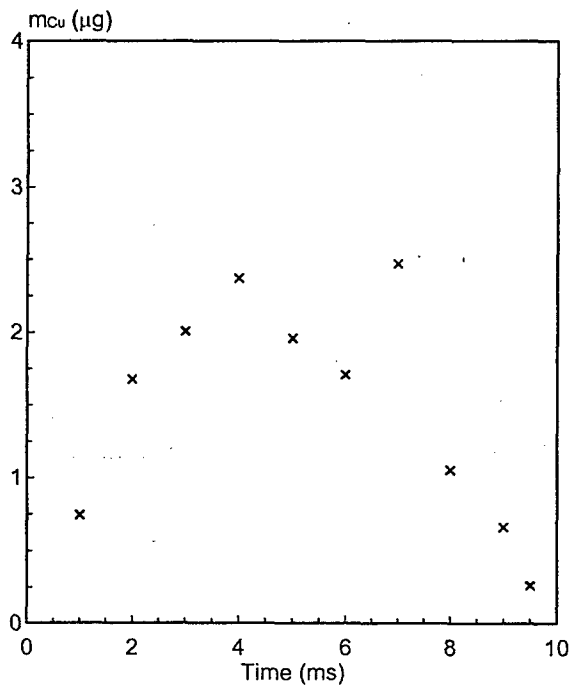


Figure 3 Time evolution of the total copper mass between the electrodes as obtained by spectroscopic measurements

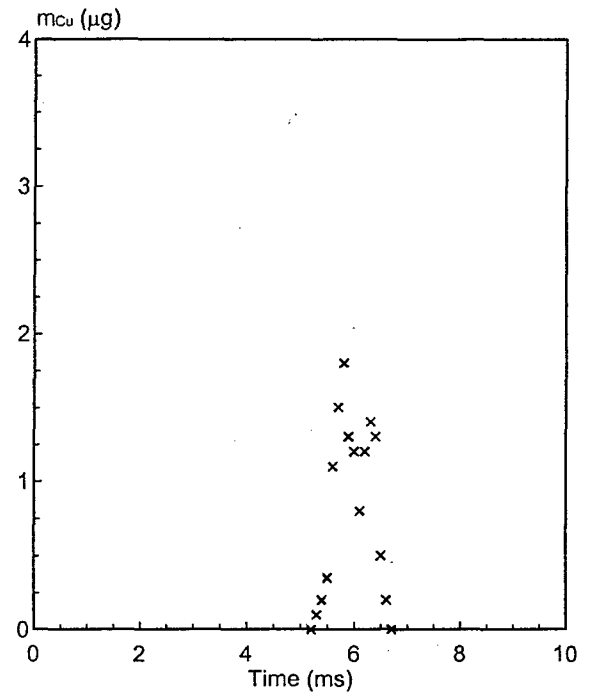


Figure 4 Time evolution of the total copper mass between the electrodes as obtained by hydrodynamic simulation

Acknowledgments: One of the authors (S.S. Ciobanu) wishes to thank GREMI and Schneider Electric for their financial support during his working stage in France.

- [1] S.S. Ciobanu, C. Fleurier, D. Hong, C. Fiévet, J. High. Temp. Chem. Processes, to appear
- [2] S.S. Ciobanu, C. Fleurier, C. Fiévet, this conference
- [3] P. Chévrier, Ph.D. Thesis, INP Grenoble, France, 1990
- [4] A. Gleizes, M. Razafinimanana, S. Vacquié, Internal Report 40277-85-1, CPAT, Université Paul Sabatier, Toulouse, France, 1985
- [5] A. Gleizes, J.J. Gonzalez, B. Liani, G. Raynal, J. Phys. D: Appl. Phys. 26(1993), 1921-1927

Experimental Study of the Electrode Vaporization in an Electrical Circuit Breaker in SF₆

S.S. Ciobanu^{§*}, C. Fleurier[§], C. Fiévet[#]

[§]GREMI, Université d'Orléans, CNRS UMR 6606, BP 6759, 45067 Orléans Cedex 2, France

[#]Centre de Recherches Schneider Electric, 38050 Grenoble Cedex, France

*On leave of absence from the Institute of Atomic Physics, INFLPR L-22, P.O.Box MG-7, 76900 Bucharest-Magurele, Romania

The interruption capabilities of an electrical circuit breaker are much influenced by the electron density. The electron density depends notably on the presence of electrode material in the arc. The high current densities at the instant of contact separation produce a strong local electrode heating so that an important initial electrode vaporization appears. After separation, the electrodes are heated and vaporized principally by the important radiation emitted by the arc and by the electron and ion bombardment.

In our experiments, we used a medium voltage circuit breaker operated in a 3 atm SF₆ gas [1]. A capacitor battery was discharged into the circuit breaker producing a half-period of a quasi-sinusoidal 50 Hz current with 4800 A peak current. The electrodes were made out of copper or a sintered mixture of copper and tungsten.

The arc rotation produced by a permanent magnet as explained in [1] helped to enhance arc cooling by thermal transfer with the surrounding gas. This rotation permits also an electrode cooling between two arc passages on the same zone.

Fluctuations of the instant of electrode separation compared to the current, the electrode surface modifications and the turbulent flows induced by the arc expansion and rotation caused a random effect of electrode vaporization from a shot to another.

The plasma parameters were obtained by simultaneous measurements using time resolved and spatially integrated emission spectroscopy, time and spectral resolved photography and electrical measurements [1]. Time and spectral resolved photographs exhibited an inhomogeneous copper presence in the arc [1]. A strong emissive copper zone (zone 1) appeared near the electrodes all along the arc evolution. A low emissive copper zone (zone 2) appeared between the first zone and the surrounding cold gas and sometimes between the two electrodes.

The electron densities in these copper dominated regions were obtained from Stark line broadening and shift. The 515.32 nm line is the *single* CuI line for which correct values of the line-width w_0 and line shift $\Delta\lambda_0$ seem to exist [2].

Due to the high electron density, the profiles of several CuI lines overlap each other, as shown in figure 1. Using a multi-Lorentz fit procedure, it was found that the CuI 515.32 nm line profile could not be fitted by *one sole* Lorentz curve. In fact the experimental profile could only be theoretically approached by using a

model with at least two different emitting regions of the arc contributing to the profile, as suggested by the photographs. Neglecting the self-absorption effect, the observed line profile is given by:

$$\Phi_\lambda = \frac{hc}{4\pi\lambda} A_{ul} \cdot (N_{u1}P_{\lambda_{01}}(\lambda) + N_{u2}P_{\lambda_{02}}(\lambda)) \quad (1)$$

where N_{ui} and n_{ei} are the number of Cu atoms in the emitting level in the zone i and the electron density respectively. The Lorentz profile is given by:

$$P_{\lambda_{0i}}(\lambda) = \frac{w_i}{\pi} \frac{1}{w_i^2 + (\lambda - \lambda_0 - \Delta\lambda_i)^2} \quad (2)$$

where w_i and $\Delta\lambda_i$ are correlated by:

$$w_i = \frac{n_{ei}}{n_0} w_0 ; \Delta\lambda_i = \frac{n_{ei}}{n_0} \Delta\lambda_0 \quad (3)$$

The line fit, the number of copper atoms in the emitting level and the electron density for each of the two regions are presented in figure 1 for one shot.

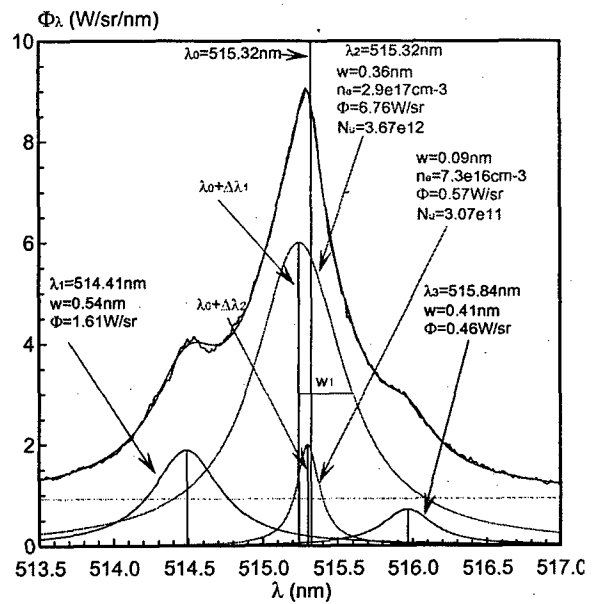


Figure 1 Experimental copper emission spectrum and its theoretical approach with the two densities model

The absolute energy calibration was performed with a tungsten ribbon lamp. We noted that the most important contribution to the line intensity was given by the emission of the high density zone.

Sometimes, in the first 2 ms of the arc life, the 515.32 nm CuI line presented also an absorption structure, as shown in figure 2. This effect was explained by the absorption of the radiation emitted in a hot central copper zone by the cold surrounding copper zone (zone 3). Neglecting the self-absorption effect in the hot region, the line profile was approached by:

$$\Phi_\lambda = \frac{hc}{4\pi\lambda} A_{ul} N_{ul} P_{\lambda_{01}}(\lambda) \cdot e^{-\tau_{03}(\lambda)} \quad (4)$$

where N_{ul} is the number of Cu atoms in the emitting level in the zone 1 and τ_3 is the optical depth of the absorption zone 3:

$$\tau_{03}(\lambda) = \pi r_0 \lambda^2 f_{lu} P_{\lambda_{03}}(\lambda) d_3 \left(1 - \frac{g_l n_{u3}}{g_u n_{l3}} \right) n_{l3} \quad (5)$$

with f_{lu} the oscillator strength, r_0 the classical electron radius, g_u and g_l the statistical weights and n_u and n_l the densities of copper atoms in the upper and lower levels.

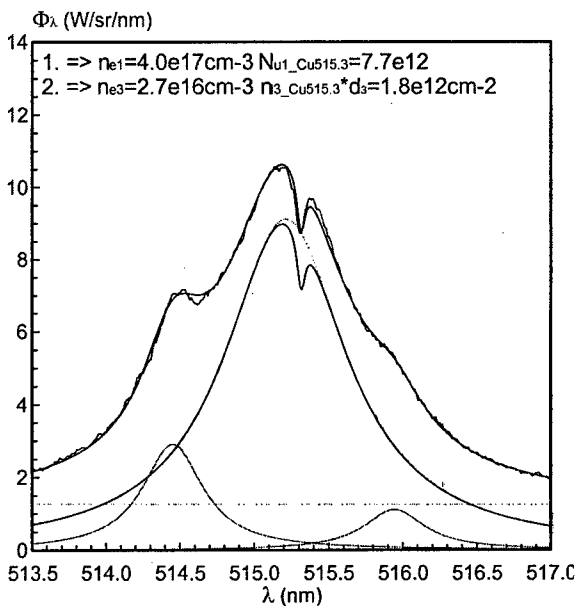


Figure 2 Absorption of the copper light emitted in a hot region by the copper atoms in a cold zone

An iterative fit of the experimental profile including also the continuum emission yielded N_{ul} , n_{e1} , n_{e3} and

$$n_{l3} d_3 \left(1 - \frac{g_l n_{u3}}{g_u n_{l3}} \right) \cong n_{l3} d_3.$$

The electron densities and plasma dimensions imply a plasma in local thermodynamic equilibrium (LTE). Thus, temperature in the copper zone 1 was obtained by an iterative procedure based on Boltzmann distribution using line intensities determined from the low resolution spectral data. Time evolution of the copper plasma temperature for the high density copper region (zone 1) was presented in [1].

Because the separation of the contributions of the different emissive copper zones was impossible with the low resolution spectrometer the temperature of the second emission zone could not be determined. It could only be estimated as follows: if we consider a $(\text{SF}_6)_{1-c}$

Cu_c plasma in LTE at 3 atm and the electron density for the emission zone 2 and the absorption zone 3 as obtained from the previous spectra, the copper concentration can be obtained as function of temperature. The temperature dependence of the copper concentration for these electron densities is presented in figure 3.

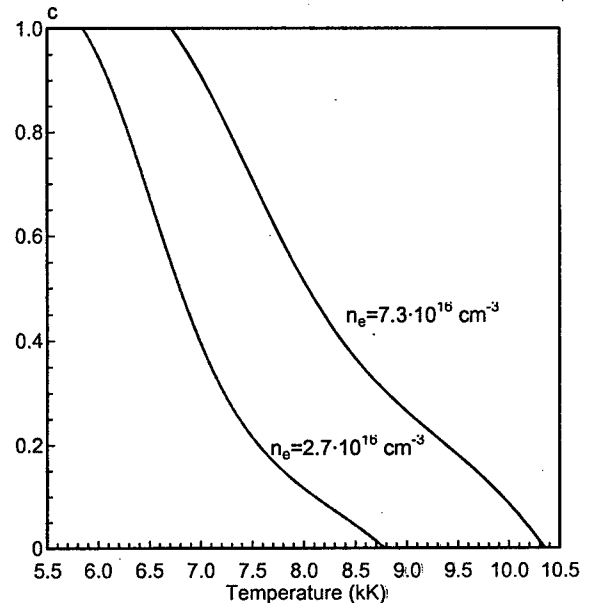


Figure 3 Copper concentration c in a $(\text{SF}_6)_{1-c} \text{Cu}_c$ in LTE at 3 atm for the electron densities in the zones 2 and 3

The figure 3 gives the range of possible temperatures for the emission zone 2 and the absorption zone 3. For the presented spectra, these temperatures are between 6700 and 10300 K for the emission zone 2 and between 5800 and 8800 K for the absorption zone 3.

Acknowledgments: One of the authors (S.S. Ciobanu) wishes to thank GREMI and Schneider Electric for their financial support during his working stage in France.

- [1] S.S. Ciobanu, C. Fleurier, D. Hong, C. Fiévet, J. High. Temp. Chem. Processes, to appear
- [2] C. Fleurier, in Spectral Line Shapes, Vol. III, Ed. R.J. Exton, A. Deepak Publ., Hampton, Va., P. 67, 1987

Electrical conductivity of an SF₆ thermal plasma at low temperature (T < 5 000 K)

B. Chervy, A. Gleizes and P. Krenek*

CPAT, ESA 5002, Université Paul Sabatier, 118 route de Narbonne, F31062 Toulouse cedex 4, France

* Institute of Electrical Engineering, Academy of Sciences, Dolejskova 5, 14200 Praha 8, Czech Republic

1) Introduction

Usually, the electrical conductivity (EC) in thermal plasmas is considered to be due to the electrons. Nevertheless, in electro-negative gases such as SF₆, the electrons may be attached to atoms to form negative ions; in this condition, occurring in SF₆ plasmas at atmospheric pressure when the temperature T < 4500 K, the charged particles are mainly positive and negative ions, so that the EC depends on these ions. This phenomenon may be important in special SF₆ circuit-breaker arcs where the surrounding SF₆ gas is heated at temperature of the order of 2000 K [1]. In this case the residual EC may strongly influence the arc decay in the presence of a fast recovery voltage.

The aim of this communication is to present the calculation method and the results concerning the SF₆ electrical conductivity in the temperature range between 1 000 and 5 000 K, and for a pressure range between 0.1 and 1.6 MPa. As a first step we shall present the plasma equilibrium composition; then we will describe the theoretical bases of the EC calculation and we will give the main results and the corresponding discussion.

2) Equilibrium composition

This calculation corresponds to an extension of a previous work [2]. Now we take 32 species into account: 7 neutral polyatomic molecules (SF₆, SF₅, SF₄, SF₃, SF₂, SSF₂, FSSF), 3 neutral diatomic molecules (F₂, S₂, SF), 2 neutral atoms (S, F), 4 atomic ions (F⁺, S⁺, F⁻, S⁻), 6 diatomic ions (F₂⁺, S₂⁺, SF⁺, F₂⁻, S₂⁻, SF⁻), 9 polyatomic ions (SF₅⁺, SF₄⁺, SF₃⁺, SF₂⁺, SF₆⁻, SF₅⁻, SF₄⁻, SF₃⁻, SF₂⁻) and the electrons. The methods of calculation of the internal partition functions were described in [2]. In figure 1, we have plotted the evolutions of the relative charged species densities in an SF₆ plasma at atmospheric pressure. It is important to note that when T < 2 500 K, the dominant positive ion is not S₂⁺ (as it was expected in [1] and computed in [3]) but SF₃⁺. This fact will have a great influence on the behaviour of the EC.

3) Bases of the calculation

Following Devoto [4] the electrical conductivity σ is given by:

$$\sigma = -\frac{e^2 n}{kT\rho} \sum_{i=1}^q Z_i \sum_{j=1}^q n_j m_j Z_j D_{ij} \quad (1)$$

where e is the electron charge, k the Boltzmann constant, n the total particle number density, ρ the mass density. Z_j , m_j and n_j are respectively the charge, the mass and the number density of particle j , and D_{ij} is the ordinary diffusion coefficient between particles i and j . These diffusion coefficients D_{ij} have been computed with the third approximation of the Chapman-Enskog method, using the general expressions given in [4]. They depend on the cross sections of the elastic collisions between all the particles, through the so-called effective collision integrals defined by [2]:

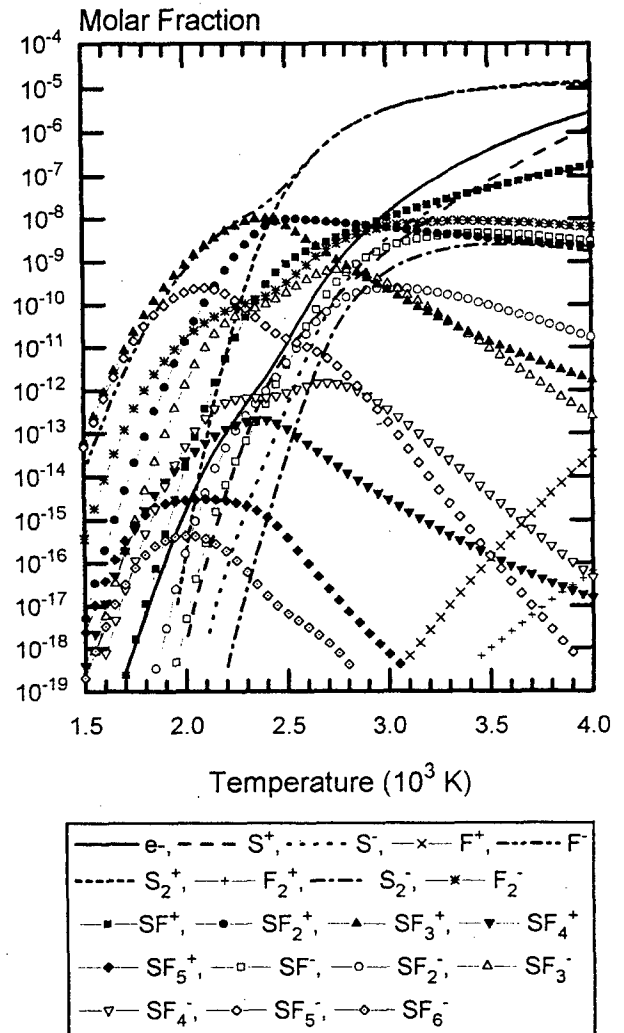


Figure 1: Relative charged particle concentration in an equilibrium SF₆ plasma at atmospheric pressure

$$\bar{\Omega}^{(l,s)} = \frac{4(l+1)}{\pi(s+1)! [2l+1 - (-1)^s]} \int_0^\pi \exp(-g^2) g^{2s+3} Q^{(l)} dg \quad (2)$$

where l and s define the order of the collision integral, g being the relative velocity and $Q^{(l)}$ the total transport cross section. The calculation of Ω depends on the kind of interaction:

* electron-neutral interaction: in general we have taken values of elastic collision cross sections from literature [2]. For the reactions between electrons and polyatomic molecules we have used either the polarization method or the hard sphere approximation.

* Collisions between charged particles: as in [2], we have adopted a screened Coulomb potential allowing to treat attractive and repulsive potentials.

* Ion-neutral interaction: purely elastic collisions and charge transfer have been considered. The methods have been described in [2]. In addition to this previous work, we must take into account F-F⁻ charge transfer. Nevertheless the cross section for this mechanism is not known. We have then calculated the corresponding collision integral by the polarization method, but the influence of this phenomenon on σ will be discussed in the last part.

4) Results

As several collision integrals are not well-known, we have considered that the best set of data (standard case for our calculation) corresponds to the following conditions:

* electron-molecule interaction: hard-sphere method;
* F-F⁻ charge transfer: values computed with the polarizability and multiplied by a factor of 10.

In order to check the dependence of the EC on these collision integrals, the evolutions of σ computed for 3 sets of data, versus the temperature T , are plotted in figure 2. The 3 sets are respectively: the standard case; a case with the electron-molecule interaction computed with polarizability; a case with the (F-F⁻) interaction without the factor of 10. We can observe that this last mechanism has a very weak influence on the calculation of σ . The role of the electron-molecule interaction is higher; by comparing the two tested methods with experimental cross sections of the literature involving other molecules (N₂, H₂, O₂, CF₄) we have found that the best approximation for electron-molecule collision is the hard sphere model.

Our results show that the values of σ for $T < 3\,000$ K depend strongly on the ionic species taken into account in the calculation of the equilibrium composition. If we consider a limited number of ions (S⁺, S₂⁺, SF⁺, F⁻ and SF⁻) the difference between the two conditions of calculation, shown in figure 3, is very important when $T < 2\,500$ K. In this same figure we have plotted experimental values indirectly deduced from post-arc current measurements [1]. These last values are in very

good agreement with our results computed by our best set of data.

References

- [1] J. Maftoul, M. Barrault, G. Bernard, P. Chevrier, S. Rowe: J. Phys. D: Appl. Phys. **28** (1995) 1133
- [2] B. Chervy, A. Gleizes, M. Razafinimanana: J. Phys. D: Appl. Phys. **27** (1994) 1133
- [3] K.P. Brand, J. Kopainsky: Appl. Phys. **18** (1978) 425
- [4] R.S. Devoto: Phys. Fluids **9** (1966) 1230

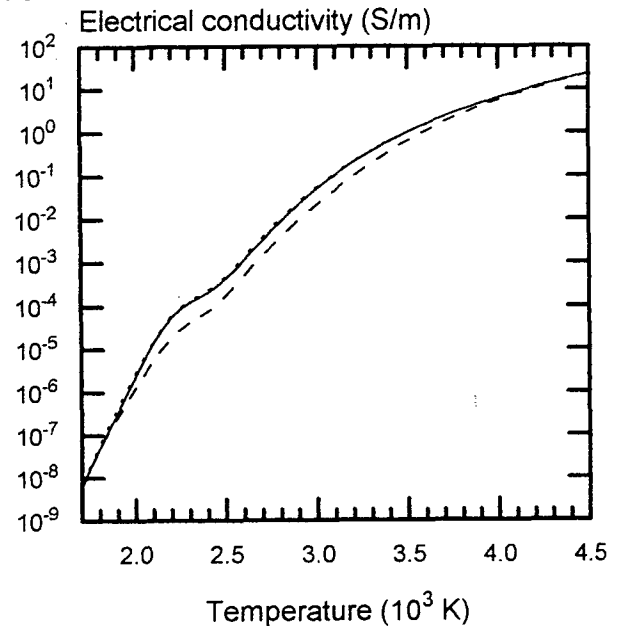


Figure 2: Computed variations of the electrical conductivity: — this calculation; - - polarizability for e-neutral; F-F- without charge transfer

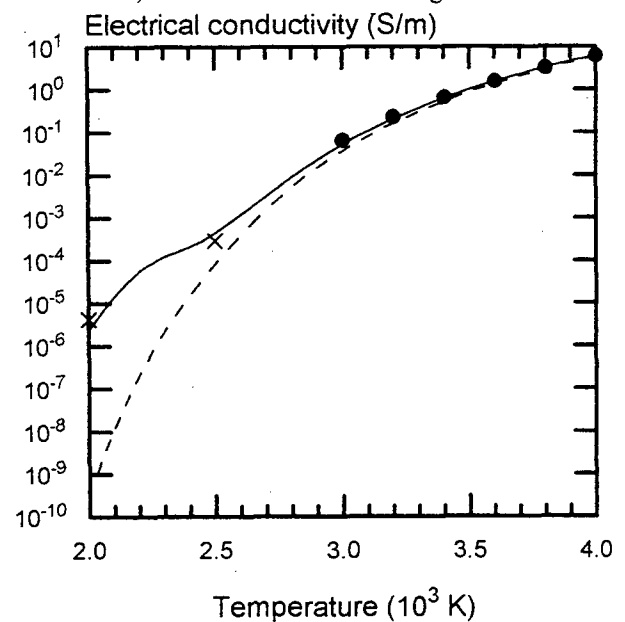


Figure 3: Variations of σ : — this calculation; - - calculated with a limited number of ionic species; ● computed by [2]; X measured by [1]

CALCULATION OF MEAN ABSORPTION COEFFICIENTS FOR THERMAL PLASMAS. APPLICATIONS TO AIR, METHANE AND ARGON-IRON

A. Gleizes, A. Erraki, Y. Naghizadeh-Kashani, H. Riad

Centre de Physique des Plasmas et de leurs Applications de Toulouse (CPAT)
ESA n° 5002 - Université Paul Sabatier, 118 Route de Narbonne - 31062 Toulouse Cedex 4 - France

1. Introduction

The calculation of radiative transfer is a time-consuming step in the numerical modelling of thermal plasmas. In the hottest regions of thermal plasmas the radiative energy losses may generally be estimated using a net emission coefficient previously computed assuming an isothermal plasma. But this coefficient is enable to calculate the real absorption of radiation in the edges of the plasma and/or in the cold gas surrounding the plasma. The best way to calculate this absorption seems to use the method of partial characteristics, proposed by Sevastyanenko [1], but the previous calculation of these characteristics, corresponding to source and sink terms of radiation, is long and complicated (see e.g. [2]). A more classical method to compute the radiative transfer is based on the assumption of grey body with one or several wavelength bands. Within each band a mean absorption coefficient is defined; it depends only on the temperature and pressure and not on the wavelength (or frequency).

The problem correlated with this method is the line radiative transfer which is not well treated and may induce large errors on the computed radiative flux. We propose here a simple method to compute the mean absorption coefficient that takes into account the strong line self-absorption in the plasma. As a consequence this new mean absorption coefficient depends on the size of the plasma. We present here results concerning thermal plasmas in various gases or mixtures of gas and vapour: air, methane and Ar-Fe.

2. Bases of the calculation

In the spectrum of radiation emitted by a thermal plasma, the real absorption coefficient may vary by several orders of magnitude. Thus it is important to define wavelength bands, where the absorption coefficient changes slowly. On the other hand the use of the method in a numerical modelling needs a small number of bands in order to limit the computation time. The criteria allowing to define the limits of the bands are mainly given by the spectral evolution of the continuum absorption coefficient showing sudden jumps due to the electronic structure

of the species. These jumps correspond to photon energy equals to ionisation or dissociation energies. The chosen band limits for the studied gases or mixtures are given in tables 1 to 3.

For a given band the mean absorption coefficient $\langle K' \rangle$ (K' takes induced emission into account) corresponds to continuum and line contributions. For the continuum we have first calculated the spectral variation of the absorption coefficient at a given temperature K'_c by considering all the mechanisms leading to the continuum emission: radiative recombination; bremsstrahlung; attachment. Details of this calculation were given previously[3]. Then the mean continuum contribution for a particular band is given by:

$$\langle K'_c(T) \rangle = \frac{\int_{\nu_1}^{\nu_2} K'_c B_\nu d\nu}{\int_{\nu_1}^{\nu_2} B_\nu d\nu} \quad (1)$$

where B_ν is the Planck function, ν_1 and ν_2 are the boundaries of the band.

band number	1	2	3	4	5	6
wave-length (nm)	30	41.8	85.2	91	106.4	1199.1
	-	-	-	-	-	-
	41.8	85.2	91	106.4	1199.1	4500

Table 1. Band limits for an air plasma.

band number	1	2	3	4	5
wavelength (nm)	30	44.8	78.4	156	1199.1
	-	-	-	-	-
	44.8	78.4	156	1199.1	4500

Table 2. Band limits for an Ar-Fe plasma.

band number	1	2	3	4	5	6	7
wave-length (nm)	30	92	110	150	190	330	3000
	-	-	-	-	-	-	-
	92	110	150	190	330	3000	30000

Table 3. Band limits for a methane plasma.

The contribution $\langle K_r' \rangle$ of a non-absorbed line to the mean absorption coefficient of a given band is given by the Ladenburg law:

$$\langle K_r' \rangle = \frac{\int_{\Delta\nu} B_0(\nu) K_r(\nu) d\nu}{\int_{\Delta\nu} B_0(\nu) d\nu} = \frac{B_0(\nu_0)}{W(\Delta\nu)} \frac{\pi e_0^2}{m_0 c} f_{lu} n_u \quad (2)$$

where $\Delta\nu$ is the frequency interval of the corresponding band and ν_0 the central frequency of the line emitted from an upper level (n_u number density of this level and f_{lu} the line oscillator strength).

For a self-absorbed line, we consider that only a part of the line contributes to the mean absorption coefficient. Thus we multiply the value of $\langle K_r' \rangle$ given in (2) by an escape factor Λ_r which value lies between 0 and 1. This escape factor depends on the plasma geometry. For calculating it we assume an isothermal plasma with a thickness R ; the total mean absorption coefficient for a given band $\langle K' \rangle$ is then depending on this parameter R .

3. Results

We present in figures 1-3 the evolution of the mean absorption coefficient $\langle K' \rangle$ versus temperature, for various bands of the considered plasmas. From figure 1 we may observe the strong effect of line self-absorption in air plasma at high temperature ($T > 8000\text{K}$) assuming that all the molecules are dissociated.

The effect of presence of a metal vapour is illustrated in figure 2, especially in the band 4 containing a lot of resonance lines of Fe and Fe^+ . Finally for methane the mean absorption coefficient takes into account the molecular absorption at low temperature ($T < 5000\text{K}$) which is due to dissociation and ionisation [4].

4. Conclusion

We have calculated values of mean absorption coefficients in various thermal plasmas that allow to compute the radiative transfer in a rather simple way but considering a local self-absorption of resonance lines. In a near future, we will use these data for radiation transfer calculations and we will compare the final results with those obtained by other methods.

References

[1] Soloukhin R.I. "Radiative heat transfer in high-temperature gases" Edition R.Goulard, Hemisphere Pub.Corp., (1987)

- [2] Raynal G., Gleizes A. *Plasma Sources Sci. Technol.*, 4, 152 (1994)
 [3] Gleizes A., Rahmani B., Gonzalez J.J., Liani B. *J. Phys. D*, 24, 1300 (1991)
 [4] H.Riad. Thèse de l'université Paul Sabatier de Toulouse n° 2465 (1996)

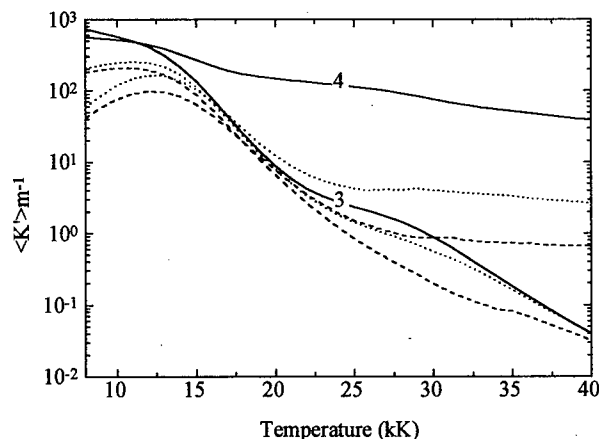


Figure 1. Evolution of $\langle K' \rangle$ in air plasma for various plasmas thicknesses ($R=0$ —, $R=1$ mm ... , $R=10$ mm ---) and 2 bands.

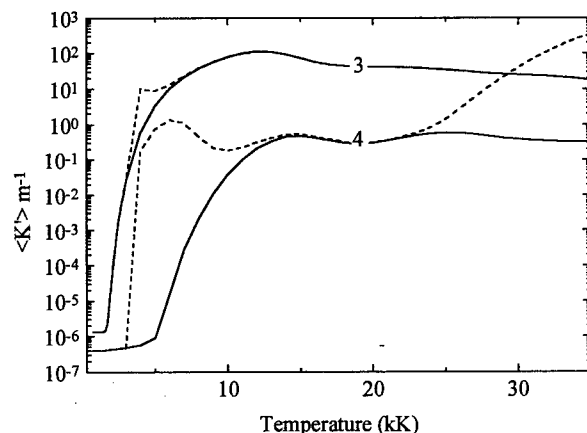


Figure 2. Evolution of $\langle K' \rangle$ in Ar-Fe plasma for pure argon plasma (—) and with 1% iron (---), $R=5$ mm.

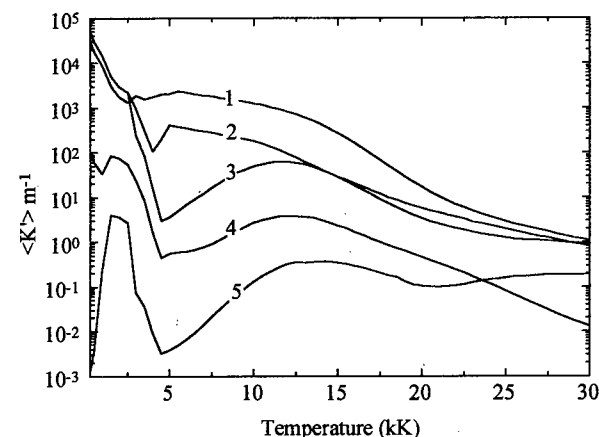


Figure 3. Evolution of $\langle K' \rangle$ in methane plasma for various bands, $R=5$ mm.

Ionisation Efficiency in a Pinched Cascaded Arc Channel

K.T.A.L.Burm, W.J. Goedheer*, J.A.M. van der Mullen, and D.C. Schram

Eindhoven University of Technology, P.O. Box 513, 5600 MB Eindhoven

*F.O.M. Institute for Plasma Physics 'Rijnhuizen', P.O. Box 1207, 3430 BE Nieuwegein

1 Introduction

In the present study, we will focus on the improvement of the ion density at the arc outlet. Efficiency increases are necessary to obtain effective remote deposition, in which the plasma source and target area are decomposed. Remote deposition is easier to control than non-remote deposition and therefore preferable. The increase in the ionisation outflow will be obtained by creating a nozzle shaped cylindrical arc channel as sketched in figure 1.

Simulations were used to obtain the results.

The arc plasma expands supersonically into a low pressure vessel. To simulate the existence of the expansion, a $Ma = 0.9$ boundary condition is implemented at the arc outlet.

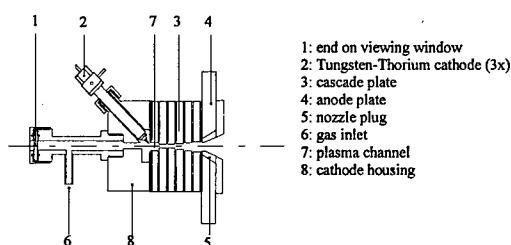


Figure 1a: The cascaded arc: a thermal plasma at atmospheric pressure is created in a D.C. arc

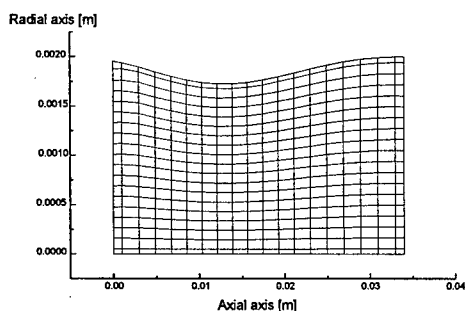


Figure 1b: Generated arc channel grid

2. Cascaded Arc Plasma Source Characteristics

Table 1 gives the operating characteristics used in the simulations.

Table 1: Operating parameters of the simulations

Gas used	Argon
Arc current (I_{arc})	25,40,50,60 and 75 A.
Total gas flow rate	10,20,30,65,100 and 150 sccs
Outlet diameter ($2 \cdot R$)	4 mm
Nozzle diameter ($2 \cdot r$)	1.5, 2, 2.5, 3, 3.5, 3.7, 4 mm
Arc channel length	34 mm or 60 mm

3 Ionisation efficiency

Gasdynamic laws were used to understand the pinch processes in the cascaded arc channel.

- Introducing a nozzle entails that the plasma flow is blocked. Slowing down the plasma at the arc inlet and increasing the electric field at the nozzle leads to a more efficient arc.

- Using Bernoulli's law together with mass conservation, we find that the ionisation rate decays exponentially with the flow.

- The ionisation coefficient S_{cr} , for which the electron energy distribution is Maxwellian, distinguishing a bulk temperature T_b and a different tail temperature T_t , can be represented[1] by:

$$S_{cr} \sim T_t^2 \sim E^2$$

Considering the resistance between consecutive arc channel plates in agreement with Dahiya e.a.[2], we get:

$$S_{cr} \sim E^2 \sim I_{arc}^2$$

4. Simulations

Stationary two-dimensional Boltzmann Transport Equations for density, momentum and energy are solved using the magnetohydrodynamic approximation[3] (MHD). The 5-point Strongly Implicit Procedure (SSIP)[4] is used to solve the discretised equations. The system of transport equations is solved numerically, using the SIMPLE algorithm[5] for the pressure and flow fields. Due to the model's ability to use orthogonal curvilinear coordinates[6], we were able to adjust the geometrical configuration.

5. Conclusions

- Pinching the arc channel is an easy but rather not unlimited way of increasing the ionisation degree at the arc outlet.
- The typical flow and power dependence of the ionisation degree was found and explained.
- The ionisation coefficient S_{cr} increases with the square of the electric field. The flow dependence remains the same at all currents.
- Simulations indicate that ionisation takes place dominantly very near the arc inlet.
- Especially for small nozzle cross-sections, temperatures (coming closer to LTE) and electric field intensity increase inside the nozzle. However, ionisation remains to take place dominantly near arc inlet.
- The decrease (or 'saturation') in arc outlet ionisation degrees for strongly pinched arcs at low flows is expected to be caused by diffusion to the wall.

6. References

- [1] K.T.A.L.Burm, report VDF/HG 95-09 Eindhoven University of Technology; F.A.S. Ligthart and R.A.J. Keijser, J. Appl. Phys. **51** (10) oct. 1980.
- [2] R.P. Dahiya, M.J. de Graaf, R.J. Severens, H. Swelsen, M.C.M. van de Sanden, and D.C. Schram, Phys. Plasmas **1** (6), June 1994.
- [3] D.A. Benoy, thesis Eindhoven University of Technology (1993).
- [4] G.E. Schneider and M. Zedan, Numerical Heat Transfer **4**, 1-19 (1981); H.L. Stone, J. Numer. Anal. Vol. **5**, No 3, 530-558 (1968).
- [5] S.V. Patankar, editor 'Numerical Heat Transfer and Fluid Flow' McGraw-Hill, New York (1980).
- [6] Mobly, C.D. and R.J. Stewart, Journal of Comp. Phys. **34**, 124-135 (1980); S.B. Pope, Journal of Comp. Phys. **26**, 197 (1978); J.F. Thompson, F.C. Thames, C.W. Mastin, Journal of Comp. Phys. **24**, 274-302 (1977); H.J. Haussling and R.M. Coleman, Journal Comp. Phys. **43**, 373-381 (1981).

Diagnostics of a thermal argon - bromine plasma created in a wall-stabilized cascade arc for determination of atomic structure constants

A. Baćłowski, A. Golly, I. Książek, T. Wujec
Opole University, Institute of Physics, 45052 Opole, Oleska 48, Poland

1. Introduction

To determine atomic structure constants like oscillator strengths (or transition probabilities) of spectral lines spectra emitted from plasma sources containing the studied element are commonly recorded. On hand of measured line intensities and some plasma parameters the desired atomic structure constants can be derived. The introduction of source elements in plasma sources is often difficult. Relatively easy is the introduction of gases or mixtures of vapours of chemical compounds, containing the studied element and a working gas (together with argon), in thermal plasma sources like the wall-stabilized cascade arc after Shumaker [1] (realised in many versions).

2. Experimental set-up

A mixture of argon and bromine vapours was introduced in the central section of a wall-stabilized arc, the parts near the electrodes were supplied with pure argon (Fig.1). In different experiments currents from 30 to 60 amps were used. The total plasma length was about 7cm (from C to A), the length of the bromine plasma 4 cm (from c to g). The amount of bromine vapours (between 10% to 20 %) was regulated by adjusting the temperature of a thermostat. The plasma column was imaged onto the entrance slit of a grating spectrometer equipped with an optical multichannel analyzer (OMA 4). Profiles of ArI, BrI and BrII spectral lines were recorded and global intensities and halfwidths were calculated.

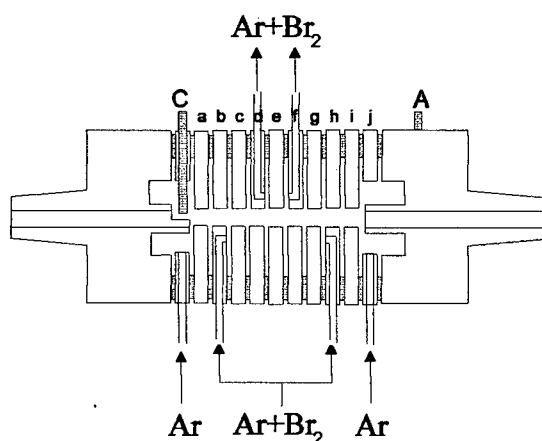


Fig. 1 Wall- stabilized dc arc applied to creation of a argon - bromine plasma

3. Plasma diagnostics using the LTE model

3.1 Set of equations linking the plasma parameters for an argon - bromine mixture

The application of the LTE model permits to establish a set of equations (1 to 7), which provides plasma parameters if global intensities of Ar and Br lines (Eqs 5 and 6) and halfwidths of some Stark broadened lines (Eq. 7) are available from experiment.

$$p = (n_e + n_{Ar} + n_{Ar}^+ + n_{Br} + n_{Br}^+) \cdot kT \quad (1)$$

$$n_e = n_{Ar}^+ + n_{Br}^+ \quad (2)$$

$$n_{Ar}^+ n_e = n_{Ar} S_{Ar}(T) \quad (3)$$

$$n_{Br}^+ n_e = n_{Br} S_{Br}(T) \quad (4)$$

$$I_{Ar} = n_{Ar} f_{Ar}(T) \quad (5)$$

$$I_{Br} = n_{Br} f_{Br}(T) \quad (6)$$

$$\Delta\lambda_{1/2} = a \cdot n_e T^b \quad (7)$$

where

$$S(T) = \frac{2U^+}{U} \left(\frac{2\pi m k T}{h^2} \right)^{3/2} e^{-\frac{\chi}{kT}} \quad (8)$$

$$f(T) = \frac{hc}{4\pi\lambda_{ki}} \cdot \frac{g_k A_{ki}}{U} n \cdot l \cdot e^{-\frac{E_k}{kT}} \quad (9)$$

A serious problem appears when the length of the argon plasma („l” in eq. 9) must be estimated. Since the influence of the presence of bromine in the argon plasma cannot be neglected, the total length of the plasma does not correspond to the argon plasma length. The observed intensity of the ArI line (4300 Å) has to be corrected because the bromine concentration in the central part of the plasma column „reduces” the length of the argon plasma to an „effective” value.

3.2 Special methods of temperature determination

The mostly used method for determination of transition probabilities is based on ratios of line intensities. The knowledge of plasma component densities is than not necessary, but the plasma temperature must be known. Two ways to obtain the plasma temperature will be presented in this work:

a) If values of transition probabilities for a number of lines are available – Boltzmann plot (see Eq. 9) may be drawn and the temperature can be easily derived from the slope of this plot (Fig. 2).

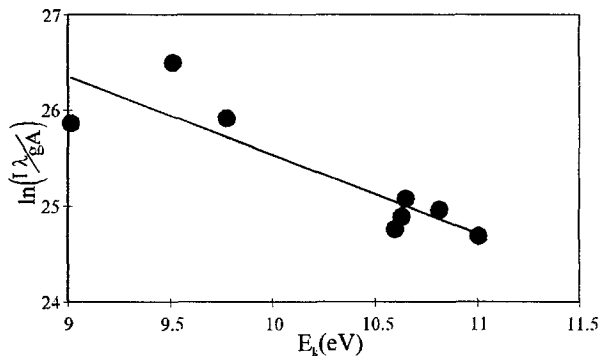


Fig. 2 Boltzmann plot obtained from some BrI- lines of known transition probabilities. The temperature derived from the slope is about 9900 K ($\pm 10\%$).

b) Another possibility appears if optically thick lines are observed in the studied plasma. It is known, that the intensity in line centres of some strongly self-absorbed lines may attain the value of the Planck function for the given plasma temperature. This effect was presumed by Boldt [2] to obtain absolute standard intensities in the VUV, where lines of this type often appear (in this case the plasma temperature must be known). In our earlier work [3] we used the inverse of this way – we measured the absolute intensity in the line center of an optically thick ArI line and from the corresponding value of the Planck function we obtained the temperature (for this work see Fig. 3).

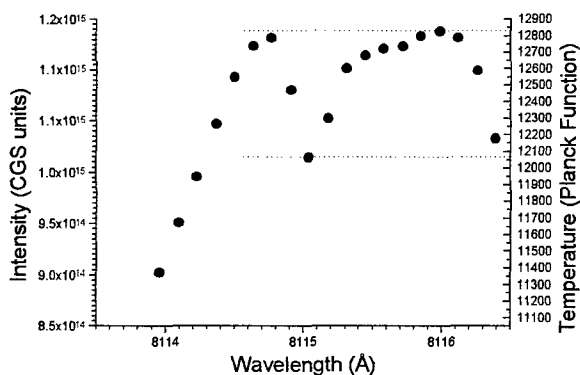


Fig. 3. Temperature measurement from intensities of line centres of the selfabsorbed ArI 8115 Å line. The right hand scale permits the estimation of the temperature from the maximum (and the minimum) of intensity observed in the figure. The minimum corresponds to the coldest region in the plasma.

4. Discussion of results

The matrix of the CCD – detector (256 × 1024 pixels) was divided into 25 tracks and covers a surface about 5 mm × 20 mm. The optical system imaged the plasma column (observed end-on through the electrode) 1:1 onto the detector plate and spectra originating from different regions of the plasma column were recorded at the same time. Radial distributions of plasma parameters were determined. For the given operating conditions in different regions of the plasma column temperatures between 9500 K and 13000 K were observed and electron densities between 10^{16} cm^{-3} and 10^{17} cm^{-3} were found. Applying an iteration method the „effective” length of the argon plasma was estimated (about 0.8 of the total plasma length). The electron densities were calculated from Stark broadening of the ArI 4300 Å line. The halfwidth of this profile depends on the physical conditions in the plasma column, which is not homogeneous, and reasonable corrections can be made only if the plasma is observed side-on and Abel inversions are performed. Thus the determined electron density values are „averaged” values only. In further experiments additionally small quantities of hydrogen will be introduced in the central part of the plasma column and the halfwidth of the H_β line will provide more accurate values of the electron density.

The temperatures obtained for the same region of the plasma column applying the above mentioned methods and values resulting from the solution of the set of equations 1 to 7 do not agree very well. Discrepancies of about 10% could be found.

5. References

- [1] J. B. Shumaker: Rev. Sci. Instrum., **32** (1961) 65
- [2] G. Boldt: Space Science Rev. **11**, (1970) 728
- [3] A. Goly, T. Wujec: 12th Int. Conf. On Spectr. Line Shapes, Toronto (1994) PB-16

Acknowledgements: This publication is based on works sponsored by the Polish-American M. Curie Joint Fund II under project MEN/NIST-94-166.

The authors wish to express their gratitude to E. Pawelec from the Jagiellonian University for substantial help in the evaluation of spectra.

MODELING AND SPECTROSCOPY STUDIES ON A CUTTING PLASMA TORCH

J.A.González Aguilar, C.Pardo, A.Rodríguez-Yunta and M.A.G.Calderón

Dpto. De Física Aplicada. Universidad de Cantabria.
Av. Los Castros s/n. 39005 Santander. SPAIN

Introduction

Plasma cutting is a widely extended industrial application of thermal plasmas. However, our knowledge of the detailed physical effects contributing to the plasma torch performance is still quite incomplete. The heat transfer to the anode, the changes in plasma properties due to the metallic vapors and to the growing hole in the cut piece, are complex but interesting phenomena to understand for future optimizations of torch performance.

1. Experimental study.

In this work we made an experimental study on the transferred arc of a cutting torch with Zirconium cathode, using air as shielding gas, and currents in the range 50 to 150 A. The light emitted by the arc was analyzed by a spectrometer Jobin-Yvon HR460 with a CCD camera and a photomultiplier.

In normal operation of the cutting torch, there are frequent double arcing and instabilities that it makes difficult to obtain the plasma parameters. An example of double arcing could be seen in the following figure, where the metallic elements and Nitrogen atomic lines show a clear deformation in the left side. This deformation is stronger for the emission of the Cu line because the nozzle of the torch is made of copper.

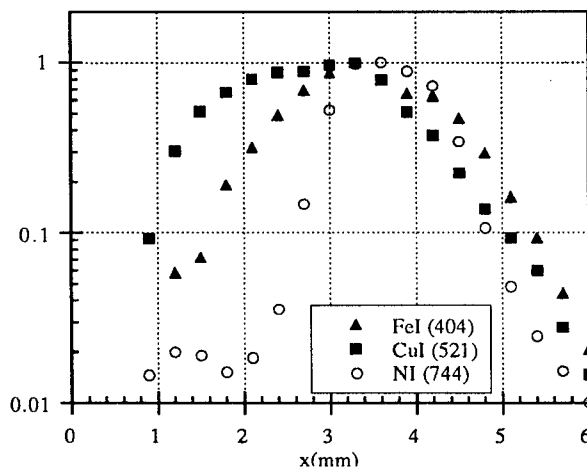


Figure 1. Radial profile, at half cathode-anode length, of emitted intensity for atomic lines of neutral N, Fe, and Cu, normalized to unity for each species, for an air arc with a current intensity of 100 A.

By using the experimental data that was taken without noticeable instabilities or movements of the plasma

column, we determined temperature, excited level populations and species concentration distributions from emission spectroscopy by assuming the validity of Boltzman law. Electron density was also obtained from Stark broadening of the H_{α} atomic line.

Figure 2 shows the obtained relative concentration of neutrals and ions, at 4 mm from the anode for a total anode to cathode length of 10 mm and a current of 100 A. As it can be seen the presence of metallic elements is not important at this distance from the anode.

The obtained radial temperature distribution, for the data of figure 2, had a maximum at the arc axis of 13 600 K. At the radial position of 0.7 mm, where the concentration of neutral and ionized Nitrogen become of equivalent magnitude, the temperature was of 10 200 K. This result is in disagreement with the standard temperature dependence of the composition of an air plasma, calculated from minimization of Gibbs free energy [2]. We must remember that the concentration of ionized atoms was obtained from the population of their excited levels, and it can be heavily overestimated due to deviations of Boltzman law.

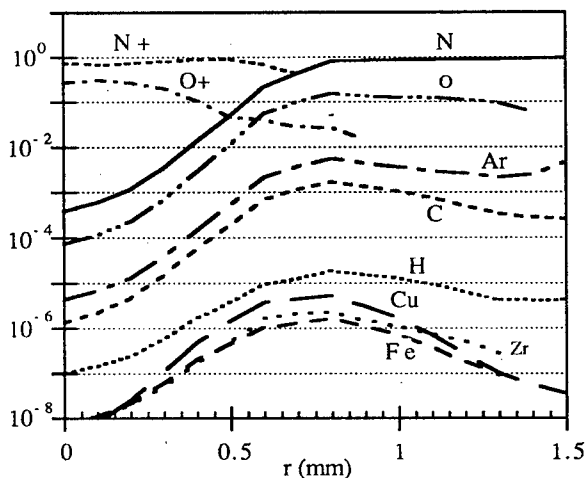


Figure 2. Radial distribution of relative concentration for several neutral and ionized atoms, at 4 mm from the anode, in an air arc transferred over mild steel with a total length of 10 mm and a current intensity of 100 A.

The temporal evolution of plasma parameters was also obtained. As the concentration of metallic vapors increases, the results show a lowering of plasma temperature and electrical conductance. This effect reaches different amounts and it has different temporal behavior for different metal pieces.

2. Modeling

Numerical modeling of the plasma torch to compare with the experimental data was also made. The model is based on cylindrical symmetry and the following equations for mass conservation:

$$\frac{1}{r} \frac{\partial}{\partial r} (r \rho v_r) + \frac{\partial}{\partial z} (\rho v_z) = 0$$

radial momentum conservation:

$$\rho \left(v_r \frac{\partial v_r}{\partial r} - \frac{v_\theta^2}{r} + v_z \frac{\partial v_r}{\partial z} \right) = -\frac{\partial P}{\partial r} - J_z B_\theta + \frac{1}{r} \frac{\partial}{\partial r} \left(2\eta r \frac{\partial v_r}{\partial r} \right) + \frac{1}{r} \frac{\partial}{\partial r} \left(2\eta r \frac{\partial v_r}{\partial r} \right) + \frac{\partial}{\partial z} \left[\eta \left(\frac{\partial v_z}{\partial r} + \frac{\partial v_r}{\partial z} \right) \right] - 2\eta \frac{v_r}{r^2}$$

azimuthal momentum conservation:

$$\rho \left(v_r \frac{\partial v_\theta}{\partial r} + \frac{v_r v_\theta}{r} + v_z \frac{\partial v_\theta}{\partial z} \right) = \frac{1}{r^2} \frac{\partial}{\partial r} \left[r^3 \eta \frac{\partial}{\partial r} \left(\frac{v_\theta}{r} \right) \right] + \frac{\partial}{\partial z} \left(\eta \frac{\partial v_\theta}{\partial z} \right)$$

axial momentum conservation:

$$\rho \left(v_r \frac{\partial v_z}{\partial r} + v_z \frac{\partial v_z}{\partial z} \right) = -\frac{\partial P}{\partial z} + J_r B_\theta + \frac{\partial}{\partial z} \left(2\eta \frac{\partial v_z}{\partial z} \right) + \frac{1}{r} \frac{\partial}{\partial r} \left[\eta r \left(\frac{\partial v_z}{\partial r} + \frac{\partial v_r}{\partial z} \right) \right]$$

energy conservation:

$$\frac{1}{r} \frac{\partial}{\partial r} (r \rho v_r h) + \frac{\partial}{\partial z} (\rho v_z h) = \frac{J_r^2 + J_z^2}{\sigma} - R + \frac{1}{r} \frac{\partial}{\partial r} \left(\frac{r \kappa}{C_p} \frac{\partial h}{\partial r} \right) + \frac{\partial}{\partial z} \left(\frac{\kappa}{C_p} \frac{\partial h}{\partial z} \right) + \frac{5\kappa}{2eC_p} \left(J_r \frac{\partial h}{\partial r} + J_z \frac{\partial h}{\partial z} \right)$$

electric current continuity:

$$\frac{1}{r} \frac{\partial}{\partial r} \left(r \sigma \frac{\partial \phi}{\partial r} \right) + \frac{\partial}{\partial z} \left(r \sigma \frac{\partial \phi}{\partial z} \right) = 0$$

$$J_r = -\sigma \frac{\partial \phi}{\partial r} ; J_z = -\sigma \frac{\partial \phi}{\partial z}$$

and magnetic field equation:

$$\frac{1}{r} \frac{\partial}{\partial r} (r B_\theta) = \mu_0 J_z$$

This set of equations was solved by Patankar's SIMPLER algorithms.[1] We used theoretical values for thermal coefficients [2] and emitted radiation power losses [3] under the assumption of LTE.

The anode domain and anode layer were taken into account in a simple way. The energy balance at the anode was made by estimating the plasma heat flux to the anode and considering the heat conductivity on the metallic piece to be cut, its vapor pressure for a given temperature and its latent heat for melting and boiling.

A more complete simulation of the cutting process, including convection on the weld pool, and metal expulsion by the gas flow, is still under development.

Figure 3 shows the calculated isotherms using a 101x101 grid, and figure 4 the stream lines in the plasma, at the beginning of the operation, when the anode is still flat.

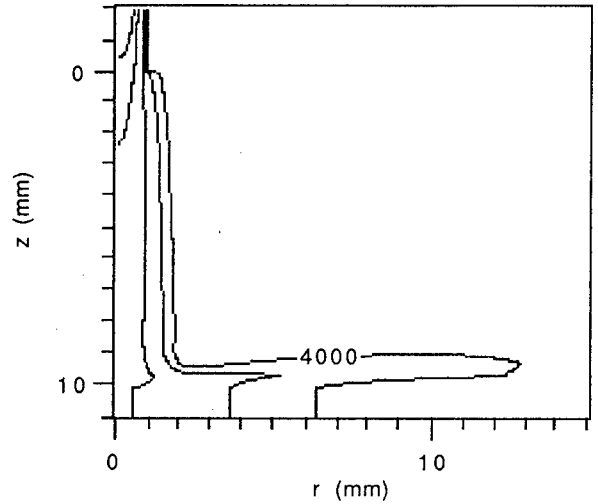


Figure 3. Isotherms (from 4 kK to 20 kK with a step of 4 kK) for a transferred arc with a current intensity of 150A and a cathode-anode length of 10 mm.

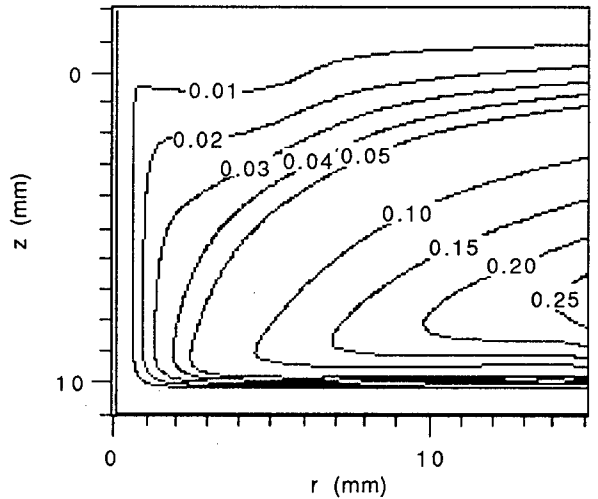


Figure 4. Stream lines in g/s for the same parameters as figure 3.

Comparison of the calculations with experimental results shows a good agreement for some properties as temperature. The observed lowering of plasma temperature, as the cutting is going on, it can be explained as a combination of changes on the anode attachment with the increase of radiation emitted by metallic vapors.

The variation on net plasma resistance is a complex interaction between changes in plasma temperature, plasma conductivity, plasma column length and also the anode attachment.

References

- [1] S.V.Patankar. *Numerical Heat Transfer and Fluid Flow*. McGraw-Hill, New York, 1980
- [2] M.I.Boulos, P.Fauchais and E.Pfender. *Thermal Plasmas*. Plenum Press, New York, 1994
- [3] A.Gleizes et al. Private communication.

DETERMINATION OF THE RADIAL TEMPERATURE DISTRIBUTION OF PULSED SODIUM ARC DISCHARGES

M. Kettlitz and H. Schöpp

Institute of Low Temperature Plasma Physics e.V. Greifswald, Robert-Blum-Str. 8-10, D-17489 Greifswald, Germany

1. Introduction

The energy demand for lighting is tremendous, and thus the reduction of costs by using more efficient light sources is an enormous challenge. Therefore research and development in this field will still be of essential interest. The application of new materials and procedures may lead to the development of new light sources. Some decades ago, light transmitting ceramic materials introduced a new quality of high-pressure sodium lamps. Also metal halide lamps made of ceramic have been available lately. These materials are highly translucent but have the disadvantage to be not transparent. That is why spatially resolved spectroscopic investigations cannot be performed on such lamps and therefore transparent alkali resistant discharge tubes, for example sapphire tubes, are required. Such sapphire tubes are used to investigate temperature profiles of pulsed sodium discharges.

2. Experiment

A special technique is used to prepare the sodium discharge tubes of sapphire. The discharge is operated in a so-called simmer mode that keeps the plasma in the conducting state by means of a dc discharge which controls the cold-spot temperature in the discharge tube

and therefore the available alkali vapour pressure. The stationary dc power is about 50 W. It is superimposed by nearly rectangular current pulses produced by a second circuit. They have a duration of 1 ms, current values from 1 A up to 50 A and a maximum power input of up to 7 kW is reached. During the pulse regime, plasma temperature and particle number densities and hence the optical output are determined by the pulse power.

The spectroscopic measurements are performed during the pulse current plateau in the visible and infrared spectral range. The radiation of the discharge passes an optical mirror system and is imaged to the entrance slit of a 0.5 m spectrograph. The side-on intensity distribution is recorded by means of a gated CCD-system connected to a computer for further processing of the images. For an absolute radiation calibration a xenon radiation standard is used.

3. Determination of the temperature

For the determination of the plasma temperatures the following methods are used:

1. The temperature can be derived from the absolute intensity of one spectral line. If the degree of ionisation is low and the vapour pressure is known the line intensity reads:

$$\varepsilon_{ki} = \frac{1}{4\pi} \frac{hc}{\lambda} \frac{p}{kT} g_k A_{ki} \exp\left(-\frac{E_k}{kT}\right)$$

ε_{ki} - emission coefficient, h - Planck constant, c - velocity of light, λ - wavelength, T - temperature, g_k , A_{ki} , E_k - statistical weight, transition probability, excitation energy of the upper level, k - Boltzmann constant.

The sodium vapour pressure p can be determined from the wavelength separation $\Delta\lambda$ between the maxima of the self-reversed sodium D-lines following de Groot [1].

2. The temperatures are derived from the intensity ratio of two atomic sodium lines:

$$\frac{\varepsilon_1}{\varepsilon_2} = \frac{A_1 g_1 \lambda_2}{A_2 g_2 \lambda_1} \exp\left(-\frac{E_1 - E_2}{kT}\right)$$

The index 1 refers to the first, 2 to the second line. This equation offers the possibility to evaluate the

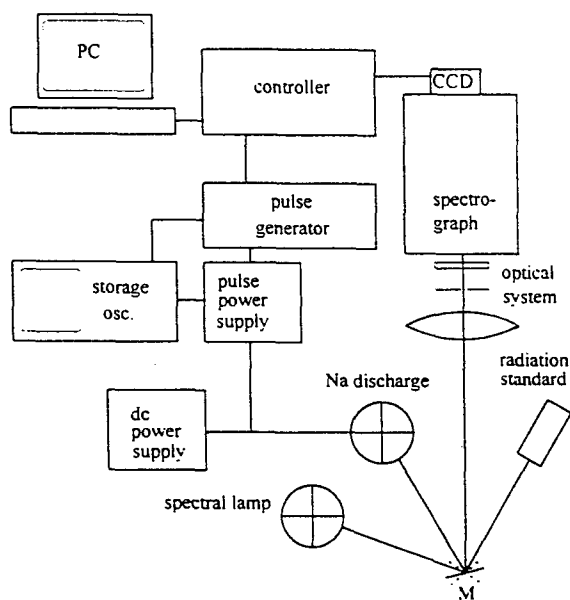


Fig. 1: Schematic view of the experimental set-up.

temperature without knowledge of the number density of sodium atoms.

3. The temperature is determined from the spectral radiance L_m in the maximum of the self-reversed Na 818.4/819.5 nm lines. Following Bartels [2], L_m is a sensitive function of the maximum temperature T_m along the line of sight:

$$L_m = C_B B_\lambda(T_m)$$

C_B is a constant and taken from de Groot [3]. The maximum temperature can be derived from the radiance via the Planck function B_λ .

4. Knowing the sodium vapour pressure, the temperature can also be derived from the recombination radiation below 408 nm. The emission coefficient for this radiation can be calculated as a function of the temperature:

$$\varepsilon_{cont.} = \kappa_{at} \xi \frac{P}{kT} B_\lambda(T)$$

κ_{at} - absorption coefficient per atom, ξ - function according to [4].

4. Results

The plasma temperatures of the sodium discharges are determined from the ratio of different Na lines, from the absolute line intensities, according to Bartels and from the recombination continuum.

A problem concerning the temperature determination from the ratio of two lines arises for the alkalis from their low excitation energies. For the temperature determination one needs the energy difference of the upper levels of the involved lines. It is seen, that the better the accuracy of the temperature determination, the larger is the energy difference of the upper levels of the two lines. But with differences of nearly 1 eV for sodium this accuracy is limited.

Best temperature values are reached for the ratio of the Na I lines 615.4/616.1 to 466.5/466.9 nm or 615.4/616.1 to 497.9/498.3 nm. The problem that the Na I 615.4/616.1 nm are situated on the red wing of the D-lines was solved by subtracting the background and leads only to small additional uncertainties. But only the temperature values for the centre of the arc are reliable and agree quite good with those of the second method. Outside the central part of the arc small deviations in the line intensities lead to large uncertainties in the shape of the temperature curve. The error of the temperature depends on the energy difference of the upper levels of the considered lines. This leads to an error of 15% at 4000 K for the ratio of the Na I 615.4/616.1 to 497.9/498.3 nm lines. Therefore this method is not preferred for the determination of the plasma temperature.

For the first and fourth method the pressure has to be determined. Using the measured wavelength separation of the maxima of the self-reversed D-lines the pressure is 0.15 bar. The temperature curves for the lower currents are derived from the absolute intensities of the 466.5/466.9 nm and also the 497.9/498.3 nm lines. Both curves agree well at low currents, but as mentioned above at high currents the Na I 466.5/466.9 nm is no longer optically thin. Therefore the lines at 497.9/498.3 nm are preferred.

So, the temperatures in the discharge axis are between 3000 and 7000 K. Figure 2 shows plasma temperature curves for lower currents received from absolute line intensities. With increasing pulse currents there is also an increase in the temperatures and a change in the shape of the temperature profiles.

For higher discharge currents the arc is more extended to the wall and the temperature profiles become flatter. Because of their higher temperatures and their flatter profiles the temperature of the arcs with higher currents could be determined closer to the wall.

Temperatures determined by the third method agree well with the first method. The fourth method gives a satisfactory agreement with the other temperature profiles for higher pulse currents.

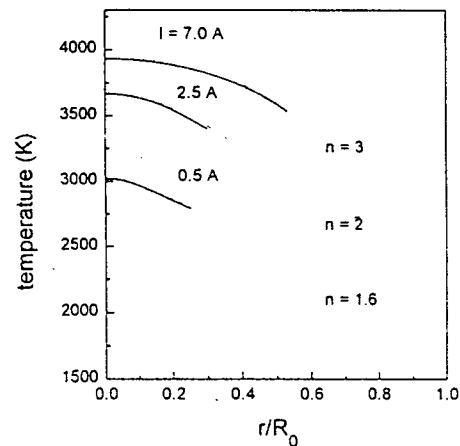


Fig. 2: Plasma temperature for lower currents in dependence on the reduced radius r/R_0 .

- [1] J. J. de Groot and van J. A. J. M. van Vliet: The High-Pressure Sodium Lamp (Deventer: Kluwer) (1986)
- [2] H. Bartels, Z. Phys. 127 (1950) 234, 128 (1951) 546
- [3] J. J. de Groot, Ph. D. thesis (1974)
- [4] D. Hofsäb, Z. Phys. A 281 (1977)

Highly structured electron energy distribution functions under expanding arc conditions

M.Capitelli*, N.Dyatko***, K.Hassouni**, C.Gorse*, S.Longo*

* Centro di Studio CNR Chimica dei Plasmi and Dipartimento di Chimica dell'Università, Via Orabona 4, Bari, Italy

** LIMHP - Universite' de Paris Nord - CNRS Villetaneuse (France)

*** Branch of the Kurchatov Institute, Troitsk, Moskow Region, Russia

In the last few years we have shown the strong coupling existing in non-equilibrium plasmas between the electron energy distribution function (eedf) and the concentrations of vibrationally and electronically excited states. These studies were performed for both discharge and post-discharge conditions. The main result of these researches is the observation of structures on eedf due to second kind collisions of the type



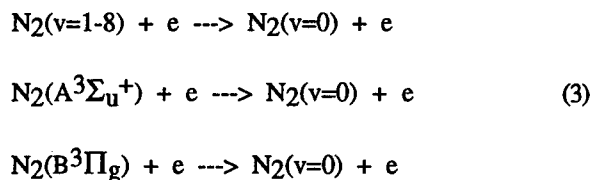
where N_2^* denotes a vibrationally or electronically excited state [1-2].

The extension of these ideas to expanding arc conditions has never been examined, because it is generally believed that the high ionization degrees present in these conditions are sufficient to maxwellize eedf through electron-electron coulomb collisions. Only recently eedf in expanding arc conditions has been studied [3]. The role of second kind collisions was in effect smoothed by electron-electron and electron-ion collisions even though memory of second kind collisions was present in the enhancement of relevant rates. In this paper we consider N_2 plasmas for conditions typically met in arc expanding flows [4].

We solve a homogeneous Boltzmann equation for eedf written in the form

$$\frac{\partial n(\epsilon, t)}{\partial t} = \frac{\partial J_{ee}}{\partial \epsilon} + \frac{\partial J_{ei}}{\partial \epsilon} + In + Sup + Ion \quad (2)$$

where $n(\epsilon, t)$ is the number density of electrons at energy ϵ and time t and the different terms on the right hand side of eq.1 represent respectively the flux of electrons along the energy axis driven by elastic, electron-electron, electron-ion, inelastic, superelastic and ionization collisions. Explicit terms can be found elsewhere [1-2]. The inelastic term includes the most important energy losses processes such as vibration and electronic excitation as well as ionization (treated as an inelastic channel). The superelastic terms include the following processes



Concentrations of vibrationally and electronically excited states as well as the ionization degree α have been considered as free parameters. In particular figure 1 reports three different eedf calculated according to different hypothesis. Curve 1 is obtained by considering concentrations (mole fraction) of electronically excited molecules in equilibrium at $T_e=T_g=5000K$, while curves 2 and 3 have been obtained by considering concentrations exceeding the equilibrium values. In all the reported cases the vibrational distribution is a Boltzmann one at $T_g=T_v$. We can see that the presence of non equilibrium concentrations of electronically excited states (curves 2 and 3) strongly enhances the eedf's tail compared to the equilibrium case (curve1).

The ionization degree is not sufficient to completely thermalize the eedf.

Figure 2 reports eedf for other conditions : in particular we are considering a higher translational temperature as well as higher concentrations of excited states. Again the effect of superelastic electronic collisions is well evident in the tail of eedf.

The main conclusion of the present paper is that in arc expanding conditions structured eedf's can persist as a result of second kind collisions. This structure can enhance by several orders of magnitude some relevant rates.

The present results must be considered as a first step toward the understanding of the role of non-equilibrium eedf under quasi equilibrium conditions. Future work in this direction should couple the Boltzmann equation for eedf with the kinetics of electronically excited states and with the fluidynamics to make more realistic either the concentrations of excited states or the conditions of the problem.

Acknowledgement

This work was partially supported by 'Progetto Strategico Applicazioni Industriali dei Plasmi' of CNR

References

- [1] G.Colonna, C.Gorse, M.Capitelli, J.Wilhelm and R.Winkler: Chem. Phys. Lett. 5 (1993) 213
- [2] C.Gorse, M.Cacciatore, M.Capitelli, S.De Benedictis and G.Dilecce: Chem. Phys. 119 (1988) 63
- [3] M. Capitelli, G.Colonna, A.Gicquel, C.Gorse, K.Hassouni and S.Longo: Phys.Rev.E 54 (1996) 1843
- [4] C.O.Laux, R.J.Gesman, and C.H.Kruger: Proc. 26th AIAA Plasmadynamics and Lasers Conference, San Diego CA AIAA 95 (1995) 1989

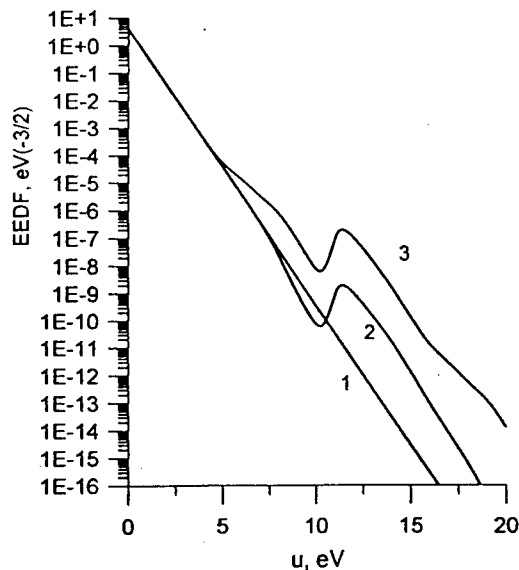


Fig.1 Electron energy distribution functions versus energy for equilibrium (curve 1) and non-equilibrium conditions (curves 2-3) in the post discharge regime (reduced electric field $E/N=0$). Conditions are: $T_v = T_g = 5000$ K, $\alpha = 2 \cdot 10^{-5}$, curve (2): $N_2(A)/N_2 = 10^{-6}$, $N_2(B,C)/N_2 = 10^{-7}$, curve (3): $N_2(A)/N_2 = 10^{-4}$, $N_2(B,C)/N_2 = 10^{-5}$

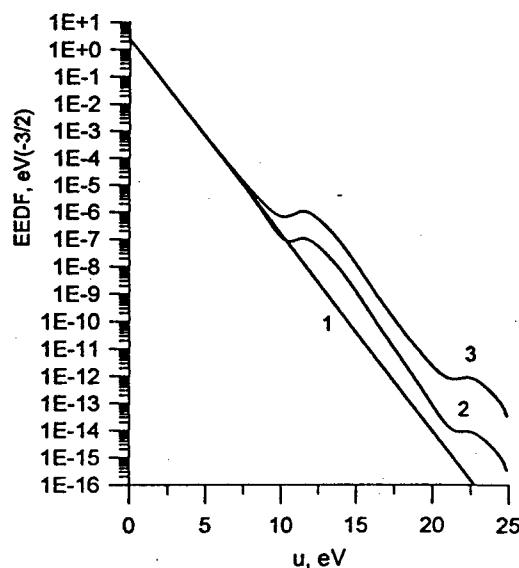


Fig.2 Electron energy distribution functions versus energy for equilibrium (curve 1) and non-equilibrium conditions (curves 2-3) in the post discharge regime (reduced electric field $E/N=0$). Conditions are: $T_v = T_g = 7000$ K, $\alpha = 8 \cdot 10^{-4}$, curve (2): $N_2(A)/N_2 = 10^{-4}$, $N_2(B,C)/N_2 = 10^{-5}$, curve (3): $N_2(A)/N_2 = 10^{-3}$, $N_2(B,C)/N_2 = 10^{-4}$

ENERGETIC IONS IN TVA (THERMIONIC VACUUM ARC) GENERATED PURE METAL VAPOR PLASMAS.

G.Musa, A.Popescu, I.Mustata, A.Salabas, F.Leu

National Inst. for Laser & Plasma Physics, PO MG-36, Bucharest Romania

H.Ehrich, J.Schumann

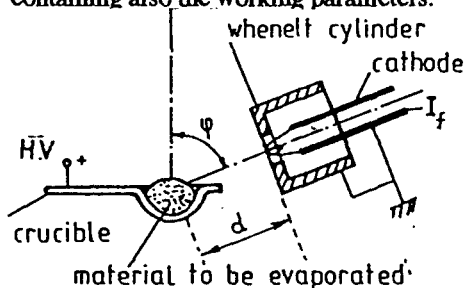
Universitat Essen, Fachb.Physik, AG Dunnschichttechnologie, Essen, Germany

Introduction.

New type of plasma sources Thermionic Vacuum Arc (TVA) and Anodic Vacuum Arc (AVA), generating pure metal vapor plasma with energetic ions content have been reported in [1]-[2]. This type of plasma source has the unique quality to deposit thin films which are bombarded during their growing, just with the ions of the depositing metal. The percentage of the incident ions on the substrate (from total particles) depends on the arc current and its value is between a few percents and 50%. In TVA discharge, directed energy of ions can easily exceed 100 eV. The aim of this paper is to present on which parameters depends this energy value and how it can be controlled in order to be able to choose in advance the energy of the ions bombarding the growing high purity thin film or even change it during deposition.

Experimental results.

TVA structure has been described before. However, for the clarity we are giving in Fig.1, a very schematic presentation, containing also the working parameters.



ϕ -angular relative position of (C) and (A)

d-distance from (C) to center of crucible

I_f - heating current of the cathode (C)

Fig.1.Schematic presentation of TVA

This arc running in vacuum conditions is self generating the "gas" in which the discharge takes place. Consequently the meanings of breakdown and arc voltage drop are different from those currently used. Indeed, for ignition, the applied voltage must generate in vacuum conditions the metal vapors in the interelectrode space. As concerning the arc voltage drop U_a , the anode voltage fall must ensure enough energy input to anode to maintain at least the same rate of evaporation of atoms from the anode as it was at the TVA ignition. Cathode fall must ensure for each

given conditions, the needed ionization rate necessary to sustain all charge losses. TVA works in high vacuum or UHV conditions. At the application of a high voltage across anode and heated cathode, due to the electron bombardment, the anode material first melts and after starts to boil, ensuring the metal vapors in the interelectrode space. At a convenient value of the applied high voltage a bright discharge is established in pure metal vapors and a sudden increase of the current and decrease of the voltage across electrodes is observed. This metal vapor plasma is continuously expanding away from its source. We measured the energy of ions at 250mm away from the plasma source, using a retarding probe energy analyzer. The unexpected high value of the energy of ions is due to the elevated potential of the metal vapor plasma at the source against the grounded vacuum vessel wall. Indeed, because cathode is grounded, the plasma source is at a potential at least equal with cathode fall (in its new acceptance). In order to prove this, using derivative of the probe characteristics taken in various points, we measured from the shift of these characteristics on voltage scale, the change of the potential from plasma source toward the wall. In Fig.2 is shown the obtained result.

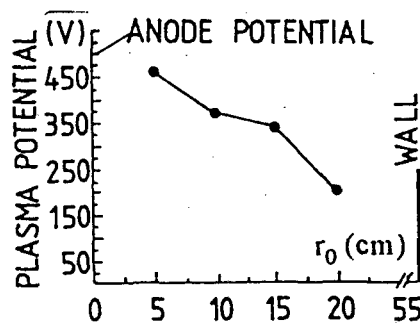


Fig.2.Potential distribution from the plasma source to the wall.

A continuous decrease of the potential can be observed, which accelerates the expanding plasma ions in their way from the source to the wall. Now we can establish the parameters and the means to control the energy of ions assuming that the energy of ions are directly related to the cathode potential fall. Unfortunately, this parameter can not be

monitored easily. A parameter which can be displayed easily and continuously is the arc voltage drop U_a , which is related to the cathode fall through the relation:

$$U_a = U(\text{cathode fall}) + \Delta U(\text{plasma}) + U(\text{anode fall})$$

The peculiarity of TVA discharge permits to change at will the cathode fall value. Indeed, if the supply of electrons from the cathode to the anode surface is worsened, in order to maintain the same arc current, a higher cathode fall is necessary to compensate the decrease of the flux of electrons. In this way, an increase of the energy of ions is obtained. Following means can be used to increase this energy:

- decrease of the cathode heating current I_f
- increase of the distance d
- increase of the angle Φ
- increase of the sample distance from source
- decrease of the arc current

The same means can be used to decrease the energy of ions.

The change of the arc voltage drop U_a with the change of the cathode heating current is shown in Fig.3 for two values of I_a and for $\Phi=60^\circ$. In Fig.4 is given the dependence of the measured energy of ions on cathode heating current I_f for $\Phi=85^\circ$. For a TVA discharge with arc current $I_a=1.25A$ and $\Phi=60^\circ$ we measured the ratio between energy of ions E_i and the arc voltage drop U_a for various U_a values obtained changing I_f . The results are shown in Fig.5 and we can see, that for a large variation of U_a values, the energy of ions represents nearly the same fraction from U_a . It results that for a given arc current I_a the voltage drop U_a can be used indeed to roughly estimate the energy of ions. The fraction E_i/U_a increase with the arc current value toward 1.

In Fig.6 is shown the change of the arc voltage drop U_a with the change of the cathode anode distance for $\Phi=0^\circ$. More than 200V increase appears at a change of the distance from 2.5 mm to 4.7mm.

We measured also an increase of the energy of ions from 120eV to 200 eV at a change of angle Φ from 60° to 85° ($I_a=3A$).

The increase of the energy of ions with the distance from the plasma source is obvious if we consider the curve given in Fig.2.

The volt-ampere characteristic of TVA is close to a hyperbola described by $U_a I_a = \text{const}$. It results that arc current is also a parameter which gives us the possibility to change arc voltage drop and consequently to control the energy of ions. This can be done only at low arc currents. At high arc currents of the order of 20-100A, voltage drop is small and nearly constant (around 20 volts) and the energy of ions can not be changed too much. The difficulties in controlling the energy of ions

are: 1.- d and Φ can not be changed easily during deposition; 2.- lowering of the cathode temperature decrease the life-time of the cathode; 3.- at low arc currents the deposition rate decrease.

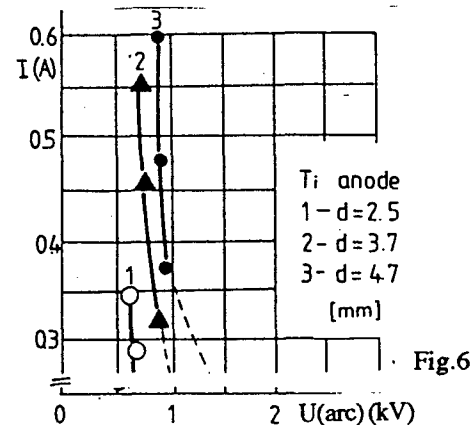
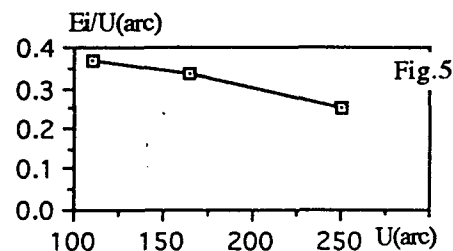
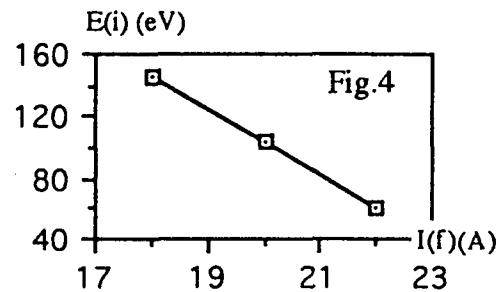
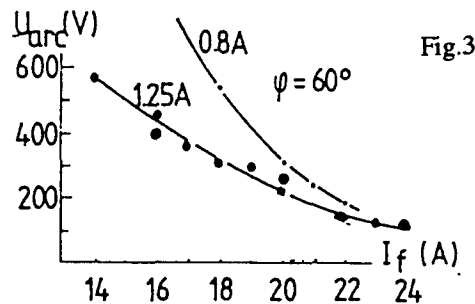


Fig.3. Arc voltage drop dependence on cathode heating current.

Fig.4. Dependence of the energy of ions on cathode heating current.

Fig.5. Ions energy to arc voltage drop ratio versus arc voltage drop for $I_a=1.25A$

Fig.6. Displacement of arc voltage drop U_a -arc-current I_a at interelectrode distance change.

[1]. H. Ehrich, B. Hasse, M. Mausbach, K. G. Muller, IEEE Trans. Plasma Sci. 18, 895, 1990

[2]. G. Musa, A. Baltog, A. Popescu, N. Betiu, I. Mustata, Contr. Plasma Phys. 6, 431, 1987

DC PLASMA TORCH THEORETICAL AND EXPERIMENTAL RESULTS

J. Pacheco¹, M. Razafinimanana², J.M. Bauchire², S. Vacqu  ² and J.J. Gonzalez²

1/ Instituto Nacional de Investigaciones Nucleares (ININ), Centre Nucl  aire du Mexique, Apartado Postal n   18-1027,
Toluca, Mexico CP 11010.

2/ Centre de Physique des Plasmas et Applications de Toulouse, ESA 5002, Universit   Paul Sabatier, 118 route de
Narbonne 31062 Toulouse Cedex 4 France Email: jjg@cpa11.ups-tlse.fr

Introduction

In recent years, thermal plasma processes have been proposed and used for the destruction of hazardous wastes. The decomposition of toxic wastes (such medical wastes) is of growing importance in connection with environmental pollution. This paper presents the first results obtained in the study of a DC plasma torch, with the object of the construction of an hazardous waste treatment facility located in Mexico. This work is a collaboration between the ININ laboratory (Mexico) for the experimental part, and the CPAT (Toulouse University) for the elaboration and the perfecting of a theoretical model describing the behaviour of the plasma torch in a first stage and the furnace in a second stage.

Experimental

Experimental set-up

The first investigations were carried out with a scale model of cylindrical furnace (20 cm diameter) running in argon and in nitrogen at atmospheric pressure. The torch is a classical model with a thoriated tungsten cathode and an anode of copper. At this time, the current intensity is limited to 200 A. Our results have been obtained with an intensity of 75 A. The temperature profiles have been determined using absolute intensity of neutral argon lines, and assuming the existence of local thermodynamic equilibrium. Abel transformation allowed us to obtain local values of the line intensities. Calibration was performed with a tungsten ribbon lamp. The influence of gas flow rate on the temperature of Ar plasma and Ar-N₂ plasma was studied for different distances from the nozzle exit z .

Experimental results

The figure 1 gives the variations of the radial temperature for a gas flow rate of 34.5 l/mn (corresponding to 1.026 g/s) in pure argon and for four values of the distance z from the nozzle exit. With a current intensity of 75A, the temperature maximum on the axis of the discharge is 11400K at the nozzle exit ($z=0$).

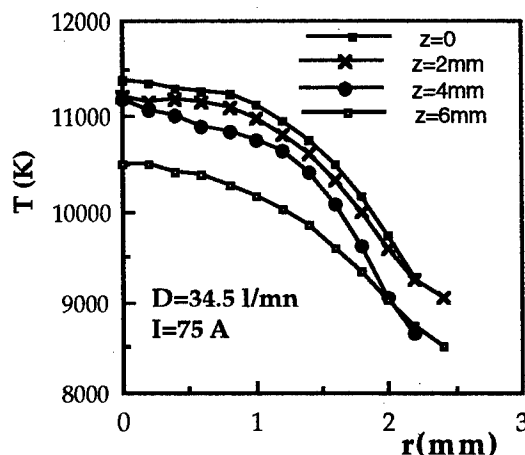


Figure 1

Other experiments with a gas flow rate of 24l/mn (corresponding to 0.7g/s) and the same value of the current intensity have been realized.

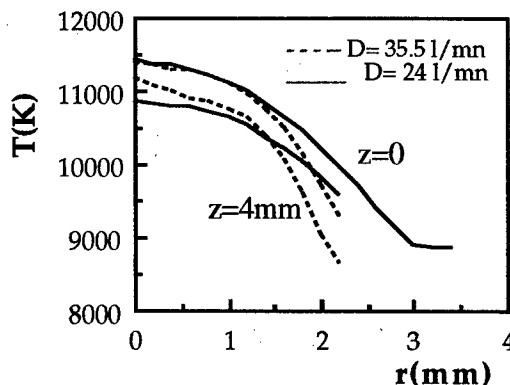


Figure 2

The figure 2 presents experimental values of $T(r)$ for these two values of the mass flow rate $D=34$ and 24 l/mn and two distances from the exit $z=0$ and $z=4$ mm.

The increase of gas flow rate constricts the plasma jet and the temperatures far from the axis are lower with an higher value of the mass flow rate. At the nozzle exit ($z=0$) an augmentation of the mass flow rate does not lead to an increase of the axis temperature.

The introduction in argon of a weak percentage of nitrogen modifies the values of temperature and arc voltage. The figure 3 gives the temperature profiles for three values of z , with a gas mixture composed of 5% N_2 and 95% Ar ($I=75A$).

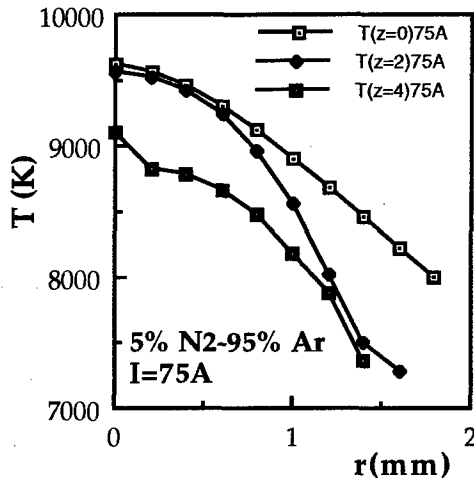


Figure 3

On the axis, the temperature for $z=0$ decreases of 1800K in comparison with pure argon. For a same gas flow rate, the decrease in T along a radius is faster with the gas mixture. We observed a clear decrease in arc voltage with the introduction of nitrogen in argon. With a same current intensity this effect leads to a decrease of the electric power injected in the discharge with a repercussion on the enthalpy of the plasma.

Modelling

Assumptions and governing equations

The governing equations are written in an axisymmetric system of coordinates and the operation of the torch is assumed to be in steady state with negligible gravity effects. The plasma is assumed to be in local thermodynamic equilibrium (LTE) and the radiation effects are considered through the net emission coefficient. This model was previously described by Bauchire et al [1]. The mathematical 2D model is limited to the free jet region and uses the SIMPLE method after Patankar [2]. So, at the inlet (the nozzle exit) the temperature and the axial component of the velocity are given by:

$$u(r) = u_0 \left(1 - \frac{r}{R}\right)^n$$

$$T(r) = T_0 \left(1 - \frac{r}{R}\right)^n + T_w$$

where u_0 and T_0 are the maximum experimental values of the axis temperature (at the exit). T_w is the value of the temperature on the edge of the anode ($n=2$). So for the comparison with the experimental results, we only give a geometrical parameter : the nozzle diameter and the values of u_0 , T_0 and T_w . On figure 4 we compare the experimental results obtained in an argon plasma at atmospheric pressure. The inlet gas flow rate is $D=24$ Nl/mn and the current intensity is equal to 75A. The temperature values are given along the axis ($r=0$). One can observe a good agreement especially in the hotter region of the plasma ($z < 1$ cm). Other results on the influence of Ar- N_2 mixtures and on the influence of the mass flow rate and current intensity will be presented during the conference.

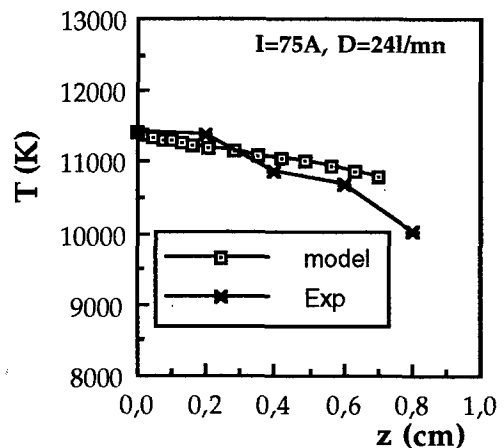


Figure 4

Conclusion

The first work of this program gave good results, particularly on the agreement between experiments and theoretical results. However, incineration leads to production of dusts and ashes necessitating the presence in the furnace of a second torch for the treatment of these products. The realization of this furnace and the adaptation of the theoretical model are currently under way.

Acknowledgements

Financial support by the Centre National de la Recherche Scientifique and the Conacyt is gratefully acknowledged.

References

- [1] J.M. Bauchire, J.J. Gonzalez and A. Gleizes, ISPC12, Minneapolis, 3 pp1761-1765, 1995.
- [2] S.V. Patankar, "Numerical Heat Transfer and Fluid Flow", McGraw-Hill (1980)

PHENOMENA IN THE ELECTRIC ARC CATHODE REGION

B. Pokrzywka[†], K. Musiol[†], S. Pellerin[‡], E. Pawelec[†], J.-M. Cormier[‡], J. Chapelle[‡]

[†] Institute of Physics, Cracow Pedagogical University, ul. Podchorążych 2, 30-084 Kraków, Poland

[‡] Institute of Physics, Jagellonian University, ul. Reymonta 4, 30-459 Kraków, Poland

[‡] GREMI, Université d'Orléans, BP 6759, 45067 Orléans Cedex 2, France

Abstract: The plasma near the cathode tip of an electric arc, shows radial dependence of its physical equilibrium state. In the hot core, the plasma is in the local thermodynamic equilibrium (LTE) state. Toward outer zones, the plasma state deviate from the LTE equilibrium. In our opinion, it is caused after all by the ArI ground state overpopulation. Results of our experiments support this conclusion. Theoretical estimations of the ArI ground state overpopulation give results consistent with experiment. Calculations show, that this overpopulation is caused by inward transport of ground state atoms into the plasma column.

I- Introduction

For last few years, the near cathode zone of an electric arc has been intensively studied. It has been observed in several experiments, that the off axis maximum value of the neutral atom line total intensity, depends on the distance from the cathode [e.g., in argon arc: 1, 2, 3, 4, 5, 6, 7, and in nitrogen arc: 8, 9].

In our previous publication [2, 3, 7], we presented results of spectroscopic diagnostic performed for an argon arc plasma burned at atmospheric pressure with the arc current of 200A where these phenomena were observed.

Formally two reasons are possible to explain this phenomena: the plasma equilibrium state depends on the distance from the cathode or pressure gradients exist in this plasma zone. To find an answer on the question which mechanism plays dominant role in phenomenon described above, we performed plasma model calculations.

II- Experimental results

Several slices at the distance h from the cathode of the electric arc have been spectroscopically investigated. Plasma was observed side-on, argon line profiles and continuous emission have been measured at various chordal positions to perform Abel's inversion. Plasma diagnostic has been performed using various methods applied to ArI, ArII and ArIII lines. From our extended analysis [7], one can conclude that:

- there is good agreement between the temperatures determined from the Boltzmann plot and Lenz-Fowler-Milne (L-F-M) method applied to 480.6nm ArII line, but not with temperature derived from the L-F-M method applied to the 696.5nm ArI line.
- population distribution of ArII excited levels was in the Boltzmann-Saha equilibrium for $T \geq 18000\text{K}$.
- very close to the cathode surface, the plasma temperature reach $\sim 29500\text{K}$. This temperature is higher than obtained from isotherms maps calculated in the frame of magneto-hydrodynamic models, for similar plasmas.
- there is good agreement between the radial free

electron density distribution, obtained from the Stark width of the 397.9nm ArII line, and that calculated from the LTE equation set (with temperature derived from the Boltzmann plot). This is a supplementary proof of existence of the Boltzmann-Saha equilibrium in the ArII levels population for $T \geq 18000\text{K}$

- Continuum radiation for the temperatures below $\sim 16000\text{K}$ deviate from the LTE isobar in the Olsen-Richter (O-R) graph, in the same manner as experimental data for ArI-ArII lines. Disagreement observed for temperatures above $\sim 19000\text{K}$, seems to be a result of underestimation of the Bibermann ξ factor for ArIII recombination radiation (the contribution of ArIII ions to continuum radiation intensity is as important as ArII ions contribution - See [7] and [10]). This hypothesis is supported by good agreement between electron density derived from the ArII lines intensity ratio measurement (the Boltzmann plot) and electron density obtained from line broadening measurements.

The arc plasma near the cathode tip shows radial dependence of the physical equilibrium state. In the hot core ($T > 17000$), close to the arc axis, the plasma is in the LTE state. In the outer zones, the plasma state deviate from the LTE state at $p = 1\text{atm}$.

For plasma column layers (slices) closer to the cathode tip, deviation from the LTE state begins at smaller distance from the axis and for higher temperature, even if the electron density is greater than $1.5 \times 10^{23} \text{m}^{-3}$. Deviation from the LTE state for $p = 1\text{atm}$ decreases with the distance from the cathode and practically vanishes for $h > 3\text{mm}$.

III- Model calculations

A deviation from the LTE state may be described only in a frame of the collisional-radiative model. One has to solve the equation set describing populations of neutral argon states, up to the ionisation limit lowered by interaction of atoms with the plasma. In the case of the argon plasma at atmospheric pressure, the transport of radiation may be described locally, using so called

escape coefficients. Furthermore, real population density n_q of atoms in the q state is written in the form $n_q = (1 + \delta_q) n_q^s$, where δ_q describe overpopulation of the q state, and n_q^s is the density in the atomic q state when the Saha equilibrium exists between the q and ionic ground state. We also introduce a transport term W_q .

To estimate the overpopulation, we assumed, according Rosado [11], that the argon energy levels system can be represented by four effective levels, the first one ($q=1$) being the ArI ground level.

To estimate the influence of the ground state atoms inward transport on the overpopulation coefficients δ_q we have calculated them for different plasma temperatures T , for various values of transport term W_q . Velocity and temperature distribution values for the estimations of W_q were taken after Lowke [12]. Atom density distributions were calculated for these temperatures, with overpopulation factors included. Then, overpopulation factors for excited states ($q>1$) remain negligible in comparison to δ_1 for W_q as high as 10^6 - 10^7 s⁻¹. Furthermore, influence of the transport of atoms in excited states is negligibly small. The dominant effect is the ArI ground state overpopulation, due to the ground state atoms transport term W_1 , which stays several order of magnitude higher than that created by ambipolar diffusion.

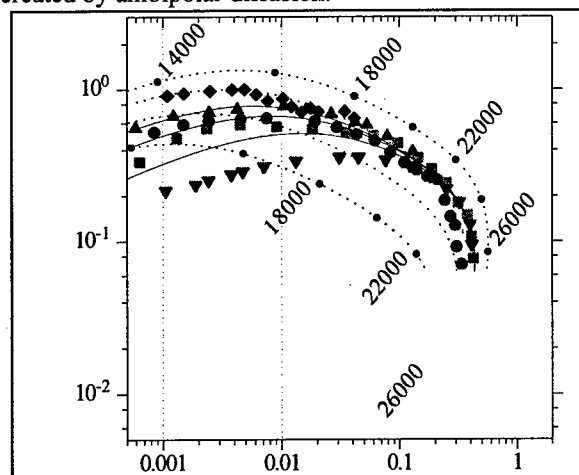


Figure 1: O-R for various physical plasma states

Plasma layers [in mm]: ▽ 0.085, 0.51, ○ 1.1, △ 2.1, ◇ 4.5
 ● temperature marks with 2000 K increment;
 --- LTE isobars for $p=0.6$ to 1.2 atm [step: 0.2 atm];
 — PLTE isobars at $p=1$ atm with overpopulation factor δ_1 for ArI ground state equal to 1.0, 2.0 and 3.0 [up to down]

In the experimental O-R graph [Cf. Fig.1], one may see, that departure from the equilibrium state exists in external plasma zones, for temperatures smaller than 17000K. One may also see that the overpopulation δ_1 qualitatively explains the behaviour of ArI lines.

We have calculated W_1 and δ_1 for some points of the plasma temperature and velocity distribution determined by Lowke [12]. Then, for example, for $h=0.1$ mm and $T=15000$ K, we obtained W_1 values as high as -5×10^5 s⁻¹, which produce the ground state

overpopulation $\delta_1 \approx 5$. This value „locates” the corresponding point in the O-R diagram on the LTE isobar $p=0.5$ atm and gives electron density 42% lower than the LTE value.

More detailed comparison of the theoretical estimation can be made. Particularly, the overpopulation δ_1 for the isotherm $T=15000$ K (determined for each slice using O-R graph for ArI-ArII pair) can be traced as a function of the distance from the cathode tip. Then, although overpopulation δ_1 seems underestimated in the model, it qualitatively explains the behaviour of neutral argon lines. Differences between measurements and the model could be attributed to following reasons: simplification in the magneto-hydrodynamical model (based on invalid LTE hypothesis), uncertainties in rate coefficient in collisional-radiative model...

IV- Conclusion

Deviation from the LTE state for $p=1$ atm can be caused by an overpopulation of the ArI ground state, that may be quite high. The dominating impact on the ArI ground state overpopulation is the inward transport of the ground state atoms.

However, it must be pointed out, that from experimental results of emission spectroscopy, it is not possible to decide which mechanism plays dominate role in this phenomenon: it is worth to notice, that formally, an assumption concerning existence of the pressure lowering in the plasma, permits also to obtain consistent results from different diagnostic methods in a mathematically simpler way [2, 3].

In the actual situation, works which would join the magneto-hydrodynamic and collisional-radiative models should be undertaken. Such a model should be made for ArII, but for this many cross sections concerning ArII should be measured or calculated.

We thanks Prof. Lowke for sending us results of his model calculations.

VI- References

- [1] G.N.Haddad and A.J.Farmer *J.Phys.D* **17** (1984) 1189
- [2] S.Pellerin, K.Musiol, B.Pokrzywka and J.Chapelle *J. High Temp.Chem.Proc Supp.3-1* (1992) 478
- [3] S.Pellerin, K.Musiol, B.Pokrzywka and J.Chapelle *J.Phys.D* **27** (1994) 522
- [4] J.Haidar and A.J.D.Farmer *J.Phys.D* **27** (1994) 555
- [5] M.Razafinimanana, P.Gudzy, A.Gleizes, L.El Hamidi and S.Vacque *J. High Temp.Chem.Proc.* **4** (1994) 51
- [6] J.Haidar *J.Phys.D* **28** (1995) 2494
- [7] B.Pokrzywka, K.Musiol, S.Pellerin, E.Pawelec and J.Chapelle *J.Phys.D* **29** (1996) 2644
- [8] J.Haidar and A.J.D.Farmer *J.Phys.D* **26** (1993) 1224
- [9] S.Megy, J.M.Baronnet and E.A.Ershov-Pavlov *J.Phys.D* **28** (1995) 344
- [10] B.Pokrzywka, K.Musiol, S.Pellerin and J.Chapelle *Int. Symp. on Plasma Research and Application*, juin 1997, Opole (Poland) (Submitted)
- [11] R.J.Rosado *Thesis* (1982) Eindhoven Univ. of Tech., Eindhoven (The Netherlands)
- [12] J.J.Lowke *Private communication*

Influence of the arc motion on the hydrodynamic flow in a three-phase AC plasma reactor

B. RAVARY*, L. FULCHERI*, F. FABRY**, G. FLAMANT**

* Centre d'Energétique
Ecole des Mines de Paris
BP 207
F-06904 SOPHIA ANTIPOLIS CEDEX
FRANCE

** IMP-CNRS
B.P. 5
Avenue Felix Trombe
F-66120 FONT ROMEU
FRANCE

1. Introduction

Three phase AC plasma technologies are particularly suitable for high power & large volume plasma systems.

This study makes part of the characterisation of a plasma reactor for carbon black production located in Odeillo, France [1][2][3].

The knowledge of temperature and velocity fields is of main importance for an efficient control of the process. Due to their specific geometry, three phase AC plasma technologies are characterised by a mutual electromagnetic influence of the arcs and consequently by a very typical arc motion which governs the general hydrodynamic flow.

A simplified model of the electromagnetic forces taking place on the arcs is proposed. This model proves to be in good agreement with high-speed cine-camera films. In order to take into account the evaluated Lorentz forces, the boundary condition of the plasma inlet velocity has been modified in an hydrodynamic model of the reactor. With this condition, the results of the numerical simulation are in good agreement with calorimetric measurements and surface wall temperatures.

2. Evaluation of the Lorentz forces

The objective of this evaluation is to develop a simplified approach allowing to take into account the electromagnetic forces on the flow in the reactor without solving the 3D time-dependent magneto-hydrodynamic equations which would be extremely high computer time consuming.

2.1. Nature of the arcs

From an hydrodynamic point of view, an arc can have two different behaviors. It can be penetrated by a transversal flow or it can behave almost like a moving solid body [4]. The transition between these two behaviours corresponds to the transition of the parameter β , ratio between the magnetic and the viscous forces. Using visual evaluations of the geometric characteristics of the arcs, β proves to be

large enough in our reactor so that arcs can be approximated as moving conducting solid bodies.

2.2. Hypothesis

Here are the main hypothesis used in our calculation :

- the currents in the three electrodes are sinusoidal with a phase shift of 120° , which is in good agreement with our oscilloscopic measurements,
- the arcs are linear and stay on the electrodes' axis as in Figure 1.

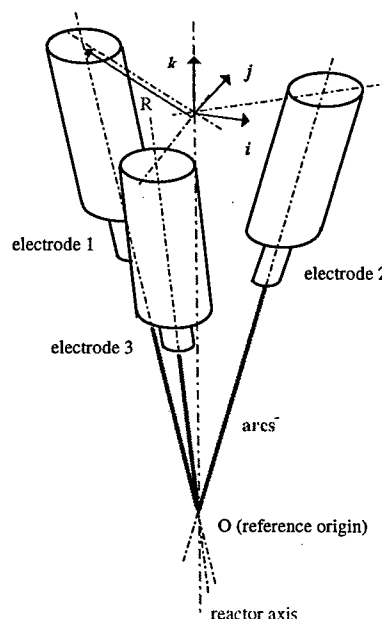


Figure 1 : Simplified geometry of the arcs used for the calculation of the induced Lorentz forces in the reference (O; i, j, k)

2.3. Calculation of the magnetic force

According to the previous hypothesis, the instantaneous current i_n in the arc from electrode n ($n \in \{1; 2; 3\}$) is :

$$i_n(t) = I \cos\left(\omega t - (n-1)\frac{2\pi}{3}\right) \quad (1)$$

where I is the maximum current and ω is the pulsation of the current.

Using the classical formulas for the magnetic field induced by a linear shape circuit, the Lorentz force induced by the arcs and the electrodes at a point P_n of the arc n is given by :

$$\vec{F}(P_n, t) = -\frac{\mu_0}{4\pi} \frac{I^2}{\pi R_{arc}^2} \cdot \frac{3}{2} \sin \alpha \cdot p \int_0^{\frac{R}{r^3}} \frac{d\tau}{r^3} \quad (2)$$

$$\begin{pmatrix} -\cos\left(\omega t - (n-1)\frac{2\pi}{3}\right) \sin\left(\omega t - (n-1)\frac{2\pi}{3}\right) \\ \cos^2\left(\omega t - (n-1)\frac{2\pi}{3}\right) \cos^2 \alpha \\ \cos^2\left(\omega t - (n-1)\frac{2\pi}{3}\right) \sin \alpha \cdot \cos \alpha \end{pmatrix}$$

where, α : angle between an electrode and the axis of the reactor,

μ_0 : magnetic permeability of vacuum,

p : curvilinear abscissa of P_n along the electrode n , $p=0$ in O .

R_{arc} : radius of the arc

This force is centrifugal with a 2ω pulsation and is maximum in the vicinity of point O .

This result is relevant with a similar calculation on a slightly different geometry used in electrometallurgy [5].

2.4. Comparisons with experiments

Several high-speed cine-camera films (7000 FPS) have been made of the arc zone from the opened bottom of the reactor. Argon and nitrogen were used as plasma gas.

In the argon case, the simplified theory gives a good approximation of the forces applying on the arcs. The force given in (2) tends to blow the arcs outward as seen on the pictures. All sequences of pictures show arc shapes in agreement with the evolution of forces on each arc as illustrated on Figure 2.

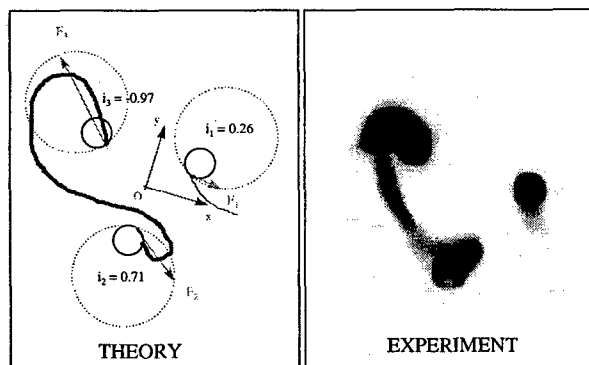


Figure 2. : Distribution of currents at electrodes and resulting Lorentz forces (left) with the corresponding picture from the high-speed cine-camera film (right).

In the nitrogen case, the arc movements are much more erratic and the interpretation is not completed yet.

3. Hydrodynamic model

The main characteristics of the hydrodynamic model of the reactor are given elsewhere [1][2]. In order to take into account the influence of the Lorentz force which cannot be neglected in the arc zone, the inlet velocity boundary condition of plasma gas has been changed. This kind of modification had already been suggested for three-phase AC metallurgical furnaces [6].

The best results of our computational laminar model were obtained with a 45° angle between the plasma gas velocity direction and the vertical axis, outwards. The distribution of calorimetric loss measured from the cooling system was less than 5% different in each part, compared with the numerical results. The wall temperature deduced from pyrometric measurements were also in good agreement.

4. Conclusions

A simplified theory to estimate the induced Lorentz forces in a three-phase AC reactor proved to be in good agreement with high-speed cine-camera pictures. In order to include the influence of these forces on the hydrodynamic flow, the plasma gas inlet velocity has been modified and the results of the simulation were in good agreement with experimental measurements.

5. References

- [1] L. Fulcheri, G. Flamant, B. Variot, B. Ravary, J.M. Badie, Characterisation of a 3-phase AC plasma reactor for carbon black synthesis from natural gas, ISPC 12, Minneapolis, MINNESOTA USA, Vol. 3, 1159-1164, (08/21-25/1995).
- [2] L. Fulcheri, G. Flamant, B. Ravary, F. Fabry, L. Menard, Characterization of a 3-phase A.C. Plasma process, 4th European Conference on thermal plasma processes, Athens 15-18 July 1996, to be published.
- [3] F. Fabry, L. Fulcheri, G. Flamant, J.M. Badie, B. Ravary, J.Y. Peroy, F. Fischer, J. Saint-Just, F. Kassabji, Heat and mass balance on a pilot plasma reactor for carbon compound synthesis from hydrocarbons, 4th European Conference on thermal plasma processes, Athens 15-18 July 1996, to be published.
- [4] G.R. Jones, M.T.C. Fang "The physics of high-power arcs" Rep. Prog. Phys., 43, 1980.
- [5] H.L. Larsen "AC electric arc models" Dr. Ing. Thesis, 1996.
- [6] P. Gardin, C. Soide, A. Dez & I. Guillaume "Use of physical and numerical simulation methods to characterize gas flow in trielectrode arc furnace" *Ironmaking & Steelmaking*, 19, 4, 1992.

EXPERIMENTAL ANALYSIS OF THE CARBON ARC FOR FULLERENE SYNTHESIS

K. Saidane, M. Razafinimanana, J. Pousse, A. Gleizes and S. Vacquié

Centre de Physique des Plasmas et de leurs Applications de Toulouse
ESA n° 5002, Université Paul Sabatier, 118 route de Narbonne 31062 Toulouse cedex 4, France

1. Introduction

Among the numerous processes allowing the production of fullerenes, the process based on the electric arc actually seems the most efficient technique for the quantitative production of this molecule [1/2/]. By this technique the carbon vaporisation is obtained by erosion of the graphite anode and the produced fullerenes are mixed with soots which settled on the cooled wall. In order to optimize this process by correlating the arc properties with fullerenes formation, it appears in a first time essential to choose arcing conditions allowing reliable spectroscopic measurements.

2. Experimental set up

The arc chamber, a hollow cylinder of 30 cm diameter and 1 m height is presented in figure 1. It has two windows to observe the arc. The two graphite electrodes of 6 mm diameter are located vertically in the centre of the arc chamber. The anode is in the upper position. Modification of the distance between the two electrodes and striking of the arc by contact was made possible from outside the chamber by means of a system allowing independent moving of the electrodes. Furthermore it is essential to control and maintain the gap length constant during the experiment. For that purpose, the image of the arc was projected on a photodiodes array coupled with a P.C. type micro-computer which drives the adjustment of the anode and cathode positions by independent motors.

The light emitted by the plasma was focused onto the entrance slit of a monochromator with a focal length of 1m and 1200 grooves/mm grating. On the outlet focal plane was placed a CCD array allowing analysis of plasma radiation. Radial exploration of the arc was made possible by means of a mirror enabling displacement in two directions. The whole spectroscopic analysis set up was driven by a PC micro computer. Electrical power was supplied by three DC sources of 100V and 100A each. Our working conditions were: 80A current intensity, 1mm and 4mm arc lengths and helium ambient gas at pressure of 13kPa.

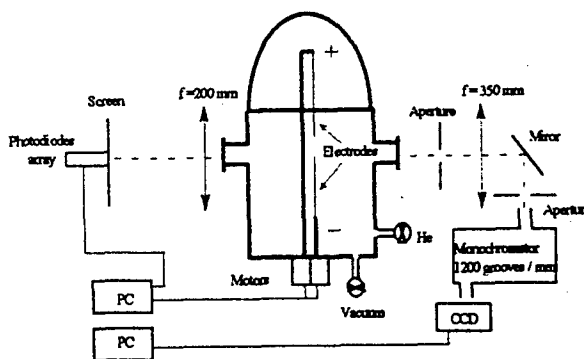


Figure 1: Block diagram of the experimental set up

3. Methods

Two emission spectroscopic methods based on the Swan band recording and assuming local thermodynamic equilibrium (L.T.E.) were carried out to determine the plasma temperature. The first one is based on the comparison of the experimental and the simulated Swan $C_2(0,0)$ rotational system spectra band as developed by Budo [3/]. The second one, in the region where the temperature is greater than 4500K, we have applied the Fowler-Milne method to the C_2 Swan band. Indeed, if the plasma is in LTE, the variation of the total intensity of a molecular band with temperature, at constant pressure, always presents a peak. The position of the peak, constant for a pure gas or a given mixture of gases, allows the isotherm ($T=T_m$) characteristic of the band in question to be deduced. In order for this technique to be applicable, the axis temperature must be greater than T_m : in the case of the Swan band studied in He-C plasma mixtures, this implies temperatures greater than 4500K. Moreover, the use of this method presents the advantage of obviating the requirement for calibration, in absolute values of the Swan band intensity.

Multiple measurements of the radial profiles of the arc were made under identical conditions. Statistical processing of the results was performed to increase their accuracy.

4. Results

The temperature profiles were strongly dependent on the experimental conditions and especially on the anode erosion rate. In figure 2 we report the recorded

anode and cathode displacement velocities during experimental acquisition time. One can mention that about 30% of the vaporized carbon due to the anode erosion deposit on the cathode surface, that explains the displacement in the same direction of the two electrodes as shown in figure 2. Different phases relative to the erosion of the anode were observed experimentally. Immediately after the arc is established, one can notice the existence of a phase which lasts about 8 minutes corresponding to a strong and relative uniform erosion of the anode and thus an important carbon vapour emission. The measured mean values of the anode erosion rate during this first phase are about 0.45g/mn and 0.15g/mn respectively for 1mm and 4mm arc lengths as shown in figure 3. The durable stability of the discharge relative to this first phase allowed us to develop emission spectroscopy methods. We have reported in figure 4 the temperature profiles at different positions z from the anode and for 1mm and 4mm electrodes gap. At $z=0.5$ mm and 1mm from the anode and for 4mm arc length, both methods were used; the two series of results relative to these cases gave a satisfactory agreement. The maximum value of the temperature on the axis does not exceed 5500K that confirms the cathode state slightly damaged during arc operating.

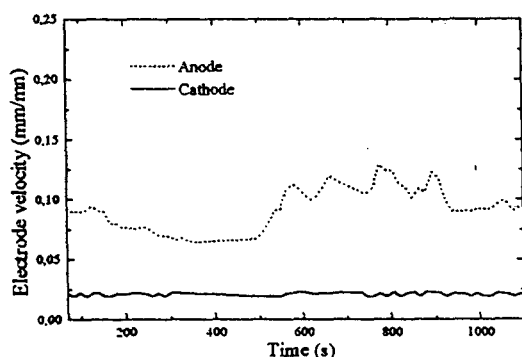


Figure 2: Electrodes velocities for 80A arc current.

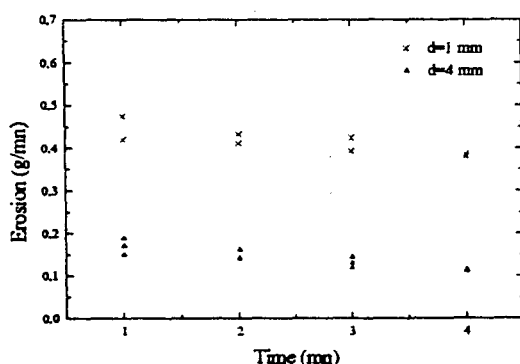


Figure 3: Anode erosion rate for two arc lengths and 80A current intensity.

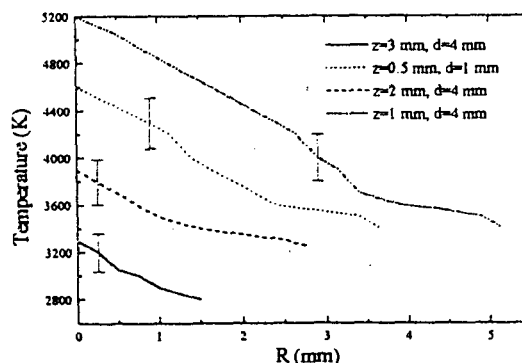


Figure 4: Temperature profiles.

5. Conclusion

The main difficulty in this study is the very fast evolution of the anode erosion. Thus, it was essential to perfect an experimental set up allowing to perform reliable spectroscopy measurements with a typical fullerenes reactor. The obtained experimental results concerning the plasma characteristics were consistent. The results we have obtained recently relative to the plasma temperature measurements by using the absolute intensities of the 247.8nm and 909.4nm CI neutral carbon lines seem to indicate an existence of departures from LTE. We intend in one hand to confirm these results and in the other hand to work with higher current intensities since the production of fullerenes was relatively weak (about 5%). Moreover, measurements of carbon concentrations fields will be the goal of the future work.

6. References

- /1/ A. Huczko, H. Lange, A. Resztak, P. Byszewski, High temp. Chem. Proc. 4 (1995) 125.
- /2/ C.N.R. Rao, T. Pradeep, R. Seshadri, R. Nagajan, V.N. Murthy, G.N. Subbanna, F. D'Souza, V. Krishnan, G.A. Nagannagowda, N.R. Suryaprakash, C.L. Khetrapal, S.V. Bhat, Indian J. of Chem. 31 A&B (1992) F5.
- /3/ A. Budo, Z.Phys. 98 (1936) 437.

Stabilization of plasma arcs when feeding with rectangular alternating currents of medium frequency

H.-J. Scheibe, H.-D. Musikowski

Otto-von-Guericke- Universität Magdeburg
Fakultät für Elektrotechnik
39016 Magdeburg / Germany

Introduction:

Application of plasma discharges operated at higher frequencies is of increasing interest for a number of plasma arrangements and procedures. It is beneficial to use advanced power electronics for discharge feeding utilizing dynamic current stabilization on IGBT basis. This allows to keep the commutation phases in the area of zero current much shorter than at sinusoidal current of medium frequency discharge. Therefore, the impact of the de-ionization time behaviour of the arc plasma on commutation will be reduced, thus allowing the operation of a stable electric arc even in plasma torches, subjected to a gas flow, without additional reignition aids. This paper describes some results obtained with regard to the impact of electric and plasma-technological parameters on the stability and changed performance parameters of the electric arc.

Methods:

Free burning electric arcs and plasma arcs in a plasma torch are fed by a current source with downstream inverter circuit whose control frequency is variable between 2 and 27 kHz. Commutation time is approximately 2 μ s. Current rise velocities of 150 A/ μ s are obtained. Fig. 1 shows the curve of the instantaneous value of current and voltage at the electric arc. Fig. 2 shows the arc power and di/dt values of the arc current.

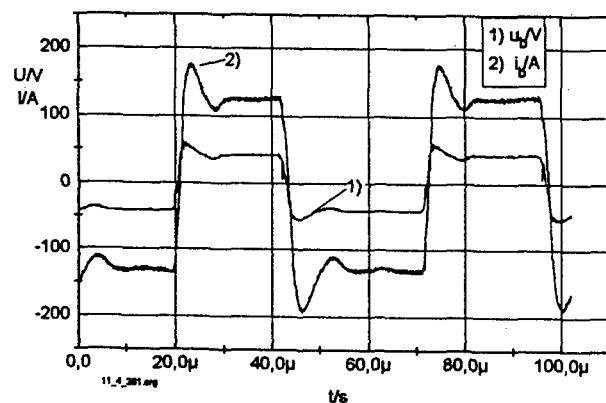


Fig. 1: Arc voltage $u_a(t)$ and current $i_a(t)$ of a free burning arc under Ar (distance of electrodes $d_{El}=5$ cm, electrodes of graphite, $I_{rms}=130$ A)

The parameters were obtained by minimizing parasitic impedances and a specific inverter control. The power $p(t)$ (Fig. 2) and the dynamic arc resistance $r_b(t)$ (Fig. 3) have been computationally corrected for the impact of a parasitic residual inductance of approximately 0.17 μ H [1].

Power pulses which are clearly to be recognized are due to the characteristics of the power electronic circuit rather than any changed arc discharge behaviour in the vicinity of zero current (see $r_b(t)$ in Fig. 3).

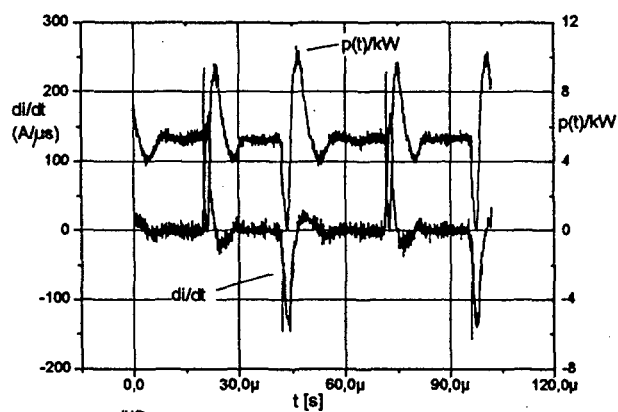


Fig. 2: Arc power $p(t)$ and current rise velocity $di/dt(t)$ of an arc according to Fig. 1

Comparative studies of the operational behaviour of an arc torch for free-burning arcs and a plasma torch set-up

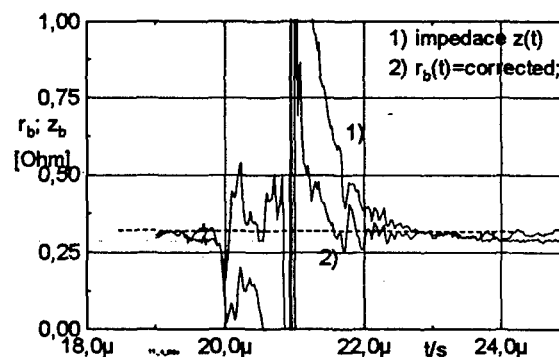


Fig. 3: Arc impedance $z(t)$ und arc resistance $r_b(t)$ in the vicinity of zero current Fig. 1

subjected to a gas flow (rod-shaped cathode $r_{Kat} = 2.5$ mm, hollow anode Cu $r_A = 6$ mm, $l_A = 62$ mm) aim to clearly show different properties and behaviours.

Results:

As expected, the investigations made on the free-burning arc under various inert gases (Ar, N_2 , H_2) with 10 to 50 mm spacing between graphite electrodes show a tendency of the r.m.s. values of the arc voltage under Ar to increase with increasing frequency (Fig. 4). This tendency was not found for molecular gases. Based on a comparative calculation on the basis of common electric conductances for argon arcs at the applied operating frequencies of up to 23 kHz and relevant harmonics (5th

harmonic still involved with 20% of the fundamental wave), the skin effect is not the main reason for the increase in the r.m.s. value of the arc voltage.

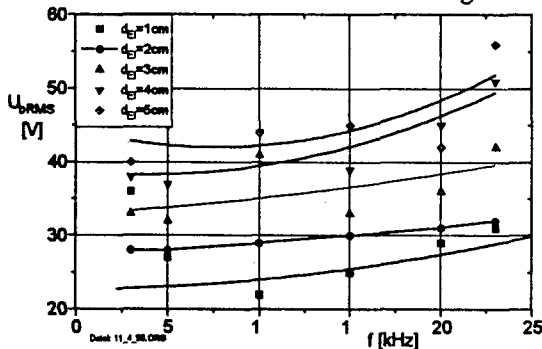


Fig. 4: Arc voltage dependence on frequency (Ar: 400 l/h; $I_{b, rms}=130$ A; parameter spacing between electrodes)

Considerable scattering of the values is primarily due to the much higher mobility of m.f. arcs compared with d.c. arcs. However, as the actual arc length cannot be quantified it does not make much sense to derive from these results a field strength characteristic.

The changed operating properties of m.f. arcs can be more clearly demonstrated in operating the plasma torch than the free-burning torch.

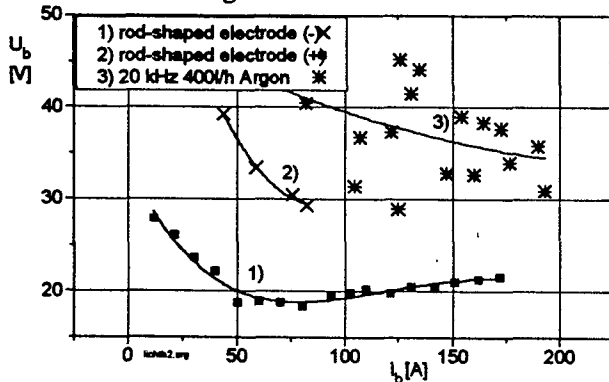


Fig. 5: Voltage characteristic of a plasma torch (rod-shaped tungsten electrode $r_W=2,5$ mm; copper hollow electrode $r_{Cu}=3$ mm; $l_{Cu}=53$ mm) 1); 2) dc-current; 3) mf-current

With all the other conditions comparable, the supply voltage of the arc when using alternating current of medium frequency (r.m.s. values) is considerably higher than when using direct current (arithmetic mean), (Fig. 5). This cannot be substantiated by the polarity effect on tungsten and copper electrodes alone (curves 1) and 2)). Caused by the temporary lack of the magnetic pinch during the commutation process the arc motion behaviour in the area of the hollow electrode is clearly pronounced even at small gas flow rates. This occurred in all gases subjected to investigation and it was particularly obvious in the case of nitrogen (Fig. 6). The control frequency was several times higher than the shunting frequency thus allowing an existing root of the arc to detach in current-free phases.

An analysis of the instantaneous value behaviour of a reduced current plasma arc under Ar (Fig. 7) shows a

tendency to reignition delays depending on polarity and gas flow rate.

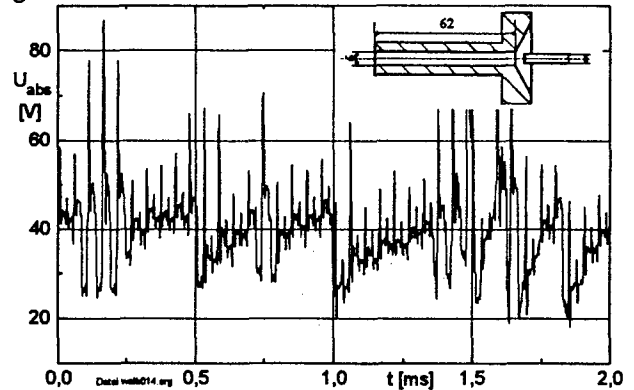


Fig. 6: Amount absolute of arc voltage of a m.f.-plasma arc under N_2

($I_{rms}=90$ A; $U_{rms}=42$ V; $\dot{V}_{N_2}=180$ l/h)

These delays may disturb stationary operation (zone A). They are caused by effects in the vicinity of the electrodes. This behaviour may be reduced by changing the available supply voltage.

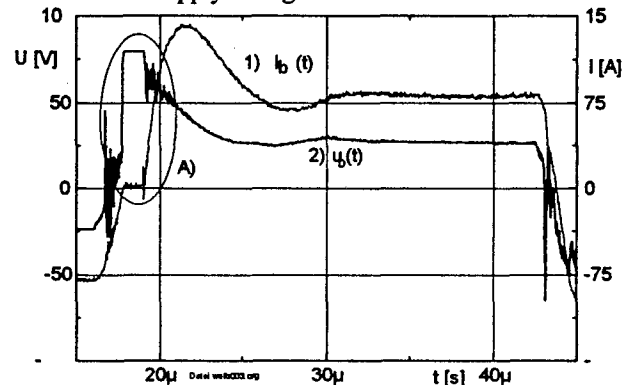


Fig. 7: Reignition behavior of a reduced current plasma arc during the positive potential on the tungsten rod-shaped electrode

($I_{rms}=60$ A; $\dot{V}_{Ar}=400$ l/h)

Conclusions:

Electric arcs and plasma arcs subjected to a gas flow can be operated at m.f. power supply. Caused by the commutation process, short-time current interruptions occur between half periods. Compared with d.c. operation, this approach allows to obtain beneficial changes in operational performance.

Even at low gas flow rates, improved mobility of the discharge channel results in a more intensive motion behaviour of the root of the arc in hollow electrodes and a tendency to better arc performances. Compared with d.c. operation, the considerable polarity effect and reignition delays, occurring at arc root areas subjected to a gas flow, point to the necessity of modifying the plasmatron design.

References:

- [1] Scheibe, H.-J.; Musikowski, D.; Hess, U: Workshop Computeranw. in d. Elektrowärmet., TU Ilmenau, 11.Okt. 1996.

RF-excitation of Cu ion laser transitions in He(Ne)-CuBr discharge

M.Grozeva, J. Schulze*, D.Teuner*, P.Telbizov, T.Petrov, N.Sabotinov, J.Mizeraczyk**, J.Mentel*

Institute of Solid State Physics, Bulgarian Academy of Sciences, 72 Tzarigradsko Chaussee, 1784 Sofia, Bulgaria

*Department of Electrotechnical Engineering, Ruhr-University, Universitätsstr. 150, D-44780 Bochum, Germany

**Institute of Fluid Flow Machinery, Polish Academy of Sciences, Fiszerka 14, PL-80952 Gdansk, Poland

1. Introduction

For the first time RF excited Cu ion laser was reported by Mikhalevskii et al. who obtained lasing at pulsed mode of excitation (100 μ s, 1 kHz) on three Cu ion lines in a transverse He-Cu⁺ discharge [1]. The copper atoms in the discharge were produced by RF sputtering of the internal copper electrode at excitation RF power of 2 kW (100 W/cm). Such high power was necessary mainly to produce the required copper atom density in the discharge.

An alternative method for producing free copper atoms is to seed the discharge with a copper halide. The use of volatile metal compounds as a source of metal vapor was successfully applied in the case of the CuBr atomic laser [2]. Later CW oscillation on Cu ion transitions in a hollow cathode (HC) discharge seeded with different copper halides was demonstrated [3]. Using copper halides instead of the elemental copper reduced the threshold current for lasing by a factor of 2-3 over those obtained for the sputtering HC discharge Cu⁺ laser [4].

We applied the same technique to develop a RF-excited Cu⁺ laser, using CuBr as a source of Cu atoms. The aim of the reported investigations was to study the possibilities for Cu⁺ lines excitation in a RF-excited He(Ne)-CuBr discharge and to obtain laser oscillation at a lower input power than in the case of the sputtering RF-excited Cu⁺ laser [1]. The emission spectra of He-CuBr and Ne-CuBr discharges were investigated. Laser oscillation on Cu⁺ transition in the near IR spectral region was obtained in He-CuBr discharge at pulsed and CW RF excitation. Laser gain on UV Cu⁺ lines was observed in Ne-CuBr discharge.

2. Spectroscopic study

To determine the discharge conditions at which efficient excitation of the Cu⁺ lines is attained we investigated the emission spectrum of RF-excited He and Ne discharges seeded with CuBr.

The experimental discharge tube (Fig. 1) was made of fused silica. The active part of the tube had 8 mm inner diameter and was 10 cm in length. At the middle of the

discharge zone a fused silica reservoir with CuBr was connected. Distilled in vacuum 98% pure p.a. CuBr from Fluka was used. The CuBr reservoir was heated separately in an oven and the CuBr vapor pressure was controlled independently from the RF power in the discharge.

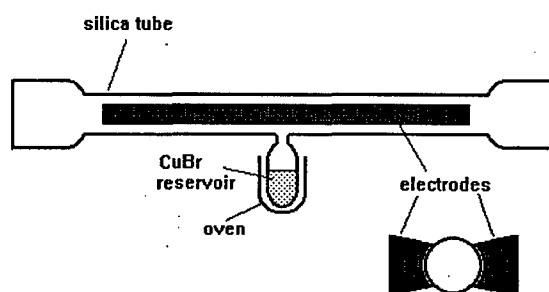


Fig. 1 Scheme of the discharge tube

The RF power was capacitively coupled into the discharge by two brass electrodes (10 cm in length, 8 mm wide) mounted along the quartz tube. The discharge was run by a generator operating at 13.56 MHz. The emitted light from the discharge was recorded by an optical simultaneous multichannel analyzer.

The emission spectra in the 740-800 nm spectral range in He-CuBr discharge and in the 240-300 nm spectral range in Ne-CuBr discharge were recorded at different RF powers and CuBr reservoir temperature. The copper ion lines intensities increased when increasing the CuBr reservoir temperature up to 500°C, the highest temperature at which stable discharge was obtained.

Efficient excitation of the copper ion laser states was achieved at RF input power 200 W, i.e. at linear power density of 20 W/cm. At a lower input power, in spite of the presence of copper atoms in the discharge, spontaneous emission on copper ion lines was hardly detected.

Except for the copper ion laser lines, no other copper ion lines were found even at higher than 200 W input power. That proves that efficient charge-exchange excitation [4] takes place at the examined discharge conditions.

3. Laser oscillation in He-CuBr discharge

Pulsed and CW lasing on four infrared Cu^+ lines (740.4 nm, 766.5 nm, 780.8 nm and 782.6 nm) was obtained in RF-excited He-CuBr discharge operated at two different frequencies: 13.56 MHz and 27.12 MHz.

3.1. Pulsed lasing

Pulsed oscillation on the 780.8 nm Cu^+ transition was obtained in a laser tube in which the CuBr was placed in the discharge volume and the discharge heating was used to evaporate the halide (Fig. 2). The laser tube was made of fused silica, the discharge channel was 400 mm long, with 8 mm bore diameter. A second fused silica tube was inserted in it, also 400 mm long, 5.5 mm bore diameter. Along its length a 4 mm slot was cut. Small pieces of CuBr were evenly spread in the internal tube under the slot. The role of the internal tube was to protect copper deposition on the inner surface of the discharge tube. The RF power was coupled in the discharge by two externally mounted brass electrodes, 400 mm long, 8 mm wide.

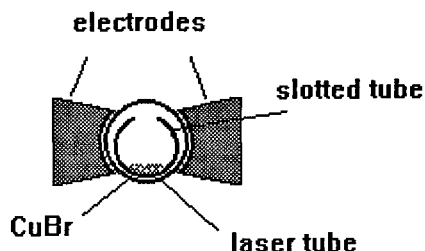


Fig. 2 Schematic cross-section of the laser tube

The discharge was excited by 27.12 MHz RF pulses with changeable pulse repetition rate from 1 kHz to 4 kHz and pulse duration from 40 μs to 150 μs . Laser oscillation was obtained at helium pressure from 1.8 kPa to 4.8 kPa, with an optimum at 4.0 kPa.

The lowest pulse power amplitude at which lasing was observed was around 500 W, which corresponds to 12.5 W/cm linear power density, much lower than the 100 W/cm necessary for lasing in the RF sputtering He-Cu system [4]. At optimal for lasing conditions: 4.0 kPa He pressure, 160°C tube wall temperature and 750 W pulse power amplitude (18.75 W/cm) a small-signal gain of 8%/m was measured at 780.8 nm Cu^+ laser line.

3.2 CW lasing

The second tube had a design similar to that used for He-Cd capacitively-coupled RF-excited laser [5]. The active volume was confined by a ceramic capillary 40 cm long and 4 mm in diameter. At the middle of the active zone a side-arm reservoir with CuBr was connected. From this reservoir the CuBr vapor diffused to the active discharge region where it was dissociated into Cu and Br atoms. The CuBr reservoir was heated separately up to 450°C and the vapor pressure was controlled independently of the RF excitation power.

Using this tube CW oscillation on four near-IR Cu^+ transitions (740.4 nm, 766.5 nm, 780.8 nm and 782.6 nm) was obtained at 13.56 MHz excitation frequency. The laser power of all lines increased linearly with increasing input power from 400 W up to 800 W. The maximum input power was limited due to arcing between the electrodes. For the 780.8 nm line which is the strongest line, an output power of 10 mW was achieved at an optimum He pressure of 7 kPa and input RF power of 800 W.

4. UV Cu^+ lines excitation in Ne-CuBr discharge

The obtained reducing of the excitation power in He-CuBr RF-excited discharge suggested that the power necessary for excitation of the UV laser transitions of Cu^+ might be reduced also in Ne-CuBr RF-excited discharge.

Using Ne as a buffer gas, in the same tube in which CW lasing was obtained, we observed laser gains on the following 14 UV Cu^+ lines: 240.3 nm, 242.4 nm, 247.3 nm, 248.6 nm, 249.6 nm, 250.6 nm, 252.9 nm, 254.5 nm, 259.1 nm, 260.0 nm, 270.3 nm, 271.4 nm, 271.9 nm, 272.2 nm. The strongest line was the 248.6 nm line with an optimum Ne pressure at 1 kPa.

5. Conclusions

For the first time laser oscillation on Cu^+ lines using dissociation of copper-halide in RF-excited discharge was reported. The threshold input power for lasing was reduced about 5 times compared to that reported for the sputtering RF-excited Cu^+ laser. CW laser action on IR Cu^+ lines at RF excitation was obtained. Laser gain in the UV spectral range was observed in Ne-CuBr discharge.

Acknowledgment

This work was supported by the European Commission Copernicus Programme CIPA-CT 93-0219.

References

- [1] E. Latush, V. Mikhalevskii, M. Sem, G. Tolmachev, and V. Khasilev, *Pisma ZETF* **24** (1976) 81.
- [2] N. Sabotinov, *Pulsed Metal Vapor Laser*, eds. C.E. Little and N. Sabotinov, Kluwer Academic Publishers (1995) 113.
- [3] J.A. Piper and D.F. Neely, *Appl. Phys. Lett.* **33** (1978) 621.
- [4] D.C. Gerstenberger, R. Solanki, and G.J. Collins, *IEEE J.Quant.Electron.*, **QE-16** (1980) 820.
- [5] N. Reich, J. Mentel, J. Mizeraczyk, *IEEE J. Quantum Electron.*, **QE -31** (1995) 1902.

Investigation of Arc Spot Ignition on Cold Electrodes by Emission Spectroscopy

M. Schumann, D. Nandelstädt, A. Korbel, J. Schein, and J. Mentel
Ruhr-Universität Bochum, Lehrstuhl für AEEO, D-44780 Bochum, Germany

1. Introduction

In preceding investigations measurements were made in air with 24 different materials of the so called arc spot formation delay time or commutation time t_c [1]. This is the time which is needed to initiate the formation of arc spots on cold electrodes after applying an electric field between an arc and a third electrode biased either negatively or positively against the bulk plasma.

The most important result of these investigations was that this arc spot formation delay time measured for freshly polished electrodes is independent of the bulk properties of the electrode material like work function or electrical conductivity. Another result was that this arc spot formation delay time is very sensitive on variations of the surface structure. SEM investigations were made revealing that the crater structure left by the ignition at the electrode surface is depending on the surface structure [2], [3].

To investigate the ignition of arc spots on cold cathodes under defined conditions and in a defined gas atmosphere a special experimental set-up was developed which is given below [4], [5]. The ignition of arc spots on the cathode was investigated as well by high speed photography as by electrical measurements. The arc traces of short current pulses were examined by in situ optical microscopy of the cathode surface.

Two different modes of arc spot ignition were observed: an initiation by a diffuse glow discharge which may pass into a constricted arc spot and an immediate formation of a constricted arc spot.

The two modes of arc spot ignition at atmospheric pressure were attributed to different surface structures, which can be characterized by the field enhancement factor [6], [7]. Field enhancement by microprotrusions may raise the local electron emission more than any known depression of the work function. A sufficiently high density of small emission sites produces by field emission locally such a high average current density that a plasma channel and an arc spot on the cathode surface is formed. With lower pressure the influence of the surface structure is reduced and pushed back by TOWNSEND- γ emission.

Characteristic spectra of the filling gas and the commutation electrode could be related to the different modes and are given further down.

2. Experimental Set-Up

The experimental set-up shown in Fig. 1 consists of a pair of horn electrodes with an anode A and a cathode C between which an arc is ignited by high voltage

breakdown. After the ignition the arc operated with a current of 25 A is blown magnetically against a diaphragm (D) positioned horizontally above the horn electrodes.

The commutation electrode (CE) is positioned behind a small aperture (diameter 2 mm) in the center of the diaphragm ensuring the ignition to take place definitely in an area of 1-2 mm². The voltage between the arc plasma and the grounded CE, given by the voltage drop of the resistor R_k , amounts to 250 V in this experiment. Up to eight CE's are fixed on the circumference of a revolver (R), turned successively behind the hole. The whole discharge arrangement is enclosed in a vacuum tight chamber made of high grade steel which is pumped to UHV and filled with pure gases. The chamber is equipped with windows for optical observation of the ignition, which is possible with sufficient spatial resolution by reason of the special set-up. A detailed description of how the experiment takes place is given in [5], [6].

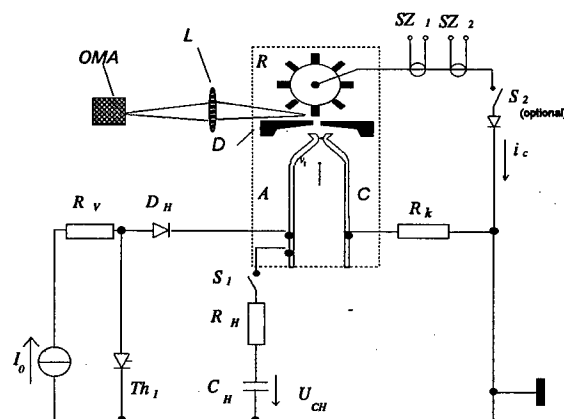


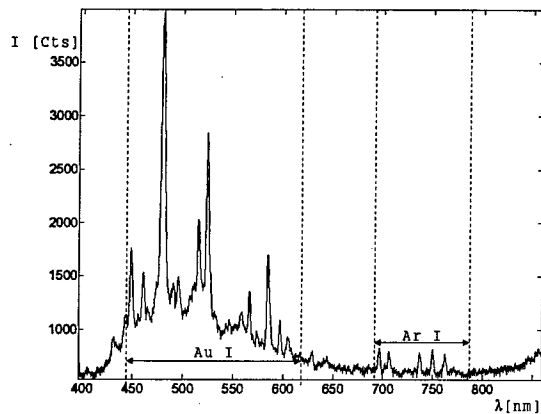
Fig. 1: Set-up with horn electrodes with A: anode; C: cathode; D: diaphragm with aperture; R: electrode revolver equipped with 8 commutation electrodes CE; OMA: optical multichannel analyser; lens L; SZ₁, SZ₂: current probes measuring i_c through CE. Ignition circuit formed by C_H , R_H and S_1 charged onto the voltage U_{CH} . Main circuit formed by current source I_0 , R_v , R_k , and diode D_H .

3. Measurements

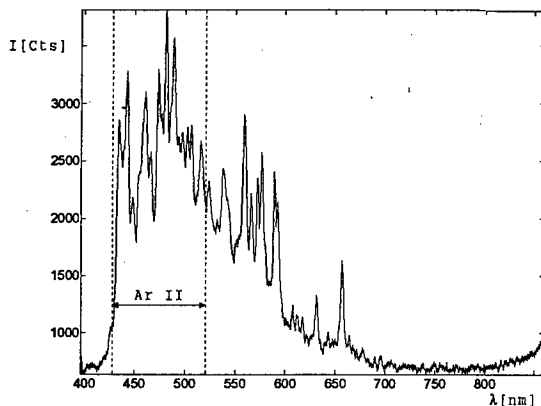
Forty ignitions in turn were made on a single electrode in pure Ar before it was replaced. Thereby the electrode surface changes from ignition to ignition. As well does the ignition itself which takes place as mentioned above in two different modes.

In the first case the ignition is initiated by a precurent larger than 1 mA lasting up to several μs . This precurent is characterized by two parameters, the

maximum precurrent i_v and precurrent flow time t_v [6]. A luminous layer becomes visible. With increasing current, a channel is forming which starts from the luminous layer and leads to the bulk plasma. In the second case an initiating precurrent could not be detected with the measuring device of this experiment. A bright plasma ball is formed in front of the cathode spanning the gap between an unstructured bulk plasma and the cathode [4], [6].



a)



b)

Fig. 2: Spectrally and spatially resolved representation of light emission in front of the CE. Its diameter is given on the right side: a) Emission of the luminous layer, Au I, Ar I: atomic Au- and Ar-lines; b) Emission of the plasma ball, Ar II: lines of single ionized Ar.

The spectrally and spatially resolved emission in front of an Au-electrode in Ar is shown in Fig. 2. Fig. 2a gives the emission of the luminous layer. It extends

over the whole electrode surface and comprises of atomic lines of the electrode material and of the filling gas Ar. Similar results are also found for cathodes made of Cu and Al. Fig. 2b represents the emission of the plasma ball. It is concentrated in a small spot with a diameter of 100-300 μm and consists mainly of ion lines of the filling gas Ar. Similar spectra are emitted by the plasma channel forming after the luminous layer. Principally the same spectra are also found for electrodes made of Cu, Al, and W, however not for graphite.

4. Conclusions

Two different kinds of arc spot ignition on cold cathodes have been identified, the modes of diffuse and constricted current transfer. It has been shown that these different kinds of current transfer emit very different optical spectra. The atomic lines of the electrode material emitted by the luminous layer indicate that electrode material is vaporized presumably by a destruction of electron emitting microprotrusions. The ion spectrum of the constricted arc spot reflects a high electrical power input into the arc spot.

Acknowledgment

This work was supported by the Deutsche Forschungsgemeinschaft grant SFB 191/A3.

References

- [1] J. Mentel, R. Bayer, J. Schein, M. Schumann, "Arc Spot Ignition on Cold Electrodes in an Ambient Gas Atmosphere," in *Phenomena in Ionized Gases*, K. H. Becker et al., Eds., Woodbury, New York: AIP Press, 1996, pp. 278-288.
- [2] K.-P. Nachtigall and J. Mentel, "Optical Investigation of Arc Spot Formation on Cold Cathodes in Air," *IEEE Trans. Plasma Sci.*, vol. 19, no. 5, pp. 947-953, 1991.
- [3] R. Bayer, J. Schein, M. Schumann, J. Mentel, "Optical Investigation of the Interaction of a Dense Plasma with Cold Cathodes in Air," *IEEE Trans. Plasma Sci.*, to be published.
- [4] J. Schein, M. Schumann, and J. Mentel, "Optical Investigation of Arc Spot Formation on Cold Cathodes in Noble Gas Atmosphere," *IEEE Trans. Plasma Sci.*, vol. 24, no. 1, pp. 59-60, 1996.
- [5] J. Schein, "Untersuchung der Wechselwirkung eines dichten Plasmas mit kalten Kathoden," Ph.D. dissertation, Ruhr-Universität Bochum, Germany, 1996.
- [6] J. Schein, M. Schumann, and J. Mentel, "Analysis of Arc Spot Ignition on Cold Lamp Electrodes," in *Conf. Record 1996 IEEE IAS, 31st IAS Annual Meeting*, vol. 4, pp. 2155-2161.
- [7] R. V. Latham, *High Voltage Vacuum Insulation*, London: Academic Press, 1981 and 1995.

Experimental Study of Cathode Region of Pulse High Current Free Burning Arc in Argon at Atmospheric Pressure

N.K.Mitrofanov and S.M.Shkol'nik

A.F.Ioffe Phys.-Techn.-Inst. Rus.Acad.Sci., Polytechnicheskaya 26, St.Petersburg 194021, Russia

1. Introduction

The cathode processes in atmospheric pressure arcs are studied for a long time. A theory of arcs with a tungsten thermionic cathode in inert gas is well advanced [1]. The experimental studies of such arcs are numerous [2,3]. An experiment and a theory do not contradict qualitatively one another: both in calculations and in experiments a weak dependence of a current density on an arc current, a falling voltage-current characteristic of near-cathode layer are observed. The quantitative distinctions also are not too great. One of the major characteristics of cathode region is a potential difference between a cathode and undisturbed plasma - a cathode potential drop V_c . In the review [1] results of comparison between V_c measurements and V_c calculations, obtained by various methods, are presented. At currents $I = (10^2+10^3)$ A in Argon the measured values of V_c are within limits of $(10+6)$ V and the calculated ones - $(12+5)$ V. Recently the calculations giving a significantly different result are published: V_c changes from 27 V up to 17 V while I is varied from 99 up to 971 A [4].

In general terms the most correct method of an electrode drop measurement is the probe technique. Such methods as the short arc voltage and calorimetric measurements have large limitations and repeatedly came under criticism. However, the probe diagnostics of a strongly ionized plasma at atmospheric pressure was not elaborated till now. It is wide-spread point of view stated in [5] on basis of qualitative consideration only that a plasma potential V_{pl} differs from a floating probe potential V_f by $(1+2)$ V. It has resulted, as the recent investigation [6] showed, in large errors of V_{pl} and so V_c determination. Recent results of the atmospheric pressure strongly ionized plasma probe diagnostics elaboration [7] were used in the present investigation.

2. Experimental setup and procedure

To perform the studies the same experimental setup as in [7] was used. The cathode was a tungsten $\varnothing 2$ mm stick with a semispheric tip. The stick was pressed in a copper water-cooled holder. The extended part was of 8+10 mm length. The copper water-cooled anode was located 12 mm above the cathode. In parallel to an on duty d.c arc (50+70) A the generator of single rectangular (≤ 1000 A) pulses of a duration up to 5 ms was connected. A pulse front when a discharge gap shorted was ~ 0.1 ms.

A spherical probe $\varnothing 0.5$ mm was shot at velocity ≥ 1 m/s through the arc channel core zone. The probe location was determined with accuracy of about 0.3 mm.

To record an arc emission spectrum a monochromator coupled with an optical analyzer was used. The spatial resolution was ≤ 0.3 mm. In one exposure a spectrum range of 25 nm was recorded. To measure a radial distribution of a spectral line intensity the analyzer camera was turned through 90° . The distribution was subjected to the Abelian inversion procedure. An analyzer start delay was set to match by an instant of probe travelling through the near-axis zone of an arc.

3. Experimental results and discussion

The range of I under examination was (250+550) A. An arc appearance at a fixed voltage of the pulse generator could change from one pulse to another. Visual observations have shown that those changes are due to either a displacement of an on duty arc attachment from a tip of the cathode or to a strong droplet erosion (at the maximum currents) in a pulse arc. The data obtained in such cases were rejected. The measurements were considered as related to the same arc mode if a current and a voltage had changed not more, than with 5 %. Measurements have shown that a current and a voltage of an arc reach new quasistationary values at $\tau \geq 1$ ms after the beginning of a pulse. Series of measurements with various delays were carried out which has shown that both spectroscopical and probe measurements at $\tau \geq 1$ ms did not depend on time. The estimation shows that during about 1 ms a temperature wave in tungsten will run a distance $\sim r_c$ (r_c - an arc attachment radius on the cathode). All mentioned above allows to consider that when we perform our measurements (3+4) ms after the pulse beginning we determine arc parameters in a quasistationary state. It is obvious that thermal mode of the cathode differs from that of d.c. arc. It should be noted that the cathode thermal mode in d.c. arc depends on conditions of the cathode cooling, i.e. on a specific design of a cathode unit. So it is necessary to take this circumstance into account when the results are compared.

The plasma temperature was determined from relative intensities of ArIII spectral lines ($\lambda = 330.19, 331.12, 333.61, 334.47$ nm). At $I > 250$ A it is necessary to use ArIII lines because they appear rather sensitive to a change of plasma temperature unlike ArII lines. The diameter of the luminous channel which we accepted

equal to that of the current channel was determined from width of radial distribution of ArIII line intensity at half of a profile height.

The dependence of plasma temperature T measured at $z \approx 0.6$ mm from the tip of the cathode on current is shown in fig.1. At $I > 450$ A a satisfactory agreement

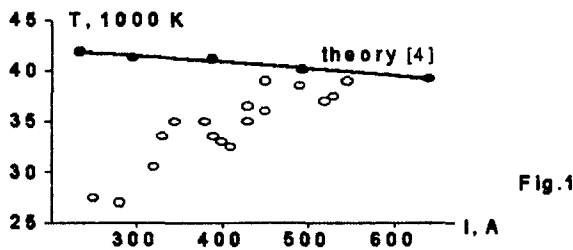


Fig.1

between the experiment and the calculations [4] is observed. However, at lower currents one can see a distinction between the calculated and experimental values which is far greater than the experimental data scatter. This fact may be explained by that the experiments and the calculations are performed at various distances from the cathode. A plasma temperature was calculated on an external boundary of the region of equalization of electrons and heavy particles temperatures which extent was estimated in [4] as 10^{-2} cm. The spatial resolution does not allow to perform the measurements so close to the cathode. The expansion of a current from the cathode attachment, a decrease of a current density j can results in a decrease of T . However, the measurements show that at $I > 450$ A close to the cathode ($z \leq 1$ mm) the diameter of the luminous channel does not practically changes as well as plasma temperature. It forms something like the slightly extended channel with high temperature in which a main current flows. It is conceivable that this is due to effect of a current self-magnetic field. At lower currents this phenomenon appears only slightly and insufficient spatial resolution results in that the measurements are carried out in the region with a temperature lower than that at the external boundary of the cathode layer.

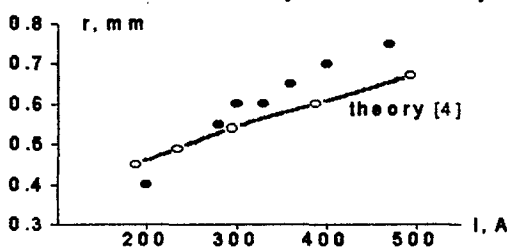


Fig.2

The dependence of the current channel radius on an arc current is shown in fig. 2. In the same figure the results of calculations [4] are presented. The results obtained show that an arc current density near the cathode is approximately constant in the investigated current range and averages $j \approx 3 \cdot 10^4$ A/cm². It should be noted that it is an estimation only.

The results of probe floating potential V_f measurements at $z \approx 1.0$ mm from tip of the cathode are shown in fig. 3. In the same figure the results of measurements [5,8] and calculations [4,9,10] are presented too. One can see that the V_f measurement results obtained in the present work

are in agreement with the previous results [5,8]. However, in [5,8] V_f was identified with V_{pl} to an accuracy within (1 ± 2) V and one can see that these results does not contradict with the calculations [9,10].

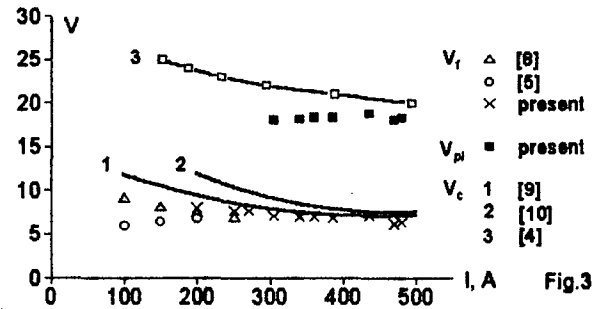


Fig.3

According to results of [7] we consider that V_f differs from V_{pl} rather considerably and at $T = (2.5 + 3.5)$ eV the difference $(V_{pl} - V_f)$ reaches (11 ± 12) V. The plasma potential values with respect to the cathode V_{pl} recalculated in accordance with [7] is also presented in fig. 3. The obtained values V_{pl} are close to the calculation results [4]. However, while determining the cathode potential drop V_c it is necessary to take into account the potential difference ΔV between the external boundary of the cathode layer and the point where the probe measurements were carried out. It is not a simple task. The rough estimation is of no interest in this case. So the value V_{pl} measured in present work can be compared with calculations in which not only the cathode layer but an arc as a whole is performed.

4. Acknowledgement

The research described in this publication was made possible in part by Grants № R5D000 and № R5D300 from the International Science Foundation

5. References

- [1] A.M.Zimin, I.P.Nazarenko, I.G.Panevin, V.I.Khvesiuk: Mathematical Simulation of Cathode Processes, Nauka, Novosibirsk, (1993) 194 p. (in Russian)
- [2] M.F.Zhukov, N.P.Kozlov, A.V.Pustogarov et al.: Electrode Processes in Arc Discharges, Nauka, Novosibirsk, (1982) 160 p. (in Russian)
- [3] V.F.Gordeev and A.V.Pustogarov: Thermionic Arc Cathodes, Moscow, Energoizdat, (1988) 192 p. (in Russian)
- [4] M.S.Benilov and A.Marotta: J. Phys. D: Appl. Phys., **28** (1995) 1869
- [5] W.Finkelburg, H.Maecker: Elektrische Boegen und thermisches Plasma, Handb. Phys., XXII (1956) 254 p
- [6] F.G.Baksht, A.Rybakov: Tech. Phys., **67** (1997) (in Russ)
- [7] F.G.Baksht, N.K.Mitrofanov, A.B.Rybakov and S.M.Shkol'nik: Proc.ICPIGXXIII(1997)Toulouse, France
- [8] B.S.Gavrjutshenko, R.Ya.Kucherov, A.V.Pustogarov et al.: J. Tech. Phys., **45** (1975) 2119 (in Russian)
- [9] W.Neumann: Beitr. Plasmaphys.: **9** (1969) 499
- [10] A.M.Zimin, N.P.Kozlov, V.I.Khvesiuk: Izv. SO Acad. Sci. USSR, Ser.Tech.Sci., **8** (1979), 17 (in Russian)

EXPERIMENTAL MEASUREMENTS ON A DC PLASMA TORCH: COMPARISON WITH THEORETICAL MODEL

N. Singh, J.M. Bauchire, M. Razafinimanana, J.J. Gonzalez, A. Gleizes

Centre de Physique des Plasmas et de leurs Applications de Toulouse
ESA n° 5002, Université Paul Sabatier, 118 route de Narbonne 31062 Toulouse cedex 4, France
Phone: +33-05-61-55-60-20 Fax: +33-05-61-55-63-32 e-mail jjg@cpa11.ups-tlse.fr

1. INTRODUCTION

This paper presents results obtained in an experimental study of a DC plasma torch. Measurements have been made on an argon plasma jet discharging into an argon environment at atmospheric pressure. We have studied the influence of the total current intensity and of the inlet gas flow rate on the characteristics of the plasma: temperature field and drop voltage.

The experimental results were compared with those predicted by our model relative only to the free jet region. The inlet conditions are given by theoretical laws classically used by other authors on the same subject.

2. EXPERIMENTAL

The DC plasma torch and the details of the experimental arrangement are given in [1]. The argon plasma jet exits into a chamber filled with argon maintained at atmospheric pressure. The typical working conditions were current intensities in the range 100 to 200A; gas flow rates varying from 15 to 35NL/mn. Emission spectroscopy method was used to determine the temperature at the nozzle exit. The measurements were carried out on the 696.5nm argon neutral line. The plasma was assumed to be in LTE. The statistical error in the determination of the temperature was estimated to be about 5%.

- Electrical characteristics

On **figure 1** is shown the variation of the drop voltage versus the current intensity for different gas flow rates. The arc voltage decrease observed is linked directly to the attachment between the arc and the anode [2]. At a fixed current and for a higher gas flow rate $D=30\text{NL/mn}$, the constriction of the plasma is enhanced and as a result the diameter of the plasma is reduced. The arc moves along the anode and attaches itself upstream further from the cathode. These results are in good agreement with those of [3]. It is noteworthy that the arc voltage for $D=30\text{NL/mn}$ tends towards a stabilised value at higher current intensities. This increase of the net power transferred to the plasma with an increase of the gas flow rate is well known. In their works, Capetti and Pfender [4] observed an increase of about 30% of the net power transferred to the plasma using a current intensity around 400A when the gas flow rate increased from 23.6 to 47.2 NL/mn. In our

case this increase is about 4 and 9% respectively for 50 and 180A and for a change on the gas flow $D=20$ to 30NL/mn .

- Temperature profiles

The influence of current intensity and gas flow rate on the temperature of an argon plasma discharging into an argon environment was studied. **Figure 2** shows the influence of gas flow rate for a current intensity $I=100\text{A}$ at two axial positions $z=1$ and 10mm from the nozzle exit. The increase in gas flow constricts the plasma jet and the temperatures near to the axis increase; the constriction is more pronounced with lower z values. The current has a more significant effect on the temperature profiles. An increase of the current intensity has a repercussion on the enthalpy of the plasma. Indeed the power applied to the torch is increased and also the gas velocities, leading to a lengthening and broadening of the plasma plume.

3. THEORETICAL MODEL

A mathematical 2D model limited to the free jet region was developed by using Patankar's [5] resolution model. The mathematical formulation was based on the main following assumptions: we consider an axisymetrical configuration in a steady state and in laminar flow conditions. The plasma was assumed to be in L.T.E and the radiation is treated using the net emission coefficient. At the inlet (nozzle exit) the temperature and the axial component of the velocity are given by:

$$u(r) = u_0 \left(1 - \left(\frac{r}{R} \right)^n \right)$$

$$T(r) = (T - T_0) \left[1 - \left(\frac{r}{R} \right)^n \right] + T_w$$

where u_0 and T_0 are the maximum experimental values of the axial velocity and temperature on the axis (at the exit). T_w is the value of the temperature on the edge of the anode ($n=2$). The mathematical model and the equations used in the entire domain are described in previous works [6]

4. DISCUSSION

On **figure 3** we present the axial temperature versus the distance from the nozzle exit. The current intensity

$I=100A$ and the inlet gas flow rate is $D=20NI/mn$. There is a satisfactory agreement between the calculated and the measured values. The axial temperature T_0 is equal to $11000K$ at $z=0mm$. The maximum velocity is not given but calculated via the knowledge of the temperature profile imposed and the inlet gas flow rate. On **figure 4** we give the temperature profile at $z=2cm$ from the exit. There is reasonable agreement between experiment and theory, especially in the hotter regions of the plasma ($r<1.5mm$); however, there are discrepancies in the cooler regions. The difference between the modelling and experimental results becomes larger for temperatures below $9000K$ and may be attributed to three reasons. Firstly, the signal becomes weak in the cooler regions of the plasma and the temperature values at the plasma edge are not that precise. Secondly, the higher temperature values given by the model at the plasma edge is linked to the boundary conditions imposed by the model. Thirdly, the discrepancies may be due to departure of the plasma from LTE. A systematic comparison was made with the experimental results, using two values of the gas flow rate 20 and $30NI/mn$ and considering two current intensities $100A$ and $200A$ at different values of z from the nozzle exit.

5. REFERENCES

- [1] J.J. Gonzalez et al, TPP4, Greece 15-18 July (1996)
- [2] S. Paik et al, Plasma Chem. Plasma Process, **11**, 379 (1993)
- [3] O. Betoule, Thèse (PhD), Univ. de Limoges, France (1994)
- [4] A. Capetti and E. Pfender, Plasma Chem. Plasma Process, **9**, 329 (1989)
- [5] S.V. Patankar, "Numerical Heat Transfer and Fluid Flow", McGraw-Hill (1980)
- [6] Gonzalez J.J et al, FSO96, Czech Republic 14-18 October (1996).

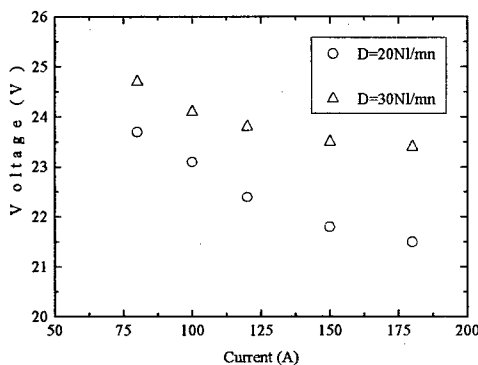


Figure 1 : Voltage current characteristics of the plasma torch

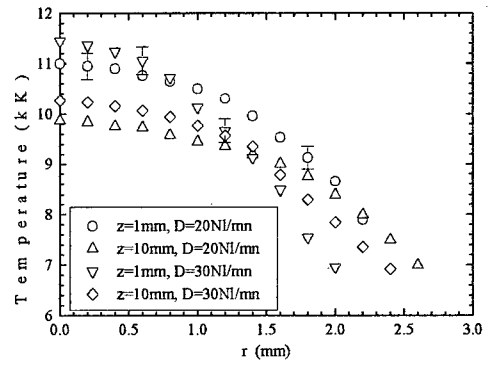


Figure 2 : Temperature profiles at different axial positions for $I=100A$ and $D=20$ and $30NI/mn$ in argon

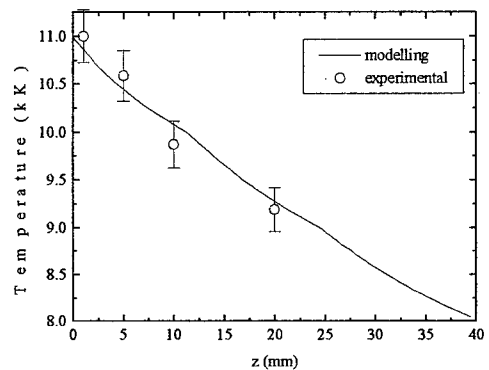


Figure 3 : Comparison of axis temperature for $I=100A$ and $D=20NI/mn$

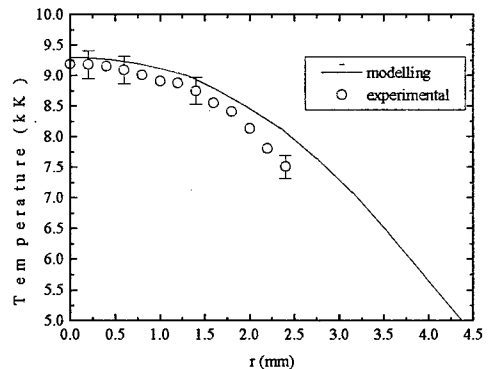


Figure 4 : Comparison of temperature profiles at $z=2cm$ for $I=100A$ and $D=20NI/mn$ in argon

STUDY OF THE PHYSICS PHENOMENA IN THE DISCHARGE CHAMBER OF AIR PLASMA GENERATOR WITH COPPER ELECTRODE FOR METALS CUTTING

Tudor Stanciu, Victor Pogora, Ion Protuc
 Technical University of Moldova (T.U.M.)
 168, bd. Stefan cel Mare, Chisinau, 2012,
 Republic of Moldova

1. Introduction

The metal cutting technology based on air plasma arc is widely used in different industrial applications. A new type of plasma generators based on copper electrode with cavity has been developed in the Technical University of Moldova [1]. One of the most important elements of the plasma generator in which a lot of different physical processes take place which deal with the transformation of the electrical energy in the thermal one is the electric arc discharge chamber.

2. The physical processes in the discharge chamber of the plasma generator

The discharge chamber of the generator consists of the copper electrode with a cavity 1 and the nozzle 2 separated by the rotator 3 (fig. 1). In the same time the last allows a tangential transport of the air into the discharge chamber.

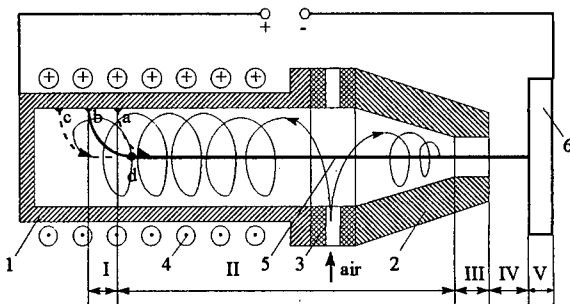


Fig. 1. The scheme of the chamber of air plasma generator based on cooper electrode with cavity

Normally the electric arc 5 occurs between the electrode and the object 6. From the physical point of view all the electric arc energy can be divided into 5 energetic zones, three of which are located into the discharge chamber. In the zones I-IV of the arc the processes of the molecules dissociation, atoms excitation, ionisation and recombination, and the photoemission take place.

In the first zone the radial part $b-d$ and the spot of the arc rotate and move on the surface of the electrode

cavity in the limits of the area $a-c$. The length of this area is determined by the balance between the gasodynamic and electrodynamic forces which are caused by the interaction of the radial part of the electric arc and the magnetic fields of the electric arc and of the winding 4 under the electric current. From the thermal point of view the electrode 1 is in the most disadvantages conditions, namely the parts on which are located the anode spot or the cathode spot of the electric arc. The life time of this electrode depends directly on the erosion speed which depends in turn on the current intensity value, on the thermal flow on the arc base spot as well as on the electrode polarity. The experimental results show that the current intensity value for the negative polarity in the centre of the cathode spot is 10 times greater and the current spot is 2 times less then for the positive polarity [1]. The electrode erosion depends mainly on the constructive parameters (electrode cavity diameter d_e and length l_e , the nozzle channel diameter d_n , the current intensity value in the arc I , the air debit G_a and the magnetic field solenoidity $I \cdot W$). The mathematical model of the specific erosion γ of the electrode with cavity has been obtain from the experimental results and is described by the following linear equation,

$$\gamma = [1.25 + 0.72 \cdot l_e - 0.39 \cdot d_e + 0.14 \cdot d_n + 0.38 \cdot G_a - 0.16 \cdot I \cdot W] \cdot 10^{-6} \text{ g} \cdot \text{C}^{-1} \quad (1)$$

In zone II the electric arc is on the action of turbulent flow of the gas being stabilised along the discharge chamber axis. When the electric arc passes through the nozzle channel (zone III) it is contracted in the radial direction. When quitting the nozzle the electric arc is dilated slightly. In the metal the electric arc is constraint into its own cut.

The presence of the tangential component of the air speed in the discharge chamber brings to the separation of the electric arc on the walls of the electrode and nozzle. As a result the difference of potentials appears between the electric arc and the walls. That is why breakdowns take place between the electric arc and the walls in the electrode with cavity as well as in the nozzle. In the electrode with cavity this breakdown causes a decrease of the arc length and does not present any danger. The breakdown between the electric arc

and the nozzle however can destroy the nozzle due to the cascade firing of the electric arc: electrode-nozzle-metal.

During the metal cutting process the nozzle is neutral from the electric point of view and it serves to concentrate the energy in the working zone as well as to stabilise the electric arc in space. In the same time the nozzle, being neutral, is a good collector or emitter (depending on the polarity of electrode with cavity) of the charged particles which penetrate from the electric arc through the separating gap due to the processes of diffusion, gas photoionisation and photoemission. In the normal mode of the generator functioning a non autonomous discharge takes place in the isolating gap with a small value of the leakage current which depends on the resistance of the isolation. This resistance is non linear and depends mainly on the gas temperature in the isolation gap which varies widely in dependence on the plasma generator parameters.

From the radial distribution of the plasma temperature at the exit from the nozzle and considering that the temperature distribution in the nozzle channel is practically the same the following three zones can be outlined (fig. 2).

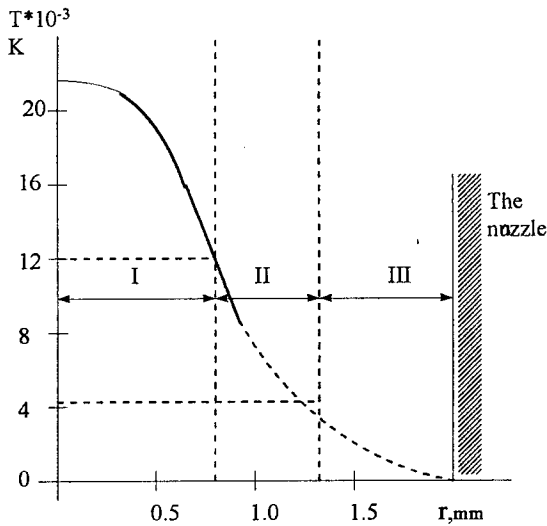


Fig. 2.

The first zone has the temperature above 12000 K and the following condition is satisfied for it,

$$n_i = n_e \approx n_p, \quad (2)$$

where n_i , n_e , n_p are the concentrations of the ions, electrons and neutral particles respectively.

In zone II called strongly non balanced zone the following condition satisfies,

$$n_i = n_e \gg n_p, \quad (3)$$

In the nozzle channel this zone is constrained between the isotherms with the temperatures of 12000

K and 4500 K where the electric conductivity is practically 4 times less than in zone I. For zone III, called zone of the saturated layer we have,

$$n_i \neq n_e \quad (4)$$

It is zone III which forms the isolation gap between the electric arc and the nozzle.

The voltage-leakage current characteristic of this zone depends on the constructive parameters, on the current, on the air debit, as well as on the length of zone IV. In fig. 3 a series of volt-ampere characteristics is represented for different values of the current from 150 A (curve 1) to 400 A (curve 2), for air debit equal to $1 \text{ g} \cdot \text{s}^{-1}$, for the nozzle diameter d_n and length l_n of 4 and 6 mm respectively and for the distance between the nozzle and the metal l_{n-m} equal to 10 mm. The dependence of the volt-ampere characteristics on other parameters has been studied. From these characteristics it follows that they all are increasing and when the leakage current is equal to 1 A the isolation gap breakdown takes place causing the cascade electric arc firing.

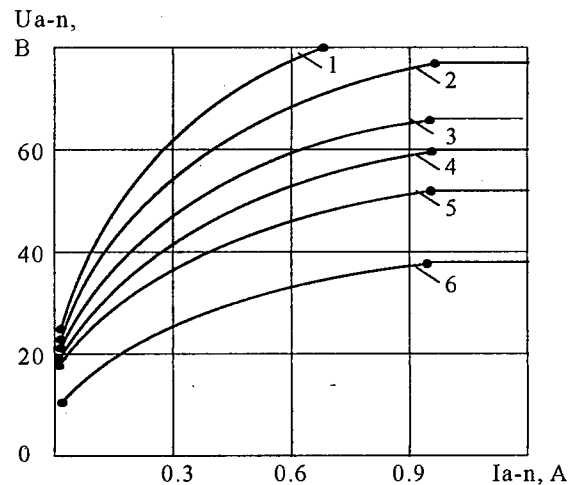


Fig. 3.

From this research where the influence on other parameters has been taken into account the following mathematical model of the leakage current between the electric arc and the nozzle has been obtained.

$$I_{a-n} = 7.57 \cdot 10^{-3} E \cdot I^{0.86} \cdot Ga^{-0.54} \cdot d_n^{-1.65} \cdot l_n^{1.67} \cdot l_{n-m}^{0.54}, \quad (5)$$

where E is the electric field intensity in the gap between the electric arc and the nozzle.

References

- [1] V. Pogora, I. Protsouc, T. Stanchou: Etude et optimisation de l'Installation de Coupure des Métaux par la Torche à Plasma d'air. UIE Congress on Electricity Applications, 1, Birmingham, UK (1996).

STUDY OF CIRCUIT BREAKER ARC DURING THERMAL CURRENT INTERRUPTION

A. Trusca, A. Gleizes, J.J. Gonzalez

Centre de Physique des Plasmas et de leurs Applications de Toulouse
ESA n° 5002, Université Paul Sabatier, 118 route de Narbonne 31062 Toulouse cedex 4, France
Phone: +33-05-61-55-68-55 Fax: +33-05-61-55-63-32 e-mail jgg@cpa11.ups-tlse.fr

INTRODUCTION

Important efforts are now devoted to improve the theoretical methods used on the development of circuit-breakers. The so called physical have a larger field of applicability than the "black-box" models. They allow to study not only the interaction between the arc and the circuit, but also the impact of the conception parameters.

In the present paper are presented the results of a theoretical study of a circuit-breaker based on a two-dimensional turbulent time-dependent calculation. The physical model used for the modelling, could be applied for the thermal current interruption phase, like in short-circuit current cutting. The consideration of the turbulence and of two kinds of radiation treatments: with and without self-absorption of the radiation on the edges of the arc, determine a greater complexity and applicability.

1. BASES OF THE MODEL

1.1 Generalities

The model, based on a system of conservation differential equations is simplified using some hypotheses. These hypotheses are adopted to the studied region and period, more exactly to the nozzle of the circuit-breaker, around zero current, without having in view the properties of the arc near the electrodes. These hypotheses, similar to those of a previous paper [1], are the followings:

- pure SF₆ plasma in local thermodynamic equilibrium, with a cylindrical symmetry;
- radial electric field and Lorentz's forces are neglected;
- radiation losses are calculated on the base of a net emission coefficient dependent on the local parameters, temperature and pressure.

The thermodynamic properties and the transport coefficients of the SF₆ plasma used in this paper are taken from [2]. The system of equations includes the conservation equations and the Ohm's law. In cylindrical coordinates they were given in [1].

1.2 Treatment of turbulence

After years of studies the role of the turbulence in explaining the behaviour of the SF₆ arc was proved and

accepted [3]. The turbulence will directly influence the heat and momentum transfer by means of two thermodynamic properties: thermal conductivity and viscosity, which have a laminar and a turbulent component. Being far from the electrodes we can consider the arc like a jet and use the Prandtl mixing length model. So, the turbulent components are:

$$\mu_t = \rho \varepsilon_t \quad K_t = \frac{C_p \mu_t}{P_r} \quad (1)$$

where: P_{rt} is the turbulent Prandtl number ($P_{rt} = 0.5$),

$$\varepsilon_t = l^2 \left| \frac{\partial v_z}{\partial r} \right|, \quad l \text{ is the mixing length } (l = 0.075 \cdot R_{jet}).$$

R_{jet} is the jet radius. To account for the enhanced effect of the turbulence in the divergent part of the nozzle, for current less than 100A we use [1]:

$$\varepsilon_t = l^2 \left| \frac{\partial v_z}{\partial r} \right| \left(1 + (p-1) \frac{z}{L} \right) \quad (2)$$

where L is the nozzle length, z is the axial coordinate. p is an adjusted coefficient between 1 and 10.

1.3 Treatment of radiation

The present calculation uses a net-emission coefficient.

ε_n , to represent the energy loss by radiation, coefficient taken from Gleizes et al [4]. In order to obtain a better agreement with the reality we have doubled this values. To account for the effect of self-absorption, especially in the cold part of the gas in the nozzle, we consider a radiation model similar to of Blundell's one [5]. We assume 2/3 of emitted radiation in the arc core (defined by temperature greater than $T_1 = 0.65 \cdot T_0$, where T_0 is the axis temperature), is absorbed in the outer region with temperature less than T_1 . For temperature greater than T_1 we use the values of Gleizes et al [4]. for a given radius of 1mm. For temperature less than T_1 we consider that the effective value of ε_n is negative and can be expressed by:

$$\varepsilon = - \frac{\frac{2}{3} \int_0^{R_a} 4\pi \varepsilon_n r dr}{\int_{R_a}^R 4\pi r dr} \quad (3)$$

Where R_a is the radius corresponding to T_1 .

2. RESULTS AND DISCUSSIONS

The proposed model allows to study the characteristics of the arc temperature and velocity, arc voltage electric field, post arc current and the influence of different physical parameters on the interrupting capability. We applied the model in order to simulate the behaviour of an electric arc of 100kV-20kA circuit breaker for which we had experimental measurements done at EDF Renardieres laboratory (7).

In fig.1 temperature field at zero current is shown for coefficient of turbulence $p=9$. We notice the temperature decreasing in the divergent part of the nozzle, where the effect of the turbulence is stronger. For the post-arc phase, in fig. 2, the variation of the axis temperature is represented in the case of a critical value of the recovery voltage with a rate of rise of $RRRV=8.7 \text{ kV}/\mu\text{s}$, applied after a delay of $0.3 \mu\text{s}$. In this case taking $p=8$ the result obtained corresponds to a cut-off failure, because after a few μs the recovery voltage leads to an increasing temperature.

Once the value of the p coefficient is adjusted with an experimental result of a cut-off/no cut-off limit, we can predict the interruption performances of the circuit-breaker versus di/dt . Limiting curves are shown in fig. 3. The case of neglected self-absorption of the radiation is indicated by dashed lines. At the instant of zero current, the maximum effect of the self-absorption phenomenon, is a temperature decrease with about 500K, but we notice an important increase of the interrupting capability. To explain this result we should consider the role of both turbulence and radiation. Considering self-absorption of radiation on the edges of the arc leads to a rather low energy losses by radiation, but also to a high mixing length. In the transient period, around current zero when the influence of the turbulence is increased, a bigger value of the mixing length will determine a smaller temperature and finally a greater interrupting capability.

Presently the models are not enough precise for being self-consistent. They require yet a few measurements to adjust them and to make a quantitative validation.

REFERENCES

- [1] A.Gleizes, T. Robert, J.J. Gonzalez, B. Liani, 1992, Plasma Sources Sci. Technol. 1, 135.
- [2] B. Chervy, A.Gleizes, M. Razafinimanana, 1994, J. Phys. D.Appl. Phys. 27, 1193-1206.
- [3] A. Gleizes, 1990, invited paper IX Symp on Phys. of Switch. Arc, Tchecoslovaquie.
- [4] A.Gleizes, B. Rahmani, J.J. Gonzalez, B. Liani, 1991, J. Phys. D.Appl. Phys., 24, 1300.
- [5] R. E. Blundell, M.T.C. Fang, 1996, XII Symp. on Phys. of Switch. Arc, Brno (CZ)
- [6] A.Gleizes, M. Bouaziz, C. Pradayrol, G. Raynal, M. Razafinimanana, 1995, 11th Conf. Gas Disch. Applic. GD95 (Tokyo)
- [7] T. Robert Thesis, 1992, n°1110, Université Paul Sabatier, Toulouse.

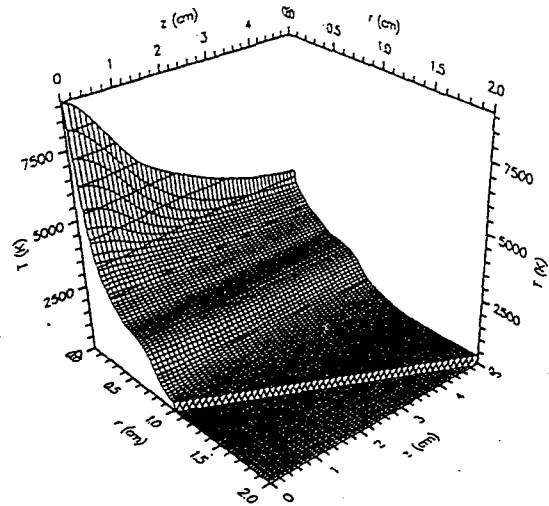


Figure 1: Temperature field at zero current, $p=9$

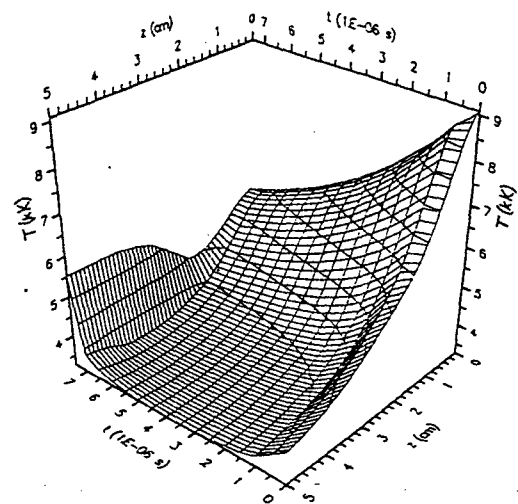


Figure 2: Axis temperature in post-arc phase, $p=8$

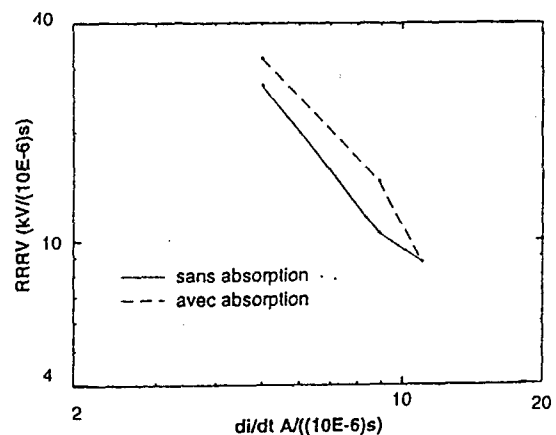


Figure 3: Limiting curves for thermal interruption

Two-Dimensional Model of the Anode Area of a Low Pressure Discharge.

K.N.Ulyanov, A.A.Filippov

The Russian Federation State Research Centre "All-Russian Electrotechnical Institute", Moscow, Russia

1. Introduction

It is considered a problem of the current density distribution at the discharge near anode area with regard for a non-linear anode drop U_a dependence on the current density j for the anode surface of different form. The paper offers analysis of the situation when a non-uniform anode drop is negative and cases of transition to a current density saturation regime on a part or the whole anode surface.

2. Physical Model

Plasma is separated from anode, cathode and walls with a space charge layer. Layers are considered as thin, collisions of electrons are important, conductivity σ is described by a Spitzer formula, electron temperature T_e doesn't depend on the coordinate, therefore $\sigma = \text{const}$. Given a cathode drop U_c doesn't depend on j ,

$$U_1 = U_{ac} - U_c, \quad U_1 = U_{pi} - U_a, \quad U_a = -(kT_e/e) \ln(j_{ch}/j),$$

where j_{ch} - the electron chaotic current density. Expression $U_a(j)$ is typical for low pressure discharges at $j < j_{ch}$. When $j = j_{ch}$ a positive anode drop may take place [1].

3. Mathematical Model

The analogy was drawn between laws of a direct current density distribution and electrostatic field strength. To calculate $j(r, z)$ integral equations method was used [2]. The problem was settled by a successive approximation method. At a zero approximation distribution j was at constant potentials at anode and cathode plasma boundaries. The obtained dependence $j_a(r)$ was used to define $U_a(r)$ for $U_a < 0$. Then a further new distribution $j(r, z)$ was found and so on. If a saturation regime occurred at a part of the anode boundary a value of the normal component $j_n = j_{ch}$ was specified.

4. Results

Fig. 1 shows a configuration of the discharge. Fig. 2 presents $j_a(r)$ for different forms of the anode surfaces at an electrostatic approximation ($U_a = \text{const}$, $U_c = \text{const}$). One should note an essential non-uniformity j_a which leads to a dependence $U_a(r)$. The influence of $U_a(j)$ may be demonstrated on an example with following parameters: $H = 0.1$ m, $r_a = 0.05$ m, $R = 0.016$ m, $kT_e = 3$ eV, $\sigma = 10^4$ Ohm $^{-1}$ m $^{-1}$, $j_{ch} = 10^6$ A/m 2 . The

generatrix of the anode projection is two sectors of the circles $R_c = 0.016$ m, conjugated at the angle of 30° .

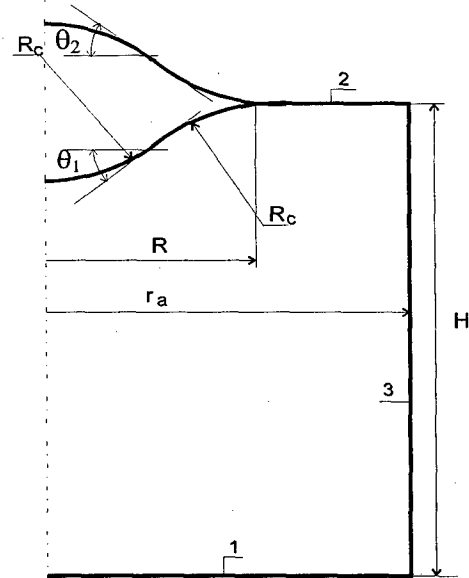


Fig. 1. Configuration of the discharge. 1- cathode. 2 - anode, 3 - isolated wall.

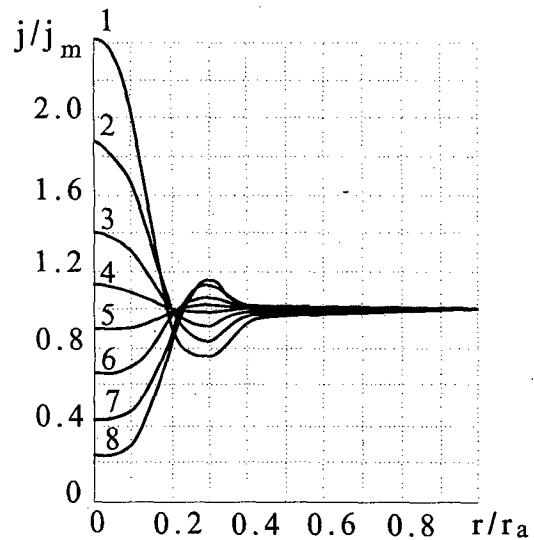


Fig. 2. Relative distribution of density of an anodic current for the different forms of the anode at an electrostatic approximation.

1 - $\theta_1 = 45^\circ$, 2 - $\theta_1 = 30^\circ$, 3 - $\theta_1 = 15^\circ$, 4 - $\theta_1 = 5^\circ$,
5 - $\theta_2 = 5^\circ$, 6 - $\theta_2 = 15^\circ$, 7 - $\theta_2 = 30^\circ$, 8 - $\theta_2 = 45^\circ$.

Fig. 3, 4 show dependencies $U_a(r)$ and $j_a(r)$ for different U_1 . As soon as $j_a < j_{ch}$ (curves 1, 2) non-uniform distributions $U_a(r)$ and $j_a(r)$ are realized; when j_a is higher $|U_a|$ is smaller. When the saturation is attained at a part of the anode (curve 3) or on its whole surface

(curve 5) $U_a > 0$ to provide $j_a = j_{ch} = \text{const.}$ However it is impossible to realize an area with $U_a > 0$ since at saturation this part of the plasma surface should be equipotential and here $U_a = 0$. Therefore regimes with $U_a > 0$ are prohibited.

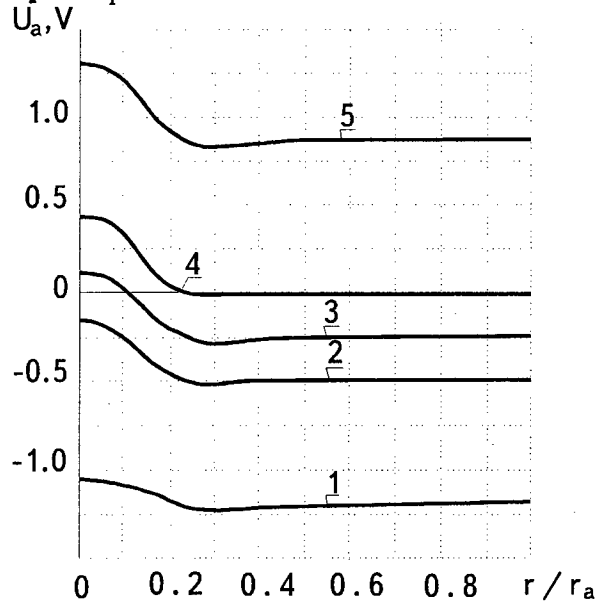


Fig. 3. Dependencies of anodic drop for different U_l .
1 - $U_l = 5$ V, 2 - $U_l = 8$ V, 3 - $U_l = 9$ V, 4 - $U_l = 10$ V,
5 - $U_l = 11$ V.

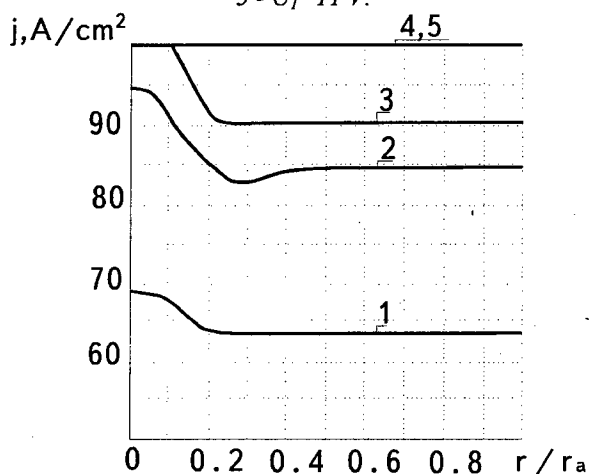


Fig. 4. Relative distribution of density of an anodic current dependencies for the different U_l .
1 - $U_l = 5$ V, 2 - $U_l = 8$ V, 3 - $U_l = 9$ V, 4 - $U_l = 10$ V,
5 - $U_l = 11$ V.

Fig. 5, 6 illustrate distributions U_a and j_a considered for $U_a = 0$ at an area with $j_a = j_{ch}$. For this area j_a depends on the coordinate, which is just the case of the similar

dependence j_{ch} , i.e. the plasma concentration, from r . But this dependence is defined by other equations and should disagree with that one which can be obtained from the solution of the given problem. Therefore the saturation regime can be realized at a part of the anode surface only in exceptional cases when distribution $j_a(r)$ obtained from this problem solution meets $j_{ch}(r)$ get with the problem solution for plasma. This agreement can be readily attained for smaller anodes for which two-dimensional effects are inessential. In this case one observe $U_a > 0$ [1].

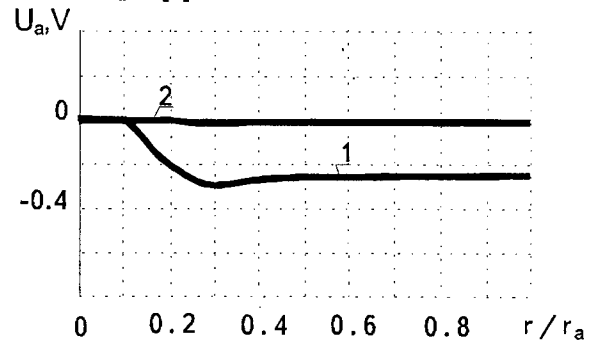


Fig. 5. Distributions $U_a(r)$ for prohibited regimes with $U_a > 0$.

1 - $U_l = 9$ V, 2 - $U_l = 10$ V

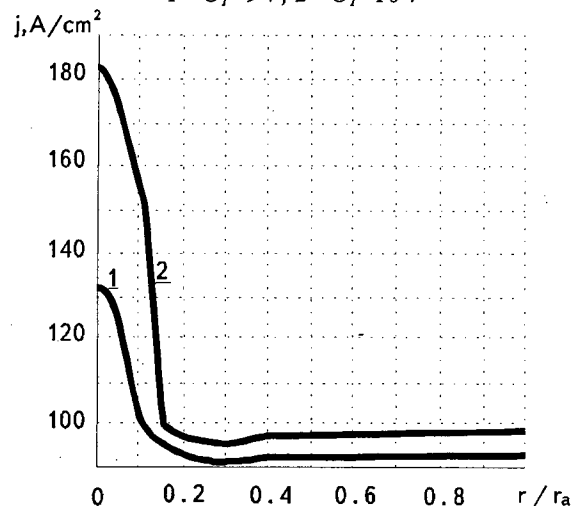


Fig. 6. Distributions $j_a(r)$ for prohibited regimes with $U_a > 0$.

1 - $U_l = 9$ V, 2 - $U_l = 10$ V

References

- [1] Clyarfeld B.N., Neretina N.A. Journal of Technical Physik, v.28 (1958), No.2, p.p.296-309.
- [2] Kolechitsky E.S. High-voltage arrangements electric fields calculation, Moscow, Energoatomisdat, 1984.

Effect of Anode Vapours on the H.C. Vacuum Arc Cathode Stream Deceleration

K.N.Ulyanov, J.I.Londer

The Russian Federation State Research Centre "All-Russian Electrotechnical Institute", Moscow, Russia

One-dimensional model of the vacuum arc plasma zone in three-liquid hydrodynamics approximations is proposed. It is assumed that atoms evaporated from the anode are ionized in a narrow near anode-zone, slow ions obtain quickly a Maxwellian distribution at the cost of Coulomb collisions, deceleration length of cathode stream ions exceeds the gap length, but the cathode stream deceleration is essential. Outside the narrow near-electrode zones streams of slow anode and fast cathode ions are kept, electron thermal conductivity equalizes the electron temperature. Estimations show for the electron movement equation changes in the kinetic energy may be neglected. By obtaining an electric field value from this equation and putting it in fast (1) and slow (2) ion movement equations one may get the following (axis X is directed to the anode, L is the gap size):

$$\frac{d\varepsilon_1}{dy} = -\frac{z_1}{n_e} \frac{dp_e}{dy} + \frac{8}{3\sqrt{\pi}} \left(\frac{m}{M}\right)^{1/2} \frac{n_{1c}}{\alpha} \frac{z_1 z_2}{t_e^{3/2}} * \\ * (z_1 - z_2) \frac{n_2}{n_e} - z_1^2 z_2^2 \frac{n_2}{\varepsilon_1} \quad (1)$$

$$\frac{d\varepsilon_2}{dy} = -\frac{z_2}{n_e} \frac{dp_e}{dy} - \frac{1}{n_2} \frac{dp_2}{dy} - \frac{8}{3\sqrt{\pi}} \left(\frac{m}{M}\right)^{1/2} \frac{n_{1c}}{\alpha} * \\ * \frac{z_1 z_2}{t_e^{3/2}} (z_1 - z_2) \frac{n_1}{n_e} + z_1 z_2 \frac{n_1}{\varepsilon_1} \quad (2)$$

The balance of slow ion energy takes into consideration the ion thermal conductivity and friction force work:

$$\frac{d^2 t_2}{dy^2} = \frac{z_2^4}{2.6} t_2^{-5/2} \left[\gamma \cdot n_{1c} \left(\frac{t_2}{n_2} \frac{dn_2}{dy} - \frac{3}{2} \frac{dt_2}{dy} \right) - \frac{4}{\sqrt{\pi}} \left(\frac{m}{M}\right)^{1/2} * \right. \\ \left. * z_2^2 n_e n_2 \frac{t_e - t_2}{t_e^{3/2}} - z_1^2 z_2^2 \frac{n_1^2 n_2}{n_{1c}} - \frac{5}{2} \frac{1}{t_2} \left(\frac{dt_2}{dy} \right)^2 \right] \quad (3)$$

Equations (1)-(3) were solved numerically with regard for quasi-neutrality and continuity equations for fast and slow ions and boundary conditions at anode and cathode:

$$n_e = Z_1 n_1 + Z_2 n_2, \quad n_1 \cdot \varepsilon_1^{1/2} = n_{1c}, \quad n_2 \cdot \varepsilon_2^{1/2} = \gamma \cdot n_{1c} \quad (4)$$

$$n_1(0) = n_{1c}, \quad n_2(0) = n_{2a}, \quad T_2(0) = T_{2c}, \quad T_2(1) = T_{2a} \quad (5)$$

In (1) to (5) the following notations are used:

$$y = X/L, \quad n_e = N_e / n^*, \quad n_1 = N_1 / n^*, \quad n_2 = N_2 / n^*,$$

$$\varepsilon_1 = E_1 / E_1(0), \quad \varepsilon_2 = E_2 / E_1(0), \quad p_e = P_e / (E_1(0) n^*), \quad (6)$$

$$p_2 = P_2 / (E_1(0) n^*), \quad t_e = (kT_2) / E_1(0), \quad t_2 = (kT_2) / E_1(0)$$

Indexes "e", "1", "2" are referred respectively to electrons, fast and slow ions. n_{1c} - the concentration of fast ions at the cathode, γ - the ratio of current densities of slow and fast ions, α - the fraction of the full current transferred by fast ions, $E_1(0)$ - the kinetic energy of fast ions at the cathode. n^* and n_{1c} are defined as follows:

$$n^* = \frac{\varepsilon_1^2(0)}{\pi \cdot e^4 \ln \Lambda L}, \quad n_{1c} = \frac{\alpha j}{t_1 j^*}, \\ j^* = \frac{\varepsilon_1^{5/2}(0)}{\pi \cdot e^3 \ln \Lambda L} \left(\frac{M}{2} \right)^{1/2} \quad (7)$$

Here, j - the arc current density. The set of equations (1)-(4) with boundary conditions (5) makes possible to determine a dependence of electron concentration, fast and slow ions, slow ion temperature and kinetic energy (directed velocity) of fast and slow ions on the dimensionless coordinate y . The set of equations was solved numerically. Physical parameters were arc current density, fast and slow ion streams, velocities of fast ions at the cathode and slow ions at the anode, electron temperature.

Typical calculation data are presented in Fig.1-3. One should note essential heat of slow ions, presence of sufficiently narrow near-electrode zones with a high gradient of ion temperature, presence irregular cathode stream deceleration and rather complex law of slow ion concentration changes. With the rise in anode vapour concentration at a given current density value the cathode stream deceleration is intensified (particularly at the near-anode zone) due to a strong dependence of ion collision Coulomb section on the relative velocity. In this case a sharply non-uniform heat is developed in the gap which affects importantly the dependence of stream parameters on coordinate y . For each set of cathode stream parameters (and value of t_e) it is possible to determine a limiting density of anode vapours which stops the cathode stream and disturbs uniform current carrying. The corresponding values are given in Fig.4. It is to be pointed out the limit values n_{2a} are in agreement with experimental results [1]. For a typical quasi-stationary a.c. vacuum arc such temperature values may be attained under heating the anode at which the

anode vapour density exceeds a critical one and the cathode stream can be forced away from the anode. In this case a positive anode drop may appear in the near-anode zone, anode vapours be ionized with electrons [2] and the gap - subjected to a breakdown resulting in formation of an anode spot.

The calculations were executed at following values of physical parameters: $L=1$ cm, $kT_e=3$ eV, $E_1(0)=30$ eV, $n^*=1.4 \cdot 10^{15} \text{ cm}^{-3}$, $j^*=210 \text{ A/cm}^2$.

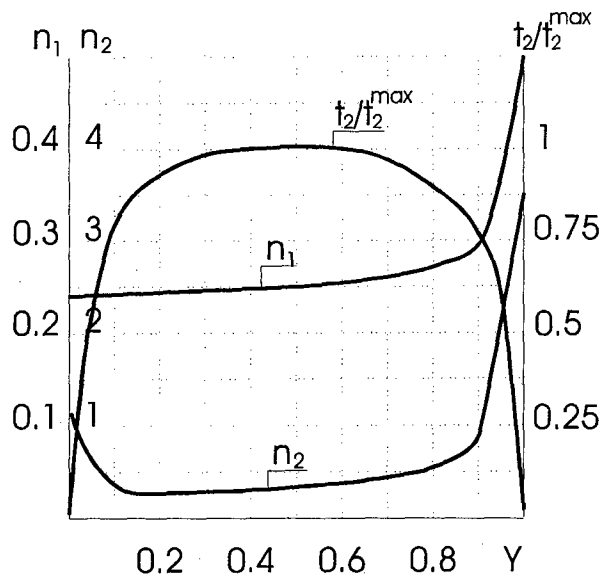


Fig.1 Dependence of the fast and slow ion concentrations and the slow ion temperature on the dimensionless coordinate ($n_{1c}=0.24$, $n_{2a}=3.5$, $j/j^*=3$).

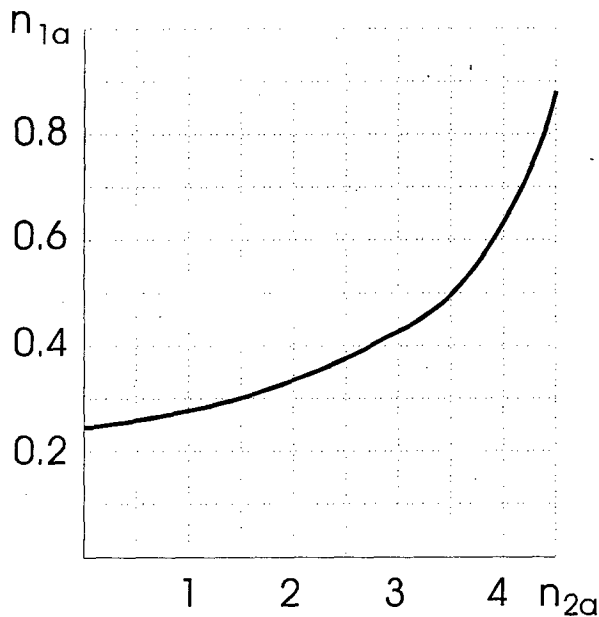


Fig.2 Dependence of the fast ion concentration at the anode on the anode vapor density ($j/j^*=3$).

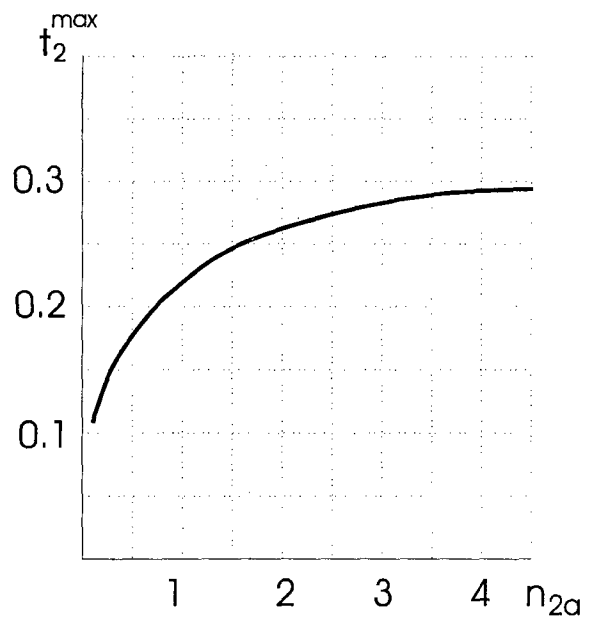


Fig.3 Dependence of the maximum slow ion temperature on the anode vapour density ($j/j^*=3$).

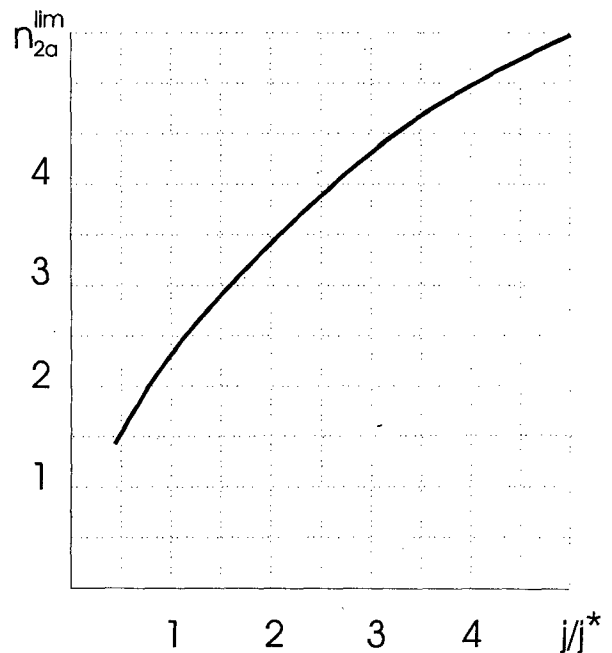


Fig.4 Dependence of the limit anode vapour density on the arc current density.

References

- [1] R.L.Boxman: Journ.Appl.Phys., v.45, (1974), N11, p.4835
- [2] V.A.Gordin, J.I.Londer, I.O. Sibiryak, N.Ulyanov: Radiotekhnika i elektronika, v.29, (1984), N4, p.774

A COMPREHENSIVE STUDY OF ARCING ON ALUMINUM ANODIZED PLATES IMMERSSED IN LOW DENSITY PLASMAS

C.V. Doreswamy*, D.C. Ferguson, J.T. Galofaro,

D.B. Snyder, and B.V. Vayner*

NASA/ Lewis Research Center, Cleveland, Ohio 44135

Abstract.

A number of experiments has been done to study characteristics of the electromagnetic radiation generated by arcing on anodized aluminum plate immersed in low density plasma. The low Earth orbit plasma environment was simulated in a plasma vacuum chamber, where the parameters could be controlled precisely. Diagnostic equipment included two antennas, a spherical Langmuir probe, a wire probe, and a very sensitive current probe to measure arc current. All data were obtained in digital form with the sampling interval of 2.5 ns that allowed us to study the radiation spectrum at frequencies up to 200 MHz. We found that the level of interference exceeds considerably the limitations on the level of electromagnetic noise determined by technical requirements on Space Shuttle operation. Experiments with two independently biased plates have shown that the arcing onset on one plate generates a pulse of current on the second plate, and that the secondary current pulse has a significant amplitude. We emphasize the necessity of the elaboration of a special tool for designers to prevent the adverse consequences of arcing on spacecraft operation.

1. Introduction.

Among the many aspects of the problem there is one which is of particular interest: arcing on spacecraft surfaces with a high negative potential and its consequences. It is quite obvious that arcs are undesirable events, and the main purpose of current research is to elaborate methods for arc mitigation. Arcing onset is a stochastic process. Arcs occur randomly on spacecraft surfaces, and it is impossible to predict the moment and site of arcing. However, it is possible to determine the most probable sites of arcing and to prevent the adverse consequences by implementing a special procedure that must be elaborated. The greater part of this tool exists now. To prevent the negative consequences of arcing at the design stage it seems necessary to determine the spectra and absolute levels of electromagnetic radiation generated by arcing (EMI), magnitudes and pulse forms of arc

current, and to investigate the influence of arcs on other spacecraft surfaces situated near the arc site. In the present paper we describe the results of experimental study and theoretical analysis that were carried out to elucidate the problems named above.

2. Experimental setup.

All our experiments were performed in a vertical vacuum tank installed at the NASA Lewis Research Center. Vacuum equipment provides pressure as low as 10^{-7} Torr. Two Penning sources generate an argon plasma with the electron density $n_e = (2-10)10^5 \text{ cm}^{-3}$, temperature $T_e = 1-1.2 \text{ eV}$, and neutral argon pressure $p = 7 \cdot 10^{-5}$ Torr which were steady during the experiment. An anodized aluminum plate ($18 \times 18 \text{ cm}$) is mounted vertically at the bottom of the chamber, and it is biased by a high voltage power supply through the resistor $R = 100 \text{ k}\Omega$. Diagnostic equipment includes two spherical Langmuir probes each with diameter $d = 5 \text{ cm}$, two perpendicular antennas each with length $l = 50 \text{ cm}$, and two wire probes. For the second part of the experiment, two pairs of plates were installed with separations of $L = 25 \text{ cm}$ and 50 cm respectively, and each plate was biased by an independent power supply. The back sides and edges of plates were insulated by Kapton films. Because the plates themselves have a low capacitance, additional capacitors $C = 0.22 \text{ }\mu\text{F}$ ($0.47 \text{ }\mu\text{F}$ for some experiments) were installed between the plates and ground. This allowed us to increase the electrical charge collected on the plates to more adequately simulate the real situation on the spacecraft. The setup provided the possibility to investigate the influence of an arc initiated on one plate on the processes that were going on on the second plate. All data were obtained in digital form with the sampling interval 2.5 ns. Thus, we are able to study electromagnetic oscillations with frequencies up to 200 MHz.

3. Experimental results.

a) *High frequency EMI.* Arc discharge current generates both plasma waves and electromagnetic radiation which can disturb the operation of electronics. The experimental study of plasma waves has shown that the most intense waves are Langmuir waves with frequencies up to 20 MHz for LEO conditions [1]. The measured electrical field strength $E \approx 0.1 \text{ V/m-MHz}$ could be considered quite significant

*Tuskegee University, Tuskegee, Alabama

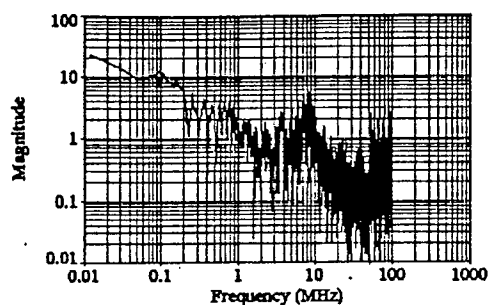
*NASA/NRC Research Associate

at distances of a few meters from arcing site, and these measurements confirmed the necessity of shielding of sensitive electronics. High frequency transverse electromagnetic waves occupy a wide range on the frequency scale (results are obtained for $f \leq 200\text{MHz}$), and their magnitudes are quite large even though the spectra demonstrate a drop of approximately 20dB/dec [1]. The EMI field strength depends on the bias voltage, decreasing by 40 dB when the voltage decreases from 1kV to 250 V. The results of one experiment are shown in Fig. 1. For most of the measurements the amplitude of voltage in the horizontal antenna is almost equal to that in the vertical antenna. However, a few experiments demonstrated some difference between the amplitudes of signals on the two antennas. Both spectra have some common features: a broad peak at the plasma frequency f_p and an almost flat spectrum at frequencies $f > f_p$. Because all measurements were performed in the near field zone, the attenuation of low frequency waves ($f < f_p$) in the plasma was negligible.

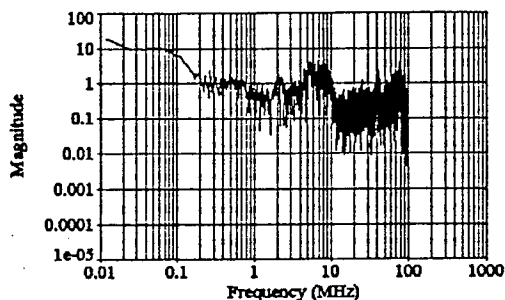
b) *Plasma effects from arcing.* The amount of electrical charge injected into the plasma is equal to 50-100 μC for all of our experiments (for more details, see [1]). We may expect some kinds of secondary effects on the independently biased plate mounted near the plate where arc occurs. Our first series of experiments was done with plates mounted at a separation of $L=25\text{cm}$, facing each other. Two different oscillograms were obtained from the experiment. In the most cases, the second probe registered a low amplitude positive current pulse. However, during a few experiments we observed an effect that could be called "induced arcing" (Fig. 2). It is seen from the graphs that an arc on the first plate generates a negative pulse of current on the second plate, and both amplitudes are comparable. This kind of event can not be explained until further experimental work will be done.

4. Conclusion.

It is well known that arcing on spacecraft surfaces is an unavoidable event with the adverse consequences. An extensive experimental and theoretical study of arcing onset and its aftermath has been carried out with the purpose of obtaining the quantitative characteristics of these physical processes. As a result of our efforts we have data regarding the arc rate dependence on the bias voltage and space environment parameters, the intensity and spectrum of the electromagnetic interference, and some other effects on the conductive surfaces situated near the arcing site. We believe that incorporation of the collected results in a well elaborated computer code for calculations of the electrostatic field distribution along the spacecraft can provide an effective tool for designers. The realization of this program will greatly increase the reliability of spacecraft operation.

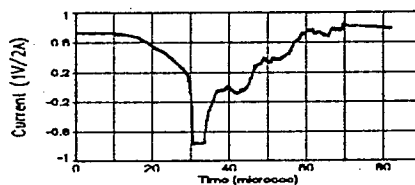


a)

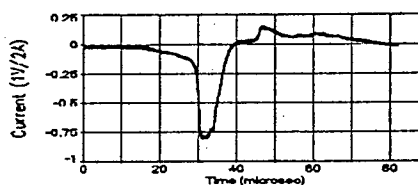


b)

Fig.1. Spectra of signals registered by two antennas
a)horizontal; b)vertical



a)



b)

Fig.2. a) Arc occurs on the plate biased -300 V.
b)Current probe registers pulse on the second plate biased -250 V.

Acknowledgments. This work was performed while B. Vayner held a National Research Council-NASA/LeRC Research Associateship.

5. References

- [1]. B.V. Vayner, D.C. Ferguson, D.B. Snyder, and C.V. Doreswamy... Electromagnetic Radiation Generated by Arcing in Low Density Plasma. NASA TM 107217, (1996), 28 pp.

The Effects of Self-induced Magnetic Field on a High Current SF₆ Arc in a Supersonic Nozzle

J.D. Yan and M.T.C. Fang

Department of Electrical Engineering and Electronics
The University of Liverpool, Liverpool L69 3BX, UK

Abstract

The effects of the self-generated Lorentz force on the electric and aerodynamic behaviour of a 30kA SF₆ arc have been investigated by solving mass, momentum, energy and charge conservation equations. Radiation and turbulence enhanced momentum and energy transport have been taken into account. Charge conservation provides an equation for the solution of electric field, the computation domain of which is larger than the domain for the flow. Although Lorentz force substantially increases the pressure level and distribution, the change in arc voltage does not exceed 10%. The influence of the Lorentz force is restricted to the region close to the upstream electrode.

1. Introduction

It is well known that the Lorentz force due to the interaction of the arcing current and its own magnetic field is the course for strong gas acceleration in a free burning arc [1]. However the effects of the self-generated Lorentz force on a nozzle arc are less clear as the arc also burns in a pressure gradient generated by a high pressure reservoir.

The objective of the present investigation is to carry out a comparative study on the importance of the Lorentz force for a 30kA SF₆ arc in an enlarged nozzle of Benenson et. al [2]. An upstream electrode is placed at the nozzle inlet. The dimensions of the nozzle are: Throat diameter=47.5mm, Axial distance of throat to nozzle inlet=59.4mm, Nozzle length=95mm, Inlet diameter=95mm, Exit diameter=59.85 mm, Electrode diameter=19.5mm, Axial distance of electrode tip to nozzle inlet = 9.5 mm.

Table 1

Equation	ϕ	Γ	S_ϕ
continuity	ρ	0	0
z-momentum	w	$\mu_l + \mu_t$	$-\partial p / \partial z$ $+ J_r B_\theta$ $+ \text{viscous terms}$
r-momentum	v	$\mu_l + \mu_t$	$-\partial p / \partial r - J_z B_\theta$ $+ \text{viscous terms}$
enthalpy	h	$(k_l k_t) / c_p$	$\sigma E^2 - q + dP/dt$ $+ \text{viscous dissipation}$

2. The Governing Equations

Computer simulation of the nozzle arc is based on the solution of four conservation equations which can be written in the following form

$$\frac{\partial(\rho\phi)}{\partial t} + \nabla \cdot (\rho \vec{V} \phi) - \nabla \cdot (\Gamma_\phi \nabla \phi) = S_\phi \quad (1)$$

where ϕ is the dependent variable, ρ the gas density and \vec{V} the velocity vector. The source terms S_ϕ and the diffusion coefficients Γ are listed in Table 1 where all notations have their conventional meaning. The subscript, l, denotes the laminar part of the transport coefficient and t the turbulent part. The boundary conditions for equation (1) are detailed in [3]. SF₆ arcs in an accelerating flow are often turbulent [4]. Prandtl mixing length model has been successfully applied to gas blast arc although it requires one test result for a given nozzle to fix the turbulence parameter [4]. Details of the calculation can be found in [3]. For the nozzle used it has been found that $c = 0.04$ is satisfactory. The magnetic field has negligible effect on the transport properties.

The source term in the energy equation due to the arc is $\sigma E^2 - q$ (Table 1). Electric power input, σE^2 , is calculated by solving the current continuity equation in the form

$$\nabla \cdot (\sigma \nabla \psi) = 0 \quad (2)$$

in a rectangular domain which is larger than the Flow domain. ψ is the electrostatic potential. The potential of the transparent current collector which is placed at the nozzle exit is set at zero. The potential at the end of the upstream electrode (flush with the inlet plane) is iteratively solved until the total current passing through the nozzle is equal to the given value. $\partial\psi/\partial n = 0$ is used for the rest of the boundaries.

The term q in Table 1 represents the net radiation loss per unit volume and time. A semi-empirical radiation transport model [5] is used to calculate q . This model has been proven to be sufficiently accurate to give very good prediction when compared with the measure radial temperature profile in SF₆ [5].

The magnetic field is purely azimuthal due to the axisymmetric distribution of the current density. The magnetic flux density is calculated by Ampere's Law.

3. Results and discussion

Version 2.0 of PHOENICS [6] is used to obtain the results. Body fitted co-ordinate is used in the grid system. A total cell number of 70×70 is used in the flow domain.

The most evident effect of the self-generated magnetic force is the modification to the pressure field which is shown in Figures 1 and 2. The pressure difference on the axis with and without the magnetic

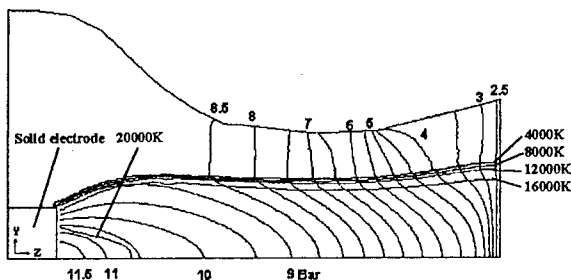


Figure 1 Pressure and temperature contours in the enlarged EPRI nozzle with self-generated Lorentz force. The upstream stagnation pressure is 9 Bar and the stagnation temperature is 313k. The exit pressure is 2.5 Bar.

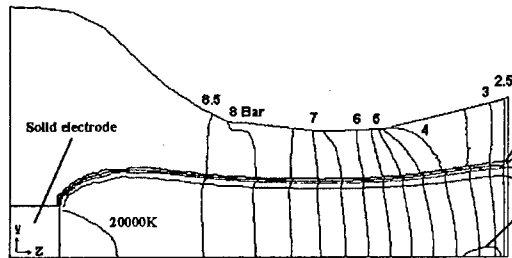


Figure 2 Pressure and temperature contours in the enlarged EPRI nozzle without self-generated Lorentz force.

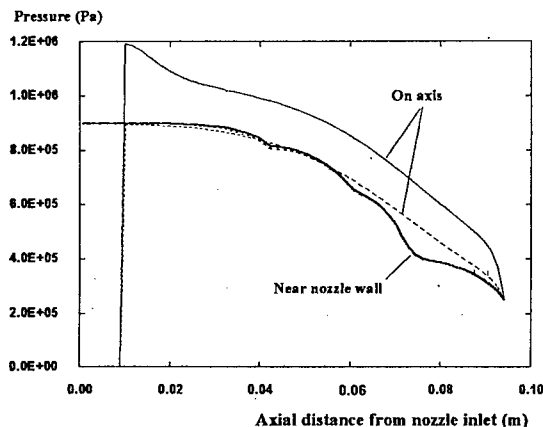


Figure 3 Pressure on nozzle axis and near the nozzle wall. Solid lines: with magnetic force; Broken lines: without magnetic force. Pressure distributions near the wall for the two cases are nearly identical.

force reaches 2 Bar (Figure 3). The gas near the cathode region is strongly accelerated by the magnetic driving force (Figure 4). A careful examination on the results shows that the flow velocity and the enthalpy at the nozzle exit are not sensitive to the magnetic field. However, the increase in gas density due to the pressure rise in the arc column enhances the axial energy convection and results in an arc voltage which is 8% higher than that without magnetic field. The energy flow rate at the exit is shown in Figure 5.

4. CONCLUSION

The most evident effect of the magnetic force is its modification to the pressure field in the nozzle. The

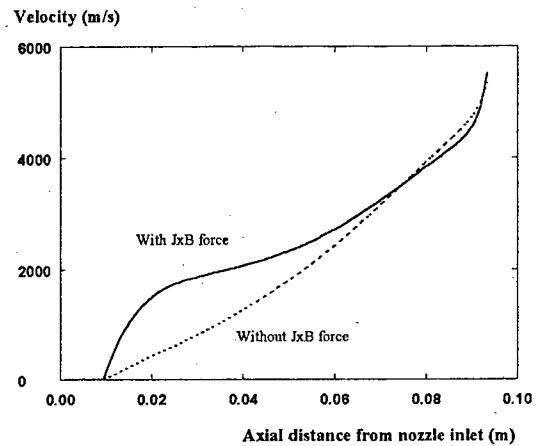


Figure 4 axial velocity component on nozzle axis

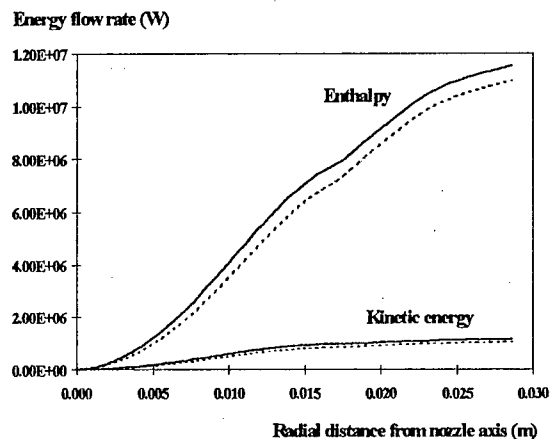


Figure 5 Radially integrated energy flow rate at the nozzle exit. The upstream stagnation pressure is 9 Bar and the stagnation temperature is 313k. The arc voltage for the 30kA SF₆ arc is 447V without magnetic field and 472V with magnetic field. The exit pressure is 2.5 Bar. Solid lines: with JxB force; Broken lines: without JxB force.

difference of axis pressure with and without the magnetic force can reach 2 Bar for a 30kA SF₆ arc. The increase in arc voltage (6%) is caused by the enhanced axial energy convection due to the density increase in the arc column.

REFERENCES

- [1] P. Kovitya and J.J.Lowke, J.Phys.D: Appl. Phys., 18, Pp. 53-70, 1985
- [2] D.M.Benenson, G.Frind, R.E.Kinsinger, H.T.Nagamatsu, H.O.Noeseke and R.E.Sheer, Jr., EPRI Report, EL-1455, Research Project 246-2, Pp.2-6 to 2-7, 1980
- [3] J.D.Yan and M.T.C.Fang, To be published on IEEE Special Issue on Plasma Science, 1997
- [4] M.T.C.Fang, Q. Zhuang and X.J.Guo., J.Phys. D:Appl. Phys., Vol. 27, Pp.74-83, 1994
- [5] J.F.Zhang, M.T.C.Fang, and D.B.Newland, J.Phys. D:Appl. Phys., Vol 20, Pp.368-79, 1987
- [6] PHOENICS is supplied by CHAM, Bakery House, 40 High Street, Wimbledon Village, London SW19 5AU, UK

The stability of argon arcs in axially accelerating flow

R E Blundell, M T C Fang and J D Yan

Department of Electrical Engineering and Electronics,
University of Liverpool, Liverpool L69 3BX, UK.

1. Introduction

High pressure arcs in predominantly axial flow occur in a number of practical applications such as circuit-breakers, arc heaters and in arc welding. The stability of the arc column is important as the arc properties depend strongly on whether the flow within the arc is laminar or turbulent. Previous attempts to explain the presence of instabilities in the arc rely on analogies with simpler flows whose stability properties are known. However, such a simple approach ignores the many closely coupled physical processes inside the arc column and cannot give a reliable picture of arc instability. The purpose of this paper, therefore, is to approach the problem more directly and attempt to give at least a qualitative description of the causes of arc instability.

The extremely complicated nature of the arc governing equations necessitates some simplification of the problem. Our analysis is therefore restricted to the self-similar arc, for which the thermodynamic properties of the arc and the axial velocity gradient are axially constant. Such arcs are found close to a stagnation point at an electrode tip in the predominantly axial flow generated by a constricting nozzle. The self-similar arc captures the qualitative features of more general arcs, while remaining tractable to stability analysis.

2. Stability equations

The non-dimensional conservation equations for an arc in predominantly axial flow may be simplified using the boundary layer approximations and are

$$\begin{aligned} \frac{\partial \rho}{\partial t} + \frac{1}{r} \frac{\partial}{\partial r} (\rho u r) + \frac{\partial}{\partial z} (\rho w) &= 0 \\ \rho \frac{\partial w}{\partial t} + \rho u \frac{\partial w}{\partial r} + \rho w \frac{\partial w}{\partial z} + \frac{\partial p}{\partial z} &= B_P \frac{1}{r} \frac{\partial}{\partial r} \left(r \eta \frac{\partial w}{\partial r} \right) \\ \rho \frac{\partial h}{\partial t} + \rho u \frac{\partial h}{\partial r} + \rho w \frac{\partial h}{\partial z} &= B_P \frac{1}{r} \frac{\partial}{\partial r} \left(r \frac{\kappa}{c_p} \frac{\partial h}{\partial r} \right) \\ &+ \sigma E^2 - B_Q q \\ I &= \int_0^\infty dr 2\pi r \sigma E \end{aligned}$$

where all notations have their conventional meaning and the normalisation quantities and similarity parameters are given in [1]. The thermodynamic and transport properties used are those of argon. Radiation is modelled using a net-emission coefficient method without including a region of net radiation reabsorption. For a self-similar arc the equations can be simplified

and their equilibrium solution can be found numerically using a finite volume method [2].

The equations are perturbed by imposing small axisymmetrical perturbations of the type $\rho(r, t, z) = \hat{\rho}(r) \exp(i\omega t + i\alpha \log(z))$ where $\log(z)$ is introduced to make the perturbed equations independent of z . Perturbations to each of the quantities in the governing equations, including all the gas properties, but excluding the pressure, are introduced. The use of the boundary layer approximations to simplify the diffusive terms and remove the pressure perturbation incurs a degree of approximation, as does the neglect of a radial current component. For a self-similar arc, these approximations can be shown to be reasonable [3]. The result is the following set of ordinary differential equations containing two parameters, α and ω :

$$\begin{aligned} \hat{\rho} u \frac{dT'}{dr} + \hat{\rho} \left(\frac{u}{r} + \frac{du}{dr} + \frac{u}{\hat{\rho}} \frac{d\hat{\rho}}{dr} + i\omega + (1 + i\alpha)f \right) T' \\ + \hat{\rho} \frac{du'}{dr} + \left(\frac{\rho}{r} + \frac{d\rho}{dr} \right) u' + (1 + i\alpha)\rho f' = 0 \\ \left(\hat{\rho} u \frac{df}{dr} + \hat{\rho} f^2 - B_P \frac{1}{r} \frac{\partial}{\partial r} \left(r \hat{\eta} \frac{\partial f}{\partial r} \right) \right) T' + 2\rho f f' \\ - B_P \hat{\eta} \frac{df}{dr} \frac{dT'}{dr} - B_P \hat{\eta} \frac{d^2 f'}{dr^2} + \rho \frac{df}{dr} u' \\ + \left(\rho u - B_P \frac{\eta}{r} - B_P \frac{d\eta}{dr} \right) \frac{df'}{dr} + (\rho i\omega + \rho f i\alpha) f' = 0 \\ B_P \left(\frac{\rho u \hat{h}}{B_P} - \frac{1}{r} \frac{d}{dr} (r \kappa \hat{h}) - \kappa \frac{dh}{dr} - \kappa \frac{d\hat{h}}{dr} \right) \frac{dT'}{dr} \\ - B_P \kappa \hat{h} \frac{d^2 T'}{dr^2} + \rho \frac{dh}{dr} u' + (\rho \hat{h} i\omega + \rho f \hat{h} i\alpha) T' \\ + \left(\hat{\rho} u \frac{dh}{dr} + \rho u \frac{d\hat{h}}{dr} - B_P \frac{1}{r} \frac{d}{dr} (r \kappa \frac{dh}{dr} \right. \\ \left. + r \kappa \frac{d\hat{h}}{dr} \right) + \hat{\sigma} E^2 + B_Q \hat{q} \Big) T' - \frac{2E}{r} \frac{d\phi'}{dr} = 0 \\ \frac{1}{\sigma r} \frac{d^2 \phi'}{dr^2} + \frac{d}{dr} \left(\frac{1}{\sigma r} \right) \frac{d\phi'}{dr} \\ - \frac{\hat{\sigma} E}{\sigma} \frac{dT'}{dr} - E \frac{d}{dr} \left(\frac{\hat{\sigma}}{\sigma} \right) T' = 0 \end{aligned}$$

where the hats represent differentiation with respect to temperature, $f = \partial w / \partial z = w/z$ is the axial velocity gradient and ϕ is a current stream function introduced in order to replace the integral equation for the current with a differential equation. Axial symmetry and constant external flow conditions outside the arc provide the required boundary conditions for the perturbed solutions. A current source is assumed so the

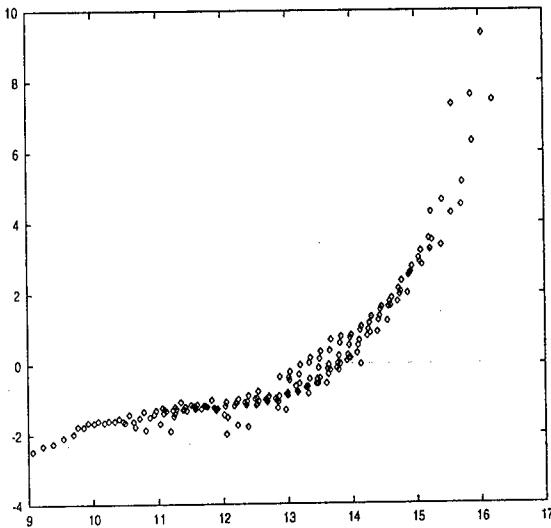


Figure 1: Amplification rate of the most unstable mode plotted against the parameter $-2\log_{10} B_P = \log_{10}(I^2 P f_\infty)$

total current remains constant although the local current density is perturbed. Instability is investigated by assigning imaginary values to ω . The value of α is then determined by satisfying the boundary conditions through the governing perturbed equations. Thus, the problem is an eigenvalue problem and the stability equations determine the corresponding dispersion relation. The perturbed equations are discretised using a Chebyshev collocation method [4] and the resulting matrix eigenvalue problem solved using the QZ and inverse Rayleigh iteration methods [3]. Instability results if α_I , the imaginary part of α , is negative for any value of ω .

3. Results

The numerically obtained solutions of the self-similar arc stability equations show that $\omega = 0$ produces the most unstable behaviour, although the dependence of α_I on ω is weak. Similarity theory suggests that two similarity parameters, $B_P = k_1(I^2 P f_\infty)^{-1/2}$ and $B_Q = k_2(P/(I^2 f_\infty^3))^{1/4}$, rather than the three discharge parameters independently should determine the stability [1]. The constants k_1 and k_2 depend on the values chosen for the characteristic gas properties and for simplicity are set to unity here and f_∞ is the axial velocity gradient of flow external to the self-similar arc. The results show that to a good approximation, B_P alone determines the stability. Figure 1 shows the numerical results obtained for $10 < I < 1000\text{A}$, $2000 < f_\infty < 15000\text{s}^{-1}$ and $1 < P < 8\text{ Bar}$ for the amplification rate $-\alpha_I$ plotted against the similarity parameter B_P^{-2} with $\omega = 0$. The scatter of the points is caused by the weak dependence of α_I on B_Q . The tendency towards instability at large values of $P I^2 f_\infty$ is clear, with the critical value in the range 10^{13} – 10^{14} .

The predictions of stability at low current must be treated with some care. Our analysis has assumed local thermodynamic equilibrium and this may be violated at the low temperatures associated with the low current.

The physical cause of instability can be determined from the terms in the equation for the mean energy of the instability [3]. For the argon arcs investigated here, analysis of this equation shows that instability arises in the shear layer between the arc core and the surrounding cold gas. The instability is driven by the radial gradient of the density which is very large in the shear layer and by fluctuations in the ohmic heating. Fluctuations in the ohmic heating always have a destabilising effect [5] but the numerical results show that the effect in argon is more important than in SF_6 [3, 5]. The thermal conduction and to a lesser extent the radiation dissipate energy from the instability. Thus the process causing instability is quite different to that of the simple flows commonly used as analogies to arc stability.

One of the more important applications of argon arcs is in arc welding. In this case, the arc burns in an accelerating flow caused by magnetic pumping near the cathode. The stability of the arc is important to the welding process and although our model is strictly applicable only to the self-similar arc there are similarities to the free-burning arc. If the flow generated by magnetic pumping is regarded as the same as that produced by a suitable nozzle shape then our results can give a qualitative idea of instability in free-burning arcs when the parameter f_∞ is adjusted accordingly. A quantitative comparison is not possible because fluctuations in the magnetic pumping have not been included in the analysis and these may be important.

References

- [1] R. E. Blundell and M. T. C. Fang, "Similarity of radiating arcs burning in a turbulent, axially-accelerating gas flow." To appear in *J. Phys. D: Appl. Phys.*
- [2] J. F. Zhang, D. B. Newland, and M. T. C. Fang, "The computation of self-similar arcs," *Comp. Phys. Comm.*, vol. 47, no. 2-3, p. 267, 1987.
- [3] R. E. Blundell, M. T. C. Fang, and A. Vourdas, "Stability of a d.c SF_6 arc in an axially accelerating flow." Submitted to *IEEE Trans. Plasma Sci.*
- [4] M. R. Malik, "Numerical methods for hypersonic boundary layer stability," *J. Comp. Phys.*, vol. 86, pp. 376-413, 1990.
- [5] R. E. Blundell, M. T. C. Fang, and A. Vourdas, "Linear stability analysis of the self-similar arc," tech. rep., EPSRC report GR/H73233-3, 1996.

The interrelation between the departure from LTE and the space modes of electric arc plasma and diagnostic problems

V.A.Zhovtyansky

Department of Radiophysics, Taras Shevchenko Kiev University, Kiev, Ukraine

It is generally agreed the local thermodynamic equilibrium (LTE) state takes place in the electric arc plasma [1]. This point of view is predominating. But our experience has shown that this widely accepted assumption is invalid often [2].

1. Nonequilibrium due to gradiental effects

The state of plasma plays a key role in the determining of the space distribution of plasma generated particles density in the arc. For example, results of investigations of electric arc plasma between evaporated copper electrodes in LTE-assumption exhibit the significant increasing of copper vapour content at the arc periphery at every its section [3,4]. Such increasing in other authors' papers is explained as a result of demixing due to ambipolar diffusion [4]. We have shown inaccuracy of this assumption by numerical calculation [3]. This corresponds with the results of our previous experiments in a part of negligible role of diffusion processes in electric arc plasma [5].

We consider the adequate explanation for obtained results is departure from the LTE-assumption in such plasma due to another kind of gradient. Namely, the partial LTE (PLTE) is caused by the resonance radiation transfer in the nonuniform plasma having the temperature gradient. Radiation from the hot arc core is able to overpopulate the resonance level of Cu atoms at the arc region where temperature is relatively small. Furthermore, one of the diagnostic spectral lines CuI 510.5 nm is ordinary self-absorbed in any experiment as may be confirmed from checking of obtained plasma parameter. It is also directly shown in our experiment based on the laser absorption spectroscopy technique [6].

The comprehensive calculation allows to specify the overpopulation extent of the atom copper resonance level with respect to the ground one at various distances away from the arc axis. This effect has been sufficiently universal for any dense plasma. It is most manifested at the periphery of the specified plasma source. That is why it went largely unnoticed under ordinary observations along the axis chord of the plasma volume, excluding tomographic procedure.

2. Simulation-adaptive spectroscopy

Plasma was produced between the end surfaces of the non cooled copper electrodes in the air, each having a diameter of 6 mm. Interelectrode distance L could be

varied between 2 and 8 mm and discharge current from 3,5 to 100 A. The electrodes was placed in a vertical position. The single square current pulse up to 100 A was put on the "duty" week-current discharge. The quasi-steady mode was investigated.

The initial experimental data acquisition was accomplished by the tomography spectrometer based on the astigmatic light-high monochromator and the electrostatic image dissector. It allows to carry out the recording of radial distributions of nonstationary arc radiation intensity in various spectral ranges simultaneously [7]. As a result the radial structure of the nonstationary plasma source may be defined.

This paper deals with problem of such non-LTE plasma diagnostic. The next idea of simulation-adaptive diagnostic procedure is proposed (Fig.1). Starting with the LTE approximation plasma parameters are calculated. In this case observed profiles of plasma radiances (integrated along spans) as a function of distance ρ from axis in a number of spectral ranges $J(\rho, \lambda_n)$ are used as initial data. In the result of inverse problem solving they are transformed to radial distribution of the emission $I(r, \lambda_n)$ in the assumption

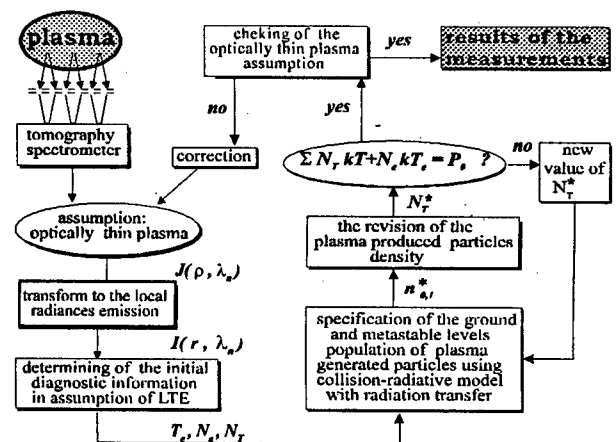


Fig.1. The diagram of simulation-adaptive diagnostic procedure

of optically thin plasma. Next stage includes iterative process of collision-radiative population of the ground and metastable levels of plasma particles with account of radiation transfer in resonance lines. The calculated plasma parameters are to be satisfied simultaneously the supposed model of the non-LTE plasma and initial values $I(r, \lambda_n)$. The last operation in this cycle is checking of plasma optical thickness in

diagnostic spectral lines. The simulation is over if the plasma is optically thin. In the contrary case the initial values $I(r, \lambda_n)$ would be corrected to new values $I_k(r, \lambda_n)$ and temperature T_k . Further previous cycle would be repeated until the result of integration of radial distribution of the emission along spans with account of radiation transfer will be coincide with initial experimental data $J(\rho, \lambda_n)$. This iterative process is over if the result of optical thickness checking corresponds to calculated temperature and levels population. The proposed method allows to exclude the "catastrophic" increasing of the copper vapour content at the arc periphery obtained by other procedures.

3. Space modes

The feature of electric arc plasma space structure in a longitudinal direction is existence of bright luminous spots nearby electrode vicinity with the characteristic size of the order 1 mm at each of electrodes. Purely speaking, an electric arc is closed through these formations with electrodes. The arc, as such, looks like as the less bright formation between these spots. It is good distinguishable if interelectrode distances exceed $L \geq 4$ mm. In other case these visually discernible separated spots are merged practically together. As illustration in Fig.2,a are presented the examples of longitudinal structure of different interelectrodes distance arcs. Here $N_e^{int}(x)$ are integrated along a diameter the electron density values:

$$N_e^{int}(x) = 2 \int_0^R N_e(x, r) dr,$$

where upper limit of an integration $R(x)$ is the radius of plasma formation in appropriate arc section. Representation about its absolute value in separate section at $L = 8$ mm gives Fig.2,b. It is possible to conclude that above mentioned spots in electrode vicinity areas correspond essentially significance of electron density N_e .

Thus, it is possible to speak about electric arc plasma space structure. In a case of long arc in the distance from electrodes the role of the hot core plays zone near its axis. There is LTE plasma in this zone. PLTE takes place in the outer periphery region. As interelectrode distance decreases the electrode vicinity area with the high contents both electron and copper vapours are merged, derivating one zone. In such short arc, where $L \leq d$ (L - vapour distance, d - arc diameter at the vapour section) or in the vicinity of electrodes $l \leq d$ (l - distance from electrode) the state of plasma is deviated from LTE even in axis zone due to influence of resonance radiation from cathode spots. For example, in short ($L = 2$ mm) free-burning electric arc between copper electrodes the overpopulation of resonance levels of Cu atoms

consists of one order with respect to LTE at the discharge current 30 A.

Thus, the properties of free burning electric arc plasma in copper vapour are largely determined by its non-uniformity.

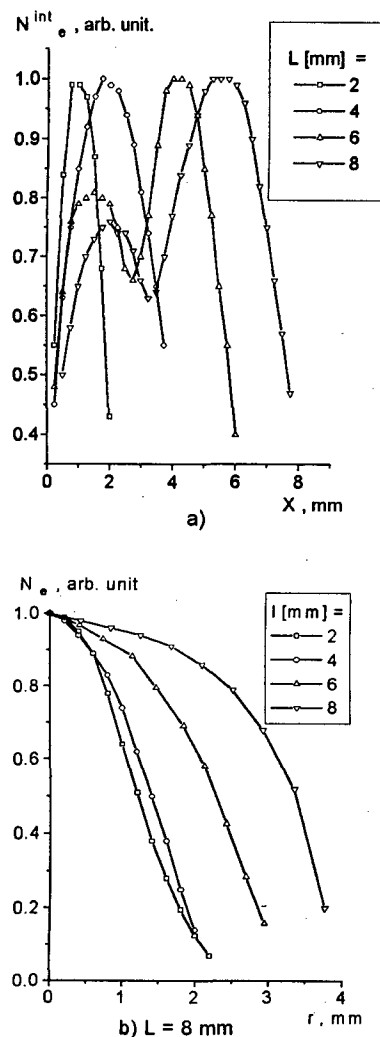


Fig.2. The longitudinal structures of electric arcs with $L = 2, 4, 6$ and 8 mm (a) and radial structure of electric arc with $L = 8$ mm (b); $I = 30$ A.

1. F.Burhorn. *Z. Phys.* 1955. V.140. P.440.
2. V.A.Zhovtyansky. *ESCAMPIG*, The Netherlands. 1994. P.254.
3. I.L.Babich, A.N.Veklich, V.A.Zhovtyansky, A.Yu.Pankin, A. I.Cheredarchuk. *Ibid*, P.310.
4. B.Cheminat, K.Gadaud, P.Andanson. *J. Phys. D: Appl. Phys.* 1987. V.20, No.4. P.444.
5. В.А.Жовтянский, О.М.Новик. *Ж. техн. физ.* 1989. Т.59, в.9. С.186.
6. I.L.Babich, A.N.Veklich, V.A.Zhovtyansky. *Journal of Applied Spectroscopy* (translated from Russian). 1989. V.51, No.4. P.1028.
7. A.N.Veklich, V.A.Zhovtyansky. *Ibid*. 1989. V.50, No.4. P.359.

Investigations of free-burning electric arc in copper vapours

I.L.Babich, A.N.Veklich, A.I.Cheredarchuk, V.A.Zhovtyansky

Radiophysics Dept., Taras Shevchenko Kyiv University, 252033, Kyiv, Ukraine

Earlier plasma of the electric arc, free-burning in air between copper electrodes, in various modes of arc operations, was experimentally investigated [1-3]. Radial distributions of temperature $T(r)$ and electron density $N_e(r)$ are measured by emission spectroscopy methods. Using the model of local thermodynamic equilibrium (LTE-assumption) it allows to calculate radial population distributions of any copper atom level. Radial distributions of absorption coefficient κ_0 in centre of a spectral line CuI 510.5 nm are measured by the laser absorption spectroscopy method. It allows to calculate the appropriate distributions of the metastable level population of Cu atom irrespective of the plasma condition. Really, the densities of absorbing particles in the bottom condition of the considered optical transition N_k in a case of Doppler and Lorentzian contours are accordingly equal:

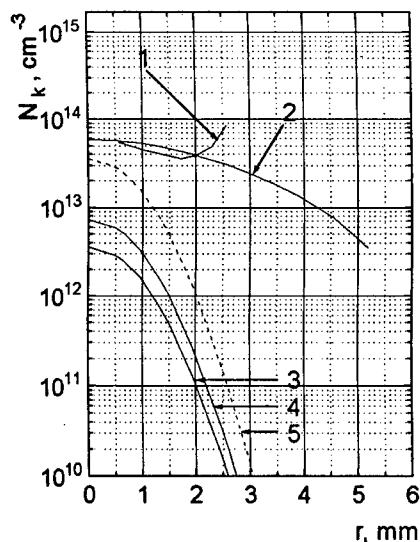
$$N_k = 9.2 \cdot 10^{15} \kappa_0 \Delta\lambda_D,$$

$$N_k = 1.2 \cdot 10^{16} \kappa_0 \Delta\lambda_L.$$

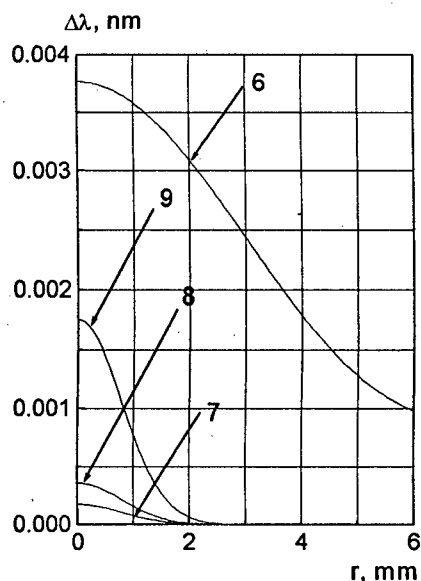
The estimated values of half-width $\Delta\lambda_D$ can be obtained from measured $T(r)$ and $\Delta\lambda_L$ - from $N_e(r)$.

In Fig. 1,a and 2,a radial distributions of $N_k(r)$ in the average cross section of the interelectrode distances $l_{ek} = 8$ mm for currents 3.5 and 30 A are given. The diagrams of estimated values of half-width $\Delta\lambda$ of a spectral line 510.5 nm in case of Doppler effect and Stark effect for two different values of broadening parameters [4] and [5] are shown, too (Fig. 1,b 2,b). The analysis of obtained results allows to make the following conclusions. For low current mode of electric arc ($I = 3.5$ A) both techniques provide practically coinciding $N_k(r)$ (curves 1 and 2). It testifies that the LTE is established in chosen plasma section. And, the coinciding just these curves was quite expected as in conditions of rather low electron density the broadening of a spectral line is caused by Doppler effect (Fig.1, b).

At increasing of the arc current ($I = 30$ A) results of $N_k(r)$ measurements by both techniques differ, as a minimum, by half order (Fig. 2, a). Two variants of an explanation are probable. The deviation from LTE is realized in plasma and/or Stark broadening parameters are incorrect. Really, in this case N_e is increased and the contribution of Stark effect in broadening of a spectral line in a zone of arc conductivity should be comparable to the contribution of Doppler effect. Therefore being available in the literature and used for estimations Stark broadening parameters [4,5] require further, more careful, analysis.



a



b

Fig.1. Radial distributions of $N_k(r)$ (a) and estimated values of half-width $\Delta\lambda(r)$ (b) of a spectral line 510.5 nm in the electric arc plasma at current $I = 3.5$ A; calculation in the LTE-assumption - curve 1; the cases of the Doppler effect - curves 2, 6 and Stark effect for three different values of broadening parameters: [4] - curves 3, 7; [5] - curves 4, 8; tenfold value of parameter [4] - curves 5, 9.

Additional width measurements of the spectral line 510.5 nm in one of arc operation modes were carried out. The contours of a spectral line were measured by a Fabry-Perot interferometer. This technique provides necessary spatial resolution [3]. For the control of obtained results independent "rough" measurements of the spectral line contour were carried out. Radiation of complete chosen section of arc column was investigated by the high-resolution spectrograph (dispersion - 2 nm/mm). The spatial resolution such technique, naturally, did not provide. However it was possible to find out the order of the spectral line width. Is shown, that Stark broadening parameters [4,5] for line 510.5 nm CuI are underestimated, as a minimum, by the order. Therefore $N_k(r)$ are in addition calculated for tenfold value of broadening parameter [4] (Fig.1,a and 2,a, curve 5). The obtained results confirm the use expediency of the offered specified value of this parameter. Thus, it is possible to state that results of measurements by both techniques are with confidence coinciding for the whole zone of discharge conductivity for arc operation mode at the current 30 A as well (Fig.2,a).

In all investigated modes at the arc periphery (outside of the conductivity zone) $N_k(r)$, measured by various methods, do not coincide. By this is meant that deviation from LTE is realized. In work [6] two-temperature model of electric arc plasma is offered. According to it at the periphery, as opposed to the axial volume, electron and the heavy components temperatures do not coincide. Not neglecting such opportunity, we nevertheless consider, that at the arc plasma periphery, where temperature is rather small, there is the deviation from LTE owing to absorption of resonance radiation from the high-temperature axial zone in this arc area [7].

[1] I.L.Babich, A.N.Veklich, V.A.Zhovtyansky. *Journal of Applied Spectroscopy* (translated from Russian). 1989. V.51, No.4. P.1028

[2] I.L.Babich, A.N.Veklich, V.A.Zhovtyansky, A.Yu.Pankin, A. I.Cheredarchuk. *ESCAMPIG*, The Netherlands. 1994. P.310

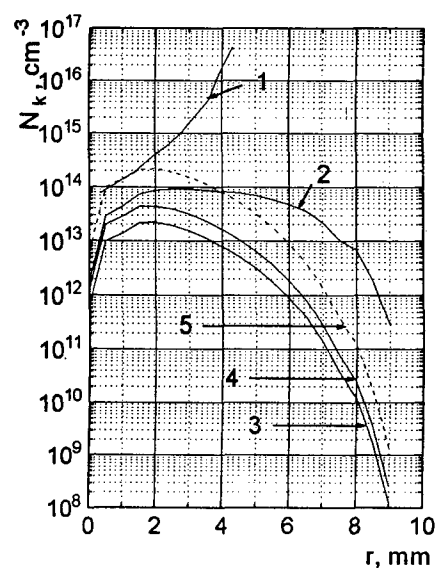
[3] I.L.Babich, A.I.Cheredarchuk, A.N.Veklich, V.A.Zhovtyansky. *12th International Symposium on Plasma Chemistry*. 1995. Minneapolis. Proceedings V.4. P.1861

[4] Konjevic R., Konjevic N. *Fizika*. 1986. V. 18, N 4. P.327

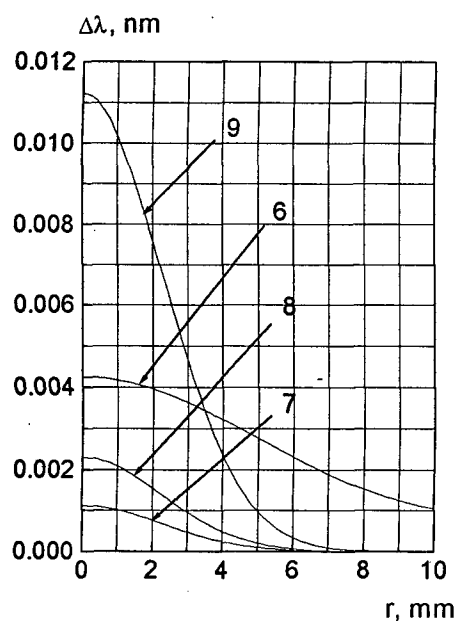
[5] Fleurier C., Manlat C. *17th Int. Conf. Phenom. Gases*. Budapest. 1985. Cont. Pap. P.981

[6] Hsu K.C., Pfender E. *J. Appl. Phys.* 1983. V.54, N8, P.4359

[7] I.L.Babich, A.I.Cheredarchuk, A.N.Veklich, V.A.Zhovtyansky. *ESCAMPIG*, Poprad, Slovakia. 1996. P.251



a



b

Fig.2. Radial distributions of $N_k(r)$ (a) and estimated values of half-width $\Delta\lambda(r)$ (b) of a spectral line 510.5 nm in the electric arc plasma at current $I = 30$ A; calculation in the LTE-assumption - curve 1; the cases of the Doppler effect - curves 2, 6 and Stark effect for three different values of broadening parameters: [4] - curves 3, 7; [5] - curves 4, 8; tenfold value of parameter [4] - curves 5, 9.

Topic 11

Generation and dynamics of plasma flows.

Generation of magnetic field by acceleration of Hall plasma and some consequences of this process

Liliya M. Alekseeva

Institute of Nuclear Physics, Lomonosov Moscow State University,
Moscow 117234, Russia

Let a planar flow of a Hall plasma be directed across a magnetic field \mathbf{H} . If all physical quantities do not vary in the direction of \mathbf{H} , the equation of electromagnetic induction has the form

$$\frac{\partial \mathbf{H}}{\partial t} = \nu \Delta \mathbf{H} + \text{curl}(\mathbf{v} \times \mathbf{H}) + \xi \nabla \frac{1}{\rho} \times \nabla \frac{H^2}{2}. \quad (1)$$

Here, we take the channel length l as a unit length and the values ρ_* and H_* of ρ and H in some characteristic point, as a unit density and a unit magnetic-field strength, respectively. Further, the Alfvén velocity at this point is assumed to be the unit of velocity v and the magnetic pressure $H_*^2/4\pi$, to be the unit of pressure P . The procedure of nondimensionalizing is described in more detail in [1]. Following [1], we assume the plasma to be isothermal. Then the state of the plasma is determined by three constant parameters: the magnetic viscosity $\nu = R_m^{-1}$ (where R_m is the magnetic Reynolds number), the ratio β of the characteristic gas pressure to the characteristic magnetic pressure, and the quantity $\xi = c_0 m_i / e l \sqrt{4\pi \rho_*}$, which characterizes the magnitude of the Hall effect (here c_0 is the speed of light).

Evidently, according to Eq. (1), the magnetic field can be generated in a Hall plasma not only by maintained motion of the fluid conductor across the magnetic field (as in the case of ordinary non-Hall conductors) but also by a maintained density gradient directed transversely to the magnetic-field gradient ∇H .

If we rewrite Eq. (1) using the Euler equation with $\nabla P = c^2 \nabla \rho$, it assumes the form

$$\frac{\partial \mathbf{H}}{\partial t} = \nu \Delta \mathbf{H} + \text{curl}(\mathbf{v} \times \mathbf{H}) + \frac{\xi}{c^2} \frac{H}{\rho} \frac{d\mathbf{v}}{dt} \times \nabla H, \quad (2)$$

where $c^2 = \beta/2$ is the gasdynamic sound speed.

We see that the Hall effect results in changes of the magnetic field precisely in those regions where the gradient ∇H transverse to the flow acceleration already exists. Therefore, there is a tendency for progressively smaller scales to arise in the distributions of physical values in the direction normal to the flow acceleration. Accordingly, dissipation becomes progressively more significant. As a consequence, an equilibrium between magnetic-field generation due to the Hall effect and dissipation should be established at a sufficiently small spatial scale. This limiting scale is a measure for the

sharp transverse nonuniformity of the stationary flow, which arises in a resistive Hall plasma in a channel. We find the small limiting scale for a given ξ value, making simple estimations for different terms of the stationary Eq. (2) (where $\partial H/\partial t = 0$ and $d\mathbf{v}/dt = \mathbf{w} = (\mathbf{v} \nabla) \mathbf{v}$).

We introduce a local Cartesian coordinate system (p, η) with the stream-aligned p -axis and the transversely directed η -axis (from the anode to the cathode), whose origin is at a certain point which we denote as $(0, 0)$. Correspondingly, the velocity component v_η is equal to zero at the local coordinate origin and small in its vicinity. This provides $(\mathbf{v} \nabla) v_\eta \ll (\mathbf{v} \nabla) v_p$ or $w_\eta \ll w_p$.

In addition, as the transverse scale is small ($l_\eta \rightarrow 0$), we have $\partial H/\partial p \ll \partial H/\partial \eta$, and the Hall term in the stationary version of Eq. (2) proves to be equal to

$$B = \frac{\xi}{c^2} w_p \frac{H}{\rho} \frac{\partial H}{\partial \eta}. \quad (3)$$

Here, we see that it is the longitudinal acceleration of the Hall plasma that gives rise to the studied effect of the generation of the small- l_η magnetic field. In other words, the longitudinal acceleration of the Hall plasma results in a strong transverse nonuniformity of the plasma flow.

Now we compare the Hall term B of Eq. (2) with the "convective" term

$$\text{curl}_z(\mathbf{v} \times \mathbf{H}) = -\frac{\partial}{\partial p}(v_p H) - \frac{\partial}{\partial \eta}(v_\eta H). \quad (4)$$

To estimate the first term in the right-hand side of Eq. (4), we replace the acceleration w_p in Eq. (3) by its part $v_p(\partial v_p/\partial p) \sim v_p^2/l_p$ (where $l_p \leq 1$ is the characteristic nondimensional longitudinal scale; note that $l_p \gg l_\eta$). To estimate the second term, we replace w_p in (3) by its another part $v_p(\partial v_\eta/\partial \eta)$. It becomes then evident that the ratio of the convective term to the Hall term in the stationary version of Eq. (2) does not exceed

$$l_\eta \frac{c^2}{\xi} \frac{\rho}{H v_p}.$$

We restrict our consideration to channels in which the gasdynamic acceleration is not too strong in comparison with the magnetic acceleration, assuming that $\beta \lesssim 1$ (or, that is the same, $c^2 \lesssim 1$). We see that

the convective term proves to be negligibly small.

Thus, the stationary version of Eq. (2) acquires the form

$$\frac{\partial j_p}{\partial \eta} + \frac{\xi}{\nu c^2} \frac{H}{\rho} w_p j_p = 0, \quad (5)$$

where $j_p = \partial H / \partial \eta$ is the longitudinal component of the electrical current. Thus, we infer that the sought-for small transverse scale l_η of the Hall-plasma flow is equal to γ^{-1} , where

$$\gamma = \frac{\xi}{\nu c^2} \frac{H}{\rho} w_p. \quad (6)$$

Let us list several conclusions.

(i) The inequality $\gamma \gg 1$ is a necessary condition for the existence of a stationary Hall-plasma flow with a sharp transverse nonuniformity.

(ii) We find, making use of the Euler equation, that

$$\gamma = -\frac{\xi}{\nu} \frac{H}{(\rho)^2} \frac{\partial}{\partial p} \left(\rho + \frac{H^2}{2c^2} \right). \quad (7)$$

Hence, the nonuniformity of the stationary Hall-plasma flow is stronger, the greater ξ and the smaller $\beta = 2c^2$ and ν . Further, in channels with a significant gasdynamical acceleration, a great value of $\xi/\nu = \omega_e \tau_e$ is necessary for the Hall effect to manifest itself in the flow, whereas this value may be small for regimes of magnetic acceleration of plasma ($\beta \ll 1$).

(iii) The flow is most strongly influenced by the Hall effect in the vicinity of the point where the product of H/ρ by the longitudinal acceleration w_p reaches its maximum.

(iv) The structure revealed in the flow is always of fixed polarity in the following sense: for accelerating channels ($w_p > 0$), the value $|j_p|$ increases in the anode direction.

(v) As we saw, the strong transverse nonuniformity of the Hall-plasma flow is due to plasma acceleration along the channel. Basically, the longitudinal acceleration w_p^0 is in essence determined by the conditions at the inlet and outlet of the channel, the magnetic field H^0 being created by the electric current j^0 directed predominantly across the channel, from the anode to the cathode. According to Eq. (5), which is "linear" with respect to j_p , we should expect a sharp nonuniformity to manifest itself in the distribution of the small longitudinal current \tilde{j}_p , if the values of the constant parameters ξ, ν , and β are such that

$$\gamma = \frac{\xi}{\nu c^2} \frac{H^0}{\rho^0} w_p^0 \gg 1. \quad (8)$$

Then the nonstationary disturbances associated with the small longitudinal current \tilde{j}_p can also be classified. Indeed, by juxtaposing the left-hand side of Eq. (5) to $\partial \tilde{H} / \partial t$ we can estimate the characteristic time $t_{\text{mag}} \sim \gamma^{-2} \nu^{-1}$ of the magnetic-field variation. The time of gasdynamic response to magnetic-pressure variations is $t_{\text{gas}} \sim \gamma^{-1} / c$. For $\xi \ll c$, we

have $t_{\text{gas}} \ll t_{\text{mag}}$, and gasdynamic quantities can be considered quasi-stationary with respect to the time-dependent magnetic field. On the contrary, if $\xi \gg c$, we have $t_{\text{gas}} \gg t_{\text{mag}}$. As this takes place, the magnetic field comes into conformity with variable gasdynamic quantities in a very short time and thus behaves as a quasi-stationary quantity. In this case, plasma perturbations appear to be of gasdynamic nature. Indeed, purely acoustic waves were found by analytically solving the full set of equations for resistive Hall-plasma flows of this type [2].

In conclusion, we note that, due to the smallness of l_η , the properties established above for planar flows should have analogues in axisymmetric resistive Hall-plasma flows with an azimuthal magnetic field. Isothermal flows of this type were investigated numerically [1]. These studies have revealed such flow properties as the important role of the longitudinal component of the electric current, the regularities in the dependence of the flow on the parameters pointed out in conclusion (ii), and the presence of the near-anode structure described in conclusion (iv).

If the thermal conductivity of the plasma is taken into account in numerical simulations, the features of the phenomena in Hall-plasma flows are found to be of the same sort, but a strong local heating of the plasma occurs in the region near the anode where an electric current with an enhanced longitudinal component is observed (see, for example, [3]).

References

- [1] K. V. Brushlinskiĭ and A. I. Morozov, in: *Voprosy teorii plazmy*, ed. by M. A. Leontovich, vol. 8, Moscow: Atomizdat, 1974, pp. 88–163 [Engl. transl.: *Reviews of Plasma Physics*, vol. 8, New York: Consultants Bureau, 1980, p. 105].
- [2] L. M. Alekseeva, *Pis'ma Zh. Tekh. Fiz.* **19**(5), 34–88 (1993) [Engl. transl.: *Sov. Tech. Phys. Lett.* **19**(3), 145–147 (1993)].
- [3] L. M. Alekseeva, A. V. Getling, and V. V. Savel'ev, *Geomagn. Aeron.* **22** (4), 612–616 (1982).

Computational analysis of a three-dimensional plasma spray jet

B.Dussoubs, A. Vardelle, M. Vardelle, P. Fauchais

Laboratoire Matériaux Céramiques et Traitements de Surface,

Equipe Plasma, Laser, Matériaux, URA 320 CNRS

Faculté des Sciences de Limoges, 123 avenue Albert Thomas, 87060 Limoges

1. Introduction

Plasma sprayed coatings are widely used in various industrial fields, mainly as wear-, corrosion- and heat-resistant coatings [1]. However, their distinctive microstructure, which consists of layers of thin lamellae with possible inclusions of unmelted particles, pores and crack network, can limit their use. The microstructure of these coatings depends on the velocity, size, molten state and surface chemistry of particles impinging on the substrate ; These parameters are linked with the macroscopic input parameters of the spray process : arc current intensity, plasma and carrier gas flow rates, plasma gas nature, injection conditions for powders... Numerical simulations, thanks to their capability to vary independently the different parameters, can contribute to a better understanding of the phenomena involved in coating formation and the setting of on-line process control.

An analysis of a d.c. plasma jet, operating under industrial conditions is presented, using a tridimensional commercial fluid dynamics code, ESTET [2]. The influence of the variation of arc current, primary (Ar) and secondary gas (H₂) flow rate on plasma flow fields and spraying reproducibility, is discussed.

2. Mathematical modeling

The ESTET software is an "hybrid" code, since the discretisation of the equations is made using both finite difference and finite volume methods. An Eulerian formulation is used for the gas phase, solving the governing equations for a turbulent-gas flow, e.g. the conservation of mass, momentum and energy, as well as the conservation for each species of the gas mixture. Computations take into account fluid turbulence using a standard k-ε model [3] with a correction for low Reynolds numbers (Launder and Sharma, [4]), e.g. in the potential core and close to the walls of the injector and substrate.

The gas flow model is based on the following assumptions : the plasma flow is turbulent, except within the potential core ; the system is steady and in local thermodynamic equilibrium (LTE) ; the plasma is optically thin. The thermodynamic and transport properties of the mixture consisting of plasma gas and air are determined using Wilkes mixing laws from the properties of pure gases [5].

The modeling domain and the boundary conditions are shown in Fig.1. A rectangular mesh is used (the axial direction is set to y-coordinate), subdivided in a non-uniform 49*43*43 grid.

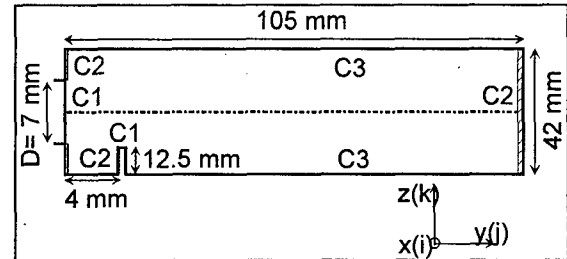


Figure 1 : the calculation domain

At the two inlets of the domain, the torch exit and the powder injector exit, the values of the different variables are fixed. At the torch exit, standard velocity and temperature profiles are used (after [6]). The remaining part of the entrance plane ($y=0$) is considered as a wall (condition C2), as well as the exit plane ($y=100$ mm) whose temperature is fixed initially at 300K. The other boundaries are free (condition C3), i.e. an imposed pressure, set equal to 1 atm is considered.

3. Results and discussion

The plasma torch operates at 600A and 65V with a torch efficiency of 55%, resulting in an effective power dissipated in the gas of 21.5 kW. The plasma-forming gas is a mixture of Argon and Hydrogen. The plasma jet issues in ambient air at 300K and at atmospheric pressure. Decreases of 10% and 20 % in total power, as well as decrease of 20% in Ar or H₂ flow rate, are investigated. In the last two cases, it should be emphasized that a decrease in the gas flow rate results in a variation of the arc tension, that is a variation of the power supplied. Table 1 summarizes the various conditions used for the present study.

Test number	Effective power input (kW)	Ar flow rate (slm)	H ₂ flow rate (slm)
1 (ref)	21.5	45	15
2	19.3	45	15
3	17.1	45	15
4	20.8	36	15
5	20.0	45	12

Table 1 : plasma spray parameters chosen for numerical simulations

The powder injector is located 4 mm downstream of the torch exit, 8.5 mm off the axis. The carrier gas flow rate (Ar) is fixed to 5 slm, which corresponds to the optimal value for the spraying of zirconia powders (particle size range : 22-45 μm) ; it ensures that the median particle trajectory makes an angle of 3-5° with the plasma jet axis. Therefore, most of particles cross the hottest zones of the plasma flow and reach the optimum acceleration and heating.

Figures 2 and 3 show the isovalues of temperature and entrained air mass fraction, respectively, in a plane orthogonal to the torch axis, for the reference case (test 1). The latter corresponds to the spraying conditions approved by the torch manufacturer for aforementioned zirconia powder. When the jet expands in the atmosphere, it transfers a part of its kinetic energy to the surrounding air which is progressively entrained within it because of the difference in density and velocity. The hot jet core, corresponding to the plasma forming gas not disturbed yet by the entrained, cold air, remains for approximately 20 mm. Then, the onset of turbulent behavior appears, leading to a rapid decrease in temperature as the mass fraction of entrained air increases. At 60 mm from the torch exit, the expanding jet is composed of 70% air, and the turbulence is completely developed.

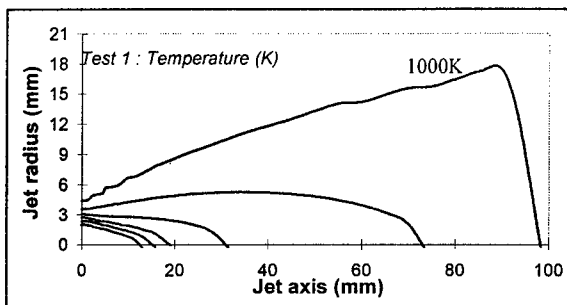


Figure 2 : isotherms (test 1). Lines are separated by 2000K

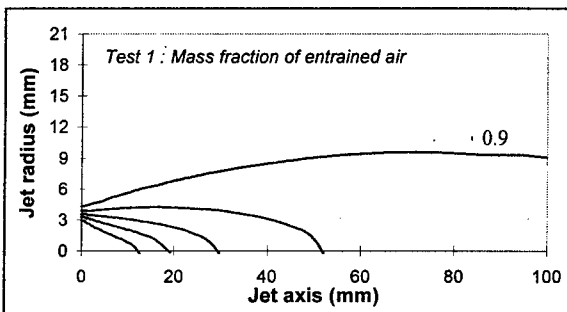


Figure 3 : isovalues of air mass fraction (test 1). Lines are separated by 0.2

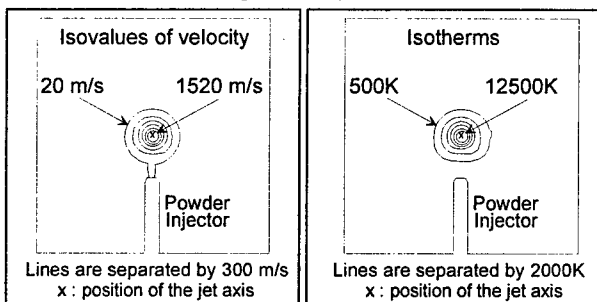


Figure 4 : isovalues of velocity (a) and temperature (b) in the injector plane (test 1).

As shown in Figures 4 (a) and (b), the effects of carrier gas injection are very weak under the spraying conditions for zirconia powder. The determination of the R_m parameter, ratio of plasma jet and carrier gas momentum (taking into

account the temperature), gives in these conditions a value of 0.5, which means that the influence of injection is relatively small, since it has been shown [7] that this effect is noticeable when R_m value exceeds 5.

Test number	T_{max} (K)	V_{max} (m/s)
1	12900	1760
2	12300	1630
3	12000	1575
4	11500	1635
5	11100	1606

Table 2 : maximum temperature and velocity on plasma jet axis at 4 mm downstream of the torch exit

The maximum temperature and velocity, on the jet axis, at a distance of 4 mm downstream of the torch exit, are reported in Table 2. The following conclusions may be drawn :

- a decrease in power input of 10 or 20% results in a decrease in temperature of 4 or 7% respectively (tests 1, 2, 3).
- when Ar or H_2 flow rate diminishes, the arc voltage, and therefore the power input, are decreased. This causes a drop in temperature and velocity (tests 4 and 5). This effect is more noticeable when H_2 flow rate is changed.

Only weak differences are observed between the various runs for the distribution of air mass fraction in the jet, especially for tests 1 to 3, showing that a decrease in power input has a weak influence on air entrainment. Indeed, the flow velocity diminishes but in the same time, temperature decreases too, and the momentum of the flow is maintained.

The variations in intensity and voltage which may be encountered during plasma spraying operations, and the related modification of flow fields may be responsible for a variation in powder treatment. This study appears as a first step that should be completed with the calculation of particles trajectory and thermal history. The 3-D resolution is essential, to predict correctly the effects of a single injection point as well as the shape and size of particle spot on the substrate.

References

- [1] P. Fauchais, M. Vardelle : Pure and Applied Chemistry, **66** (6) (1994) 1247-1258.
- [2] J.D. Mattei, O. Simonin : Logiciel ESTET. EDF Report n° HE 44/92.38B. EDF-LNH, 6 quai Watier, 78400 Chatou-France.
- [3] B.E. Launder, D.B. Spalding : Computer Methods in Applied Mechanics and Engineering, **3** (1974) 269-289.
- [4] B.E. Launder, B.I. Sharma, Letters in Heat and Mass Transfer, **1** (1974) 131-138.
- [5] R.C. Reid, T.K. Sherwood : The Properties of Gases and Liquids, 2nd ed., Mc Graw Hill (1966).
- [6] C.H. Chang, J.D. Ramshaw : Plasma Chemistry and Plasma Processing, **16** (1996) supplement 5S-17S
- [7] Z. Njah, J. Mostaghimi and M.I. Boulos, International Journal of Heat and Mass Transfer, **36** (16) (1993) 3909-3919.

AN ATTEMPT TO SIMULATE RADIATIVE EMISSION FROM NONEQUILIBRIUM HYPERSONIC AIR FLOWS

A. Epifanie, J.P. Sarrette, A.M. Gomes

Centre de Physique des Plasmas et de leurs Applications de Toulouse, ESA 5002. Université Paul Sabatier, 31062 Toulouse Cedex 4, France

ABSTRACT

Since the early 70's and the development of atmospheric flights, considerable effort has been expended to numerically compute the thermodynamic and chemical state of the highly nonequilibrium air plasma created in the flow around hypersonic vehicles. The accuracy of such models can be tested by comparing experimental spectra with an air plasma radiative emission simulation. This simulation can be achieved in three steps: first, the computation of the chemical and thermal flow conditions; second, a collisional radiative model (CR) to access the densities of the atomic and molecular excited states; and finally, modeling of the corresponding emitted spectrum.

This work describes the first results of the coupling of an original CR air model [1] with a hypersonic flow field calculation. The influence of chemical, thermal and radiative nonequilibrium on the shape and intensity of the emitted spectrum is studied.

1. Introduction

An eleven-species reactive air mixture is considered here, including N_2 , N , O_2 , O , NO , N_2^+ , N^+ , O_2^+ , O^+ , NO^+ , and e^- . The behavior of this chemically reactive and thermally excited one-dimensional flow field is described by the Navier-Stokes equations.

In this first attempt, a two-temperature (T, T_v) model is built and equations are solved using an implicit higher-order symmetric scheme based on a generalized Roe's approximate Riemann solver. The gas kinetic model used is derived from Park's model [2], where the effective dissociation rates are controlled by an average temperature $T_a = T^{0.7} T_v^{0.3}$.

The temperatures and densities given by this aerothermodynamical code are fed into a CR model in which the populations of the different excited states are calculated in the optically thin case and using the quasi steady state (QSS) approximation. It is also assumed that radiative energy losses do not affect the thermochemical state of the plasma.

2. Flow-field calculation

2.1 Governing Equations

One-dimensional Navier-Stokes equations incorporating nonequilibrium effects are written in a conservative form:

$$\frac{\partial U}{\partial t} + \frac{\partial F_c}{\partial x} + \frac{\partial F_v}{\partial x} = S$$

$$U = ((\rho_s)_{s=1,11}, \rho u, E, E_v)^T$$

$$F_c = ((\rho_s u)_{s=1,11}, \rho u^2 + p, u(E + p), u E_v)^T$$

$$F_v = ((\rho_s u_s)_{s=1,11}, -\tau_{xx}, q_x - u\tau_{xx}, q_v + \sum_{s=mol} E_v^s u_s)^T$$

$$S = ((w_s)_{s=1,11}, 0, 0, Q_{v-t} + Q_{v-c})^T$$

where

$$E_v = \sum_{s=mol} E_v^s(T_v) = \sum_{s=mol} \rho_s e_v^s(T_v)$$

$$E = \sum_{s=c} E_v^s(T) + E_v(T_v) + \sum_{s=c} \rho_s h_s^0 + \frac{1}{2} \rho u^2$$

$$\rho_s u_s = -\rho D_s \frac{\partial X_s}{\partial x}, \quad \tau_{xx} = 4\mu \frac{\partial u}{\partial x}, \quad q_v = -\lambda_v \frac{\partial T_v}{\partial x}$$

$$q_x = -\lambda_v \frac{\partial T}{\partial x} + q_v + \sum_{s=1}^{11} \rho_s h_s u_s$$

Calculation of transport properties closely follows the example of Gnoffo [3] where the collision integrals are taken and reviewed as according to Raffanel [4].

2.2 Vibrational Model

The source term of the average vibrational energy equation is made up of two terms which mirror the various exchanges between the different modes.

The V-T energy exchanges are described by the Landau-Teller formula

$$Q_{v-t} = \sum_{s=mol} \left(\frac{e_v^s(T) - e_v^s(T_v)}{\tau_{v-t}^s} \right)$$

The total relaxation time τ_{v-t}^s for each molecule s is obtained using a combination of the Landau-Teller relaxation time and a vibrational collision time. If anharmonicity is to be taken into account, Losev's expression [5], developed to modify the Landau-Teller relaxation time, can be used.

For the C-V coupling Olejniczak [6] proposed the generalized expression

$$Q_{c-v} = N_a \sum_{s=mol} \left(\frac{w_s^f \bar{E}(T, T_v) + w_s^b \bar{E}(T, T)}{M_s} \right)$$

where the mass source term is separated in two contributions: $w_s = w_s^f + w_s^b$.

2.3 Numerical Method

An implicit second-order accurate TVD scheme using a symmetric modified flux approach developed by Yee [7] is used to solve the Navier-Stokes equations. The Roe average state for the nonequilibrium gas is determined using Liu and Vinokur's equation [8]. The resulting tridiagonal matrix system is solved by a biconjugate gradient method.

3. Collisional-Radiative Model

An extended description of the model used can be found in [1]. The endothermic rate coefficients for radiative and electronic inelastic collisional processes (excitation, ionization, dissociation, spontaneous emission, radiative recombination) between the different electronic molecular states are calculated using the method given by Bacri [9]. For all collisional processes, reverse rate coefficients are obtained applying the detailed balance relations. A plasma that is optically thin for all transitions is considered and rate coefficients are assumed to be dependent on the vibrational temperature T_v only.

4. Radiation simulation

Once the densities of the excited emitting states are obtained, it is possible to simulate radiative emission of the air plasma in a given spectral window. Because of its significance in reentry plasma, the emission of the N_2^+ first negative system in the 385-395 nm spectral region has been particularly studied. The numerical method is close to the one described by Whiting [10] and the spectroscopic constants used are taken from the work of Klynning [11]. Vibrational transition probabilities are taken from Laux [12].

5. Results

Emitted intensities have been calculated in four cases, showing the influence of the different nonequilibria upon the spectrum. The flow conditions used in each case are summarized in Table 1. Chemical equilibrium means that the temperatures and pressure obtained in the complete model (case d) have been used to calculate a corresponding chemical equilibrium plasma composition. The maximum intensity of the N_2^+ first negative (0-0) band is also given for each case, considering that the integrated intensity of each rotational line is distributed spectrally with a Gaussian line profile having a 0.2 nm full width at half maximum.

The normalized profiles obtained in the different cases are exactly superimposed when thermal conditions are equal. The intensity ratio between the (0-0) and (1-1) band peaks depends only and weakly on T_v (Fig. 1).

6. Conclusion

The coupling between a 'laboratory' aerothermodynamical model, capable of easily integrating various physical approaches of high-temperature flow-field phenomena, and an original molecular CR model should allow us to compare our results with experimental nonequilibrium spectra. The CR model used is markedly different from the one described in NEQAIR [13], which is based on an extension to the excited states of Park's rate coefficients calculated for the fundamental electronic states.

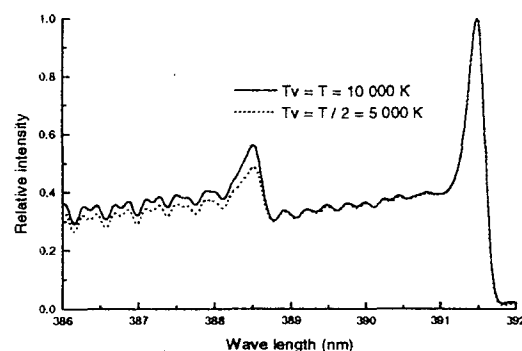
REFERENCES

1. J.P. Sarrette *et al.*, J. Quant. Spectrosc. Radiat. Transfer, **53**, (1995), 125.
2. C. Park, J. Thermophys. Heat Tr., **7**, (1993), 385.
3. P. A. Gnoffo *et al.*, NASA TP-2867, (1989).
4. S. Raffanel, thesis n° 170, Paul Sabatier University, Toulouse, (1987).
5. S. A. Losev, Gasdynamic Laser, Springer-Verlag, New York, (1981).
6. J. Olejniczak *et al.*, AIAA Paper 94-1983, (1994).
7. H. C. Yee, NASA TM-89464, (1987).
8. Y. Liu *et al.*, J. Comput Phys., **83**, (1989), 373.
9. J. Bacri *et al.*, Physica, **101C**, (1980), 399.
10. E. E. Whiting *et al.*, J. Quant. Spectrosc. Radiat. Transfer, **7**, (1967), 725.
11. L. Klynning *et al.*, Phys. Scripta, **25**, (1982), 543.
12. C.O. Laux *et al.*, J. Quant. Spectrosc. Radiat. Transfer, **48**, (1992), 9.
13. C. Park, NEQAIR: User's Manual, NASA TM86607, (1985).

Table 1: The different cases studied

	T (K)	T_v (K)	Flow	I ($W\ cm^{-3}\ sr^{-1}\ \mu m^{-1}$)
Case a	10097	10097	Chem. Eq.	1.250
Case b	10097	7435	Chem. Eq.	0.574
Case c	10097	10097	Chem. Noneq.	0.083
Case d	10097	7435	Chem. Noneq.	0.025

Fig. 1: Effects of thermal nonequilibrium on band spectrum



Collection of isotopically enriched lithium in plasma by means of ion cyclotron resonance

D.A.Dolgolenko, A.N.Ezubchenko, V.S.Laz'ko, A.I.Karchevsky, Yu.A.Muromkin, V.G.Pashkovsky, A.L.Ustinov

Russian Research Center Kurchatov Institute, Kurchatov sq. 1, 123182, Moscow, Russia

1. Introduction

Lithium is one of the few elements which isotope separation by ion cyclotron resonance can be demonstrated in laboratory. Investigations of lithium isotope separation began with registration of selective cyclotron heating of ions ${}^6\text{Li}^+$ and ${}^7\text{Li}^+$ in plasma [1]. After that microgram amounts of lithium were obtained, where ${}^6\text{Li}$ isotope concentration corresponded to separation degree $q = C_p(1-C_i)/[C_i(1-C_p)] > 80$, where C_p is resulting concentration and C_i is initial concentration of the isotope [2]. Further experiments were devoted to obtain extraction coefficient of ${}^6\text{Li}$ from the plasma flow $\gamma = m_p C_p / (m_i C_i)$, where m_p - mass of ${}^6\text{Li}$ in product and m_i - mass of ${}^6\text{Li}$, transferred by the plasma flow during the collection. Results of the enriched lithium collection obtained on the collector system of initial construction corresponded to the value $\gamma \leq 0.10$ with $q \geq 19$ [3].

To increase the extraction coefficient, investigation of isotopically selective heating of ions was continued, and the other construction of the collector system was used.

2. Experimental installation

Layout of the experimental installation, described in detail in [2], is presented in Fig. 1. Longitudinal discharge in lithium vapor was initiated in vacuum chamber 1 in magnetic field, between heated cathode 2 and grid anode 5. Selective heating of ${}^6\text{Li}$ was performed using 65-cm long 4-entry helical antenna 6 with spiral step 65 cm. Collector system 7 was placed at the end of the heating region.

Principal parameters of the installation are: uniform magnetic field 0.2-0.27 T; lithium plasma density $n_e = 10^{12} \text{ cm}^{-3}$; diameter of the plasma column is 6 cm; initial electron and ion temperature $T_e, T_i = 4 \pm 10 \text{ eV}$, temperature if ions heated under ICR conditions up to 100 eV. Frequency of the RF-field was equal 656 kHz.

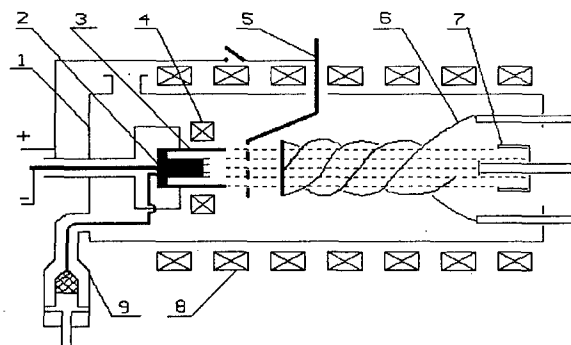


Fig. 1 Scheme of the experimental installation

The measurements of plasma parameters and ICR diagnostics were performed using double electric probes and electrostatic analyzers, described in [2].

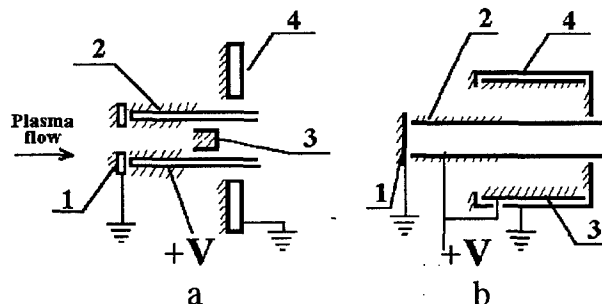


Fig. 2. Collector system design.

Construction of the collector system is presented in Fig. 2. In initial construction of the collector system (Fig. 2a) hollow water-cooled cylinder 2 with outer diameter 32 mm and inner diameter 26 mm, covered from plasma flow by ring water-cooled screen 1, was used for target isotope ions collection. Other matter was gathered on inner 3 and outer 4 waste collectors.

To diminish plasma loss on screen 1 another design of collector system was used (Fig 2b) with disc screen 1 ($\varnothing 20 \text{ mm}$, 2 mm thick), placed under floating voltage; main collector 2 of enriched lithium ($\varnothing 16 \text{ mm}$) and additional collector 3 of enriched lithium ($\varnothing 64 \text{ mm}$). Both collectors were electrically

insulated and positive voltage $V_r = 0 \div 150$ V relative to other parts of the collector system can be applied to them. Left part of cylinder 4 ($\varnothing 75$ mm) also was used as a screen and on its bottom the depleted lithium was gathered. All parts of the collector unit were made from copper and were water-cooled. Places of lithium deposition are marked with dashes.

3. Results of experiments

Ion cyclotron resonance in moving plasma is observed on frequencies, shifted from stationary ions resonance frequencies $\omega_{ci} = eB/M_i$. Value of this shift is defined by Doppler effect, and its value is equal to $k_z v_{iz}$. Here k_z is axial wave vector of antenna and v_{iz} - axial ion velocity. For separation of isotopes of medium and heavy masses the value of $\Delta\omega/\omega_{ci}$ is about 1% [4]. Frequency difference is higher for lithium because of big lithium ions velocity $v_{iz} > 10^6$ cm/c and relatively short used antenna with $k_z \sim 0.1$ cm⁻¹. Magnetic field, created by this antenna, is traveling in axial direction with phase velocity $v_{ph} = -\omega/k_z$ and can accelerate or slow down ions, in dependence of v_{ph} sign. This effect of antenna magnetic field influence is described in [5].

Resonance curves, obtained using electrostatic analyzer, are presented in Fig 3. The curves on Fig 3a were obtained, when $v_{ph} \uparrow \uparrow v_{iz}$, and the curves in Fig 3b correspond to $v_{ph} \uparrow \downarrow v_{iz}$. Value of the retarding potential V_r in electrostatic analyzer was varied: 140 V at $I_a=150$ A, 90 V at $I_a=100$ A and 40 V at $I_a=150$ A.

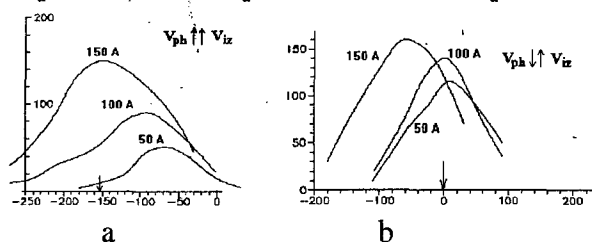


Fig. 3. Heated ion current versus detuning of resonant magnetic field for stationary ions ($B_0 = 0.256$ T) for different RF antenna currents.

As it is seen from Fig 3, increase of antenna current led to additional resonance frequency shift. This shift can be explained by acceleration or slow down of resonance ions in axial direction under influence of transverse component of RF magnetic field [5].

In these experiments, lithium samples were taken using collector system, shown in Fig 2b, at antenna current $I_a = 100$ A, at two directions of v_{ph} .

and duration of deposition 3 min. Values of base magnetic field for collection were defined from resonance curves: these values are indicated in Fig 3. by arrows. These results are presented in Table 1 (N 2, 3). Results obtained using collector system of initial design (Fig 2a) are presented for comparison (N 1).

Table 1

N	collec. system	relation. V_{ph} и v_{iz}	total. Li mass, mg	Ret. potential
1	2a	$V_{ph} \uparrow \uparrow v_{iz}$	50,1	20 V
2	2b	$V_{ph} \uparrow \uparrow v_{iz}$	49,0	40 V
3	2b	$V_{ph} \uparrow \downarrow v_{iz}$	45,5	40 V

N	mean conc.	product mass, mg	$C(^6\text{Li})$ in product	extract coeff. γ
1	7,8	2,9	28,3	0,21
2	7,1	3,9	26,5	0,3
3	7,0	3,0	23,5	0,22

N	waste mass, mg	$C(^6\text{Li})$ in waste	Li mass at screen, mg	$C(^6\text{Li})$ at screen
1	22,1	4,4	18,6	7,5
2	37,1	5,4	8,0	5,5
3	36,5	5,6	6,0	7,5

It is shown, that smaller screen surface results in better extraction of the target isotope from the plasma flow. Comparison of results, obtained at different directions of phase wavefront, showed that at the regime of plasma flow "accelerating" ($v_{ph} \uparrow \uparrow v_{iz}$) higher value of extraction coefficient γ is obtained.

4. References

- [1] A.I.Karchevskii, V.S.Laz'ko, Yu.A.Muromkin, A.I.Myachikov, V.G.Pashkovskii, A.L.Ustinov, A.V.Chepkasov: XX-th ICPIG, 8-12 July 1991, Pisa, Italy. Contributed papers, 1, pp. 331 - 332.
- [2] A.I.Karchevskii, V.S.Laz'ko, Yu.A.Muromkin, A.I.Myachikov, V.G.Pashkovskii, A.L.Ustinov, A.V.Chepkasov: Plasma Phys. Rep, 19 (1993) 214-218.
- [3] D.A.Dolgolenko, A.I.Karchevskii, V.S.Laz'ko, Yu.A.Muromkin, V.G.Pashkovskii, A.L.Ustinov: Compte rendu des Journees sur les Isotopes Stables, pp. 348 - 353. 24-25 Novembre 1993, Saclay, France.
- [4] A.Compant La Fontaine et P.Louvet: Compte rendu des Journees sur les Isotopes Stables, pp. 332 - 336.
- [5] V.S.Laz'ko. Plasma Phys.Rep,20,5(1994) 470 - 472

Topic 14

**Non-linear phenomena and
self-organization processes.**

Control of the chaotic regimes of a driven thermionic discharge

C. Arnas-Capeau and Th. Pierre*

Laboratoire PIIM, UMR 6633 CNRS-Université de Provence, IMT, 13451 Marseille Cedex 20, France

*Laboratoire P.M.I., URA 835 du CNRS, Université Nancy I, BP 239 54506 Vandœuvre Cedex, France

e_mail : pierre@lpmi.u-nancy.fr

1. Introduction

During the last few years, various studies have been devoted to the study of unstable and chaotic regimes of plasma discharges. This was motivated in part by the necessity to extend the operating parameters of plasma sources in technological applications and to control the unstable regimes of the low pressure infra-red laser systems. In fact, this type of very simple plasma systems exhibits many interesting features whose investigation is valuable for the general dynamical study of nonlinear systems.

In recent years, the ability to stimulate or control the dynamics of chaotic systems has been pointed out, for instance by Hübner [1] who developed the H method using nonresonant parametric perturbations, or by Ott, Grebogi and Yorke [2]. Delayed feedback methods have also been proposed by Pyragas [3]. All these techniques have been tested on various chaotic systems. Among these techniques, the delayed feedback method, often referred to as the TDAS method (Time Delay AutoSynchronization) is often most easy to implement on physical systems. Moreover, this method is not very sensitive to noise and this last point is of practical interest in plasmas. The success is however not granted, because it is related to some peculiar topological characteristics of the strange attractor associated with the chaotic system under study [4].

Low-frequency oscillations of various discharges have recently been studied from the view-point of nonlinear dynamics [5]. A period doubling route to chaos was observed in self-excited ionization waves [6,7], as well as for periodically driven discharges of various kinds. Many investigations have been focused on studying the relaxation oscillations of discharges with filaments cathode [8,9]

The system considered here is constituted by a hot cathode (32 tungsten filaments) located inside a magnetic multipolar chamber (stainless steel vessel equipped with rows of permanent magnets). The anode is the wall of the chamber. The emitted electrons are accelerated in the electric field created

between cathode and anode by the discharge voltage supply. This classical device can be operated in two very different regimes, namely the Anode Glow Mode (AGM) and the Temperature Limited Mode (TLM). The AGM is obtained at low discharge voltage, close to the ionization potential, leading to a low electron density and to the creation of ions only near the anode. In the TLM on the other hand, ions are produced in the whole volume and the plasma density is limited by the electronic emission of the filaments. Moreover, self-oscillations are observed at the transition between AGM and TLM. Numerical simulations [10] have carefully investigated the mechanism of this phenomenon. The period of this relaxation instability is related to the discharge voltage and the collision frequency, i.e. to the gas pressure. Undriven chaotic regimes have already been reported [11]. Driven regimes are very easily chaotic, exhibiting a low-dimensional chaos, triggered by the discharge voltage as control parameter.

We are reporting here on the dynamical control of a low-frequency driven thermionic discharge in the AGM, allowing to extend the regular regimes of the plasma density in such devices.

2. Experimental results

The cylindrical discharge chamber (80 cm in diameter, 60 cm in length) with a 32-filaments cathode is filled with argon at a low pressure (10^{-4} torr). The electron density, plasma potential and electron temperature are measured using several Langmuir probes. The discharge is obtained using a DC-power supply in series with a controllable power supply (DC- 100 kHz) which is driven by a sinusoidal function generator. We obtain then a modulated plasma density inside the chamber in either the AGM or TLM. Increasing the discharge voltage and choosing a driving frequency non-resonant with the natural oscillation frequency, we obtain easily a chaotic regime of the discharge in the AGM.

Typical frequency spectra corresponding to time series recorded by the Langmuir probe biased in the electron saturation regime exhibit broadened peaks between the harmonics of the driving frequency. A numerical analysis of long time-series has been performed, giving an estimated dimension $D=2.2 \pm 0.4$. Classical analysis leads to the conclusion that this system is a low-dimensional chaotic system.

The control method used [7] is derived from the TDAS method: the real-time chaotic signal is digitized and processed inside FIFO memories in order to obtain a delayed signal. This delay is chosen equal to the period of the targeted unstable periodic orbit (UPO), namely the period of the driving signal. The delayed and real-time signals are then subtracted in order to get an error signal which is applied to the control parameter (discharge voltage). Figure 1 displays the transition between the uncontrolled and controlled regimes for the probe signal (trace a) and the control signal (trace b). A transient high level control signal is obtained during the controlling process. The control signal is reduced afterward to a low level. This last point is consistent with the standard schemes of chaos control. The intrinsic high sensitivity to initial conditions of chaotic systems is the basic reason for obtaining a dynamical control of this nonlinear system with only a very weak perturbation.

3. Conclusions

We have obtained the control of a driven thermionic discharge in the anode glow mode exhibiting low-dimensional chaos using a time-delay autosynchronization method. The low-level control information is derived continuously from the signal of a monitoring Langmuir probe and applied to the control parameter (discharge voltage).

4. References

- [1] A.W. Hübler, *Helv. Phys. Acta*, **62** (1989) 343
- [2] E. Ott, C. Grebogi, J.A. Yorke, *Phys. Rev. Lett.*, **64** (1990) 1196
- [3] K. Pyragas, *Phys. Lett. A*, **170** (1992) 421
- [4] W. Just, T. Bernard, M. Ostheimer, E. Reibold, H. Benner, *Phys. Rev. Lett.*, **78** (1997) 203
- [5] A. Piel, T. Klinger, in *Proc. XIIth ICPIG*, AIP Conf. Proc. 363, AIP Press (1996) 90
- [6] K.D. Weltmann, H. Deutsch, H. Unger, C. Wilke, *Contr. Plasma Phys.* **33** (1993) 73
- [7] Th. Pierre, G. Bonhomme, A. Atipo, *Phys. Rev. Lett.*, **76** (1996) 2290
- [8] R. Timm, A. Piel, *Contr. Plasma Phys.* **32** (1992) 539
- [9] C. Arnas Capeau, G. Bachet, F. Doveil, *Phys. Plasmas*, **2** (1995) 4650
- [10] F. Greiner, T. Klinger, A. Piel, *Phys. Plasmas*, **2** (1995) 1810
- [11] T. Klinger, F. Greiner, A. Piel, *Phys. Plasmas*, **2** (1995) 1822

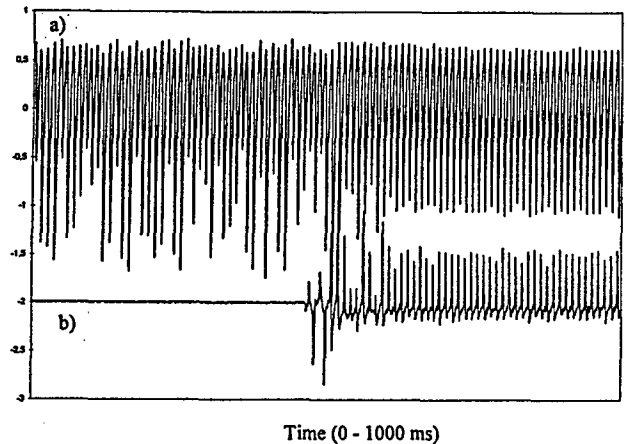


Figure 1

Time-series of the probe signal before and after switching on the control. The second trace is the control signal exhibiting the transient high level allowing to target the UPO corresponding to the period of the driving signal.

Dynamical force-free zero-net-current layer in compressing turbulent plasma

A. F. Djakov, Yu. K. Bobrov* and A. V. Sorokin*

Russian Joint-Stock Company of Energy and Electrification "EES Rossii", Moscow, Russia

*High Voltage Research Centre of All-Russian Electrotechnical Institute, Istra, Moscow region, Russia

1. Basic equations

The self-organization final stage of a large-scale high magnetic field structure in the turbulent pressureless plasma is considered. It is suggested that mean magnetic field is purely force-free, $\nabla \times \vec{B} = \gamma \vec{B}$, and is maintained both by a large-scale plasma flow \vec{v} and by a turbulent MHD dynamo action (α -effect [1] is taken into account). Within the framework of one-dimensional model, in Cartesian coordinates $\{x, y, z\}$ the dimensionless values \vec{B} , γ , \vec{v} have the form

$$\vec{B} = \{\cos \varphi, \sin \varphi, 0\}, \quad \gamma = -\partial \varphi(t, z) / \partial z, \\ \vec{v} = \{0, 0, v(t, z)\},$$

where the magnetic shear φ and velocity v obey the equations [2,3]

$$\frac{\partial \varphi}{\partial t} + v \frac{\partial \varphi}{\partial z} - \frac{1}{\text{Re}_m} \frac{\partial^2 \varphi}{\partial z^2} = 0, \quad (1)$$

$$\frac{\partial \varphi}{\partial z} \left(R_\alpha + \frac{\partial \varphi}{\partial z} \right) + \text{Re}_m \frac{\partial v}{\partial z} = 0.$$

Here $\text{Re}_m = VL/\eta$, $R_\alpha = \alpha L/\eta$, $\eta = \eta_M + \eta_T$; V is a velocity and L a length characteristic of the system considered, α is a dynamo coefficient that is assumed to be constant, η_M and η_T are the respective magnetic diffusivities of the ohmic and turbulent origin.

2. Zero-net-current (ZNC) layer solution

One exact solution to (1) corresponding to a "force-free wave" with $\gamma = R_\alpha = \text{constant}$ has been discussed in [3]. There exists another exact stationary solution to (1) that gives

$$B_x = [1 - (R_\alpha z)^2] F(z), \quad B_y = -2R_\alpha z F(z), \quad (2)$$

$$\gamma = 2R_\alpha F(z), \quad v = -2R_\alpha^2 z F(z) / \text{Re}_m,$$

where $F(z) = 1/[1 + (R_\alpha z)^2]$. These relationships are plotted in Fig. 1. The function γ is not constant here

and peaks at $z = 0$, where $\gamma(0) = 2R_\alpha$. Electric current concentrates in the vicinity of xy -plane, plasma moves toward this plane on each side of it and magnetic field vector is rotated through one complete revolution as it runs the entire length of z -axis. It should be noted that the current density drops in order of magnitude even at a distance of $\Delta \approx 3L/R_\alpha$ away from the plane, but the plasma velocity at the distance comprises more than half its maximum value.

Thus, one possible steady state of the force-free magnetic field in the turbulent resistive plasma corresponds with a compression of the plasma into a layer with net electric current inside being equal to zero. In so doing, both the convective transfer of the magnetic field into the layer by mean plasma flow and the dynamo action maintain precisely the steady force-free field against its decay owing to magnetic diffusion. At infinity the magnetic field is a potential one (γ tends to zero) and is in opposition to a positive direction of x -axis. Therefore, the electric field generated by turbulent dynamo in the current-free plasma must be balanced by an external homogeneous electric field in the form $\vec{E} = \{R_\alpha, 0, 0\}$. It may be concluded that the expressions (2) describe a continuous one-dimensional model of the force-free ZNC layer placed in the homogeneous collinear electric and magnetic field.

3. β -effect in the force-free ZNC layer

It is necessary to stress that α -effect plays a crucial role in the formation of ZNC layer because the solution (2) to equations (1) disappears in the limit $\alpha \rightarrow 0$. This is a reason to consider the characteristics of MHD turbulence in the force-free magnetic field.

In so much strong magnetic field the turbulence, possessing the property of magnetic field generation, can be present only as a random MHD waves of two modes: Alfvén waves and fast magneto-acoustic waves with nearly equal frequencies. The wave turbulence may acquire nonzero mean helicity of the velocity fluctuations \vec{u} needed for an existence of α -effect ($\alpha \propto \langle \vec{u} \cdot (\nabla \times \vec{u}) \rangle$) by virtue of nonlinear interaction between the waves of distinct modes. But, as is shown in [4], this interaction causes concurrently the

spectral transfer of large-scale magnetic field helicity $\vec{B} \cdot (\nabla \times \vec{B}) = \gamma B^2$ to the short-wave region of magnetic fluctuations \vec{b} . This in turn gives rise to the main nonlinear dynamo process - so called β -effect - wherein the coefficient α in (1) has to be replaced by a sum of $\alpha + \beta$, where $\beta \propto \langle \vec{b} \cdot (\nabla \times \vec{b}) \rangle$. The coefficient β is always opposite in sign to α , that is why β -effect may weaken the dynamo action tangibly. The quantity β is governed by equation [5] that can be represented in the case of the force-free mean magnetic field and high conducting plasma ($\eta_m \rightarrow 0$) as

$$\frac{\partial \beta}{\partial t} + \nabla \cdot (\beta \vec{v}) = \frac{4c_A^2}{3} \left(\gamma - \frac{\alpha + \beta}{\eta_r} \right), \quad (3)$$

where c_A is the instantaneous Alfvén velocity. The solution of (3), being averaged over the characteristic width $L = 2\Delta \approx 6\eta_r/\alpha$ of ZNC layer, has been found for the function γ from (2) and initial condition $\beta(t=0) = 0$ in the form

$$\beta = -\frac{\alpha}{6} \left[1 - \exp \left(-\frac{4}{3\eta_r} \int_0^t c_A^2 d\tau \right) \right].$$

As can be seen from this expression, $\beta(t \rightarrow \infty) \rightarrow -\alpha/6$ and $\alpha + \beta \approx 0.8\alpha$ in the steady state. It means that the main part of magnetic helicity of the large-scale force-free field being considered is conserved in the long wave region of turbulent spectrum. Therefore negative influence of β -effect on the formation of the force-free ZNC layer in turbulent plasma can be neglected to a first approximation.

4. Conclusion

The static force-free ZNC layer, as applied to the problem of explosive release of magnetic energy stored in many natural objects, has been considered in [6]. This layer is supposed to be a simple model of linearly unstable magnetic configuration, which may be formed and energized by the relative or differential motion of line-tied ends of the localized part of pre-existing potential field imbedded in a high conducting plasma. In reality, however, convective flows of the plasma, stressing the initial equilibrium field and giving rise to its energy build-up, are far more complex and diversified.

Because of this, the study of the nonlinear magnetic-energy release, stored in the dynamical force-free ZNC layer by the opposing large-scale plasma flows, seems to be of a substantial interest for understanding of the unstable relaxation of magnetic systems being often observed both in astrophysics (solar and magnetospheric activity) and in laboratories as well.

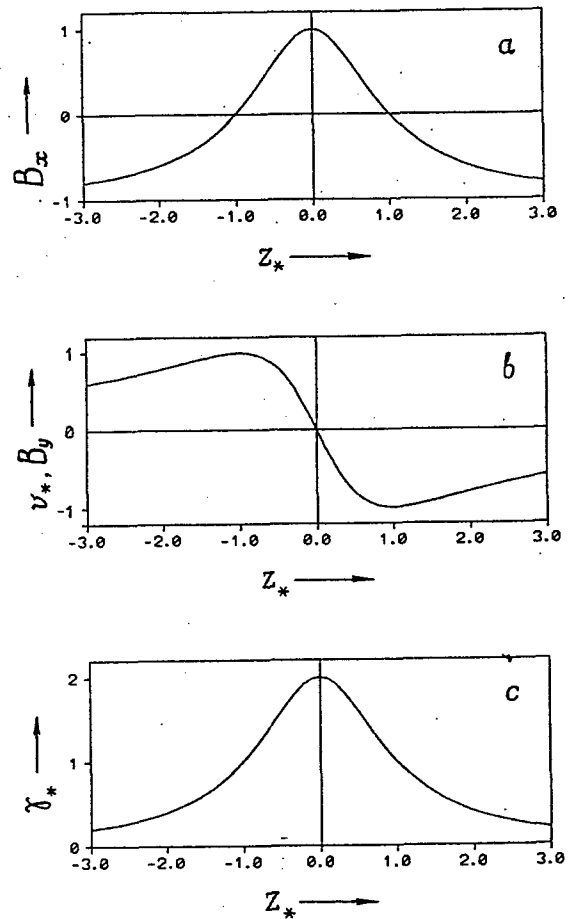


Fig.1. The distributions of the magnetic field components B_x (curve a) and B_y (curve b), plasma velocity $v_* = v(R_{em}/R_\alpha)$ (coincides with curve b) and function $\gamma_* = \gamma/R_\alpha$ (curve c) along the axis $z_* = zR_\alpha$ in the dynamical force-free zero-net-current layer.

5. References

- [1] H. K. Moffatt: 1978, "Magnetic Field Generation in Electrically Conducting Fluids", University Press, Cambridge
- [2] B. C. Low: Rev. Geophys. Sp. Phys., **20** (1982) 145
- [3] Yu. P. Emets, A. V. Sorokin: 1989, Proc. XIX ICPIG, Belgrad, Contr. Pap. 2, 264
- [4] S. I. Vainshtein: 1983, "Cosmical Magnetic Fields", Nauka, Moscow (in Russian)
- [5] S. I. Vainshtein: Magnetohydrodynamics, N 3 (1980) 3 (in Russian)
- [6] J.-S. Kim et al: J. Plasma Phys., **45**(1) (1991) 71

Adiabatic evolution of force-free plasmoid with surface currents

A. F. Djakov, Yu. K. Bobrov* and A. V. Sorokin*

Russian Joint-Stock Company of Energy and Electrification "EES Rossii", Moscow, Russia

*High Voltage Research Centre of All-Russian Electrotechnical Institute, Istra, Moscow region, Russia

1. Introduction

A wide range of phenomena in plasmas is described by the one-fluid magnetohydrodynamic equations with isotropic pressure. Using nondimensional variables the equation of steady laminar motion of the plasma may be written in the form

$$M_A^2 \rho (\bar{v} \nabla) \bar{v} + (\beta/2) \nabla p + \bar{B} \times (\nabla \times \bar{B}) = 0, \quad (1)$$

where $M_A = v/c_A$ is the hydromagnetic Mach number, $\beta = p/p_m$ is the "plasma beta", $c_A = B/\sqrt{\mu_0 \rho}$ is the Alfvén velocity, $p_m = B^2/2\mu_0$ is the magnetic pressure. Since in the nearly incompressible magnetized plasma the density disturbances propagate with velocity c_A then $\beta, M_A \ll 1$ for slow (subsonic) motions. As this takes place, the magnetic field to a first approximation has, according to (1), force-free structure and satisfies the equations

$$\nabla \times \bar{B} = \gamma \bar{B}, \quad \nabla \cdot \bar{B} = 0, \quad (2)$$

where γ is a scalar function. An immediate consequence of these equations is that $\bar{B} \nabla \gamma = 0$, i.e. γ is constant along a force line of the field.

Analysis of stability of the magnetic field frozen into a closed volume of perfectly conducting plasma, so that magnetic helicity $H = \int \bar{A} \bar{B} dV$ ($\bar{A} = \nabla^{-1} \times \bar{B}$) is a topological invariant, leads to conception of the force-free field as well. In this case magnetic field possessing a minimum of energy is governed by equations (2) with constant γ [1].

2. Force-free plasmoid with surface currents

Further a quasistatic expansion (or contraction) of the plasma volume bounded by the sphere $r = R(t)$ with axisymmetric force-free magnetic field inside is considered. The rate of volume change is assumed to be much less than instantaneous average value of Alfvén velocity in the plasma, i.e. $dR/dt \ll c_A$. That is the force-free configuration may be treated as is in equilibrium with external plasma at every instant. Following integral values remain constant during the

evolution: mass m of the plasma and azimuthal magnetic flux Ψ , both are confined in the volume $r < R$, as well as the helicity H (three invariants of the process).

It is supposed that force-free magnetic field is generated rapidly in the domain $r < R(0)$ embedded in an infinitely conducting plasma. Then surface currents are present on the domain free boundary over a period of ensuing evolution of the force-free plasmoid. These currents prevent the magnetic field penetration into outer region and create an extraneous field (para to magnetic field of volume currents in the plasma) that is required to an existence of the finite force-free system. In spherical coordinates $\{r, \theta, \varphi\}$ equations (2) have a solution of "classical spheromak" type [2], whereby

$$B_r = B_\varphi = 0, \quad B_\theta = \sqrt{2/\pi D} \gamma^2 \cos \omega \sin \theta \quad \text{for } r = R, \quad (3)$$

where $\omega = \gamma R$, $D = D(\psi) = \text{constant}$. According to (3) there is only azimuthal component i_φ of the surface

current \bar{i} being equal to $i_\varphi = -B_\theta(R, \theta)/\mu_0$. Parameter ω must obey the equation $\omega = \tan \omega$ and is the fourth invariant of the process considered ($\omega = 4.49...$ for a lowest magnetic energy state of the plasmoid).

The condition of a slow (adiabatic) evolution of the plasmoid may be expressed in the form

$$d(R^{3/2})/dt \ll 6\Psi/\sqrt{3\pi\mu_0 m} = \text{inv}, \quad (4)$$

where the term on the right-hand side is constant for all t . Therefore an inequality (4) comprises a criterium for the rate of change of the plasmoid radius which preserves the force-free character of the magnetic field.

3. Potential function of the force-free system

The relationship between radius R and gasdynamic pressure on the plasmoid surface is established by means of a potential function of the force-free plasma system confined inside a closed boundary with surface currents by external medium pressure. By a potential function is meant an integral energy characteristic of the magnetic system a variation in which is equal but opposite in sign to an infinitesimal mechanical work of the forces operating in the system. If an expression of the potential function U for the system under consideration is known then a condition of quasistatic equilibrium of the system is represented as $dU/dR = 0$.

In the absence of external medium pressure, the potential function of the spherical axisymmetric force-free domain with surface currents has been derived in [3] in the form

$$U_m = U_0/R, \quad U_0 = \omega H/2\mu_0. \quad (5)$$

It is easily seen that this force-free configuration cannot be even in quasistatic equilibrium because of $dU_m/dR \neq 0$ for any R . An equilibrium is possible in the pressure-balanced system where the gasdynamic pressure of external plasma equalizes the electromagnetic forces acting on the surface currents and tending to expand the configuration.

Let $\tilde{p}(t)$ be the average boundary pressure of external plasma over the surface of the sphere. By virtue of the fact that $R = R(t)$, the time-dependent pressure \tilde{p} may be rewritten as $\tilde{p} = \tilde{p}(R)$. When radius R gains a variation δR , an infinitesimal work of the surface pressure forces becomes

$$(\delta W)_p = -\delta U_p = -\tilde{p}(R)\delta V(R), \quad (6)$$

where $\delta V(R) = 4\pi R^2 \delta R$ is the variation of spherical volume. From (5) and (6) it follows that the potential function for the force-free system involved has the form

$$U = U_m + U_p = U_0/R + 4\pi \int \tilde{p}(R) R^2 dR. \quad (7)$$

According to quasistatic equilibrium condition, the relationship between R and \tilde{p} can be obtained from (7) as

$$R(t) = \sqrt[4]{U_0/4\pi\tilde{p}(t)}. \quad (8)$$

4. Conclusions

1. The model of linear expansion of the force-free plasmoid from volume V to V' has been discussed in [4]. In this model the coordinates x_i ($i = 1, 2, 3$) of an arbitrary point lying on some magnetic line vary linearly in the laboratory frame of reference, so that $x'_i = \xi_i x_i$, $\xi_i = \text{const}$. It has been shown that magnetic field is kept force-free one in the course of the expansion only if $\xi_i = \xi$ for any i . Equation (8) makes it possible to express the parameter ξ in terms of the mean boundary pressure as

$$\xi = R(t')/R(t) = \sqrt[4]{\tilde{p}(t)/\tilde{p}(t')}, \quad t' > t.$$

2. It should be noted that the rate of change of the average boundary pressure depends strongly on the plasmoid radius. From (8) follows

$$\frac{d\tilde{p}/dt}{dR/dt} \propto \frac{1}{R^5} \rightarrow 0 \quad \text{for } R \rightarrow \infty.$$

The rate of pressure decrease falls steeply compared to the rate of plasmoid expansion with increasing radius R . Therefore the process may be considered as going on at the constant "background" pressure of the plasma outside the force-free domain late in the expansion.

3. This "background" pressure is not fully arbitrary one but has its lower limit. For example, in the case of constant-rate adiabatic expansion of the force-free sphere, when $R(t) = R(0) + at$ (a is a positive constant), throughout the expansion the pressure \tilde{p} must satisfy the inequality

$$\frac{a}{\sqrt[8]{\tilde{p}}} < < \frac{4\Psi\sqrt{2/3m}}{\sqrt[8]{2\omega H(\pi\mu_0)^3}} = \text{inv},$$

following from (4) and (8). The minimum \tilde{p}_{\min} of the outer pressure depends heavily on the rate of expansion; a comparison of two regimes with $a^{(2)} = 0.1a^{(1)}$ gives $\tilde{p}_{\min}^{(2)} = 10^{-8} \tilde{p}_{\min}^{(1)}$.

5. Applications

These results may be applied to further development of the evolution theory of solar-originated magnetized plasmoids (magnetic clouds) observed in the interplanetary space [4]. They also make a contribution to the study of compact toroidal magnetic confinement devices described by Taylor relaxed state [5].

It is evident that the principal results relating to plasmoid dynamics are valid whether force-free plasmoid is confined by gasdynamic pressure of the outer high conducting plasma, or it is situated in vacuum and balanced owing to the magnetic pressure of external confining field (in the latter case the surface currents are absent and plasmoid is force-free entirely). For example, adiabatic expansion may occur early in the formation of spheromak configuration in the plasma produced by a coaxial gun and injected into the confinement chamber (flux conserver) [6]. On the contrary, the compression governed by (4) and (8) may be expected to attend a passage of the relaxed compact toroids through the converging section of high energy accelerator like MARAUDER [7]. In both cases the confining magnetic field is generated in self-consistent manner by the eddy currents induced in the well conducting walls of experimental setups.

6. References

- [1] L. Woltjer: Proc. Nat. Acad. Sci.(USA), **44** (1958) 489
- [2] M. N. Rosenbluth, M.N.Bussac: Nucl. Fusion, **19** (1979) 489
- [3] A. V. Sorokin: 1988, In: "Electromagnetic Field of Electric Power Setups", Nat. Acad. Sci.(Ukraine), Kiev, p. 112 (in Russian)
- [4] W.-H. Yang: Astrophys. J., **344** (1989) 966
- [5] J. B. Taylor: Rev. Mod. Phys., **58** (1986) 741
- [6] B. L. Wright: Nucl. Fusion, **30** (1990) 1739
- [7] J. H. Degnan et al: Phys. Fluids, **B5** (1993) 2938

Spatiotemporal dynamics and control of ionization waves in an undriven neon glow discharge

A. Atipo, Th. Pierre and G. Bonhomme

Laboratoire de Physique des Milieux Ionisés et Applications, U.R.A 835 du C.N.R.S.
Université Henri Poincaré, Nancy I, B.P. 239 54506 Vandoeuvre Cedex FRANCE
e.mail:atipo@lpmi.u-nancy.fr

1. Introduction

Gas discharges offer a paradigm for nonlinear processes, which in recent decades have received a growing interest [1-5]. These nonlinear behaviours, as it is well known, have an important role in plasma physics. Consequently their study is of greatest importance. There are now several works reporting on experimental and theoretical studies on nonlinear phenomena in plasma systems [1,6], but they are mostly made through a local measurement of the temporal behaviour. However, to improve and to get a better understanding of chaotic phenomena and turbulence in spatially extended plasmas, spatiotemporal investigations are needed. The goal of this paper is to present the spatiotemporal experimental investigations of the chaotic regimes of ionization waves in an undriven glow discharge, and to demonstrate that it is possible to control these chaotic regimes.

2. Experiment

The experiments are carried out in a conventional cold-cathode glow discharge, filled with neon gas under pressures from 1 torr to 10 torrs. The discharge voltage is applied between the end electrodes; the current discharge can be varied between 0 to 100 mA. In the chosen pressure range the plasma is collisional and a positive column forms in an extended region of the discharge (30cm in length). Ionization waves which are related to the modulation of the electron temperature and to the subsequent modulation of the ionization rate propagate in the positive column [7]. Different types of ionization waves which are in nonlinear saturation can propagate simultaneously in the discharge. The existence of several eigenmodes with strong couplings leads to self-excited chaotic dynamics [8]. The discharge current fluctuations are measured through a resistor inserted in the discharge circuit. The local fluctuating wave fields are observed by detecting the fluctuations in the light emission flux, using fast collimated photodiodes. At aiming to make the spatiotemporal investigations of the ionization waves chaotic dynamics, a fast 16-channels VXI digitizing plug-in unit is used. It performs synchronized acquisition of the signals from 16 axially

regularly spaced photodiodes. The signals are then stored and processed in a computer. A digital oscilloscope and a high resolution spectrum analyzer are also used.

3. Results

Typical ionization waves regimes observed in a neon glow discharge are shown in figure 2 and 3, where the signals are plotted versus time and space. It is obvious that the two regimes shown below are basically different: the first (figure 2) is a periodic regime, while a detailed analysis of the second has shown typical features of a chaotic regime.

The control of these chaotic regimes has been achieved using two different methods: the Time Delay Autosynchronization method (TDAS) [9, 10], and the Spatial Autosynchronization method, in which the signals obtained from two distant axially movable detectors are subtracted, using a differential amplifier. The amplifier output signal is applied to the control parameter (discharge current), achieving thus the control of the chaotic regime.

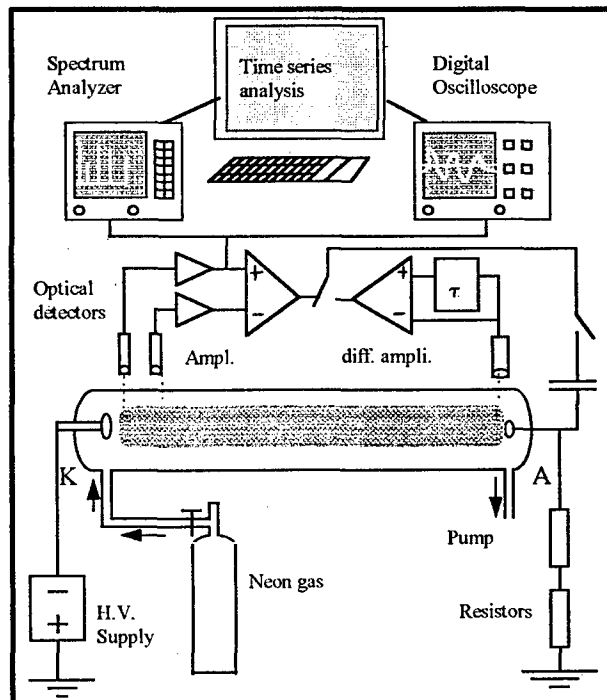


Figure 1: Experimental set-up

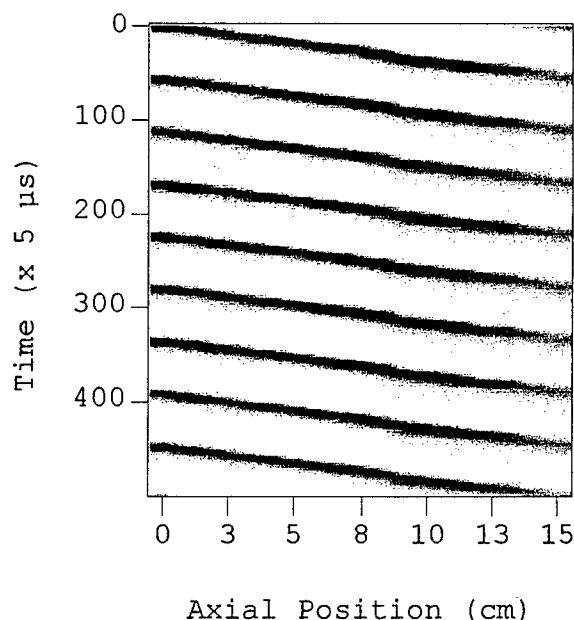


Figure 2: Periodic regime of ionization waves.

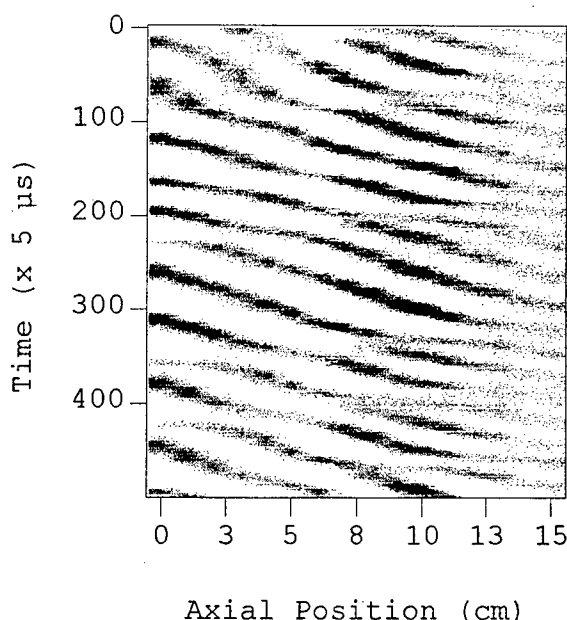


Figure 3: Spatiotemporal chaotic regime of ionization waves

When switching on the control in the chaotic regime, the system remains chaotic during a certain time interval until the stable orbit is approached.

Such transient dynamics which precede the stabilization of a periodic orbit are studied by means of spatiotemporal investigations.

4. Conclusion

Undriven chaotic regimes of ionization waves in a neon glow discharge have been investigated from extended spatial analysis for spatiotemporal behaviours.

Chaotic regimes are controlled using two different control techniques.

The chaotic and periodic transient dynamics preceding the stabilization of a given periodic orbit has also been experimentally studied.

5. References

- [1] A. Piel, T. Klinger, in Proc. of XIIth ICPIG, Invited Papers, edited by K. H. Becker, W. E. Carr, E. E. Kunhardt, page 90, AIP Conf. Proc. 363, AIP Press, (1996).
- [2] P. Y. Cheung and A. Y. Wong, Phys. Rev. Lett. **59** 551 (1987).
- [3] T. Braun, J. A. Lisboa, R. E. Francke and J. A. C. Gallas, Phys. Rev. Lett. **59** 613 (1987).
- [4] K. Ohe and H. Tanaka, J. Phys. D, Appl. Phys. **21**, 1391 (1988).
- [5] C. Wilke, H. Deutsch and R. W. Leven, Phys. Lett. **136**, 114 (1989).
- [6] T. Klinger et al., Nonlinear dynamics and chaos in gas discharge systems, Journal de Physique IV, Vol.5, C6-131 (1995).
- [7] L. Pekarek, Ion waves and ionization waves, in Proc. of Xth ICPIG, Invited Papers, edited by P.A. Davenport, page 365, Oxford, UK (1971).
- [8] K. D. Weltmann, T. Klinger, and C. Wilke, Phys. Rev. E **52**, 2106 (1995).
- [9] K. Pyragas and A. Tomasevicius, Phys. Lett. A **180**, 99 (1993).
- [10] T. Pierre, G. Bonhomme and A. Atipo, Phys. Rev. Lett. **76**, 2290 (1996).

Comparative studies performed on "fireballs" formed in direct current and high frequency discharges

M. Sanduloviciu, C. Borcia[†], V. Melnig and C. Gherman

"Al.I. Cuza" University, Department of Plasma Physics, 6600 Iasi, Romania

[†]present address: Université Paris-Sud, L.P.G.P., bât. 212, 91405 Orsay cedex, France

The appearance of spherical coherent space charge configurations, in the form of a fireball or of a plasmoid, is a phenomenon well known by the physicists that have worked in d.c. and h.f. gas discharges. Concerning their spontaneous appearance, recent investigations have proved the presence of the same self-organization mechanism [1,2]. In this paper we present, additionally, a comparative study of the generation process and the behavior of a nearly spherical fireball formed in a low voltage d.c. arc and of a plasmoid formed in a h.f. electric field.

The presence of the self-organization process can be evidenced by plotting the diagram (characteristic) of a system parameter as a function of a control parameter. The nonlinearity evidenced in this characteristic related to hysteresis cycles, bistabilities, oscillations, period multiplications, and transitions to chaos, are strong arguments for the presence of self-organization [3,4].

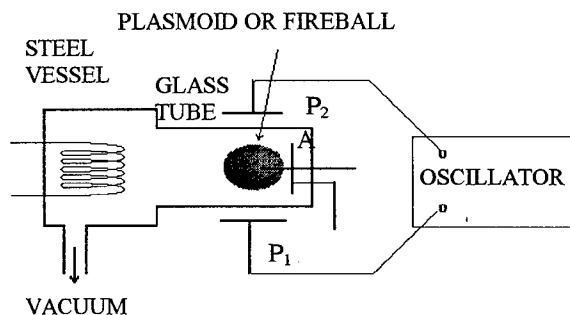


Fig. 1 Experimental device

The experimental device is schematically shown in Fig. 1. It consists of a plasma source containing a heated tungsten wire whose potential is biased negatively with respect to the surrounding steel vessel. At the one end of the vessel a glass tube is attached. It contains, at its free end, a circular plate anode (A). The steel vessel is connected at a vacuum device. The working gas (Argon) is introduced through a needle valve at pressures in the range $10^{-1} \div 10^{-3}$ Torr. One obtains the typical $I(V)$ characteristic shown in Fig. 2(a) by increasing and decreasing slowly the positive voltage of A. In this characteristic the current I collected by A represents the system parameter and the anode voltage V the control parameter. As known [1-3], the nearly spherical space charge configuration appears in front of the anode when its voltage reaches a certain critical value for which the current suddenly increases. This behavior proves that for this critical value the ohmic resistance of the gaseous conductor suddenly decreases. The single possible explanation of

this sudden resistance decrease is, in our opinion, the formation of an electrical double layer at the border of the fireball, able to act as a source of new charged particles. Evidently, this is possible when the potential

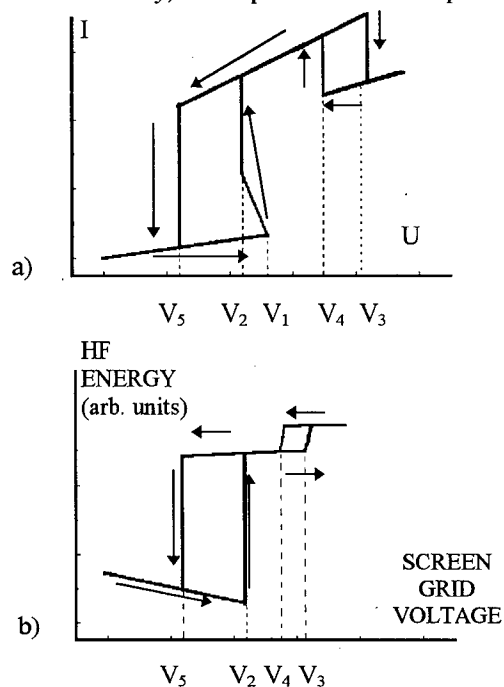


Fig. 2 Critical points in the diagram in which the system parameter current is plotted as a function of the control parameter anode voltage, related to the self-organization scenario at the origin of the spherical space charge configuration; V_1 -appearance of the negative resistance branch (a); V_2 -spontaneously formation of the fireball attached at the A surface (a) and of the plasmoid (b); V_3 -transition into an oscillatory regime; V_4 -disappearance of the oscillatory regime; V_5 -disruption of the fireball (a) and of the plasmoid (b)

developed over the double layer reaches or exceeds the ionization potential of the Argon (15.6V). The presence of such a potential gradient is proved by measurements performed with a heated probe and presented in Fig. 3. The diminishing of the internal resistance, firstly evidenced by the negative slope of the $I(V)$ characteristic, appears when the ionization cross section suddenly increases. Consequently, a relative great number of electrical charged particles is produced.

In order to prove the possibility to determine the transition from the nearly spherical fireball attached at the anode surface into a free floating plasmoid sustained by a high frequency electric field,

we have placed the region around A within two plates P_1 and P_2 connected to a high frequency oscillator. The h.f. energy of the oscillator can be varied continuously by the mean of the screen grid voltage.

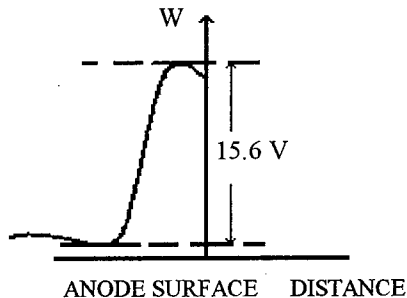


Fig. 3 The axial potential in front of the anode of the plasma diode when the fireball is present

We perform our investigations producing firstly the nearly spherical fireball attached at the anode by fixing its voltage at the first critical value, V_2 . If, under these conditions, a h.f. electric field is created within the two plates P_1 and P_2 , it becomes possible to determine the detachment of the fireball from the anode surface and, after that, its further sustenance only by the h.f. electric field. Using the same heated probe we have measured the allure of the potential around and inside the spherical space charge structure, i.e. the plasmoid. The measurement results are shown in Fig. 4 and prove a similar internal structure as that of the fireball produced in the d.c. discharge. Using as a system parameter the energy transferred from the oscillator through the discharge and, as a control parameter, the screen grid voltage, we obtain the diagram presented in Fig. 2(b). This diagram shows also the presence of critical points. The first one, V_2 , in which the energy transferred to the discharge abruptly increases, proves a sudden diminishing of the discharge impedance. Evidently, such a behavior can be explained in the same way as for the current increase showed in Fig. 2(a), i.e. the creation of a new source of electrical charged particles. This fact appears when the potential drop on the spherical double layer that borders the plasmoid becomes equal or greater than the ionization potential of the Argon.

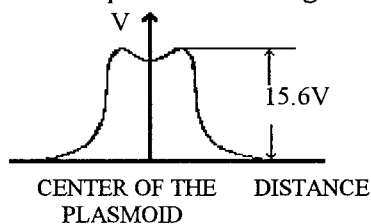


Fig. 4 The axial profile of the potential through the plasmoid

The described results prove that both the formations of the nearly spherical fireball attached to the anode of a d.c. discharge and of the plasmoid generated by the h.f. electric field are related with the nonlinear behavior of the system. In both cases the

spatial coherence of the structures is assured by an electrical double layer that protects the system from the surrounding plasma.

Another critical point, V_3 , present in both characteristics, is related to the transition into an autonomous state evidenced by the fact that the spherical double layer detaches from the anode surface and runs through the plasma column, toward the plasma source. The periodical formation and disruption of the double layer in front of the anode [3] are accompanied by a periodical exchange of matter and energy with the surrounding environment. This is evidenced in the appearance of periodical modulations of the system parameters [3]. The presence of hysteresis phenomena when the control parameter is slowly decreased proves also that both coherent structures have the ability to memorize their past history, a phenomenon usually proper to self-organized systems.

On the basis of these experimental results we conclude that it is possible to control the transition from a fireball generated in a d.c. discharge into a h.f. plasmoid. After the disconnection of the d.c. power supply the existence of the spherical space charge structure is sustained by radiation energy produced at resonance.

Our results prove that a space charge structure whose coherence is assured by a spherical double layer behaves as a cavity able to absorb radiant energy at resonance. The described results prove also that the plasma inside the cavity is heated by radiative energy absorption and that, due to the difference between the electrons and positive ions mobility and diffusivity, it becomes possible to maintain an excess of positive ions inside the plasmoid nucleus. The unstable state of the plasmoid, already described as a pulsating phenomenon [2], relieves its property to act as an autonomous body. The autonomy of the system is realized by a periodical exchange of matter and energy within the plasmoid and the surrounding plasma.

All the above briefly described experimental results are arguments which demonstrate the presence of a similar self-organization process at the origin of fireballs formed in d.c. discharges and of plasmoids formed in h.f. electric fields. As a consequence of their similar internal structures it becomes possible to produce, in a controlled way, the transition from a fireball, initially generated in a d.c. discharge, into a plasmoid whose further existence can be assured only by a h.f. electric field.

Bibliography:

- [1]. M.Sanduloviciu, E.Lozneanu, Plasma Phys. Contrl. Fusion, **28** (1986) 585
- [2]. M.Sanduloviciu, Plasma Phys. Contrl. Fusion, **29** (1987) 1687
- [3]. M.Sanduloviciu, C.Borcia, Gabriela Leu, Phys. Lett. A, **208** (1995) 136
- [4]. G.Nicolis and I.Prigogine, 1987, Exploring Complexity, Piper Munich

Self-organization of autonomic chaotic regimes in striated low-temperature plasma of a glow discharge

M.V. Chirkin, V.V. Solonin, V.A. Stepanov

Department of Physics, Pedagogical University

46 Svoboda St., 390000 Ryazan, Russia

e-mail: yastreb@ttc.ryazan.ru

1. Introduction

The control of the chaotic state of ionization waves in the positive column of a periodically driven neon glow discharge was achieved by an active feedback technique [1]. It was shown that an unstable periodic orbits (UPO's) in chaotic state could be stabilized by small, time-dependent variations of the modulation amplitude.

In the present paper there has been studied the phenomenon of self-organization of chaotic regimes in the autonomous striated low-temperature plasma of a neon glow discharge. The purpose of the investigation is to explain the mechanism of self-organization by means of analysis of UPO's inside the phase space chaotic attractor.

2. Methods of investigation

The experimental set-up consists of discharge tube (10 mm in internal diameter, 203 mm in length, filled with pure neon, pressure 3 Torr), current supply and the equipment for measurement of the integral light intensity $X(t)$ from the positive column. As one parameter the discharge current was varied between 16.85 and 18.2 mA.

As the plasma is considered to be an open system, a method of renormalized entropy, based on the Klimontovich S-theorem [2], has been applied. This method serves a quantitative measure of relative degrees of order in different regimes of a system. In our case different regimes of moving striations were realised at discharge current variation. To compare the relative degrees of order in two different regimes "0" and "1" (two time series recorded at corresponding discharge currents) there has been calculated a deviation of entropies:

$$\Delta S = \begin{cases} S_0 - \tilde{S}_1, X_0^{max} > X_1^{max}, \\ \tilde{S}_0 - S_1, X_0^{max} < X_1^{max}, \end{cases} \quad (1)$$

$$S_{0,1} = - \int_0^{X^{max}} f_{0,1}(X) \ln f_{0,1}(X) dX, \quad (2a)$$

$$\tilde{S}_{0,1} = - \int_0^{X^{max}} \tilde{f}_{0,1}(X) \ln \tilde{f}_{0,1}(X) dX \quad (2b)$$

where $f_{0,1}(X)$ - distribution functions calculated from a

time series of light intensity oscillations, $\tilde{f}_{0,1}(X)$ - renormalized distribution functions. The procedure of such renorming was described in [3]. The positive value of ΔS means that self-organization has occurred in the system and regime "0" has less order than "1" one.

Together with this method non-linear dynamic tools were used. There has been reconstructed the attractor in the m -dimensional phase space from a time series of one observable (it was the light intensity obtained from the photoelectric multiplier fixed at some point of axial position) according to the Takens theorem [4], and its correlation dimension has been calculated by means of the Grassberger-Procaccia algorithm [5]. Unstable periodic orbits have been extracted from the attractor with the help of Lathrop-Kostelich method [6].

3. Experimental results

With the "0" regime a regime at a minimal discharge current - the onset of chaos - was used in our case. Further the discharge current was increased and we had other regimes (more chaotic states than "0"); we named each of them "1". They were analysed versus the regime "0" in pairs. The calculated entropy shows that the states with more order follow the ones with less order (Fig. 1). The last deviation is $\tilde{S}_0 - S_1 > 0$ and it means that self-organization has taken place in our system. As it will be shown later that state looks like a quasi-periodic motion.

Also the correlation dimension of the reconstructed attractors versus discharge current was valued and unstable periodic orbits were extracted from the time series. It showed the route "chaos onset - chaos - quasiperiodicity" that meant the effect of self-organization in our system.

Next we were interested in a low-period unstable periodic orbits. No low-period orbits were found at a low current, but with the current increased many unstable periodic orbits appear. Looking at a Poincare section (Fig. 2) of three different regimes of the plasma one could suggest that synchronisation of the autonomic chaotic regime or self-organization of the complicated behaviour of moving striates occurs through two unstable periodic orbits.

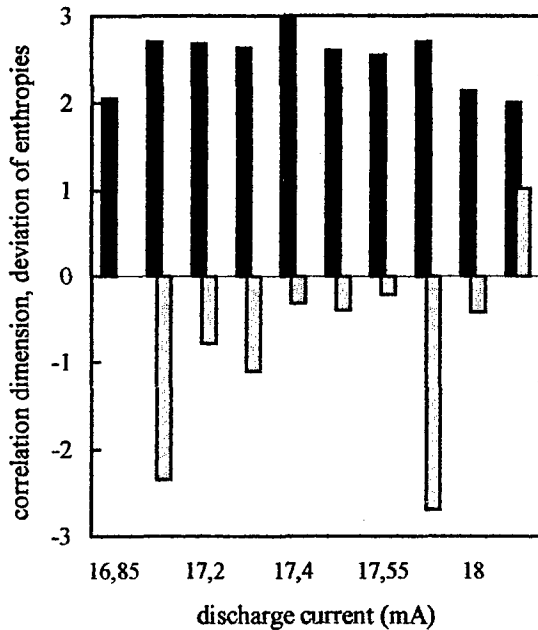


Figure 1: Characteristics of the striated plasma dynamics versus discharge current: light gray columns - deviations of entropies ($10^{-4} S$), black columns - correlation dimensions of the phase space attractors

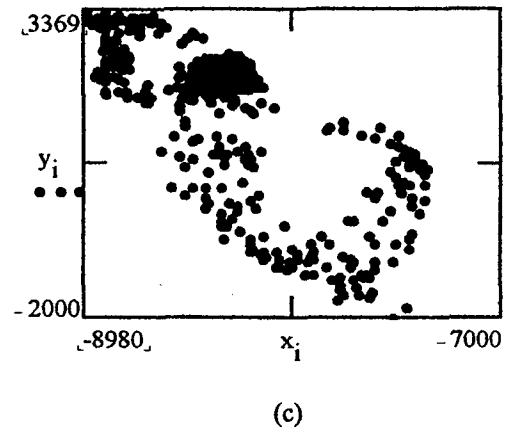
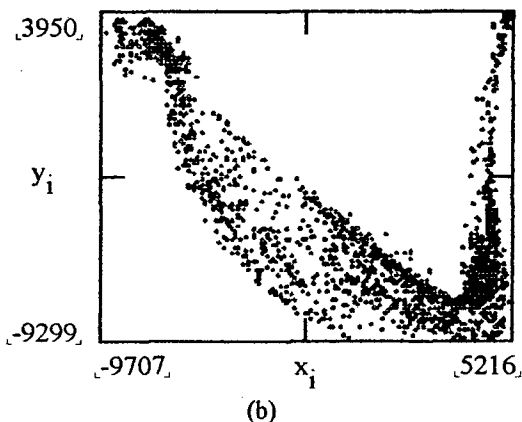
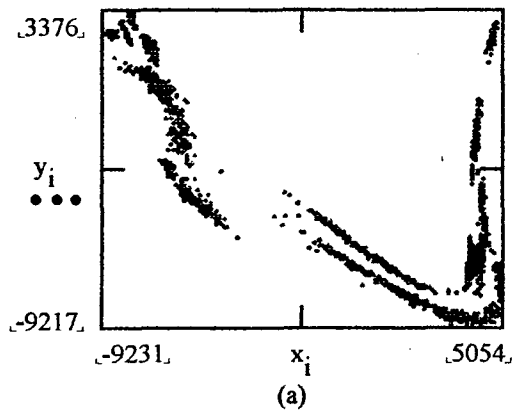


Figure 2: Poincaré sections of the phase space attractors: $x_i = X(t_i - 2\tau)$, $y_i = X(t_i - \tau)$, $z_i = X(t_i) = \text{const}$. Discharge current (mA): a) - 16,85, b) - 17,4, c) - 18,2

4. Conclusions

By means of the method of renormalized entropy, based on the Klimontovich S-theorem, there has been found self-organization of moving striations in a neon discharge. The measurements of correlation dimension of reconstructed attractors at different discharge currents and Poincaré section also confirm that phenomenon. The analysis of unstable periodic motions shows that mode-locking regimes appear through two base orbits that correspond to domains of points at a Poincaré section. It makes us suggests an analogy with the chaos control algorithm [7] though achieved without any temporal program, only by a simple increase in the discharge current.

5. References

- [1] K.-D. Weltmann, T. Klinger, C. Wilke: Phys. Rev. E, 52 (1995) 2106
- [2] Yu.L. Klimontovich: Techn. Phys. Letters, 9 (1983) 1412
- [3] Yu.L. Klimontovich: Techn. Phys. Letters, 14 (1988) 631
- [4] F. Takens: Dynamical systems and turbulence, Berlin, Springer-Verlag (1981)
- [5] P. Grassberger, I. Procaccia: Phys. Rev. Lett., 50 (1983) 346
- [6] D.P. Lathrop, I.J. Kostelich: Phys. Rev. A, 40 (1989) 4028
- [7] E. Ott, C. Grebogy, J.A. Yorke: Phys. Rev. Lett., 64 (1990) 1196

Parametric and nonlinear effects in a UHF resonator loaded by a plasma layer perturbed by ion-sound oscillations.

G. Cicconi and C. Rosatelli

Dipartimento Ingegneria Elettrica, Università di Genova (Italy),
via all'Opera Pia, 11/A I-16145 Genova

1. Introduction

Some preliminary results of an experiment to observe parametric and nonlinear effects produced in a high-Q UHF resonator where a collisionless plasma layer, diffused in a section of this resonator, is extruded by DC discharges modulated by LF low frequency oscillations. The plasma high frequency (Langmuir) steady-state turbulence is enhanced by the LF oscillations applied to grids that control the DC discharges generating the plasma, and then converted in electromagnetic oscillations of the resonator. The turbulent spectra of Langmuir and electromagnetic radiation are strongly attenuated when LF frequency is increased whereas the spectra frequencies of turbulent modes increase with plasma density. To explain the conversion mode is invoked a weakly turbulence model in the context of a three-waves, random phase, nonlinear process [1] in the presence of a modulational instability generated by a ponderomotive force present in particular near the walls.

2. Test set

A detailed description of the plasma loaded resonator (PLR) was reported elsewhere [2] [3]. In particular we give here the essential characteristics of this experiment test set. The diffusion partially ionized extruded plasma (technical quality argon at a pressure of $4 \cdot 10^{-4}$ Torr with an ionization degree of the order of 10^{-4}) is produced by 4 DC discharges located symmetrically upon the inside cylindrical wall of the resonator: the electrons emitted by hot filaments are accelerated and focalised towards the resonator wall by planar grids (50 cm^2 about) having narrow meshes (less than the Debye length). The plasma is confined in a volume of 40 liters at one end of the resonator, which is 1/4 of the maximum volume of the piston-tunable resonator (50 cm diameter and 82 cm max length). At the other end of the resonator (vacuum section) is located a dipole antenna. This PLR, divided in the two section plasma/vacuum, could be considered as a double plasma source [4].

3. Experimental condition

The plasma parameters are the following:

electron density $n_e = (1 \div 6) \cdot 10^9 \text{ cm}^{-3}$,

electron temperature $T_e = (1,7 \pm 0,2) \cdot \text{eV}$,

ion temperature $T_i = (0,2 \pm 0,1) \cdot \text{eV}$,

metastable atom density $n_m = (9 \cdot 0 \pm 1) \cdot 10^8 \text{ cm}^{-3}$,

metastable temperature $T_n = (400 \pm 20) \text{ K}$.

Resonator conditions: length constant $L = 82 \pm 2 \text{ cm}$; lower resonance frequencies (plasma absent): TE(111) dominant mode 398 MHz, TE (112) 514 MHz, TM(012) 592 MHz, TM(013) 726 MHz; loaded Quality factor 500;

modulation conditions: LF variable in the range $(10 \text{ Hz} \div 2 \text{ MHz})$, sine and square wave operation, amplitude peak-to-peak applied to the grids 20 V in the presence of RC coupling.

4. Experimental results

In this paper some preliminary results are shown concerning the excitation, by LF signals in the presence of plasma, of TE(111) dipolar and TM(012) electric monopolar resonant modes. The effects produced on these resonant modes by the LF frequency of excitation were observed by means the following diagnostics:

a) diagnostics of density fluctuations in turbulent regime performed on the resonator antenna measuring the reflexion of a swept nonperturbing electromagnetic wave. The swept antenna reflexion is observed in a band of 50 MHz around the turbulent plasma resonance. The more important nonlinear observed effect is a strongly decreasing in amplitude of the turbulent bands when the LF frequency increases. A sweep RF generator is connected to the antenna. In figs. 1 and 2 are shown the oscilloscope displays of the resonance mode TE(111) for 1 and 10 kHz LF modulation. In figs. 3 and 4, in the same condition of figs. 1 and 2, are shown the displays for the resonance TM(012).

b) diagnostics of RF (or microwave) emission by a spectrum analyser SA connected to the resonator antenna. In this case the dominant nonlinear effect is the radiation band that appears as splitted in two lateral bands (lower and upper bands). The upper band is strongly attenuated when the frequency of the LF excitation is increased. In figs. 5 and 6 are shown the SA displays for 1 and 10 kHz LF (sine) excitation (TE111). A similar observation may be made for (TM012) mode.

5. Theoretical model and comments

A simple theoretical model suitable to explain, in a first approximation, the experimental results here presented based on a three-waves interaction (plasmon description: $l+s \rightarrow t$) may be phenomenologically synthesized by the following three nonlinear inhomogeneous equations:

s-wave (Korteweg de Vries):

$$\Psi_t + \alpha \Psi_x + \beta \Psi_{xxx} = \gamma |\Psi_0|^2 \Psi,$$

l-wave (Schrodinger):

$$\phi_{xx} + K\phi + K_0 |\phi|^2 \phi \pm i\phi_t = K_1 |\Psi|^2 \phi,$$

t-wave : (resonator m,n mode)

$$\left(\frac{\omega^2}{\omega_{m,n}^2} - \frac{\omega_{m,n}^2}{\omega^2} \right) + \frac{i}{Q_{m,n}} = \frac{y_g(\psi, \phi)}{y_{m,n}}$$

where Ψ_0 is the LF external pump potential.

In principle this simple model gives us an unidimensional phenomenological solution describing, in a first approximation, our experiment results. However surface effects generating an electric ponderomotive force, which could be responsible for the excitation of the lower and upper resonance bands, growing by parametric modulational instabilities [5], cannot be taken into account. A more refined theory, along with other experiment results in which the level of LF pump is varied, is necessary.

References

- [1] V.N. Tsytovich. Nonlinear Effects in Plasmas, Plenum Press (1970)
- [2] G. Cicconi and A. Tarditi. Plasma Sources Science & Technology 4,13 (1995)
- [3] G. Cicconi and C. Rosatelli. ICPP 96 Nagoya Abstract 9J05. Contributed Paper (in press)
- [4] H. Ikezi et al. Fifth Conf. on Plasma Physics and Controlled Nucl. Research (Tokyo 1974) H4-3,732
- [5] F. Cap. Handbook of Plasma Instabilities. Vol. 2 Academic Press (1978)

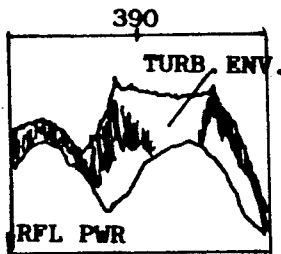


FIG. 1

TE(111)
 $f_0 = 390\text{MHz}$
 $\Delta f_0 = 40\text{MHz}$
 $f_m = 1\text{kHz}$

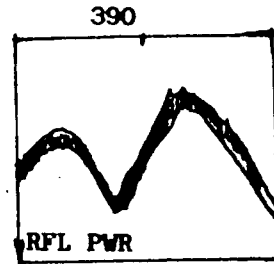


FIG. 2

TE(111)

$f_0 = 390\text{MHz}$
 $\Delta f_0 = 40\text{MHz}$
 $f_m = 10\text{kHz}$

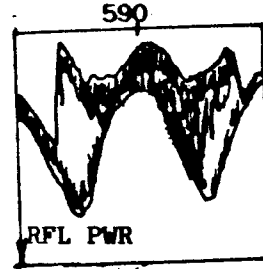


FIG. 3

TM(012)
 $f_0 = 590\text{MHz}$
 $\Delta f_0 = 40\text{MHz}$
 $f_m = 1\text{kHz}$

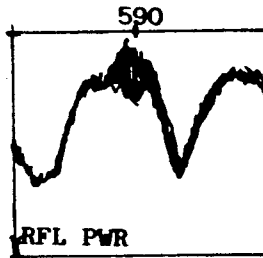


FIG. 4

TM(012)
 $f_0 = 590\text{MHz}$
 $\Delta f_0 = 40\text{MHz}$
 $f_m = 10\text{kHz}$

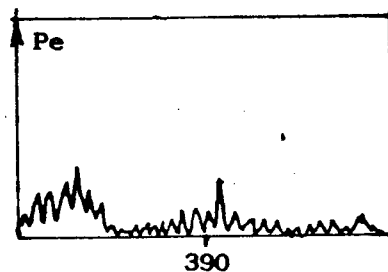


FIG. 5

TE(111)
 $f_0 = 390\text{MHz}$
 $\Delta f_0 = 30\text{MHz}$
 $f_m = 1\text{kHz}$
 $10\mu\text{W/cm}$

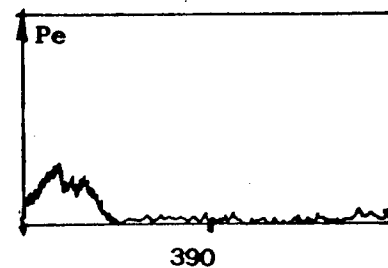


FIG. 6

TE(111)
 $f_0 = 390\text{MHz}$
 $\Delta f_0 = 30\text{MHz}$
 $f_m = 10\text{kHz}$
 $10\mu\text{W/cm}$

The waves scattering processes in the magnetized plasma with upper hybrid pump.

V.N. Pavlenko, V.G. Panchenko, I.N. Rosum

Institute for Nuclear Research,
prospect Nauki 47, 252028, Kiev, Ukraine.

Investigation of electromagnetic wave scattering by density fluctuations are important for studying such problems as wave transportation mechanism in plasmas, measurements of the efficiency of the HF pump power dissipation, plasma diagnostics etc. .

In previous works [1-3] the waves scattering processes in homogeneous plasma and in the plasma with density gradient subjected by lower hybrid radiation have been investigated.

We investigate now the scattering of electromagnetic wave by density fluctuations when the frequency of the pump wave ω_0 is close to the upper-hybrid frequency ω_u .

We then suppose that electron-ion plasma imbedded to the magnetic field $B_0 = B_0 z$ and pump wave electric field $E_0 = E_0 y \cos \omega_0 t$ excites ion-sound waves and the modified convective cells. We can write the differential cross section in the form [1,2]:

$$d\Sigma = \frac{1}{2\pi} \left(\frac{e^2}{mc^2} \right)^2 \frac{\omega'^2 \omega''^2}{\omega_{pe}^4} \times \quad (1)$$

$$R|\xi|^2 \langle \delta n_e^2 \rangle_{\Delta\omega, \vec{q}} d\omega'' d\theta$$

where $\Delta\omega = \omega' - \omega''$, $\vec{q} = \vec{k}' - \vec{k}''$; ω' , ω'' and k' , k'' are the frequencies and the wave vectors of the incident and scattered waves, θ is the space angle, $\langle \delta n_e^2 \rangle_{\Delta\omega, \vec{q}}$ is the correlator of the electron density fluctuations at the combination frequency $\Delta\omega$. As our first example we consider the decay of the pump wave ω_0 into upper-hybrid wave $\omega_{u1} \approx (\omega_{pe}^2 + \Omega_e^2)^{1/2}$ ($\omega_{pe} > \Omega_e$, ω_{pe} and Ω_e are the electron plasma and gyrofrequencies) and modified convective cells $\omega_c = (k_z/k) (m_i/m_e)^{1/2} \Omega_i \ll \Omega_i$. Note that convective modes arise in a magnetized plasma with a small value of β and can occur in the ionospheric plasma [4].

The parametric instability threshold field for this decay is following:

$$E_{th1}^2 = 16 \frac{\omega_o^2 B_o^2}{k^2 c^2} \frac{m_e v_{et}^2 \omega_{u1}}{m_i \omega_c \Omega_e^2} \quad (2)$$

In the region above threshold ($E_o > E_{th1}$) the plasma becomes turbulent and we use the non-linear stabilization mechanism described in [2]. Thus the differential cross section is given by "pump field" term:

$$\frac{d\Sigma_+}{d\Omega} \approx \left(\frac{e^2}{mc^2} \right)^2 \frac{\omega'^2 (\omega' \pm \omega_o)^2}{\omega_{pe}^4} \times$$

$$R|\xi|^2 \frac{q^2 E_o^2 c^2}{\omega_o^2 B_o^2} \left(\frac{\omega_{pt}}{\Omega_i} \right) \frac{\omega_c^4}{\omega_{u1}^2 v_{et}^2} \times$$

$$\frac{q^2 T_e^2}{128 \pi e^2} \frac{\Omega_e^2}{\omega_{pe}^2} \quad (3)$$

For typical ionospheric plasma parameters in the F layer at about 250 km $n_o = 10^6 \text{ sm}^{-3}$, $T_e \sim T_i \approx 0,1 \text{ eV}$, $B_o = 0,45 \text{ G}$, $v_{et} \approx 5 \times 10^2 \text{ sec}^{-1}$ the differential cross section given by (3) exceeds the corresponding one due to thermal noise by several orders of magnitude.

For next our decay of pump wave into upper hybrid

$\omega_{u2} \approx \Omega_e (1 + \omega_{pe}^2 k_z^2 / 2 \Omega_e^2 k^2)$
(for this case $\omega_{pe} < \Omega_e$) and ion-sound wave $\omega_s = kV_s$,
($V_s = (T_e / m_i)^{1/2}$ is the ion-sound velocity) the threshold field is given by :

$$E_{th2}^2 \approx \frac{25}{2} \left(\frac{5\pi m_e}{2 m_i} \right)^{1/2} \frac{v_{Te}^2}{c^2} \times$$

$$B_o \frac{\omega_o^2 (\omega_o^2 - \Omega_e^2) v_{et}}{\omega_{pe}^4 \Omega_e^3} \quad (4)$$

We calculate also in similar manner the differential cross section in the region above threshold ($E_o > E_{th2}$) and estimate that for typical parameters of hot plasma $n_o = 10^{14} \text{ sm}^{-3}$, $T_e = 10 \text{ keV}$, $B_o = 50 \text{ kG}$, the pump field differential cross section is greater than usual thermal noise term by 2-3 orders of value.

The result of this paper should be useful for understanding the processes of electromagnetic wave scattering in the laboratory and ionospheric plasma with upper hybrid pump.

References.

- [1] V.N.Pavlenko, V.G.Panchenko: J. Plasma Physics, **43** (1990) 165.
- [2] H.Wilhelmsson, V.N.Pavlenko, V.G.Panchenko: Phys. Scripta, **44** (1991) 599.
- [3] V.N.Pavlenko, V.G.Panchenko, I.N.Rosum: Abstr., Intern. Conf. on Plasma Physics (Nagoya, Japan, 1996) p.232.
- [4] V.N.Pavlenko, V.G.Panchenko, P.K.Shukla: Sov. J. Plasma Phys., **15** (1989) 531.

Influence of density gradient on absorption of upper hybrid pump energy in turbulent plasma

V.N.Pavlenko, V.G.Panchenko, I.N.Rosum

Institute for Nuclear Research,
prospect Nauki 47, 252028, Kiev, Ukraine.

The absorption mechanism of high-frequency radiation in the plasma by upper hybrid pump wave in the presence of parametric instability have been extensively investigated in recent years [1,2]. The important role of parametric instabilities in the region of upper hybrid resonance was pointed out in [1]. In present report on the base of kinetic fluctuation theory we study the absorption of upper hybrid wave in magnetized inhomogeneous plasma with density gradient. We have calculated the effective collision frequency ν_{eff} in the turbulent state of such plasma when the amplitude of pump wave E_0 exceeds the parametric instability threshold E_{th} . As it turns out $\nu_{eff} \gg \nu_{ei}$, where ν_{ei} is the electron-ion collision frequency. Note that for the case of homogeneous plasma the similar problem was studied in [2]. We consider the inhomogeneous plasma with exponential density gradient when the distribution function $f_{oe,i}$ is proportional to $\exp(\alpha' y)$,

$\alpha' = n_0^{-1} dn_0/dy$ is the plasma inhomogeneity parameter. We suppose that such plasma subjected to the magnetic field $B_0 = B_0 \vec{z}$ and pump wave electric field $E_0 = E_0 \vec{y} \cos \omega_0 t$ excites upper hybrid and electron drift waves. We consider upper hybrid wave satisfying the dispersion relation

$$\omega_U = \Omega_e (1 + \omega_{pe}^2 \sin^2 \theta / 2\Omega_e^2) \quad (1)$$

when ω_{pe} and Ω_e are the electron plasma and cyclotron frequencies, θ is the angle between the wave vector and B_0 . The expression (1) is valid in strongly magnetized plasma for $\omega_{pe} \ll \Omega_e$. We assume that the damping rate of the upper hybrid wave $\gamma_U \approx \nu_{ei}$. The frequency and the damping rate of electron drift wave are:

$$\omega_D \approx -k_{\perp} \alpha' T_e / m_e \Omega_e,$$

$$\gamma_D \approx -(\pi/2)^{1/2} \omega_D (-\omega_D^2 k_{\perp}^2 \rho_i^2 \times (1 + T_e/T_i) / 2k_{\parallel} v_{Te} + T_e \omega_D \times (1 + T_i/T_e) \exp(-\omega_D^2 / 2k_{\parallel}^2 v_{Ti}^2) / k_{\parallel} v_{Ti}) \quad (2)$$

where ρ_i is the ion Larmor radius and $v_{Te,i}$ is the thermal

mal velocity of particles. According to (2) the interaction between the wave and the electrons is destabilizing and we have well known drift instability, which for along time considered to be unavoidable in a finite size plasma. Note however that the ion Landau-damping term will become important in a short device where k_{\parallel} has to take rather large values. Moreover, in a device with magnetic shear, k_{\parallel} can take small values only locally and damping is obtained by convection into regions with larger k_{\parallel} . Consider the parametric decay of pump wave into upper hybrid and electron drift wave

$$\omega_o = \omega_U + \omega_D \quad (3)$$

In the region above threshold ($E_o > E_{th}$, where $E_{th}^2 = 8\omega_o^2 B_o^2 \omega_{pe}^2 \times (kr_{De})^2 \nu_{ei} \gamma_D / k^2 c^2 \Omega_e^3 \omega_D$) plasma

becomes turbulent. We suppose that the scattering of charged particles on the turbulent fluctuations is the nonlinear stabilization mechanism of parametric instability [3]. Thus we introduce the effective collision frequency ν_{eff} that describes such mechanism and defines the velocity of plasma heating. It is shown in [2,3] that ν_{eff} is determined by spectral density of turbulent fluctuations. Under assumption $\gamma_D, \gamma_U < \nu_{eff} < \omega_D$ we find:

$$\nu_{eff} \approx \frac{k_o^2 c^2 \Omega_e^3 \omega_D E_o^2}{8\omega_o^2 B_o^2 (k_o r_{De})^2 \omega_{pe}^2 \nu_{ei}} \quad (4)$$

where k_o is defined by decay condition (3). It can be seen from (4) that ν_{eff} grows with increasing density gradient and intensity of pump wave.

These results agree with experimental data of the anomalous absorption of electromagnetic wave energy in a turbulent magnetized plasma. We note that for typical hot plasma parameters, i.e. $k_o r_{De} = 0,2$, $B_o = 50$ kG, $n_o = 10^{14} \text{ cm}^{-3}$ and $T_e = 5$ keV the present value of ν_{eff} is much greater than ν_{ei} . We have thus deduced the efficiency for the absorption of upper hybrid wave energy in a plasma, as the absorbed power is proportional to $\nu_{eff} E_o^2$. Our results can thus be of interest for upper hybrid heating of plasmas.

References

- [1] R.P.Sharma, P.K.Shukla: Phys.Fluids, 26 (1983) 87.
- [2] V.N.Pavlenko, V.G.Panchenko L.Stenflo, H.Wilhelmsson: Physica Scripta, 44 (1992) 257.
- [3] V.N.Pavlenko, V.G.Panchenko P.K.Shukla: Sov. J. Plasma Phys., 15 (1989) 531.

Interaction of filaments in an a.c.-driven planar gas discharge system

I. Müller, E. Ammelt, H.-G. Purwins

Institute of Applied Physics, University of Münster, D-48149 Münster, Germany

Until now, relatively little research has been done on pattern formation in lateral gas discharge systems, that is, upon non-homogeneous current density distributions perpendicular to the main current flow [1][2]. In our experiments, we investigate a lateral high frequency glow discharge system from the point of view of pattern formation. This paper presents results of the interaction of solitary-like filaments. Our measurements are motivated by theoretical approaches developed in the field of self-organization, more exactly in the field of reaction-diffusion systems of the activator-inhibitor type [3].

The investigated system consists of a planar arrangement of two glass plates which enclose a gas layer (Fig. 1). One of these glass plates has a transparent, conductive ITO(Indium-Tin-Oxide)-layer covering the entire surface. The other glass plate has on its surface an aluminium contact of radial symmetry of a diameter which is smaller than the diameter of the ITO-layer, so that the extension of the active discharge region is defined by the aluminium contact. Typical dimensions of the apparatus are represented in Fig. 1. The system is supplied by a sinusoidal high a.c. voltage with voltage amplitudes U up to 1200V and at frequencies in the range of $f = 100\text{--}300\text{kHz}$. The gas used is helium at pressures between $p = 10\text{--}1000\text{hPa}$.

Experiments have shown that the current density in the system is proportional to the luminous density of the emitted light in good approximation for all represented measurements. We therefore examine the current density distribution by registering the lateral distribution of the emitted luminous density with video or high-speed cameras.

Over a wide range of parameters, the system shows patterns that consist of solitary-like current density filaments. If the supply voltage is increased beyond the ignition voltage, several filaments are abruptly

generated. The diameters of the filaments, which is in the order of 1mm or less, is very much smaller than the diameter of the active domain, therefore the filaments usually do not come into contact with the system boundary. Should a filament actually reach the boundary, it is repelled. In this context, it is remarkable that for given parameters all filaments have equal size and act as quasi-particles.

Filaments may be stationary or in motion, generally at low speed. For certain parameter sets stationary and moving filaments may coexist. Towards higher voltage amplitudes their number increases.

In various parameter ranges, in particular at rather low voltage amplitudes moving filaments may collide. If such a collision occurs, one of the filaments disappears while the other one remains unchanged. By this scenario the number of filaments decreases successively until only one single filament remains.

Investigations of two filaments have shown that the global luminous density Φ of these filaments decreases with decreasing distance r between them (Fig. 2). This

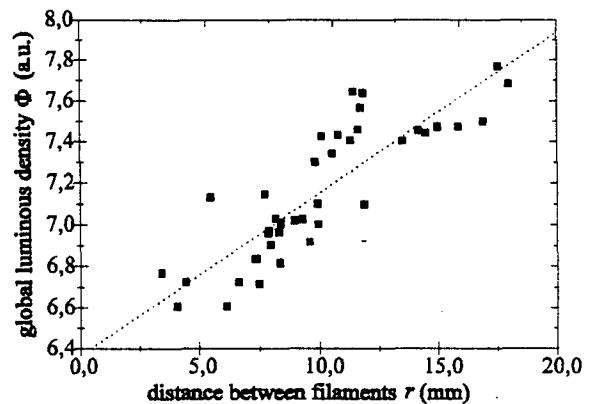


Fig. 2. Relation between the global luminous density of two filaments and the distance between these filaments. The dotted line represents a linear fit. The parameters are $D = 50\text{mm}$, $a = 0.50\text{mm}$, $b = c = 0.55\text{mm}$, $f = 200\text{kHz}$, $p = 642\text{hPa He}$, $U = 547\text{V}$.

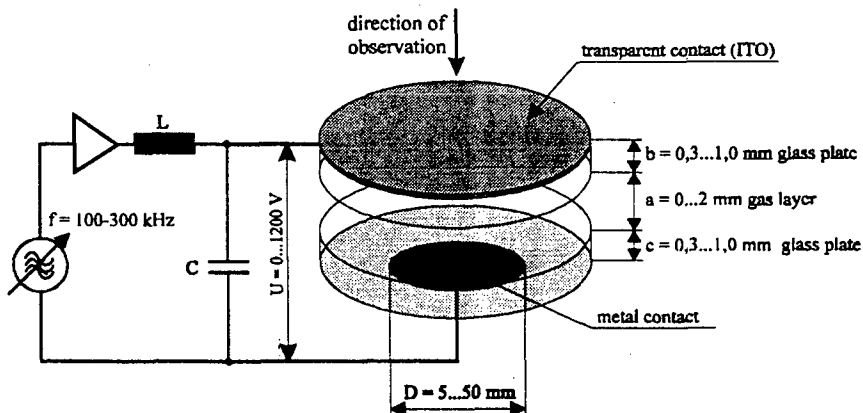


Fig. 1. Cross section of the experimental setup and electrical circuit of the a.c.-driven gas discharge system.

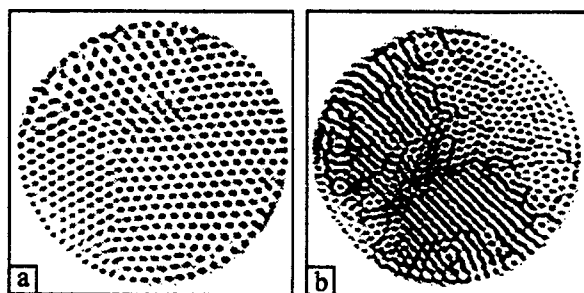


Fig. 3. a) Hexagonal arrangement of current density filaments.

b) Coexistence of stationary filaments and stripe-like patterns.

Both pictures represent single frames of a video recording. The grey-scale was inverted. The parameters are in a): $D = 50\text{mm}$, $a = 0,50\text{mm}$, $b = c = 0,55\text{mm}$, $f = 200\text{kHz}$, $p = 419\text{ hPa He}$, $U = 474\text{ V}$, in b): $D = 50\text{mm}$, $a = 0,50\text{mm}$, $b = c = 0,55\text{mm}$, $f = 200\text{kHz}$, $p = 243\text{ hPa He}$, $U = 870\text{ V}$.

is true for many different values of the gas pressure. Moreover, this phenomenon is found in other gases as well, e.g. in nitrogen or in mixtures of helium and nitrogen. This result points to an inhibiting effect between converging filaments under appropriate parameters.

At relatively high voltages the extinction process becomes less important, while new filaments are generated. Due to repulsive interactions these filaments form a hexagonal pattern (Fig. 3a). Such patterns usually consist of several so-called structure domains, which are separated by some kind of grain boundaries. By the generation of filaments at the system boundary and extinction at the grain boundaries the domains may move and change shape.

In a narrow range of parameters, clusters of filaments appear (Fig. 4) [4]. A cluster is an arrangement of several filaments sticking together with constant, characteristic distances between them. Clusters can be composed of different numbers of filaments with various geometries. They can be generated starting with a hexagonal pattern consisting of many filaments. By lowering the amplitude of the driving voltage the outer filaments vanish one after the other until geometries like those in Fig. 4 are achieved. As it is represented in Fig. 4, the number of filaments belonging to a cluster depends directly on the voltage amplitude, whereas the geometrical arrangement of the filaments is independent of the voltage. In clusters, attractive and repulsive interactions must be balanced.

As a last example, Fig. 3b shows a snapshot of another discharge pattern. This is one frame of a video recording. In contrast to the other examples, in this case we do not only find filaments but at the same time slowly moving stripe-like patterns appear. This is a long time scale pattern, though, related to the relatively long exposure time of 20ms. In reality the stripes consist of rapidly moving filaments. This could be proved by pictures taken at an exposure time of $5\mu\text{s}$ with a high-speed camera, thus measuring just one

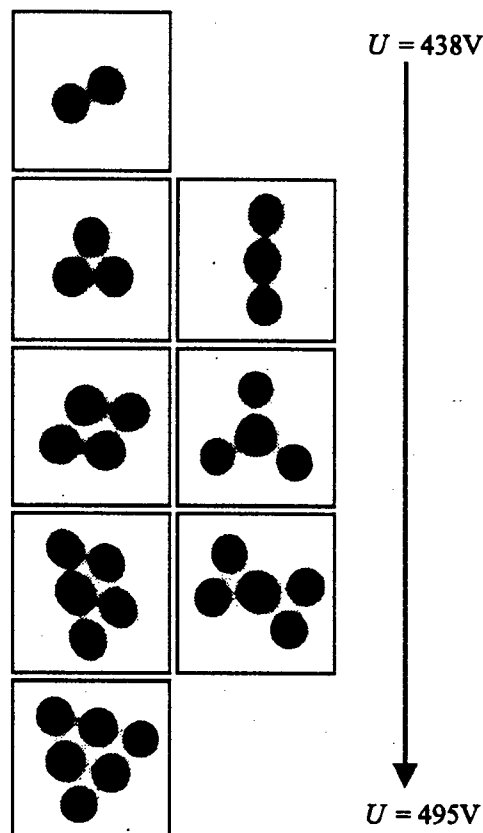


Fig. 4. Photographs of stationary clusters consisting of current density filaments. An inverted grey-scale was chosen. The voltage amplitude rises from top to bottom. The parameters are $D = 13\text{mm}$, $a = 0,55\text{mm}$, $b = 0,7\text{mm}$, $c = 0,3\text{mm}$, $f = 200\text{kHz}$, $p = 419\text{ hPa He}$.

breakthrough of the discharge. These pictures show filaments spread across the entire discharge system. The above-mentioned examples give a brief insight into the multifarious patterns that are created due to the attraction and repulsion between current filaments.

Besides the a.c. powered gas discharge system presented in this paper, we also investigate a d.c. powered system consisting of a gas layer and a high-resistance semiconductor layer arranged in parallel [5]. For the latter system a phenomenological model, which describes the observed patterns qualitatively, was derived [3].

References

- [1] D.G. Boyers, W.A. Tiller, J. Appl. Phys. 41 (1), 28 (1982)
- [2] W. Breazeal, K.M. Flynn and E.G. Gwinn, Phys. Rev. E 52 (2), 1503 (1995)
- [3] C. Radehaus, H. Willebrand, R. Dohmen, F.-J. Niedernostheide, G. Bengel, H.-G. Purwins, Phys. Rev. A 45 (4), 2546 (1992)
- [4] E. Ammelt, D. Schweng and H.-G. Purwins, Phys. Lett. A 179, 348 (1993)
- [5] Y. Astrov, E. Ammelt, S. Teperick, H.-G. Purwins, Phys. Lett. A 211, 184 (1996)

Cell like structures formed in plasma after self-organization

M. Sanduloviciu, E. Lozneanu and Gabriela Leu

Department of Plasma Physics and Structure of Matter

"Al.I.Cuza" University of Iasi, 6600 Iasi, Romania

The creation of ordered structures against the second law of the thermodynamics requires answers to two essential questions. The first one is the question why do the particles available in an asymptotic stable milieu spontaneously self-assemble into an ordered complexity whose self-consistence is assured by a system boundary structure. The second one is the question why does the system boundary structure assures, after its "birth", the exchange of matter and transduction of energy necessary for its autonomous existence and subsequent evolution.

In this paper we show that, from phenomenological point of view, possible answers to the above questions are implicitly contained in a recently published self-organization physical scenario able to explain the spontaneous formation of self-consistent space charge configurations in plasma [1-6]. This scenario describes the "birth" of an ordered structure involving entropy "expulsion" [7] and then, its transition into an open system. This is a system able to assure its "autonomy" by an exchange of matter and transduction of energy with the surrounding environment that is periodically produced [1-6].

Here we describe a tentative model process, based on the above mentioned self-organization mechanism, able to give answers to the question why a membranous "vesicle", perhaps an essential step in the origin and evolution of the earliest cell, could emerge under controllable laboratory conditions. We start from the well-established fact that an electrical spark, produced in a plasma device, is able to generate, in certain conditions, a spherical space charge configuration which appears as a free floating fireball [8,10]. Its appearance is evident related to the creation of a hot plasma in the impact point of the spark. Considering the differences between the mobility and the diffusivity of the electrons and the positive ions, an electrical space charge separation finished with the nucleation of a plasma enriched in positive ions appears. Acting as a gas anode, the electrons from the surrounding plasma are accelerated toward it so that, the series of physical processes whose final product is a self-organized space charge configuration bordered by an electrical double layer can be successively developed [6]. The "birth" of the space charge configuration is spontaneous because it corresponds to the transition into a configuration characterized by a local minimum of the free energy. During the birth process the entropy is locally diminished.

As it is known, the formation of a free floating fireball is a phenomenon frequently observed in low voltage arcs and thermoionic converters [10]. The news

of our experimental investigation consists in the fact that we have started the generation of the fireball by an electrical spark in a pre-existent plasma. Adjusting the experimental conditions it is possible to maintain the fireball (after its genesis) in an unstable state during which intensive periodical modulations of the d.c. current, initially used for the plasma production, can be observed. The origin of the periodical current modulation is the proper dynamics of the fireball. In this state the double layer at its border acts as a cell membrane sustaining and controlling a preferential and periodical exchange of matter with the environment and also a periodical transduction of the kinetic energy of the electrons in electric field energy. These current modulations are evidenced by the periodical expansion and constriction of the fireball visual image. The dynamics assures the "viability" of the fireball also for anode voltages much lower than that necessary for its generation. Experimentally, this is evidenced by the presence of a hysteresis phenomenon that proves the ability of the fireball to memorize its past history [6].

Briefly speaking the self-sustained dynamics, that attributes to the fireball the behavior of a "viable" autonomous body, is related to the self-assemblage mechanism of the spherical double layer at its border [9]. During this self-assemblage process the potential drop over the double layer becomes so high that the electrons accelerated inside it attain energies for which the ionization rate in the nucleus suddenly increases. Under such conditions the net positive space charge at the positive side of the double layer overcompensates that at its negative side. Consequently the space charge configuration expands [3-5]. In this expanding process the self-consistent double layer [9] accelerates toward the nucleus the thermalized electrons from the plasma through which the double layer runs. They produce besides new positive ions a local heating process too so that, owing to the difference in the diffusivity of electrons and positive ions a new opposite space charge separation is initiated. In this way the cycle of the space charge configuration dynamics is enclosed and the reformation process of a double layer around the positive nucleus can again begin. Evidently, the described dynamics involves a matter exchange with the environment related to the periodical formation and disruption of the double layer at the fireball border and also a transduction of kinetic energy of electrons in heat but also in electric energy stored in the field of the double layer structure.

The described phenomenology suggests that a gaseous vesicle in the form of a fireball, perhaps able for subsequent evolution into a prebiotic structure,

could be created by an electrical spark. We note additionally that such a fireball relieves other interesting properties as self-replication, transmission of information, intercommunication using radiant energy [2] and other behaviors usually attributed to biotic systems. In spite of the fact that the spherical space charge configuration generated after the described self-organization process is very primitive, we think that the knowledge of its generation scenario, under controllable laboratory conditions, could be relevant for the modeling of the genesis, self-sustenance and evolution possibilities of a prebiotic structure in the early Earth atmosphere (a plasma like medium in which electrical sparks are present).

References:

- [1]. M.Sanduloviciu, Proc. XXI ICPIG Bochum 1993, Proc. III Inv. Papers, 279
- [2]. M.Sanduloviciu, Romanian Reports in Physics, **45** (1993) 355
- [3]. M.Sanduloviciu and E.Loizneanu, Plasma Physics Contrl. Fusion, **28** (1996) 585
- [4]. D.Alexandroaiei and M.Sanduloviciu, Phys. Lett A, **122** (1987) 173
- [5]. M.Sanduloviciu, Plasma Phys. Contrl. Fusion, **29** (1987) 1687
- [6]. M.Sanduloviciu, C.Borcia and Gabriela Leu, Phys. Lett A, **208** (1995) 136
- [7]. T.Sato et al, Res. Rep. 318 National Inst. Fusion Science, Nagoya, 464-01, Japan
- [8]. Roth Reece, J. Fus. Technology, **27** (1994) 225
- [9]. M.Sanduloviciu, Proc XXII ICPIG New Jersey 1995, Contr. Paper 1, p.21
- [10]. M.Sanduloviciu, Int. Conf. Plasma Phys, 1996 Nagoya (in print)

On the so called Turing structures formed in gas discharges

E.Lozoneanu, Gabriela Leu and M. Sanduloviciu
 "Al. I. Cuza" University, Department of Plasma Physics
 6600 Iasi, Romania

Recently in many papers [2-4] were reported the results of the investigations performed on the formation of spatial structures in semiconductors and gas discharge systems. The authors consider that the basic physical processes involved in the pattern formation are that predicted by Turing [1] for the generation of homogeneous stationary patterns.

The goal of this paper is to attract the attention on some similarities which can be observed when the results described in [2,3] are compared with those observed in the usual gas discharges. These similarities seem to suggest the possibility to explain the formation of spatial patterns as a result of a self-organization process whose physical scenario was already described [6]. The final product of such a self-organization process is a well-localized, nearly spherical, space charge configuration (SCC), usually known as anode spot [5-8]. Using the anode voltage as a control parameter it becomes possible to generate SCC visible as luminous globes [5-8], at the anode surface of a dc glow discharge. In Fig. 1 are presented

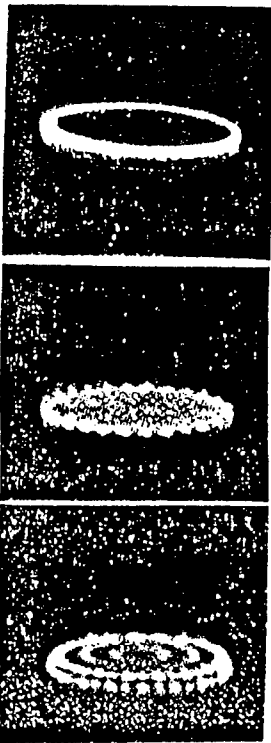


Fig.1.
Continuously distributed ring-like luminous space charge configuration at the border of a disc anode in a dc glow discharge and its transition into symmetrical distributed anode spots.

photographs of a disc anode surface that evidence the transition from a uniform ring like distributed luminous space charge configuration at its border into a series of spatially periodic structures (anode spots) when the anode voltage is decreased. These results suggest comparison with the periodic structure shown in Fig. 2 obtained in a d.c. gas discharge in a quasi-one-dimensional system consisting of a semiconductor and a metal electrode [2,3].

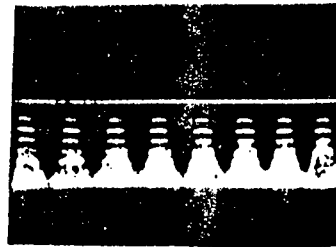


Fig.2 Photograph of the spatially periodic structure of the luminous density in a quasi-linear semiconductor-metal-electrodes discharge system (from ref. 3).

The spontaneous formation of the anode spots in a glow discharge can be related to the nonlinear behavior of the current versus voltage characteristic [5,6]. The negative resistance behavior evidenced in the nonlinear $I(V)$ -characteristic (a requirement necessary for the model developed in [2]) appears under conditions when the formation of double layers in front of the anode becomes possible [5,6]. In the experiment described in [2,3] this is realized when the distance between the electrodes exceeds a certain value. Concerning the basic physical processes that produce the negative resistance behavior of the glow discharge, these are essentially related to the self-organization process during which, in front of the anode, a double layer is formed [5,6]. When the anode surface is small, and consequently a SCC, bordered by a spherical double layer, is forming, the negative resistance behavior appears in the $I(V)$ -characteristic (Fig. 3).

To explain the "filamentation" of the discharge current it is necessary to consider the phenomena at the origin of the spontaneous formation of an anode spot bordered by a nearly spherical electrical double layer. The anode spot appears when, by decreasing the anode voltage, the current at the anode of a glow discharge would be too small to maintain the discharge [8]. Under such conditions the requisite extra-ionization can be provided after acceleration of the electrons in a double layer structure

whose potential drop is equal to or exceeds the ionization potential of the gas [5-7]. After the appearance of self-consistent double layers, the discharge becomes able to maintain its existence for anode voltages for which this is not possible in the absence of the double layers [5].

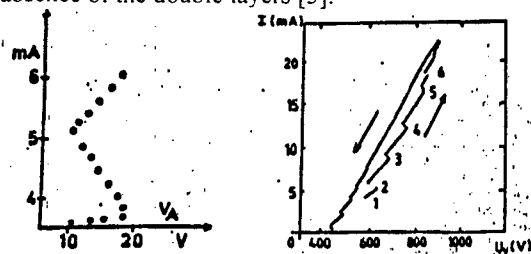


Fig. 3 Current-voltage characteristic whose negative resistance branch corresponds to the formation of a single anode spot (from ref. 4) and current-voltage characteristic under variation of the applied anode voltage for a quasi-one-dimensional semiconductor-metal electrodes system (from ref. 3).

The globular aspect of the anode spot is a consequence of the tendency of every double layer to transit into a state characterized by a local minimum of the potential energy [6]. After the self-assemblage process of the anode spot, this acts as a well-localized new source of charged particles determining a concentration (filamentation) of the d.c. current. Therefore, when the applied voltage diminishes, the discharge "reacts" creating the anode spots and, consequently, the current filamentation as is shown in Fig. 2 for a quasi-one-dimensional discharge. By the transition into a nearly self-consistent spherical double layer, a new source of charged particles appears in the discharge [9]. So, the conditions for the discharge maintenance are fulfilled also for an anode voltage smaller than that necessary when spherical double layers are not present at the anode surface.

As was shown [5,6] each anode spot is bordered by a spherical double layer whose external side is formed after electron accumulation. Consequently, the repulsive electrostatic forces acting between different anode spots determine their reciprocal position on the anode surface. This is the reason why the anode spots are symmetrically distributed on the anode surface (Fig. 1).

The spatially periodic structure on a quasi-one-dimensional anode, shown in Fig. 2, is related to the presence of striations, i.e. of a set of hemispherical double layers, generated after "multiplication" of an anode spot [5,6]. Consequently, between different striated columns repulsive forces act determining their spatial separation evidenced, in the quasi-one-dimensional discharge, as luminous filaments. By increasing the applied voltage to critical values, luminous filaments are spontaneously generated, one after another, while the $I(V)$ characteristic exhibits discontinuities, as a set of negative resistances (Fig. 3). By decreasing the applied voltage, the discontinuities in

the $I(V)$ characteristic (accompanied by successively disappearance of luminous filaments) are shifted toward lower voltages, proving the presence of hysteresis phenomena, usually proper to self-organization [6].

For proving the above proposed new explanation of the patterns formation, we have repeated the experiments described in [2,3] with the single essential difference that the discharge was produced within two identical metal plates. The obtained results show that the presence of a semiconductor electrode is not necessary for evidencing the current filamentation. As it was already mentioned, it is probable that the negative resistance is directly related to the formation process of the spatial pattern

We notice that similar filamentation of the current is observed also in other experimental devices as for example in plasma focus [10] (Fig. 4).

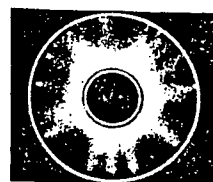


Fig. 4 Current filamentation in a plasma focus device (from ref. 10)

The experimental results obtained by us up today, that will be published in the future, prove that the current filamentations similar to those described in the papers of Radehaus et. al. ([2,3]), can be understood considering the self-organization physical scenario already described [5,6].

The variety of nonstationary pattern, mentioned in the paper of Astrov et al. [4], can be explained, in our opinion, considering the dynamical behavior of double layers as described in [6].

References:

- [1]. A.M. Turing, *Phyl. Trans. R. Soc. B* 327 (1952) 37
- [2]. C. Radehaus, H. Willebrand, R. Dohmen, F.J. Niedernostheide, G. Bengel, and H.G. Purwins, *Phys. Rev. A* 45 (1992) 2546
- [3]. C. Radehaus, R. Dohmen, H. Willebrand and F.J. Niedernostheide, *Phys. Rev. A* 12 (1990) 7426
- [4]. Y.U. Astrov, E. Ammelt, S. Teperick, H.G. Purwins, *Phys. Lett. A*, 211 (1996) 184
- [5]. M. Sanduloviciu and E. Lozneau, *Plasma Phys. Contr. Fusion* 28 (1986) 585
- [6]. M. Sanduloviciu, C. Borcia and Gabriela Leu, *Phys. Lett. A*, 208 (1995) 136
- [7]. Bing Song, N. D'Angelo, and R.L. Merlino, *J. Phys. Appl. Phys.* 24; (1991) 1789
- [8]. K.G. Emelous, *Int. J. Electron.* 52 (1982) 407
- [9]. M. Sanduloviciu, E. Lozneau, XX ICPIG New Jersey 1995, *Contr. Papers* 1, p. 21
- [10]. H. Kromholz, W. Neff, F. Ruhl, K. Schonbach and G. Herziger, *Phys. Lett. A* 77 (1980) 247.

On the temporal structures generated by a Thermionic Vacuum Arc discharge

M. Sanduloviciu, C. Stan, G. Musa¹, A. Popescu¹, I. Mustata¹, F. Leu¹

"Al. I. Cuza" University, Department of Plasma Physics, 6600, Iasi, Romania

¹Inst. of Physics and Technology of Radiation Device, P.O. Box MG-07 Bucharest, Romania

1. Introduction

Oscillatory phenomena in plasma devices have a long history but, not general accepted theory has been developed up to now. This is one of the essential reasons why the oscillating regimes can not be controlled in fundamental and applicative investigations. In this context, the specialists interest are in thermionic vacuum arc discharge, especially from the practical reasons in the coating applications and film deposition [1,2]. The oscillating phenomena present in the working regime of such a device, was used by us to make a lot of experimental observations and to explain them using the physical scenario of self-organization [3,4].

2. Experimental device

The experimental device used in our observations (Fig. 1) consists of a wolfram heated filament (16 - 20 A) placed at controllable distances (5 - 10 mm) and angles ($\varphi \in (0^\circ - 90^\circ)$) from a wolfram crucible containing the material to be evaporated (copper in our case). The two electrodes are mounted in the centre of a vacuum cylindrical stainless chamber with a base pressure of $\approx 10^{-5}$ Torr. The thermoelectrons emitted by the cathode are focalised by the Whent cylinder and are accelerated toward the anode by a high potential (\approx KV). The thermoelectrons collide the anode heating it until the melting point. In this moment the anode material starts to evaporate, the pressure in front of it increases and the discharge is ignited.

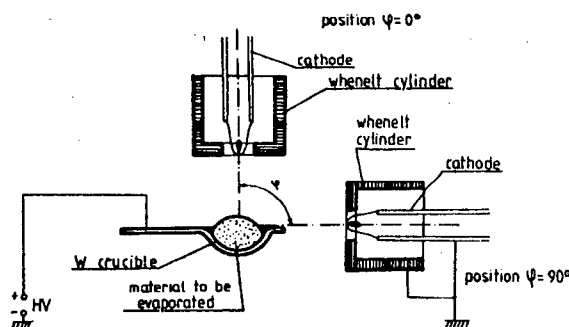


Fig. 1 Scheme of the experimental arrangement

3. Experimental results

The current -voltage characteristic of such a discharge, reveals a lot of nonlinear features (hysteresis, negative resistance, critical points, modulations, etc.). Our

experimental observations of the thermionic vacuum arc discharge are mainly focused on the oscillations regimes appeared at the critical external condition (such as anode voltage, filament temperature, pressure, anode-cathode distances and orientation, ballast resistor, etc.). Fig. 2 shows the simultaneous visualisation of the time variation of the discharge current (curve 1) and of the voltage (curve 2) for a continuous variation of the dc power supply, marking the beginning of the oscillating regime ($p=1.5 \cdot 10^{-6}$ Torr, $I_f=18$ A, $d_{A-K}=6$ mm, $\varphi=45^\circ$). This regime appears after the strong increase of the current simultaneously with the voltage decrease in the arc working zone. Analysing only the oscillations from this region we find two distinct regimes:

- a random regime, with frequency of the oscillations in the range of few Hz and with large amplitudes;
- a periodic regime, with frequency of the oscillations in the range of hundred of kHz and with small amplitudes.

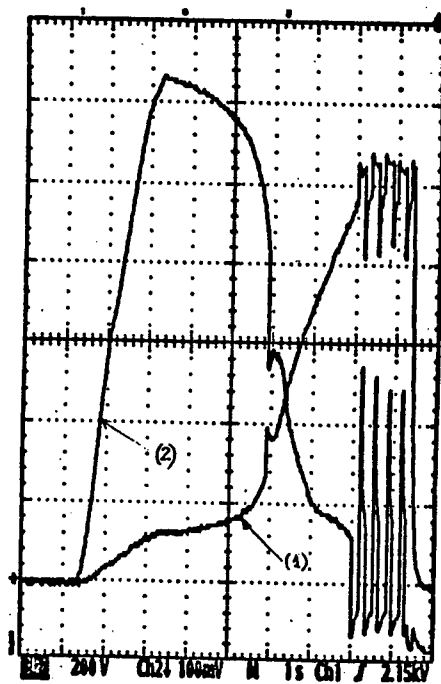


Fig. 2 Current discharge (curve 1) and voltage (curve 2) for a continuous variation of the dc power supply ($p=1.5 \cdot 10^{-6}$ Torr, $I_f=18$ A, $d_{A-K}=6$ mm, $\varphi=45^\circ$)

Fig. 3 shows these two types of oscillation regimes in current (curve 1) and voltage (curve 2).



Fig. 3 Aleatory appearance of the self-organized structure in front of the anode, evidencing the determinist chaotic behaviour

Small oscillations with the shape indicated in Fig. 4. appear during each aleatory oscillation.

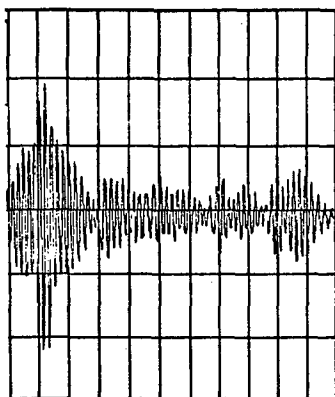


Fig. 4 Periodic current modulation produced by the proper dynamic of the self-organized anode configuration.

4. Discussions

Based on the similarities with a low voltage discharge, we propose the same physical scenario [3,4,5] standing at the origin of the current modulations. Random internal or external factors generate the premises for the appearance of the bipotential structures in front of the anode (in the evaporating phase) through a self-organization phenomenon. After its genesis, the localised structures bordered by double layers, begin to manifest a proper dynamics. In this context, we consider that the periodic current modulations observed in a thermionic vacuum arc discharge are not genuine oscillations because they result after successive generations and disruptions of the self-consistent double layers [3,4].

5. Conclusions

Our experimental results prove that in a thermionic vacuum arc discharge, used especially for practical

reasons, two kind of instabilities appear. One of them is related with the aleatory appearance of a self-organised configuration in front of the anode, when the formation is supposed to be in a determinist chaotic regime and the other one appears as ordered temporal structures evidenced as coherent oscillations. The last one is related to the proper dynamics of the anode configuration which is required for the self-maintenance of such a self-organised structure. During this oscillating phase, the anode configuration behaves as an autonomous body, able to self-sustain a periodical exchange of matter and energy with the surrounding plasma [4,5].

The chaotic behaviour of the temporal structures generated by the thermionic vacuum arc discharge is under considerations.

6. References:

- [1]. G. Musa, H. Ehrich, M. Monsback, J. Vac. Sci. Technol. A **12** (1994) 2887-2895
- [2]. G. Musa, I. Mustata, I. Popescu, A. Baltag, G. Dinescu, Rom. Rep. in Phys. **46** (1994) 601
- [3]. M. Sanduloviciu, E. Lozneanu, Plasma Phys. Contrl. Fusion, **28** (1986) 585
- [4]. M. Sanduloviciu, C. Borcia, G. Leu, Phys. Lett. A, **208** (1995) 136
- [5]. M. Sanduloviciu, C. Stan, G. Musa, A. Popescu, I. Mustata, A. Sabalas, Symposium on Double Layers - Potential Formation and Related Nonlinear Phenomena in Plasmas (17-19 September 1996, Sendai, Japan)

The Effect of the Magnetic Field on the Hollow Cathode Generated Electron Beam

L. Biborosch, M. Toma and M. Sanduloviciu
Department of Plasma Physics, Al. I. Cuza University
Blvd. Copou 11, 6600 Iasi, Romania

1. Introduction

Investigations of a hollow cathode discharge in helium with a cylindrical cathode have indicated that the first step in their development can be a high impedance mode of operation in which an axial electron beam is produced [1]. These beam electrons with energies determined by the full applied voltage do not suffer any collision with the gas atoms so that they can carry up to 20% from the whole discharge current [2]. In spite of the spatial compression of the electron generation this does not lead to the pinching of the discharge. The same electron beam mode constitute the predischage stage for the radial hollow cathode discharge or for the main discharge of a pseudospark discharge. Consequently, even a narrow transverse magnetic field must have an important effect on the breakdown of this high impedance mode of the hollow cathode discharge and the corresponding spatial distribution of the generated electron beam. Some data about this effect are discussed in the present contribution.

2. Experimental Device

The experimental set-up is shown in figure 1. More details can be found elsewhere [3]. The beam mode of operation occurs over a limited range of discharge parameters, so that we are restricting to helium pressures lower than 0.5 Torr and discharge currents smaller than 10 mA. To obtain the electron beam mode the voltage of the current-controlled power supply was smoothly increased at nearly a constant discharge current.

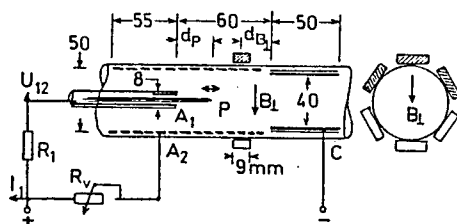


Fig. 1. Experimental set-up of the discharge device.

The diagnostic tools of the discharge plasma was an axially movable double probe P for the plasma density measurements or an emissive probe to measure the plasma potential. The probes were made of tantalum wire 0.1 mm in diameter and 3 mm in length. The

small permanent magnets which produce the narrow transverse magnetic field are also movable along the axial direction of the cylindrical discharge tube. The dc discharge can be run with two different cylindrical hollow anodes; a small anode A_1 , located at 60 mm from the cathode exist in the front of the electron beam and a very large mesh-anode A_2 covering the whole discharge tube walls over the cathode-anode A_1 length. In the electron beam mode of operation the transition between these two different anodes can be obtained by their relatively biasing with a large variable resistor R_v or an auxiliary power supply.

3. Experimental Data and Discussion

In the absence of the transverse magnetic field (in the top of figure 2), a positively bias of the small anode A_1 of only a few volts in the respect to the large one is sufficiently to carry about 80 % from the discharge current through this small anode. One can be noted that, under the same conditions, i.e. with the small electrode A_1 acting as anode, the electron beam is more confined. Then, if a narrow transverse magnetic field with a relatively small strength is applied in the front of the small anode, a much larger positively biasing (comparable with ionisation potential of helium) must be used in order to obtain the same current values through the small anode. This positively biasing increases further with the magnetic field strengths as shown in the bottom of figure 2.

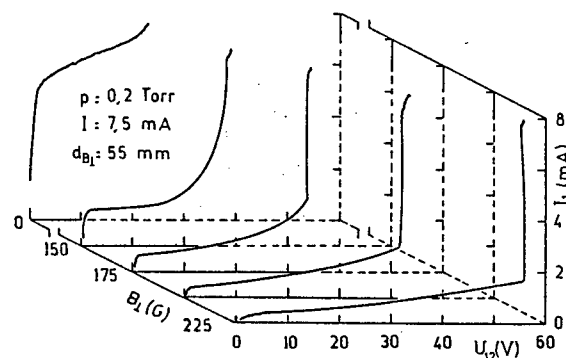


Fig. 2. The dependence of the current voltage characteristics of the small anode on the magnetic field strength in the beam mode.

Alternatively, if the same transverse magnetic field but with a given field strength "is moved" axially towards

the hollow cathode, these current-voltage characteristics of the anode circuit are not qualitatively changed. The exceptions are the magnetic field localisation near the hollow cathode exit when it prevents the appearance of the electron beam mode itself in the top of figure 3.

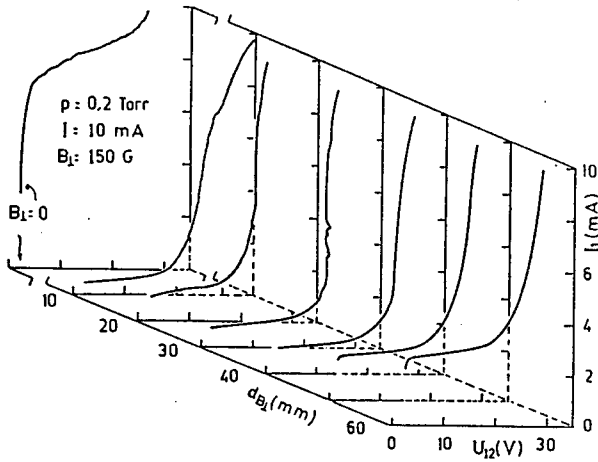


Fig.3. The dependence of the current-voltage characteristics of the small anode on the axial location of the narrow transverse magnetic field.

The axial profiles of the plasma density measured along a direction which make a small angle with the direction of the electron beam are shown in figure 4.

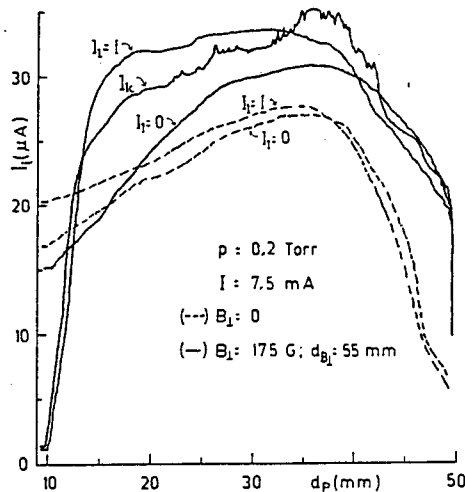


Fig.4. The axial profiles of the plasma density for the beam mode. I_k is the anode current value for which the discharge switch to the small anode.

The discharge conditions are the same as in figure 2, but the magnetic field strengths and anode current I_1 are now the curve parameters. Therefore, as long as the double probes are inside the electron beam, the plasma density remains nearly constant along the cathode-anode A_1 region. Only at the axial edges of the electron beam, i.e. nearly to the hollow cathode exit or near the small anode, when the probes go out from the

beam, the plasma density abruptly decrease. The last decreases of the plasma density in front of the small anode occurs only if a larger field strength is applied here. For these larger magnetic field strengths the electron beam is more deflected from its axial direction and also impeded to touch the small anode. Thus, a new secondary anode structure must be formed in front of the small anode in order to carry the same discharge current through A_1 region. This new anode structure, known as anode spot or ball of fire is bordered towards the cathode by an anode double layer [4]. In fact, if we extend the plasma potential measurements over the whole cathode-anode A_1 distance we found a certain two step double layer structure for a radial hollow cathode discharge [5]. The same behaviour of the plasma potential are also observed for the present electron beam mode if larger magnetic field strengths and maximum anode currents $I_1 = I$ are used, (see in figure 5).

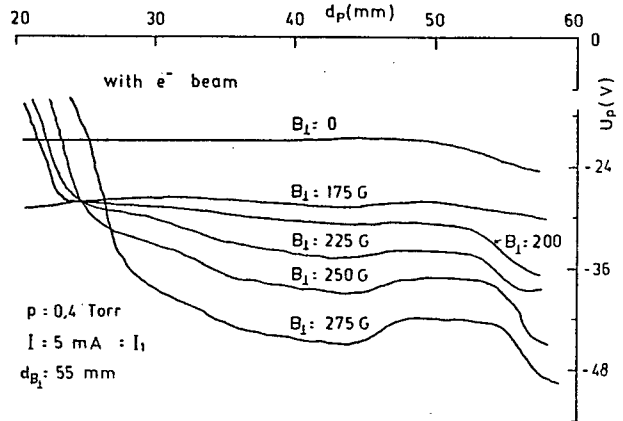


Fig.5. Axial profiles of the plasma potential with the magnetic field strength as parameter. The small anode current has its maximum value.

In conclusion, the effect of a narrow transverse magnetic field on a hollow cathode discharge which generate an electron beam is rather important, especially when it is located at the axial edges of the discharge. The hollow anode dimensions are actually not restricted as is proved by our experimental results for the electron beam mode operation of the hollow cathode discharge.

4. References

- [1] K.H. Schoenbach, XXI-th ICPIG, Bochum, 1993, Inv. Pap., p.287
- [2] G. Popa, M. Sanduloviciu, P. Croitoru and C. Moldoveanu, XIV-th ICPIG, Grenoble 1979, J. de Phys., 40 (1979) C7-187
- [3] L. Biborosch and M. Sanduloviciu, 4th SDL, Innsbruck, 1992, Ex. -183
- [4] M. Sanduloviciu and E. Lozneanu, Plasma Phys. and Fus. Contr., 28 (1986) 585
- [5] L. Biborosch, I. Grosu and M. Sanduloviciu, XXII-th ICPIG, Hoboken 1995, Contr. Pap., II-151

Filamentation of surface wave sustained discharges

N. Dzermanova, D. Grozev, K. Kirov, A. Shivarova and Ts. Tsvetkov
Faculty of Physics, Sofia University, BG-1164 Sofia, Bulgaria

1. Introduction

As it is known [1,2], waveguided discharges sustained by surface wave (SW) propagation can be produced in a wide range of variation of the gas pressure starting from several mTorr up to atmospheric one. Both the long columns of quite and stable plasmas at low pressure and the plasma torches at high pressure provide many possibilities for application of the discharges. However the results presented here show that the transition from low to high pressures passes through formation of unstable structures of the type of filaments. Studies on the behaviour of these structures could be of interest with respect to fundamental aspects of maintenance of the discharges and their application.

2. Experimental arrangements

The experimental set-up is shown in Fig.1. By applying

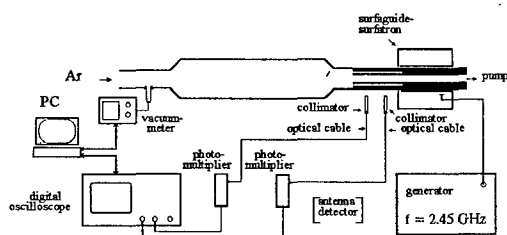


Fig. 1. Experimental arrangements.

a powerful signal ($P_0 = 140$ W in the case presented here) at frequency of 2.45 GHz to a surfaguide-surfatron device [2], a SW sustained discharge in Ar is created in a cw regime. The discharge is produced in a tapered tube [3], in which formation of the unstable structures is observed at lower applied power. Such a shape of the tube is closer to those of the plasma reactors. The experiments are performed in flowing gas by varying the gas pressure from $p = 0.1$ Torr till 1 Atm. The total light emission giving information about the plasma density, is registered by photomultipliers (PHMs). For measuring the velocity V_r of rotation of the filaments, signals from two collimators situated at an angle of 30° in a plane perpendicular to the tube axis are compared. Method of correlation analysis of the registered, by the oscilloscope, signals is also used. The interrelation between electric field power and plasma density is registered by comparing the signal from one of the

PHMs with a signal from a microwave antenna.

3. Qualitative observations

The instabilities studied are macroscopic structures which are of the type of filaments. They change in number, shape, width and length and usually rotate. The development of their formation is observed in unstationary conditions determined by changes of p . With increasing p , the dynamics of the discharge develops in two unstable stages.

The development of the first stage (at $p = 0.1$ -50 Torr) starts from the stationary state of the plasma column. The increase of p causes the following changes which go in a consequence on the background of plasma which completely fills the tube: (i) the length of the plasma column shortens; (ii) the oscillations of its end which is a cone-shape region whose top is at the discharge end, become more pronounced; (iii) strata—several brighter and darker slabs perpendicular to the discharge axis—appears close to the end; (iv) the plasma at the end of the column concentrates in the outer region in a dipole-type azimuthal structure and the cone-shaped darker region in the center has its base at the end of the discharge; (v) formation of filaments starts from the outer region.

A contraction of the discharge in the filaments is the second stage ($p = 50$ Torr-1 Atm). There is no plasma between these isolated structures, with azimuthal rotation, situated in the outer region of the tube. With increasing p , they become brighter, V_r changes. At first they are four, later they reduce consequently to three, two, one. Their length L decreases with the increase of p . The act of each reduction of their number is accompanied with an increase of L . At high pressure ($p > 100$ -200 Torr) an unmovable filament in the center of the tube formes the discharge.

At lower power ($P_0 = 40$ -100 W) the plasma column and the filaments are shorter, the process develops more quickly, the time duration of the stages is shorter and some of them disappear. The rate dp/dt of the pressure variation strongly influences the picture. At higher dp/dt , the development is faster and the different stages are hardly distinguished.

4. Results

The presented results give the microscopic parameters

of the filaments obtained at a stage of uniform rotation (Fig.2). V_r is determined by measuring the time delay between the signals from the two PHMs. With increas-

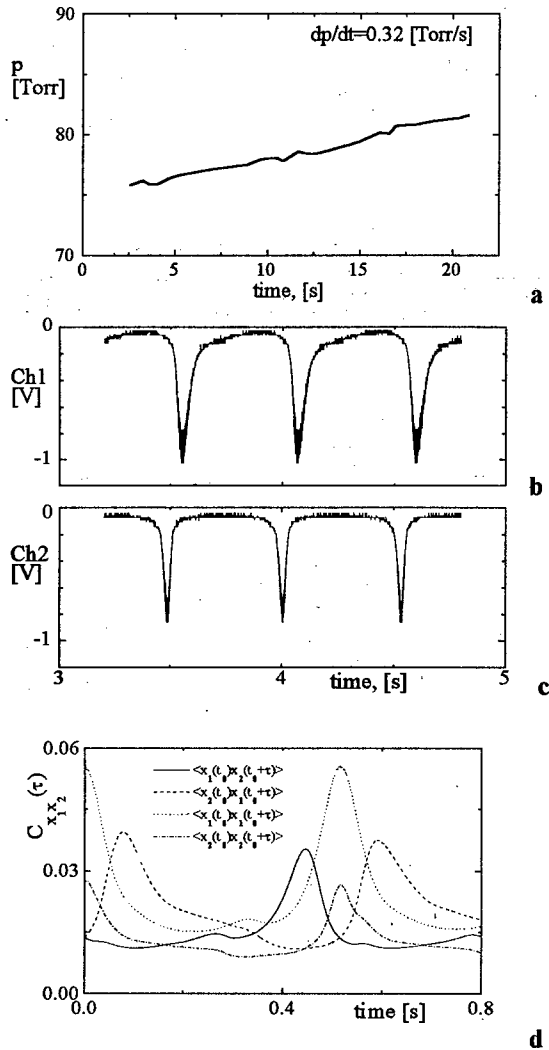


Fig. 2. Time evolution of the signals from the two PHMs (b) and (c) at $dp/dt = 0.32$ Torr/s obtained from (a). Results from correlation analysis in (d).

ing dp/dt , V_r increases, the p -range of uniform rotation narrows and shifts towards lower p -values (Table 1). In general, V_r is in the limits: (2-12) cm/s. The filaments are (7-2.5) mm in a diameter. For studying the stages of nonregular behaviour, a correlation method analysis is developed. The method is demonstrated in Fig. 2d. The time-shifts of the maxima of the correlation functions $\langle x_1(t_0)x_2(t_0+\tau) \rangle$, $\langle x_1(t_0)x_1(t_0+\tau) \rangle$ and $\langle x_2(t_0)x_1(t_0+\tau) \rangle$, $\langle x_2(t_0)x_2(t_0+\tau) \rangle$ determine V_r .

At $dp/dt < 1.5$ Torr s^{-1} , the filaments are structures which concentrate wave energy and plasma bunches (Fig. 3). In the cases when the variation of the density is from a zero level (i.e. filaments without plasma between them), the variation of the electric field power is from a given constant value. Therefore there is a threshold field amplitude for creation the discharge in the filaments.

Gas flow dp/dt [Torr/s]	Velocity of rotation V_r [rad/s]			Pressure range p [Torr]
0.32	7.7	7	6.8	76÷87
0.38	8.5	8	7.7	64÷71
0.9	11.3		8.5	57÷62

Table 1.

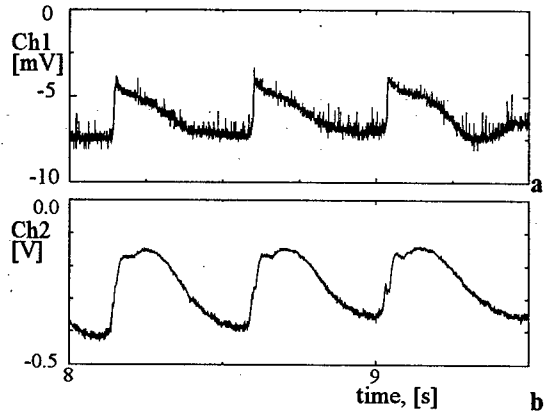


Fig.3. Time variation of the electric field power (antenna signal in (a)) and the plasma density (signal from photomultiplier in (b)).

Formations like tongues at the end of the filaments are also observed. The time evolution of the signal (Fig. 4) picked by a PHM from the end of a filament shows that it vibrates in axial direction with frequency of 40 Hz.

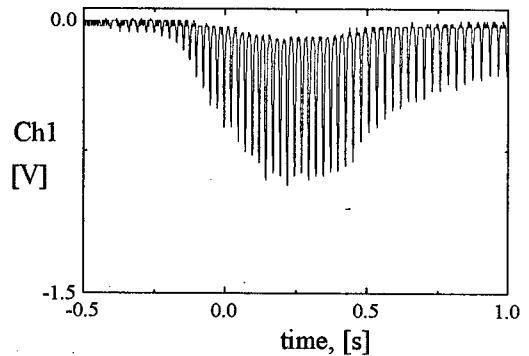


Fig.4. Axial vibration of the end of a filament (signal from a photomultiplier).

In conclusion, results on unstable evolution of SW sustained discharges at varying p are presented. The instabilities—macroscopic formations with a shape of filaments—are nonlinear structures of space concentration of wave energy and plasma density.

Acknowledgements. This work was supported by the EC-project n0 CIPA-CT-0101 and the NFSR-project n0 F-409.

References

- [1] M. Moisan, *et al*: *Rev. Phys. Appl.*, **17** (1982) 707
- [2] C. M. Ferreira and M. Moisan, Eds.: *Microwave Discharges: Fundamentals and Application* (N. Y., Plenum, 1993)
- [3] M. Moisan and Z. Zakrzewski: *XVII ICPIG* (1985), p. 712

On Behaviour of Electron Beam Exciting Strong Langmuir Turbulence in Plasma

I.A.Sychov

General Physics Institute of the Russian Academy of Sciences, Plasma Physics Division

117942, 38 Vavilov St., Moscow, Russia

Within the problem of the Strong Langmuir Turbulence (SLT) relaxation of electron beam exciting SLT remains a little studied. This problem had studied theoretically (see for ex. [1] and ref. therein) and experimentally [2,3] but discordance of results and interpretations bears the problem continue to be interesting.

This report concerns the evolution of beam electron distribution function (EDF) under conditions $\delta < 1$ and $\delta > 1$, where [4]

$$\delta = A(n_b / n_0) \cdot (mv_0^2 / T_e)^2 \quad (1)$$

is the beam parameter characterizing Langmuir field intensity, A - kinetic coefficient, which is equal to $6 \cdot 10^{-3}$ for our experimental conditions, v_0 - velocity of beam electrons injected into the plasma. The value $\delta = 1$ corresponds to the SLT threshold.

EFD was defined by differentiation of the delay curve of multigrid analyzer with applying of linear voltage on analyzing grid of the amplitude 450 V and duration 0,5 μ s compared with Langmuir cavity collapsing time from its initial size $L_0 = 2\pi / k_0$, where $k_0 = \omega_{pe} / v_0$, down to its final size $L_{\min} \approx 10r_{De}$. Thus one could consider the delay curves measured to be instant (with definit accuracy), i.e. no averaging was made through cavities anseml. Typical experimental parameters was: argon plasma density $n_0 \cong 2,5 \cdot 10^{11} \text{ cm}^{-3}$, $T_e \cong 2,5 \text{ eV}$, beam energy $\varepsilon_0 = 300 \text{ eV}$ and pressure $P_{Ar} = 5 \cdot 10^{-4} \text{ Torr}$.

Consider the relaxation picture as dependance from pumping parameter δ . Fig.1 represents the EFD family on various distance from injection point for subthreshold case. One can see that in the case $\delta = 0,2$ the beam is yet monoenergetic at the distance $z = 10 \text{ cm}$ from injection point and its velocity width is small $\Delta v / v_0 \ll 1$. Furthermore during passing through the plasma EDF is broadened and at the distance $z = 30 \text{ cm}$ looks nearly as "plateau" with $\Delta v / v_0 \sim 1$. (Note that our planar analyzer doesn't see the bulk of plasma electrons at velocities $\sim 10^8 \text{ cm/s}$ due to its aperture). Beam EDF behaviour at subthreshold value $\delta = 0,8$ is quite analogous with those difference that EDF "washing-away" in velocities occurs to be more quickly.

Fig.2 illustrates the beam EDF at parameters exceeding the SLT threshold ($\delta = 2,5$ and $\delta = 7$). One can see many beams on the EFD plot, i.e. particle movement becomes manyflowing. Note that EDF is nonstationary at every spatial point; at the next moment it may have quite different view, but never takes a form of "plateau". By the way one can see appearance of tails of fast electrons from the bulk accelerated in collapsing cavities and contributing to the beam EDF.

Let's discuss these results. First of all the relaxation length under subthreshold values δ is not described by the quasilinear formulae [1]:

$$l_{QL} = (v_0 / \omega_{pe}) \cdot (T_e / mv_0^2) \cdot (n_b / n_0) \cdot \Lambda \quad (2)$$

(Λ is of order Coulomb logarithm) because for our parameters it must give $l_{QL} \sim 5 \text{ cm}$ for $\delta = 0,2$ and

$l_{QL} \sim 1 \text{ cm}$ for $\delta = 0,8$ while experimental value is much more: $l_{QL} \sim 25 \div 30 \text{ cm}$. Second, although the

SLT reduces the beam relaxation, however nonlinear relaxation length appears always to be (according to theory [1]) less than quasilinear. This contradicts our experiment because as follows from Fig.2 no relaxation appears to be at all under SLT conditions. The latter proposition is confirmed by the fact that no difference in turbulence intensity, measured by bursts of field in collapsing cavities according to methodic described in [4], was found along the beam path.

Manyflowing character of the EDF one could probably explain by that the beam electrons accelerated in cavities considered at final stage as thin plane capacitors filled with oscillating field, suffer the modulation in velocities resulting in the grouping at some spatial point. The grouping distance is

$$z_{gr} = v_0 / \alpha \omega \quad (3)$$

where $\alpha \ll 1$ is modulation depth defined by cavity potential $\alpha = \varphi_{cav} / 2\varepsilon_0$, ω - modulation frequency.

Assuming $\varphi_{cav} \approx 30 \text{ V}$ (corresponding to $E_L^2 / 8\pi n_0 T_e \sim 1$, where E_L - Langmuir field of cavity) for $\varepsilon_0 = 300 \text{ eV}$ we obtaine $z_{gr} \sim 1 \text{ cm}$, so that there are many of grouping points at our experimental length where electron current is locally high.

In conclusion the increase of upper energy of beam electrons due to small transient time for particles

passed through collapsed cavities were measured. Measurements were made for constant beam pumping $\delta=3$ varying beam energy in the range 150-300 eV. The results are performed in Fig.3 as dependence of upper energy increase $\Delta\epsilon_0$ from parameter $k_0 L_{\min}$. This dependence allows to say a few words about Langmuir field in the plasma. The initial scale of Langmuir waves excited by electron beam decreases with the beam energy decreasing, so that Langmuir energy is gathered to collapsing cavity from less space. From the energy conservation law we have for maximum electric field of the cavity on final stage of transient electrons

$$\Delta\epsilon_0 \propto e E_{\max} L_{\min} \sin(k_0 L_{\min} / 2) / (k_0 L_{\min} / 2)$$

takes the form:

$$\Delta\epsilon_0 \propto \frac{1}{(k_0 L_{\min})^{3/2}} \frac{\sin(k_0 L_{\min} / 2)}{k_0 L_{\min} / 2} \quad (4)$$

Excellent coincidence of experimental values with this dependence allows to conclude that although the average spatial Langmuir field defined only by pumping parameter δ is constant, the maximum electric field of the cavity on final stage is varying while the beam energy is varying. For example for our experimental parameters one could obtain $E_{\max} \cong 1,2 \cdot 10^3$ V/cm ($W_{L,\max} / n_0 T_e = 0,6$) for $\epsilon_0 = 150$ eV and $E_{\max} \cong 2 \cdot 10^3$ V/cm ($W_{L,\max} / n_0 T_e = 1,7$) for $\epsilon_0 = 300$ eV.

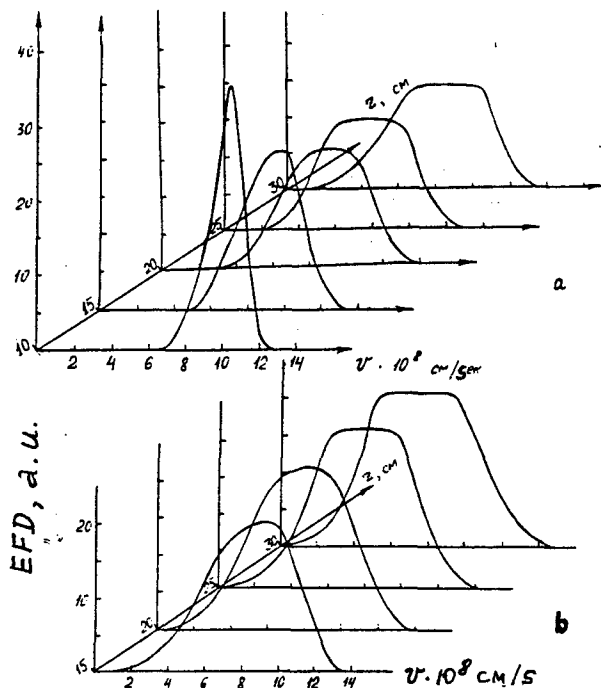


Fig.1. Spatial evolution of electron beam under subthreshold values: a - $\delta=0,2$; b - $\delta=0,8$

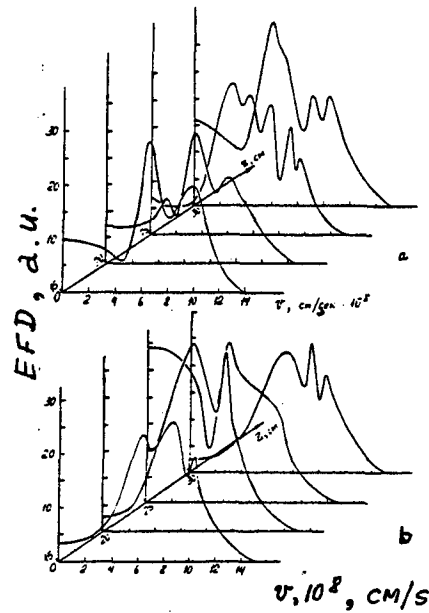


Fig.2. Spatial evolution of electron beam under overthreshold values: a - $\delta=2,5$; b - $\delta=7$

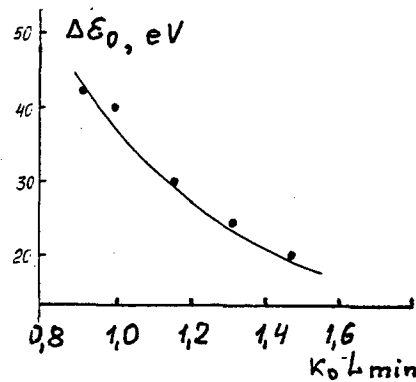


Fig.3. Beam energy increase of transient electrons under $\delta=3$ from $k_0 L_{\min}$ (dots). Solid line - function (4)

Author thanks Dr. Sergeichev for discussion.

References:

- [1] V.D.Shapiro, V.I.Shevchenko, in Handbook of Plasma Physics, edited by A.A.Galeev and R.N.Sudan, 1984, Vol.2
- [2] D.M.Karfidov et all, Laser and Particle Beams, 1988, Vol.6, Part 3, p.607
- [3] D.M.Karfidov et all, in Proc. of 4-th Brazilian Plasma Astrophysics Workshop, 1993, p.122
- [4] D.M.Karfidov, A.M.Rubenchik, K.F.Sergeichev and I.A.Sychov, Sov. JETP, 1990, Vol.98, N5, p.1592

Radiation Spectra of Langmuir Cavities in a Weak Magnetized Turbulent Plasma

K.F.Sergeichev and I.A.Sychov

General Physics Institute of the Russian Academy of Sciences, Plasma Division

117942, 38 Vavilov St., Moscow, Russia

Strong Langmuir turbulence (SLT) is characterized by a collection of collapsing cavities with entrapped bunches of Langmuir waves [1]. At the terminal collapsing stage before burnout the wave bunch radiates a small part of its energy stores nearly to the plasma frequency [2]. There are some expectations that cavity radiation carries information on the field structure of the cavity [3]. This report is devoted to a study of the radiation spectra of a single Langmuir cavity in the turbulent plasma disturbed by an electron beam in a presence of weak confining magnetic field, $\omega_H / \omega_{pe} \ll 1$.

The experimental device have been described in [2]. Plasma parameters were $n_0 \cong 4.2 \text{ cm}^{-3}$, $T_e \cong 2.5$ eV, $H_0 \cong 45$ Gs, working gas - argon under pressure $P_{Ar} \cong 5 \cdot 10^{-4}$ Torr. The plasma oscillations of Langmuir bunches had been received by thin wire antenna submerged in the turbulent plasma with passband measured within the limits of 3 dB to be 5.5-6.15 GHz. SLT was excited in the quiescent plasma by electron beam with parameters exceeding the SLT threshold, i.e. under $\delta > 1$, where $\delta = 6 \cdot 10^{-3} \cdot (n_b / n_0) \cdot (mv_0^2 / T_e)^2$ [2].

The radiation spectra of single flash were studied by the sensitive spectrum analyzer having the property of strobe a pulse in time with a control of gate delay. For gate duration 0.5 μs (while the duration of the final stage of the cavity to be near 0.2 μs) at leading edge of the beam pulse and moderate pumping parameter δ over SLT threshold the separate flash regime was realized, with the first, moreover single, flash trapped in the gate with high probability. Its spectrum was viewed in the band 25 MHz. The spectrum pattern is shown in Fig.1 for the bearing plasma frequency 5.72 GHz. Note first of all that it has line structure with lines to be distant for instance on 3.6 ; 5.4; 11.5 MHz suggesting to idea that ion-acoustic waves with wavenumbers $k_{De} \cong 0.18 ; 0.28 ; 0.7$ modify the electromagnetic spectrum of the cavity. The result confirms a thesis that the cavity radiation occurs near to the final stage of the collapse, when strong ion sound is generated by the cavity walls movement.

For to reveal a spectral form of the collapsing cavity radiation the spectral patterns were averaged over the large number of single flashe realizations (of 100

pulses) at every frequency point. The results of such procedure for beam parameter $\delta=2$ and plasma frequency $f_{pe} = 5.74$ GHz are presented in Fig.2. It's clear from Fig.2a that the spectrum form of single cavity consists of three lines separated with interval 120-150 MHz, which is approximately equal to electron gyrofrequency and varies proportionally to the magnetic field strength. Thus for external magnetic field $H_1=30$ Gs this interval decreases to 90 MHz, i.e. for $H_0 / H_1=1.5$ $\Delta f_0 / \Delta f_1$ is approximately the same 1.5. It immediately follows that the cavity field oscillations undergo modulation with the electron gyrofrequency, thus spectral peaks are presented at the frequencies $\omega = \omega_{pe}, \omega_{pe} \pm \omega_H$. Note that the same effect takes place for the radiation of second harmonic (see Fig.3). For its observing by the same antenna we had decreased the plasma density by 4 times so the main plasma frequency observed by the cavity radiation is equal to 2.87 GHz. The intensity of second harmonic is 10 times lower in comparison with the first harmonic intensity.

As was mentioned above the form of spectral line could give a useful information about cavity field structure. According to [3] the radiation line form of the N-th harmonic of the Langmuir soliton is defined as

$$I_N(\Delta\omega) \propto \Delta\omega^{-7/4} \Delta\omega^{5/2(N-2)} \times \\ \times [1 + \xi \frac{c^2}{v_{Te}^2} \left(\frac{\Delta\omega}{N\omega_{pe}} \right)^3] \quad (1)$$

where $\Delta\omega$ is frequency shift to the red side respectively to the main line, $\xi \sim 1$. The first term in brackets is responsible for quadrupole radiation, while the second term - for dipole radiation.

Fig.4 shows spectral form of the I and II harmonics obtained from our measurements. It follows that for $\Delta\omega / \omega > 5 \cdot 10^{-3}$ the dependance has polynomial form with degree $\cong -3.5$. It follows from (1) that in the case of pure dipole radiation $I_1(\Delta\omega) \propto \Delta\omega^{-5/4}$, while in the case of pure quadrupole radiation $I_1(\Delta\omega) \propto \Delta\omega^{-17/4}$. Thus comparing experimental and teoretical degrees one could suppose the quadrupole radiation to

be dominant.

The structure of the second harmonic (Fig.4) gives the degree $n \cong -1,3$ which is closed to the degree for quadrupole radiation $n \cong -1,75$. However one could note from (1) that the line form of the second harmonic has nontrivial structure; the intensity falls down from the beginning but then begins to grow behind some value of $\Delta\omega$. It is that dependance which we observed experimentally (Fig.3).

Thus our conclusion is that the Langmuir cavity as a radiation source represents the mixture of dipole and quadrupole with predomination of the latter. This conclusion coincides with those pointed in [4], which concerned the numerical simulation of Zakharov equations.

At last let's note that the line splitting in magnetic field to three lines of approximately equal intensity is surprisingly analogous to Zeeman effect of atomic line splitting: $\Delta\varepsilon = \mu_0 g M_J H$, $M_J = -J, \dots, J$, μ_0 - Bohr magneton, g - Lande factor, J - total momentum. Using this analogy and multiplet of three lines we could say that Langmuir cavity looks as particle with $J = 1$ from the point of view of quantum mechanics.

This work was supported by the Russian Fundamental Science Foundation, Project No 96-02-17640.

References:

- [1] P.Y.Cheung, A.Y.Wong, Phys.Fluids, 1985, V.28, N5, p.1538
- [2] D.M.Karfidov, A.M.Rubenchik, K.F.Sergeichev and I.A.Sychov, Sov. JETP, 1990, V.98, N5, p.1592.
- [3] V.V.Yan'kov, Sov. Plasma Physics, 1985, V.8, N1, p.86
- [4] K.Akimoto, H.L.Rowland, K.Papadopoulos, Phys.Fluids, 1988, V.31(8), p.2185

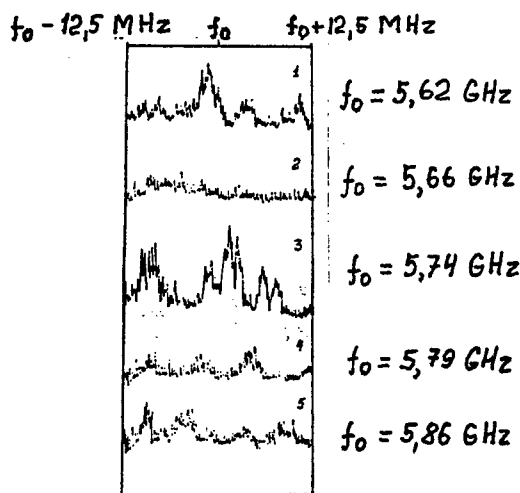


Fig.1. Spectrum pattern of the single cavity radiation in the band 25 MHz (single pulse, not averaged)

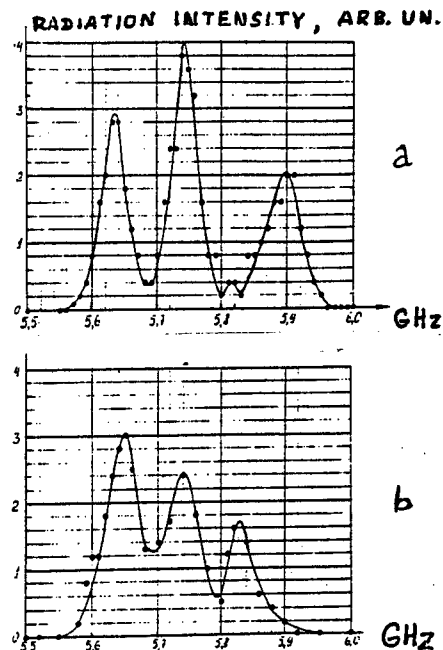


Fig.2. Spectral form of the single cavity radiation on the main frequency ($f_{pe} = 5,74$ GHz):

a - $H_0 = 45$ Gs; b - $H_0 = 30$ Gs.

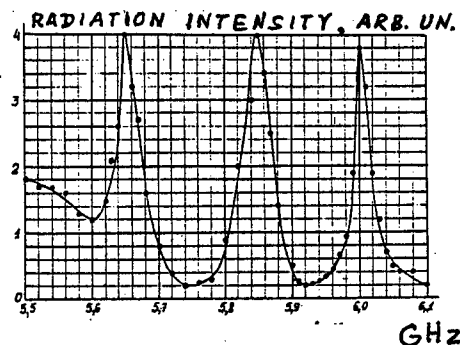


Fig.3. Spectral form of the single cavity radiation on the second harmonic ($f_{pe} = 2,87$ GHz),

$H_0 = 55$ Gs.

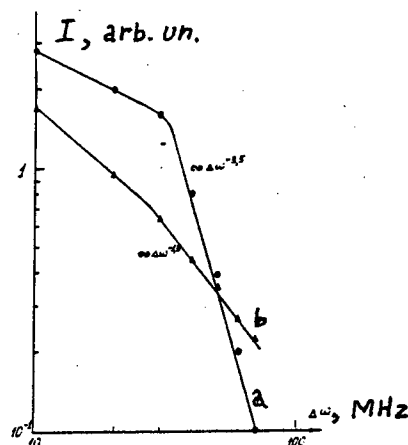


Fig.4. The dependance of line intensity from frequency deviation: a - first harmonic, b - second harmonic.

OBSERVATION OF INTERMITTENT CHAOTIC PHENOMENA CAUSED BY ION ACOUSTIC INSTABILITY

K. Taniguchi, H. Kuwae, N. Hayashi, Y. Kawai
Interdisciplinary Graduate School of Engineering Sciences,
Kyushu University, Kasuga, Fukuoka 816, Japan

1. Introduction

Recently there has been great interest in chaotic phenomena in plasma physics. Chaotic phenomena have been observed in the nonlinearity of plasma sheath [1] or the instability of discharge. For the present, the chaos phenomena via frequency bifurcation was reported in an electron beam plasma system [2] and DC discharge plasma. Intermittency is well known as one of the typical route to chaos. As the characteristic of intermittent chaos, the burst type time series which consist of a periodic laminar motion and a turbulent nonperiodic burst is observed.

In the DC discharge plasma system, it was reported that an ion acoustic wave instability including the burst type oscillation is excited, when the plasma is biased by the static field [3]. When the electron drift velocity is larger than the ion acoustic velocity, the ion acoustic instability is excited [4], and then the burst type autonomous oscillations appear. In this paper, we present the first investigations of the chaotic analysis of autonomous oscillation caused by an ion acoustic instability.

2. Experimental

The experiments are carried out using a Double plasma device. The chamber dimensions are 70 cm in diameter and 120 cm in axial length. Argon gases are introduced into the chamber with pressures of $4.0\text{--}5.0 \times 10^{-4}$ Torr. The chamber is separated into a driver region and a target one at the center by a separation grid kept at a floating potential, and the experimental region is target region. Plasma is generated only in the target region, and two parallel mesh electrodes (10 cm in diameter, 50 mesh/inch) are installed in the region at interval of about 3 cm. One electrode (chamber wall side) is biased positively and the other (separation grid side) is kept at floating. The discharge current I_T and discharge voltage V_T in the target region are kept at 60 mA and at 150 V, respectively. Only voltage biased to the mesh grid is varied as a control parameter of the system (V_m). All of the experimental measurements are obtained from the perturbation components of the currents on the biased mesh. Typical plasma parameters are follows: the electron density $n_e \sim 2\text{--}5 \times 10^8 \text{ cm}^{-3}$, the electron temperature and the ion temperature near the mesh electrode are $T_e \sim 1\text{--}2 \text{ eV}$ and $T_i \sim T_e/10$, respectively.

3. Results and Discussion

When V_m exceeds a certain threshold with gradually biasing the mesh electrode, an instability is found to be excited around the ion plasma frequency f_{pi} (~ 500 kHz). Figure 1 shows the typical example of frequency spectra measured by the biased mesh. At $V_m = 25 \text{ V}$, a broad peak of instability excited around f_{pi} . We consider that the broad peak frequency is slightly smaller than f_{pi} since the plasma density between mesh electrodes is lower than that in the outside region. With increasing the V_m , it grows and moves in the lower frequency region, and a few broad peaks appear. In the low frequency region, the frequency difference between two neighboring peaks is almost constant, and it decreases for higher frequency components, as shown in Fig. 1. Since it is found that the observed frequency spectra become discrete and the interval of observed frequency spectra independent of the distance between electrodes in preliminary experiments, the observed phenomena is not excited by the traveling double layer.

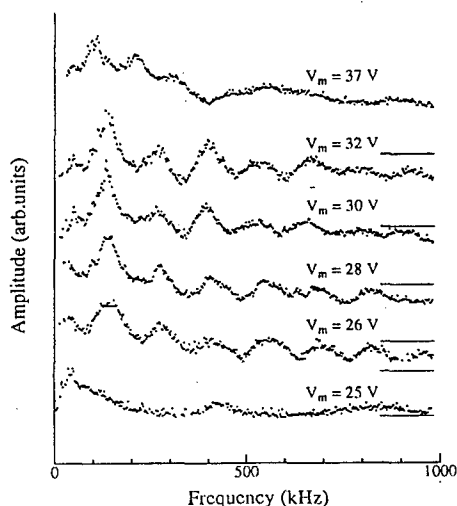


Fig. 1 Typical frequency spectra of the perturbation components of the biased mesh. Solid line denotes the noise level.

These spectrum represents the dispersion of the wave. The n th wave number k_n corresponding to the n th spectrum component f_n , is given by $k_n = 2\pi n/L$, where L is the distance between electrodes. Then, n th wave number k_n and $\omega_n (=2\pi f_n)$ is obtained as a k - ω diagram [3]. The dispersion relation of the observed wave agree

with a theoretical dispersion of the ion acoustic wave.

In order to investigate the behavior of the system, we measure the time series by the biased mesh, and reconstruct phase portraits using the embedding method. Figures 2 (a) and 2 (b) show the typical time series and phase portraits for $V_m=26$ V and $V_m=30$ V, respectively. The time delay is set as $\tau=1.0 \times 10^{-6}$ s. The burst type oscillation is found to appear at $V_m=26$ V. With increasing V_m , the interval of bursts is shorten, and the system becomes turbulent.

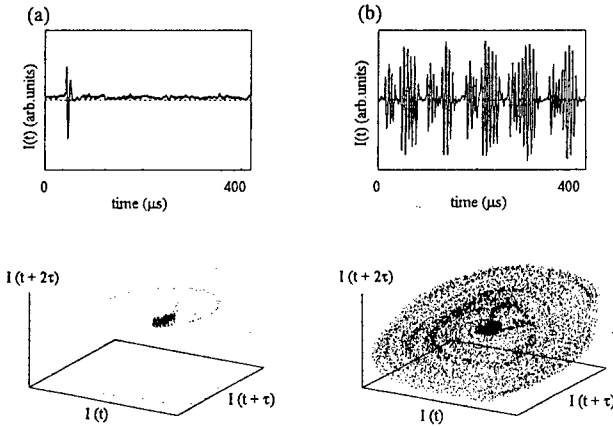


Fig. 2 Typical time series and phase portraits: (a) $V_m=26$ V and (b) $V_m=30$ V.

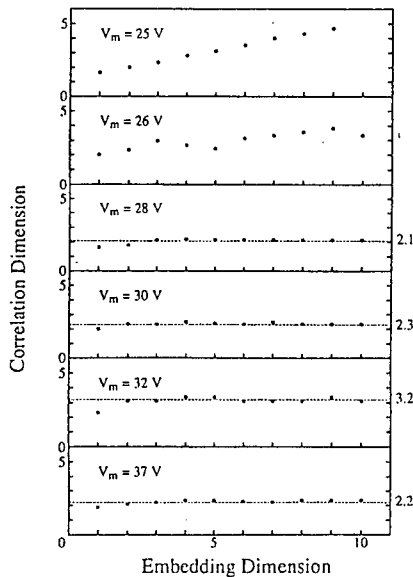


Fig. 3 Correlation dimension of the attractors reconstructed from time series for each V_m of Fig. 1.

Figure 3 shows the correlation dimension which correspond to each V_m of Fig.1. For the $V_m=25$ V and 26 V, the correlation dimensions are not saturated, in spite of the increase of the embedding dimension. Thus, the system is not chaotic. On the other hand, when

$V_m \geq 28$ V, the correlation dimensions are saturated. At $V_m=30$ V, especially, the correlation dimension is about 2.3. Therefore, the system may be in an intermittent chaotic state, since it have the burst type oscillations and the fractal dimension.

For the $V_m=26$ V and $V_m=30$ V, we calculate the Lyapunov exponent, as shown in Fig.4. As seen in this figure, the largest Lyapunov exponent is about 1.9. Since the Lyapunov exponent is positive and the correlation dimension is fractal, this system is intermittent chaos. Concerning to the determination of type of intermittency, the result of the numerical prediction of $1/f$ noise and of the probability distribution of laminar length almost agree with the theory of type-I intermittency. Thus, the present system may be in type I intermittent chaos state.

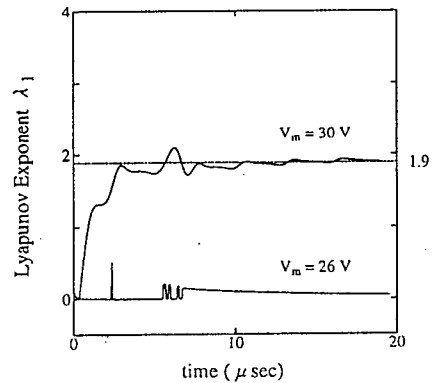


Fig. 4 Largest Lyapunov exponents of the attractors of (a) not chaotic state (b) chaotic state.

4. Conclusion

Using two parallel mesh electrodes which are biased positively, we excite an ion acoustic wave instability. The control parameter of this system is the mesh biased voltage (V_m). When $V_m \geq 26$ V, the burst type autonomous oscillation is experimentally observed around the ion plasma frequency ($f_{pi}=500$ kHz). For the $V_m \geq 30$ V, the phase portraits reconstructed from observed time series are chaotic, and the correlation dimensions are above 2 and fractal. Furthermore, at $V_m=30$ V, the largest Lyapunov exponent is positive, 1.9. These results suggest that the system reaches intermittent chaos.

Reference

- [1] A. Komori, N. Ohno, T. Yamaura and Y. Kawai, Phys. Lett. **170A**, 439 (1992).
- [2] N. Hayashi and Y. Kawai, Phys. Plasmas **3**, 4440 (1996).
- [3] H. Tanaka, A. Hirose and M. Koganei, Phys. Rev. **161**, 94 (1967).
- [4] D.B. Fenneman, M. Raether and M. Yamada, Phys. Fluids **16**, 871 (1973).

Observation of the Eckhaus Instability in a Glow Discharge Plasma

A. Dinklage, B. Bruhn, H. Deutsch, S. Gubsch, B.-P. Koch and C. Wilke

Institut für Physik, Ernst-Moritz-Arndt Universität Greifswald, Domstr. 10a, D-17489 Greifswald, Germany

1. Theoretical remarks

The Eckhaus instability [1] is a pattern selecting instability of the uniform state in the vicinity of the threshold of the instability owing to nonlinearities. This instability appears whenever the system is forced to have a wave number outside a nonlinear stable band that is not limited by linear mechanisms. Experimentally, instability mechanisms of this kind were found in hydrodynamic systems (e.g. [2]) and the effect of the Eckhaus mechanism can be shown experimentally by spatio-temporal observations of the pattern formation in the vicinity of the stability limits.

Theoretically it is well known that there are model equations that are susceptible to the Eckhaus instability, like equations of the Ginzburg-Landau (GL) type [3]. In the case of a transition from sub- to supercritical Hopf bifurcations in the vicinity of threshold the GL equation has to be modified by further nonlinear terms [4]. It has been shown that additional nonlinear terms of such kind are essential for a proper description of the bifurcation behavior of ionization waves [5], which are well known to exhibit a variety of nonlinear behaviors (e.g. [6]). A review on ionization waves was given by Ohe [7] depicting the properties of this nonlinear wave phenomenon.

In this paper we report on the observation of the Eckhaus instability in a glow discharge plasma.

2. Experimental results

The experiments presented in this paper were performed in a neon glow discharge tube ($p_0=1.5$ Torr, $r_0=1$ cm) driven by a current source ($i<20$ mA). The spatio-temporal variation of the light intensity was observed, which was due to the metastable atoms that are involved in the physical mechanism of ionization waves. It is a peculiarity of bounded systems of a length L to show a discrete spectrum of allowed wave states that may be represented by a wave number k_n

$$k_n = 2\pi n/L. \quad (1)$$

In the experiments described here only wave modes with a discrete power spectrum are observed above a critical current ($i_c=9$ mA). Below this threshold no self-excited ionization waves are observable representing a uniform state. If the current is increased, mode transitions appear for well defined current values. If the current is decreased from the

experimentally limited maximum, mode transitions appear as well. However, the currents corresponding to mode transitions were different indicating a hysteresis [see Fig. (1)]. We should remark that our system always contains only one wave mode which is nonlinearly stable in between the transition currents.

The linear stability of the uniform state to a perturbation with a wave number k is given, if the growth is less than zero, reflecting a decaying wave state. We performed a linear stability analysis experimentally by the temporal observation of an externally driven p-wave. We are able to prepare wave states of any wave number and amplitude by applying a modulated current to the discharge current. The amplitude of the driven waves was chosen to be small compared to the saturated amplitude of the self-excited, nonlinear waves. If the current is varied for a perturbation of a fixed wave number k , we identify a critical current $i_l(k)$ corresponding to the amplitude of the perturbation that represents a zero growth rate σ . This procedure yields the neutral curve in Fig. (1).

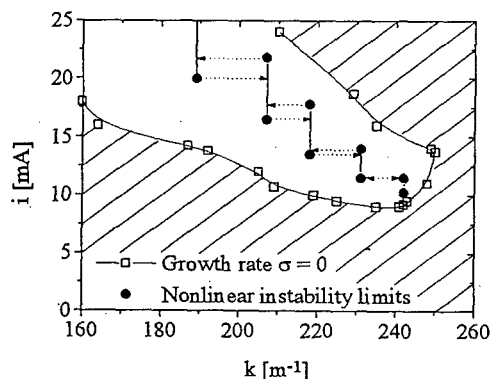


Figure 1: Stability diagram of p-waves in a neon glow discharge. Solid, vertical lines represent stable, self excited wave modes. Horizontal arrows indicate mode transitions. Hollow squares connected by the spline curve represent the curve of linear stability of the uniform state (hatched area).

In order to confirm a pattern selecting mechanism, we observed the spatio-temporal behavior of a mode transition given in Fig. (2) using a stroboscopic imaging technique. The discharge current was slowly varied in order to arrive at the stability limit of the wave pattern. The mode transition $k_n \rightarrow k_{n+1}$ was observed. The diagram shows wave crests and troughs (density of black dye) representing equal phases of the waves as a function of space (abscissa) and time. The spatial range given in Fig. 2 represents

locations where the p-waves were found to be saturated. In the center of the diagram a bifurcation of the lines, representing the waves' phases, can be identified. Thus, the pattern selecting process appears in the volume of the system as it would be predicted by theory. We should mention that the exact position of a mode transition is not predictable, neither in space nor in time. The mode transition was accompanied by a rise of side-bands that could be observed if the system was driven in the vicinity of the instability.

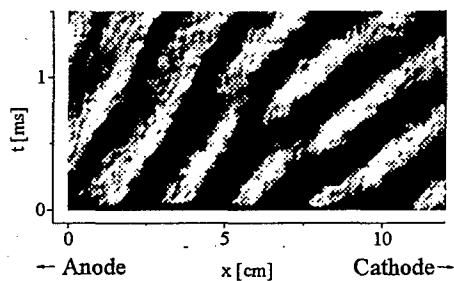


Figure 2: Space time diagram of a mode transition of saturated p-waves in the positive column of a neon glow discharge. The shade of the black colour represents the phases of the waves.

3. Conclusions

We have presented experimental investigations of linear and nonlinear stability of ionizations waves (p-waves). We observed the spatio-temporal behavior of a mode transition of different nonlinear stable wave states, suggesting a mechanism related to a general nonlinear instability, the Eckhaus instability. Theoretical considerations led to a model equation of the GL type, supporting the experimental results. In conclusion, we reported on the observation of the Eckhaus instability in a glow discharge plasma. Comparing our results to other experiments we found our system to exhibit a strong pattern selection [5].

Finally, we would like to point out that instabilities of the Eckhaus type should be expected to appear in completely different plasma states related to nonlinear wave phenomena owing to the universality of the instability mechanism.

The authors acknowledge helpful discussion with Dr. W. Zimmermann and Prof. K. Fesser. This work was funded by the Sonderforschungsbereich 198 'Kinetik partiell ionisierter Plasmen', Projekt A7 of the Deutsche Forschungsgemeinschaft.

4. References

- [1] W. Eckhaus: *Studies in Non-Linear Stability Theory*, Springer: Berlin (1965); L. Kramer and W. Zimmermann: *Physica D*, **16** (1985) 221
- [2] B. Jانياود, A. Pumir, D. Bensiomon et al.: *Physica D*, **55** (1992) 269; P. Kolodner: *Phys. Rev. A*, **46** (1992) 6431; S. Rasenat, E. Braun and V. Steinberg: *Phys. Rev. A*, **43** (1991) 5728
- [3] M.C. Cross and P.C. Hohenberg: *Rev. Mod. Phys.*, **65** (1993) 851 and references therein
- [4] W. Eckhaus and G. Iooss: *Physica D*, **39** (1989) 124
- [5] B. Bruhn and B.-P. Koch (to be published)
- [6] W.X. Ding, H. Deutsch, A. Dinklage and C. Wilke: *Phys. Rev. E* (publication in march 1997); K.-K.-D. Weltmann, H. Deutsch, H. Unger and C. Wilke: *Contrib. Plasma Phys.*, **33** (1993) 73
- [7] K. Ohe: *Current Topics in The Physics of Fluids*, **1** (1994), 319

Topic 17

Numerical modeling.

Hot ions in multi-component plasmas

Anschütz, F.-B.[†], Awakowicz, P.[†], Scheubert, P.[†], Valentini, H.-B.[‡]

[†] Physics of Electrotechnology, Technical University of Munich, Arcisstr. 21, 80290 München, Germany

[‡] Institut für Physikalische Hochtechnologie, Helmholtzweg 4, 07743 Jena, Germany

Abstract

Fluid dynamic modelling of multi-component plasmas leads to a multi point boundary value problem if the ion inertia as well as an isotropic ion partial pressure are taken into account. A numerical solution to this task is presented.

Physical model and basic equations

A multi fluid model of a low pressure gas discharge is considered. Each species (electrons, different kinds of positive ions) is described by the equations of particle balance and momentum conservation. Models describing several ion species were previously treated, but simplifications were used. The static ion pressure was neglected in [1], while quasineutrality was assumed in [2]. In this work, a homogenous ion pressure as well as the space charge density are taken into account. Therefore, the model describes the bulk and the sheath simultaneously.

The particles are generated within the plasma by electron impact ionisation of the neutral gas. The neutral gases are regarded as motionless with spatially constant densities. The carrier motion is influenced by the electric field, the elastic collisions, Coulomb collisions, the inertia and the partial pressure gradient. The electric field is calculated from the Poisson equation.

The model describes the positive column of a cylindrical, axially homogenous and time invariant discharge. Only one spatial dimension (radius) has to be considered. The governing equations are:

$$\begin{aligned} \frac{1}{r} \frac{d}{dr} (r n_j v_j) &= n_e G_j \\ \frac{1}{r} \frac{d}{dr} (r m_j v_j^2) + k_B T_j \frac{dn_j}{dr} &= q_j n_j E - n_j m_j v_j v_j + \Delta P_j^C \\ \epsilon_0 \frac{1}{r} \frac{d}{dr} (r E) &= \left(\sum_i q_i n_i + q_e n_e \right) \end{aligned}$$

The variables are the particle densities n_j , the radial components of the drift velocities v_j and radial component of the electric field E . $n_e G_j$ denotes the generation of particles of species j (j =electrons, ion species) by electron impact ionisation. G_j depends on the electron temperature and the neutral gas density of species j . The mass m_j , the temperature T_j and the charge q_j describe the particle j . v_j is the elastic collision frequency and ΔP_j^C the Coulomb collision term.

The boundary conditions have to be stated at the axis, within the plasma and at the wall. The radial vector components have to vanish on the axis. Electron and neutral densities may be chosen on the axis. The electron drift speed at the wall is nearly sound speed [3],

which leads to an eigenvalue problem for the electron temperature. One more boundary condition per ion is needed. These boundary conditions have to be stated at the points where one ion species attains its sound speed. The left hand sides of the particle and the momentum balance are linearly dependent at the point of sound speed (singular point). In order to obtain a physically reasonable solution, the right hand sides must be linearly dependant too, which is the boundary condition for this ion species [4].

Solution method

The set of differential equations is transformed to a set of nonlinear algebraic equations by finite volume discretisation. The resulting set of algebraic equations and the boundary conditions are solved by Newton iteration.

Treatment of the boundary conditions

In addition to the densities and velocities the locations of the ion sound speed points must be calculated in each step of the iteration from the current guess of the radial velocity profiles. The boundary condition for each singular point is evaluated by interpolating the grid point values to the point of sound speed. The interpolation requires a very fine grid in the region of the singular points.

Numerical treatment

The Jacobian of the system is very ill conditioned. This is caused by the difference between the masses of ions and electrons and the steep gradients in the sheath, where the mean drift velocity of electrons rises to approximately sound speed. Therefore, a direct matrix solver must be used. In this work, a standard subroutine Gauss solver for banded matrices was used in order to exploit the sparsity. A minimal band width of the Jacobian requires dynamic reordering of the linearized equations when the radii of the singularities change.

The Newton iteration fails due to the strong coupling of the differential equations unless an excellent initial guess is used. This guess is obtained by solving the two point boundary value problem, which is obtained by assuming zero ion temperature [1][5].

All discretisation was done by using an implicit scheme. At higher ion temperatures a fully implicit scheme is recommended for the discretisation of the source term of the Poisson equation, although it is less precise for small integration steps [6]. On the other hand, a fully implicit scheme is more stable.

Results

Calculations are carried out for a helium plasma with admixtures of hydrogen and nitrogen. According to an experimental setup, the positive column of a cylindrical

cascade arc at a pressure of 100 Pa with a tube radius of 3.5 mm was assumed. As in the experiment, a ratio of generated carriers of 0.964: 0.027: 0.009 from helium, nitrogen and hydrogen respectively was adjusted by choosing neutral gas densities. Under the experimental conditions, all ion temperatures are small compared to the electron temperature. The ion densities are normalized to the measured electron density on the axis ($2.2 \cdot 10^{19} \text{ m}^{-3}$). The calculated electron temperature is 12 eV.

Fig. 1 shows the fraction of the different ion species at vanishing ion temperature and neglected Coulomb interaction. In Fig. 1, the densities are multiplied by additional factors in order to allow comparison between the profiles. The hydrogen profile's dip is due to a runaway effect of the mobility [7]. The ion fractions on the axis are calculated from the boundary conditions by use of the generation ratios, which depend on the densities of neutrals and the electron temperature.

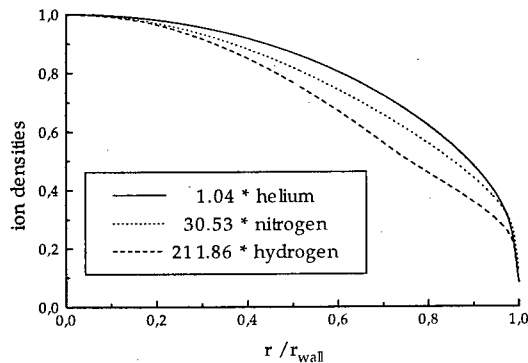


Fig. 1: Densities of cold ions without Coulomb collisions.

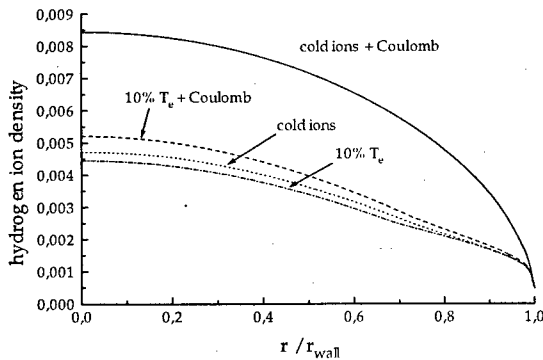


Fig. 2: The effect of temperature and Coulomb collisions on the hydrogen density.

In the following, four cases are examined. Calculations are carried out for two ion temperatures (zero, 10% of T_e) with and without Coulomb interaction. In Fig. 2 and 3, the density profiles are shown for hydrogen and nitrogen. The density of hydrogen ions is decreased with increasing temperature. This is caused by increased diffusion towards the wall. Coulomb friction with other ions reduce the diffusion of hydrogen, thus leading to higher densities.

The effect of temperature on the nitrogen density is more complicated. Neglecting Coulomb collisions, the density of nitrogen is decreased with increasing temperature. If Coulomb collisions are taken into account, the density is increased with the ion temperature. This might be understood by the following considerations: due to their mass, cold nitrogen ions are drifting to the wall at relatively low speed. If Coulomb friction is taken into account, nitrogen is pushed to the wall by ions of the much lighter helium buffer gas. Therefore, the nitrogen ion density is decreased on the axis while the helium ion density is increased. At high temperature, thermal diffusion increases the nitrogen ion flux and decreases the Coulomb friction and the push out by lighter atoms.

Due to the higher temperatures, the net space charge density at the axis is reduced by 9 %.

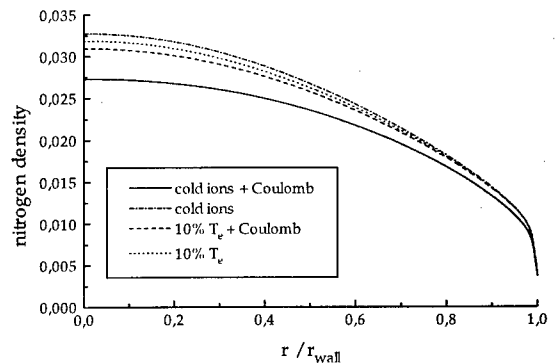


Fig. 3: The effect of temperature and Coulomb collisions on the nitrogen density

Discussion

It is well known that the influence of ion temperatures on the radial distributions of densities and velocities is small. In multi-component plasmas, the ion temperatures may influence the mixtures of positive ions. Different behavior is observed for ions lighter and heavier than the buffer gas, if ion-ion interactions are taken into account.

References

- [1] Valentini, H.-B., *Beiträge Plasmaphys.* **20** (1980) 243
- [2] Shapiro, D.A., Valentini, H.-B., *Contrib. Plasma Phys.* **31** (1991) 391
- [3] Valentini, H.-B., *Contrib. Plas. Phys.* **31** (1991) 211
- [4] Franklin, R.N., "Plasma Phenomena in Gas Discharges" Clarendon Press, Oxford 1976
- Wieckert, C., *Contrib. Plasma Phys.* **27** (1987) 309
- Valentini, H.-B., *J. Phys. D: Appl. Phys.* **21** (1988) 311
- [5] Forrest, J.R., Franklin, R.N., *Br. J. Appl. Phys.* **19** (1968) 1357
- Ingold, J.H., *Phys. Fluids* **15** (1972) 75
- [6] Patankar, S.V., "Numerical Heat Transfer and Fluid Flow", Hemisphere, Washington, D.C. 1980
- [7] Howorka, F., Fehsenfeld, F.C., Albritton, D.L., *J. Phys. B: Atom. Molec. Phys.* **12** (1979) 4189

A hydrodynamic model for a cylindrical Langmuir probe in a low pressure discharge

P. Scheubert, P. Awakowicz, B. Anschütz, G. Wachutka

Lehrstuhl für Technische Elektrophysik, Technische Universität München, Arcisstr. 21, D-80290 München, Germany

Abstract

A hydrodynamic model for cylindrical Langmuir probes is suggested. For negatively biased probes, the collection of positive ions is calculated. The space charge in the sheaths, inertia of ions and electrons are considered. Collisions of charge carriers and a non zero ion temperature are taken into account. Finally, the model is compared with measurements.

A hydrodynamic plasma model

Single Langmuir probes are widely used for diagnostics of low pressure discharges. Normally, it is assumed that a probe immersed in a plasma only has minor influence on the discharge itself [1]. The influence of probes on low pressure discharges was already investigated by Waymouth [2] and Valentini [3], [4]. Therefrom it is known that the region influenced by a probe is much more extent than a few Debye lengths.

To get an appropriate description for a probe influencing the discharge, the whole system must be modelled. This can be achieved by using a two fluid hydrodynamic model.

From the Boltzmann equation, a set of conservation equations can be derived to describe the behaviour of low pressure discharges [5].

We restrict ourselves to a two moment model and the case of a steady state. For a cylindrical, one dimensional geometry the governing equations are:

$$\frac{1}{r} \frac{d}{dr} (r n_{e,i} v_{e,i}) = n_e G$$

$$\frac{1}{r} \frac{d}{dr} (r n_{e,i} m_{e,i} v_{e,i}^2) = q_{e,i} n_{e,i} E - k T_{e,i} \frac{dn_{e,i}}{dr} - n_{e,i} m_{e,i} v_{e,i} v_{e,i}$$

where r denotes the distance from the axis, $n_{e,i}$ and $m_{e,i}$ the number densities and masses of electrons and ions, respectively. The corresponding radial drift velocities are $v_{e,i}$. The charge of electrons and ions are described by $q_{e,i}$.

The carriers are considered to have constant, non zero temperatures denoted by $T_{e,i}$. Inelastic collisions are taken into account by assuming a rate G which describes the generation of electrons and ions by impact ionisation. Hereby G depends on the electron temperature T_e and the density of the neutral gas from which electrons and ions are produced. Elastic collisions with neutral particles which cause a loss of momentum for charged carriers are taken into account by the effective collision frequencies $\nu_{e,i}$.

With respect to the sign of their charge, the particles are accelerated or decelerated by an electric field strength E .

The dependence of the field strength on the space charge is given by the Poisson equation:

$$\frac{1}{r} \frac{d}{dr} (rE) = \epsilon_0 (q_i n_i + q_e n_e)$$

where ϵ_0 is the permittivity of the vacuum.

Geometry and boundary conditions

A cylindrical geometry consisting of two coaxial electrodes is investigated.

The outer electrode is hollow and serves as the discharge vessel. The discharge is assumed to be powered by an external RF magnetic field. The inner electrode is considered to be a probe and therefore has a much smaller diameter. By applying a voltage between the two electrodes a current is drawn.

The formulation of appropriate boundary conditions [4], [5] leads to a multipoint boundary value problem. The model has to be supplied with the following data: probe and reactor radius, neutral gas temperature and pressure, the peak ion density, and the current drawn by the inner electrode. The ion temperature is assumed to be equal to the temperature of neutral particles.

The electron temperature, the potential difference between the electrodes, density distributions for electrons and ions, respectively, as well as the corresponding distributions of radial velocities and the electric field are calculated.

Discussion of theoretical results

Especially the assumption of a non zero ion temperature results in numerical difficulties. The system consisting of 5 ordinary nonlinear differential equation can not be solved by standard integration algorithms.

A solution can be found by using a finite volume discretisation and a deformable grid.

Theoretical results will be presented in the following for a cylindrical discharge vessel with a radius of 0.1 m. An Argon discharge ($p_N = 1.0 - 100$ Pa) with a peak ion density of 10^{16} m^{-3} is investigated. The assumed probe radius was 50 μm .

Fig. 1 shows the radial electron density distribution for 3 different neutral gas pressures. With increasing pressure, the discharge becomes more diffusion dominated and the profiles flatten.

The influence of the probe voltage on the sheath region surrounding the probe is shown in Fig. 2. A significant difference between electron and ion density occurs and decreases towards the plasma. The distribution of electron and ion density is shown for two applied

voltages (5.8V, -29V). In the first case, the probe is floating, the net current drawn by the probe equals zero. In the second case, the probe is negatively biased which leads to a depletion of electrons in the sheath region. For both voltages the cylindrical geometry causes an increase of the ion number density in a layer very close to the probe.

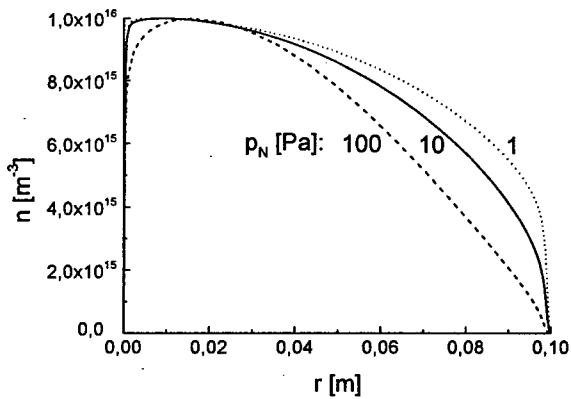


Fig. 1. Radial electron density profiles for a neutral gas pressure range from 1 Pa to 100 Pa

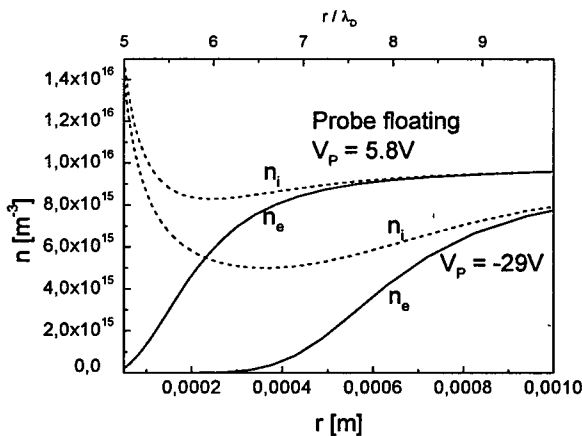


Fig. 2. Radial electron and ion density profiles in the sheath region close to the probe for a neutral gas pressure of 10 Pa.

Comparison with experiment

Experiments were carried out in an ICP reactor with argon in a pressure range from 1-100 Pa. To determine electron density and temperature a Langmuir probe with diameter 50 μm and a length of 5 mm was used. The electron density was obtained from the current at the plasma potential, the electron temperature was calculated from the slope of the current in this point.

In order to check the validity of the model, first of all calculated and measured values of the mean electron energy were compared. Figure 3 shows the excellent agreement.

The dependence of the probe current on the applied voltage is shown in Fig. 4. Over the pressure range from 5-100 Pa a good correlation between simulation and measurement can be observed. As an example the current-voltage characteristics for two neutral gas pressures are shown in Fig. 4.

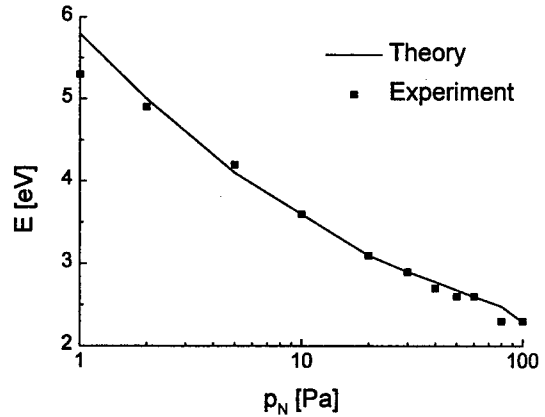


Fig. 3. Mean Electron Energy in dependence of the neutral gas pressure: comparison between theory and experiment

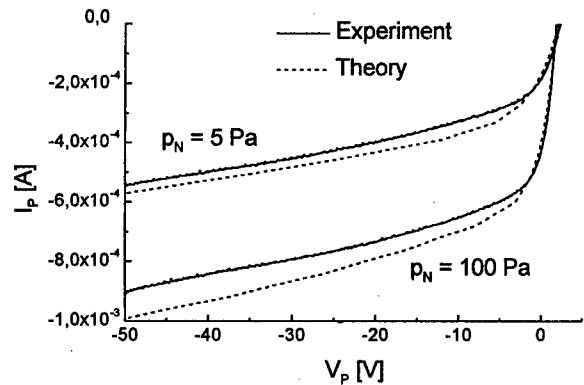


Fig. 4. Probe currents in dependence of applied voltage for neutral gas pressures 5 Pa and 100 Pa.

Acknowledgements

For his assistance in performing the measurements shown above I would like to thank my colleague Dr. W. Kasper.

References

- [1] J. D. Swift, M. J. R. Schwar: *Electrical Probes for Plasma Diagnostics*, Iliffe Books, London (1970)
- [2] J. F. Waymouth: *Phys. Fluids* 7 (1994) 1843
- [3] H.-B. Valentini: *Contr. plasma Phys.* 31 (1991) 2, 211-229
- [4] H.-B. Valentini, E. Glauche: *Plasma Sources Sci. Technology*, 4 (1995) 353-365
- [5] H.-B. Valentini: *J. Phys D: Appl. Phys.* 27 (1994) 119 - 128

METALLIC POWDERS IN A PLASMA TORCH : NUMERICAL MODELLING OF THE CURRENT INTENSITY EFFECT

J. M. Bauchire¹, J. J. Gonzalez¹ and P. Proulx²

¹ Centre de Physique des Plasmas et de leurs Applications de Toulouse (CPAT)

ESA n° 5002 - Université Paul Sabatier

118 Route de Narbonne - 31062 Toulouse Cedex 4 - France

² Centre de Recherche en Technologie des Plasmas (CRTP)

Département de génie chimique - Université de Sherbrooke

Sherbrooke, Québec, J1K2R1 - Canada

1. Introduction

The use of plasma jets for spray coating plays an important role of the thermal plasmas applications. However, the injection of particles in a plasma jet modifies its structure, leading to a cooling of the jet and a contraction of the flow. A good knowledge of these phenomena is necessary to improve the quality of the processes and numerical modelling appears to be an interesting tool to predict plasma behaviour.

Crowe *et al* [1] have developed the PSI-Cell technique to take into account the presence of particles in a flow. This technique was applied by Proulx *et al* [2-3] to plasma jets and RF plasma torches. On the other hand, we have developed a model of a DC plasma torch [4-5] including both the nozzle and the plasma jet.

The objective of this work is to study the interaction between an argon plasma at atmospheric pressure and metallic powders in a DC plasma torch. We show the effect of the iron and tungsten particles loading on the total absorbed power and on the thermal treatment of the particles.

2. Mathematical model

2.1. The plasma-particles interaction

The PSI-Cell model allows a coupling of the particulate phase described by the Lagrangian approach with the Eulerian system of equations describing the plasma flow. This technique, first calculates the undisturbed flow and temperature fields, then uses them to calculate the particle trajectories. In the particle trajectory calculation, the momentum, heat and mass transfer between the particulate phase and the plasma are integrated over the control volumes used to calculate the flow field. The exchange terms are included in the plasma flow calculation and the particle trajectories are calculated with the updated plasma flow conditions. The injection of the particles in the plasma is done in a single point source, at the exit of the torch (figure 1) and with a Gaussian size distribution contained between -2 and +2 μm around the mean diameter. The particle concentration in a control volume (of location ij) is calculated simply as :

$$C_{ij}^l = \frac{N_{ij}^l \tau_{ij}^l}{V_{ij}} \quad (1)$$

where N_{ij}^l is the number of particles size l injected per unit time (l is the coordinate for the particle size distribution), τ_{ij}^l is the time of flight of the particles in the control volume of volume V_{ij} . This concentration is then used to calculate the source/sink terms, used in the flow and temperature fields :

$$S_{p\phi_{ij}} = \left(\sum_l C_{ij}^l \frac{\Delta m_p \phi_{ij}^l}{\tau_{ij}^l} \right) \quad (2)$$

ϕ stands for the appropriate intensive fluid and Δm_p is the variation of the particle mass in cell. The particles trajectories and thermal histories are described by Proulx *et al* [2-3].

2.2. Assumptions and governing equations of the plasma

The model of the DC plasma torch, described in previous works [4-5] is based on the local thermodynamic equilibrium hypothesis. The governing equations are written in an axisymmetric system of coordinates, for a laminar flow in a steady state. The radiation effects are considered through the net emission coefficient at atmospheric pressure. The inlet and the carrier gases are argon at atmospheric pressure.

For the plasma, solutions are sought for a set of elliptical partial differential transport equations, solved using Patankar's algorithms [6]. All the equations can be written in the same form :

$$\nabla \cdot (\rho U \phi) = \nabla \cdot (\Gamma_\phi (\nabla \phi)) + S_\phi + S_{p\phi} \quad (3)$$

where ϕ again is general variable, Γ_ϕ the corresponding diffusion coefficient and S_ϕ the source term. $S_{p\phi}$ is the particles perturbation on the property ϕ calculated through the PSI-Cell technique. U is the velocity and ρ is the mass density. The calculation region and the corresponding boundary conditions are sketched in figure 1. V and j_x are respectively the electric potential and the axial current density component. At the cathode tip, the current density profile is given by Hsu *et al* [7].

The inlet velocity profile $u(r)$ is parabolic and the computational domain is a grid of 87×38 (x, r) points.

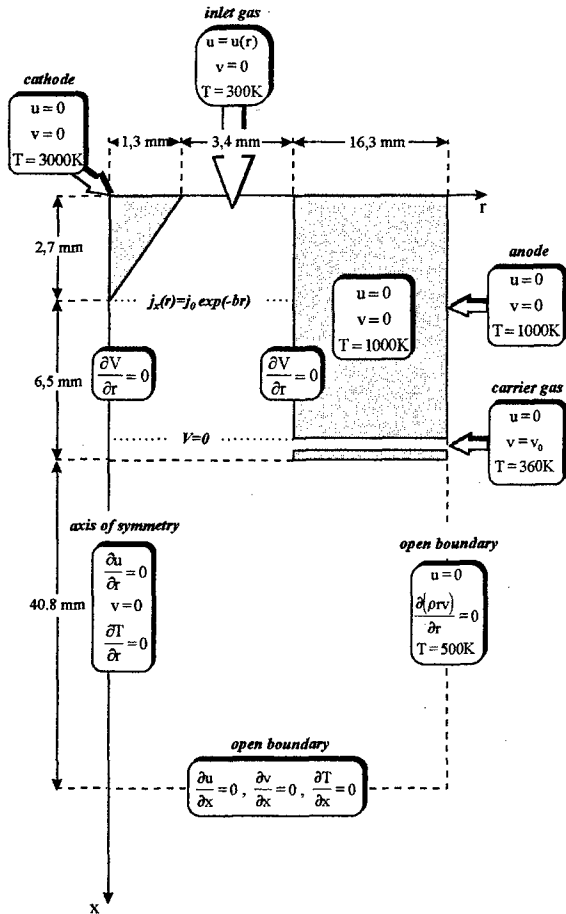


Figure 1. Computation domain and boundary conditions

3. Results and discussion

The calculation was made with the following operating conditions : the inlet mass flow rate $D_0 = 0.5$ g/s, the carrier gas flow rate $D = 0.01$ g/s and the particle diameter $d_p = 25$ μ m. We have summarized in Table 1 the power absorbed by the particles for two values of the current intensity $I = 100$ A and $I = 180$ A, which correspond to a net power of the torch of, respectively, 1.1 kW and 2.1 kW.

	Iron	Tungsten
$I = 100$ A	99.9	38.0
$I = 180$ A	163.6	57.1

Table 1. Power absorbed (W)

The results show that the absorbed power is greater using iron than tungsten particles. The specific heats and the latent heats are higher for iron than for tungsten which contributes to a more important energy absorption by this material. We can also see, on figure 2, that the mean particle temperature is not very modified by the current intensity increase, contrary to the axial velocity (figure 3). These phenomena linked to the velocity and the temperature fields of the plasma are important in spray coating. The rise of the current

intensity leads to a diminution of the particle flight time which is not compensated by a rise of the temperature. However, the increase of the velocity can improve the flattening and the adherence on the substrate [8].

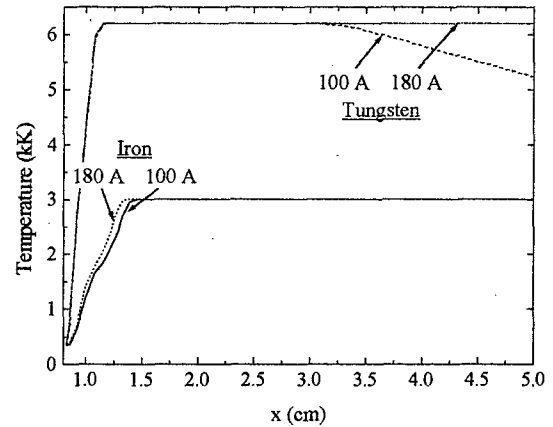


Figure 2. Mean temperature the particles versus axial position

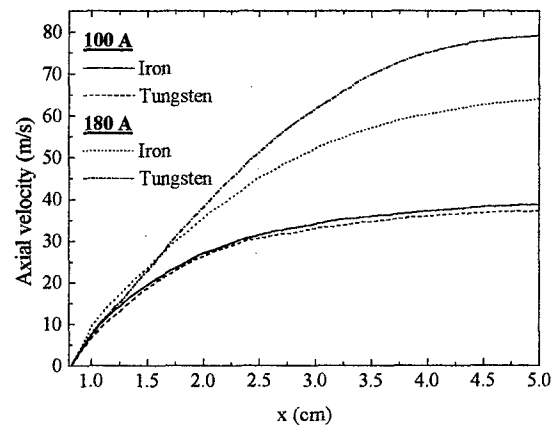


Figure 3. Mean axial velocity of the particles versus axial position

4. References

- [1] Crowe C. T., Sharma M. P. and Stock D. E. 1977 J. Fluid. Eng. **99** 325
- [2] Proulx P. 1987 Thèse de Doctorat, Université de Sherbrooke (Canada)
- [3] Proulx P., Mostaghimi J. T. and Boulos M. I. 1985 Int. J. Heat Mass Transf. **28** 1327
- [4] Bauchire J. M., Gonzalez J. J. and Gleizes A. 1995 12th ISPC (Minneapolis, USA) **3** 1761
- [5] Gonzalez J. J., Bauchire J. M. and Gleizes A. 1996 12th Symp. Phys. Switching Arc (Brno, Czech Republic) **1** 49
- [6] Patankar S. V. 1980 "Numerical heat transfer and fluid flow" ed. McGraw-Hill
- [7] Hsu K. C., Etemadi K. and Pfender E. 1983 J. Appl. Phys. **54** pp 1293-1301
- [8] Vardelle M., Vardelle A., Besson J. L. and Fauchais P. 1981 Revue Phys. Appl. **16** 425

Simulation of positive streamers in air.

I. Two-step algorithm based on van Leer type upwind schemes.

A.F. Djakov, Yu.K. Bobrov*, I.A. Solntsev†, Yu.V. Yurghelenas*

Russian Joint Stock Company of Energy and Electrification "EES ROSSII", 7 Kitaigorodsky proezd, Moscow, 103074, RUSSIA

*High Voltage Research Center of All-Russia Electrotechnical Institute, Istra-2, Moscow Region, 143500, RUSSIA

†Central Aerohydrodynamical Institute, Zhukovskij, Moscow Region, RUSSIA

1. Introduction.

Since the works of Morrow [1] an application of flux-corrected transport (FCT) algorithms for solution of continuity equations has led to the essential progress in streamer and corona discharge simulation. But further investigations shown that using of FCT generates numerical errors concerned with "stepping" of exponential profiles on the fronts of ionization waves. To overcome them the two-step van Leer type algorithm of the solution of continuity equations suitable to streamer simulation is proposed here. Solution of test problems and comparative analysis of wide class of finite-difference schemes including FCT is performed.

2. Description of the method.

Numerical solution of the continuity equation:

$$\partial n / \partial t + \partial(vn) / \partial x - \partial(D \cdot \partial n / \partial x) = I \quad (1)$$

in case $D=0$ is based on the van Leer's idea of finite-volume approximation by piecewise-linear functions:

$n(x) \cong \bar{n}_{i+1/2}^0 + s_{i+1/2}(x - x_{i+1/2})$ [2]. Here $\bar{n}_{i+1/2}^0$ is an average value on the grid cell $\Delta_{i+1/2} = (x_i, x_{i+1})$, which is second order - identical to $n(x_{i+1/2})$, $s_{i+1/2}$ - the slope value. To maintain monotonicity of the scheme all the slopes are defined by flux-limiter function FL [3]:

$$s_{i+1/2} = FL(s_p s_{i+1}), \quad s_i = (\bar{n}_{i+1/2}^0 - \bar{n}_{i-1/2}^0) / (x_{i+1/2} - x_{i-1/2}), \\ x_{i+1/2} = 0.5(x_{i+1} + x_i).$$

The algorithm can be written in the conservative form:

$$\bar{n}_{i+1/2}^1 = \bar{n}_{i+1/2}^0 + (\delta n_{i+1/2})^{\text{conv}} + (\delta n_{i+1/2})^{\text{ion}}, \quad (2)$$

where $(\delta n_{i+1/2})^{\text{conv}} = -(f_{i+1}^{1/2} - f_i^{1/2}) \delta t / \delta x_{i+1/2}$,

$(\delta n_{i+1/2})^{\text{ion}} = I_{i+1/2}^{1/2} \delta t$. Upper index "1" corresponds to the solution on the next time step $t+\delta t$ and "1/2" - to the half time step. $f_i^{1/2} = v_i^{1/2} \bar{n}_i^{1/2}$ - the fluxes through interface boundaries $x = x_i$, $\bar{n}_i^{1/2}$ - interface values, defined in upwind manner. For $v_{i+1/2}^0 > 0$

$$\bar{n}_{i+1}^{1/2} = \bar{n}_{i+1}^0 + 0.5 \cdot \delta t [I_{i+1/2}^0 - (\bar{n}_{i+1}^0 v_{i+1}^0 - \bar{n}_i^0 v_i^0) / \delta x_{i+1/2}],$$

$$\bar{n}_{i+1}^0 = \bar{n}_{i+1/2}^0 + 0.5 s_{i+1/2} \delta x_{i+1/2}.$$

In streamer discharge problems the coefficients of (1) are functions of electric field strength E , which depends on total discharge density by Poisson equation [4].

Therefore to obtain values $v_i^{1/2}$, $I_{i+1/2}^{1/2}$ the execution of the half step is needed. The formulae for $\bar{n}_{i+1/2}^{1/2}$ are similar to (2):

$$(\delta n_{i+1/2}^{1/2})^{\text{conv}} = -0.5(f_{i+1}^0 - f_i^0) \cdot \delta t / \delta x_{i+1/2},$$

$$f_i^0 = v_i^0 \bar{n}_i^0, (\delta n_{i+1/2}^{1/2})^{\text{ion}} = 0.5 I_{i+1/2}^0 \delta t.$$

The calculation of coefficients of (1) on a half step is to be performed using $\bar{n}_{i+1/2}^{1/2}$ values.

A simple modification of fluxes f_i is needed for including a diffusion term:

$$f_i^{1/2} = v_i^{1/2} \bar{n}_i^{1/2} - 0.5 D_i^{1/2} (\bar{n}_{i+1/2}^{1/2} - \bar{n}_{i-1/2}^{1/2} + \bar{n}_{i+1/2}^0 - \bar{n}_{i-1/2}^0) / \delta x_i, \\ \delta x_i = 0.5(\delta x_{i+1/2} + \delta x_{i-1/2}). \text{ So, the finite difference}$$

scheme becomes implicit and $\bar{n}_{i+1/2}^{1/2}$ values can be obtained by the standard method. The expression for $\bar{n}_{i+1/2}^{1/2}$ must be corrected as well.

When choosing an appropriate flux-limiter function FL one can construct various high resolution schemes.

3. Test problems.

It is very essential to choose adequate test problems for analysis of algorithms. The analysis given in [1] was quite poor because such profiles as "step" and "triangle" are not similar to ionization wave forms.

For the analysis of convective term approximation, ignoring diffusion, the equation (1) is considered in dimensionless form, so that $v \sim 1$, $n \sim 1$ and characteristic length size is of order of 1. A lot of finite difference schemes (more than 10) defined by a choice of flux-limiter FL in comparison with FCT (Phoenical LPE

SHASTA) were tested. Many of flux-limiters being used can be found in [3].

In the first class of problems ($v=1$, $I=0$) the solution $n(x,t)=n_0(x-t)$ describes a movement of a given profile of number density $n_0(\xi)$. For the testing of the methods the exponential profiles "cosh": $n_0(\xi)=\cosh^{-2}[4(\xi-x_0)]$ and "gaussian": $n_0(\xi)=\exp[-8(\xi-x_0)^2]$ and traditional ones: "triangle" and "step" [1] are considered. The results of calculation have shown that FCT method, giving good results for the profiles "step" and "triangle", leads to "stepping" on a left-hand side of exponential profiles. It is most critical for positive streamer simulation. The schemes with the flux-limiters of van Leer [2,5] have given the best results between considered. The typical result for "cosh" profile (mesh size $\delta x=0.025$, time step $\delta t=0.005$, total time $T=10$) is presented in Fig.1.

In the second class of problems ($v=v_0+\alpha x$, $I=0$ or $I=\beta n$) the movement in a non-uniform velocity field with external sources was considered. Both van Leer's and FCT methods have given good results in this case.

The third class of problems with analytic solutions of the type: $[v(\xi)-u_0] \cdot n(\xi)=const$, $\xi=x-u_0 t$, describes a wave which phase velocity u_0 exceeds drift value v . The results of calculations for $n(\xi)=0.5+0.5/\cosh^2(4\xi)$, $v(\xi)=3-2\cosh^2(4\xi)/[1+\cosh^2(4\xi)]$, $u_0=3$, $T=5$, shown in Fig.2, testify to a large phase error of the method FCT, followed by macroscopic oscillations. The absolute error of the FCT exceeds even an error of the Lax-Wendroff method and coincides by an order to an error of the Courant-Isaacson-Rees scheme. At the same time the van Leer methods [2,5] have given excellent results as in this case as at greater magnitude of a phase velocity, so the inequality $u_0 \cdot \delta t / \delta x > 1$ takes place.

4. Conclusions.

The two-step algorithm of the solution of the continuity equation based on van Leer type finite-volume schemes, suitable for positive streamer simulation, is proposed here. Being economic on time of calculation, given method allows to overcome numerical errors of FCT method such, as "stepping" of exponential profiles of ionization waves.

The simulation of positive streamers in air [5] demonstrates great effectiveness of the algorithm.

The work has been carried out according to the project "Fundamental theory of electrical discharges in energetics" of Russian Joint Stock Company "EES ROSSII".

5. References.

- [1] R. Morrow: J. Comp. Phys., 43 (1981) 1
[2] B. van Leer: J. Comp. Phys., 14 (1974) 361

- [3] C.D. Munz: J. Comp. Phys., 77 (1988) 18
[4] A.F. Djakov et al. Simulation of positive streamers in air. II. (Contribution paper at this conference)
[5] B. van Leer: J. Comp. Phys., 23 (1977) 263

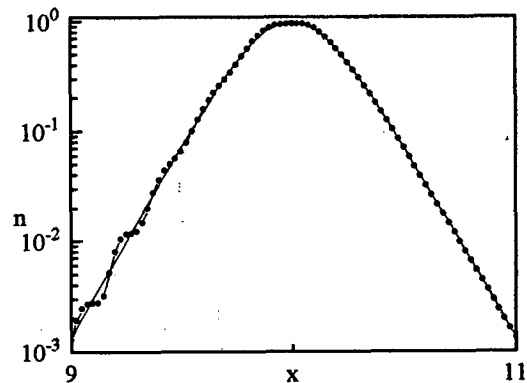


Fig.1. Results of calculation for "cosh" profile:

— exact solution, —•— FCT.

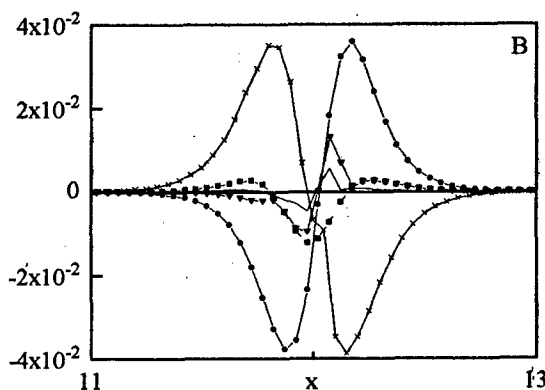
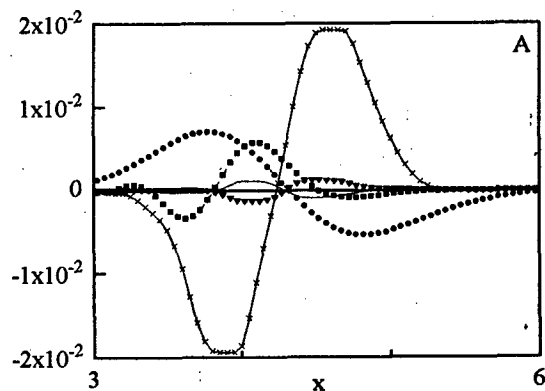


Fig.2, A-B. Absolute error of wave calculation by various methods.

— [2], — [4], —•— Lax-Wendroff, —x— FCT,
—+— Courant-Isaacson-Rees

Simulation of positive streamers in air.

II. Positive streamer propagation in a non-uniform field

A.F. Djakov, Yu.K. Bobrov*, Yu.V. Scherbakov*, Yu.V. Yurghelenas*

Russian Joint-Stock Company of Energy and Electrification "EES ROSSII", 7 Kitaigorodsky proezd, Moscow, 103074, RUSSIA

*High Voltage Research Center of All-Russia Electrotechnical Institute, Istra-2, Moscow Region, 143500, RUSSIA

1. Streamer dynamics model.

Positive streamer dynamics in air at atmospheric pressure and temperature = 300 K in a non-uniform external electric field which average value is much less than threshold value E_t is investigated here.

The dynamics of streamer is described by the system of continuity equations and Poisson equation:

$$\begin{aligned} \partial n_e / \partial t + \nabla \cdot (\bar{v}_e n_e) - \nabla \cdot (D_e \nabla n_e) &= q_e + I_{ph} \\ \partial n_+ / \partial t + \nabla \cdot (\bar{v}_+ n_+) &= q_+ + I_{ph} \\ \partial n_- / \partial t + \nabla \cdot (\bar{v}_- n_-) &= q_- \end{aligned} \quad (1)$$

$$\partial n_k^* / \partial t = q_k^+$$

$$-\nabla \cdot (\nabla \varphi) = \rho / \epsilon_0$$

Here n_+ , n_- , n_e , n_k^* - positive, negative ions, electrons and metastable molecules number densities respectively, \bar{v} - drift velocities, D_e - diffusion coefficient, $\rho = e(n_+ - n_- - n_e)$ - electric charge density, φ - electric potential. The source terms q include the ionization by electron impact, attachment, recombination and excitation of metastable states of molecules, $q_+ = q_- + q_e$. Quantities q , \bar{v} , D depend on the electric field strength $|\bar{E}|$, $\bar{E} = -\nabla \varphi$. The term I_{ph} describes photoionization of gas molecules.

Dependencies of the coefficients in (1) and source terms q on the reduced electric field magnitude have been obtained by the solution of Boltzmann equation. As for the rates of reactions between heavy particles the approximations [2] used to apply. Photoionization by radiation of excited nitrogen molecules is accepted according to [3].

In the quasi-two-dimensional approach the fixed radius of streamer R_c is supposed to be in a range $R_c = 0.03 + 0.10$ cm. Space charge is assumed to be uniformly distributed in radial direction, and electric field on axis is defined by disk method accounting image charges on electrodes [1].

Calculation of I_{ph} on the axis of discharge have been performed accounting of supposed cylindrical configuration. For the optimization the exponential approximation of kernels of integrals and factorization method have been used. Numerical solution of the

continuity equations was performed by the algorithm [4]. Increment of electric charge density $\rho = e(n_+ - n_- - n_e)$ was obtained in every time step according to the formula:

$$\delta \rho = e[(\delta n_+)^{\text{conv}} - (\delta n_-)^{\text{conv}} - (\delta n_e)^{\text{conv}}],$$

where $(\delta n)^{\text{conv}}$ is the increment of particles number density due to convection and diffusion [4]. This critically improves the accuracy of calculations because of $\rho \ll en_+$, en_- , $(\delta n)^{\text{conv}} \ll (\delta n)^{\text{ion}}$, and the separate solution of the equation for $\rho(x, t)$ proposed in [2] is not required.

2. Initial electrons.

In case of plane anode a quasi-neutral layer of electrons and positive ions with exponential profile near the anode is supposed for the streamer initiation. In case of spherical anode the electron detachment from ozone negative ions for seed electron generation [5] is assumed. Stationary number density of ions O_3^- of order of 10^3 cm^{-3} is supposed. The electron detachment rate is obtained by the formulae [5]:

$$v = k v_{el} \exp(-\epsilon/W), \quad W = 0.5 M (\mu_- E)^2,$$

where ϵ - bond electron energy in negative ion, W - random ion energy, μ_- - ions mobility, v_{el} - elastic collision frequency, M - mass of ion, $k \approx 0.1 + 0.01$.

3. Streamer dynamics in small external field.

For the analysis of streamer properties under propagation in external electric field with a strength much smaller than E_t , the parallel plane electrodes configuration is considered. For $0 < x < 2$ cm streamer formation in uniform external field $E_0 = 40 \text{ kV/cm}$ takes place. After that the streamer propagates in the electric field $E_1 < E_t$.

During the avalanche-streamer transition stage polarization of charge leads to formation of the ionization front where electric field, electric current and Joule electric power are strictly localized (Fig.1). Electron number density and electric field strength reach the values of order of $n \sim 10^{14} + 10^{15} \text{ cm}^{-3}$, $E \sim 100 + 200 \text{ kV/cm}$ correspondingly, so that the electric field of space charge is much greater than external electric field (Fig.2). While streamer moving in the field E_1 charge depolarization time is much greater than the time of propagation on the distance equal to the width

of the front. This causes the streamer can propagate even in an absence of external electric field. The values of charged particles number densities and electric field strength depend on R_c , but there is almost no dependency of streamer velocity on R_c in the supposed range (Fig.2).

For the analysis of streamer formation and propagation in a strongly non-uniform external electric field a sphere-plane gap (sphere radius - 0.5 cm, gap length - 5 cm) is considered. Simulations have been performed for the voltage range $U=30+50$ kV.

After entering the region of almost zero-value external field streamer is essentially decelerated (Fig.3). But for the stopping of streamer a definite time is needed and at sufficiently great potential value of $U \sim 50$ kV streamer can reach cathode. During the movement on the initial distance ~ 2 cm streamer has got almost constant velocity. This is found to be in agreement with the experimental results for streamer propagation in short air gaps [6].

4. Conclusions.

Numerical modeling of streamers have been performed here enables to study the main mechanisms of discharge formation and propagation and to obtain reliable characteristics of electric discharges.

The account of electron detachment from O_3^- ions as a possible mechanism of seed electron generation lets to avoid the influence of initial electron concentration arbitrary choice on streamer formation. The method [4] allows to perform stable calculation of the solutions of continuity equations for the exponential profiles of ionization waves fronts. The method of the calculation of the photoionization term is appeared to be optimal for calculation time and amount of computer memory.

The results of the numeric simulation are in a good qualitative agreement with the results of the experiments. Right after the period of streamer formation electric field, electric current and Joule electric power are strictly localized in a short region of the wave front which causes a streamer propagation. While propagating in a relative small electric field either stopping of the streamer or formation of stable propagation regime takes place. The streamer velocities as qualitative dependencies of streamer parameters are in a weak dependency on the supposed values of streamer radius R_c .

The work has been carried out according to the project "Fundamental theory of electrical discharges in energetic" of Russian Joint Stock Company "EES Rossii".

5. References.

[1] A.J. Davies, C.J. Evans: Proc.IEE.-114 (1967) 1547

[2] I.A. Kossyi et al.: Plasma Sources Sci. Technol.- 1 (1992) 207

[3] M.B. Zheleznyak M.B., A.Ch. Mnatsakanyan, S.V. Sizykh: Teplofiz. Vys. Temp.- 20 (1982) 423 (in Russian)

[4] A.F. Djakov et al. Simulation of positive streamers in air. I. (Contribution paper at this conference)

[5] Yu.K. Bobrov, Yu.V. Scherbakov: Proc. Sci.-Tech. Conf. "Design of electrotechnical equipment of complexes of high-voltage, converter, high-current and semi-conductor technics".- 14-18 Apr. 1994.- Moscow.- 1994.- P.30-35 (In Russian)

[6] F. Grange et al.: J. Phys. D.- 28 (1995) 1619

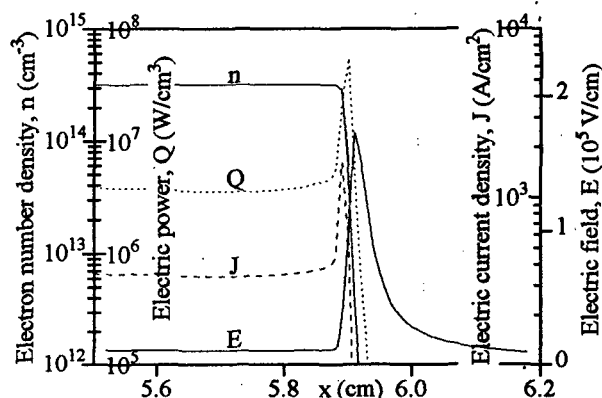


Fig.1. Spatial dependencies of streamer parameters, $E_1 = 8$ kV/cm, $R_c = 0.03$ cm.

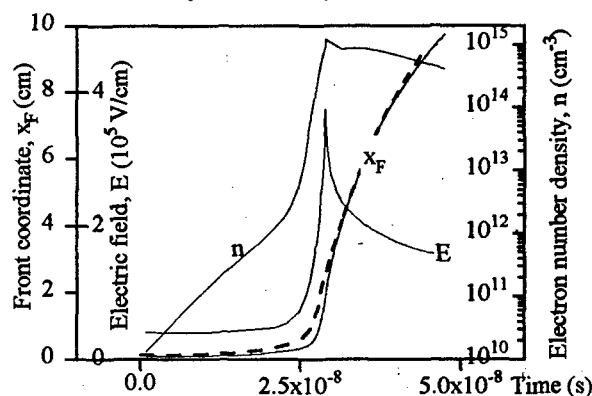


Fig. 2. Streamer propagation in a small field. $E_1 = 8$ kV/cm, $R_c = 0.03$ cm. Dash line: $R_c = 0.1$ cm.

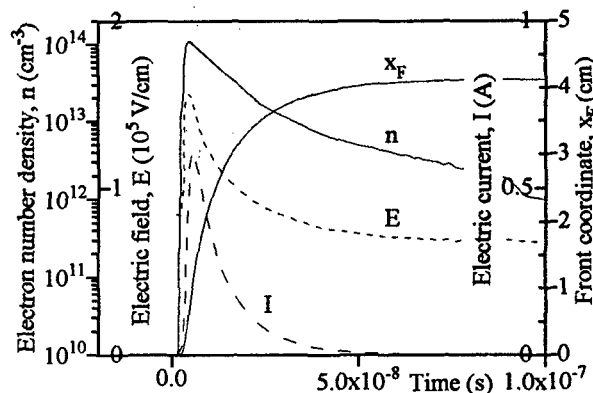


Fig.3. Streamer propagation in sphere-plane gap. $U = 40$ kV, $R_c = 0.05$ cm

SPUTTERED PARTICLES TRANSPORT STUDY IN A RF MAGNETRON DISCHARGE.

F. Clénet, Ph. Briaud, G. Lempérière, G. Turban.

Laboratoire des Plasmas et des Couches Minces.

Institut des Matériaux de Nantes. UMR 110 - CNRS

2, rue de la Houssinière. 44 072 Nantes cedex 03 - France.

Introduction.

Sputter deposited $Ti_{1-x}W_x$ thin films are widely used in microelectronic device fabrication as diffusion barrier between Al contact layers and Si (or silicide) underlayers. The efficiency of W based diffusion barriers has been shown to be a strong function of alloy composition through changes in film properties. Differences in sputtering emission, scattering behavior and redistribution process on substrate of the constituent atoms are the major factors which alter the composition of the sputter deposited film from an alloy target in argon sputtering gas [1].

In this paper we present a combined experimental and modelling study of the Ti and W atoms densities ratio in the plasma and in the film deposited onto a substrate in a R.F magnetron discharge.

Transport model.

The transport model is based on the PIC-MC method [2]. The simulation particle represents about $10^7 - 10^9$ real neutral atoms. An artificial grid in a cylindrical coordinate is introduced. To obtain atoms density the simulation particles is weighted onto the grids points. The motion of particles is followed as they travel through the scattering gas. The Monte Carlo method is used to model collisions between sputtered atoms and gas atoms.

Particles are assumed to be emitted from the target at random positions in the erosion profile ('race track') of the sputtered target with the Thompson energy distribution [3]. This energy is characterised by the sputtering voltage, the binding energy of the Ti and W atoms in the bulk. The emission direction is defined by two independent angles φ and θ . The azimuthal one (φ) is calculated using an isotropic distribution and the direction of ejected atoms trajectory from a normal to the cathode is determined from the angular distribution $f(\theta)$.

Due to the relatively weak densities of sputtered atoms in the discharge we consider only elastic collisions between these particles and the sputtering gas atoms. The distance λ between two collisions is assumed to follow a Poisson distribution and can be calculated using the relation $\lambda = -\lambda_m \ln(u)$ where λ_m is the sputtered atom mean free path and u is an uniform random number between 0 and 1. The elastic interaction is characterized by the relative velocity of the incident particle, the impact parameter and the Born-Mayer interaction potentiel [4]. After a collision the energy and the

scattering angle of the sputtered atom are calculated from the classical mechanical laws.

The relative theoretical thickness of the deposited WTi layer is determined by counting impinging superparticles along the coordinate z normal to the target. Sticking coefficient of the particle is taken equal to unity.

Optical model.

By analyzing the optical emission spectrum of the discharge plasma, tungsten to titanium densities ratio can be determined by the method described as follows [5]. Assuming a direct process for electronic excitation, an uniform plasma emission and no reabsorption effect, the signal intensity detected at the frequency ν_{ij} , is given by:

$$I_{ij} = [X^*_i] \cdot R_{ij} \cdot h\nu_{ij} \cdot A_{ij} \cdot d\Omega. \quad (1)$$

R_{ij} is the spectral response of the apparatus, A_{ij} is the transition probability of the transition $i \rightarrow j$, $d\Omega$ is the solid angle that is assumed to remain constant. If we consider that the formation of excited state X^*_i is direct through electron impact and the decay is purely radiative, the density $[X^*_i]$ can be write :

$$[X^*_i] = [X_i] \cdot n_e \cdot \tau_k \cdot K^{e_{exc}} \quad (2)$$

where X_i is the density of atoms in the fundamental state, τ_k the radiation lifetime, n_e the electron density, and $K^{e_{exc}}$ the electronic excitation rate. $K^{e_{exc}}$ is given by the integration of the theoretical cross section $\sigma^{e_{exc}}(E)$ and the energy distribution $f(E)$, which is assumed to be Maxwellian, from a threshold E_s up to infinity. Considering the Ti ($i \rightarrow j$) and W ($l \rightarrow k$) transitions, the set of equations (1) and (2) allows us to calculate the tungsten to titanium densities ratio $[W]/[Ti]$ for different pressures of the argon gas discharge.

To perform spectroscopy measurements, we used an HR320 Jobin-Yvon monochromator having a focal length of 0.32 m. The detector was situated outside a quartz window in such a way that we detect the maximum of light emission. The Ti (365.3 nm), Ti (399.8 nm), W (407.34 nm) and W (400.8 nm) lines were selected due to their strong intensities.

Results and discussion.

The R.F magnetron sputtering is performed from an alloy target of composition $W_{70}Ti_{30}$ (atomic per cent) in argon gas. The magnetron is a circular, planar device,

with 5 cm cathode diameter placed 5 cm away from the substrate [6]. Discharge R.F power is 150W and pressure is in the range 0.67 to 2 Pa.

In our computer simulation code of the sputtered atoms transport in gas, the angular distribution of sputtered particles $f(\theta)$ obey to a subcosinus law, so the θ angle is generated from [7]:

$$\theta = \arccos \left[\sqrt{\frac{\alpha^{2(u-1)} - 1}{\alpha^2 - 1}} \right]$$

α is a parameter which depends on the target material and is adjusted to obtain a good fit between simulation and experimental results. Figure 1 shows the variation of the atomic densities ratio (W/Ti) versus distance from the target as obtained by experiment with an argon pressure of 2.0 Pa and by simulation with $\alpha_{Ti} = 2.8$ and $\alpha_W = 1.2$. The composition of the deposited film on a Si substrate at different positions on the lateral walls from the target is measured by Energy Dispersive X-ray Spectroscopy (EDXS).

Figure 2 shows the variation of Ti and W densities in the discharge, resulting from simulation versus the distance from the cathode, for two pressures, 0.67 and 2.0 Pa. As the argon pressure increases a broad maximum in the density profiles is observed which is more pronounced for case of Ti. This result is explained by the thermalization of the sputtered atoms as a function of pressure. Collisions with argon neutrals affect primarily the lighter sputtered atoms so, for low pressure values Ti concentration increases faster than W and closer to the cathode with increasing argon pressure. Their mean energy is reduced by collisions with argon neutrals, which is confirmed by the model. As a consequence sputtered species accumulate into the discharge. Variations of the W/Ti ratio in the discharge as a function of pressure is also observed by emission spectroscopy. Figure 3 shows the changes of the tungsten to titanium densities ratio, when the pressure varies, obtained from the optical model described above. At low pressure, 0.67 Pa, this ratio is close to the target composition (2.3) and diminishes when the pressure increases up to 2.0 Pa. A similar result is obtained using the transport model, but in this case the ratio decreases faster and is equal to 0.6 at 2.0 Pa. In figure 4 we present the radial thickness of a film deposited on an anode substrate placed at 5 cm from the cathode. A good agreement between the experimental thickness measurements and the corresponding transport model result is observed.

Conclusion.

A PIC-MC model has been used to simulate the transport and the thermalization of sputtered atoms from a TiW target. Relative Ti and W densities obtained by particles simulation fit well with those obtained from spectroscopic measurements.

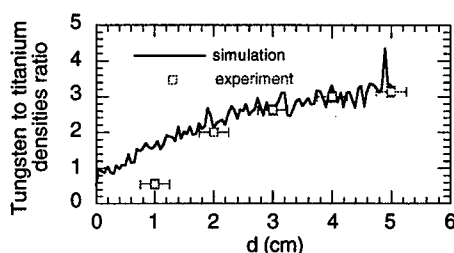


Figure 1: Variation of the tungsten to titanium densities ratio versus the distance from the cathode for an argon pressure of 2.0 Pa.

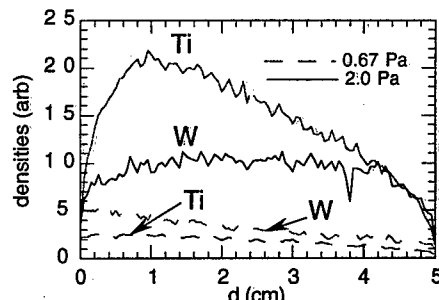


Figure 2: Variation of the sputtered atoms densities versus the distance from the cathode for argon pressures 0.67 Pa and 2.0 Pa.

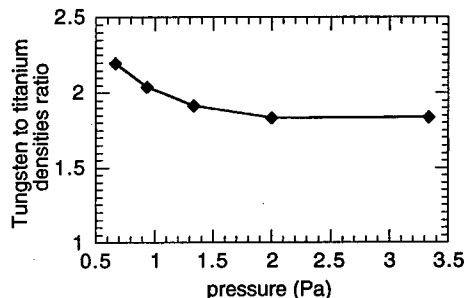


Figure 3: Variation of the tungsten to titanium densities ratio against the pressure.

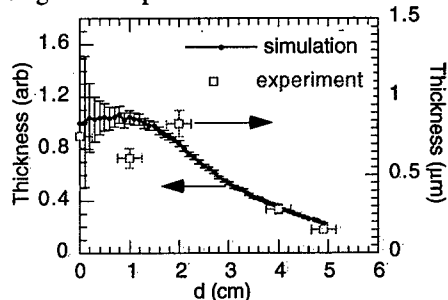


Figure 4: Relative thickness profile from transport model in arbitrary units and thickness profile from SEM measurements.

References.

- [1] T. Motohiro, J. Vac. Technol. A 4 (2), (1996).
- [2] C. K. Birsdall, A. B. Langon, New York: MacGraw-Hill, 1985.
- [3] M. W. Thompson, Philos. Mag. 18 (1968), 377.
- [4] A. A. Abrahamson, Phys. Rev. 178 (1969), 76-79.
- [5] J. F. Guimaraes, J. B. Almeida, J. Bretagne, Plasma Sources Sci. Technol. 2 (1993), 138-144.
- [6] H. Ramarotafika, G. Lemperiere, Thin Solid Films. 266 (1995), 267-273.
- [7] H. Oechsner, Appl. Phys. 8 (1975), 185-198.

NUMERICAL MODELLING OF THE IGNITION TRANSIENT IN INDUCTIVELY COUPLED PLASMA TORCHES

F. Taddei^{}, V. Colombo^{*}, G.G.M. Coppa^{**}, C. Panciatichi^{***}*

^{*} Università degli Studi di Bologna, Dipartimento di Matematica, C.I.R.A.M., Via Saragozza 8, 40123 Bologna - Italy
e-mail: colombo@boltzmann.ing.unibo.it

^{**} Politecnico di Torino, Dipartimento di Energetica, Corso Duca degli Abruzzi 24, 10129 Torino - Italy
e-mail: ggmcpa@polito.it

^{***} C.S.E.L.T. Centro Studi E Laboratori Telecomunicazioni, Via G. Reiss Romoli 274, 10148 Torino - Italy
e-mail: cpnciat@lemon.cselt.stet.it

1. INTRODUCTION

The aim of the work is to obtain a quantitative description of the physical behaviour of an inductively coupled plasma torch during the ignition transient, in order to optimize the procedures required to obtain a stable discharge. The study, originally devoted to understand the physical behaviour of an already existing system (a torch working at atmospheric pressure, connected to a 13.56 MHz, 5.4 kW RF generator [1], realized in the framework of a new technological process for the production of optical fibres), has been extended to other types of torch, including ICPTs for waste treatment applications [2]. In the Authors' opinion, simulating the procedures that induce plasma initiation is a useful tool in many applications: for example, in systems in which a sharp pointed graphite rod is positioned inside the torch in the coil region and, once heated by induction currents, slowly pulled out and then completely extracted when the discharge is established. A time-dependent study, instead of a static analysis, usually performed in this kind of problems, has the advantage to allow one to select different starting conditions that will finally lead to stable plasma discharges. The time-dependent fluid-magnetic study has been performed within the frame of the SIMPLER algorithm [3]: this involves the simultaneous solution of the continuity, flow and energy equations for the gas together with equations for the electric and magnetic fields, under the assumptions of axially symmetric, optically thin plasma in LTE, with laminar flow for both the plasma and the confinement gas. The results obtained for various flow rates using pure Argon as cooling and plasma gases and different power operating conditions give a description of the velocity and temperature fields during the initiation and in the final self-sustained plasma; comparisons can be done with temperature radial profiles obtained with AES temperature diagnostics for an already existing system [4]; this could finally allow one to select a rigorous set of starting procedures that lead to the desired conditions of plasma discharge.

2. NUMERICAL SIMULATION

The numerical simulation of ignition transients leading to a stable configuration has been performed under the following assumptions [5]:

- two-dimensional (r, z) dependence for temperature, velocity and electromagnetic fields;
- laminar flow for carrier and confinement gas;

- local thermodynamic equilibrium for the axially symmetric and optically thin plasma;
- negligible effect of viscous dissipation and pressure work in energy equation;
- the electric current density is simply given by σE , neglecting the effect of the magnetic field.

The continuity equation,

$$\frac{\partial \rho}{\partial t} + \text{div}(\rho u) = 0 \quad (1)$$

the radial and axial momentum equations

$$\frac{\partial(\rho u_r)}{\partial t} + \text{div}(\rho u u_r) = -\frac{\partial p}{\partial r} + \text{div}\left(\mu \nabla u_r + \mu \frac{\partial u}{\partial r}\right) + G_r \quad (2)$$

$$\frac{\partial(\rho u_z)}{\partial t} + \text{div}(\rho u u_z) = -\frac{\partial p}{\partial z} + \text{div}\left(\mu \nabla u_z + \mu \frac{\partial u}{\partial z}\right) + G_z \quad (3)$$

(where G_r and G_z represent the time-averaged radial and axial force densities due to the interaction with the electromagnetic field) and the enthalpy equation

$$\frac{\partial(\rho h)}{\partial t} + \text{div}(\rho u h) = \text{div}\left(\frac{k}{C_p} \nabla h\right) + Q_J - Q_R \quad (5)$$

(where Q_J and Q_R are the ohmic heating and radiation loss terms, respectively) are solved by using a fully implicit time discretization method together with the finite volume method for space discretization. In order to obtain a good electromagnetic description of the system during the initiation of the plasma, a 2-D treatment has been carried out, by discretizing the equation for the amplitude E_ϕ of the azimuthal component of the electric field

$$\frac{1}{r} \frac{\partial}{\partial r} \left(r \frac{\partial E_\phi}{\partial r} \right) - \frac{E_\phi}{r^2} + \frac{\partial^2 E_\phi}{\partial z^2} - i \omega \mu_0 (\sigma E_\phi + J) = 0 \quad (4)$$

on a domain far bigger than the torch region and using boundary conditions that regard the torch as a magnetic dipole [1]. The electric field obtained from Eq. (4) is then used to evaluate the magnetic field. The presence of the graphite is simulated by imposing a very high conductivity in the region occupied by the rod.

3. SELECTED RESULTS

In Figs. 1 and 2 some selected results are presented, showing temperature distributions in an Argon plasma with RF excitation at 13.56 MHz. Firstly, a starting condition is considered: the RF generator is switched on (the input power is set to 0.7 kW), with the graphite rod completely inserted, while the gas initially flows (8 liters/min) at a temperature of 20 °C; once a steady condition is reached, the code simulates a step extraction of the rod while the input power is also raised, till the system eventually reaches a new stable state. This procedure is repeated, up to complete extraction of the rod, with a final input power of 1.5 kW; Fig. 1 refers to the temperature distribution at the beginning of the ignition transient, when numerical convergence is reached with the graphite rod completely inserted in the coil region; Fig. 2 refers to the temperature in the final stable configuration when the rod is extracted.

ACKNOWLEDGMENTS

Work performed within the Strategic Project of Italian C.N.R. on Industrial Applications of Plasmas; partial financial support by A.S.P. Scientific Association, Torino, Italy (Plasma Torch/Plasma Processing Project) is acknowledged.

REFERENCES

1. G. Cocito, L. Cognolato, V. Colombo, G. Dellapiana, C. Panciatici, *Modeling, Project and Numerical Simulation of an Inductively Coupled Plasma Torch for the Deposition of SiO₂*, 48th Annual Gaseous Electronics Conference, Berkeley, U.S.A., 1995.
2. E. Pfender, *Thermal Plasma Processing in the Nineties*, Pure & Applied Chemistry, **60**, 591, 1988.
3. S.V. Patankar, *Numerical Heat Transfer and Fluid Flow*, McGraw-Hill, New York, 1980.
4. G. Cocito, L. Cognolato, V. Colombo, C. Panciatici, A. Zazo, *AES Temperature Diagnostics in an Inductively Coupled Plasma Torch for the Deposition of High Purity Fused Silica for Optical Waveguides*, 49th Annual Gaseous Electronics Conference, Argonne, U.S.A., 1996.
5. Xi Chen, E. Pfender, *Modeling of RF Plasma Torch with a Metallic Tube Inserted for Reactant Injection*, Plasma Chemistry and Plasma Processing, **11**, 103, 1991.

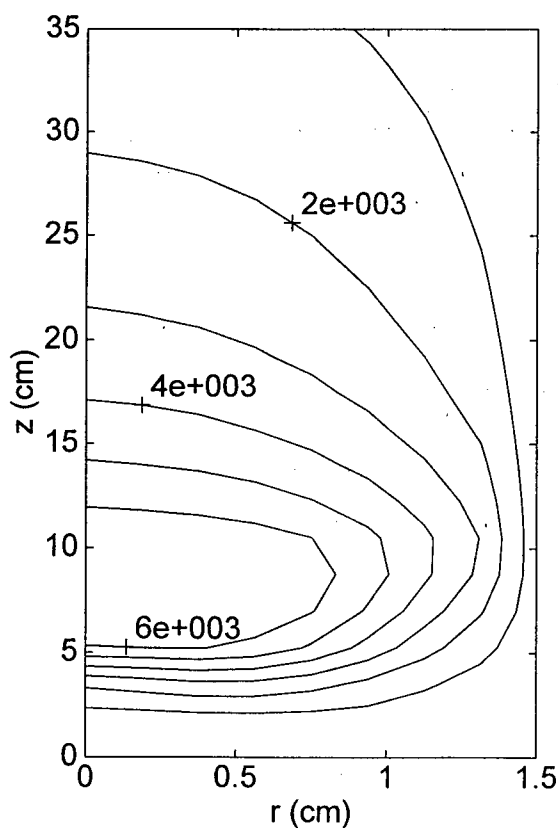


Fig. 1 - Temperature distribution (in K) inside the torch with the graphite rod completely inserted.

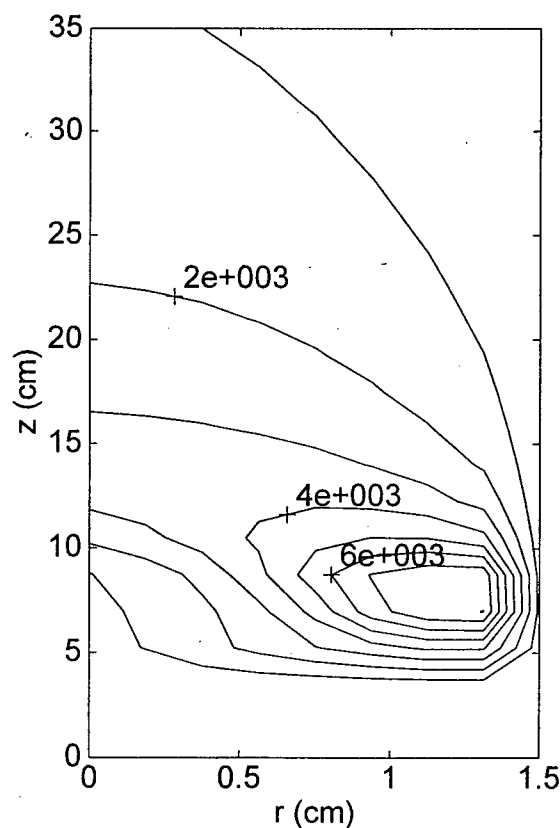


Fig. 2 - Temperature distribution inside the torch when the graphite rod is extracted.

Recent High-Resolution Studies of Pseudospark Discharge

A. Al-Hussany and A.J. Davies

Department of Physics, University of Wales Swansea, Singleton Park, Swansea SA2 8PP, U.K.

1. Introduction

Boeuf and Pitchford [1] have developed a hybrid fluid-particle model for describing the initiation phase of pseudospark discharges. In this model the time-dependent fluid equations for the electrons and positive ions are solved self-consistently with Poisson's equation for a two-dimensional axially symmetric geometry. A three-dimensional Monte-Carlo simulation was used to obtain the ionization source term in the fluid equations.

The continuity equations were solved by the exponential scheme of Scharfetter and Gummel. This scheme is described in a companion paper [2] where it is shown that it is essentially of first order accuracy in space when the principal transport process is drift rather than diffusion. In [2] the extension of the exponential algorithm to give second order spatial accuracy is described which results in considerable reduction in the degree of numerical diffusion so that the scheme is able to resolve discontinuities and sharp gradients without introducing spurious oscillations or ripples.

The present paper describes typical simulations of the initial stages of pseudospark development where the hybrid scheme of Boeuf and Pitchford has been updated to employ the second-order exponential scheme as an alternative to the original algorithm. The geometry chosen for the present simulations consisted of a hollow cathode and plane anode as in Fig. 1.

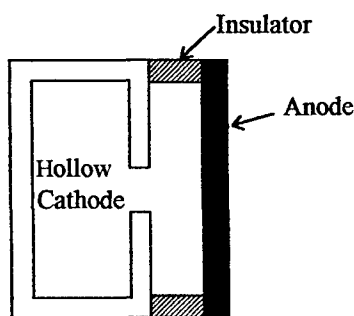


Fig. 1. Typical model pseudospark diode geometry. Internal radius 1.54 cm, cathode hole radius 0.33 cm, cathode-anode distance 0.57 cm, aperture thickness 0.2 cm, depth of hollow cathode 0.77 cm.

2. Results

The aim of the present simulations was to investigate the effect of the second-order algorithm on the simulation of the initial stages of pseudospark development. The gas filling was taken to be nitrogen at 0.67 Torr pressure with an applied voltage of 2 kV. The secondary electron mechanism was assumed to be

ionic with secondary emission coefficient $\gamma_i = 0.07$ and the ionization source term was obtained as in [1]. The electron and positive ion drift velocities were assumed to be functions of the local value of the parameter E/p and to be given by the relations [3]

$$w_e = 2.9 \times 10^5 E/p$$

and

$$w_p = \begin{cases} 2 \times 10^3 \left(1 - 4 \times 10^{-3} \frac{E}{p} \right) \frac{E}{p}, & \frac{E}{p} \leq 80 \text{ V/cmTorr} \\ 1.25 \times 10^4 \left(\frac{E}{p} \right)^{\frac{1}{2}} - 2.5 \times 10^3 \left(\frac{E}{p} \right)^{-1} & \text{otherwise.} \end{cases}$$

Fig. 2 illustrates the evolution of the potential distribution using (a) the original exponential algorithm and (b) using the second-order exponential scheme. Both calculations are very similar with the virtual anode moving into the hollow cathode and the development of a sheath over the whole surface of the cathode as has been previously reported by, for example, Boeuf and Pitchford [1]. The time scale of the development of the virtual anode is much quicker for the second-order calculation with comparable potential distributions being reached in about half the time of the original exponential scheme. This is due to the effect of numerical diffusion in the first-order scheme which tends to smooth the charged particle distributions and reduce the effect of space-charge.

Fig. 3 shows the electron multiplication factor as a function of time for the two schemes as the discharge plasma enters the hollow cathode. We see that the electron multiplication is much higher in the second-order scheme.

In a range of low-voltage simulations, where diffusion is considerable, it was found that the general features of the discharge development were very similar for both algorithms except for the time-scale of the growth which was considerably faster for the high resolution scheme.

Tests of the second order algorithm have been carried out at higher applied voltages and for conditions where the photonic secondary process is present in addition to the ionic secondary process, thus leading to much more rapid discharge growth. In all cases the method has worked extremely well although the stability criteria for the time step are more critical for the second-order scheme at high voltages, where drift predominates, and this may lead to excessively small steps being needed in the later stages of the development.

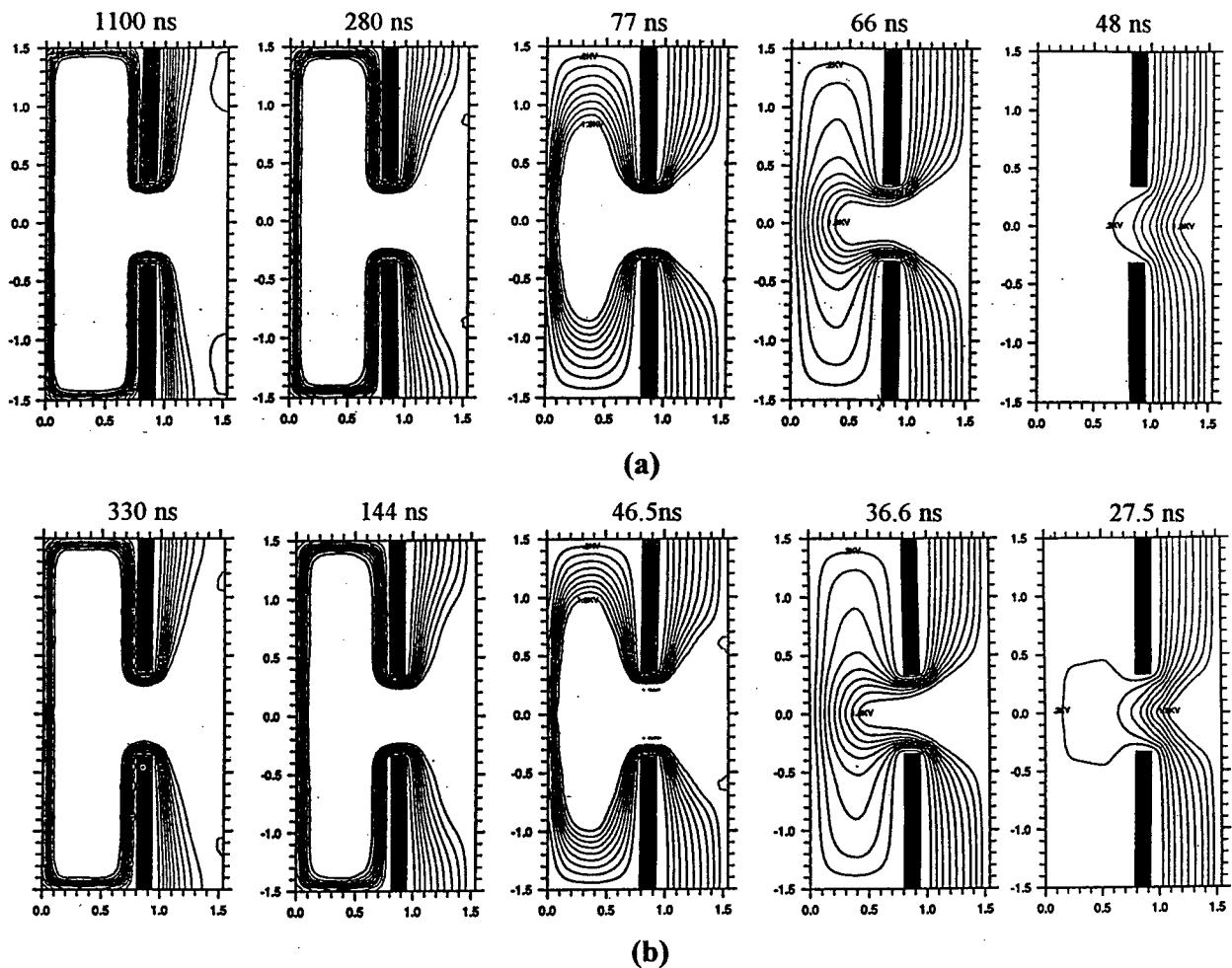


Fig. 2. Evolution of the equi-potential distribution of a pseudospark discharge in nitrogen for the geometry of Fig. 1 using (a) first-order and (b) second order exponential schemes in the hybrid method of Boeuf and Pitchford.

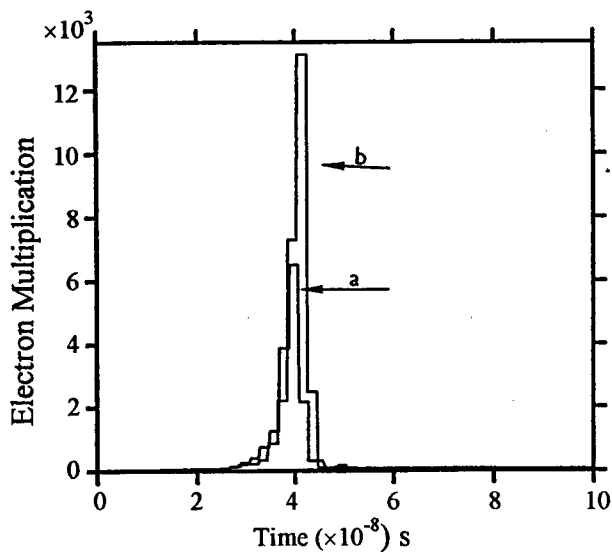


Fig. 2. Electron multiplication as a function of time calculated using the hybrid fluid-particle model based (a) on the first- and (b) on the second- order exponential schemes

3. Conclusions

The first- and second- order exponential schemes are powerful tools in simulating the early stages of pseudospark discharge development. The second order scheme offers improved accuracy and reduced numerical diffusion but may require smaller time-steps in order to satisfy the stability criteria.

4. References

- [1] J. Boeuf and L.C. Pitchford: IEEE Trans Plasma Sci, No 19, 2 (1991) 286.
- [2] A. Al-Hussany and A.J. Davies, "A Stable High Resolution Integration Scheme for Discharge Simulation", Proc. ICPIG XXIII (1997).
- [3] A.J. Davies: IEE Proc, 133 (1986) 217.

A Stable High Resolution Integration Scheme for Discharge Simulation

A. Al-Hussany and A.J. Davies

Department of Physics, University of Wales Swansea, Singleton Park, Swansea SA2 8PP, U.K.

1. Numerical Scheme

In the simulation of electrical discharge development the continuity equations expressing charge conservation for each particle species are solved subject to the appropriate boundary conditions, with the electric field distribution being determined by Poisson's equation.

One powerful and very stable method for solving the continuity and momentum transfer equations is the exponential scheme originally used by Scharfetter and Gummel [1] in describing the transport of electrons and holes in semiconductors. Boeuf et al [2] have shown how this scheme may be also used to solve the linked system of continuity plus Poisson equation. In outline, the exponential scheme may be summarised as follows.

In one dimension the current density of electrons is

$$J_e = e\mu_e n_e E - eD_e \frac{dn_e}{dx},$$

and, if E , J_e , μ_e , and D_e are taken to be constant between two successive mesh spaces, integration with respect to x within a cell yields

$$n_e(x) = n_e(0) \exp\left(\frac{\mu_e Ex}{D_e}\right) + \frac{J_e}{e\mu_e E} \left(1 - \exp\left(\frac{\mu_e Ex}{D_e}\right)\right).$$

The current density may thus be found from this integral form by rearranging the expression to give

$$J_e = -\frac{e\mu_e E}{1 - \exp\left(\frac{\mu_e Ex}{D_e}\right)} \left[n_e(0) \exp\left(\frac{\mu_e Ex}{D_e}\right) - n(x) \right].$$

Denoting values of parameters at the centre of a cell by the subscript i and at the right and left hand boundaries by $i+\frac{1}{2}$ and $i-\frac{1}{2}$ so that $\Delta x_i = x_{i+\frac{1}{2}} - x_{i-\frac{1}{2}}$, the electric field is given to second order accuracy by

$$E_{i+\frac{1}{2}} = \frac{\phi_{i+1} - \phi_i}{x_{i+1} - x_i}.$$

The flux at the $i+\frac{1}{2}$ cell interface, obtained from J_e , is

$$F_{i+\frac{1}{2}} = \frac{1}{\Delta x_i} \left[n_i D_i e^{Z_{i+\frac{1}{2}}} - n_{i+1} D_{i+1} \right] \frac{Z_{i+\frac{1}{2}}}{e^{Z_{i+\frac{1}{2}}} - 1},$$

where

$$Z_{i+\frac{1}{2}} = \frac{\mu_{i+\frac{1}{2}}(\phi_{i+1} - \phi_i)}{D_i}.$$

A similar expression can be obtained for $F_{i-\frac{1}{2}}$. For small changes of potential between two successive grid points this expression approaches the standard difference relation for the diffusion flux while, if the change in potential is large, it approaches the drift flux. The main deficiency in this scheme is the accuracy,

which is only of first order in space when drift dominates and can lead to considerable numerical diffusion. This may be seen by letting $Z_{i+\frac{1}{2}} \rightarrow \infty$ (i.e. negligible diffusion and particles moving in the positive x direction) in which case $F_{i+\frac{1}{2}} = n_i \mu_{i+\frac{1}{2}} E_{i+\frac{1}{2}}$ which is a simple first-order upwind scheme.

The spatial resolution may be increased, however, by representing the density as being piecewise linear within a cell leading to the expression

$$F_{i+\frac{1}{2}} = \frac{1}{\Delta x_i} \left[(n_i + \frac{1}{2} \Delta x_i S_i) D_i e^{Z_{i+\frac{1}{2}}} - (n_{i+1} + \frac{1}{2} \Delta x_i S_i) D_{i+1} \right] \frac{Z_{i+\frac{1}{2}}}{e^{Z_{i+\frac{1}{2}}} - 1}$$

(where S_i is the slope function) which makes the scheme of second order accuracy since, for $Z_{i+\frac{1}{2}} \rightarrow \infty$, we now have $F_{i+\frac{1}{2}} = (n_i + \frac{1}{2} \Delta x_i S_i) \mu_{i+\frac{1}{2}} E_{i+\frac{1}{2}}$. Choice of slope function has been discussed by Munz [3]

2. Tests of the Algorithm

Practical application of the second order exponential scheme has shown it be stable and of second order accuracy provided the slope function is suitable chosen.

A comparison between the first and second order exponential schemes is shown in Fig. 1 which traces the drift of a rectangular box shape of electrons in a two-dimensional z - r geometry having axial symmetry. The high degree of dissipation due to numerical diffusion is clearly seen in the original exponential scheme and care must be taken in any given application to ensure that the effects of numerical diffusion do not swamp that of the actual physical diffusion. Numerical diffusion is greatly reduced in the second order scheme.

A typical simulation using the enhanced exponential scheme is shown in Fig. 2. Here the evolution of electron density between parallel plate electrodes is traced following the release of a pulse of initiatory electrons from the surface of the cathode. Values of the primary ionization coefficient were taken from [4] and the secondary electron emission from the cathode was assumed to be photonic with a value of 3.5×10^{-4} . The movement of the primary avalanche and cathode streamer are clearly seen with no signs of instability.

3. Conclusions

The original exponential scheme of Scharfetter and Gummel is a powerful and stable method but can have a high degree of numerical diffusion. Increasing the spatial resolution to second order results in greater accuracy and considerably reduced numerical diffusion.

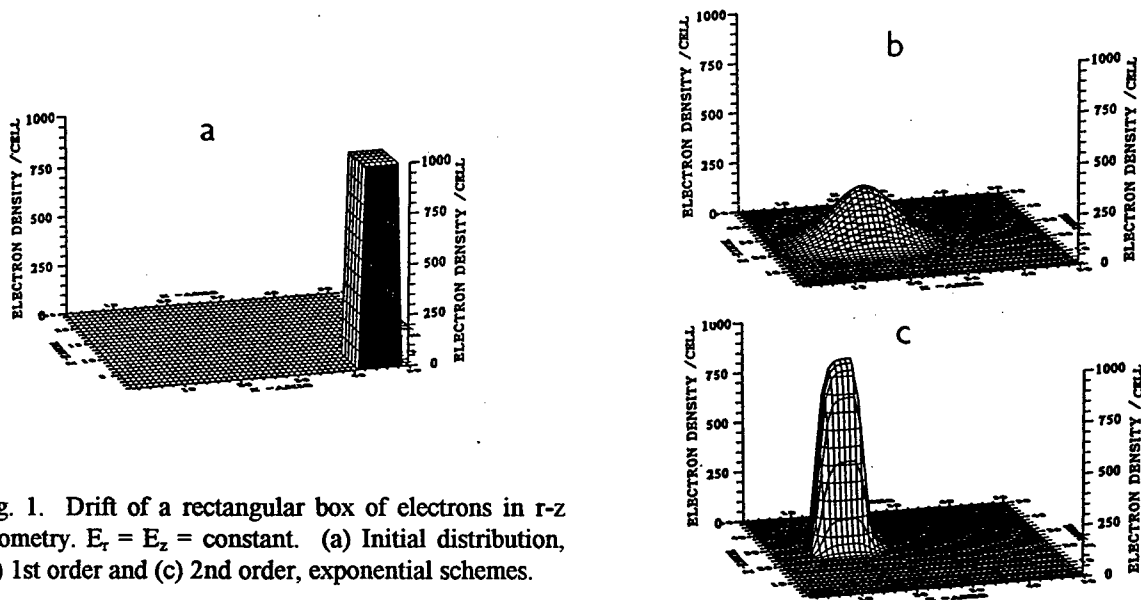


Fig. 1. Drift of a rectangular box of electrons in r - z geometry. $E_r = E_z = \text{constant}$. (a) Initial distribution, (b) 1st order and (c) 2nd order, exponential schemes.

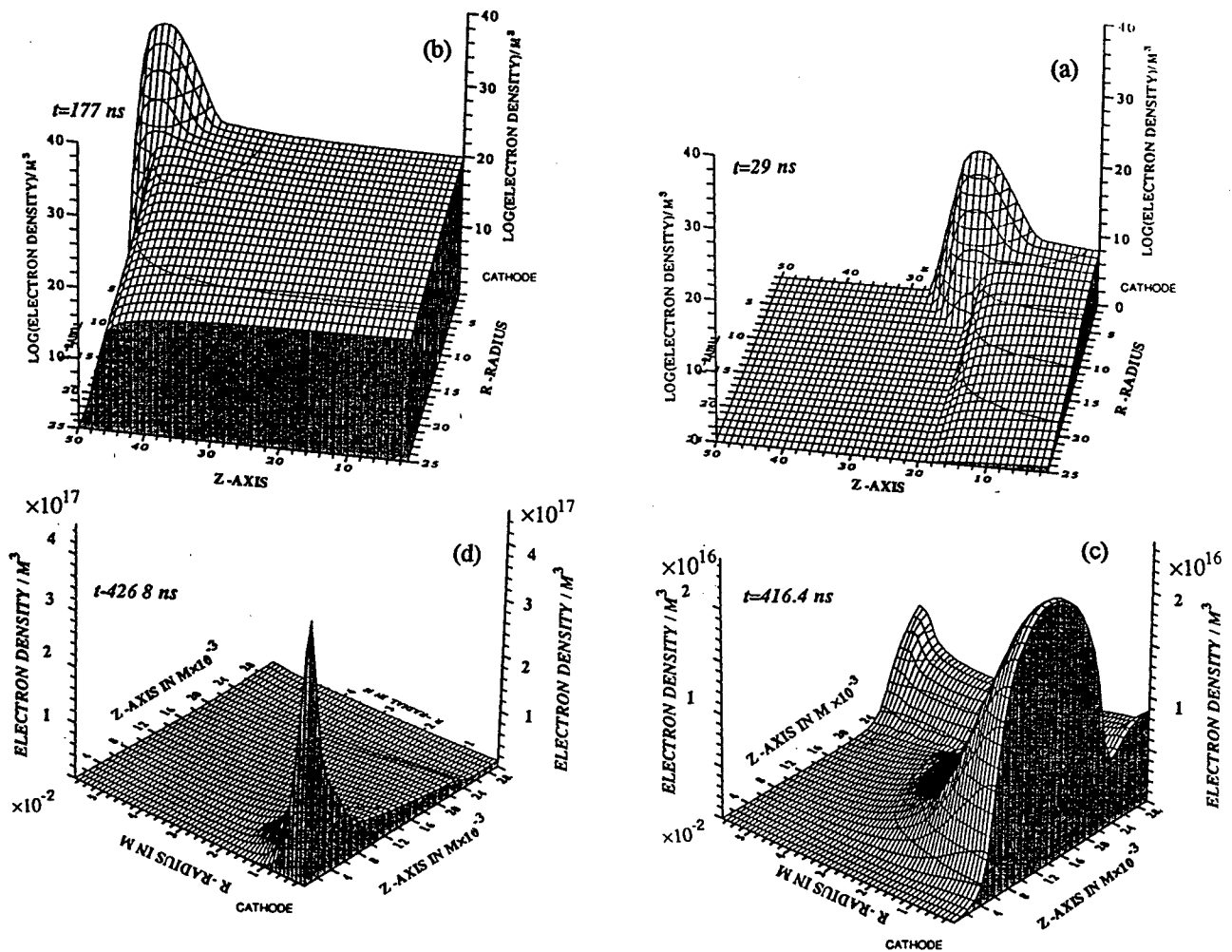


Fig. 2. Evolution of electron density between parallel plane electrodes of 6 cm radius and 3 cm separation in nitrogen at a pressure of 12000 Pa. The applied voltage is 16.7 kV. (a) and (b) on log scales; (c) and (d) on linear scales.

4. References

- [1] D.L. Scharfetter and H.K. Gummel: IEEE Trans on Electron Devices, **Ed-16** (1969) 64.
- [2] J. Boeuf and L.C. Pitchford: IEEE Trans Plasma Sci, No 19, 2 (1991) 286.
- [3] C.D. Munz: J Comp Phys, 77 (1988) 18.
- [4] A.J. Davies: IEE Proc, 133 (1986) 217.

Analysis of a H_2 short-gap spark channel with a hybrid model of neutral and charged particle dynamics

M. Jugroot, O. Eichwald, M. Yousfi, P. Bayle*

C.P.A.T, ESA n° 5002, 118 route de Narbonne, 31062 Toulouse, France

*CEMES-LOE, 29 rue J.Marvig, 31055 Toulouse, France

1. Introduction

The electric breakdown of hydrogen is examined by means of a two dimensional hybrid model applied to the case of a short (1.8mm) hydrogen gap at 500torr. Previous and numerous photographic studies of the static breakdown have identified several steps in the breakdown, namely, the formation of a glow-like discharge followed by the growth of a thin filamentary channel which bridges the electrodes and causes complete voltage collapse [1-2]. Our model of the complex physical processes occurring in the discharge couples both electrical (resulting from space charge effects) and neutral density heterogeneities in order to explain the different steps observed before the spark channel. We study a low overvolted ($\sim 1\%$ above sparking voltage $V_s=2750V$) discharge and describe major features of the different steps leading to the spark channel, with particular emphasis laid on the luminous appearance of the discharge.

2. Hybrid model

Our model is described by the fluid equations of electrons and ions coupled to the Poisson equation whereas neutral particle equations are described in [3]. However, source terms representing momentum and energy transfers, i.e. the action of the discharge on the neutral gas, are calculated precisely from the charged particles simulation. Thus, the Joule heating term, resulting from the global elastic and inelastic collisions between charged and neutral particles in the energy equation is equal to $J \cdot E$, where E is the total electric field encompassing space charge effects. To summarize, our hybrid model includes two strongly coupled submodels of charged and neutral particles. In fact, as all governing terms of the discharge obey to the reduced field (E/N), it implies that the hybrid modelling no longer treats the neutral gas to be passive and includes counter-reactions (i.e. heterogeneous electric field resulting from space charge effects are superimposed to neutral heterogeneities).

As photoelectron emission dominates in hydrogen, the cathode boundary condition in electron conservation encompasses the condition of balance between the electron flux near the surface and the photoelectron flux as described in [4]. The area of the cathode, ($\sim 3cm^2$ in our case) plays a leading role in the evolution of the discharge as it determines the lifetime of the pseudoglow. The luminosity due to radiative excited states $C_1\Pi_u$ and $B_1\Sigma_u^+$ is assumed to be proportional to $L=v_{ex}n_e$. The photofrequency v_{ex} like all discharge parameters (ionisation frequency,

mobility, etc.) involved in the calculations have been calculated from a Boltzmann multi-term equation [5].

3. Results

The initial conditions correspond to a number of electrons ($\sim 10^5$) created at the cathode. Under the action of the applied electric field, these primary electrons proceed rapidly to the anode where they are absorbed. However, electrons are produced simultaneously with the emission of the corresponding photon and hence electronic and ionic growth rapidly leads to a pseudoglow configuration consisting of three distinct parts : a cathode region (CR), a negative glow (NG) and a positive column (PC). This particular structure of the discharge is clearly expressed by its luminous appearance with a bright luminous region in front of the cathode surface, a narrow dark space and a uniform glow extending to the anode (fig.1). The high space charge at the cathode due to uncompensated ionic charge, generates an important electric field which maintains the intense luminous region during the entire pseudoglow stage. The radial structure of luminosity of the anodic zone (fig.2) ($\sim 0.1mm$ from the anode) shows a tendency towards constriction, measured by a decrease in the distance corresponding to $L_{max}/2$, (for instance reduction of $\sim 10\%$ from 65ns to 70.1ns) hence initiating the filamentary glow at the anode. The intensity of the end of the PC (fig.3) matches an interesting experimental feature [1-2] which revealed in the radial structure, a central peak in intensity, surrounded by a less intense luminous ring. The double nature of the PC, i.e. expansion and partial constriction is reflected by the multiple maxima in the radial direction (fig.3) ($\sim 1.6mm$ from the anode). In fact, the partial constriction is due the nature of radial electric field which reverses a few mms from the axis. Consequently, the sign of the radial field induces an inward electronic motion near the axis and an outward motion off the axis (a few mms away). Furthermore, the inward radial electron drift induced by the space charge produces detectable constriction in the electronic density contour lines (fig.4) with a clearly formed 'neck' in the PC.

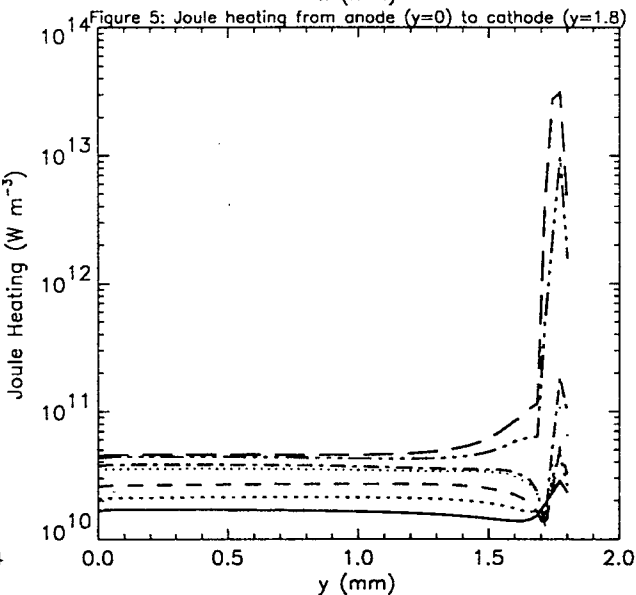
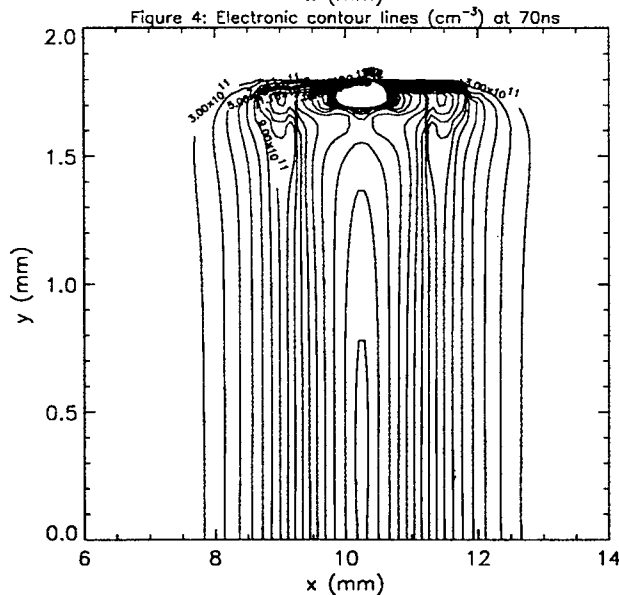
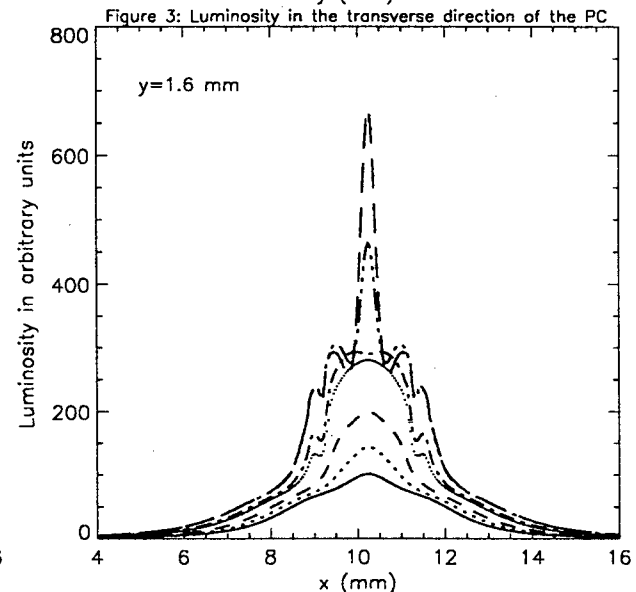
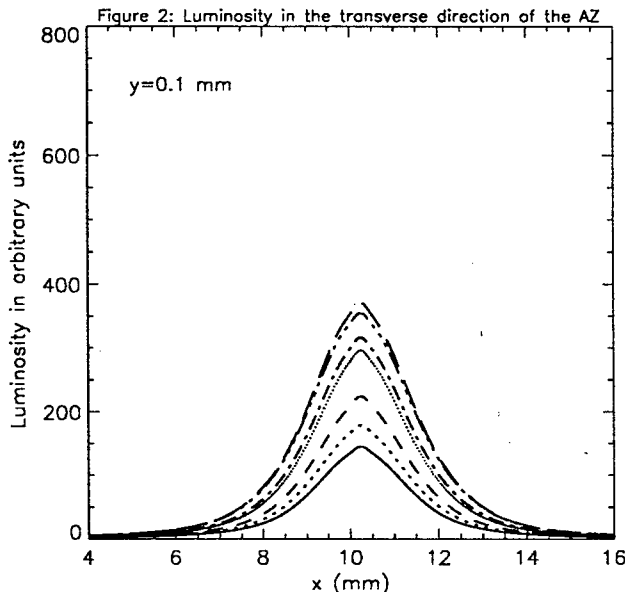
The high electric field and charged particle densities at the CR provides an important Joule heating (fig.5) which shoots the neutral gas temperature above 2500 K instants following 70.1ns, thereby triggering dissociation in the CR. Thus, the Joule heating effect, corresponding to the energy dissipated in the gap, is much more important in that region. A similar behaviour has been detected experimentally in nitrogen [6].

4. Conclusion

The present hybrid model shows that the radial evolution of the electric field generates a partial constriction of the positive column displayed by multiple radial maxima in the luminosity. It also gives rise to a clearly detectable constriction of the electronic density in the PC. Furthermore, the energy dissipated in the CR is of prime importance compared to that in the PC.

5. References

- [1] S.C. Haydon, Invited Papers, Proc. 8th ICPIG, (Vienna), (1967), 495
- [2] M. C. Cavenor, J. Meyer, Aust. J. Phys., **22**, (1969), 155
- [3] O. Eichwald, M. Jugroot, P. Bayle, M. Yousfi, J. Appl. Phys., **80**, (1996), 694
- [4] J.P. Novak, R. Bartnikas, IEEE Trans. Plasma Sc., **18**, (1990), 775
- [5] M. Yousfi, M.D. Benabdessadok, J. Appl. Phys., **80**, (1996), 6619
- [6] T. Fujiwara, T. Sato, J. Sekikawa, H. Yamada, J. Phys. D: Appl. Phys., **27**, (1994), 826



A 2-D fluid model for dust particles in an RF discharge

W.J. Goedheer

FOM-Institute for Plasmaphysics Rijnhuizen
P.O. Box 1207, 3430 BE Nieuwegein, The Netherlands

1. Introduction

When dust particles of a given size are introduced in a discharge, they will be charged until they reach the floating potential. As a result of their negative charge they are confined by the space charge sheath electric fields. Forces opposing this confinement are, for instance, the drag exerted by the flux of positive ions and gravity. Selfconsistent modelling of the dust behaviour is hampered by the fact that the transport of dust has a timescale far beyond typical RF periods, while the presence of the dust influences the behaviour of the other charged species on the RF timescale. Especially the spatial distribution of the electric field and its time average play an important role. We have constructed a 2-D fluid model, which simulates the behaviour of a given amount of dust of a given size in a cylindrically symmetric RF discharge.

2. The fluid model

The fluid model is based on the equations of continuity for the density and the drift-diffusion approximation for the flux of each charged species with mobility μ_s and diffusion coefficient D_s [1]:

$$\frac{\partial N_s}{\partial t} + \vec{\nabla} \cdot \vec{\Gamma}_s = S_s, \quad \vec{\Gamma}_s = \mu_s N_s \vec{E} - D_s \vec{\nabla} N_s. \quad (1)$$

The inertia of the ions is corrected for by replacing the actual electric field by an effective field [2], for an ion with a momentum scattering frequency ν_m given by:

$$\frac{\partial \vec{E}_{\text{eff}}}{\partial t} = \nu_m (\vec{E} - \vec{E}_{\text{eff}}). \quad (2)$$

The actual electric field is computed from Poisson's equation:

$$\nabla^2 V(\vec{r}) = \frac{e}{\epsilon_0} \left(\sum_s \frac{q_s}{e} N_s \right), \quad \vec{E} = -\vec{\nabla} V, \quad (3)$$

where the sum contains all charges species s .

The rates for processes like excitation, ionization and attachment are prescribed as a function of the average electron energy. These prescriptions are either obtained from literature or computed from a two-term Boltzmann solver for the electron energy distribution function. The average electron energy is obtained from the electron energy balance [1].

3. Charge on a dust particle

A dust particle in the discharge is charged up to the floating potential. This potential depends on the local ion and electron density. For a spherical particle,

the orbital motion limited theory [3] predicts a positive ion current

$$I_+ = 4\pi r_d^2 e N_+ \sqrt{\frac{kT_+}{2\pi M_+}} \left(1 - \frac{eV_p}{kT_+}\right) \quad (4a)$$

and an electron current

$$I_e = 4\pi r_d^2 e N_e \sqrt{\frac{kT_e}{2\pi m_e}} \exp\left(\frac{eV_p}{kT_e}\right) \quad (4b)$$

Equating these expressions gives the floating potential V_p and the charge, $q_d = 4\pi\epsilon_0 r_d V_p$. In the calculations a fixed ratio of the electron and ion temperature of 160 has been used.

4. Forces on a dust particle

Apart from trivial forces like gravity and the electric force, the motion of a dust particle is influenced by the neutral drag,

$$\vec{F}_n = -\frac{4}{3}\pi r_d^2 N_n m_n v_{th,n} \vec{v}_d, \quad (5)$$

which is exerted by a flux of neutrals with density N_n , mass m_n and a thermal velocity $v_{th,n}$ on a particle with a velocity \vec{v}_d relative to the gas [4], and by the ion drag,

$$\vec{F}_i = 4\pi m_i \vec{\Gamma}_i \sqrt{\left(\frac{8kT_i}{\pi m_i} + v_i^2\right)} \times \left(\frac{eq_d}{4\pi\epsilon_0 m_i v_i^2}\right)^2 \ln \left[\sqrt{1 + \frac{b_{max}^2}{r_d^2}} \right], \quad (6)$$

which is exerted by the Coulomb interaction between a flux $\vec{\Gamma}_i = N_i \vec{v}_i$ of ions with temperature T_i . b_{max} is a screening distance related to the Debye length [4]. Because the gas temperature is assumed not to vary in space, the thermophoretic force is neglected. The gravitational force can usually be neglected as well; it becomes important only when the size of the particles is large enough.

Since the dust has a large mass, it will only be able to react to the average RF electric field; also variations in the ion drag and in the charge will average out.

5. Drift-diffusion equation for dust

In equilibrium, the neutral drag, the electric force and the ion drag balance. Introduction of a momentum loss frequency ν_{md} , a mobility μ_d and a diffusion coefficient D_d for the dust,

$$\nu_{md} = \frac{4}{3}\pi R_d^2 N_n \frac{m_n}{m_d} v_{th,n}, \quad (7a)$$

$$\mu_d = \frac{Q_d}{m_d \nu_{md}}, \quad D_d = \mu \frac{kT_d}{Q_d}, \quad (7b, c)$$

and addition of a diffusive velocity yields the average flux of the dust, which can be treated with the same numerical procedures as the fluxes of the other charged particles:

$$N_d \vec{v}_d = \frac{4\pi m_i N_d \vec{\Gamma}_{i,av}}{m_d \nu_{md}} \sqrt{\left(\frac{8kT_i}{\pi m_i} + v_{i,av}^2\right)} \times \left(\frac{eq_d}{4\pi\epsilon_0 m_i v_{i,av}^2}\right)^2 \ln \left[\sqrt{\left(1 + \frac{b_{max}^2}{R_d^2}\right)} \right] + \mu_d N_d \vec{E}_{av} - D_d \vec{\nabla} N_d. \quad (8)$$

6. Recombination on a dust particle

The fluxes of ions and electrons arriving at the dust surface will recombine to form neutral gas. The recombination rate is readily obtained from equation 4b. With the charge inserted instead of the floating potential, it reads:

$$R = 4\pi r_d^2 N_d N_e \sqrt{\frac{kT_e}{2\pi m_e}} \exp\left(\frac{eq_d}{4\pi\epsilon_0 kT_e r_d}\right) \quad (9)$$

7. Results

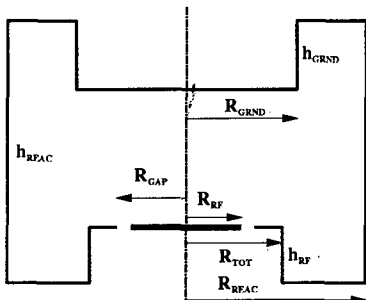


Fig.1. The geometry used in the 2-D model

Simulations were done in a geometry as sketched in figure 1, with a total reactor height and radius of 8 and 12 cm, respectively. Both electrode heights are 2 cm and have a radius of 6 (RF) and 8 (grounded) cm. The grounded ring around the RF electrode has a radius of 6.5 cm, with a gap of 1 mm.

Figure 2 shows the distribution of dust with a radius of 20 nm in an electronegative discharge operated at 13.56 MHz and a pressure of 250 mTorr. The power is 20W. Only the zone between the planes of the electrodes is shown. As is known from experiments, large dust accumulates at the transition between the bulk and the sheath. The maximum density is $1.4 \cdot 10^{14} \text{ m}^{-3}$ and the charge -100e. When the dust becomes smaller, the ion drag decreases, and the dust accumulates more in the centre of the discharge. This is illustrated for an electropositive discharge in figure 3. The dust radius is now 2 nm, the maximum $2.2 \cdot 10^{15} \text{ m}^{-3}$ and the charge -18e.

Figures 4 and 5 show the electron density with and without small dust in units of 10^{16} m^{-3} . Due to the

recombination, the maximum off-axis vanishes when dust is present.

8. References and acknowledgements

- [1] J.D.P. Passchier and W.J. Goedheer, J. Appl. Phys. 73 (1992) 1073.
- [2] A.D. Richards, B.E. Thompson and H.H. Sawin, Appl. Phys. Lett. 50, (1987) 492.
- [3] J.E. Allen, Physica Scripta 45 (1992) 497.
- [4] D. Winske and M.E. Jones, IEEE Trans. Plasma Sci. PS-22 (1994) 454.

This work was performed under the EURATOM-FOM Association agreement and supported by the Netherlands Organization for Scientific Research (NWO).

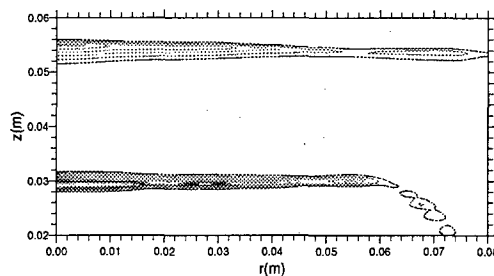


Fig.2. A distribution of dust with a radius of 20 nm.

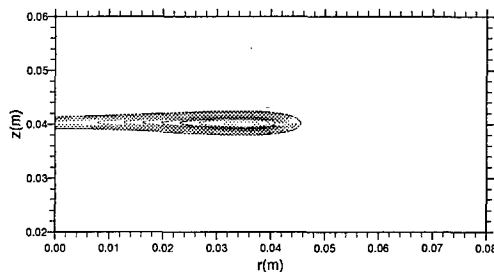


Fig.3. A distribution of dust with a radius of 2 nm.

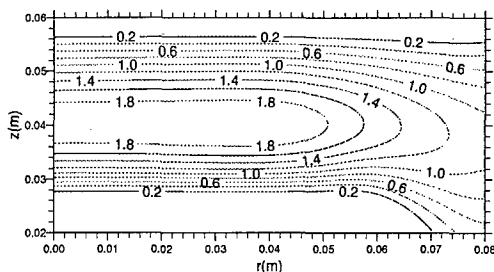


Figure 4. The electron density with small dust.

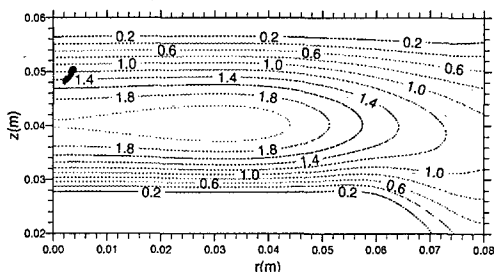


Figure 5. The electron density without dust.

Modeling results of $\text{SiH}_4\text{-H}_2$ RF/VHF deposition discharges compared to experiments

G.J. Nienhuis¹⁾, W.J. Goedheer¹⁾, E.A.G. Hamers²⁾, J. Bezemer²⁾

- 1) FOM-Institute for Plasmaphysics 'Rijnhuizen'
P.O. box 1207, 3430 BE Nieuwegein, the Netherlands
- 2) Dept. of Atomic and Interface Physics, Debye Institute, Utrecht University
P.O. box 80000, 3508 TA Utrecht, the Netherlands

1. Introduction

Hydrogenated amorphous silicon (a-Si:H) has an extensive field of applications. Important applications are the use in solar cells and in thin film transistors for LCD panels. At Utrecht University thin films of a-Si:H are deposited using plasma enhanced chemical vapor deposition (PECVD) in a parallel plate reactor operated at very high frequencies (VHF). The properties of the a-Si:H film (band gap, hydrogen content, refractive index, etc.) can be controlled by adjusting the parameters of the process, such as pressure, RF-frequency, RF-power, and gas mixture. However, a major problem in optimizing material properties is the complex chemistry of the silane plasma and the plasma-wall interaction (deposition process). Modeling provides knowledge of the deposition process and a way to find the optimum parameter space of the reactor.

An existing 1-D fluid model has been compared to experiment. Some discrepancies arose, because the width of the deposition reactor is not very large compared to the electrode distance. Therefore, the model is extended to two dimensions (cylindrical symmetric).

2. Description of the fluid model

The fluid-model presented is a self consistent fluid model which describes the electron kinetics and the chemistry in the discharge as well as the deposition process at the walls. In Figure 1 the cylindrical symmetric geometry of the 2-D model is shown. Fluid models describe the discharge by a combination of balances for the particle, momentum and energy densities of the ions, electrons, neutrals and radicals. The electric field is solved self-consistently using the Poisson equation. An effective electric field is used for the ions.

Rates for electron impact collisions as well as the electron transport coefficients depend on the electron energy distribution function (EEDF). The collision rates, the electron transport coefficients, and the average electron energy are obtained by solving the Boltzmann equation for the EEDF. This EEDF has been expanded in two terms with respect to the velocity. The EEDF is calculated as function of the electric field for a given composition of the neutral background density. A look-up table has been constructed to obtain the collision rates

and electron transport coefficients as function of the

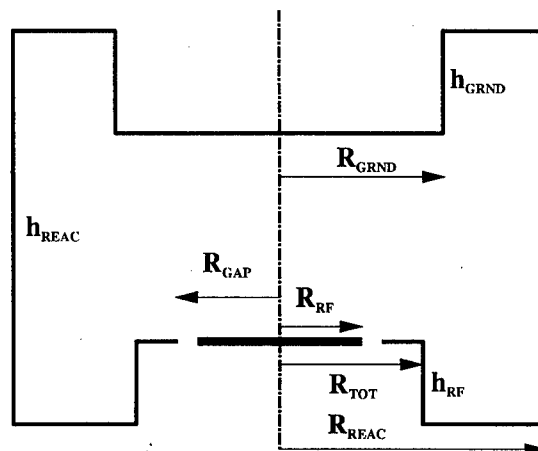


Figure 1 : Geometry used in 2-D model.

average electron energy. These tables are used in the fluid model, where the average electron energy is computed.

In order to model an SiH_4/H_2 discharge in a realistic way, a number of different species and reactions must be included. However, a minimum number of different particles and reactions is desired to keep the computational effort low. A sensitivity study with a 1-D model has been used to find a minimum set of different particles and reactions.

The actual deposition process is modeled by introducing sticking coefficients. Gas inlet and pumping and the gas transport are calculated consistently. They are assumed to be diffusive.

3. Experimental setup

The experiments have been performed in the ASTER [1] (Amorphous Semiconductor Thin film Experimental Reactor) at the Utrecht University. The deposition reactor has an inner volume of 10 liters, an inner diameter of 20 cm. The upper electrode is grounded. The powered electrode is placed 2.7 cm below the upper one. The electrodes have a radius of 8.0 cm. A dark space shield positioned a few millimeters below the powered electrode is used to shield the rest of the reactor from this

electrode. For the power coupling a π -type matching network is used at 13.56 MHz, while an L-type network is used at frequencies between 30 and 65 MHz. The partial pressures of the neutrals are measured with a mass spectrometer during plasma deposition. The growth rate of the deposited layer is measured ex-situ. Ion energy distributions are measured at the position where normally the substrate for deposition is placed.

4. Results of a 1-D model

The results of an existing 1-D model [2] of a SiH_4/H_2 discharge have been compared with experiment. The partial pressures of SiH_4 , H_2 , and Si_2H_6 and the growth rate have been compared, because these are accessible both by model and experiment. The plasma characteristics have been measured/calculated as function of RF-frequency, RF-power and total pressure in the reactor. After comparing the results of the 1-D model with the experimental data in a wide range of operating parameters, it is concluded the model can predict tendencies in the so-called α -regime i.e. the dust free regime. An example is given in Figure 3, where the

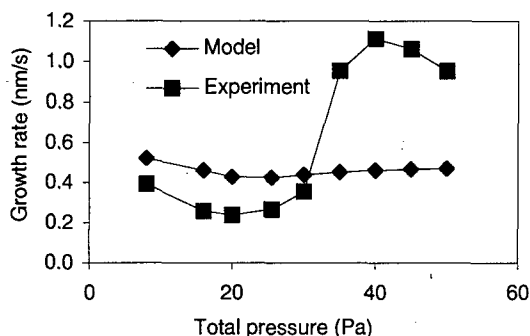


Figure 3 : Growth rate vs. total pressure.

behavior of the growth rate is shown as function of the total pressure in the reactor. At lower pressures the tendencies between model and experiment agree. Above a critical pressure (≈ 30 Pa) the growth rate increases strongly (the so called α - γ' transition [3]).

In the α -regime, calculation of correct absolute values of the plasma parameters is not possible with this 1-D model. This can be observed in Figure 3 and in Figure 2 where the partial pressure of SiH_4 and H_2 are shown as function of the RF-frequency.

A possible cause of the discrepancy between experiment and model in the α -regime, is that the model is one dimensional, i.e. the intrinsic assumption of this model that the discharge is assumed to be symmetric. In the 1-D model, the DC bias voltage is assumed to be equal to zero. In practice this is not the case. With a 2-D model, an asymmetric discharge can be simulated.

A further advantage of the 2-D model is that the modeling of gas inlet and pumping in the reactor

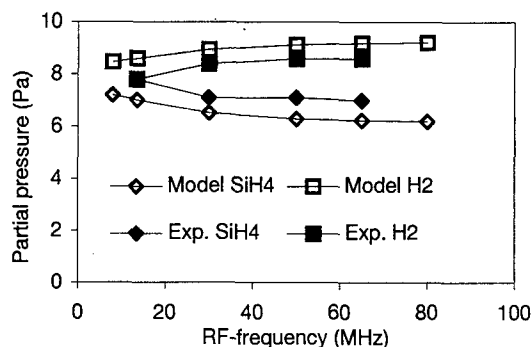


Figure 2 : Partial pressure of SiH_4 and H_2 vs. RF-frequency

pumping can be modeled more appropriate. Finally, with a 2-D model, the bias voltage and uniformity of the deposition can be calculated and thus a more extensive comparison between experiment and model is possible.

An advantage of the 1-D model of course is the reduced computational effort compared to the 2-D model.

A major problem in plasma modeling is the inaccuracy or even lack of elementary data (cross-sections for ionization, dissociation, etc. and the coefficients for chemical reactions and transport). The sensitivity of the results with respect to the elementary data can be determined by calculating the change in the characteristics of the plasma as a results of a change in the elementary data. An overview will be given of the important processes and particle in the SiH_4/H_2 discharge.

5. Results of the 2-D model

Results of the 2-D model will be shown and compared both with the 1-D model and the experiments. The 2-D model allows for the calculation of other experimental accessible discharge parameters such as the DC self bias voltage and sheath characteristics, which are deduced from the ion energy distributions.

ACKNOWLEDGMENTS

This work was performed under the EURATOM-FOM Association agreement and was supported by the Netherlands Organization for Scientific Research (NWO), the Netherlands Agency for Energy and the Environment (NOVEM).

- [1] C.A.M. Stap, et al., Proc. ninth E.C. Photovoltaic Solar Energy Conf., Freiburg Germany, 74 (1989)
- [2] G.J. Nienhuis et al., submitted to J.A.P.
- [3] L. Andújar, et al. J. Vac. Sci. Technol. **A9**, 2216 (1991).

Modelling of ECR Discharges

D. Hemmers, W. Biel, M. David, H. Kempkens, J. Uhlenbusch
Heinrich-Heine-Universität Düsseldorf
Institut für Laser- und Plasmaphysik
D-40223 Düsseldorf

1. Introduction

Electron cyclotron resonance (ECR) plasma sources are widely used in experimental investigations of dry etching and plasma assisted chemical vapour deposition. In order to optimize the coupling of the microwave into the plasma and investigate the influence of the magnetic field on the discharge we developed a numerical model which is able to compute self-consistently the electron density and temperature of an ECR discharge in two dimensions. The model gas is argon. We discuss results of the calculations for different neutral pressures and different magnetic field configurations.

2. Experimental Setup

The discharge vessel as shown in fig. 1 is nearly ready for the first experimental runs. It consists of three parts made from stainless steel. The outer parts with a length of 685 mm and several observation ports have a circular cross section ($d=180$ mm) to enable the microwave to propagate to the center nearly undisturbed. The inner segment has a squared cross section (180×180 mm²) and a length of 220 mm. On the inner part there are mounted four main ports to apply simultaneously several diagnostic techniques (e.g. Thomson scattering).

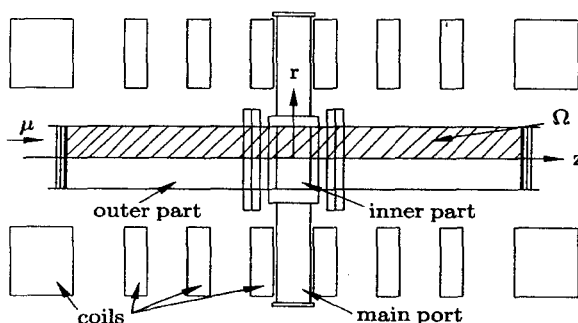


Fig.1: Experimental setup

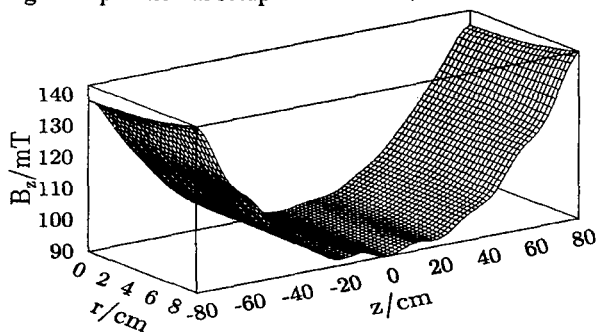


Fig. 2: Magnetic field inside the discharge vessel

The microwave enters the vessel from the left hand side through a quartz window as a right-hand circular polarized TE₁₁-Mode with a power of up to 6000 W parallel to the magnetic field. The magnetic field is produced by 58 coils with an inner radius of 200 mm. The coils are piled up to 8 packages of 14 and 5 coils each as shown in fig. 1. The outer two packages are driven with a higher current (80 A) than the inner ones (62 A), so that the resulting field is a magnetic mirror with a mirror ratio of $M=1.5$, cf. fig. 2.

3. Modelling

The modelling of ECR discharges requires the self-consistent solution of Maxwell's equations and plasma transport equations. From the first ones the following wave equation for the electric field \vec{E} can be obtained:

$$\frac{\partial^2 \vec{E}}{\partial t^2} = -\frac{c^2}{\epsilon_r} \nabla \times \nabla \times \vec{E} - \frac{\sigma}{\epsilon_0 \epsilon_r} \frac{\partial \vec{E}}{\partial t} \quad (1)$$

In eqn. (1) the material properties of the plasma are included by the relative dielectricity ϵ_r and the conductivity σ which are computed from the dispersion relation for right circular polarized waves propagating parallel to the magnetic field using the cold plasma approximation [1]. The dependence of \vec{E} on the azimuthal coordinate is eliminated by using periodic boundary conditions thus setting $E(r, \theta, z, t) = e^{i\theta} E(r, z, t)$.

The plasma model treats the electrons as a fluid assuming a Maxwellian electron energy distribution function, cf. [2]. After Braginskii [3] the particle balance using the diffusion approximation is given by

$$-\nabla \cdot \underline{\underline{D}} \cdot \nabla n_e = R_{ion} \quad (2)$$

where R_{ion} is the temperature dependent ionisation rate. $\underline{\underline{D}}$ is the diffusion tensor for electrons in the applied magnetic field. It is assumed that the electrons diffuse ambipolar in the direction parallel to B . To describe the cross field transport we assumed Bohm diffusion. The second equation is a simplified energy balance for the electrons

$$-\nabla \cdot \underline{\underline{\kappa}} \cdot \nabla T_e + \frac{5}{2} k T_e R_{ion} = \frac{1}{2} \sigma \vec{E}^* \cdot \vec{E} - Q_{coll} \quad (3)$$

The source term $1/2 \sigma \vec{E}^* \cdot \vec{E}$ on the right hand side of eqn. (2) describes the heating of the plasma by microwave absorption. The term Q_{coll} takes into account the energy losses of electrons by collisions. $\underline{\underline{\kappa}}$ denotes the heat conductivity tensor of electrons after [2]. The quantities n_e and T_e are assumed to be independent of θ . The boundary conditions for eqns. (2) and (3) prescribe the particle and energy fluxes to the walls:

$$\Gamma_{e,wall} = -(\underline{D} \cdot \nabla n_e) \cdot \underline{\bar{e}}_n = \frac{1}{4} n_{e,s} v_{e,s} \exp\left(-\frac{e\Delta\Phi}{kT_{e,s}}\right) \sin \alpha \quad (4)$$

$$q_{e,wall} = -(\underline{\kappa} \cdot \nabla T_e) \cdot \underline{\bar{e}}_n = \Gamma_{e,wall} kT_{e,s} \left(2 + \frac{e\Delta\Phi}{kT_{e,s}}\right) \quad (5)$$

$n_{e,s}$, $T_{e,s}$ and $v_{e,s}$ are electron density, temperature and thermal speed at the plasma-sheath boundary. $\Delta\Phi$ is the potential difference between plasma and wall. α denotes the angle between the local magnetic field and the wall. On the axis the gradients of n_e and T_e in the radial direction are set to zero.

The ion density is given by quasineutrality, $n_i = n_e$, the ion temperature is set to $T_i = 5000$ K. The neutral temperature is calculated from a global energy balance.

Eqns. (1) to (3) are solved in r - z -geometry on the area Ω , cf. fig. 1, using a Galerkin finite element method.

4. Results

Figs. 3 to 5 show the radial component of the electric field, the electron density and temperature for a neutral pressure of 0.5 Pa and a microwave power of 200 W.

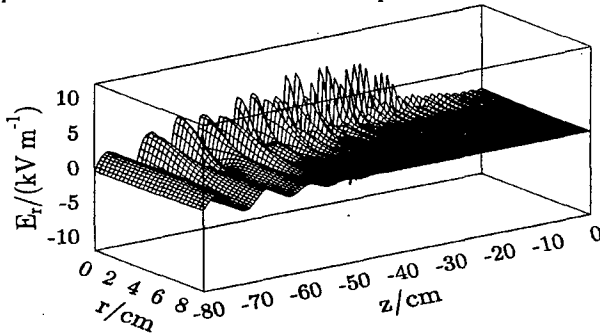


Fig. 3: Radial component of the electric field

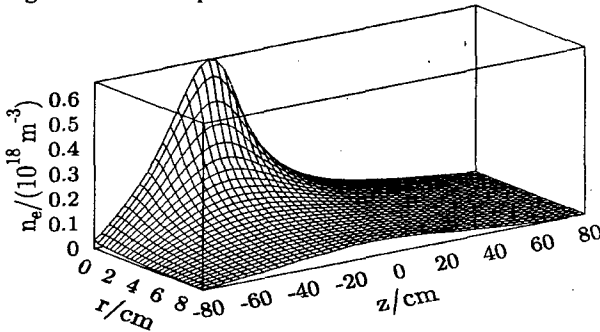


Fig. 4: Electron density

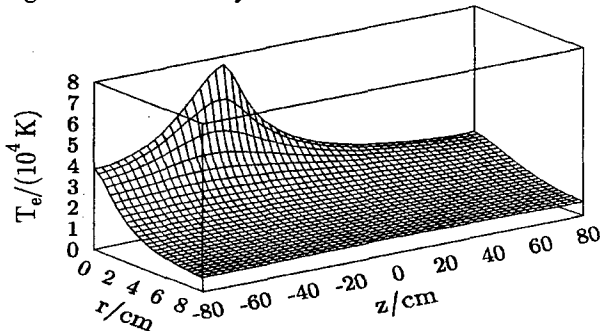


Fig. 5: Electron temperature

The microwave is focussed towards the axis and strongly absorbed at magnetic fields between 100 mT and 90 mT which is higher than the resonant field strength of 87.5 mT. This localized absorption leads to a sharp peak in the electron temperature with a maximum value of 6.5 eV. The electron density shows at the same position a maximum of $0.7 \cdot 10^{18} \text{ m}^{-3}$ which is higher than the critical density. The decrease of the electron density towards the quartz windows is caused by wall recombination.

In calculations with increasing neutral pressures (0.2 Pa, 0.5 Pa, 1.0 Pa) the electron density shows a sublinear increase while the electron temperature remains nearly constant. The position of maximum power absorption shifts to higher magnetic field strengths due to higher source density and increased collision frequencies. Furthermore, the increased electron density leads to a stronger focussing of the microwave.

To investigate the influence of the magnetic field on the discharge the mirror ratio was changed from 1.5 to 1.7 and 1.9 thus increasing the gradient of B . While the electron density and temperature remain nearly unchanged the position of maximum absorption shifts to a position more distant from the quartz window. Finally, the width of the absorption maximum is small when the gradient of the magnetic field is large as predicted by [4].

5. Conclusion

We have presented a model which computes electron density and temperature of an ECR discharge self-consistently. Calculations have shown that the plasma together with the magnetic field behaves as a lens as expected from ray tracing calculations [5]. Due to collisions the absorption at high pressures takes place at magnetic field strengths well above resonance. Coupling of the microwave to the plasma from the high magnetic field side can lead to overcritical densities. The magnetic field strongly effects the plasma, especially its position and the width of the absorption maximum zone are influenced.

6. References

- [1] Stix, *Waves in Plasmas*, American Institute of Physics, New York, 1992
- [2] Bowden et al., *Thomson scattering measurements of electron temperature and density in an electron cyclotron resonance plasma*, J. Appl. Phys. 73(6), 1993
- [3] Braginskii, *Transport Processes in a Plasmas*, Reviews of Plasma Physics 1, Consultants Bureau, New York, 1965
- [4] Kuckes, *Resonant absorption of electromagnetic waves in a non-uniformly magnetized plasma*, Plasma Physics, Vol. 10, 1968
- [5] Veerasingam et al., *Ray tracing calculations of ECR absorption in plasma etching and deposition devices*, Plasma Sources Sci. Technol. 3, 1994

One-Dimensional Hybrid Fluid-Monte Carlo Model of a AC Matrix Plasma Display Panel Cell

A. Hirech and J.P. Boeuf

Centre de Physique des Plasmas et Applications de Toulouse (E.S.A. 5002), UPS,

118 route de Narbonne, 31062 Toulouse Cedex, France

Email: hamid@cpa01.ups-tlse.fr

This work presents results from a self-consistent 1D hybrid model of the discharge initiated in an ac plasma display panel cell. The ionization rate in the hybrid model is calculated using a Monte Carlo simulation. The aim is to check the validity of simpler (fully fluid) plasma display models based on the local field approximation [1]. Results are presented in a 10% xenon, 90 % neon mixture, for a gap length of 100 μm and gas pressure of 560 Torr at ambient temperature.

1. Introduction

Plasma display panels [2, 3] consist of two glass plates, each with parallel electrodes deposited on their surface. In the matrix configuration the two sets of electrodes are orthogonal. The electrodes are covered with a dielectric film above which a protective MgO layer is deposited. Each picture element, at the intersection between a line and column electrode, can be illuminated independently when a voltage pulse is applied between the two electrodes. The capacity of the dielectric layer above each electrode is taken to be 460 pF/cm² in the simulation. The model is used in this paper to simulate a discharge pulse for an applied voltage of 310 V across the electrodes, with no memory charges on the dielectric surface at $t=0$. The resulting discharge pulse is identical to a "ON" state pulse (with memory charges), for a value of the sustaining voltage equals to 155 V (in the "ON" state, the voltage due to the memory charges is equal to the sustaining voltage). This value corresponds to the middle of the margin.

2. Hybrid model of the discharge

The fluid model is based on a two-moments description of electron and ion transport, coupled with Poisson's equation, and with a set of kinetic equations characterizing the evolution of the population of excited states leading to UV emission in neon-xenon mixtures. The main difference with the model of [1] (referred to as the "fluid, local model" below) is that the ionization source term in the continuity equation is deduced from a Monte Carlo simulation of the electrons emitted by the surface (these electrons are followed until their energy becomes too small to ionize the gas before they reach the surface). Since this procedure is more accurate than the local field approximation, this model can help validating the approach of [1].

3. Current and voltage across the gap

Figure 1 shows the time evolution of the gap voltage and the current density in the cell, deduced from the model. The discharge is initiated in the gap after a time delay of about 230 ns and the current density reaches a peak value of 6 A/cm² in about 10 ns. The decrease of the current density is due to the charging of the dielectric surface and the resulting decrease of the voltage across the gap.

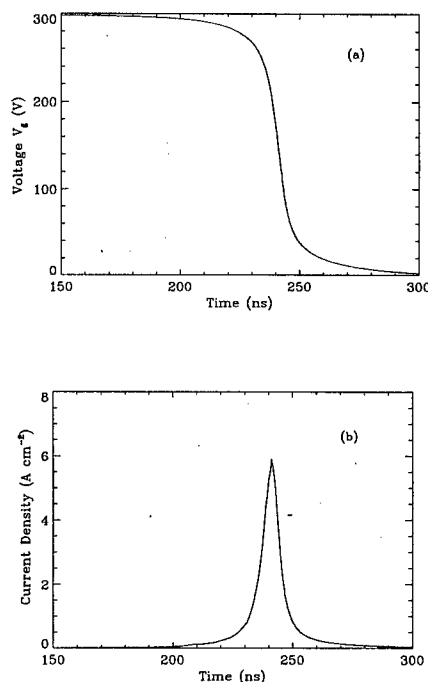


Fig.1. (a) Voltage (V_g) across the cell and (b) discharge current density as a function of time for a discharge in (90-10) neon-xenon mixture, gap length 100 μm , gas pressure 560 Torr (300 K), dielectric capacitance 460 pF/cm², initial gap voltage 298 V (310 V across the electrodes).

4. Electric field, charged particle densities and excitation rates

Figure 2 shows the spatial distribution of the electric field and charged particle densities in the gap at $t = 240$ ns (time of maximum current density). The dominant ion is Xe⁺ and the concentration of molecular ions is

negligible under these conditions. The value of the ion density in the sheath at the peak current is on the order of 10^{14} cm^{-3} , as in the fluid, local model of [1] while the maximum plasma density is about 10^{14} cm^{-3} , instead of $0.6 \cdot 10^{14} \text{ cm}^{-3}$ in [1] (this is because of non local ionization). The spatial distribution of the electric field is very similar to the one deduced from the local model.

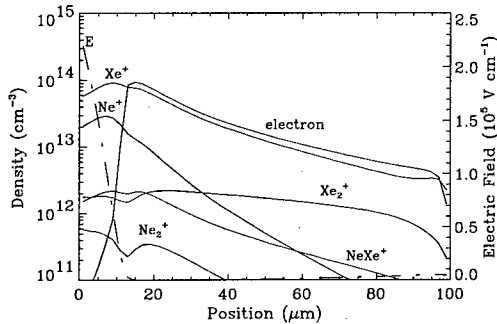


Fig. 2. Space variations of the density of electron and ions at the time of maximum current in the cell ($t=240\text{ns}$).

Figure 3 shows the spatial distribution of the production rates of $\text{Xe}^*(^3\text{P}_1)$, $\text{Xe}^*(^3\text{P}_2)$ and Xe^{**} at time $t=240 \text{ ns}$ (see [1] for a definition of Xe^{**}). The shape and values of these rates are similar to those deduced from the fluid, local model (Fig. 14 of [1]). However, as expected, the hybrid model predicts more excitation inside the negative glow plasma than the local model. The excitation profile in the plasma further away from the sheath region is different from the one predicted by the local model, but the hybrid model still predicts an increase of the excitation rate in the column plasma at the peak current (see the discussion in [1]).

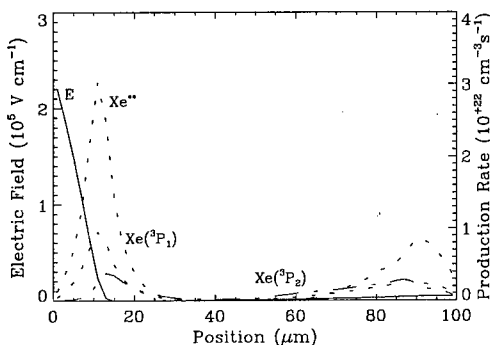


Fig. 3. Spatial variations of the production rates of $\text{Xe}^*(^3\text{P}_1)$, $\text{Xe}^*(^3\text{P}_2)$ and Xe^{**} across the gap at time $t=240 \text{ ns}$ (same conditions as in Fig. 1).

Note that the time of maximum current corresponds to the time of largest discrepancy between fluid and hybrid models since it corresponds to the minimum sheath length (and therefore strongest non equilibrium

effects).

5. Comparisons between fluid and hybrid models for different conditions

Table I presents a systematic comparison between fluid and local models for different concentrations of xenon. The values of the applied voltage, maximum current, pulse duration (at half the peak current), time of maximum current, and UV production efficiency are represented in this table. For a meaningful comparison, the applied voltage in each case has been chosen so that the discharge pulse is equivalent to a "ON" state pulse with a sustaining voltage in the mid-margin.

Xe	1%		5%		10%		30%	
	F	H	F	H	F	H	F	H
V_s (V)	112	125	131	142	142	155	175	185
J_m (A/cm ²)	4.0	2.75	6.0	4.3	7.35	6.0	12.	9.0
Δt (ns)	10.	13.5	8.0	9.5	5.6	7.8	4.0	6.2
t_m (s)	350	385	235	270	213	241	230	287
ρ_{UV} (%)	3.0	3.1	7.1	7.3	10.1	9.9	16.4	16.

Table I. Comparisons between results from the fluid (F) and hybrid (H) models showing the sustaining voltage V_s (at mid-margin), maximum current J_m , pulse duration Δt (at half the peak current), time of maximum current t_m and UV production efficiency ρ_{UV} .

The agreement between fluid and hybrid models is good. The discrepancies in the applied voltage (mid-margin) and delay time is actually due to the fact that the ionization coefficients used in the fluid model have been obtained from a Boltzmann code and that the Monte Carlo simulation performed under a constant field (i.e. during the prebreakdown phase) provides values of the ionization coefficients slightly different from those from the Boltzmann solver. The discrepancy is therefore not due to non equilibrium effects.

5. Conclusion

Fluid models of plasma display panel cells based on the local equilibrium assumption are accurate enough for usual working conditions.

6. Acknowledgments

This work has been supported by Thomson Tubes Electroniques.

7. References

- [1] J. Meunier, Ph. Belenguer and J.P. Boeuf, J. Appl. Phys. **78** (2), 15 July 1995.
- [2] J. L. Deschamps, Proceedings of the Society for Information Display International Symposium, San Jose CA, 1994, SID 94 Digest, p. 315.
- [3] A. Sobel, IEEE Trans. Plasma Sci. **PS-19**, 1032 (1991).

Study of Plasma Oxidation of Metals: Charge Transport through Plasma

R. Hrach

Department of Electronics and Vacuum Physics, Faculty of Mathematics and Physics, Charles University
V Holešovičkách 2, 180 00 Prague 8, Czech Republic

1. Introduction

In our laboratory the plasma oxidation of aluminium has been studied by the combination of experiments and modelling. The complete plasma oxidation process [1] consists of several parts: volume processes in the chemically active plasma of oxygen or O_2/Ar mixture, transport of charged particles through the transient region between undisturbed plasma and metal sample immersed into plasma, processes on the surface of the sample and the transport of ions of both oxygen and metal through the growing oxide layer. As the whole set of processes is too complicated, models of various parts of plasma oxidation have been studied separately.

2. Volume processes

Physical and chemical processes in the bulk of oxygen plasma have been studied by the computer experiment based on a macroscopic kinetic approach [2]. The model consists of 107 reactions between 12 neutral, charged and excited species. As a result of analysis the steady-state concentrations of stable products were derived for various experimental parameters. For our conditions (dc glow discharge, $E/N = 60$ Td) following concentrations of charged species were found: $1.7 \cdot 10^{-6}$ of O_2^+ , $1.4 \cdot 10^{-6}$ of electrons, $2.4 \cdot 10^{-7}$ of O^- , $1.1 \cdot 10^{-8}$ of O_2^- , etc. (all concentrations are given in relation to neutral O_2). Similar calculations for O_2/Ar plasma now are performed. These particles cross the region of disturbed plasma in the vicinity of substrate changing both their velocities and concentrations. Since it is supposed [1] that especially the O^- ions are the most important species for the creation of alumina (either coming directly from the discharge or created by electron bombardment on the substrate), the transport of electrons and ions must be studied in detail.

3. Transport of charged particles

The model of charge transport through both the sheath and presheath is based on the combination of molecular dynamics and Monte Carlo method [3]. The simplified version of model was presented in [4]. In the computer experiment the transport of all kinds of charged species originated from oxygen molecules in Ar or O_2/Ar plasma is studied under the following assumptions:

- Maxwell distribution of charged particles exists in undisturbed plasma (temperatures T_e and T_g)
- the distributions of charged particles are influenced by both the geometrical factor and electrical forces: by local electric field created by these particles and by positive or negative bias of metal substrate

- only elastic interactions are taken into account.

For the derivation of velocity and angular distributions of particles near the planar electrode the simplified $1d2v$ model is fully sufficient (one space co-ordinate x and two velocity co-ordinates v and v_x , x being perpendicular to the substrate plane).

Some results of simulation are shown in Figs. 1 and 2. The undisturbed plasma is placed on the left side and the metal substrate on the right side (at position $x = 0$).

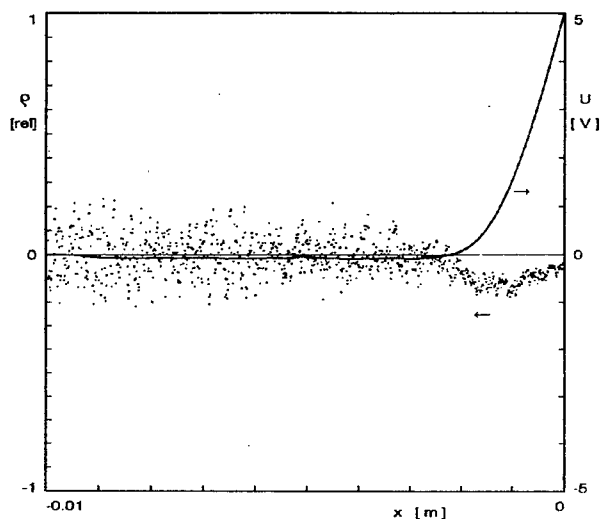


Fig. 1: Distribution of electric potential $U(x)$ and space charge $\rho(x)$ (ρ is given relatively to the steady-state concentration of electrons). Bias +5 V, total number of charged particles 200 000.

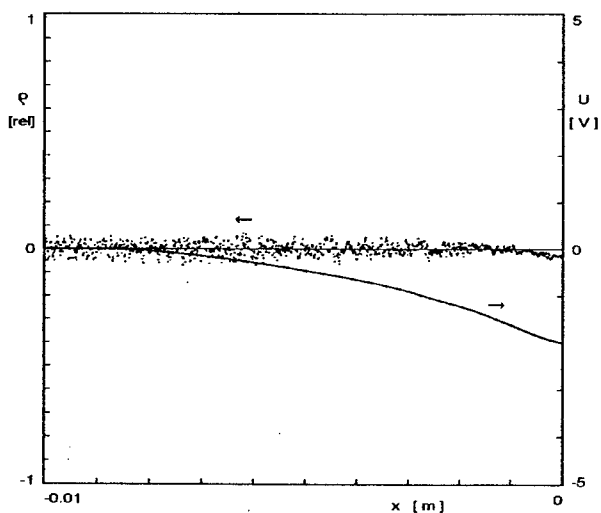


Fig. 2: Distribution of electric potential $U(x)$ and space charge $\rho(x)$. Negative bias -2 V, total number of charged particles 2 000 000.

4. Distributions of charged particles

The transport of charged particles through the sheath in non-collisional or slightly collisional plasma can be calculated analytically [4]. In the plasma oxidation process, however, the situation is different - the scattering of all kinds of charged particles (especially ions) must be taken into account and the processes in presheath cannot be neglected, too.

As for the further study of processes on the surface of metal samples the total velocity and its normal component are applied, the velocity distributions $N(v)$, $N(v_x)$ and the angular distribution $N(\theta)$ being calculated by hybrid particle simulation. Examples of these distributions are shown in Figs. 3-5. The exact forms of distributions depend not only on the bias of metal sample against the undisturbed plasma but also on the intensity of scattering events in the vicinity of samples, i.e. on the composition of plasma. The data presented in Figs. 3-5 were derived for electrons with temperature 23200 K passing through the Ar plasma of dc glow discharge at 133 Pa (ion temperatures 300 K). It was found that the distributions both of electrons and ions showed changes as compared to the original Maxwell distribution (denoted by thin lines in figures) already in rather large distances from the substrate.

5. Conclusion

In [4] it was shown that the large metal substrates used for plasmachemical technologies influence the charged particles in plasma by their presence far above the sheath region owing to so-called geometrical factor. This screening effect is partially compensated by the space charge of particles, the resulting change of energy distributions being, however, dramatic enough to be taken into account in all further studies.

6. Acknowledgements

The research has been sponsored by the European Community through the COPERNICUS Grant No. CIPA-CT94-0123. The partial financial support of the Charles University Prague under Grants No. GAUK-15 and GAUK-167 is gratefully acknowledged.

7. References

- [1] J. Siejka, J. Perriere: *Plasma Oxidation*, in *Physics of Thin Films*, Academic Press Inc., Boston 1989, Vol. 14, p. 81
- [2] P. Odehnal, R. Hrach and V. Hrachová: Proc. ESCAMPIG XIII, Poprad 1996, Slovakia, European Phys. Soc., Vol. 20 E, Part B, p. 357
- [3] C.K. Birdsall, A.B. Langdon: *Plasma Physics via Computer Simulation*, IOP Publ. Ltd., Bristol 1991
- [4] R. Hrach, P. Kuba: Proc. 10th Int. Conf. on Thin Films / 5th European Vac. Conf., Salamanca 1996, Spain, Asociacion Española de Vacio, p. 262.

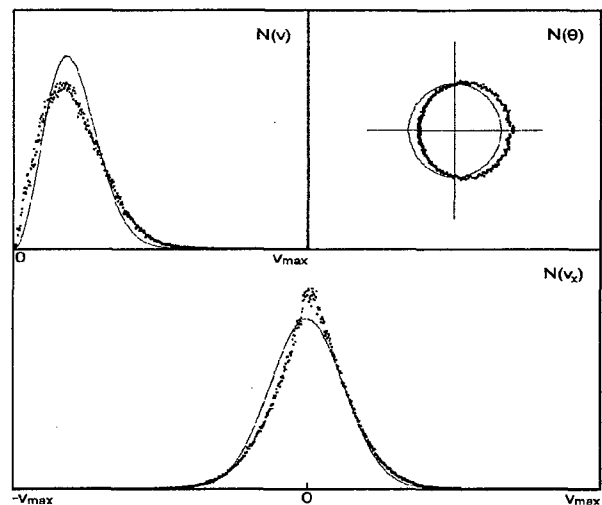


Fig. 3: Distributions of electrons for positive bias +5 V. Total number of particles 1 000 000. Distance from the substrate $d = 0.005$ m.

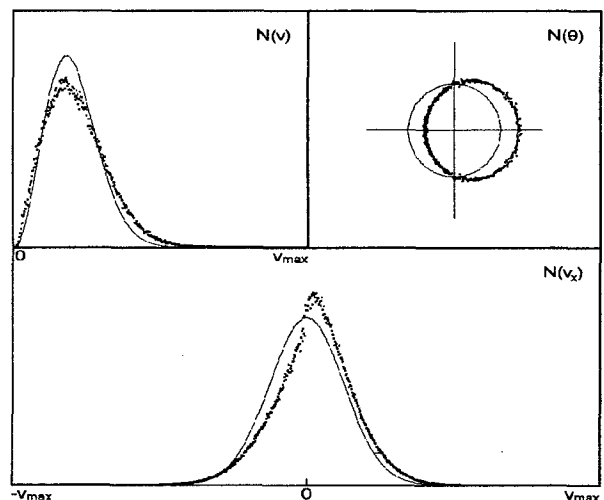


Fig. 4: See Fig. 3, but the distance being $d = 0.003$ m.

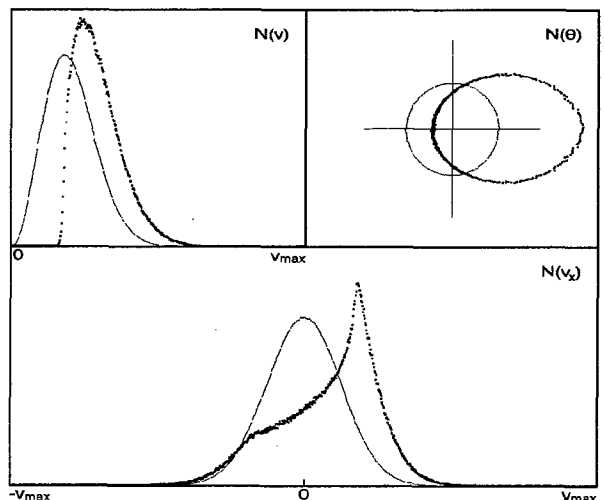


Fig. 5: See Fig. 3, but the distance being $d = 0.001$ m.

Simplified Particle Model of Collision Processes in Ar Plasma

R. Hrach, M. Entlicher, M. Horváth

Department of Electronics and Vacuum Physics, Faculty of Mathematics and Physics, Charles University
V Holešovičkách 2, 180 00 Prague 8, Czech Republic

1. Introduction

The physical processes occurring during plasma oxidation of metals has been studied by means of computer modelling combined with direct measurement. As a first step for a realistic computer experiment it is necessary to build a model of both undisturbed inert gas plasma and resulting O_2/Ar mixture. The complete list of various reactions and scattering processes in Ar glow discharge is too large for effective implementation. The aim of our present study is:

- to create a simplified qualitative model of Ar plasma as a source of particles for the modelling of plasma-solid interactions [1]
- to introduce and test new effective algorithms for hybrid particle simulation in plasma.

2. Model

The electron component of Ar plasma was simulated under the following assumptions:

- the total number of electrons is constant - processes leading to the increase and decrease of their number compensate each other
- the external electric field is constant
- the angular distribution of scattered electrons is isotropic.

These assumptions are approximately fulfilled in the positive column of dc glow discharge.

From possible interactions of electrons with other particles in plasma, a minimal set sufficient for plasma simulation was chosen. The qualitatively correct model must provide the Maxwell distribution of electrons (another assumption). It was found (see [2]) that at least the following four types of scattering events for electrons must be present:

- elastic collisions with neutral atoms in plasma
- excitations of neutral gas atoms
- ionisation of neutral gas atoms
- interactions with charged species in plasma (with electrons and positive ions or with electrons only).

This set of interactions compensate the influence of the electric field and contribute to Maxwellisation of the electron energy distribution function. Experimentally derived cross-sections of all four interactions in Ar can be found in the literature [2].

The model was based on the particle simulation technique. The group of electrons was treated in the 3D rectangular working area with cyclic boundary conditions. For time integration of electron trajectories

two methods were used: the well-known second-order Verlet algorithm and the adaptive fourth-order predictor-corrector scheme.

The collisions of electrons with neutral particles were simulated by the Monte Carlo method, the 'null collision' method being applied. For the simulation of electron-electron and electron-positive ion collisions two different types of techniques were tried.

3. Molecular dynamics algorithms

Interactions of electrons were calculated by three different algorithms, one classical and two modern:

- Particle-Particle Method [3] (direct summation of Coulomb forces), which is of order $O(N^2)$, N being the number of interacting charged particles.
- Fast Multipole Method [4], which is based on an oct-tree hierarchical spatial decomposition of the cubic simulation region into hierarchical grids of cells and replacement of most particle-to-particle with cell-to-cell interactions. Multiple expansions are used to represent the effects of all particles in a cell. Forces among close particles are calculated by the Particle-Particle method. This method has a good feature when it is implemented in a molecular dynamics program, because multiple interactions do not have to be recalculated in every time step due to small moves of particles in every step. It was found, that one update of multipole expansions per approximately 10 time steps is sufficient (this value strongly depends on velocities of particles), which enables to speed up the computation by factor 4 approximately. This method is of order $O(N)$.
- Smooth Particle Mesh Ewald Method [5], where the energy of the system is split into direct and reciprocal energy like in standard Ewald method, but allows significant speed up in computation by approximation of the reciprocal energy by cardinal B-splines. The order of this method is $O(N \cdot \log N)$.

All molecular dynamics algorithms in our tests had periodical boundary conditions in all three dimensions.

4. Monte Carlo algorithms

As a second technique the interactions of electrons with other charged particles were calculated by two stochastic approaches:

- MC1: In the simple one electron approximation [6] the electron-electron collision is treated completely statistically. It is supposed that the energy

dependence of e-e cross-section is K/E^2 , E being the electron energy, and K a constant of order of $10^{-19} \text{ m}^2\text{eV}^2$. In this approach E is the energy of studied electron before the interaction and this energy is shared randomly with arbitrary electron from our model. This is the quickest algorithm, but K is an external parameter, which must be fitted from the experimental data (energy distribution function, ...).

- MC2: The more sophisticated method simulate the e-e or e- Ar^+ interactions according to the relations for the Rutherford scattering, but the distances of particles are treated statistically. In comparison with the first Monte Carlo approach there are no external parameters and the electron energy distribution function can be simulated more precisely, however, the performance of the method is worse.

5. Results

All these methods were implemented either in the C language and tested on a Silicon Graphics Power Challenge XL computer (with 12 processors R 10000, 195 MHz and 2 GB of shared memory) or in the FORTRAN-77 language and solved on a PC microcomputer (Pentium Pro processor, 200 MHz and 64 MB of RAM memory). All further results are given for one processor R 10000, which is approximately two times faster than the Pentium Pro microcomputer.

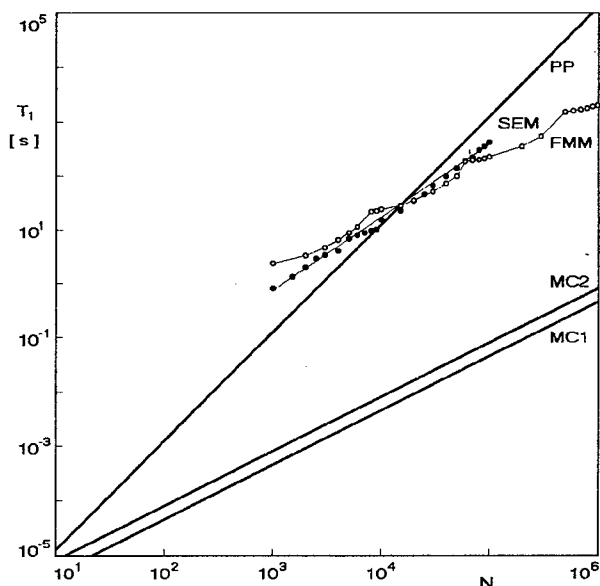


Fig. 1: The times of force calculation T_f in dependence on the number of particles N for: PP - direct summation, FMM - Fast Multipole Method, SEM - Smooth Ewald Method, MC1 and MC2 - two Monte Carlo methods. Relative accuracies for FMM and SEM methods were $1 \cdot 10^{-6}$.

In Fig. 1 the performance of various algorithms expressed in times T_f , necessary for moving of N particles over one time step is demonstrated.

As a main physical result it was found that the simplified model of Ar plasma with a reduced set of scattering events can be used for the qualitative simulation of electrons in positive column of dc glow discharge. Detailed calculations performed with various algorithms and plasma parameters proved that:

- the presence of positive ions in the model does not influence the electron energy distribution function in large extent compared to other scattering events
- the steady-state conditions in plasma are reached after a relatively long time of simulation (typically after $1 \cdot 10^5$ time steps, every step being of the order of 10^{-11} s), this time depends on the initial mean energy of modelled particles

In the computational physics direction the following results were derived:

- better agreement with experimental data can be achieved with the molecular dynamics algorithms than with the present types of Monte Carlo models
- the effectivity of the one-particle Monte Carlo algorithms is much better than even the best deterministic algorithms
- the new deterministic algorithms (FMM and SEM) are effective only for large models with 10^5 to 10^6 particles, however, in this case the demands on the computer memory are enormous
- the advantage of the statistical approach is its indifference to the effect of non-physical heating of plasma, as a consequence of finite time steps
- in the deterministic approach the non-physical heating can be reduced for electron-electron interactions, if the time step is lower than 10^{-11} s, however, for electron-positive ion interactions this effect cannot be fully nullified for any nonzero steps
- the adaptive method for the solving of the equations of motion was found to be very useful, because it reduces a non-physical heating of the system [3].

Acknowledgements

This research has been sponsored by the European Community through the COPERNICUS Grant No. CIPA-CT-94-0183, and partially by Charles University, Prague, under Grant No. GAUK-167/95 and by Czech Ministry of Education under Grant No. FR-0999/96.

References

- [1] Hrach R.: Proc. ICPIG XXIII, Toulouse 1997 France
- [2] Hrachová V., Hrach R.: Acta Phys. Slov. **41** (1991) 345
- [3] Hockney R.W., Eastwood J.W.: *Computer simulation using particles*, Adam Hilger, Bristol 1988
- [4] Greengard L., Rokhlin V.: J. Comput. Phys. **73** (1987) 325
- [5] Petersen H.G.: J. Chem. Phys. **103** (1995) 3668
- [6] Hrach R., Entlicher M., Hrach R.: Proc. 8th Joint EPS-APS Intern. Conf. "Physics Computing '96", Krakow 1996, Poland, p. 49.

One -dimensional hybrid model of plasma display cell.

V.V. Ivanov, K.S. Klopovskiy, Yu.A. Mankelevich, O.V. Proshina, A.T. Rakhimov, T.V. Rakhimova

119899, Nuclear Physics Institute, Moscow State University, Moscow, Russia

Non-stationary gas discharge in an AC plasma display panel (PDP) cell is of interest for several reasons. The understanding of complex electrodynamical and plasma-chemical processes in PDP cells is required to design the driving electronic circuits, to enhance UV emission from a weakly ionized plasma and to improve the picture quality. On the other hand, fundamental gas discharge processes and features (the electrical breakdown, cathode fall and quasi-neutral ambipolar plasma formation, plasma decay, charges deposition on the dielectric layers) are appeared in operation of an AC PDP cell. In addition, the effects of non-locality and non-stationarity of electron energy distribution function are important for electrodynamics and plasma kinetics of considered discharges because of the dimensions of a few hundred microns and gas pressure of a few hundred Torr. Standard approaches commonly used for RF and DC discharge simulations may be inapplicable for a PDP cell plasma.

In this report the developed hybrid one dimensional model of the AC PDP cell discharge is presented. The calculated discharge dynamics are given and compared with the results of drift-diffusion modeling. The conservation equations for plasma-chemical species in 10%Xe/Ne mixture and Poisson equation for electric field were self-consistently solved in the 1D model. Chemical kinetics system and discharge geometry were chosen similar to [1] (the distance between flat electrodes 100 μm , gas pressure 300 Torr, gas temperature $T=300\text{K}$). 1D hybrid model has been developed to study the electrical and optical properties of an AC PDP cell. Electric field in the discharge is substantively varied both in time and space. In operation, cathode fall are formed with the typical length at 10 μm and reduced electric field of about 10^3 Td.

Electron energy relaxation length in this region is comparable with characteristic length of electric field variation. At the boundary of cathode fall region and adjacent low field region high energy electron beam with anisotropic angle distribution are appeared. The ionization ability of these electrons cannot be related with local field. So, in our hybrid model we have divided electrons on two groups - "fast" and "slow". Fast electrons motion and relaxation are determined by solving non-stationary Boltzmann equation taking into account non-locality of EEDF. Boltzmann equation are

solved using Monte-Carlo particle in cell method (MC PIC). Slow electrons as well as ions are described in drift-diffusion approach (DDA). Charge particles balance equations and neutral species concentrations equations are self-consistently solved with Poisson's equation for electric field. Fast electrons pass in a slow electron group if two conditions are simultaneously realized $|E(z)| < E_{tr}$, $\varepsilon < \varepsilon_{tr}$. Here $E(z)$ is an electric field in the point - z , ε is an electron energy. The threshold electric field - E_{tr} is chosen according to a representation of all electrons in high electric field region as the fast ones. The energy threshold - ε_{tr} is found to be close to the lowest threshold of inelastic processes. The pulse discharge calculations by using the hybrid model are started beginning from the initial gap voltage - 273.5 V as it was done in [2]. The voltage as well as the secondary electron emission coefficients are chosen the same as in [2]. Time and spatial behavior of reduced electric field and electron, ion Xe^+ and Ne^+ densities calculated by using hybrid model are shown in Fig. 1-3 respectively. As it is seen before time $t_1 = 420$ ns the field is still uniform and is not distorted by the charge particle densities. The ion density grows and starts to decrease the field on the anode side. To $t_2 = 490$ ns quasineutral plasma occupies almost all right (anode) half of the discharge. Moment $t_3 = 509$ ns corresponds to maximum of the current density. Electric field at that time has a typical DC glow discharge cathode sheath with the length of about 10 μm with maximal reduced electric field of about 1400 Td at the left dielectric surface ($z = 0$) and the quasineutral plasma region with the field close to zero. After this moment the field starts to reduce and cathode fall starts to decay due to the charging of dielectric layers. At time $t_4 = 514$ ns maximal electric field in the cathode fall drops to 400 Td and the voltage across the gap is equal 18 V. The discharge fastly decays.

To estimate the effects of non-local discharge properties the same discharge has been simulated using drift-diffusion model (DDM). Electron rate coefficients and other parameters were calculated by solving the Boltzmann equation in two-term approximation for a required range of reduced electric field.

The first significant difference of DDM calculations from hybrid model is the time of discharge breakdown development. The maximal current density is reached

at $t=190\text{ns}$, that is 2.5 times shorter than in hybrid model. This is connected with higher ionization rates calculated for the local field in DDM. As a result, the discharge proceeds more intensively. Maximal value of reduced electric field in cathode sheath in DDM is higher (about 2000Td). Therefore the maximal ions density in DDM is two times higher than in hybrid model. On the other hand the electron density in DDM is about two times lower than in hybrid model. This result deals with non-local effects. Temporal-spatial Xe^+ distributions calculated in hybrid model and DDM were shown in Fig.3 and Fig.4 respectively. Figures show two maxima in ion distribution. The second maximum of ion concentration in Fig.4 deals only with transient discharge features and is three times smaller than in Fig.3.

Thus, the simulation results show a substantial difference between DDM and hybrid model, related with non-local effects. As a result, the redistribution of input power between ion and electron components is different in these models. It defines the different kinetic of Xe^+ atoms and Xe_2^+ dimers, which determines VUV emission from PDP cell plasma.

The work is supported by the Russian Foundation of Fundamental Research (grant 96-02-18770).

References

- [1]. L. F. Weber :Flat Panel Displays and CRT's, ed. by L. E. Tannas, Jr. (Van Rostand Reinhold, New York, 1985), p. 322.
- [2]. J. Meunier, Ph. Belenguer and J. P. Boeuf : J. Appl. Phys. 78(2) (1995) 731.

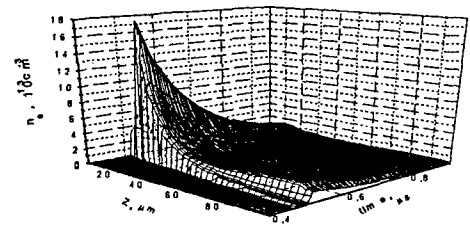


Fig.2

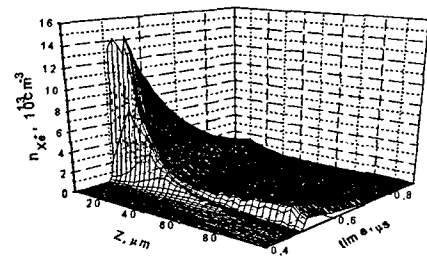


Fig.3

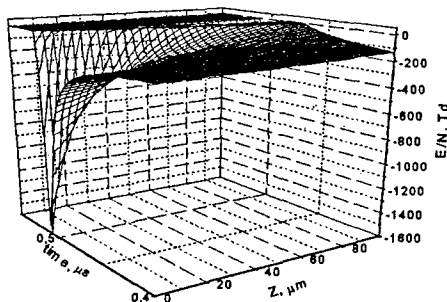


Fig. 1

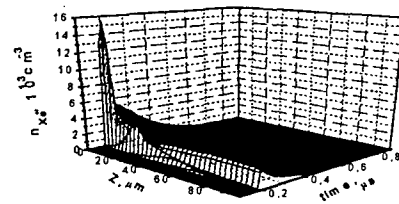


Fig.4

Pulsed Corona in an Electrostatic Precipitator Configuration

W.Egli*, U.Kogelschatz* and E.Gerteisen**

* ABB Corporate Research Ltd., 5405 Baden, Switzerland

** CSCS/SCSC, Swiss Center for Scientific Computing, 6928 Manno, Switzerland

1. SUMMARY

Many modern electrostatic precipitators (ESPs) use pulsed or intermittent energization in which a transient corona discharge is utilized for particle charging and precipitation. The time dependent solutions for the electric field and ion distribution are presented for a classical ESP configuration. We treat the dynamics of the transient ion motion by switching the applied voltage between levels above and below corona onset for the given electrode configuration. As a consequence of corona quenching the onset level is raised by the presence of additional space charge due to charged particles in the volume.

2. INTRODUCTION

A geometry bounded by two plane grounded collecting plates with parallel equidistant wires at negative high voltage in the center plane is considered [1-4]. The understanding and simulation of the full dynamics of transient coronas are considered as essential tools for improved ESP design and energization. A first attempt where the corona was modulated by switching the emission at constant applied voltage was presented in [3]. The considered geometry, simpler ones were considered in [5], consists of a plane channel configuration with straight walls Γ_2 , with one high voltage electrode Γ_1 placed in the symmetry line and the computational domain Ω , respectively the half plane between the electrode and the wall.

3. GOVERNING EQUATIONS

For simplicity we assume that the ion current flow is essentially determined by one major species of negative ions. With this simplification the ion drift region can be described by the following equations:

$$\nabla \cdot \mathbf{E} = \frac{(\rho + \rho_p)}{\epsilon}, \quad (1)$$

where ϵ , μ are the permittivity and the ion mobility, and \mathbf{E} , ρ , ρ_p are denoting the electric field vector, ion charge density and particle charge density respectively. The (eq.1) is closed by the potential relation $\mathbf{E} = -\nabla\Phi$. The boundary conditions are $\Phi=0$ at the collecting plates and $\Phi=-U$ at the surface of the corona electrode. The unsteady continuity equation for the current is given by the physical law of conservation of charge and together with the particle velocity vector it becomes:

$$\frac{\partial \rho}{\partial t} + \nabla \cdot \mathbf{j} = 0, \quad \mathbf{j} = \rho_i \mu \mathbf{E} + \rho_p \mathbf{v}_p \quad (2)$$

The contribution of the particle movement to the electrical current is neglected.

The boundary conditions for the potential are $\Phi=0$ at the collecting plates and $\Phi=-U(t)$ at the surface (Γ_1) of the corona electrode. The corona is described by the approximation [2]. With $\rho(t, \mathbf{x})$ being the negative ion space

charge density at the wire surface Γ_1 , the thickness of the corona layer being $L(\mathbf{x})=L(\Gamma_1)$ at the wire surface and with the effective ionization coefficient $\bar{\alpha}(E(L))$, the boundary and initial conditions become:

$$\left. \begin{aligned} \rho(t, \mathbf{x}) &= c(e^{\bar{\alpha} L} - 1), & t > 0 \\ \rho(t, \mathbf{x}) &= 0, & t \leq 0 \end{aligned} \right\}, \text{ at } \Gamma_1 \quad (3)$$

$$\rho(t, \mathbf{x}) = 0, \quad t \leq 0, \quad \text{in } \Omega$$

The voltage pulse applied is defined as:

$$\begin{aligned} U(t) &= U_1, & 0 < t \leq t_1 \\ U(t) &= U_2, & t > t_1 \end{aligned} \quad (4)$$

where t_1 constitutes the pulse length.

4. SOLUTION METHOD

The 2D computational domain (Fig.1-4) is discretized by four structured mesh blocks with matching grid points at internal boundaries. The timewise discretization is carried out by equidistant time steps

$$t_i = i \cdot \Delta t, \quad 0 \leq i \leq n \quad (5)$$

At each time t_i the electric field distribution \mathbf{E}_i and the consistent distribution of the space charge density ρ_i can be found by solving the equation (eq. 1-2) together with the boundary conditions (eq. 3-4). For the computation of the space charge ρ (eq.2) is transformed into the canonical form,

$$\frac{\partial \rho}{\partial t} + \mu \mathbf{E} \cdot \nabla \rho = f(\rho), \quad (6)$$

$$\frac{dx}{dt} = \mu \mathbf{E} \quad \text{along a characteristic line}$$

and the space distribution of ρ is computed by the characteristic method, i.e. integration along the characteristics that essentially correspond to the electric field lines. These are time dependent and therefore the computation of the space charge at time t_i must be expressed by some additional time delay relation. The integration of $f(\rho)$ can be expressed analytically according to [6] by

$$\rho(t_i, \mathbf{x}_1) = \frac{\rho(t_i - \tau, \mathbf{x}_c) \cdot Q_p e^{-\mu/\epsilon \cdot Q_p \tau}}{Q(t_i - \tau, \mathbf{x}_c) \cdot (1 - e^{-\mu/\epsilon \cdot Q_p \tau}) + Q_p} \quad (7)$$

Hereby, the field line is specified by the point \mathbf{x}_1 , which actually represents a mesh point, and it ends at Γ_1 referred to as \mathbf{x}_c . The travel time for the point (\mathbf{x}_1) is specified by

$$\tau = \sum \frac{|\Delta \mathbf{x}|}{\mu \|\mathbf{E}\|} \quad (8)$$

according to the canonical form (eq. 6) of the continuity equation

5. RESULTS

A first case (I) is introduced to demonstrate the response of field distribution and ion motion to a voltage pulse of

$t_1=0.3\text{ms}$, where the voltage peak $U_1=76\text{kV}$ and the corona turn off voltage $U_2=38\text{kV}$ are specified. The discrete time step Δt is set to 0.05ms . The space charge has the maximum in the front of the propagating ion cloud. The highest value of the electric field occurs at the high voltage electrode and at the initial time, $t=0$, where no space charge is in the volume (Laplace field). As a consequence of the decreasing field and the assumed constant ion mobility the drift velocity at the front of the ion cloud is always smaller than that at the rear edge (Fig. 1, Fig. 3). The apparent azimuthal structures of the ring shaped ion cloud are caused by the coarse discretization.

The second case (II) illustrates a situation with substantial corona suppression. The background space charge can originate from particles charged in upstream sections. A homogeneous and constant (in time) space charge density $\rho_p=10\mu\text{As}/\text{m}^3$ is assumed. In this case a moderate decrease of voltage is enough to quench the corona. The voltage drop is set from 76kV to 60kV after the same pulse length as in the first case. The form of the ion

space charge cloud is seriously distorted (Fig. 2). The high electric fields in the whole volume lead to a considerable reduction of ion transit time. Due to space charge effects this time can be shorter than one would expect from the first order $1/U_1$ approximation. High background space charge causes an increase in the electric field close to the collecting plate (Fig. 4).

6. REFERENCES

- [1]: W.Egli, U.Kogelschatz, ICPIG XXII, 1995, 119–120
- [2]: W.Egli, U.Kogelschatz, E.A.Gerteisen and R.Gruber, 8th Int. Conf. on Electrostatics, Poitiers, June 4–8, 1997
- [3]: W.Egli and U.Kogelschatz, Helvetica Physica Acta, 69/Separanda 2, Dec.1996, 37–38
- [4]: A.M.Meroth, R.Gerber, C.D.Munz, A.J.Schwab, VI ICESP, Budapest June 18–21, 1996
- [5]: M.Zahn, IEEE Trans. EI-11(1976), 150 – 157
- [6]: J.E.Jones, J.Phys.D:Appl.Phys.27(1994) 1835–1847

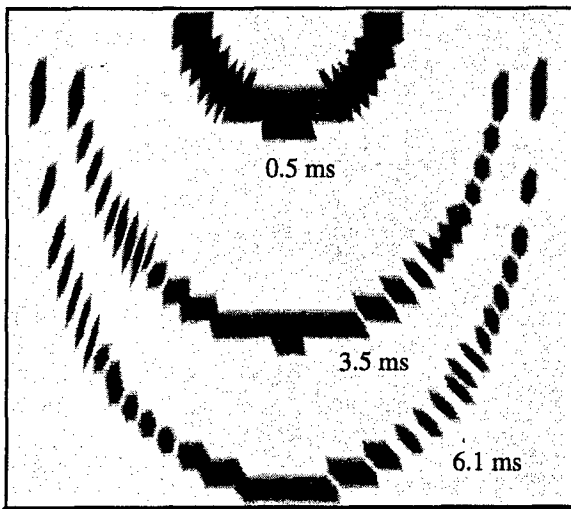


Fig. 1: Ion space charge distribution at different times without particle background charge (case I).

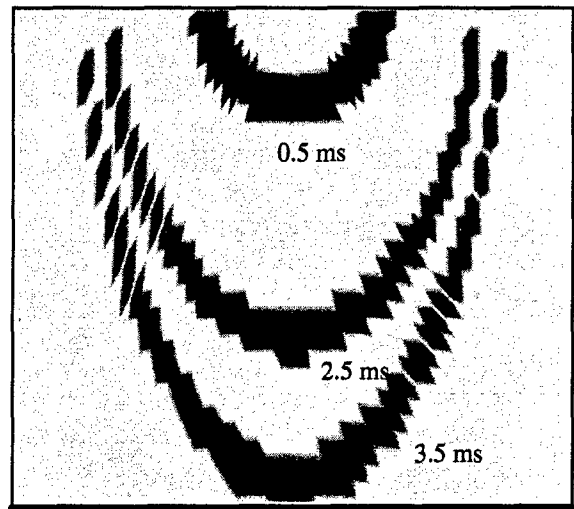


Fig. 2: Ion space charge distribution at different times with particle background charge (case II).

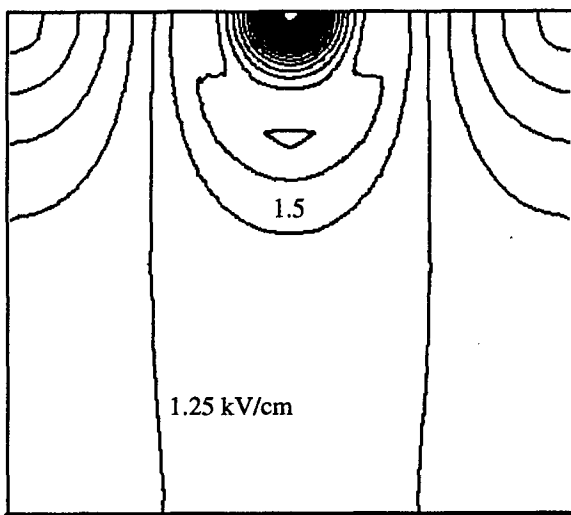


Fig. 3: Electric field distribution $\|E\|$ (case I) at $t=0.5$ ms. Spacing of iso-contours is 0.25 kV/cm

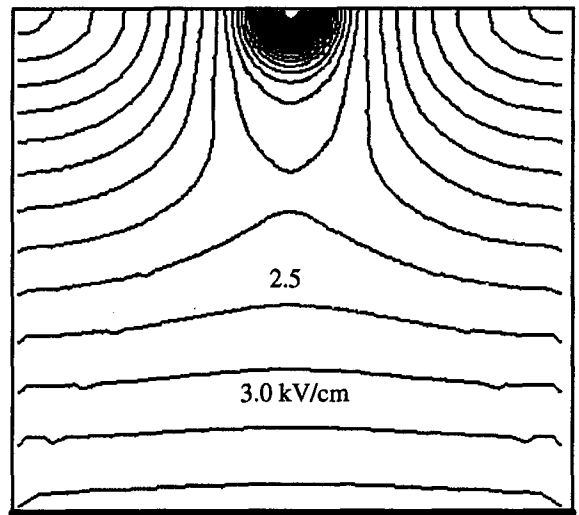


Fig. 4: Electric field distribution $\|E\|$ (case II) at $t=0.5$ ms. Spacing of iso-contours is 0.25 kV/cm

Numerical Simulation of hypersonic air nozzle flow in thermal and chemical non-equilibrium

A. Leroux, P. Domingo, P. Vervisch

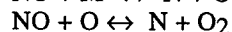
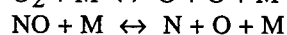
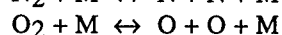
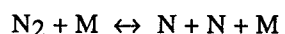
UMR 6614 CNRS CORIA - 76821 Mont-Saint-Aignan Cedex, France

The field of hypersonic aerodynamics has seen a rebirth in the past years due to the proposed development of several hypersonic vehicles (i.e. space shuttle). In particular, the reentry of vehicles in the atmosphere is a challenging problem. Considering the shock induced by the reentry, the gas reaches high temperature. This causes thermal excitation and chemical reactions to occur in the flow.

An experiment was carried out in 1991 by Lionel Robin from the CORIA of Rouen. The measurements were performed on the TT1 nozzle from the TSNIIMACH facility in Moscow. TT1 is a supersonic nozzle that was used in order to simulate the reentry of a vehicle into the atmosphere. The complete experimental facility was built of a supersonic nozzle followed by a jet in which had been placed an oblique climbing step. This step was a model of the protection material surrounding a shuttle.

The scope of this work is to simulate the flow inside the nozzle taking into account both chemical and thermal non-equilibrium. Moreover, the influence of various chemical and vibrational models are to be studied. The available experimental data related to this study are the molar fraction of NO at the exit of the nozzle as well as the velocity and the translational temperature.

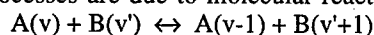
Air is taken as the simulation fluid composed of 5 species which are N_2 , O_2 , NO, N and O. The kinetic scheme is a 17 reactions scheme. Dissociation/Recombination of each molecule and 2 exchange reactions are taken into account:



M being one of the 5 species.

The basic chemistry model, used as a validation of the numerical code is Park's model[1]. Thermal non equilibrium is modeled for each molecule. Thus each molecule is characterized by its own vibrational temperature. Terms contributing to the vibrational non equilibrium can be divided in 3 parts: vibrational energy gained or removed by chemistry (a molecule being removed takes back its vibrational energy), Vibration-Translation (V-T) processes and Vibration-Vibration (V-V) processes.

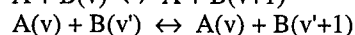
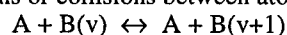
V-V processes are due to molecular reactions such as:



Source terms due to (V-V) collisions are calculated using Candler's expression [2] and supposing that the collision probability is constant and equal to 10^{-2} . It

should be noticed that only monoquantum collisions are considered here.

V-T processes are due to either molecular collisions or collisions between atoms and molecules:



The V-T processes are modeled using Landau-Teller's relaxation formula. The prediction of the relaxation time of this phenomena is an open subject. The first model used in this study is the one of Millikan and White[3].

The system to solve is composed of 11 equations: 5 transport equations for species, 3 equations for the transport of vibrational energy, 2 equations for momentum (x and y direction) and one for the conservation of overall energy. The flow is supposed to be axisymmetric but the numerical code can also solve 2 dimensional problems.

The numerical scheme used to solve these equations is an upwind Non MUSCL TVD scheme based on the work of Yee [4]. The code is explicit/implicit so that it can treat time-accurate as well as steady state calculations.

Two chemistry models have been used in this work. The first one is commonly known as Park's model[1]. This "universal" model is very useful since it can serve as a validation of the code by comparison with other numerical results.

In this model, forward reaction rates k_f are given as Arrhenius laws: $k_f = AT_a^n \exp(-\frac{\theta}{T_a})$

whereas backward reaction rates are obtained using equilibrium constants.

The other chemical model used in this study is based on the works of Krivonosova and Losev[5] and hereafter referred as Losev's model. The 2 models mainly differ on the expressions of the backward reaction rates. It should be noted that they are the most important rates since, in expanding flows, recombination processes are dominant.

Park's model tends to underestimate the values of backward reaction rates at low temperatures. Consequently the recombination processes are underestimated. This leads to underpredicted values for N_2 and O_2 in comparison to Losev's model. On the opposite, the calculated values of N mass fractions seem to be overpredicted with Park's model. The O mass fraction is almost the same with both models.

As far as NO mass fraction is concerned, 2 antagonist processes take place. Using Losev's model should give a higher value of NO due to a more efficient recombination. However, in this flow, NO is mostly produced by the exchange reaction $O_2 + N \leftrightarrow O + NO$.

In Park's model, the mass fraction of N is higher in the divergent part of the nozzle than in Losev's model. Then the amount of N is more important in the case of Park's chemistry and produces more NO than with Losev's reaction rates. Moreover, at low temperatures, (which is the case in the divergent part of the nozzle), the reaction $\text{NO} + \text{N} \leftrightarrow \text{O} + \text{N}_2$ is faster and leads to a larger removal of NO than with Park's model. Calculating the molar fraction of NO at the nozzle exit leads to values of $5.1 \cdot 10^{-3} \text{ mol/m}^3$ according to Park's model and $3.82 \cdot 10^{-3} \text{ mol/m}^3$ according to Losev's model. The experimental data is $3.70 \cdot 10^{-3} \text{ mol/m}^3$ and so Losev's model is closer to the reality than Park's model as can be seen on figure 1 where the mass fraction of NO along the axis of the nozzle is plotted.

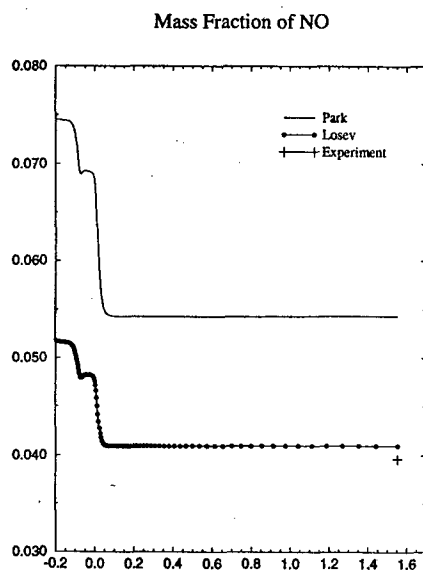


Fig. 1. Mass fraction of NO along the nozzle axis

Vibrational relaxation has also been studied. We focused on the study of relaxation times in V-T processes. Indeed, these relaxation times are highly important in vibrational nonequilibrium but not very well known. In our basic model, relaxation times were those given by Millikan and White [3]. Their work gives quite inaccurate results for atom/molecule relaxation times. In their model, the relaxation times are calculated assuming the same relaxation for atom/molecule collisions and molecule/molecule collision. The other model is based on Makarov's works [6] and gives results close to those of Millikan and White. The last model we tested in our calculations is based on the works of Doroshenko [7]. His relaxation times give vibrational temperatures close to equilibrium values. The vibrational temperature of N_2 along the axis of the nozzle is plotted on figure 2 for the 3 vibrational models. Millikan&White and Makarov's models lead to a complete freezing of the vibration in the divergent part of the nozzle whereas Doroshenko's model tend to place vibration close to equilibrium.

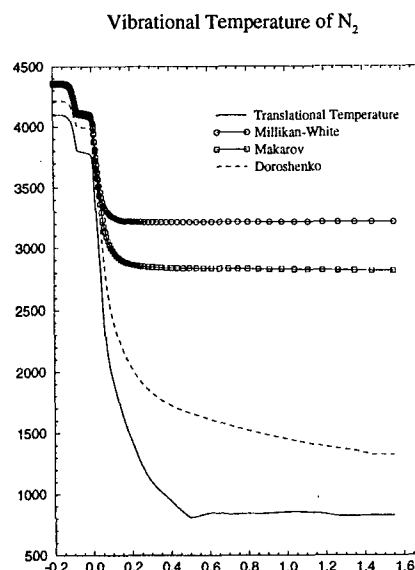


Fig. 2. Vibrational temperature of N_2 along the nozzle axis

The calculated velocity at the exit of the nozzle (3030 m/s) is fairly correct compared to the measurements (3275 m/s). However, none of the models implemented so far is able to correctly predict the translational temperature. As can be seen on figure 2, the calculated temperature is close to 800 K whereas the experimental value is around 1200 K. This discrepancy has also been seen in other nozzles where the experimental temperature is close to an equilibrium value. This problem is still under investigation.

In this work, we have tested different models to better understand the physics of flows expanding in nozzles. 2 chemical and 3 vibrational models have been implemented. The results given by a new chemistry model seem to give results closer to experimental data.

- [1] C.Park: AIAA Paper (89-1740) 1989
- [2] G.V Candler: PhD Thesis, Stanford (1988)
- [3] R.C Millikan and D.R White: Journal of Chemical Physics, **39**(12) 1963
- [4] H.C. Yee: Journal of Computational Physics, **68** (1987)
- [5] Krivonosova, Losev: Review of Plasma Chemistry, **1** (1991)
- [6] V.N Makarov: High Temperature, **33**(4) 1995
- [7] V.M Doroshenko, N.N Kudryatsev and V.V Smetanin: Moscow Physics and Technology Institute, **29**(5), April 1991

Solution of the Fokker-Planck Equation for azimuthally-symmetric 2V-distribution function using splitting scheme

Konstantin V. Telegov and Vadim D. Levchenko

M.V.Keldysh Institute of Applied Mathematics, Miusskaya Square 4, Moscow 125047, Russia

Abstract

The paper contains description of a numerical solution of the Fokker-Planck Equation for the azimuthally-symmetric in momentum space distribution function of electrons. The presented calculations are based on the successive splitting technique using divergent scheme. As an example the code is applied to the problem of the Coulomb scattering of a spatially uniform monochromatic beam of charged particles, in their passage through field charged particles with Maxwellian distribution function. We study the relation between the distribution function and its velocity moments, as well as the mean value of slowing-down time, obtained in [1],[4] and in our numerical consideration.

1. Introduction

Paper [1] describes a method of obtaining the implicit formula for the distribution function of charged particles which diffuses in a plasma. The distribution function in velocity, angle and time is presented on the base of the Fokker-Planck equation solution. Temperature, average velocity and energy of charged particles are also calculated as functions of time.

In their passage through matter electrons or fast charged particles lose energy and change direction by multiple interactions with field particles. The dominant slowing-down effect is the Coulomb scattering of beam (test particles), interacting with charged field particles. In our model we use the spatially uniform monochromatic beam of charged particles, moving through field charged particles with Maxwellian distribution function (in contrast to δ -shaped distribution function, used in [1]). We also disregard the 'test particle-test particle' interactions because the ratio between the density of test particles and field particles is supposed to be small. The test particles slow down starting from fast velocities, while the field particles are assumed to be given. No external forces act on the test particles.

Our purpose is to define the time-behavior of the distribution function of passing beam. We study accordance of directly obtained behavior of momentum, energy, temperature in time and value of slowing-down time with our numerical solution. We check also preservation of total charge of test particles to examine the accuracy of our method.

2. Mathematical model

The considered problem is subjected to Fokker-Planck (FP) formulation. The collision term of FP equation can be written in the following divergent form:

$$\frac{1}{\Gamma_\alpha} I_\alpha^{col} = -\nabla^i \left(f_\alpha \nabla_i H_\alpha + \frac{1}{2} \nabla^j (f_\alpha \nabla_i \nabla_j G_\alpha) \right); \quad (1)$$

where coefficients of friction ∇H_α and diffusion $\nabla \nabla G_\alpha$ can be calculated in terms of the Trubnikov-Rosenbluth potentials [2-3].

Adding the initial distribution of each species of particles and boundary conditions we come to total formulation of the problem.

In our case $f_\beta = A \exp\left(-\frac{p^2}{2}\right)$ and $\int f_\beta d\vec{p} = n_\beta$, where A and B can be found from the normalization condition: $f_\alpha(0) = B\delta(\vec{p}' - \vec{p})$ and $\int f_\alpha(0) d\vec{p} = n_\alpha$ consequently. Boundary condition is $f_\alpha(p_{max}) = 0$. We use adimensional form of FP equation. Momentum is measuring in units of initial momentum p_0 , adimensional time t^0 is $n_\beta e^4 Z_\beta^2 m_\alpha / p_0^3 t$.

Let us introduce spherical axially-symmetric coordinates $p = |\vec{p}|$, ψ ; here ψ is the angle between current momentum and initial momentum directions. Then we can rewrite (1) in the form (taking into account independence of G_α, H_α on ψ):

$$\begin{aligned} \frac{2p^2}{\Gamma_\alpha} I_\alpha^{col} &= -\frac{\partial}{\partial p} [p^2 W_\alpha] + \frac{1}{\sin \psi} \frac{\partial}{\partial \psi} [\sin \psi U_\alpha]; \\ W_\alpha &= \frac{\partial^2 G_\alpha}{\partial p^2} \frac{\partial f_\alpha}{\partial p} - 2 \frac{\partial H_\alpha}{\partial p} f_\alpha; \\ U_\alpha &= \frac{1}{p} \frac{\partial G_\alpha}{\partial p} \frac{\partial f_\alpha}{\partial \psi}. \end{aligned} \quad (2)$$

3. Numerical scheme

The presented Numerical solution is based on the successive splitting technique [5-7]. For splitting of equation (2) one can use (at the time step n) the scheme of splitting as follows.

$$\frac{1}{\Gamma_\alpha} \frac{f_\alpha^{n+1/2} - f_\alpha^n}{\Delta t} = L^p f_\alpha^{n+1/2}; \quad (3)$$

$$\frac{1}{\Gamma_\alpha} \frac{f_\alpha^{n+1} - f_\alpha^{n+1/2}}{\Delta t} = L^\psi f_\alpha^{n+1/2}. \quad (4)$$

where L^p, L^ψ are operators, defined on (i, j) -net in the momentum-angle space. Each of the above schemes (3,4) is solved with the sweep method.

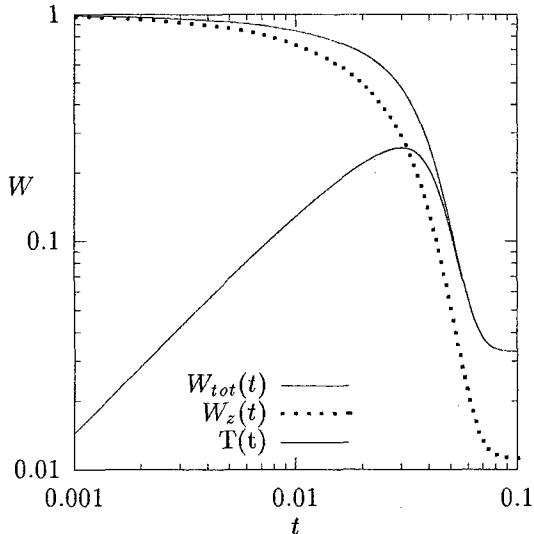


Fig 1. Time dependence of test particles' kinetic energy W and temperature T .

4. Results

We checked conservation of total charge of test particles via calculation on each time step the normalizing integral $\int f_{\alpha} d\vec{p} = n_{\alpha}$ in the same form that we had used for developing our splitting scheme: $\sum_{i,j} f_{ij}^{\alpha} d0p_i d0\psi_j$. Total charge does not keep strictly constant value due to our right-hand boundary condition, $f_{\alpha}(p_{max}) = 0$.

We calculate the time-behavior of 'parallel' (along the z axis) momentum p_z , W_z , temperature T and total energy W (in units of p_0^2) in time by calculation of appropriate integrals $p = \int f_{\alpha} p d\vec{p}$, $W = \int f_{\alpha} p^2 d\vec{p}$ and $T = \int f_{\alpha} (\vec{p} - \langle \vec{p} \rangle)^2 d\vec{p}$ in accordance with formulae $\sum_{i,j} f_{ij}^{\alpha} p_i d0p_i d0\psi_j$, $\sum_{i,j} f_{ij}^{\alpha} p_i^2 d0p_i d0\psi_j$ and $\sum_{i,j} f_{ij}^{\alpha} (p_i^2 + \langle \vec{p} \rangle^2 - 2p_i \langle \vec{p} \rangle \cos \psi) d0p_i d0\psi_j$ respectively (Fig.(1)). One can see that we got picture which is completely adequate to [1] for momentum. As to energy and temperature there are some difference. As it is known, the test particles obtain after relaxation the same temperature as the field ones. In our case the field particles have nonzero temperature. So one can see that our curve tends to stationary solution.

The time-behavior of distribution function of test beam particles is shown on Fig. (2).

At last we checked dependence of the slowing-time τ on the initial energy/momentum value which is $\tau \sim E_0^{3/2}$ (see [3], [4]). Due to this relation slower particles relax faster than particles with higher energy. It leads to 'two-hump' distribution function. Numerical solution confirms this dependence (see Fig. (2)).

We have tested our solution for various values of time-, momentum- and angle-step. We found that our solution is stable and accurate for the chosen set of parameters.

References.

- [1] V.G.Molinari and S.Manservigi: Il nuovo cimento. **14** (1992) 9.
- [2] M.Rosenbluth and C.S.Liu: Phys.Rev.Lett., **29** (1972) 701.
- [3] B.A.Trubnikov. Particle interaction in a fully ionized plasma: Consultants Bureau, New York, (1965) 105.
- [4] V.G.Molinari and S.Manservigi: Nuclear science and engineering, **112** (1992) 296.
- [5] I.F.Potapenko, V.A.Chuyanov: Sov. J.V.M.&M.Ph. **22** (1982) 513.
- [6] J.Killeen, A.A.Mirin and M.E.Rensink, in Controlled Fusion, ed by J.Killeen: Methods in computational physics, v.16. Academic Press, (1976) 419.
- [7] G.I.Marchuk. Methods of splitting. Nauka, Moscow (1988).

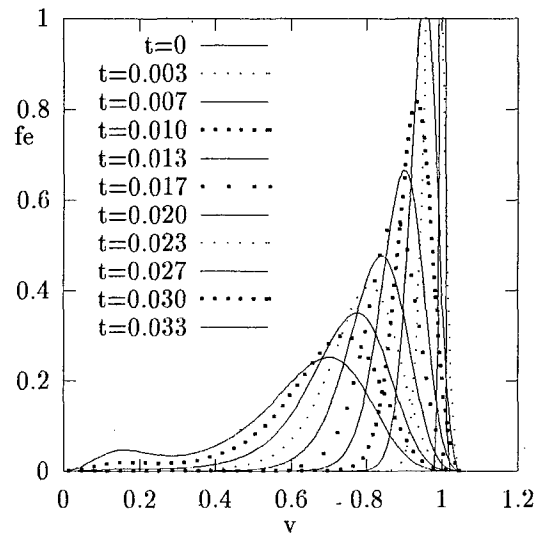


Fig 2. Distribution function profiles $f(p)$ for several time moments.

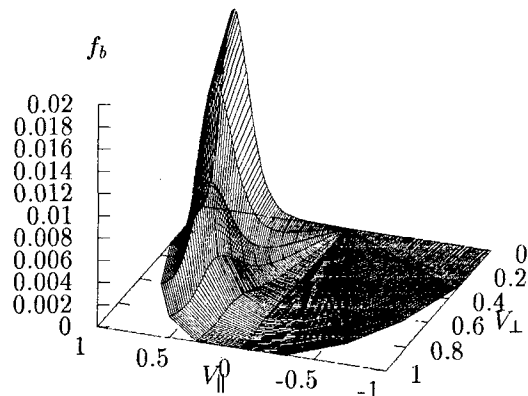


Fig 3. Distribution function $f(p, \psi)$ time moments $t = 0.02$.

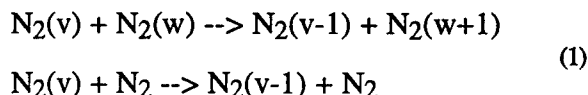
Direct Simulation Monte Carlo modeling of vibrational relaxation

D. Bruno*, M.Capitelli*, M.S.Ivanov**, S.Longo*

* Centro di Studio CNR Chimica dei Plasmi and Dipartimento di Chimica dell'Università, Via Orabona 4, Bari, Italy

** Institute of Theoretical and Applied Mechanics, Novosibirsk, Russia

The inclusion of a real state-to-state vibrational kinetics is a challenge for modern fluid dynamics, in the attempt to describe accurately strongly non-equilibrium systems such as the airflow near a reentry body or hypersonic vehicle, or the gas flow inside a plasma processing reactor. In this work we want to show the possibility to take into account a realistic description of the time-dependent kinetics of the vibrational manifold of a molecular gas (nitrogen) by using a particle approach specially suitable for fluid dynamics problems, i.e. the Direct Simulation Monte Carlo (DSMC) method [1]. This method has been considered as an alternative to continuum fluid dynamics in order to treat complex flow field, for example in shock wave and reentry airflow near flight control structures of spaceships. Despite the potential capabilities of state-to-state direct description of the chemical kinetics offered by this method, phenomenological models for internal state kinetics has been applied to this method as a rule (e.g the Larsen-Borgnakke model [1]). The kinetic scheme considered in this work includes VV (vibration vibrationa) and VT (vibration-translation) energy relaxation processes, i.e.



The relative probabilities for different processes have been calculated by using the following equations [2]

$$\begin{aligned} p_{i \rightarrow k}(g_i) &= b_{i \rightarrow k}(g_i) g_k^2 \\ \sum_k b_{k \rightarrow i}(g_k) g_k^2 &= 1 \\ b_{i \rightarrow k}(g_i) &= b_{k \rightarrow i}(g_k) \end{aligned} \quad (2)$$

where g_i is the relative velocity of the colliding molecules in the i -th internal state. This approach ensures fulfillment of the detailed balance principle. The total collision frequency is calculated according to the rigid-sphere model. We have modified this formulation in order to get a more realistic fitting of the real rate coefficients keeping the fulfillment of detailed balance. The resulting values for the coefficients b_k which enter into the expression (2) of $p(i \rightarrow k)$ can be written as follows:

$$\begin{aligned} b \left(\begin{matrix} v \rightarrow v+1 \\ w \rightarrow w \end{matrix} \right) &= (v+1) \alpha(E_{TOT}) \\ b \left(\begin{matrix} v \rightarrow v+1 \\ w \rightarrow w-1 \end{matrix} \right) &= w(v+1) \mu_{VV} \alpha(E_{TOT}) \\ b \left(\begin{matrix} v \rightarrow v \\ w \rightarrow w \end{matrix} \right) &= \mu_{eI} \alpha(E_{TOT}) \end{aligned} \quad (3)$$

where v is the number of vibrational quanta, μ_{VV} and μ_{eI} two coefficients used to scale VV and TT relaxation times with respect to the VT one, and α a normalization coefficient which depends only on the total energy. The value of μ_{VV} has been selected to approximately reproduce the results of Billing [3] for the state-to-state *ab initio* calculations of the VV rate coefficients. The nitrogen gas is treated as a gas of anharmonic oscillators, using a Morse potential law.

We have applied the model to the vibrational relaxation of a homogeneous pure nitrogen gas with a number density $N = 10^{17} \text{ cm}^{-3}$, assuming as initial conditions a Boltzmann distribution at $T_v = 8000 \text{ K}$ for the vibrational states, and a Maxwell distribution at $T_t = 1000 \text{ K}$ for the molecular

velocity. The simulated ensemble included 50000 molecules. In the early stage of relaxation the shape of the vdf departs from the equilibrium Boltzmann distribution specially in the high v region due to VV relaxation processes. This phenomenon is connected with the global non-equilibrium state of the gas (two very different temperatures) and the anharmonicity of the oscillators. In figure 1 it is shown the time evolution of the vdf: one can observe that the tail of the vdf (high v) very rapidly increases by order of magnitudes with respect to the equilibrium one. These results closely follow those reported by Cacciatore et.al. [4] by using a standard master equation approach. The first part of these distributions follows a Treanor's law as can be noted by comparing the vibrational 'temperatures' $T_{k,k+1}$ defined as

$$T_{k,k+1} = (\epsilon_{k+1} - \epsilon_k) / \ln(N_k / N_{k+1}) \quad (4)$$

with the corresponding ones obtained by the Treanor's theory. The results for T_{34} is reported in fig.2, and one can see that, apart from strong oscillations due to statistical fluctuations, the two approaches give similar results. Our results illustrate the possibility of describing the vibrational relaxation of pure nitrogen gas in strongly non-equilibrium states by using the DSMC method, provided a large ensemble of molecules is considered in the simulation.

Acknowledgement

This work was partially supported by ASI (Agenzia Spaziale Italiana)

References

- [1] G.A.Bird, "Molecular gas dynamics and the direct simulation of gas flows", Clarendon Press, Oxford (1994)
- [2] S.M.Dunn, J.B.Anderson: J.Chem.Phys. 99 (1993) 6607

- [3] G.D.Billing, in "Nonequilibrium vibrational kinetics", ed. M.Capitelli, Springer-Verlag,Berlin (1986)
- [4] M.Cacciatore et al., in "Nonequilibrium vibrational kinetics", ed.M.Capitelli, Springer-Verlag, Berlin (1986)

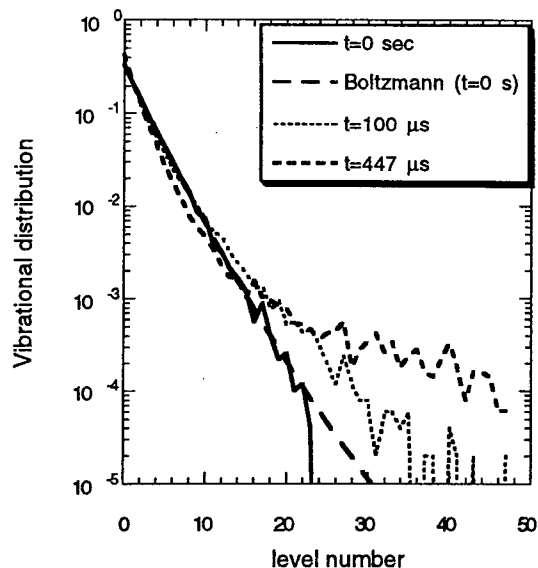


Fig.1 Vibrational distribution function as a function of time resulting from the DSMC model

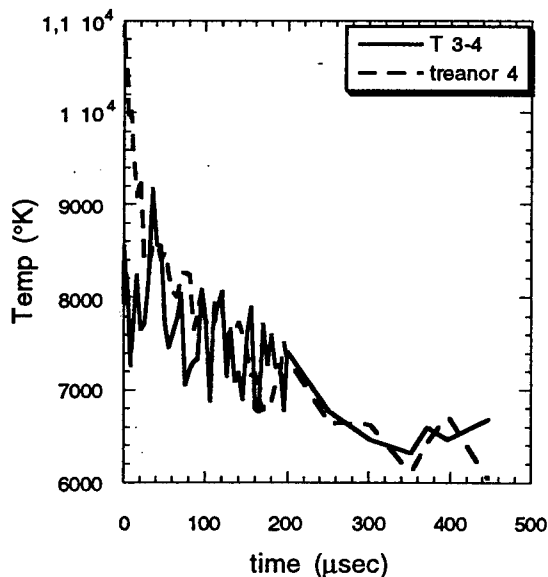


Fig.2 Comparison of the T_{34} temperature (see text for definition) resulting from the DSMC model and calculated according to Treanor's theory from the T_{01}

Numerical modeling of a fast-axial-flow CO₂ laser

F. SI-SERIR, D. LOUHIBI and A. E. MOKHTARI

Laboratoire des Lasers et Applications, Centre de Développement des Technologies Avancées
128, Chemin Mohamed Gacem, B.P.245, El-Madania, Alger, Algérie

1. Introduction

High-power CO₂ lasers are increasingly used in industrial tasks such as cutting, drilling, welding and thermal treatment of materials. In this contribution, a six-temperature kinetic model in the case of a CO₂/N₂/He/H₂O gas mixture is used to predict the performance of a fast-axial-flow CO₂ laser, pumped by a longitudinal electrical discharge. Numerical predictions are compared with experimental results obtained [1].

The model consists of a set of eight coupled differential equations [2] describing the evolution, along the discharge tube axis, of five vibrational temperatures in addition to the gas kinetic temperature and the light intensities of the two counter-propagating waves. It takes into account the effects of electrical excitation, VT and VV collisional relaxation, thermal energy transport and light intensity amplification inside the medium.

Using a numerical method to solve the system, we deduce the distribution of important parameters such as gas temperature, gain and light intensity. Conclusions are also drawn on the gain saturation process which reflects an inhomogeneous type of line broadening at low-level intensities.

The state of the active medium can be described by the population on five vibrational modes : the three normal modes v_1 (symmetric), v_2 (bending) and v_3 (asymmetric) of CO₂, the N₂ vibrational mode and the H₂O bending mode. They will be denoted by s, b, a, n and w, respectively.

The modeled cavity configuration is displayed on Figure 1. We will determine the vibrational populations, the gas temperature T and the light intensities I^+ and I^- of waves propagating in both directions inside the cavity as a function of z, neglecting the dependence of these parameters on radial coordinates [3].

2. Description of the model

Notations

The population distribution inside each vibrational mode β can be described by a Boltzmann factor $\beta = \exp(-h\nu_\beta/kT_\beta)$. ν_β represent the mode frequency and T_β its vibrational temperature. For a given vibrational level, the population distribution over the rotational sub-levels is determined by the gas kinetic temperature T. In our simulation, we consider the laser transition P(20) in the 001→001 band.

The gas mixture proportions are denoted by f_c , f_n , f_h and f_w . At the tube entrance, the gas flow velocity is v_0 , the temperature is T_0 and the pressure is P_0 . The pressure is supposed to be constant along the discharge tube. N_i represents the number density of particle i ($i=c,n,h,w$). N_s , N_b and N_a represent the number densities for the three CO₂ vibrational modes.

Other Boltzmann and energy defect factors present in the set of equations are :

$$\bar{b} = \exp(-h\nu_b/kT), \quad \bar{n} = \exp(-h\nu_n/kT), \quad \bar{w} = \exp(-h\nu_w/kT), \\ D_{\alpha,\beta} = \exp[-h(\nu_\alpha - \nu_\beta)/kT].$$

$R_{\alpha\beta}$ (resp. R_α) represent VV (resp. VT) transition rates due to collisions between molecules [4]. Γ is the stimulated emission rate. U_β represent the electrical pumping rates. F_e is the gas discharge direct heating rate. C_i is the specific heat of specie i at constant pressure. α is the gain per unit length in the gas medium.

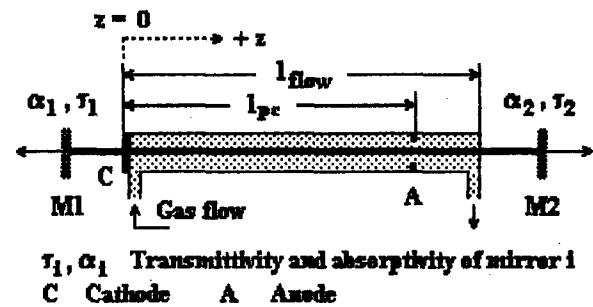


Figure 1 Geometry of the modeled fast-axial-flow CO₂ laser

The model

The set of coupled differential equations describing the evolution of the five Boltzmann factors, of the gas temperature T and of the light intensities I^+ and I^- reads :

$$\frac{v}{(1-a)^2} \frac{da}{dz} = R_{an} \frac{(nD_{a,n}-a)}{(1-n)(1-a)} + R_{aw} \frac{(wD_{a,w}-a)}{(1-w)(1-a)} \\ + R_{ab} \frac{(b^3 D_{a,b}-a)}{(1-b)^3 (1-a)} - (1-a)(1-s)(1-b)^2 \Gamma + U_a \quad (1)$$

and similar equations for s, b, n and w (2) - (5)

$$\frac{N_0}{N_A} (f_c C_c + f_n C_n + f_h C_h + f_w C_w) v_0 \frac{dT}{dz} = \\ -h(\nu_a - \nu_n) N_a R_{an} \frac{(nD_{a,n}-a)}{(1-n)(1-a)} - h(\nu_a - \nu_w) N_a R_{aw} \frac{(wD_{a,w}-a)}{(1-w)(1-a)} \\ - h(\nu_a - \nu_b) N_a R_{ab} \frac{(b^3 D_{a,b}-a)}{(1-b)^3 (1-a)} - h(\nu_s - \nu_b) N_s R_{sb} \frac{(b^2 D_{s,b}-s)}{(1-b)^2 (1-s)} \\ - 2h\nu_b N_b \frac{(\bar{b}-b)}{(1-b)} + F_e \quad (6)$$

$$\frac{dI^+}{dz} = \alpha I^+ \quad \text{and} \quad \frac{dI^-}{dz} = -\alpha I^- \quad (7), (8)$$

At $z = 0$, Boltzmann factors are evaluated on the basis of Boltzmann temperatures equal to the gas

temperature T_0 . The boundary conditions relative to the light intensities I^+ and I^- can be written :

$$I^+(0) = (1 - \alpha_1 - \tau_1)I(0) \text{ and } I(l_{\text{flow}}) = (1 - \alpha_2 - \tau_2)I^+(l_{\text{flow}}) \quad (9)$$

The numerical resolution of the differential equations system has been achieved using a finite-difference method. The used step on the z -axis was reduced until the solution becomes stationary. Our program was built using Matlab environment on a PC computer.

3. Results and discussion

The parameters used for our simulation are given in Table 1. The chosen discharge parameter E/N leads to an optimal electrical energy transfer to the N_2 and CO_2 (a) vibrational modes. The discharge current was set to the maximum value beyond which discharge instabilities appear. It corresponds to a volumetric power density jE of 1.2 W/cm^3 , the gas residence time being 5 ms [2].

Table 1 Operating specifications of the simulated setup

Tube length l_{flow}	60 cm
Positive column length l_{pc}	50 cm
Tube diameter d	5 cm
Cavity mirrors characteristics	
M1 : $\tau_1 = 0, \alpha_1 = 0$	M2 : $\tau_2 = 0.2, \alpha_2 = 0$
Entrance gas mixture pressure P_0	20 Torr
Entrance gas flow velocity v_0	100 m s^{-1}
Entrance gas mixture temperature T_0	293 K
CO ₂ / N ₂ / He / H ₂ O gas mixture proportions	
$f_c = 0.04$ $f_n = 0.4$ $f_h = 0.56$ $f_w = 5 \cdot 10^{-5}$	
Discharge parameter E/N	$3 \cdot 10^{-16} \text{ Vcm}^2$
Discharge current	120 mA

The obtained gas kinetic temperature distribution shows a slight increase from 293 K at $z = 0$ to 294.5 K at $z = l_{\text{flow}}$. Heat dissipation effects can therefore be neglected.

The evolution of the gain per unit length α along the tube axis is displayed on Figure 2. The corresponding overall small-signal gain after one round-trip through the active medium, $\exp[2 \int_0^{l_{\text{flow}}} \alpha_0(z) dz]$, is 4.00.

Figure 3 shows the light intensity distribution for both counter-propagating waves. The output intensity $I_{\text{out}} = \tau_2 I^+(l_{\text{flow}})$ is 21.6 W/cm^2 , leading to a laser output power $P_L = \pi d^2/4 \cdot I_{\text{out}}$, is 424 W. The extracted laser power per unit volume of the active medium is thus 0.36 W/cm^3 . As a comparison, the same parameter in the experimental setup described in [1] is 0.22 W/cm^3 .

In addition to the determination of the operating characteristics of the laser, we have investigated the gain saturation process in the gas medium. It is known that in the case of a homogeneously broadened line, the dependence of the gain saturation ratio α/α_0 on the light intensity I is given by the relation $\alpha/\alpha_0 = (1 + I/I_s)^{-1}$, where I_s is the saturation intensity. α_0/α is plotted as a function of I in Figure 4.

The gain is half its unsaturated value for an intensity $I_{1/2} = 35.4 \text{ W/cm}^2$. One clearly sees that the variation of α_0/α is linear for values of I higher than 50 W/cm^2 , whereas the slope is lower at low intensities. For high-level intensities, the gain behavior fits to a homogeneous type of saturation. The saturation intensity I_s , equal to the slope inverse, is 19.9 W/cm^2 . The curvature at lower values of I indicates that the inhomogeneous character of the line broadening plays an important role. In our mixture conditions, the homogeneous linewidth-FWHM of the laser line Lorentzian profile- due to collisions is 105 Mhz, whereas the Doppler width is 52 Mhz and cannot be neglected, thus.

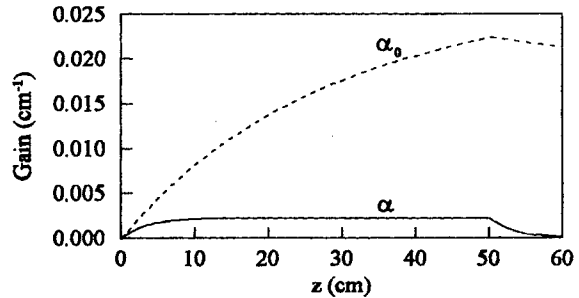


Figure 2 Distribution of the gain per unit length along the tube, in unsaturated (broken line) and saturated regimes (solid line)

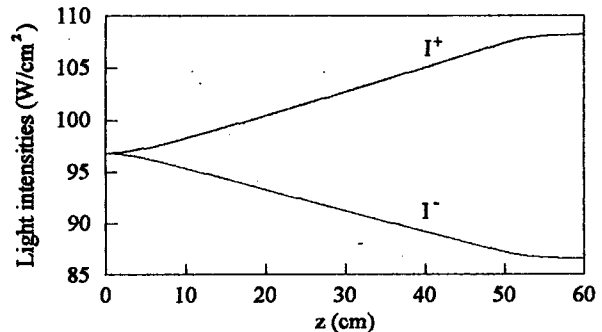


Figure 3 Light intensity distribution for forward (+) and reverse (-) waves inside the tube

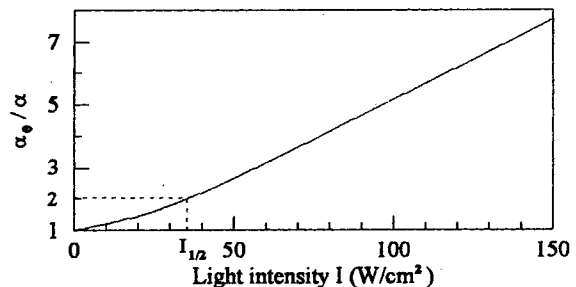


Figure 4 Ratio of unsaturated to saturated gain in the gas medium, as a function of light intensity

References

- [1] H. Sugawara *and al.* : Rev. Laser Eng. 9 (1981) 21
- [2] R.E. Beverly III : Opt. Quant. Elect. 14 (1982) 25
- [3] C. Carlhoff *and al.* : Proc. Gas Flow and Chemical Lasers (New-York : Plenum, 1984) 621
- [4] R.L. Taylor *and al.* : Rev. Mod. Phys 41 (1969) 26

Simulation of Positive Streamer Propagation in Flue Gases

N.Yu.Babaeva and G.V.Naidis

Institute for High Temperatures, Moscow 127412, Russia

Pulsed positive corona discharges in flue gases are actively studied now in connection with their use for gas cleaning from toxic components NO_x and CO_2 [1]. Active particles participating in removal of toxic components are produced in the regions of high electric field – in the heads of streamers propagating in discharge gap. Calculation of the rates of active particle production is of great importance for prediction of the efficiency of pulsed corona for cleaning. In previous works [2]–[4] such calculations have been done with use of one-dimensional (1D) streamer model. In the frame of 1D models the results depend on the choice of the value of streamer radius which is input parameter of the model. More rigorous approach is based on two-dimensional (2D) streamer model. In the present paper the results of 2D simulation of positive streamer propagation in flue gas are given. The G -values (numbers of particles produced per 100 eV of input electrical energy) for the production of primary chemically active components are obtained.

The 2D streamer model is analogous to that used earlier for air and described in detail in [5]. Streamer propagation in sphere-plane gap (the sphere radius $R_{sph} = 0.05 - 0.2$ cm, the ratio of the gap length d to the sphere radius $d/R_{sph} = 5 - 20$) in the mixture $\text{N}_2:\text{O}_2:\text{CO}_2:\text{H}_2\text{O} = 0.71:0.05:0.08:0.16$ at the molecule number density $n_m = 2.5 \cdot 10^{19} \text{ cm}^{-3}$ and the gas temperature $T = 340$ K has been simulated. As it has been shown in [2], the electron energy distribution function (EEDF) in flue gas mixtures is close to the EEDF in air. So in our model for flue gases the rate constants of excitation and dissociation of gas components have been taken calculated with EEDF in air [6]. The data [7] on the nitrogen dissociation rate constant have been used. Ionization coefficient in flue gas has been taken the same as in air, in accordance with [2]. Attachment coefficient in

flue gas differs from that in air, but the role of attachment is not essential for short streamers considered here. The main factor that determines the difference between parameters of streamers in air and flue gases is photoionization: the path length of ionizing photons in flue gases is significantly less than in air due to strong absorption by H_2O and CO_2 molecules. In figure 1 the distributions of the electric field E and the electron number density n_e along the streamer axis z are presented for $R_{sph} = 0.2$ cm, $d = 1$ cm, the applied voltage $U = 14$ kV. The value of electric field in streamer head E_h in flue gas is greater than in air. Correspondingly, the electron number density in streamer channel n_e in flue gas is also greater than in air (correlation of E_h and n_e obtained by 2D simulation agrees with the results of analytical streamer theory, see [5]). The velocity of streamer propagating in flue gas is slightly higher and streamer radius is slightly less than in air (for the same external conditions).

The results of calculation of active particles production by streamers in flue gases show that the dependence of the G -values on external conditions is weak, as in air [8]. The main chemically active components generated in considered mixture are electronically excited nitrogen molecules N_2^* (which produce radicals in collisions with O_2 , CO_2 and H_2O molecules), nitrogen atoms N , oxygen atoms in ground state $\text{O}(^3\text{P})$ and in excited state $\text{O}(^1\text{D})$. Calculated G -values for production of these components are: $G_{\text{N}_2^*} = 1.39 - 1.55$; $G_{\text{N}} = 0.34 - 0.38$; $G_{\text{O}(^3\text{P})} = 0.33 - 0.37$; $G_{\text{O}(^1\text{D})} = 0.16 - 0.19$.

It is interesting to compare the relations between G -values obtained by 2D modeling and estimated with use of simple analytical relations. In [8] for the ratio of G -values corresponding to production of particles of sorts i and j in reactions with high enough energy thresholds (when particles are generated main-

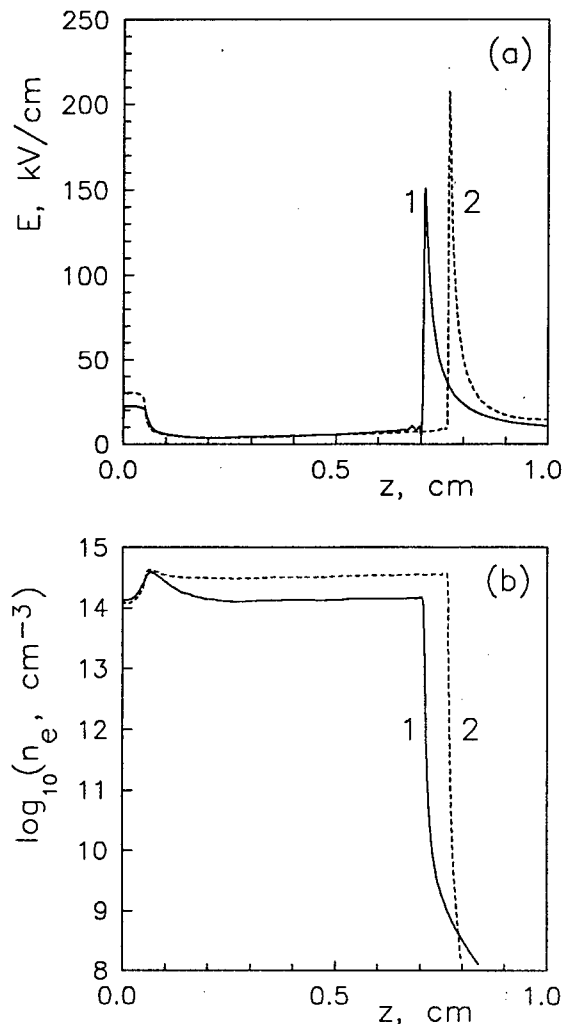


Figure 1: Electric field (a) and electron number density (b) distributions along the streamer axis for air (lines 1) and flue gas (lines 2).

ly in streamer head) the expression has been obtained:

$$\frac{G_i}{G_j} = \frac{\int_{E_c}^{E_h} \alpha_i(E) dE}{\int_{E_c}^{E_h} \alpha_j(E) dE}. \quad (1)$$

Here α_i is the reaction rate coefficient in given gas mixture ($\alpha_i = \sum x_l K_{li}(E)/V_{dr}(E)$, where x_l is the relative concentration of molecules of sort l in the mixture, K_{li} is the reaction rate constant for the production of particles i in collisions of electrons with molecules l , V_{dr} is the drift velocity of electrons). The upper limit of integrals in (1) is the maximal value of electric field in the streamer head E_h , the lower limit

is the field in the streamer channel E_c (note that the dependence of (1) on the lower limit is very weak). The results of comparison of 2D data with (1) are given in the table.

	G_N/G_{N_2}	$G_{O(^3P)}/G_{N_2}$	$G_{O(^1D)}/G_{N_2}$
2D	0.23-0.26	0.22-0.25	0.11-0.13
(1)	0.30	0.21	0.11

It is seen that the relative values of G can be estimated analytically with accuracy about 20-30 %.

The work was supported by INTAS (project 94-4207) and by the Netherlands Science Foundation (NWO). The authors would like to thank Dr. E.M. van Veldhuizen and Prof. W.R. Rutgers for helpful discussions.

References

- [1] Non-Thermal Plasma Techniques for Pollution Control, ed. by B.M. Penetrante and S.E. Schultheis (Springer, Berlin, 1993)
- [2] I. Gallimberti: Pure Appl. Chem., **60** (1988) 663
- [3] A.A. Kulikovskiy, A.Kh. Mnatsakanian, G.V. Naidis and Yu.M. Solozobov: XXI Int. Conf. on Phenom. Ioniz. Gases (Bochum, 1993), **1**, 297
- [4] R. Morrow, J.J. Lowke, A.J. Paulson and A.J. Prokopiuk: XXII Int. Conf. on Phenom. Ioniz. Gases (Hoboken, 1995), **1**, 143
- [5] N.Yu. Babaeva and G.V. Naidis: J. Phys. D: Appl. Phys., **29** (1996) 2423
- [6] N.L. Aleksandrov, A.E. Bazelyan, E.M. Bazelyan and I.V. Kochetov: Plasma Phys. Rep., **21** (1995) 57
- [7] B.M. Penetrante, M.C. Hsiao, B.T. Merritt, et al: IEEE Trans. Plasma Sci., **23** (1995) 679
- [8] G.V. Naidis: XIII Europ. Sect. Conf. on Atom. Molec. Phys. Ioniz. Gases (Poprad, 1996), 127

Study of electrical properties of the sheath in a direct current glow discharge

Stanislav Novák,

Department of Physics, J.E.Purkyně University, České mládeže 8, 400 96 Ústí nad Labem, Czech Republic

1. Introduction

Plasma oxidation, applying an activated oxygen plasma, is one of the most promising low temperature techniques used to grow oxide dielectric films on metal or semiconductor surfaces. There exist several possibilities of plasma oxidation. One point of view is connected with energies of electrons and oxide ions which take part in the oxidation - it is possible to apply plasma anodization (oxidation under positive bias of sample according to plasma potential in the same place), oxidation without external bias and oxidation under negative bias [1]. In these processes the important role is played by a sheath which is the transition region between the undisturbed plasma and the oxidized solid surface. In this region there occurs the plasma-surface interaction, and understanding the sheath is one of the key parts of plasma chemistry. Plasma physicists pay attention to the problem of the sheath for many decades [2,3]. To obtain better results in this field, a quantitative understanding of the sheath region is required. We are trying to use computer modelling for it. Many authors have modelled the entire direct current glow discharge [4-7], but not so many have dealt with the problem of the sheath by this technique [8].

The sheath near a charged surface of metal under conditions of the plasma oxidation of aluminium films in oxygen plasma in the positive column of a dc glow discharge was studied in the present paper by the computer experiment. The complete process of the plasma oxidation of metals consists of three parts - (i) volume processes in oxygen plasma, (ii) interaction of the oxygen plasma with the surface of metal and/or growing oxide film and (iii) the diffusion of charged species through the growing alumina film. The model for analyzing the volume processes [9] yielded us the steady-state concentrations of all considered kinds of particles in an oxygen plasma for various combinations of experimental parameters - gas pressure, discharge current, applied electric field, electron temperature, etc.

2. The description of the simulation

The model of the sheath in oxygen plasma is based on Monte Carlo simulations when we simulate a large number of charged particles. The basic scheme of modelled region is seen in Fig. 1. The charged particles are passing through the sheath under the influence of an electric field; collisions with neutrals are taken into account. The trajectory of the particles is given by

Newton's laws. The probability of a collision is calculated by random numbers. The Poisson equation for the electric field is solved in a self-consistent way. The source can give particles with diverse velocity distributions. In the model we used two values of time steps for electrons and for ions because of their different mobility. The calculations are made for electrons first, in the M electron time step, where M is a given number. Then the new electric field is evaluated and the motion of all ions is computed in the M ion time steps. The "zero size particle" method is used.

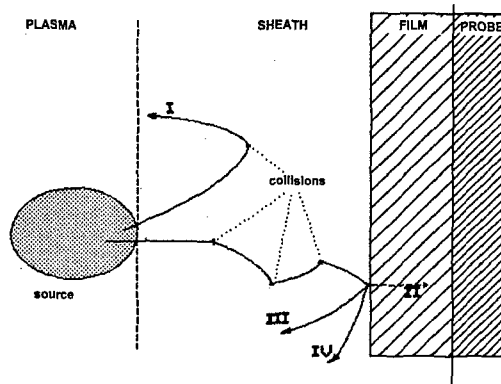


Figure 1. Model region schematic diagram with illustrated trajectories of particles: PLASMA - undisturbed plasma (source of particles), SHEATH - region of the sheath with electric field that returns a part of particles into the undisturbed plasma (I), FILM, PROBE - metallic surface covered with an oxide film. There are processes of interaction demonstrated between a particle and the film: passing through the film (II), reflection (III), secondary emission (IV).

In the model we assume a planar film surface. The model simulates the motion of charged particles only as they are influenced by the electric field in the sheath. The neutral oxygen atoms at rest cause many collisions with the charged particles. As input values for the model the data for the four species - electrons, ions O^- , O_2^+ and O_2^- - were used [10] (only ions with sufficient concentrations were taken into account). The values of mean free paths of the charged particles in neutral gas were derived from the experimental values [11] and calculated from the values of mobility. Because the values for ions have the same order of magnitude, we have used in the first approximation the values 1×10^{-5} m for ions and 1×10^{-3} m for electrons. The source of particles in the undisturbed plasma region, which we

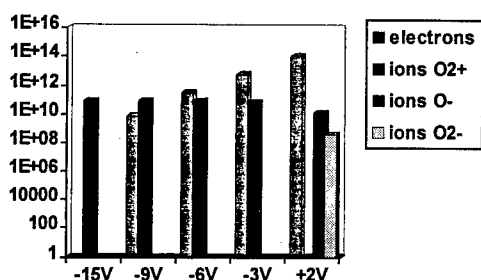


Figure 2. Fluxes (in arbitrary units) of charged particles hitting the sample surface at various sample potentials.

assume in the first approach, has a Maxwellian velocity distribution.

3. Results

Some results for oxygen plasma (for typical experimental parameters: 100 Pa gas pressure, 11 600 K electron temperature, 300 K gas temperature, length of glow discharge tube about 30 cm) are shown. The concentrations of species applied are $2.9 \times 10^{10} \text{ cm}^{-3}$ for electrons and $3.4 \times 10^{10} \text{ cm}^{-3}$, $4.9 \times 10^9 \text{ cm}^{-3}$, $2.2 \times 10^8 \text{ cm}^{-3}$ for ions O_2^+ , O^- , O_2^- , respectively.

We calculated both the concentration and the energy distribution of the impinging charged particles on the sample. In Fig. 2 the changes of fluxes of the four mentioned kinds of charged particles for various sample potentials are shown. It is seen that negatively charged particles dominate at positive bias and vice versa. The flux changes are between -10V and 0V for electrons and near zero sample potential for ions.

In Figs. 3 and 4 we can see the energy distribution of impinging electrons varying with the sample potential. Fig. 3 shows it in a smaller range of negative potentials, and the next Figure in a more wide range of potentials. It is clear that when the potential changes from more negative value towards zero then the number of

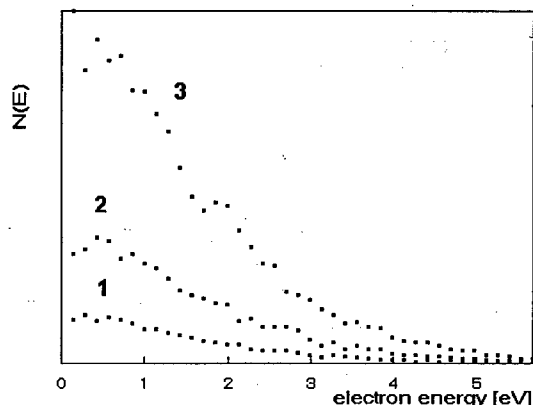


Figure 3. Energy distribution of the impact electrons at the sample potential of -3.5 V (1), -2.5 V (2), -1.5 V (3).

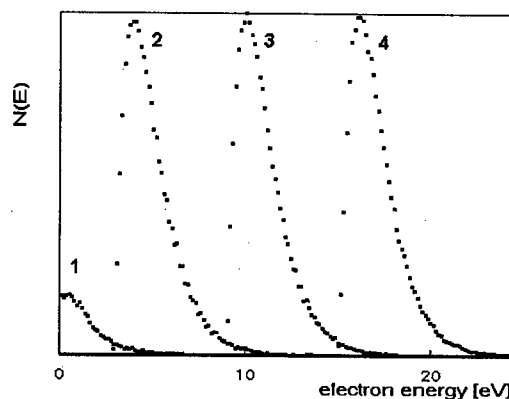


Figure 4. Energy distribution of the impact electrons at the sample potential of -2 V (1), 3 V (2), 9 V (3), 15 V (4).

impinging electrons is higher. But when the potential increases to positive values the number of electrons does not change, however, the distribution shifts to higher energies as the electrons are accelerated by the electric field in the sheath.

The model of the sheath in oxygen dc glow discharge give us positive new knowledge about processes in the sheath when collisions are considered. In the paper there are the fluxes and the energy distributions of the charged particles impinging the sample surface mentioned.

4. References

- [1] J. Siejka, J. Perriere, In: Physics of Thin Films - Advances in Research and Development, Vol. 14, p. 81. Academic Press Inc., Boston (1989)
- [2] Ed. C.G. Suits: The Collected Works of Irving Langmuir, Vol. 4. Pergamon, New York (1961)
- [3] M.J. Goeckner, J. Goree, T.E. Sheridan: Phys. Fluids B, 4 (1992) 1663
- [4] J.-P. Boeuf: J. Appl. Phys., 63 (1988) 1342
- [5] A. Bogaerts, R. Gijbels, W.J. Goedheer: J. Appl. Phys., 78 (1995) 2233
- [6] W.D. Davis, T.A. Vanderslice: Phys. Rev., 131 (1963) 219
- [7] D.B. Graves, K.F. Jensen: IEEE Trans. Plasma Sci., PS-14 (1986) 78
- [8] B.E. Thompson, H.H. Sawin: J. Appl. Phys., 63 (1988) 2241
- [9] R. Hrach, P. Odehnal, V. Hrachová: Proc. Sixth Joint Vacuum Conf., p. 154. Slovenian Vacuum Society, Bled (1995)
- [10] S. Novák, R. Hrach, J. Pavlík, V. Hrachová, In: Metal/Nonmetal Microsystems: Physics, Technology, and Applications, Proc. SPIE, Vol. 2780, p.76 (1996)
- [11] L. Láská, K. Mašek: Proc. 3rd Symposium on Elementary Processes and Chemical Reactions in Low Temperature Plasma, p.5, Krpáčovo, Czechoslovakia (1980)

Numerical simulation of a Trichel pulse in air at atmospheric pressure

T. Reess, J. Paillol

L.G.E, Université de Pau, F-64000 PAU, France

Abstract

Several theories have been proposed to explain the Trichel current shape, at low pressure, in good agreement with experimental results. Nevertheless, these theories failed to explain very fast rise time (few nanoseconds) observed at high pressure. The aim of this paper is to present a numerical simulation of the Trichel pulse which explain the typical current shape observed in air at atmospheric pressure in terms of field effect emission.

I - Introduction

When a sufficiently high negative voltage is applied to a point-plane gap in an electronegative gas such as air, regular corona current pulses are observed. These regular current pulses, called Trichel pulses, have been first studied by Trichel [1].

A model of the pulse formation was developed by Loeb [2]. His predictions were confirmed by Morrow [3], [4] who has developed a theoretical calculation which account for the Trichel pulse development in oxygen at low pressure (6.67kPa). Morrow's theory explains the current pulse formation in terms of photoelectric effect and ion secondary processes at the cathode.

Nevertheless, at high pressure (above 30kPa), Loeb [2] and Cernak and Hosokawa [5] have pointed out that the rise time of the current pulse cannot only be explained by the photoelectric effect.

We propose here a numerical simulation of Trichel current pulse in air at atmospheric pressure. This simulation takes field emission from the cathode into account and allows to explain the very fast rise time characteristic which is observed at high pressure.

II - Theory

The theory is based on a one-dimensional model in which continuity equation for electrons, positive ions and negative ions are used to describe only the axial development of the discharge.

$$\begin{aligned} \frac{\partial}{\partial t} N_e + \frac{\partial}{\partial x} N_e W_e &= (\alpha - \eta) W_e N_e - \beta N_e N_p \\ \frac{\partial}{\partial t} N_p + \frac{\partial}{\partial x} N_p W_p &= \alpha W_e N_e - \beta N_e N_p - \beta N_n N_p \\ \frac{\partial}{\partial t} N_n + \frac{\partial}{\partial x} N_n W_n &= \eta W_e N_e - \beta N_n N_p \end{aligned}$$

Here, t is time, x distance from the cathode, N_e , N_p , N_n are the electron, positive ion and negative ion densities,

respectively, and W_e , W_p , W_n are electron, positive ion and negative ion drift velocities, respectively. The material functions α , β , η are, respectively ionization, recombination and attachment coefficients.

These equations are solved numerically on a nonuniform mesh using a Flux Corrected Transport (FCT) algorithm based on techniques described by Boris and Book [6] and Morrow [3].

The continuity equations are coupled to Poisson's equation via the charge densities. Thus, the axial electric field $E(x)$ is evaluated using the classic method of Davies' disk [7]. The discharge is considered to be an r -radius-cylinder centered on the axis of symmetry of the system.

Two electron emission processes are used. At the cathode we set :

$$N_e(0,t) = N_{e(\text{Fowler})} + N_{e(\gamma)}$$

• $N_{e(\gamma)}$ is the density of secondary electrons emitted at time t :

$$N_{e(\gamma)}(0,t) = \gamma \frac{N_p(0,t) |W_p(0,t)|}{|W_e(0,t)|}$$

$\gamma = 10^{-2}$ is the ion-secondary-emission coefficient.

• $N_{e(\text{Fowler})}$ is the electron density emitted from the cathode by field effect. This density is calculated using Fowler-Nordheim relationship [8] :

$$j = B_1 \frac{E^2}{\Phi t^2(y)} \exp \left[-B_2 v(y) \frac{\Phi^{3/2}}{E} \right]$$

where j is the current density (A/m^2), E is the electric field on the cathode surface (V/m) and Φ the metal work function (eV) (B_1 , B_2 , $t(y)$, $v(y)$ are defined in [8]).

Moreover, we take cathode surface state into account using a multiplier coefficient β^* of the electric field [9].

The current I in the external circuit due to the motion of electrons and ions is calculated using Sato's equation [10].

III - Results

Typical Trichel current pulse shapes in air at atmospheric pressure obtained by Torsethaugen and Sigmond [11] are shown in fig.1 in a point-plane system with a 0.074mm radius point and a 16mm gap. The applied voltage was -4.25kV. Two kinds of cathode materials were used. The main features of the impulse shape obtained using Mo and Au cathode are a rise time shorter than 3ns, a peak value of 4mA and a step on the leading edge.

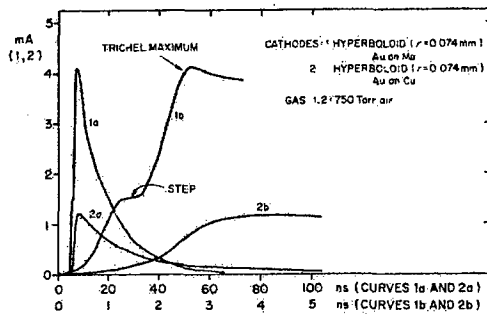


Fig. 1. Trichel current pulses in air at atmospheric pressure (Torsethaugen and Sigmond [11])

Computed current obtained for the same experimental configuration is shown in fig. 2. The discharge is considered to be an 0.5mm radius cylinder [2]. For the calculation presented we use a value of $\Phi=4.5\text{eV}$ corresponding to the mean value of Mo and Au work functions. The value of the multiplier coefficient field β^* is 120. This value is in good agreement with the experimental one [9].

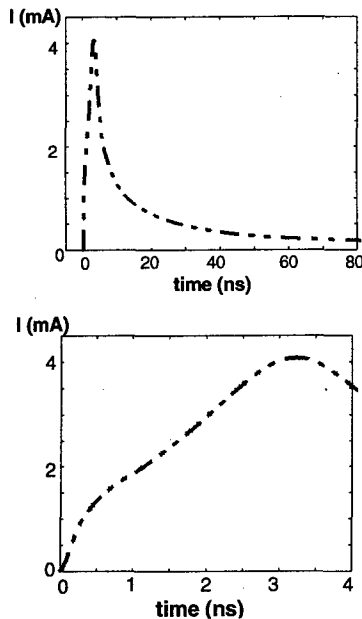


Fig. 2. Computed current versus time
d=16mm; R=0.074mm; U=-4.25kV
 $\Phi=4.5\text{eV}$; $\beta^*=120$; r=0.5mm

The main features of the theoretical current pulse are in good agreement with the experimental results: rise time $\sim 3\text{ns}$, peak value $\sim 4\text{mA}$ and a step on the leading edge.

To explain the step on the leading edge we have artificially set the secondary emission coefficient γ to zero. The two current pulses obtained are strictly similar. Therefore, the step on the leading edge, at high pressure, cannot be explained in terms of positive ion impact as it has been shown at low pressure [4].

To clarify the step origin at high pressure, we have to examine the temporal evolution of the number of electrons released at the cathode by field effect emission (fig. 3).

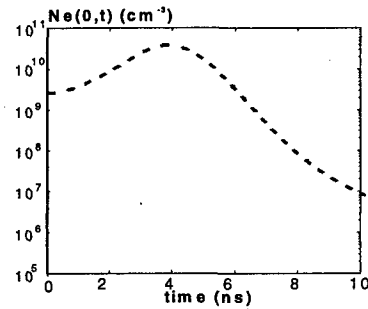


Fig. 3. density of secondary electrons released at the cathode by field effect versus time.

d=16mm; R=0.074mm; U=-4.25kV
 $\Phi=4.5\text{eV}$; $\beta^*=120$; r=0.5mm

From $t=0$ to $\sim 1\text{ns}$, the effect of space charge is negligible and the current growth is due to electron multiplication process. At the end of this phase, space charge effects start to enhance the electric field near the cathode. Therefore, electron density released by field effect significantly increases and the current is enhanced at the same time. Consequently, the step on the leading edge, at high pressure, can be explained in terms of cathode sheath formation leading to a large increase of the number of electrons released at the cathode by field emission.

IV - Conclusion

We have presented a numerical simulation of a Trichel pulse in air at atmospheric pressure in good agreement with experimental results. This simulation explains, for the first time, the fast rise time of the current pulse in terms of field effect emission. We have demonstrated the negligible role of secondary emission at high pressure in comparison with field effect emission. The step on the leading edge of the Trichel pulse can be explained in terms of a large increase of the number of electrons releases by field effect due to a cathode sheath formation. Moreover, this simulation allows to take the cathode material and its surface state into account.

Acknowledgement

The authors are grateful to CNUSC for its support and help.

References

- [1] - Trichel G.W., Phys. Rev., 54, page 1078, (1938).
- [2] - Loeb L.B., University of California Press, (1965).
- [3] - Morrow R., Phys. Rev. A, vol. 32, n°3, pp 1799-1809, (1985)
- [4] - Morrow R., Phys. Rev. A, vol. 35, n°6, pp 3821-3824, (1985)
- [5] - Cernak M., Hosokawa T., Aust. J. Phys., 45, pp 193-219, (1992)
- [6] - Borris J.P., Book D.L., J. Comp. Phys., 20, pp 397-431, (1976)
- [7] - Davies A.J., Evans C.J., Llewellyn Jones F. Proc. Roy. Soc., 281, pp 164-183 (1964)
- [8] - Fowler R.H., Nordheim L., Proc. Roy. Soc., A119, p173, (1928)
- [9] - Rohrbach F., CERN 71-5, Div. des chambres à traces, (1971)
- [10] - Sato N., J. Phys. D: Appl. Phys. 13, L3, (1980)
- [11] - Torsethaugen K., Sigmond R.S. Proc. 11th Int. Conf. on Phenomena in Ionized Gases, Prague, (1973).

Ion density distributions in the cathode region of glow discharges in gas mixtures

C. Pédoussat, L.C. Pitchford and J.P. Boeuf

Centre de Physique des Plasmas et Applications de Toulouse (E.S.A. 5002), UPS,
118 route de Narbonne, 31062 Toulouse Cedex 04, France

1. Introduction

We have used a one-dimensional, self-consistent fluid model of glow discharges developed previously in this laboratory to calculate the current-voltage characteristic and the ion density distributions in the cathode region of glow discharges in gas mixtures of Ar and Xe and for small admixtures of Hg in Ar.

2. Description of the model

The fluid model used has been described elsewhere [1], and only a brief outline is given here. The fundamental variables are the electron density, two positive ion densities, and the potential distribution. These variables are functions of space (in the axial direction) and of time. The charged particles densities are described by continuity equations in the drift diffusion approximation, and the space charge electric field is given by Poisson's equation. The continuity equations are discretized using the Scharfetter-Gummel exponential scheme. The coupled system of continuity equations and Poisson's equation are solved simultaneously using an implicit integration technique. The charged particle diffusion coefficients and mobilities as well as the ionization source term are supposed to depend on E/p (the reduced electric field strength). The model includes the option of using a Monte Carlo simulation to determine the ionization source term.

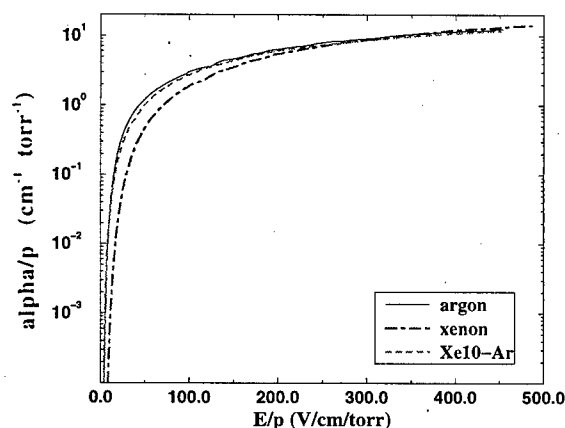


Figure 1: ionization coefficient versus E/p

In calculations for mixtures of Ar and Xe, the background gas is supposed to be cold and unexcited. The ionization rate coefficients as functions of E/p are calculated for each mixture using a 0-D Boltzmann solver in the two term

approximation. The total ionization rate coefficients are shown in Fig. 1 as function of E/p for pure argon, pure xenon, and for 10% Xe in argon.

Argon metastable atoms are included in the calculations for mixtures of Ar and Hg, and these are supposed to be produced by electron impact ionization from the ground state of argon atoms. Penning ionization (with a rate taken to be $10^{-9} \text{ cm}^3 \cdot \text{s}^{-1}$) and associative ionization (with a rate of $6.4 \cdot 10^{-10} \text{ cm}^3 \cdot \text{s}^{-1}$) are included as loss terms for metastables.

3. Results of our model

3.1 Mixtures of Ar and Xe

The calculated steady-state current-voltage characteristics in pure argon, in pure xenon, and in a mixture of 10% of Xe in Ar are shown in Fig. 2. At fixed voltage, the current density decreases when xenon is introduced. Donko finds similar results for mixtures of Xe and He [2]. This characteristic depends on the ion mobilities and on the secondary electron emission coefficients γ due to cathode bombardment by the respective ions. The mobilities of singly charged positive ions in their parent gas are reasonably well known, but the ion mobilities in gas mixtures must usually be estimated [3].

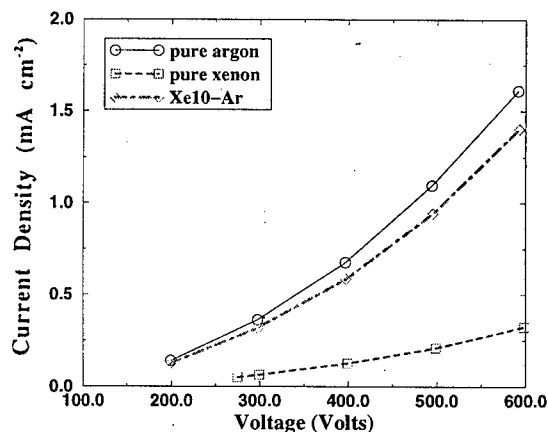


Figure 2: Calculated steady-state current-voltage characteristics in argon, in xenon and in a mixture of 10%Xe in Ar (Pressure = 1Torr, 4 cm electrode spacing)

We have performed parametric calculations to estimate the effect of the uncertainty in the values of γ and the ion mobilities on the predicted I-V characteristic. In pure argon, a change in the ion-induced secondary emission

coefficient modifies the slope of the characteristic. (The slope increases with increasing γ .)

In the mixture (10% Xe in Ar), a relative change in Xe^+ mobility of $\pm 33\%$ leads to a small change total current density (less than 2% over the range of conditions studied). A relative increase of 50% in the secondary emission coefficient due to Xe^+ increases the total current density by a maximum of 10%.

The calculated Ar^+ and Xe^+ ion density distributions in the discharge are shown in Fig. 3 along with the field distribution and the electron density for one point along the characteristic. The conditions of these calculations are: 10% Xe in Ar, Xe^+ mobility equal to $1500 \text{ cm}^2 \text{ torr/V/s}$, and Ar^+ mobility equal that in pure Ar [3]. The secondary electron emission coefficients are taken to be 0.07 for Ar^+ and 0.03 for Xe^+ . For these conditions, the Xe^+ density in the cathode fall is less than the Ar^+ density. Xe^+ is the predominant ion in the cathode fall when the xenon concentration increases above 30% for otherwise same conditions.

As mentioned above, the ionization coefficient in these calculations was supposed to be a function of the local reduced field strength, E/p . The charged particle densities in the plasma are thus considerably less than they would be if the ionization source term were determined from a Monte Carlo simulation. However, the ion density distributions in the cathode region and the components of the current density at the cathode are not much affected by the local field approximation.

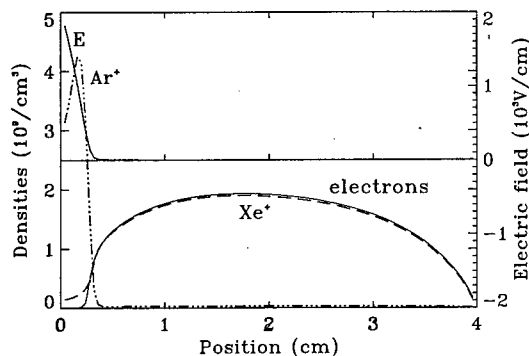


Figure 3: Charged particles densities and the magnitude of electric field versus position between electrodes for 10% Xe in Ar (Pressure = 1 Torr, Voltage = 300 Volts)

3.2 Small concentrations of Hg in Ar

The steady-state characteristic and the components of the current at the cathode in a mixture of 0.1% Hg in Ar are shown in fig. 4. Penning ionization can occur in Hg/Ar mixtures, and this has a considerable effect on the predicted discharge characteristics. Associate ionization is not very important for these conditions. The Hg^+ current is about 25% of the total current at the cathode at 200 V,

and this fraction decreases slightly with increasing voltage.

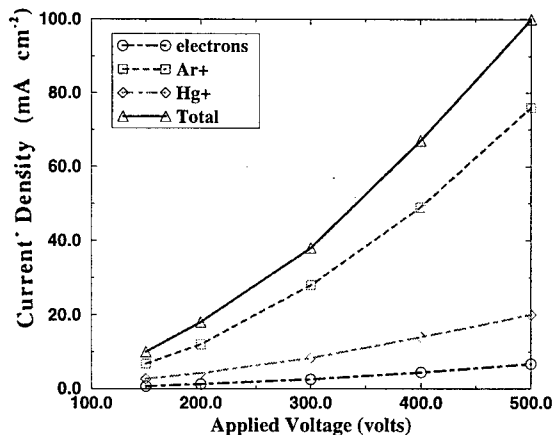


Figure 4: Steady-state current-voltage characteristic and components of the current density at the cathode (0.1% Hg in Ar, 10 torr, 0.3 cm electrode separation)

4. Conclusion

We have presented results for the current-voltage characteristics in mixtures of Ar/Xe and Ar/Hg. The purpose of these calculations was to quantify the relative contributions of each ion to the total current density at the cathode and to evaluate the effect of uncertainties in the data on the results of the calculations. This work is a step towards the development of a self-consistent model of cathode sputtering in glow discharges.

5. References

- [1] A. Fiala, L. C. Pitchford, and J. P. Boeuf, *Phys. Rev. E* **49**, 5607 (1994).
- [2] Z. Donko, and M. Janossy, *J. Phys. D: Appl. Phys.* **25**, 1323 (1992).
- [3] L. A. Vielhand, and E. A. Mason, *Atomic Data and Nuclear Data Tables* **60**, 37 (1995).

Propagation of High Power Microwaves around a Local Perturbation

G. Peres, J.P. Bœuf

Centre de Physique des Plasmas et Applications de Toulouse (E.S.A. 5002), UPS,
118 route de Narbonne, 31062 Toulouse Cedex, France

C. Theroude

Matra Marconi Space
31, rue des cosmonautes, Z.I. du Palays
31 Toulouse Cedex, France

1. Introduction

High Power Microwave pulses can have destructive effects on solid-state electronic systems. Information on the energy and the peak power that are transmitted through the atmosphere are therefore needed in evaluating the threat posed by microwave pulses on communication equipment, radar, computers, etc.

Collisional absorption during propagation through the atmosphere has been described by Yee et al. [1]. In this paper we study the lowering of the breakdown threshold in the vicinity of a conducting object at low altitudes. We have developed a three dimensional computer code using a Finite Volume in the Temporal Domain method (FVTD) in an unstructured meshing. In this model, electrons are treated as a fluid, and the avalanche growth due to the microwave field is considered. Maxwell equations are solved together with the electron continuity equations in the presence of a conducting sphere.

2. Description of the model

The system of Maxwell equations and electron continuity equation can be written as :

$$\text{rot}(\vec{E}) = -\frac{\partial \vec{B}}{\partial t} \quad (1)$$

$$\text{rot}(\vec{B}) = \mu_0 \vec{J} + \epsilon_0 \mu_0 \frac{\partial \vec{E}}{\partial t} \quad (2)$$

$$\vec{J} = -ne\langle \vec{V} \rangle \quad (3)$$

$$\frac{\partial n}{\partial t} = n(v_i - v_a) \quad (4)$$

$$\vec{V} = -\mu_e \vec{E} \quad (5)$$

(1) and (2) are Maxwell's equations where \vec{E} is the electric field and \vec{B} is the magnetic field. (4) and (5) are the electron transport equations coupled to Maxwell's equations through equation (3). J is the electron current density, n the electron density, V the drift velocity.

The set of equations (1-5) has been closed by assuming that the electron-molecule collision frequencies (momentum, attachment, ionization) depend only on the local reduced electric field E/N where N is the molecule

density. This is a reasonable assumption at sea level since the wave frequency (in the GHz range) is much smaller than the collision frequency. The ionization frequency ν_i , attachment frequency ν_a and mobility μ_e , are therefore supposed to depend only on E/N .

In this first approach we also assume quasineutrality of the forming plasma and we neglect diffusive effects (the diffusive effects combined with intense ionization can actually lead to a fast expansion of the plasma [2], [3]).

3. Numerical Scheme

We have used a Finite Volume in the Temporal Domain method to solve numerically the set of equation (1-5). This method allows to take into account a scattering object with complex geometry [4].

Maxwell's equations are written in the form :

$$\frac{\partial}{\partial t} \begin{bmatrix} E_x \\ E_y \\ E_z \\ cB_x \\ cB_y \\ cB_z \end{bmatrix} + \frac{\partial}{\partial x} \begin{bmatrix} 0 \\ c^2 B_z \\ -c^2 B_y \\ 0 \\ -cE_z \\ cE_y \end{bmatrix} + \frac{\partial}{\partial y} \begin{bmatrix} -c^2 B_z \\ 0 \\ c^2 B_x \\ cE_z \\ 0 \\ -cE_x \end{bmatrix} + \frac{\partial}{\partial z} \begin{bmatrix} c^2 B_y \\ -c^2 B_x \\ 0 \\ -cE_y \\ cE_x \\ 0 \end{bmatrix} = \begin{bmatrix} -J_x \\ -J_y \\ -J_z \\ 0 \\ 0 \\ 0 \end{bmatrix}$$

F G H

where F, G and H are fluxes functions in the x, y and z directions.

This system can be written as :

$$\frac{\partial U}{\partial t} + \text{div}[F|G|H]U = I(U)$$

where $U = (E_x, E_y, E_z, cB_x, cB_y, cB_z)$ is the cell centered state vector and I a source term depending of J .

This equation is integrated over the tetrahedral cell of the computational domain, and solved using a first order in time (Euler) and in space (Godunov) scheme.

The complete system (1-5) is solved with a 'flux splitting' method. It consists in a separate resolution of the above equation, first without the source term, which gives an intermediate state vector U^* , and then with the source term which gives the state vector $U^{t+\Delta t}$ at the next time-step.

4. Results

When a High Power Microwave propagates through the atmosphere, the electric field of the wave can be strong enough to generate an electron avalanche which leads to the rapid absorption of the wave. Below a critical electric field the wave can propagate without noticeable absorption. The enhanced field in the vicinity of a conducting object can lead to gas breakdown even though the field of the incoming wave is below the breakdown field. The results below illustrate this effect. We consider an electromagnetic plane wave propagating around a perfectly conducting sphere. The pulse duration is half a cycle of a 700 MHz wave (i.e. 0.7 ns). Figure 1 shows the scattering of the wave by the conducting sphere in vacuum, i.e. without ionization effects. Figure 2 shows the scattering of the wave in the atmosphere at altitude 0 km. The initial electric field is 55% of the theoretical breakdown threshold.

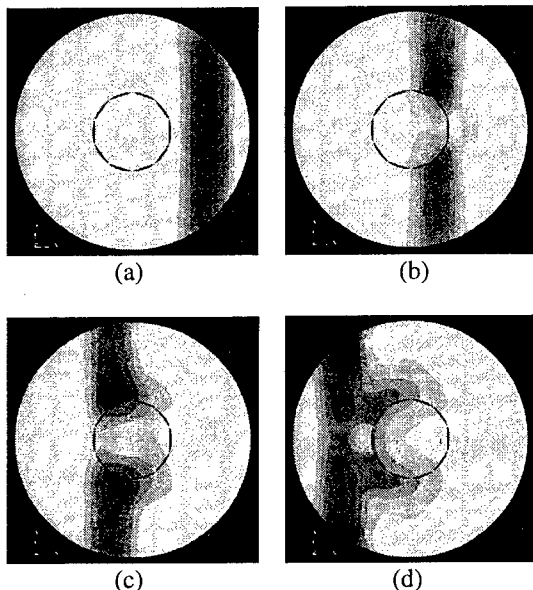


Figure 1: Scattering of a High Power Microwave pulse by a perfectly conducting sphere, in vacuum (no ionization). The electric field is parallel to the (vertical) y axis and propagates along the (horizontal) x axis, from right to left. Its modulus is represented in the xy cut plane of the sphere at four different times during propagation. The values displayed inside the sphere correspond to the field on the sphere surface, at the same xy location.

We can see in Fig. 1 the perturbation induced on the wave propagation by the presence of the sphere. In Fig. 1c the electric field has been enhanced around the sphere up to more than twice its initial value. One can therefore expect to have gas breakdown under the same conditions if the sphere is immersed in air at atmospheric pressure. This can be seen in Fig. 2 where ionization and plasma formation are now taken into account. The field distribution is clearly different from the distribution in vacuum.

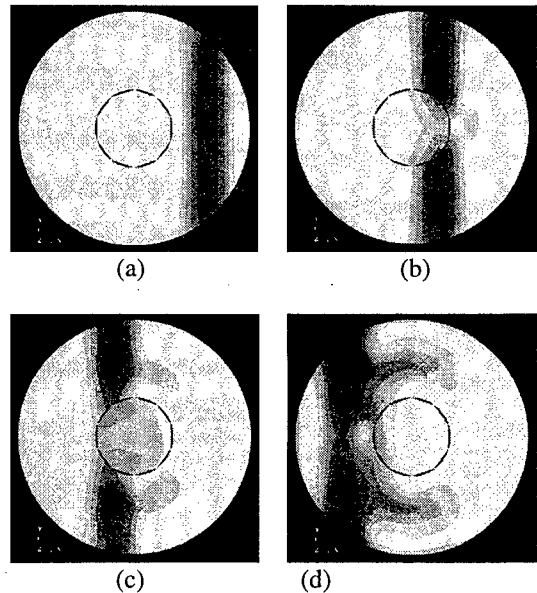


Figure 2: Scattering of a High Power Microwave by a perfectly conducting sphere, in the atmosphere. The electric field is represented as in the Fig 1.

This is due to the presence of the plasma at the location of maximum field in Figs 1c and 1d. The plasma acts as a conductive medium and the electric field maxima are now located further away from the sphere, at the interface between the plasma and the non ionized gas. This leads to the expansion of the plasma away from the sphere, in a direction parallel to the electric field.

5. Conclusion

A three dimensional model has been developed to simulate the interaction of a High Power Microwave with a complex object. Breakdown can occur in these conditions even if the field of the incoming wave is below breakdown. The model makes possible quantitative prediction of the lowering of the breakdown threshold and of the plasma expansion during the pulse.

6. Acknowledgments

This work has been supported by DGA/DRET and Matra Marconi Space.

7. References

- [1] J.H.Yee, R.A. Avarez, D.J.Mayhall, D.P.Byrne, J.S. Degroot, Physics of Fluids, B29, 1238 (1986).
- [2] V.B. Gildenburg, I.S. Guschin, S.A. Dvinin, and A.V. Kim, Sov. Phys. JETP 70, 645 (1990).
- [3] J.P. Boeuf and Ph. Belenguer, Electromagnetic Environments and Consequences, Eds. D.J. Serafin, J. Ch. Bolomey and D. Dupouy, part 1, p 523 (EUROEM 1995).
- [4] V. Shankar, A.H. Mohammadian, W.F. Hall, Finite volume traitment for the Maxwell's equations, Electromagnetics 10, 127 (1990).

Theoretical Determination of the Electron Distribution Function in an Electron Cyclotron Resonance Ion Source.

C. PERRET, A. GIRARD, C. LECOT*

Département de Recherche Fondamentale sur la Matière Condensée,
Service des Ions, des Atomes et des Agrégats,
CEA-Grenoble, 17 rue des Martyrs 38054 GRENOBLE CEDEX 9 FRANCE

* Laboratoire de Mathématiques,
Université de Savoie 73376 Le Bourget-du-Lac CEDEX FRANCE

Introduction :

Electron Cyclotron Resonance Ion Sources (ECRIS) are mirror machines which can deliver large fluxes of highly charged ions [1]. Their performance depends on the Electron Distribution Function (EDF), which has been shown to be non Maxwellian [2,3]. A one-dimensional Fokker-Planck code has been developed to determine this EDF. This code is described in this paper and the first results are presented.

I Basic principles of ECRIS

The ECRIS are open-ended magnetic traps that confine a hot electron plasma. In these plasmas (fig. 1), the particles are trapped by the magnetic configuration: two coils (1,2) produce the axial field and a multipole (3) generates the radial field. The combination of these two components leads to a minimum-B structure. A RF wave is injected into the plasma to heat the electrons by cyclotron resonance. The energy of the electrons determines the ionic charge obtained, since the ionisation potential increases with it. The magnetic configuration leads to a closed resonance surface (4), defined by $\omega = \omega_e$, with ω the RF wave frequency and ω_e the electron cyclotron frequency.

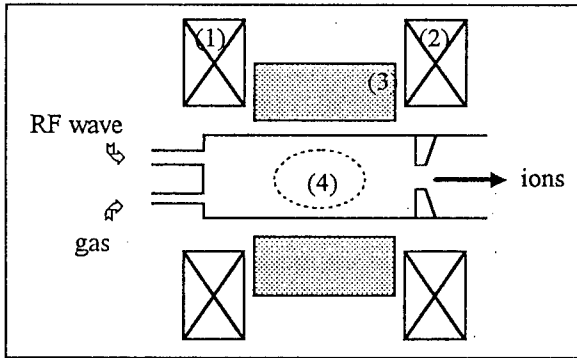


figure 1 : ECR ion source.

II The model :

The evolution of the EDF, $f(x,v,t)$ depends on various phenomena : (i) electron-electron collisions tend to restore a Maxwellian population and electrons pitch angle scattering on other electrons and ions

induces diffusion into the loss cone, (ii) the RF wave heats the electrons, (iii) inelastic collisions (ionisation) are the source of electrons in the plasma. Considering all these phenomena, we obtain :

$$\frac{\partial f}{\partial t} = \left(\frac{\partial f}{\partial t} \right)_{\text{ioni.}} + \left(\frac{\partial f}{\partial t} \right)_{\text{coll.}} + \left(\frac{\partial f}{\partial t} \right)_{\text{R.F.}} \quad (1)$$

Such a non-linear integro-differential equation is difficult to solve. Therefore some approximations are made : we assume the plasma to be homogeneous and that is possible to work in the (v, μ) space of the midplane with $\mu = v_{\parallel} / v$. Fig. 2 shows the exact loss cone in the midplane (dotted line) and the approximation made in the code (full line).

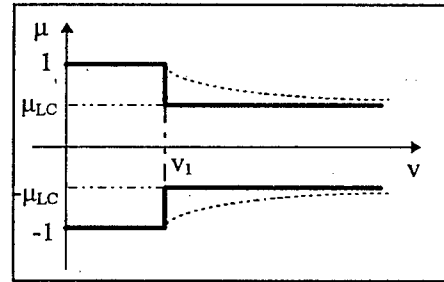


figure 2 : domain of calculation

This domain of calculation separates f into two populations : (i) below the velocity v_1 , $v_1 = \sqrt{\frac{2eV_{pl}}{m_e}}$,

the electrons are electrostatically confined by the plasma potential V_{pl} ; (ii) beyond that velocity, the electrons can leave the plasma owing to pitch angle scattering.

The ionisation term in equation (1) is an integral function of the EDF and depends on the electron-impact ionisation cross-sections given by W. Lotz [4] :

$$\left(\frac{\partial f}{\partial t} \right)_{\text{ioni.}} = \sum_{i=0}^{N-1} n_i \int f_e(v) \sigma_{i \rightarrow i+1}(v) v \cdot dv \cdot r_0(v)$$

where n_0 is the density of neutral particles, n_i the density of ions $i+$ and $r_0(v)$ a function normalised such

that $4\pi \int_0^{v_1} r_0(v) v^2 dv = 1$ because the electrons are

assumed to be created with an energy between 0 and the plasma potential.

The collisions are modelled by the Landau collision operator [5], by considering the Rosenbluth potentials [6] as isotropic. As these potentials still depend on the EDF, the equation (1) remains an integro-differential equation.

The effect of the RF wave on the electrons may be considered as a diffusion process in velocity space. Considering the equation of motion, quasilinear theory [7] leads to the determination of two diffusion coefficients (2) which depend on v , μ and v_ϕ the phase velocity of the wave :

$$D_{vv} = D(1 - \mu^2) \quad \text{and} \quad D_{\mu\mu} = D \left(\mu - \frac{v}{v_\phi} \right)^2 \quad (2)$$

$$\text{where} \quad D = \frac{\pi}{(d\omega_c/dz)L} \left(\frac{eE}{m_e} \right)^2$$

with L the length of the flux line, e , m_e the charge and mass of the electron, z the axis parallel to the magnetic field B_0 , E the amplitude of the electric component of the RF wave and $\omega_c(z)$ the cyclotron frequency.

The diffusion in angle ($D_{\mu\mu}$) becomes important for electrons with a velocity beyond the phase velocity when the magnetic component of the wave is taken into account.

III 1D code :

We solve two one-dimensional equations by separating the variables as was done by Killeen [8]. The angular part is a solution of the Sturm-Liouville problem and the module part is solved by an implicit finite volumes scheme. The integration over μ leads to diffusion terms in the velocity space and to loss terms which are due to the collisional and RF wave-induced pitch angle scattering.

The input parameters of the code are : the mirror ratio $R = B_{\max} / B_{\min}$, the neutral density n_0 , the diffusion coefficient D , the phase velocity of the wave v_ϕ and the plasma potential. Fig. 3 shows the shape of the EDF obtained with this code, using typical physical values for the various parameters, compared to a Maxwellian function. The difference between the two curves is induced by the electron cyclotron heating which overcomes collisional relaxation.

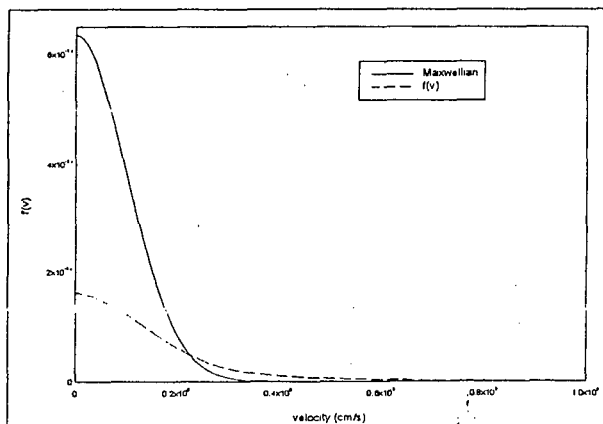


Figure 3 : shape of $f(v)$

A study of the evolution of $f(v)$ with different parameters has begun : an increase of the mirror ratio R leads to an increase of the total density, since the loss cone is smaller and particles with greater energies can stay in the plasma. As D , i.e. the RF wave power, is varied, we observe variations of densities in the two domains : the greater D , the greater the density of the domain 2 and the smaller the density of the domain 1 (fig. 4). This is consistent with the fact that the RF Wave heats the electrons. However, we can observe a saturation of the total density beyond a given value of D . This can be explained by a reduction of the ionisation term as the number of electrons capable of ionising decreases when heating is too strong.

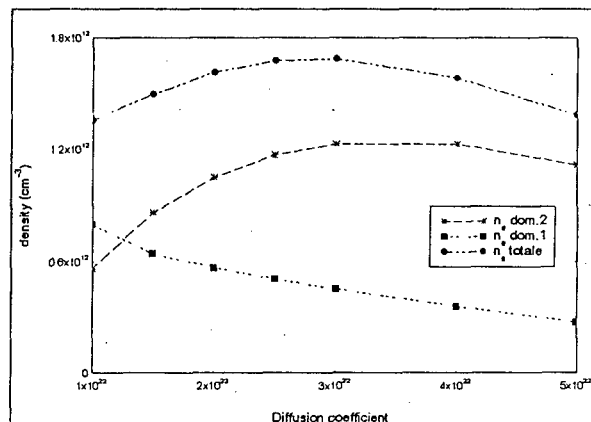


Figure 4 : densities' evolution.

IV Conclusions :

The first results show a very good qualitative evolution of the EDF with the various parameters. However, some quantitative differences between the experimental and calculated values (electronic density, electronic current, absorbed power and energetic content) still remain to be studied. Moreover, a two dimensional code is under development in order to have a better treatment of the loss cone.

References :

- [1] R. Geller, IEEE Trans. Nucl. Sci. NS 26 (1979) 2120
- [2] A. Girard, C. Perret, C. Lecot, F. Bourg, H. Khodja, G. Melin, Proc. of the ICPP Nagoya (Sep.1996) to be published.
- [3] C. Barué, M. Lamoureux, P. Briand, A. Girard, G. Melin, J. Appl. Phys., 76 (1994) 2662.
- [4] W. Lotz, Z. Physik 216 (1968) 241.
- [5] B. A. Trubnikov, Reviews of plasma Physics 1, p.105.
- [6] M.N. Rosenbluth, W.M. MacDonald & D.J. Judd, Phys. Rev. 107 (1957) 1.
- [7] C.F. Kennel & F. Engelmann, Phys. Fluids, 9(1966) 2377.
- [8] J. Killeen, G.D. Kerbel, M.G. McCoy, A.A. Mirin, Computational Methods for Kinetic Models of Magnetically Confined Plasmas, Springer Verlag, NY (1986)

Modelling of the plasma kinetics in the electrode sheath regions of a pulsed copper vapour laser

K Satoh^{1,3} R Morrow² and R J Carman¹

- 1 Centre for Lasers and Applications, Macquarie University, Sydney, NSW 2019, Australia
- 2 CSIRO Div. of Telecommunications and Industrial Physics, Sydney, NSW 2070, Australia
- 3 Dept. of Electrical and Electronic Eng., Muroran Institute of Technology, Muroran 050, Japan

1. Introduction

The copper vapour laser (CVL) is well known as a source of high average-power (~10-100W), pulsed radiation (~50ns) in the visible (510.6 & 578.2nm) operating at high repetition frequency (5-20kHz). These devices are currently used for a wide variety of scientific, medical and industrial applications including micromachining. Numerical modelling of the plasma kinetics in the pulsed glow discharge (Cu-Ne), including the laser characteristics and behaviour of the external circuit, has been done previously [1]. In the model, the discharge parameters were temporally and radially dependent (transverse to applied electric field), but were assumed longitudinal homogeneous. The evolution of the plasma near the electrodes was not described. However, it remains unclear whether the sheath impedance directly influences the discharge current during excitation pulse thereby reducing the electric field in the main Cu-Ne plasma. Experimental data describing influence of the electrodes and the formation of the electrode sheaths in CVLs is very scarce [2]. However, discharge current instabilities originating at the cathode are known to degrade laser performance [3].

The purpose of this work is to clarify the plasma kinetics in the electrode sheath regions. The Propagator Method [4] is used to describe electron and ion behaviour under non-equilibrium conditions, coupled with Poisson's equation, the impedance of the main Cu-Ne plasma and external circuit. Time variation of voltage, current and resistance in the sheath, spatio-temporal evolution of electric field and electron energy and angular distributions are shown in this article. Results from Propagator Method are also compared to those calculated assuming the local field approximation [5].

2. Model description

A one dimensional model in the field direction is used. The main Ne-Cu plasma is assumed to be a fixed resistance R_p during the early time of the excitation pulse (~50ns), since R_p depends on the conductivity of the main plasma which increases after 50ns [1]. Electrode sheath regions of the CVL plasma containing pure neon are considered as a discharge space with parallel electrodes, and R_p is connected to the discharge space in series. Figure 1 shows the simplified external circuit, which is basically similar to that used in paper [1]. The equivalent circuit of the sheath regions is assumed to consist of a resistance R_{th} and a capacitor C_3 . Loop currents I_1 , I_2 and I_3 and voltages V_1 , V_2 and V_3 across the capacitors C_1 , C_2 and C_3

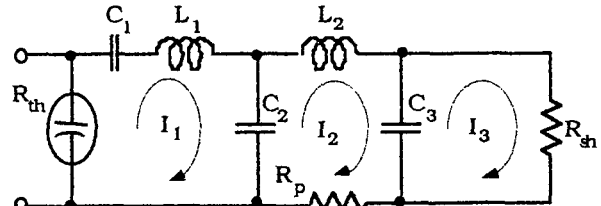


Figure 1. Simplified external circuit. $C_1=6.0\text{nF}$, $C_2=2.0\text{nF}$, $C_3=8.0\text{nF}$, $L_1=1.0\mu\text{H}$, $L_2=0.5\mu\text{H}$ and $R_p=20.0\Omega$.

respectively are calculated from following circuit equations,

$$\frac{dV_1(t)}{dt} = -\frac{1}{C_1} I_1(t) \quad (1) \quad \frac{dV_2(t)}{dt} = -\frac{1}{C_2} [I_2(t) - I_1(t)] \quad (2)$$

$$\frac{dV_3(t)}{dt} = -\frac{1}{C_3} [I_3(t) - I_2(t)] \quad (3)$$

$$\frac{dI_1(t)}{dt} = \frac{1}{L_1} [V_1(t) - V_2(t) - R_{th} \cdot I_1(t)] \quad (4)$$

$$\frac{dI_2(t)}{dt} = \frac{1}{L_2} [V_2(t) - I_2(t) \cdot R_p - V_3(t)] \quad (5)$$

$$I_3(t) = \frac{eS}{d} \int_0^d [n_p(x, t) \cdot W_p(x, t) - n_e(x, t) \cdot W_e(x, t)] dx \quad (6)$$

where e is the electronic charge, S is area of electrode, d is the length of discharge space and R_{th} is the thyatron resistance, n_e and n_p are densities of electrons and ions respectively, and W_e and W_p are average velocities of electrons and ions respectively. The densities and the average velocities are given as a function of both position x and time t , where x is the position in the field direction. Poisson's equation represented by equation (7) is used for the electric field.

$$\nabla^2 V = -1/\epsilon [n_p(x, t) - n_e(x, t)] \quad (7)$$

To describe behaviour of electron and ion in the sheath regions accurately, the Propagator Method (PM) [4] is used in this work, since PM is applicable under the condition at which local equilibrium is not achieved. The behaviour of the particles is calculated from their velocity distributions, collision cross sections between the particles and collision targets, densities of the particles and collision targets and given electric field.

The velocity distributions of electrons and ions used here have 60 mesh points for energy and 6 mesh points for polar angle. The discharge space (1.5mm long) is divided into 300 slabs and the velocity distributions are defined in each of the slabs. At this stage, momentum, eight kinds of excitation and ionisation collisions between electrons and

Ne atoms and momentum collision between Ne positive ions and Ne atoms are considered. Pressure and temperature of neon are assumed to be 30 Torr and 1273 K, respectively. Also electrodes are assumed to be fully absorbing wall and secondary coefficient due ion bombardment is assumed 0.066[6].

3. Simulation results

The calculation is initiated at $t=0$ and $V_1=8800\text{V}$. Electron and ion are parabolically distributed across the discharge space in the field direction initially and their densities are 10^{19}m^{-3} at the centre of the space, taking into account the pre-pulse condition[1]. Figure 2 shows the time variations of the voltage across the capacitor C_3 , the current I_3 and the sheath resistance R_{sh} . It is found that both V_3 and I_3 increase after 10 ns, which is similar to the time variations of V_2 and I_2 (not shown). However, R_{sh} increases rapidly and has a tendency to saturate after 25 ns.

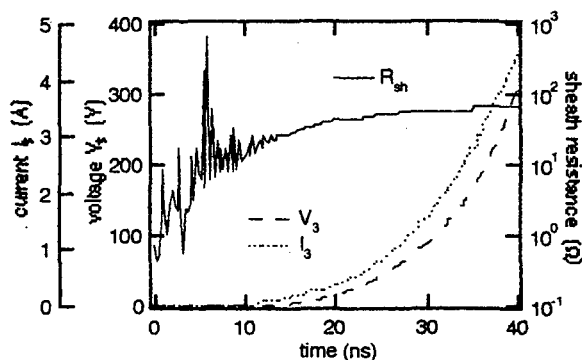


Figure 2. The time variations of V_3 , I_3 and R_{sh} .

Figure 3 shows the spatio-temporal variations of electric field in the discharge space. It is found that plasma sheaths are created near both the electrodes. Since the electric field applied by the external circuit is small during beginning of the excitation pulse and space charge due to electron diffusion is dominant, the sheaths at both electrodes are initially symmetrical. After 20 ns, the voltage applied by the external circuit begins to affect electron motion, and the formation of a cathode sheath (cathode is at $x=1.5\text{mm}$) towards the center with increasing of electric field, becomes clear. At the anode (at $x=0\text{mm}$), the electric field reduces gradually. The cathode sheath formation process qualitatively agrees with that shown by Morrow[5].

Figure 4 shows the electron energy and angular distributions in the cathode sheath region at $t=40\text{ns}$ together with that at the centre of the discharge space. It is seen that the tails of energy distributions in the sheath are spread out to high energy region and angular distributions in sheath are shifted to the opposite direction of the field due to the large sheath electric field. It is found that each of energy distributions (1), (2) and (3) in the cathode sheath shows different shape although electric field at these points are almost same. It is also seen the energy and angular distributions at the end of the sheath shown in (5) are similar to those at the centre of the discharge region at which electric field is about 200 times smaller than that at $x=1.28\text{mm}$.

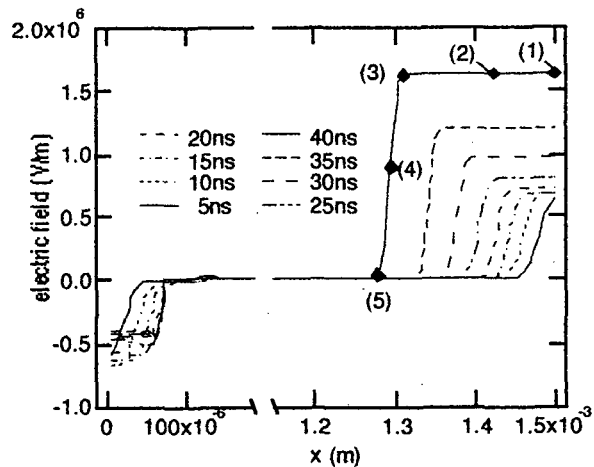


Figure 3. Spatio-temporal distributions of electric field.

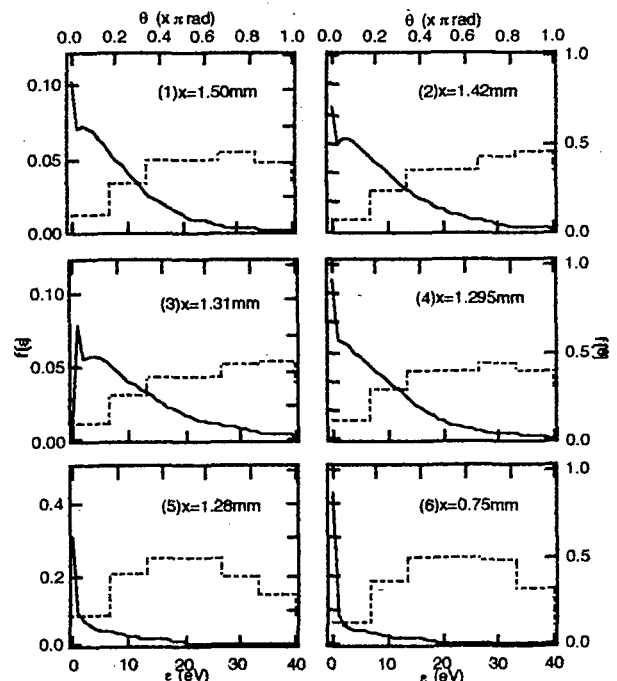


Figure 4. Electron energy (—) and angular (---) distributions at $t=40\text{ns}$. Numbers (1)~(5) correspond to those in figure 3. (6) is at the centre of the discharge space.

4. Acknowledgments

This work was supported by the Japan Society for the Promotion of Science and the Australian Research Council.

5. References

- [1] R J Carman, D J W Brown and J A Piper, IEEE, J. Quantum, Electron., **30**, No. 8, 1876 (1994)
- [2] M.A. Lesnoi, Sov. J. Quant. Electron., **14**, 142 (1984)
- [3] M.J. Withford, private communication
- [4] H Sugawara, Y Sakai and H Tagashira, J. Appl. Phys. D: Appl. Phys. **27**, 90 (1994)
- [5] R. Morrow, Phys. Rev. A, **32**, 1799 (1985)
- [6] B. Chapman, "Glow Discharge Processes", John Wiley & Sons (1980)

Self-consistent determination of the electric field in a stationary low-pressure glow discharge using microscopic treatment for the motion of electrons

by

A. Zahraoui, P. Ségur and A. Alkaa

Centre de Physique des Plasmas et de leurs Applications de Toulouse

Université Paul Sabatier, 118 route de Narbonne

31062 Toulouse Cedex, FRANCE

I. Introduction :

Recently many works have been devoted to the self-consistent determination of the electric field in a low-pressure stationary glow discharge. In some works (Kolobov and Godyak [1], Boeuf and Pitchford [2], 1995), simple analytical models are used to predict the basic properties of the discharge. These studies are very interesting as they are able to predict the general tendency of the discharge (for example occurrence of a reverse field in the negative glow). However, they are not able to give accurate quantitative predictions of the discharge characteristics. To enable that, pure numerical methods must be developed.

The first numerical model of a low-pressure glow discharge was made solving the continuity equations for electrons and ions coupled to the Poisson equation and assuming the Local Field Approximation (LFA) (Ward [3]). It is now well known that the local field approximation is not valid to describe a low-pressure glow discharge and that a more sophisticated approach (normally a microscopic approach) must be used.

As the pure microscopic approach would be too time consuming, many people have used approximate descriptions. In one of these descriptions, an energy equation is added to the continuity and to the momentum transfer equations. Most of the macroscopic parameters are then expressed versus the mean energy of charged particles instead of versus the ratio E/P (E electric field, P pressure of the background gas). This approach was adopted by Bayle [4] and a detailed analysis can be found in Gogolides [5]. The main problem in this description is that the assumption made on the shape of the distribution function is never consistent with the real shape of the distribution function in the cathode region of the glow discharge. It follows that unpredictable errors can occur.

To overcome this drawback, a new method has been developed (Fiala et al [6]) in which the electron distribution function is separated into a 'fast' and a 'slow' component. The 'slow' component is assumed to be in equilibrium with the electric field and can thus be treated by macroscopic equations within the LFA approximation. The motion of electrons in the 'fast' component is determined using a Monte Carlo method. With this description, the description of the electron energy distribution in the cathode region of the discharge is improved and, furthermore, the treatment of two dimensional geometries is now possible.

However this description may fail in some situations in

which the shape of the distribution function is strongly modified due to the occurrence of superelastic collisions and electron-electron interactions. In this case a purely microscopic treatment of electron motion becomes necessary. Hitchon et al in 1994 [7] carried out a complete microscopic description of a glow discharge using the so-called convective scheme to solve the Boltzmann equation. They showed the importance of the accurate treatment of electron scattering in inelastic collisions.

To improve the efficiency of the microscopic approach, some simplifications must be made in the treatment of the Boltzmann equation. In the following, we will show that the use of the well known Two-Term Approximation allows accurate treatment of a normal glow discharge.

II - Description of the model :

Our numerical description of a one-dimensional glow discharge (in which the position is designated by z) is based on the following equations

$$\frac{\partial j_z(z)}{\partial z} = \alpha j_z(z) \quad (1)$$

$$j_z(z) = e n_i(z) v_i(z) \quad (2)$$

$$\frac{\partial E(z)}{\partial z} = \frac{e}{\epsilon_0} (n_i(z) - n_e(z)) \quad (3)$$

$$j_z(z_c) = \gamma j_z(z_c) + j_0 \quad (4)$$

In these equations, $j_z(z)$ is the ion or electron current density, $v_i(z)$ is the mean velocity of ions or electrons and $n_i(z)$ their respective densities. Furthermore, e is the unit charge and ϵ_0 is the permittivity of a vacuum; α and γ are respectively the first ionisation coefficient and the secondary emission coefficient. Equation (4) is the usual boundary condition at the cathode (located at z_c); j_0 is the initial current at the cathode. It can be seen that knowing of γ , the product $z \cdot p$ (p being the gas pressure) and the total current J/p^2 is sufficient to obtain a unique solution of the above equations.

These expressions constitute a set of non-linear equations which can be combined to give the following differential equation for the space charge electric field (Druyvesteyn [8]) :

$$\frac{\partial}{\partial z} \left(\frac{v_i}{v_i + v_e} \frac{\partial E/p}{\partial z} \right) - \frac{\alpha v_i}{p v_i + v_e} \frac{\partial E/p}{\partial z} = \frac{e J}{\epsilon_0 p} \left[\frac{\partial}{\partial z} \left(\frac{v_e}{v_i + v_e} \right) - \frac{\alpha v_e}{p v_i + v_e} \right] \quad (5)$$

With the appropriate boundary conditions this equation can be solved iteratively to obtain E .

Equation (6) is exact if the values of $v_i(z)$ and of α/p are known exactly. In the LFA, these parameters are

obtained from equilibrium values calculated for example by numerically solving the Boltzmann equation. Accurate treatment can be made by solving the Boltzmann equation in energy and position space. In this work we use a numerical solution of the Boltzmann equation based on the two-term expansion Approximation. the equation is solved in a new space defined by the position z and the total energy w of the electrons (Winkler [9]).

It is then possible to compare the results obtained using the LFA approximation for $v_z(z)$ and α/p together with the results obtained with the microscopic calculations.

III - Results :

Figure 1 gives the space charge electric field obtained using the LFA and the solution of the Boltzmann equation. As expected, the results are very different, those obtained using the Boltzmann equation being in agreement with the experiment of Doughty et al [10]. Furthermore, they are consistent with the results obtained by other authors taking into account the non-equilibrium of electrons.

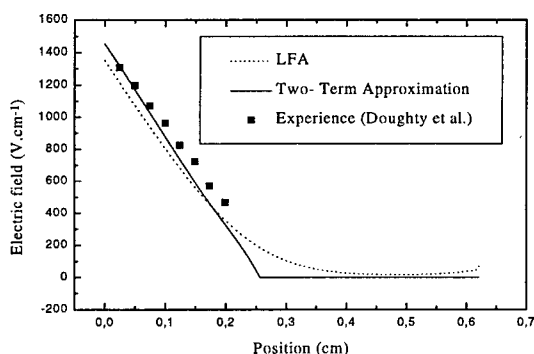


Figure 1 : Helium, $j/p^2=4.2 \cdot 10^{-3} \text{ A cm}^{-2} \text{ Torr}^{-2}$, $p=3.5 \text{ Torr}$
Self consistent electric field calculated using the Two Term Approximation and the LFA, compared to experiment

Obviously, the validity of these numerical calculations is strongly dependent on the accuracy of the Two-Term Approximation. It is possible to check this accuracy by comparing for example the ionisation coefficient calculated using the electric field given in figure 1 and corresponding to the Two-Term Approximation. We see that some difference occur. We see first that the ionisation coefficients calculated assuming isotropic collisions are slightly different in the case of Monte Carlo calculations and in the case of the Two-Term Approximation. The main differences occur in the region where α is maximum. As it is known (Hitchon [7]) that the scattering of electrons during inelastic collisions plays an important role on the determination of the electric field, we made some MC calculations

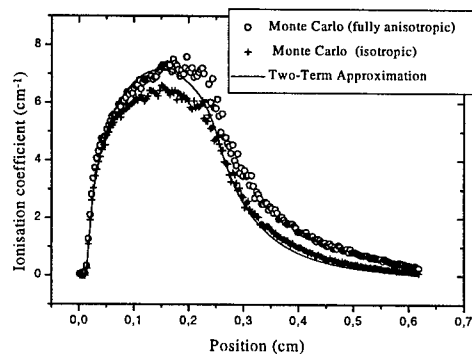


Figure 2 : Helium, $j/p^2=4.2 \cdot 10^{-3} \text{ A cm}^{-2} \text{ Torr}^{-2}$, $p=3.5 \text{ Torr}$
Comparison between various ionisation coefficients calculated with the Monte Carlo method and Boltzmann equation for different scattering laws

assuming no scattering of electrons during inelastic collisions. We see in figure 2 that the ionisation coefficient is strongly dependent on the scattering law.

IV - Conclusions :

The above results indicate that the Two-Term Approximation method employed here to determine the space charge electric field in a low-pressure glow discharge gives very interesting results. However, it is not able to take into account the importance of collision anisotropy. It follows that, for the treatment of a general glow discharge, the Two-Term Approximation must be used to treat low energy electrons (corresponding to low values of the electric field and of w). Monte Carlo calculations or accurate solutions of the Boltzmann equation must be used for the highest values of w .

V - References :

- [1] J. P. Boeuf, and L. C. Pitchford, J. Phys. D: Appl. Phys. 28 2083-2088 (1995).
- [2] V. I. Kolobov and V. A. Godyak, IEEE Transactions on plasma science, 23, n° 4 (1995).
- [3] A. L Ward., J. Appl. Phys., 33, 9, 2789-94 (1962).
- [4] P. Bayle, J. Vacuie and M. Bayle, Phys. Rev. A 34, 372 (1986).
- [5] J. Gogolides and H. H. Sawin, J. Appl. Phys. 72 (9) (1992).
- [6] A. Fiala, L. C. Pitchford and J. P. Boeuf, Phys. Rev. E 49, 5607 (1994).
- [7] W. N. G. Hitchon, G. J. Parker, and J. E Lawler, IEEE Transactions on plasma science, 22, n° 3 (1994).
- [8] M. J. Druyvesteyn and F. M. Penning, Rev. Mod. Phys. 12, 87 (1940).
- [9] R. Winkler and F. Sigeneger, XXIIth E.S.C.A.M.P.I.G., 18E, Noordwijkerhout, The Netherlands, August 23-26 (1994).
- [10] D. A. Doughty, E. A. Den Hartog and J. E. Lawler, Phys. Lett. 58, 25 (1987).

Transmission of charged particles through probe apertures in magnetised and drifting plasmas

L. Tramontin, G. Serianni, V. Antoni, M. Bagatin, D. Desideri

Consorzio RFX
Padova, Italy

1. Introduction

In magnetised plasma diagnostics and plasma processing the probes are often recessed into the supporting structure, so that the measurements on the probe surfaces are affected by the transmission coefficient of the aperture. This coefficient can be evaluated by means of analytical methods when the magnetic field is perpendicular to the probe surface [1].

In this paper a numerical model is presented, which accounts for any angle between the magnetic field and the probe and also for particle drifts along and across the magnetic field lines. Single-particle treatment is adopted while the influence of the Debye sheath on the particle trajectory is neglected.

This model provides the particle impact probability and the average impact energy in different positions on the probe. By integrating over the exposed surface, the transmission coefficient of the aperture is computed.

The model has been applied to the analysis of data obtained in the Reversed Field Pinch experiment RFX, where samples have been exposed to different angles with respect to the magnetic field and in presence of drift motions.

2. The single-particle model

In the edge region of the RFX experiment for thermonuclear fusion studies [2], typical electron temperature and density are of the order of 10 eV and $10^{18} - 10^{19} \text{ m}^{-3}$ respectively, giving a collisional mean free path between particles larger than 0.1 m. In RFX a sample-holder is used housing six samples in apertures whose width is 10 mm [3], much less than the mean free path. Thus, to this and similar situations the single-particle approximation can be applied.

The effects of the Debye sheath have been neglected in a first approximation, assuming that the sheath extension (some tens of microns) is much smaller than the aperture dimension.

Under these hypotheses a numerical model has been developed in which the geometry of the probe holder is considered for the RFX case (see figure 1) and the equations of motion for the particles have been solved. In the schematic geometry of the model one single aperture has been considered, whose details are shown in fig. 1. The motion along the y axis, perpendicular to the figure, is neglected since the parameters are assumed to be constant on the Larmor-radius (r_L) scale. The magnetic field is directed along the z axis; the α angle between the magnetic field and the normal to the probe surface can be varied. The slit of infinite length is characterised by its thickness h and width l. In the (x,z) co-ordinate system the motion is described by the following equations:

$$\begin{cases} x = x_0 + r_L \cos(\varphi + \tau) + r_L \frac{v_{dx}}{v_{\perp}} \tau \\ z = z_0 + r_L \frac{v_{//}}{v_{\perp}} \tau + r_L \frac{v_{dz}}{v_{\perp}} \tau \end{cases} \quad (1)$$

where x_0 and z_0 are the initial positions, φ is the initial phase, $v_{//} = (kT_{//}/m)^{1/2}$ and $v_{\perp} = (2kT_{\perp}/m)^{1/2}$, v_{dx} and v_{dz} are the components of the drift velocity and τ is the dimensionless product of time and cyclotron frequency.

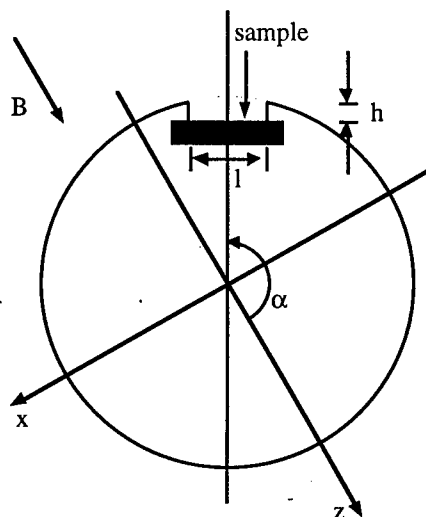


Fig. 1: Scheme of the sample-holder.

The particles start from a planar grid which is perpendicular to the motion of their gyration centres and is located at a distance from the sample-holder larger than one pitch of the Larmor orbit. The global grid width equals the sum of the slit width, as seen from the starting angle, and two Larmor radii; it is divided into N equal cells each containing M particles whose initial phases are equispaced. Also the probe surface is divided into intervals.

The impact probability of the particles over the sample surface for each grid cell is defined as the ratio between the number of particles hitting the sample and M. The width of each cell is weighed with its impact probability; the weighed sum of the width, divided by the slit width, gives the transmission coefficient.

The model has been implemented in a code whose results have been tested using the analytical solution [1] with $\alpha = 180^\circ$ (magnetic field perpendicular to the sample surface) and with no drift. By varying the parameters N and M, a compromise between computing time and accuracy of the results has been attained.

Choosing $N = 100$ and $M = 100$, the achieved accuracy is better than 1%.

It has been found that the effect of a maxwellian velocity distribution function can be well represented by a set of monoenergetic particles having the characteristic energy of the maxwellian distribution.

3. Results and applications

The model has been applied to the case of carbon impurities in the edge plasma of the RFX experiment. The sample-holder presently used is a graphite cylinder with 50 mm diameter and 6 lateral apertures [3].

With $kT_{||} = kT_{\perp} = 10$ eV, $h = 2.2$ mm, $l = 10$ mm, $B = 0.2$ T, a unidirectional flow of singly-ionised carbon gives the pattern shown in fig. 2 for the case of no drift. The average energy deposited over the sample surface varies as a function of the angle α . This result suggests that care is to be taken when the impinging energy is to be deduced from the ion implantation depth, although no sheath effects are taken into account.

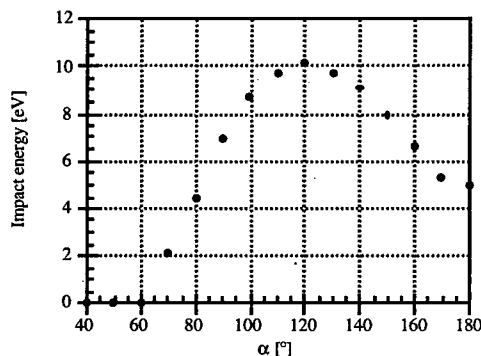


Fig. 2: Impact energy as a function of the angle α .

When the angle α is varied the polar patterns shown in figure 3 are obtained for the transmission coefficient of the central sample interval, as this is the position where the measurement is performed. It is worth noting that the coefficient is larger than 1 due to the assumption of equiprobability for the particles to come from both sides along the magnetic field. When no drift is present, the transmission coefficient is symmetric relative to the magnetic field direction, along which it possesses two maxima. With a perpendicular drift velocity ($v_{dx} = 10$ km/s), the maxima tend to overlap in the direction perpendicular to the magnetic field; relative to this direction, the transmission coefficient is symmetric. A parallel drift destroys such a symmetry and shifts the angular position of the resulting maximum.

Silicon samples were exposed to RFX plasmas and the deposited concentration of carbon was derived by means of the $^{12}\text{C}(d,p)^{13}\text{C}$ nuclear reaction [4] with the aim of studying impurity flow at the edge region of the experiment. The normalised areal density of the six samples is plotted in fig. 4. By repeatedly running the code, the optimum set of parameters has been deduced, accounting for the angular dependence of the drift

motion shown by the data. For the experimental data of fig. 4, it corresponds to a perpendicular drift velocity, v_{dx} , of 8 km/s and a parallel drift velocity, v_{dz} , of -4 km/s. These results are consistent with independent measurements obtained in analogous conditions by applying different measurement techniques [5].

The numerical model presented above can be easily modified to reproduce even more complicated geometries and three-dimensional problems. It represents a useful tool in the interpretation of results from probes recessed into apertures [6].

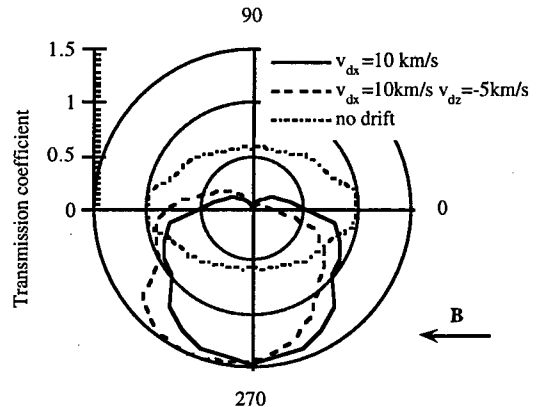


Fig. 3: Transmission coefficient in various conditions.

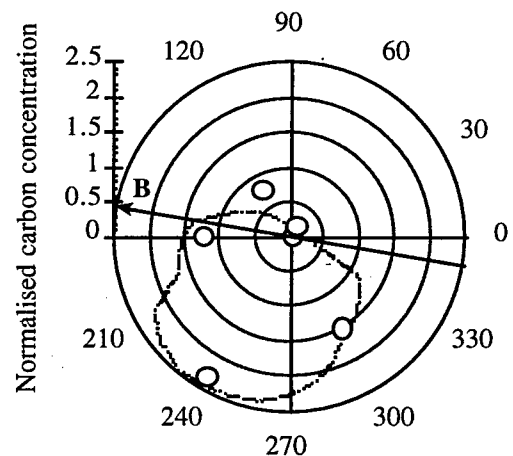


Fig. 4: Comparison of the single-particle model with experimental data.

References

- [1] S  therblom H.-E., Nucl. Instrum. Meth. Phys. Res. **A252** (1986) 107
- [2] Fellin L. et al., Fusion Eng. Des. **25** (1995) 315
- [3] Bagatin M. et al., Fusion Eng. Des. **25** (1995) 425
- [4] Handbook of modern ion beam materials analysis, ed. Tesmer, Nastasi, MRS, 1995
- [5] Antoni V. et al., Nucl. Fusion **36** (1996) 1561
- [6] Antoni V. et al., Nucl. Fusion **36** (1996) 435

CREATION OF DOUBLE LAYER IN ASYMMETRIC DC DISCHARGE

P.Vrba

Institute of Plasma Physics, Academy of Science of the Czech Republic
Za Slovankou 3, 180 69 Prague 8, Czech Republic

Particle-in-cell Monte Carlo code has been used to simulate the DC discharge in strongly inhomogeneous cylindrical and spherical electric fields. Such a discharge occurs in gaseous medium between a thin wire and coaxial cylinder, or between sharp tip and sphere at high voltage. The discharge threshold conditions has been specified and corresponding threshold voltage (threshold electric field intensity) has been determined numerically. The threshold voltage varies with the electrode geometry, the polarity of active electrodes, gas composition (H, Ar, N₂) and gas pressure. In case of positively charged inner electrode, a thin boundary sheet is developed in the vicinity of the electrode, when the quasineutrality of ionized gas is violated and the electron current is closed via external RLC circuit. In the opposite case of negatively charged inner electrode, a double layer is developed inside ionized gas.

Numerical Codes

The codes **PDC1** and **PDS1** has been used to simulate the discharge between a thin wire and coaxial electrode and between sharp tip and sphere. The codes are electrostatic, many charged particle simulations, with particle displacements in one dimension and three velocity components in own and external electric fields [1]. Monte Carlo simulation of collision processes has been added, including ionization, excitation, charge exchange, and elastic scattering. Initial conditions include uniform density thermal drifting electron and ion species. The distribution of free electrons and ions conforms the quasineutrality condition. The neutral gas has been characterized by its temperature and pressure. Boundary conditions include an external series RLC circuit with time-dependent voltage source. In our case, the applied voltage ramped to its final DC value sinusoidally with rise time $T = 2 \times 10^{-9}$ s. The secondary electron emission due to ion electrode bombardment was taken into account.

Breakdown Conditions

The breakdown condition for the discharge in inhomogeneous electric fields [2] can be

Table 1: BREAKDOWN VOLTAGE

γ	intersection point	U_b Volt
0.00035	0.225	650.0
0.001	0.257	495.5
0.005	0.310	340.5
0.01	0.340	283.1
0.05	0.435	172.9

written as

$$\int_{r_1}^{r_2} p A e^{\frac{-Bp}{E}} dr = \ln\left(\frac{1+\gamma}{\gamma}\right), \quad (1)$$

where $A, B = AV_i$ are parameters depending on gas temperature and V_i is the first ionization potential of the atom. The electric field in radial direction can be written as $E_r = E_1\left(\frac{r_1}{r}\right)^n$, where E_1 is the electric field intensity at inner electrode. In the cylindrical case ($n = 1$), the integration leads to a simple formula for the **breakdown voltage**

$$U_b = \frac{Bpr_1 \ln(1+\delta)}{\ln \frac{Apr_1 \delta}{\ln(1+1/\gamma)}}. \quad (2)$$

In the spherical case ($n = 2$), the breakdown voltage is determined solving transcendent

equation

$$\frac{\sqrt{\pi}Ap}{2q} \{ \Phi[(1+\delta)qr_1] - \Phi[qr_1] \} = \ln(1+1/\gamma), \quad (3)$$

where $\Phi(qr) = 2q/\sqrt{\pi} \int_0^r e^{-(qr')^2} dr'$, and the quantity $q = \sqrt{\frac{\delta}{1+\delta}} \sqrt{\frac{Bp}{r_1 U_b}}$. Some results of this calculation are summarized in Tab. 1. The following parameters for Ar gas were used: $p = 4$ torr, $V_i = 15,7$ V, $A = 14$ ionizations/cm-torr, $B = 180$ V/cm-torr and geometrical factor: $\delta = \frac{r_2-r_1}{r_1} = 10$.

Numerical Simulation

Breakdown Potential in Spherical Geometry

The simulations of the discharge ignition between sharp tip ($r_1 = 0.5$ mm), and sphere ($r_2 = 5.5$ mm) have been performed for argon gas at various pressures $p = (0.5 \div 100)$ torr. The breakdown potential U_b has been determined (see Fig. 1) for both polarity electrode. The discharge is easily burned up when the inner electrode is anode.

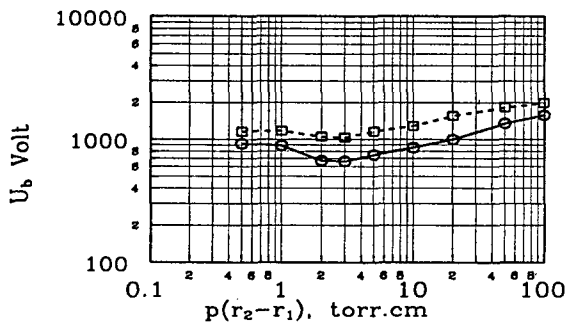


Figure 1: The dependence of breakdown potential U_b on $p \times \Delta R$ for Ar gas, $\gamma < 0.001$.

Double Layer Creation in Cylindrical Geometry

(hydrogen, $p = 100$ torr, $\Delta R = 5$ mm)

a) Wire anode

The head of electron avalanche is created closed to the anode surface. The avalanche dimension is $\approx 1/10$ of spacing of electrodes. The rest of the discharge contains less energetic electrons (and ions) with smaller density than in the avalanche region.

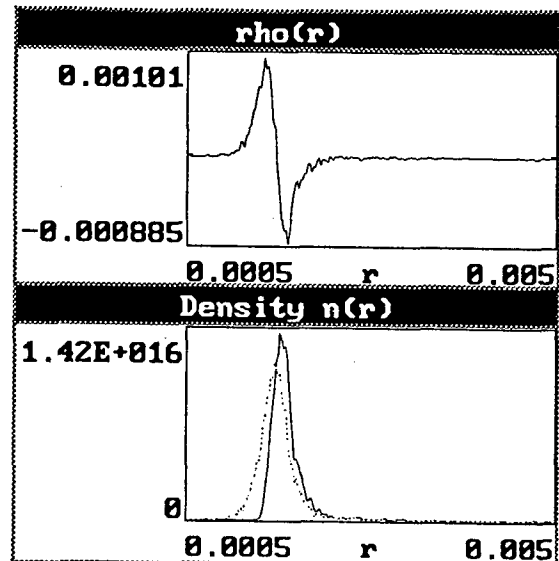


Figure 2: Radial dependence of space charge and particle densities when DL is created.

b) Wire cathode

The electron avalanche is developed quickly ($t_{av} = 9.5 \times 10^{-10}$ s), being followed by the electron (ion) ensemble rearrangement. The electrostatic **double layer** (DL) between the wire and the cylinder is formed (see Fig. 2). The external electric field is disturbed here by the space charge. The dimension of DL is $\approx 1/5$ of the discharge volume and the center of DL ($\rho \approx 0$) lies at the distance $2.3 \times r_1$. The positively charged part of DL lies near the wire while the negatively charged part next to the cylinder (see Fig. 2). The rest part of discharge volume outside the DL and cylinder is filled by electrons and ions and plays a role of a **reservoir of charged particles**.

[1] J. P. Verboncoeur, V. Vahedi, M. V. Alves, C. K. Birdsall.: *Reference Manual PDx1 PC version 2.1*, University of California, Berkeley, 1992.

[2] E. Nasser.: *Fundamentals of Gaseous Ionization & Plasma Electronics*. J. Wiley & Sons, Inc., 1971.

[3] Vrba P., : Czech. Journal of Physics, **45** (1995) 1083

The work was supported by the Grant Agency of the Czech. Acad. Sci. under Contract No. 202/1022.

An Efficient Procedure for Determining Electron Kinetic Properties in the Cathode Region of DC Glow Discharges

R. Winkler and G. Petrov

Institut für Niedertemperatur-Plasmaphysik, 17489 Greifswald, Germany

1. Introduction

The cathode region of low pressure glow discharges is of particular interest in various technological applications as well as in the understanding of the non-equilibrium behaviour of the electrons. This region is usually divided into the cathode fall and the negative glow with a less pronounced boundary between them. Large electric fields and high energy electrons of low density are found in the cathode fall however small electric fields and low energy electrons of high density in the negative glow. The distinctly non-hydrodynamic behaviour of the electrons in the cathode region is mainly caused by the large electric field close to the cathode and its strong decrease down to a low value in the negative glow with increasing distance from the cathode. As a consequence the spatial evolution of the kinetic properties of the electrons undergoes a drastic change from an electric field dominated behaviour in the cathode fall to a collision dominated behaviour in the negative glow. These are the main reasons which make the kinetic analysis of the electron behaviour in the cathode region complicated and laborious. To study this problem apart from basically simplified analytical investigations either particle simulation methods as Monte Carlo and Convective Scheme techniques or solution approaches of the full Boltzmann equation have been used. However these techniques are often limited by a low energy resolution and large computational expenditures.

It is the objective of this contribution to demonstrate that the multi-term approach recently developed in [1] to solve the space-dependent electron Boltzmann equation can be adapted to determine the energy distribution and the important macroscopic quantities of the electrons in the cathode region. It is shown that even under the difficult conditions in the cathode region an efficient determination of significant components of the velocity distribution and of related macroscopic quantities of the electrons becomes possible by the multi-term approach with a good energy resolution and with relatively less computational expenditure.

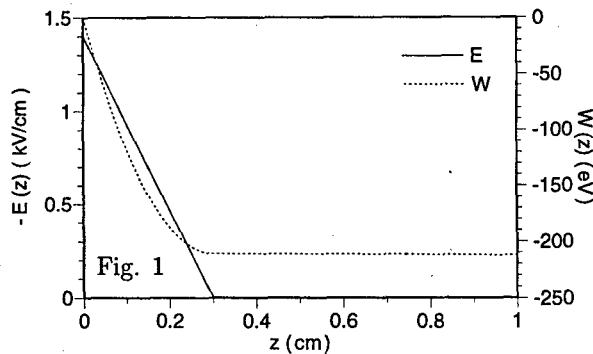
2. Main Aspects of the Approach

When considering a plane cathode perpendicular to the spatial \vec{e}_z direction along which the electric field $\vec{E}(z) = E(z)\vec{e}_z$ acts, the space-dependent velocity distribution function of the electrons becomes rotationally symmetric around \vec{e}_z and can be given the multi-term expansion $F(U, v_z/v, z) =$

$(2\pi(2/m)^{3/2})^{-1} \sum_{k=0}^{n-1} f^k(U, z) P_k(v_z/v)$ in Legendre polynomials $P_k(v_z/v)$ with $U = mv^2/2$, v_z and $v = |\vec{v}|$ being the kinetic energy, the z -component and the magnitude of the velocity \vec{v} . The lowest two coefficients $f^0(U, z)$ and $f^1(U, z)$ of this n -term expansion, i.e. the isotropic (or energy) distribution and the first anisotropy component, determine by appropriate energy space averaging over these coefficients the most important macroscopic electron quantities, as the electron density, mean energy, particle and energy current density, mean collision frequencies and energy gain and loss rates. The kinetics of the electrons in the cathode region is studied by the space-dependent electron Boltzmann equation with the inclusion of the electric field action and of elastic, exciting and ionizing electron collisions with the gas atoms. The substitution of the n -term expansion of the velocity distribution into such kinetic equation finally leads to a system of n partial differential equations for the expansion coefficients $f^k(U, z)$. This system describes the evolution of these coefficients and thus of the velocity distribution in dependence on the kinetic energy U and the space coordinate z . An examination of this system makes evident that in the k -th equation of the system with $0 < k < n-1$ only the three consecutive coefficients f^{k-1} , f^k and f^{k+1} occur, however in the lowest and the last equation of the system only the two coefficients f^0 , f^1 and f^{n-2} , f^{n-1} , respectively are included. Due to this coupling of neighbouring coefficients only and the orthogonality of the Legendre polynomials it should be expected that with increasing approximation order n the higher expansion coefficients have a decreasing impact on the lowest and particularly on the lowest two coefficients f^0 and f^1 . Therefore a sufficiently rapid convergence of the lowest two coefficients and thus of the related macroscopic quantities should occur despite the fact that the strong and rapid change of the electric field near the cathode establishes a distinct anisotropy in the velocity distribution. Following this idea the mentioned system of partial differential equations has been numerically solved as initial boundary value problem for various approximation orders n using appropriate initial and boundary conditions for the expansion coefficients. Even under the difficult conditions with respect to the electric field in the cathode region a sufficiently fast convergence of the lowest two expansion coefficients and thus of the related macroscopic electron properties has been found by using the multi-term solution approach of the space-dependent electron kinetic equation for typical spatial courses of the electric field.

3. Results and Discussion

To illustrate the possibilities of the multi-term approach for conditions occurring in the cathode region, a helium glow discharge with a pressure of 3.5 Torr and a current density j of 0.519 mA/cm² is considered. For these discharge conditions the course of the electric field $E(z)$ in the cathode region, taken from corresponding measurements in [2], and the related potential energy $W(z) = -\int_0^z E(z')dz' (-e_0)$ are shown in Fig. 1. For the negative glow at $z \geq 0.3$ cm a space-independent field strength of -2 V/cm has been chosen. The electron particle current density $j_z(z) = (2/m)^{1/2} \int_0^\infty U f^1(U, z) dU/3$ in the cathode region, which is determined by the first anisotropy component, has been fixed at the cathode surface $z = 0$ by a Gaussian-like boundary value for $f^1(U, z = 0)$ with its maximum at 10 eV and with a width of 5 eV. The secondary electron emission due to ion bombardment at the cathode has been described by an emission coefficient of $\gamma = 0.3$.



By using the multi-term approach the space-dependent electron Boltzmann equation has been solved in various approximation orders n . To illustrate the convergence behaviour with increasing approximation order, Fig. 2 shows as a function of the electron energy at some positions in the cathode fall and negative glow the ratio of the isotropic distribution obtained by a n -term to that obtained by a 10-term approximation for the case of isotropic scattering in elastic and inelastic collisions. Large deviations between the 2-term and the 10-term course of the isotropic distribution at all space positions can be observed from this figure. However when increasing the approximation order of the multi-term approach a rapid convergence of the isotropic distribution in the entire energy space and for all space positions can be clearly seen. A similar behaviour as that of the isotropic distribution has been obtained for the lowest anisotropy component $f^1(U, z)$. It has been found that sufficiently convergent results for the lowest two expansion coefficients f^0 and f^1 and thus for the related macroscopic properties of the electrons can be obtained when solving the kinetic equation in an approximation order with about ten terms. The corresponding evolution of the convergent isotropic distribution in dependence on the electron energy

U for the entire cathode region is shown in Fig. 3.

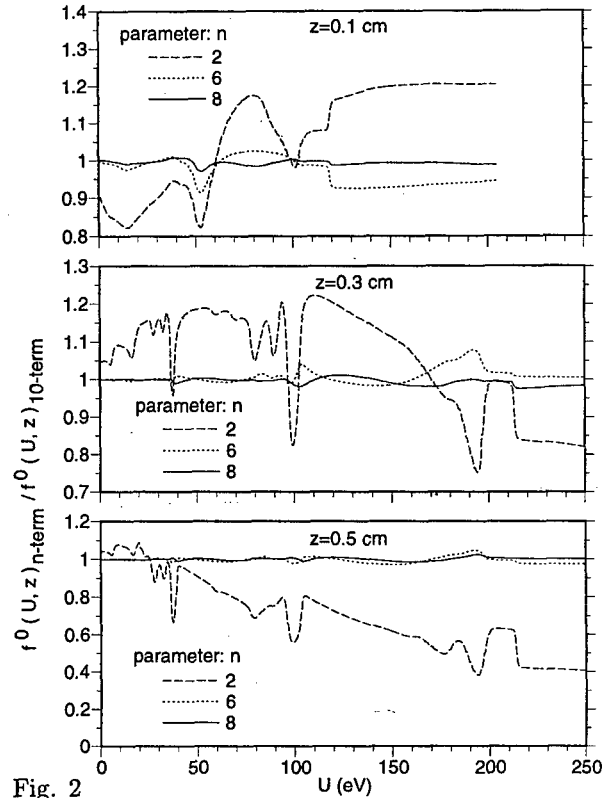


Fig. 2

This figure clearly demonstrates the pronouncedly non-hydrodynamic evolution of the isotropic distribution with increasing distance from the cathode, i.e. the rapid gain of almost the whole potential energy $W(z)$ of the electric field by the electrons in the cathode fall and their pronounced relaxation by collisions in the negative glow.

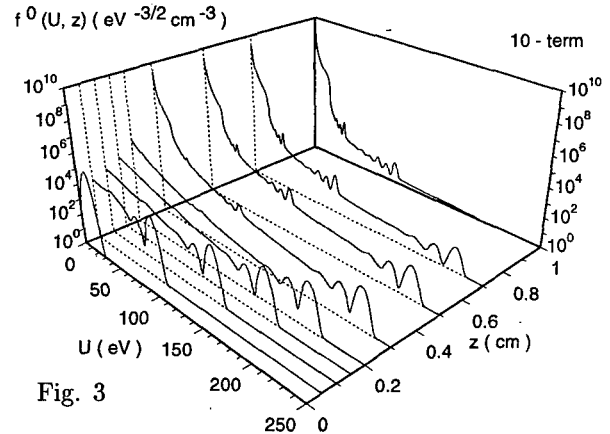


Fig. 3

4. References

- [1] G. Petrov, R. Winkler: J. Phys. D: Appl. Phys., **30** (1997) 53
- [2] E. A. Den Hartog, D. A. Doughty, J. E. Lawler: Phys. Rev., **A38** (1988) 2471

Imitation models of charged particle unipolar beam formation and acceleration processes.

Rostislav K. Tchuyan

Moscow State Aviation Institute / Technical University/
4 Volokolamskoe Shosse, 125871, Moscow, Russia

High - energy beam of charged particles have many applications in various branches of science and industry and there are usually used rather dense beams of positive or (less often) negative ions accelerated in strong electrostatic fields. A particle source is usually gas-discharge plasma. At the accelerator outlet the space charge of the beam is neutralized. This paper is dedicated to imitation (mathematical) modeling of the charged particle beams formation and acceleration in electrostatic fields. However, when studying the IOS operation one should take into account the following features: For the first, ion beams have high density and low velocities that requires taking into account the beam space charge effect when defining the electrostatic forming and accelerating field configuration. For the second, the gas-discharge plasma used as emitter and collector of the particles makes the boundaries of the beam acceleration zone vague, so that they have to be defined via modeling.

For the third, the field-forming electrodes are bombarded by secondary particles which come from the acceleration channel and neutralization plasma, and thus, the electrodes may change their shape during operation. This, in turn, changes configuration of the forming and accelerating field. Mathematical model of IOS comprises a rather typical equation system which describes, charged particle motion in electrostatic field (Poisson equation, equation of motion and continuity equation).

The equation incorporate members accounting the secondary particles born in the acceleration channel as a result of interactions between the beam ions themselves and between the beam ions and neutrals. Besides, the mathematical model has to have a condition which would define location of the gas-discharge plasma and neutralization plasma boundaries. It may be specified in various forms.

This paper considers that the boundary location (plasma meniscus) is defined by equilibrium of plasma kinetic pressure and electrostatic field pressure:

$$E^2/(8 \cdot \pi) = A \cdot n_e \cdot k \cdot T_e$$

Where coefficient A characterizes length of the integration base for finite-difference approximation. For the calculation we used the Monte-Carlo method. To define the initial beam (when the boundaries are fixed), there was calculated a set of random trajectories of ions. Since the space charge of the beam as well as the forming field both depend on the beam configuration, the calculation was

performed by an iterative method (inner iterative loop).

Some results of calculation are showed on figures. Fig.1 shows possible changes of the primary beam configuration associated with gas discharge plasma oscillations.

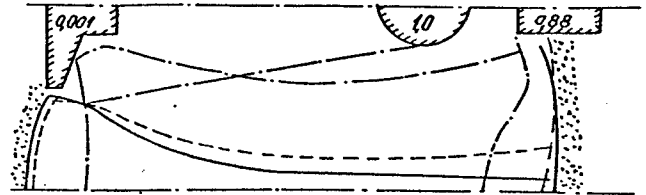


Fig.1. Modeling trajectories of primary particles in IOS.

The same concept is used to calculate the trajectories of the secondary ions (Fig.2). To define the ion birth points, the distribution of initial beam ions and the background neutral atoms was taken into account. The impact of the secondary atoms on to the IOS electrostatic field could be neglected. Once the beam configurations is calculated, the location of the acceleration zone boundaries could be checked and corrected. This generates the second (outer) iterative loop. Secondary particle flux fall out on to the IOS electrodes, change their shape, and thus, change configuration of the forming and accelerating field. Therefore, the second large block of the model is the electrode erosion calculation based on finite-difference interpretation of other electrode surfaces and the system operating time.

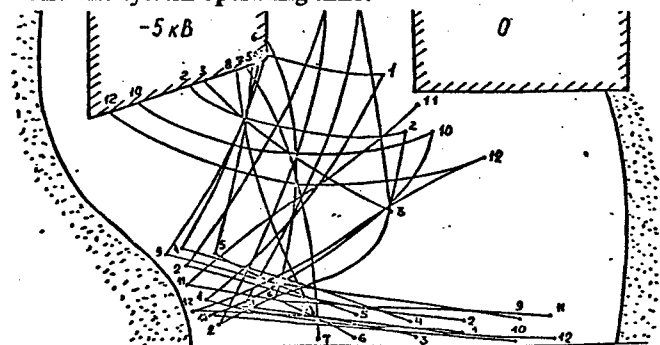


Fig.2 Modeling trajectories of second particles in IOS.

This paper shows the solutions of some methodical and practical problems. The results obtained could be used for studying the charged particle beams as well as designing the devices with such beams.

Authors Index

A

Abbaoui M. I-4
 Abdelli S. IV-264
 Abdullin I.Sh. IV-72
 Ablitzer D. IV-200
 Abramzon N. I-62
 Adachi K. I-246
 Adler H.G. III-22
 Afanas'ev V.P. III-104
 Ahedo E. I-2
 I-204
 Akaishi K. IV-156
 Akhmedzhanov R.A. I-272
 I-274
 Alcaide I. II-2
 Aldea E. IV-254
 Alekseeva L.M. I-206
 II-156
 Alexandrov A.F. I-44
 I-108
 III-88
 Alexandrov L.S. I-208
 Alexandrovich B. IV-76
 Alexeff I. III-102
 Al-Hussany A. II-216
 II-218
 Alkaa A. II-260
 Allen J.E. I-116
 I-132
 I-192
 I-194
 Almi A. I-254
 Alnot P. IV-244
 Alvarez I. I-18
 Alves L. I-120
 Amakawa T. I-246
 Amemiya H. I-110
 IV-60
 IV-62
 Amirov A.H. IV-262
 Ammelt E. II-182
 Amorim J. IV-232
 Andre P. I-4
 III-104
 Andrezza P. IV-252
 Andrezza-Vignolles C. IV-252
 Andrieux M. IV-192
 Anikin N.B. IV-48
 Annaratone B.M. I-116
 I-132
 I-192
 I-194

Anschutz B. II-204
 Anschutz F.B. II-202
 Antoni V. II-262
 IV-134
 Antonova T.B. III-88
 Arai T. IV-86
 IV-88
 IV-90
 Arnal Y. IV-230
 Arnas-Capeau C. I-202
 II-164
 Arriaga C. I-18
 Asselman A. III-24
 Atipo A. II-170
 Aubes M. III-16
 IV-64
 Aubrecht V. II-78
 II-80
 II-82
 Aubreton J. I-4
 IV-102
 IV-220
 Auday G. I-58
 Averyanov V.P. I-188
 Awakowicz P. I-60
 II-202
 II-204

B

Babaeva N.Yu. II-246
 Babaritskiy A. IV-224
 Babich I.L. II-154
 Babich L.P. I-6
 I-8
 I-10
 IV-2
 Babich M.L. I-10
 Babicky V. I-248
 IV-14
 Bacal M. I-12
 III-78
 Bachev K. I-160
 I-162
 Baclawski A. II-110
 Badie J.M. IV-192
 Bagatin M. II-262
 IV-134
 Bagautdinov A. IV-222
 Baksht F.G. I-12
 IV-138
 Baldwin M. IV-194
 Baltog A. I-94
 Bano G. III-96
 IV-212
 Baranov I.E. IV-224
 Baravian G. IV-232
 Barinov Yu.A. III-104
 Barj M. IV-142
 Bartlova M. II-80
 Bashutin O.A. IV-112
 Basner R. IV-196
 Basurto E. I-18
 Batanov G.M. I-138
 Bauchire J.M. II-120
 II-136
 II-206
 Baude S. III-86
 Bayle P. I-252
 II-220
 IV-154
 Becker K. I-62
 I-64
 IV-196
 Behnke J. IV-226
 II-4
 Behnke J.F. II-4
 II-6
 II-8
 Beilis I.I. I-14
 II-84
 Belenguer Ph. I-100
 Belhaouari J.B. II-86
 Belmonte T. IV-66
 IV-198
 Ben Gadri R. IV-44
 Benabdessadok M.D. I-252
 Bernard J.F. IV-130
 Berreby R. III-92
 Berthomieu D. I-148
 Bezborodko P. IV-68
 Bezemer J. II-224
 Bhattacharjee S. I-110
 Biborosch L. II-190
 Biel W. II-226
 Bilikmen S. I-172
 Bindemann Th. II-6
 Birau M. III-46
 Bisch C. IV-192
 Blaise G. III-86
 Blanc E. III-10
 Blois D. IV-142
 Blundell R.E. II-150
 Bobrov Yu.K. II-166
 II-168

Bobrov Yu.K.	II-208 II-210 IV-4 IV-6	Busov B. Buzzi J.M. Bykanov A.N.	II-78 III-46 IV-72	Choi W.K. Chorazy J. Christophorou L.G. Chuaqui H.	III-88 I-82 I-68 II-12 III-28
Bobrova L.N.	IV-6	C		Chumak G.M.	IV-206
Bockel S.	IV-200			Cicconi G.	II-176
Boeuf J.P.	I-112 II-56 II-228 II-252 II-254 III-42 III-70		Cachoncinlle C.	Cicman P.	IV-250
				Cinelli M.J.	IV-102 IV-220
Bogaerts A.	II-10		Cahoreau M.	Ciobanu S.S.	II-100 II-102 IV-150
Bonhomme G.	II-16 II-170		Caillez Y.		
Bonifaci N.	IV-10 IV-12		Cajal D.	Cisneros C.	I-18
Booth J.P.	IV-70 IV-202		Calderon M.A.G.	Clavreul R.	III-94
Borcia C.	II-172		Capitelli M.	Clenet F.	II-212
Bordage M.C.	IV-44			Clupek M.	I-248 IV-14
Borisenko A.G.	I-38 IV-248			Coitout H.	II-96 IV-78
Borodin V.	III-18	Cardinaud C.	III-90	Collins G.	IV-194
Bouaziz M.	II-88	Carman R.J.	II-258	Colombo V.	II-214
Boubert P.	IV-152	Cartry G.	II-70 II-72	Conde L.	I-70 II-2
Boucher I.	III-2	Catherinot A.	IV-102 IV-220	Coppa G.G.M.	II-214
Bouchoule A.	I-200 III-66	Cenian A.	I-16 III-18	Cormier J.M.	II-122
Boudjella A.	IV-16	Censor D.	I-234	Coste C.	I-268
Boufendi L.	IV-204	Cercek M.	IV-162	Coulombe S.	II-98
Bougdira J.	IV-244	Cernak M.	I-248 IV-8	Courtois L.	II-42
Bougrov G.E.	III-88	Cernogora G.	I-102 II-70 II-72	Csambal C.	II-8
Boxman R.L.	II-84			Cunge G.	IV-202
Bozin J.V.	I-98	Chabert P.	IV-202	Czerwicz T.	IV-66 IV-198
Brablec A.	I-128 IV-226	Chaker M.	I-166 I-168	D	
Bragin V.E.	IV-72	Champaign H.	IV-94	D'yachkov L.	I-188 I-190
Braginskiy O.V.	III-76	Chapelle J.	II-122	Damelincourt J.J.	III-16 III-24
Brasile J.P.	II-42	Chapput A.	IV-142	Darnon F.	III-66
Bratescu M.A.	I-92	Charles C.	IV-252	Dauchot J.P.	IV-210
Brault P.	IV-252	Chatei H.	IV-244	David M.	II-226
Bretagne J.	III-80 IV-184 IV-210	Chebotaiev A.V.	IV-110	Davies A.J.	II-216 II-218
		Chenevier M.	IV-70	De Benedictis S.	I-72 IV-14 IV-80
Brethes S.	I-268	Cheredarchuk A.I.	II-154		
Briaud Ph.	II-212 III-72	Chernukho A.	III-18	De Graaf A.	IV-254
Bruhn B.	II-200	Chernyshev A.V.	I-176	De Hoog F.J.	I-152 IV-246
Brunet H.	I-58 III-100	Cheron B.G.	II-90	De Souza A.R.	IV-46
Bruno D.	II-242	Chervy B.	II-104	De Urquijo J.	I-18
Bugrova A.I.	II-76 III-68	Chevolleau T.	III-90	Debal F.	IV-210
		Chevrier P.	II-100 II-102	Decomps Ph.	III-106
Bultel A.	II-90	Chinnov V.F.	II-94	Deegan C.M.	I-114
Burke R.	IV-230	Chirkin M.V.	IV-262	Degond P.	III-64
Burm K.T.A.L.	II-108	Chizhik A.	I-208 II-174	Deha I.	IV-116
Bursikova V.	IV-260	Choi P.	II-12 III-28		

Gleizes A.	II-86 II-88 II-104 II-106 II-126 II-136 II-140	Gross B. Grosswendt B. Grozev D.	II-82 I-78 I-156 II-192	Henrion G. Herben P.G.J.M. Hertl M.	II-16 III-63 IV-216
Glisic S.	IV-42	Grozeva M.	II-130	Heuraux S.	III-2
Glosik J.	III-96 IV-212	Gryaznov V.	I-212	Higaki H.	I-230
Godyak V.	IV-76	Gubsch S.	II-200	Hipp M.	IV-122 IV-126
Goedheer W.J.	II-108 II-222 II-224	Guerra V.	IV-160	Hirech A.	II-230
Goldman A.	III-98	Guerrini G.	III-78	Hirota A.	III-100
Goldman M.	III-98	Guiberteau E.	II-16	Hitz D.	I-228
Goldsmith S.	II-84	Guillot Ph.	I-58	Hoang T.G	III-92
Golly A.	II-110	Guilloteau E.	III-100	Hoffmann D.H.H.	III-94
Golosnoy I.O.	IV-84	Gyergyek T.	IV-162		I-212 II-52
Golubev A.	I-212			Hoffmann V.	I-146
Golubovskii Yu.B.	I-36	H		Holzinger R.	I-260
Golubovskii Yu.B.	II-4 II-6 II-54 II-62	Hacquin S.	III-2	Hong D.	III-44 IV-150
Gombert M.M.	I-22	Hadi H.	IV-16		
Gomes A.M.	I-254 II-160	Hadjadj A.	IV-204	Hopkins M.B.	I-114
Gonzalez J.J.	II-86 II-120 II-136 II-140 II-206	Hajek V.	IV-258	Horikoshi K.	IV-88 IV-90
Gonzalez-Aguilar J.A.	II-112	Hallil A.	IV-62	Horvath M.	II-232
Gorbachev A.M.	I-272 I-274	Hamada T.	IV-118	Hosokawa T.	IV-16 IV-168
Gorbunov N.A.	I-80 I-82	Hamers E.A.G.	II-224	Houska A.	II-82
Gordeev O.A.	IV-136	Hanacek P.	II-78	Hrach R.	II-230 II-232 IV-128 IV-218
Gordiats B.F.	I-124	Hangai N.	I-144		
Gorse C.	I-26 II-116	Hanitz F.	I-266	Hrachova V.	II-18 II-20 IV-218
Gortchakov S.	III-58	Hansel A.	I-84 I-260 I-126	Hubicka Z.	I-130 IV-228
Goto M.	I-96 IV-86 IV-88 IV-90	Harendt A.	I-126	Huet S.	IV-204
Goudmand P.	IV-142	Hartgers A.	III-108	Hugon R.	II-16
Goulet J.C.	I-218	Hartmann G.	IV-94 IV-96 IV-164	Hure L.	III-44
Gousset G.	I-120 III-80 IV-92 IV-184	Hartmann W.	II-116		
Grabowski D.	III-50	Hassouni K.	IV-70	Ieda Y.	II-22
Graham W.G.	IV-151	Hatano Y.	IV-96	Ignatov A.M.	I-180
Granier A.	III-72 III-74	Haug R.	I-74 III-98 IV-96 IV-166	Inagaki K.	IV-140
Gregor J.	II-30	Hava O.	II-18	Inomata T.	IV-26 IV-236 IV-238
Gresser L.	IV-180	Hayashi N.	I-216 II-198	Ion L.	IV-236 IV-238
		Haydon S.	IV-194	Isakaev E.H.	II-94
		Hbid T.	I-152	Iserov A.D.	II-94
		Hebner G.A.	IV-246	Ishida A.	IV-118
		Hecq M.	IV-214	Ivanov M.S.	II-242
		Helbig V.	IV-210	Ivanov O.A.	I-272 I-274
		Held B.	II-8 I-268 III-84 IV-180 IV-236 IV-238	Ivanov V.G.	I-12
		Heldt J.	III-50	Ivanov V.V.	I-86 I-182 II-28 II-234 III-40
		Hemmati M.	I-214		
		Hemmers D.	II-226		
		Hempel F.	IV-196		
		Henneberger K.	I-40		
		Hennig A.	II-8		

J

Jacobsen L.M. III-4
 Jager H. IV-122
 IV-124
 IV-126
 Janca J. I-256
 IV-98
 IV-100
 IV-260
 Jang H.G. III-88
 Jastrabik L. IV-226
 IV-228
 Jauberteau I. IV-102
 IV-220
 Jauberteau J.L. IV-102
 IV-220
 Jelenkovic B.M. I-98
 Jivotov V.K. IV-222
 IV-224
 Johnston C. III-62
 Jolly J. IV-190
 IV-216
 Jones J.E. IV-18
 IV-20
 IV-22
 Jonkers J. III-62
 III-63
 III-108
 Jordan A. I-260
 Jugroot M. II-220
 IV-154
 Jung H.J. III-88

K

Kalachov I. IV-222
 Kalinin A.V. II-60
 Kameta K. I-74
 Kandah M. IV-176
 Kando M. IV-104
 Kaneda T. IV-168
 Kanka A. II-18
 II-20
 Kapicka V. I-128
 IV-226
 IV-228
 Kaplan V.B. III-104
 Kapoun K. I-130
 IV-228
 Karchevsky A.I. II-162
 IV-106
 Karderinis S.N. I-132
 Katkalo A.A. IV-234
 Kawaguchi M. I-134
 II-34
 IV-132
 Kawai Y. I-136
 I-216
 I-244

Kawakami R. II-198
 IV-266
 Kawamura K. IV-144
 IV-186
 Keidar M. I-14
 Kempkens H. II-226
 Kerdja T. IV-264
 Kettlitz M. II-114
 IV-108
 Khacef A. III-30
 III-32
 Khadka D.B. I-74
 Kharchevnickov V.K. II-76
 Khodachenko G.V. II-24
 Khodataev K.V. IV-24
 Khodja H. I-140
 Kidalov S.V. III-54
 III-56
 Kimura T. I-76
 II-22
 Kindel E. III-34
 IV-108
 Kinoh Y. IV-104
 Kirillin A. I-184
 Kirnev G.S. II-26
 Kirov K. I-156
 II-192
 Kiyooka C. IV-156
 Klima M. I-128
 IV-226
 Kling R. III-36
 Klopovskiy K.S. I-86
 I-88
 II-28
 II-234
 III-40
 Kobayashi Y. I-164
 IV-144
 Koch A.W. IV-54
 IV-56
 Koch B.P. II-200
 Kocik M. III-50
 Kof L.M. IV-58
 Koga K. I-216
 I-244
 Kogelschatz U. II-236
 Kogoma M. IV-26
 Koh S.K. III-88
 Kolenic F. IV-128
 Kolisko A.L. I-272
 I-274
 Kolosov V.Yu. IV-170
 IV-172
 Kondranin S.G. III-88
 Konjevic N. IV-146
 Konstantinov E. IV-222
 Kopytin A.A. III-40
 Korbel A. II-132
 Korge H. III-110

Korolev Yu.D. IV-174
 Korshunov O.V. IV-262
 Kosbagarov A. IV-222
 Kosecek A.M. IV-128
 Kossyi I.A. I-138
 IV-110
 Kouchi N. I-74
 Kovalev A.S. III-76
 Kozyrev A.V. III-54
 III-56
 IV-174
 Krajcar-Bronic I. I-78
 Kralkina E.A. III-88
 Krasa J. IV-272
 Krasilnikov M.A. III-46
 Krcma F. IV-100
 Krenek P. II-104
 Kriha V. I-266
 Kroesen G.M.W. I-152
 IV-246
 Ksiazek I. II-110
 Kuba P. IV-128
 Kubota Y. IV-156
 Kudelcik J. IV-8
 Kudrle V. IV-28
 Kudryavtsev A.Yu. I-6
 I-10
 IV-2
 Kudu K. IV-34
 Kulikovskiy A.A. I-258
 IV-30
 Kulish M. I-212
 Kumar S. IV-194
 Kuraica M.M. IV-146
 Kurilenkov Yu.K. I-186
 I-188
 I-190
 Kurnaev V.A. II-24
 II-26
 IV-112
 Kurunczi P. I-64
 Kutsyk I.M. I-6
 I-8
 IV-2
 Kuwae H. II-198
 Kuzelev M.V. III-46
 Kuzovnikov A.A. I-154

L

Laan M. IV-32
 Lagstad I.H. IV-34
 Lamoureux M. I-140
 Lancellotti C. I-210
 Lange H. IV-36
 Lapuerta V. I-204
 Laroussi M. III-102
 Lasgorceix P. IV-102
 Laska L. IV-272

Latocha V. III-64
 Latyshev Ph.E. I-80
 I-82
 Laure C. IV-252
 Laurent A. II-92
 IV-74
 Law D.A. ‡ I-192
 I-194
 Laz'ko V.S. II-162
 Le Brizoual L. III-72
 Le Guen C. I-188
 Leborgne L. I-218
 Leclert G. III-2
 Le Coeur F. IV-230
 Lecot C. II-256
 Le Duc E. IV-28
 Lee Z.H. IV-112
 Lefort A. I-4
 III-104
 Legrand J.C. IV-218
 Lemaire P. IV-114
 Lemeur F. II-90
 Lemperiere G. II-214
 Leon L. I-70
 Leprince P. I-120
 IV-92
 Leroux A. II-238
 Leroy O. IV-216
 Lesage A. I-174
 Leu F. II-118
 II-188
 Leu G. II-184
 II-186
 Levchenko V.D. I-220
 II-240
 Leys C. III-38
 Li Bo I-52
 Li Y.M. III-20
 Lindinger W. I-84
 I-260
 IV-212
 Lino J. IV-232
 Lipaev A.M. I-178
 Lipatov A.S. II-76
 Lister G.G. III-22
 Loffhagen D. III-34
 III-58
 Loiseau J.F. III-84
 Lomakin B.N. IV-262
 Londer J.I. II-144
 Longo S. I-24
 I-26
 II-116
 II-242
 Lopaev D.V. I-86
 I-88
 II-28
 III-40
 III-76

Lorthioir S. III-86
 Louhibi D. II-244
 Loureiro J. I-90
 I-102
 IV-160
 IV-232
 Louvet G. I-186
 Loza O.T. III-46
 Lozneau E. II-184
 II-186
 Luca A. IV-212
 Lungu C.P. I-94
 Lyapin A.I. IV-234
 Lyszyk M. III-66

M

Machala Z. I-262
 Maftoul J. IV-74
 Mage L. III-74
 Magne L. II-70
 II-72
 Maheu B. II-90
 Mahony C.M.O. IV-151
 Makasheva K. I-156
 Malek S. IV-264
 Malinowsky G.Y. I-48
 Malovic G.N. I-98
 Malykh N.I. I-138
 Mandache N.B. II-50
 II-52
 Manheimer W. II-30
 Mankelevich Yu.A. II-234
 Maouhoub E. II-96
 Marchal F. I-104
 Margot J. I-166
 Mark T.D. IV-250
 Markovic V.Lj. II-46
 IV-178
 Marliere C. I-148
 Marode E. IV-46
 Martines E. IV-134
 Martus K. I-64
 Marty-Dessus D. IV-236
 IV-238
 Masek J. II-78
 II-82
 Masek K. IV-272
 Mashino S. IV-88
 IV-90
 Massines F. III-106
 IV-44
 Matejcik S. IV-250
 Matheron P. IV-116
 Mathew J. II-30
 Matsui T. I-142
 Matsumoto M. I-238
 II-58

Matsuoka M. I-134
 II-34
 IV-132
 Matveev A.A. I-138
 Maury J. IV-114
 Maximov A.I. I-256
 Mayoux C. III-106
 McFarland J. IV-151
 Meger R. II-30
 Melin G. I-140
 Melnig V. II-172
 Melnikov A.S. I-80
 Mentel J. II-130
 II-132
 III-48
 III-50
 Merad A. I-112
 Mercier M. II-92
 IV-74
 Merel P. I-168
 Mesyats G.A. II-32
 Meunier J.L. II-98
 IV-176
 Mezhiba A. I-212
 Michaut C. III-78
 Michel H. IV-66
 IV-198
 IV-200
 Michishita T. I-230
 Mikheev L.D. I-48
 IV-52
 Mikikian M. I-202
 Milenin V.M. III-54
 III-56
 Milic B.S. I-28
 I-222
 I-224
 I-226
 I-104
 Millet P. IV-118
 Mimura M. I-144
 Minami K. I-228
 Minea T.M. III-80
 Mintsev V.B. I-212
 Mitrofanov N.K. II-134
 IV-138
 Mizeraczyk J. I-250
 II-130
 III-50
 Mobasher M. I-118
 Modreanu G. II-50
 Mohri A. I-230
 Moisan M. I-168
 Mokhtari A.E. II-244
 Molotkov V.I. I-178
 Mond M. I-236
 Monin M.P. I-270

Moreno J.	II-12	Neuilly F.	IV-202	Pauna O.	I-166
	III-28	Nichipor G.V.	I-250	Pavlenko V.N.	I-232
Mori A.	II-34	Nicolazo F.	III-74		II-178
Mori I.	IV-266	Nienhuis G.J.	II-224		II-180
Morimoto T.	IV-266	Niessen W.	I-264		IV-240
Morozov A.	IV-124	Nikulín S.P.	II-36		IV-248
Morozov A.I.	II-76	Nishioka T.	II-58	Pavlik J.	IV-128
	III-68	Nistor M.	II-50	Pavlik M.	IV-250
Morozov D.A.	I-208		II-52	Pavlov V.B.	III-88
Morrow R.	II-258	Nogaki M.	IV-40	Pawelec E.	II-122
	IV-38	Novak M.	IV-226	Pealat M.	IV-216
Morvova M.	I-262		IV-228	Pechacek R.	II-30
Mouadili A.	III-24	Novak S.	II-248	Pedoussat C.	II-252
Movtchan I.A.	I-80		IV-128	Pejovic M.M.	II-46
Mozgovoi A.L.	I-6	Novakovic N.V.	I-28		IV-178
Mozgrin D.V.	II-24	Nunomura S.	I-196	Pekarek S.	I-266
Muller H.J.	IV-54	Nur M.	IV-10	Pellerin S.	II-122
Muller I.	II-182		IV-12	Pelletier J.	IV-230
Muller S.	IV-120			Peres G.	II-254
Murata T.	III-82	O		Perret C.	II-256
Muromkin Yu. A.	II-162	Odagiri T.	I-74	Perrin J.	IV-190
Murphy D.	II-30	Ohe K.	I-76	Peska L.	II-78
Musa G.	I-92		II-22		II-82
	I-94		II-66	Petit L.	III-98
	II-118		IV-140	Petrov G.	II-266
	II-188	Ohno N.	I-196	Petrov O.F.	I-176
Mushiaki M.	IV-156	Ohtani K.	IV-86		I-178
Musikowski H.D.	II-128	Oien A.H.	I-32	Petrov T.	II-130
Musinov S.	IV-222		III-4	Petrovic Z.Lj.	I-34
Musiol K.	II-122	Oishi H.	I-230		I-98
Mustata I.	II-118	Okada T.	I-96		II-44
	II-188	Okazaki S.	IV-26		II-46
Myamoto K.	I-92	Okita Y.	III-82		IV-42
		Olthoff J.K.	I-68		IV-178
N		Ono M.	IV-186	Peyrous R.	I-268
Nagahama T.	I-228	Onoda H.	II-68		III-84
Naghizadeh-Kashani Y.	II-106	Onose H.	I-144		IV-180
Nagorny V.P.	I-30	Otorbaev D.K.	IV-110	Pfau S.	II-38
Naidis G.V.	II-246	Otte M.	II-38		II-40
Naito Y.	I-144		II-40	Phelps A.V.	II-48
Nakamura M.	I-76	Overchuk K.	IV-222	Piejak R.	IV-76
	I-196			Pierre Th.	II-164
Nakamura Y.	I-242	P			II-170
	I-244	Pacheco J.	II-120	Pierson J.F.	IV-198
Nandelstädt D.	II-132	Paillol J.	II-42	Pignolet P.	II-42
Napartovich A.P.	I-24		II-250	Pinheiro M.J.	IV-232
	I-66	Panchenko V.G.	II-178		I-124
Nefedov A.P.	I-176		II-180	Pintassilgo C.D.	I-102
	I-178		IV-240	Pitchford L.C.	I-100
Neger T.	IV-122		IV-248		II-56
	IV-124	Pancheshnyi S.V.	IV-48		II-252
	IV-126	Panciatichi C.	II-214		III-42
Neiger M.	I-264	Pardo C.	II-112		III-70
	II-36	Paris P.	IV-32		III-86
Nekuchaev V.O.	I-36	Parizet M.J.	II-96	Placinta G.	IV-242
	II-54	Parys P.	IV-272	Pogora V.	II-138
Nerushev O.A.	I-198	Pashkovsky V.G.	II-162	Pointu A.M.	II-50
Ness K.F.	I-54	Passoth E.	II-8	Pokrzywka B.	II-52
					II-122

Ponomarev N.S.	I-36	Revel I.	II-56	Sadeghi N.	I-150
	II-54	Riad H.	II-106		I-152
Popa G.	II-66	Ricard A.	I-168		IV-202
	IV-242		IV-66		IV-246
Popescu A.	II-118		IV-198	Saenko V.A.	I-38
	II-188		IV-200		IV-182
Popescu I.I.	II-50		IV-210		IV-248
	II-52	Richou J.	I-174	Saidane K.	II-126
Popov A.M.	II-28		IV-116	Sakai T.	IV-16
Popov N.A.	I-88	Rivaletto M.	II-42	Sakai Y.	I-92
Poppe F.	III-38	Robert E.	III-30	Sakamoto S.	IV-186
Porokhova I.A.	II-4		III-32	Salabas A.	II-118
	II-6	Robin L.	IV-152	Salamero Y.	I-104
	II-62	Robson R.E.	I-52	Samarian A.	I-184
	III-60		I-54	Sando K.	I-164
Porras D.	I-270	Roca i Cabarrocas P.	IV-204	Sanduloviciu M.	II-172
Postel C.	IV-106	Rodriguez-Yunta A.	II-112		II-184
Potantin E.P.	IV-224	Rohlén K.	IV-272		II-186
Potapkin B.V.	II-126	Rohmann J.	II-38		II-188
Pousse J.	III-30		II-40		II-190
Pouvesle J.M.	III-32	Romeas P.	I-186	Sapozhnikov A.V.	I-138
	III-44	Rosatelli C.	II-176	Sarrette J.P.	I-254
Praessler F.	I-146	Rosenfeld W.	III-44		II-160
Prazeller P.	I-260	Rosenkranz J.	I-266	Sarroukh H.	III-24
Proshina O.V.	I-88	Rosum I.N.	II-178	Sarytchev D.V.	II-26
	II-234		II-180	Sasada T.	IV-132
Protuc I.	II-138	Roth M.	I-212	Sato K.	IV-118
Proulx P.	II-206	Rousseau A.	IV-92	Sato S.	I-242
Puech V.	I-270	Roussel J.	IV-130	Sato T.	I-164
Punset C.	III-42	Roussel-Dupre R.T.	III-6	Satoh H.	I-238
Purwins H.G.	II-182		III-8		II-58
			III-10	Satoh K.	II-260
R			III-12	Saulle C.	III-46
Rabehi A.	IV-44		III-52	Savinov V.P.	I-108
Rahal H.	I-22	Rovtar J.	IV-162	Savjолоv A.S.	II-24
Rahel J.	IV-250	Rozoy M.	I-270		II-26
Rakhimov A.T.	I-86	Rozsa K.	II-64		IV-112
	I-88	Rudakowski S.	IV-148	Sayler G.S.	III-102
Rakhimov A.T.	II-28	Rudnitsky V.A.	I-38	Scheibe H.J.	II-128
	II-234	Rukhadze A.A.	I-172	Scheibner H.	IV-188
	III-40		III-46	Schein J.	II-132
Rakhimova T.V.	I-86		III-88	Scheiring Ch.	I-84
	I-88	Rulev G.B.	I-86	Scherbakov Yu.V.	II-210
	I-182	Rusanov V.	IV-222	Schepe R.	I-40
	II-28	Rusanov V.D.	IV-224	Scheubert P.	II-202
	II-234	Rusnak K.	IV-258		II-204
	III-40	Rutkevich I.	I-234	Schimke C.	III-34
	II-124		I-236		IV-108
Ravary B.	I-148	Ryazantsev E.I.	IV-224	Schmidt E.	III-48
Raynaud P.	III-74	Rybakov A.B.	IV-138	Schmidt M.	IV-196
	II-88	Rybakov V.V.	I-240	Schmoll R.	IV-164
Razafinimanana M.	II-120			Schopp H.	II-114
	II-126	S			IV-108
	II-136	Sa P.A.	I-90	Schram D.C.	II-108
Redon R.	IV-116	Sabonnadiere M.P.	I-48		III-62
Reess T.	II-250	Sabotinov N.	II-130		III-63
Remscheid A.	IV-148				III-108
Remy M.	IV-244				IV-254
				Schruft R.	I-264

[illegible]

Theroude C. II-254
 Thomann A.L. IV-252
 Thomaz J. IV-232
 Tichonov M.G. IV-262
 Tichy M. IV-226
 Tiirik A. IV-32
 Timofeev N.A. III-54
 III-56
 Tioursi M. IV-96
 IV-166
 Toader E.I. IV-151
 Toedter O. IV-54
 IV-56
 Tokumasu H. I-228
 Toma M. II-190
 Tominaga K. IV-266
 Tonegawa A. IV-144
 IV-186
 Torchinskii V.M. I-178
 Tous M. IV-226
 Touzeau M. II-70
 II-72
 IV-46
 IV-160
 Tramontin L. II-262
 Trepanier J.Y. I-50
 Treshchalov A. III-110
 Trinquescoste M. IV-236
 Trusca A. II-140
 Tsuda N. IV-268
 Tsuda S. I-142
 Tsukabayashi I. I-242
 Tsvetkov T.S. II-192
 Turban G. II-212
 III-74
 III-90

U

Udrea M. II-50
 Ueda Y. I-136
 Uhlenbusch J. II-226
 Uhrlandt D. II-74
 Ukai M. I-74
 Ulyanov D.K. III-46
 Ulyanov K.N. II-142
 II-144
 Uneyama T. IV-118
 Ustalov V.V. IV-240
 Ustinov A.L. II-162
 Uteza O. III-26

V

Vacquie S. II-120
 II-126
 Valentini H.B. II-202
 Vallee C. III-74
 Vallone F. IV-134
 Van Bever T. I-106

Van de Grift M. I-152
 IV-246
 Van de Sanden M.C.M. IV-254
 Van der Mullen J.A.M. II-108
 III-62
 III-63
 III-108
 Van Dijk J. III-63
 Van Egmond C. III-38
 Van Ootegem B. I-218
 Vardelle A. II-158
 Vardelle M. II-158
 Vaselli M. I-44
 I-154
 II-60
 Vasenkov A.V. I-56
 IV-256
 Vasilieva A.N. III-76
 Vaulina O. I-184
 Vayner B.V. II-146
 Veis P. III-98
 Veklich A.N. II-154
 Velleaud G. II-92
 IV-74
 IV-242
 Verdes D. IV-242
 Vereshchagin K.A. I-42
 IV-136
 Vervisch P. I-218
 II-238
 IV-152
 Vervloet M. III-74
 Vesselovzorov A.N. III-78
 Vialle M. II-70
 II-72
 Videlot H. IV-190
 Videnovic I.R. IV-146
 Viel V. IV-130
 Vikharev A.L. I-272
 I-274
 Viladrosa R. III-30
 III-32
 III-44
 III-110
 Vill A. III-110
 Vitel Y. I-188
 I-190
 I-200
 Vivet F. I-200
 Vizgalov I.V. II-26
 Vlcek J. IV-258
 Vogel N.I. III-14
 IV-270
 Voitik M. III-26
 Vovchenko E.D. IV-112
 Vrba P. II-264
 Vrhovac S.B. II-44
 Vul A.Ya. III-54
 III-56

W

Wachutka G. II-204
 Wakabayashi Y. II-58
 Wang Yicheng I-68
 Watanabe T. I-244
 Watanabe Y. I-170
 Wautelet M. IV-210
 Wendt R. IV-36
 Wetzig K. I-146
 White R.D. I-52
 I-54
 Wieme W. I-20
 Wiesemann K. IV-148
 Wilke C. II-74
 II-200
 Winkler R. IV-188
 II-62
 II-266
 III-58
 Wiolland R. III-46
 Wolf O. I-264
 Wolowski J. IV-272
 Woryna E. IV-272
 Wujec T. II-110
 Wuttmann M. I-118
 Wyndham E. II-12
 III-28

Y

Yagi Y. IV-134
 Yamada J. IV-268
 Yamada K. I-74
 I-142
 Yamazawa Y. I-230
 Yan J.D. II-148
 II-150
 Yasuda M. I-170
 Yasui S. I-246
 Yatsu M. II-68
 Yilmaz A. I-172
 Yoshida M. I-134
 Yoshimura S. I-244
 Yousfi M. I-252
 II-220
 IV-154
 Yukhimuk V. III-6
 III-8
 III-12
 III-52
 Yumoto M. IV-16
 Yurghelenas Yu.V. II-208
 II-210
 Yuyama T. I-230

Z

Zahoranova A. IV-8
 Zahraoui A. II-260

Zajickova L.	IV-260
Zakouril P.	III-96
Zambra M.	II-12
	III-28
Zaretsky E	I-236
Zatsepin D.V.	IV-50
Zhelyazkov I.	I-160
	I-162
Zheng X.	I-228
Zhovtyansky V.A.	II-152
	II-154
Zicha J.	II-18
Zigman V.J.	I-226
Zissis G.	III-60
Zivkovic J.V.	IV-42
Zobnin A.V.	II-94
Zoller V.	IV-222
Zuev V.S.	IV-52
Zvonicek V.	IV-160